AJNR

AMERICAN JOURNAL OF NEURORADIOLOGY

AUGUST 2015
VOLUME 36
NUMBER 8
WWW.AJNR.ORG

THE JOURNAL OF DIAGNOSTIC AND INTERVENTIONAL NEURORADIOLOGY

Reversible cerebral vasoconstriction syndrome

Proton beam radiation necrosis in pediatric patients

Woven EndoBridge flow disrupter

Official Journal ASNR • ASFNR • ASHNR • ASPNR • ASSR

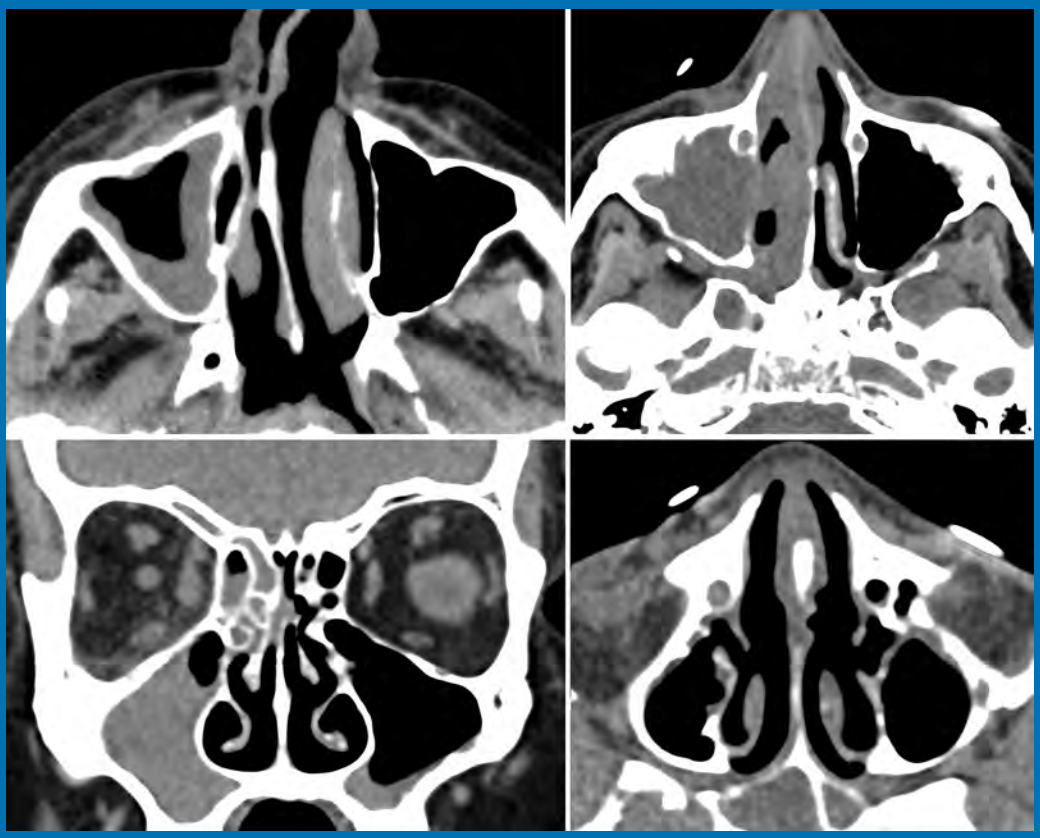

Engineered

by MicroVention®

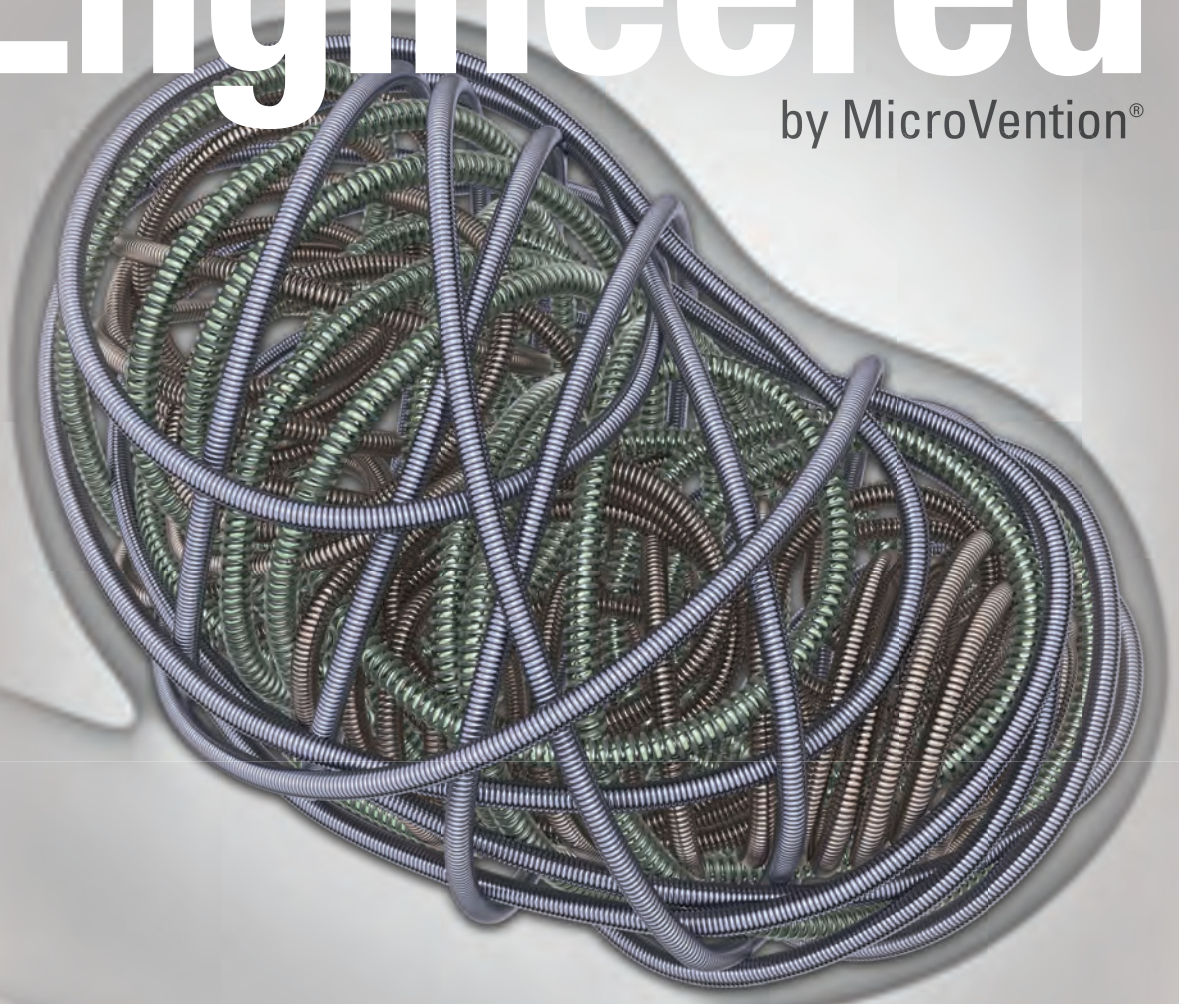

HYDROGEL ADVANCED COILS

The clinical benefits of **hydrogel** NOW engineered with the softness of bare platinum on the **V-Trak® Advanced Coil System**.

INDICATIONS FOR USE:
The HydroCoil® Embolic System (HES) is intended for the endovascular embolization of intracranial aneurysms and other neurovascular abnormalities such as arteriovenous malformations and arteriovenous fistulae. The HES is also intended for vascular occlusion of blood vessels within the neurovascular system to permanently obstruct blood flow to an aneurysm or other vascular malformation and for arterial and venous embolizations in the peripheral vasculature. The device should only be used by physicians who have undergone pre-clinical training in all aspects of HES procedures as prescribed by MicroVention.

CE 0297

Frame, Fill, Finish

HydroFrame®
HydroCoil® Embolic System

HydroFill®
HydroCoil® Embolic System

HydroSoft®
HydroCoil® Embolic System

- CLINICALLY STUDIED HYDROGEL
- EFFECTIVE[1,2,3]
- ESTABLISHED SAFETY PROFILE[4]
- SOFTER DESIGN[5]

For more information or a product demonstration, contact your local MicroVention representative:

MicroVention® TERUMO

MicroVention, Inc.
Worldwide Headquarters PH +1.714.247.8000
1311 Valencia Avenue
Tustin, CA 92780 USA
MicroVention UK Limited PH +44 (0) 191 258 6777
MicroVention Europe, S.A.R.L. PH +33 (1) 39 21 77 46
MicroVention Deutschland GmbH PH +49 211 210 798-0
microvention.com

References
1. Speirs, Burke, Lee, and Ala. The next generation HydroCoil: initial clinical experience with the HydroFill embolic coil. J NeuroIntervent Surg, 2013.
2. Brinjikiji et al. Abstract 112. Presented at: International Stroke Conference 2015, Nashville, Tennessee, February 11-13, 2015.
3. Lee, Seo, Less, Cho, Kang and Han. Mid-term outcome of intracranial aneurysms treated with HydroSoft coils compared to historical controls treated with bare platinum coils: a single-center experience. Acta Neurochir, 156:1687-1694, 2014.
4. Laymond et al. Patients prone to recurrence after endovascular treatment: periprocedural results of the PRET randomized trial on large and recurrent aneurysms, AJNR AM J Neuroradiol, 2014.
5. Data on file at MicroVention, Inc.

V-Trak® Advanced Coil System

COILING OPTIMIZED

NOW AVAILABLE

BARRICADE COMPLEX
FINISHING COIL

- Extremely soft profile of The Barricade Finishing coil now in a complex shape
- Excellent microcatheter stability for confident coil placement
- Available in a size range of 1mm-5mm

BARRICADE™ COIL SYSTEM

MADE IN AMERICA

The Barricade Coil System is intended for the endovascular embolization of intracranial aneurysms and other neurovascular abnormalities such as arteriovenous malformations and arteriovenous fistulae. The System is also intended for vascular occlusion of blood vessels within the neurovascular system to permanently obstruct blood flow to an aneurysm or other vascular malformation and for arterial and venous embolizations in the peripheral vasculature. Refer to the instructions for use for complete product information.

18 TECHNOLOGY DRIVE #169, IRVINE CA 92618
p: 949.788.1443 | f: 949.788.1444

WWW.BLOCKADEMEDICAL.COM

MKTG-031 Rev. A

BLOCKADE MEDICAL

AJNR

AMERICAN JOURNAL OF NEURORADIOLOGY

AUGUST 2015
VOLUME 36
NUMBER 8
WWW.AJNR.ORG

Publication Preview at www.ajnr.org features articles released in advance of print. Visit www.ajnrblog.org to comment on AJNR content and chat with colleagues and AJNR's News Digest at http://ajnrdigest.org to read the stories behind the latest research in neuroimaging.

Indicates Editor's Choices selection

Indicates Fellows' Journal Club selection

Indicates open access to non-subscribers at www.ajnr.org

Indicates article with supplemental on-line table

Indicates article with supplemental on-line photo

Indicates article with supplemental on-line video

Indicates Evidence-Based Medicine Level 1

Indicates Evidence-Based Medicine Level 2

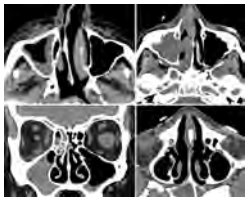

CT images showing findings of acute invasive fungal rhinosinusitis including periantral fat involvement, and soft tissue within the sphenopalatine foramen.

Trevo® XP

PROVUE RETRIEVER

Take Control. Capture More.

The newly designed Trevo® XP ProVue Retriever takes proven Trevo Retriever performance to new levels for **easy delivery, easy placement,** and **easy visualization.**

When you're in control, it's amazing what you can capture.

stryker® Neurovascular

Stroke: *Our Only Focus. Our Ongoing Promise.*

ASNR 2016
Washington, DC

ASFNR • ASHNR • ASPNR • ASSR • SNIS

THE FOUNDATION OF THE ASNR

THE FOUNDATION OF THE ASNR SYMPOSIUM 2016: EMERGENCY NEURORADIOLOGY
MAY 21-22

ASNR 54TH ANNUAL MEETING
MAY 23-26

Howard A. Rowley, MD, ASNR 2016 Program Chair/President-Elect
Programming developed in cooperation with …

American Society of Functional Neuroradiology (ASFNR)
Christopher G. Filippi, MD

American Society of Head and Neck Radiology (ASHNR)
Lindell R. Gentry, MD

American Society of Pediatric Neuroradiology (ASPNR)
Erin Simon Schwartz, MD

American Society of Spine Radiology (ASSR)
Gregory J. Lawler, MD

Society of NeuroInterventional Surgery (SNIS)
Charles J. Prestigiacomo, MD

American Society of Neuroradiology (ASNR) Health Policy Committee
Robert M. Barr, MD, FACR

Computer Science and Informatics (CSI) Committee
John L. Go, MD

Research Scientists Committee
Dikoma C. Shungu, PhD

ABSTRACT DEADLINE:
Friday, December 11, 2015

Please visit www.asnr.org/2016 for more information

ASNR 54TH ANNUAL MEETING
c/o American Society of Neuroradiology
800 Enterprise Drive, Suite 205
Oak Brook, Illinois 60523-4216
Phone: 630-574-0220
Fax: 630 574-0661
www.asnr.org/2016

SCAN NOW TO VISIT OUR WEBSITE

SAVE THE DATE... MAY 21-26, 2016
WASHINGTON MARRIOTT WARDMAN PARK • WASHINGTON DC

American Society of Spine Radiology

2016 Annual Symposium • February 18-21, 2016

Hyatt Regency Coconut Point • Bonita Springs, FL

- Stillwater Spa with 18 treatment rooms, Watsu pool, and beauty salon
- Big Hickory Island Beach
- Spectacular waterfalls and pool features, as well as a spacious sundeck
- Family pool with 140-foot corkscrew water slide and hot tub, heated adult pool with hot tub, cold-plunge pool with waterfall
- 18-hole Raymond Floyd designed Raptor Bay golf course and club
- 24-hour Hyatt StayFit gym with cardio theater
- Bicycle and kayak rentals
- Dolphin watch eco-tours and sunset cruises
- Video arcade
- Har-Tru clay tennis courts
- Camp Hyatt®

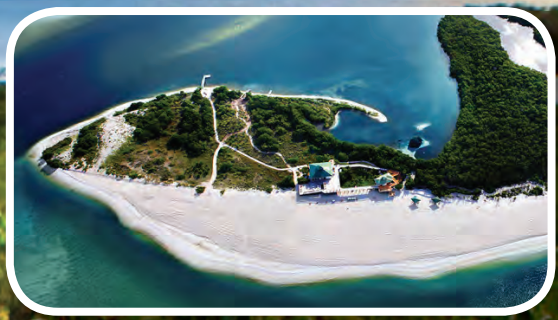

A tropical paradise centrally located between Fort Myers and Naples, Florida in the upscale community of Bonita Springs. With stunning views of the Gulf Coast, Hyatt Regency Coconut Point Resort and Spa offers casual elegance and southern style hospitality, personalized service and attention to detail at every turn.

SAVE THE DATE

AJNR

AMERICAN JOURNAL OF NEURORADIOLOGY

Publication Preview at www.ajnr.org features articles released in advance of print. Visit www.ajnrblog.org to comment on AJNR content and chat with colleagues and AJNR's News Digest at http://ajnrdigest.org to read the stories behind the latest research in neuroimaging.

AUGUST 2015 • VOLUME 36 • NUMBER 8 • WWW.AJNR.ORG

Official Journal:
American Society of Neuroradiology
American Society of Functional Neuroradiology
American Society of Head and Neck Radiology
American Society of Pediatric Neuroradiology
American Society of Spine Radiology

AJNR (Am J Neuroradiol ISSN 0195–6108) is a journal published monthly, owned and published by the American Society of Neuroradiology (ASNR), 800 Enterprise Drive, Suite 205, Oak Brook, IL 60523. Annual dues for the ASNR include $170.00 for journal subscription. The journal is printed by Cadmus Journal Services, 5457 Twin Knolls Road, Suite 200, Columbia, MD 21045; Periodicals postage paid at Oak Brook, IL and additional mailing offices. Printed in the U.S.A. POSTMASTER: Please send address changes to American Journal of Neuroradiology, P.O. Box 3000, Denville, NJ 07834, U.S.A. Subscription rates: nonmember $380 ($450 foreign) print and online, $305 online only; institutions $440 ($510 foreign) print and basic online, $875 ($940 foreign) print and extended online, $365 online only (basic), extended online $790; single copies are $35 each ($40 foreign). Indexed by PubMed/Medline, BIOSIS Previews, Current Contents (Clinical Medicine and Life Sciences), EMBASE, Google Scholar, HighWire Press, Q-Sensei, RefSeek, Science Citation Index, and SCI Expanded.

ASHNR
American Society of
Head & Neck Radiology

49th Annual Meeting | **American Society of**

Head & Neck Radiology

Comprehensive Head and Neck Imaging

September 9 - 13, 2015

Naples Grande Beach Resort
Naples, Florida

27.5 *AMA PRA Category 1 Credit(s)™*

Certain sessions of the meeting program will be submitted for SAM qualification.

Hands-on US and US-Guided Biopsy Seminar
Friday, September 11, 2015

Separate Registration Required
Registration is Limited to 20 Attendees Per Session.

Not accredited for *AMA PRA Category 1 Credit(s)™*

For More Information, visit **www.ashnr.org**

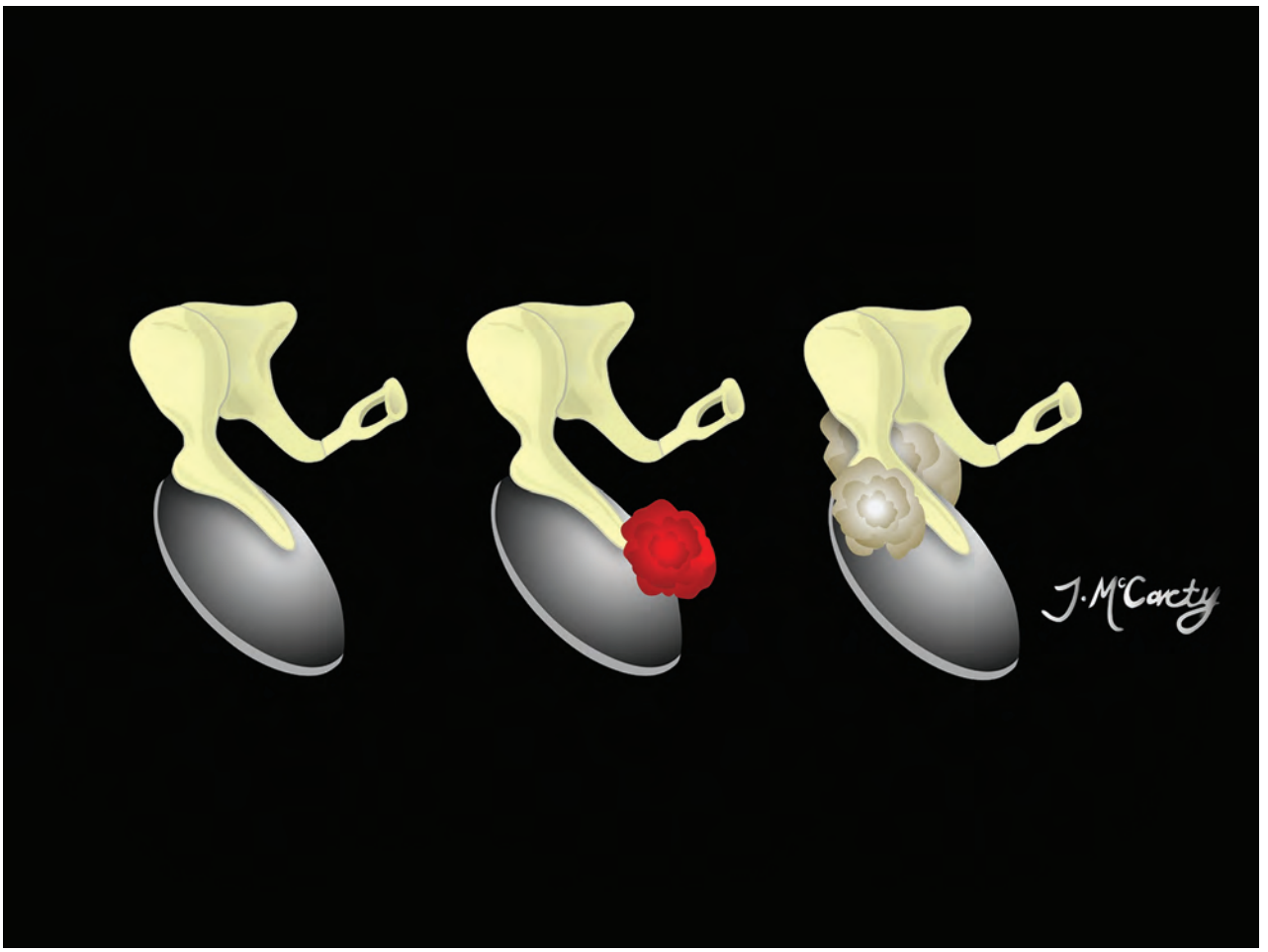

Ossicular Chain Trio: The normal ossicular chain (*left*), a red vascular glomus tympanicum involving the manubrium of the malleus (*middle*), and a pearly white cholesteatoma encompassing the malleus and incus (*right*). Drawn using the Inkpad app for iPad.

Jennifer McCarty, PGY5 Radiology Resident, University of Arkansas for Medical Sciences, Little Rock, Arkansas; jmccarty@uams.edu

Reversible Cerebral Vasoconstriction Syndrome, Part 1: Epidemiology, Pathogenesis, and Clinical Course

T.R. Miller, R. Shivashankar, M. Mossa-Basha, and D. Gandhi

ABSTRACT

SUMMARY: Reversible cerebral vasoconstriction syndrome is a clinical and radiologic syndrome that represents a common presentation of a diverse group of disorders. The syndrome is characterized by thunderclap headache and reversible vasoconstriction of cerebral arteries, which can either be spontaneous or related to an exogenous trigger. The pathophysiology of reversible cerebral vasoconstriction syndrome is unknown, though alterations in cerebral vascular tone are thought to be a key underlying mechanism. The syndrome typically follows a benign course; however, reversible cerebral vasoconstriction syndrome may result in permanent disability or death in a small minority of patients secondary to complications such as ischemic stroke or intracranial hemorrhage.

ABBREVIATIONS: RCVS = reversible cerebral vasoconstriction syndrome; PRES = posterior reversible encephalopathy syndrome

Reversible cerebral vasoconstriction syndrome (RCVS) is a clinical and radiologic syndrome whose primary features include the hyperacute onset of severe headache and segmental vasoconstriction of cerebral arteries that resolves by 3 months.[1-5] RCVS is not a single disease entity but should be considered a common presentation of multiple disorders characterized by reversible vasoconstriction of the cerebral vasculature.[3,6-8] The term "RCVS" now encompasses what was previously thought to be a group of distinct clinical entities, including Call-Fleming syndrome, thunderclap headache, and postpartum angiopathy.[4-6,8-11]

Timely and accurate diagnosis of RCVS is essential to ensuring appropriate patient care and avoiding unnecessary diagnostic tests. However, the diagnosis can be challenging because its signs and symptoms can overlap those of better known disorders of the central nervous system, including aneurysmal subarachnoid hemorrhage and primary angiitis of the CNS.[1,2,6,12-14] Furthermore, a key feature of RCVS, segmental arterial vasoconstriction, may be absent early in the course of the disease.[1,2,4,5,14] Consequently, both the clinician and radiologist must maintain a high level of suspicion for this entity in patients presenting with characteristic features.

The first part of this article will review the history of RCVS, including the previously described clinical entities that it is now thought to include. We will then discuss the epidemiology, diagnostic criteria, and clinical presentations of this disorder and explore the association of RCVS with posterior reversible encephalopathy syndrome (PRES). In the second part, we will review the imaging features of RCVS, including more recent work exploring associated imaging changes in the cerebral arterial vasculature beyond segmental vasoconstriction.

Historical Background

Reversible segmental cerebral vasoconstriction has been described in the medical literature in a diverse array of clinical settings dating back to the 1960s.[15-17] The earliest clinical reports associated this finding with the postpartum state, migraine headaches, unruptured cerebral aneurysms, and the use of vasoactive medication such as ergot derivatives. Initially, patients presenting with cerebral vasoconstriction were thought to have unique disease entities, depending on the given clinical scenario and specialist treating the patient (Table 1).[4-6,8-11] The common features of these cases, including clinical presentation with severe headache, reversibility of angiographic findings, and lack of histologic abnormalities on arterial biopsy, were not well appreciated or understood.

In 1988, Gregory Call and Marie Fleming described a unique clinical and radiographic syndrome in a small case series of 4 patients presenting with acute headache and reversible cerebral artery vasoconstriction.[18] When the authors included 12 previ-

From the Department of Diagnostic Radiology (T.R.M., R.S., D.G.), Section of Neuroradiology, University of Maryland Medical Center, Baltimore, Maryland; and Department of Diagnostic Radiology (M.M.-B.), Section of Neuroradiology, University of Washington, Seattle, Washington.

Please address correspondence to Dheeraj Gandhi, MD, University of Maryland Medical Center, Department of Diagnostic Radiology, Room N2W78, 22 South Greene St, Baltimore, MD 21201; e-mail: Dgandhi@umm.edu

http://dx.doi.org/10.3174/ajnr.A4214

Table 1: Prior terms for RCVS

Prior Terms
Migrainous vasospasm
Benign angiopathy of the central nervous system
Postpartum angiopathy
Thunderclap headache with reversible vasospasm
Sexual headache
Drug-induced angiopathy
Call-Fleming syndrome

Table 2: Diagnostic criteria for RCVS

Criteria
Severe, acute headaches, with or without additional neurologic signs or symptoms
Uniphasic disease course with no new symptoms after 1 month of onset
No evidence for aneurysmal SAH
Normal or near-normal findings on CSF analysis (protein level, <80 mg/dL; leukocyte level, <10/mm^3; normal glucose level)
Multifocal segmental cerebral artery vasoconstriction demonstrated on either catheter angiography or indirectly on CTA/MRA
Reversibility of angiographic abnormalities within 12 weeks after onset. If death occurs before the follow-up studies are completed, postmortem rules out such conditions as vasculitis, intracranial atherosclerosis, and aneurysmal SAH, which can also manifest with headache and stroke

ously published case reports of patients presenting with similar findings, comprising some associated with migraines and postpartum state, they noted distinctive features of the syndrome, such as its association with hyperacute headache, transient or permanent neurologic deficits, normal or nonspecific findings on CSF analysis, and the lack of correlation between the resolution of patient symptoms and arterial vasoconstriction. In this small series, the authors demonstrated a wide range of possible clinical outcomes, from complete resolution of symptoms to permanent disability with hemiparesis and/or cortical blindness. The eponym "Call-Fleming syndrome" was subsequently used to describe the entity.

In 2007, Calabrese et al,[6] made a case for unifying the various cerebral vasoconstriction syndromes, including Call-Fleming, under the term "reversible cerebral vasoconstriction syndrome" and proposed specific diagnostic criteria (Table 2). In recent years, our understanding of possible triggers, imaging findings, and the clinical course of RCVS has greatly improved. However, a good deal remains unknown about the syndrome. Although RCVS is becoming more widely recognized in the medical community, the overlap of its features with other conditions such as primary angiitis of the CNS continues to be a challenge. Finally, the heterogeneity of clinical and radiologic manifestations of RCVS, along with the diverse clinical settings in which it is encountered, strongly suggests that the syndrome represents a common end point of numerous disease processes, as opposed to a specific disease entity.[3,6-8]

Diagnostic Criteria

The key diagnostic criteria for RCVS proposed by Calabrese et al[6] have since been slightly modified by the International Headache Society (Table 2). Although these criteria have not been validated in any prospective study, they have proved very useful clinically to diagnose RCVS and to increase physician awareness of the disease.

Epidemiology and Potential Triggers

Although the true incidence of RCVS remains uncertain, the syndrome does not appear rare on the basis of the rates of patient recruitment or presentation into prospective and retrospective studies.[19] Furthermore, recent reports have suggested that the incidence of RCVS may be increasing, though it is unclear whether this reflects a true increase in the incidence of the syndrome versus a consequence of improved imaging techniques and physician awareness.[20,21] Nevertheless, RCVS likely remains underdiagnosed and should be included in the differential diagnosis of young patients presenting with severe headache or cryptogenic stroke.[1,5,21,22]

RCVS commonly affects patients 20–50 years of age (mean, 42–45 years), though other age groups, including children and adolescents, can be affected.[1,2,5,6,17,23-27] Most interesting, the mean age of men presenting with RCVS tends to be a decade younger than that of female patients (fourth decade).[9,12] There is a female predominance, with an average female/male ratio from 3 large series of patients of approximately 2.4:1.[2,5,9,17,23,24] RCVS does not appear to be limited to any single ethnic or racial group.[19] As Ducros[19] highlighted in her review of RCVS, differences in patient characteristics in large published series could reflect either intrinsic differences in RCVS among various patient populations and/or differences in patient recruitment criteria.

RCVS can occur spontaneously, without an obvious underlying cause, or can be secondary to an identifiable trigger (roughly 25%–60% of cases).[2,3] The delay in exposure to an exogenous trigger and the development of RCVS can be anywhere between a few days and several months.[2] In cases in which medications act as the exogenous trigger for the syndrome, patients may be taking the drug on a regular basis or infrequently, either at recommended dosages or in excess.[2] For those patients without an obvious precipitant, RCVS may be induced in vulnerable individuals due to spontaneous or evoked vascular and/or neuronal discharges.[6]

A diverse group of possible exogenous triggers for secondary RCVS have been proposed, though the potential delay between exposure and development of the syndrome (in some cases weeks to months) and the ubiquity of some triggers (coughing, laughing, and so forth) raise the possibility that some of these associations may be coincidental (Table 1).[2,3,6,11,23,28-38] However, the association of RCVS with the most commonly reported triggers is more compelling, including the use of vasoactive drugs and the postpartum state, which together account for more than half of cases in most published series (approximately 50% and 9%–10% of cases respectively).[7,17,39] Sympathomimetic drugs commonly taken over the counter for upper respiratory tract infections, including phenylpropanolamine and pseudoephedrine, as well as antimigrainous medications, have historically been associated with subarachnoid hemorrhage and ischemic stroke in rare cases, which in retrospect likely reflects the sequelae of drug-induced RCVS.[40,41] The association between RCVS and the postpartum state is thought to possibly reflect increased levels of both pro- and antiangiogenic factors, some of which have also been associated

with eclampsia, such as placental growth factor.[5] RCVS encountered in the postpartum period typically is encountered anywhere from 1 to 3 weeks following an uncomplicated pregnancy, though presentation as late as 6 weeks has been reported.[42,43]

RCVS is commonly associated with a history of migraine headaches (20%–40% of cases), which may, in part, be due to the known role of migraine medications as a trigger for the syndrome.[1,5,17] Cervical arterial dissection has also been associated with RCVS, though it remains uncertain whether this represents a potential etiology or complication of the syndrome.[7,9,44-47] In a prospective study identifying patients with RCVS or cervical arterial dissection, Mawet et al[45] found that 12% of patients in the RCVS cohort ($n = 173$) had or developed cervical arterial dissection, while 7% of patients in the cervical dissection cohort ($n = 285$) developed RCVS. In rare cases, multiple cervical arterial dissections may be present.[47] Finally, some published series have noted a significant association between RCVS and cannabis use.[22]

Pathogenesis

The pathophysiology of RCVS remains unknown. However, alterations in cerebral vascular tone leading to vasoconstriction are thought to be a key pathophysiologic mechanism underlying the development of RCVS.[1,2,6,9,23,43] This hypothesis is supported by the lack of histologic changes noted in and around the cerebral vasculature in patients with RCVS who have undergone brain biopsy.[1,43] Specifically, histologic and electron-microscopic analyses have failed to demonstrate evidence of active inflammation or vasculitis.[1] Deregulation of cerebral vascular tone in RCVS may be induced by sympathetic overactivity, endothelial dysfunction, and oxidative stress.[3,5,11,12,23,48,49] The association of RCVS with blood pressure surges, ingestion of sympathomimetic vasoactive substances, and pheochromocytoma support the role of sympathetic overactivity in its pathogenesis. On the other hand, a significant overlap between RCVS and PRES supports the importance of endothelial dysfunction, which is known to play an important pathophysiologic role in the latter. Because RCVS likely represents a common end point of a diverse group of disease processes, it is possible that the contribution of sympathetic overactivity and endothelial dysfunction to the onset of the syndrome varies depending on the incitant event in a given patient.

Various hormonal and biochemical factors have been suggested to play a role in the deregulation of cerebral vascular tone in RCVS, including estrogen, endothelin-1, serotonin, nitric oxide, and prostaglandins, some of which have been also associated with vasoconstriction following aneurysmal subarachnoid hemorrhage.[5,6,11,48] For example, urine levels of 8-iso-prostaglandin $F_{2\alpha}$, a marker of oxidative stress and a potent vasoconstrictor, were found to correlate with disease severity in patients with RCVS.[48] This finding suggests that oxidative stress may play a role in the pathogenesis of RCVS. It is unclear whether the vasoconstrictive properties of 8-iso-prostaglandin $F_{2\alpha}$ contribute to the segmental vasoconstriction found in RCVS.[48] Other factors, including placental growth factor, soluble placental growth factor receptor (soluble fms-like tyrosine kinase-1), and soluble endoglin, play a role in angiogenesis and have been implicated in the development of RCVS in the postpartum period.[8]

Genetic factors may influence an individual's susceptibility to developing RCVS and the severity of its subsequent clinical course. A specific genetic polymorphism (Val66Met) in the gene for brain-derived neurotrophic factor, which is important for neuronal survival, neurogenesis, and synaptic plasticity, has been associated with more severe vasoconstriction in patients with RCVS.[50] Most interesting, brain-derived neurotrophic factor can also affect vascular function and has been associated with disorders of abnormal vascular tone and unstable angina.

Thunderclap Headache

The thunderclap headache is a defining clinical feature of RCVS and is defined as a severe, throbbing headache that reaches peak intensity within 60 seconds of onset (Fig 1). In RCVS, the pain is often bilateral and diffuse, though it can originate in the occipital region.[1,2,5,6,9,14] Thunderclap headache has been reported in 94%–100% of patients with RCVS and may be the sole presenting symptom in 70%–76% of cases.[2,6,9,51,52] Often, there is significant delay between the onset of headache and patient presentation for medical care (average, 7 days).[9] The thunderclap headache can be associated with other symptoms, including nausea, emesis, diplopia, elevations in blood pressure, and photosensitivity.[1,2,6,9,42,44] In patients with RCVS who have migraines, the thunderclap headache is typically described as differing in location, degree, and quality from their usual migraines.[13] A minority of patients with RCVS may present with a more mild or subacute headache, though the complete absence of headache is rare.[2,3,19]

Thunderclap headache is not specific for RCVS and can be associated with various other medical conditions, including aneurysmal subarachnoid hemorrhage, primary headache disorder, pituitary apoplexy, cerebral venous sinus thrombosis, unruptured cerebral aneurysm, cervical arterial dissection, and third ventricle colloid cyst, among others.[53] In fact, prior reports suggest that RCVS will ultimately be diagnosed in less than half (45%) of patients presenting with a thunderclap headache.[14,51] For example, Grooters et al[14] found that only 8.8% of patients presenting to a single center with thunderclap headache and no evidence of aneurysmal subarachnoid hemorrhage were ultimately diagnosed with RCVS.

However, some characteristics of the thunderclap headache associated with RCVS may be more specific for the syndrome. For example, in contradistinction to patients with aneurysmal subarachnoid hemorrhage, the thunderclap headache associated with RCVS typically demonstrates a waxing and waning course, often completely resolving within 3 hours (range, minutes to days), only to recur repeatedly during 1–3 weeks.[1,2,9,14,19,23,44] On average, the last episode occurs 7–8 days after symptom onset.[19] In RCVS, the number of exacerbations may vary between 1 and 20 episodes and often are triggered by bathing, stress, sexual intercourse, change in position, exertion, and coughing.[1,2,6,7,16,42,54,55] A more moderate headache may persist between the acute episodes.[2,5,19]

The exact etiology of the thunderclap headache encountered in CVS remains uncertain. Some authors have postulated that cerebral vasoconstriction may be the cause because the cerebral

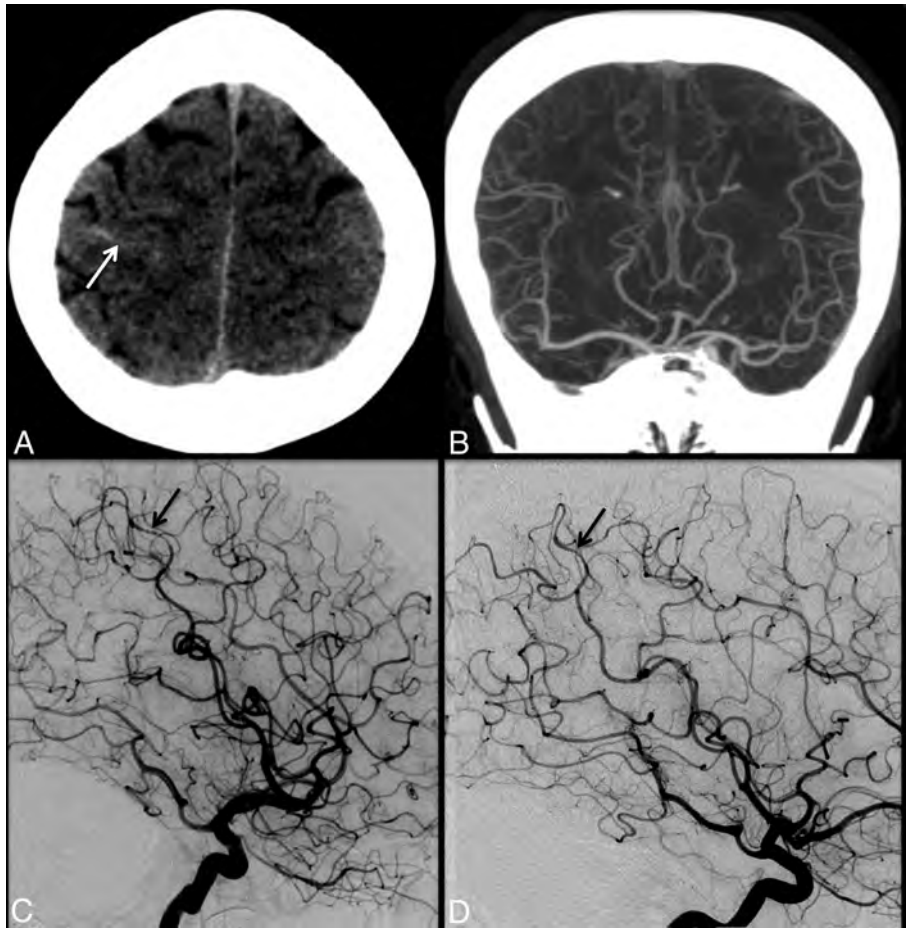

FIG 1. A 47-year-old woman with the sudden onset of severe headache. Initial noncontrast head CT (*A*) demonstrates trace sulcal subarachnoid hemorrhage (*white arrow*) near the vertex. CT angiography performed at the same time (*B*) is interpreted as having unremarkable findings. Conventional angiography (*C*) demonstrates mild diffuse irregularity with multifocal narrowings throughout the cerebral vasculature with a beaded appearance, most pronounced in distal right middle cerebral artery cortical branches (*black arrow*). Findings are most consistent with RCVS. Follow-up catheter angiogram performed 1 month later (*D*) demonstrates complete resolution of cerebral vasoconstriction (*black arrow*).

vasculature receives innervation from the first division of the trigeminal nerve and the dorsal ganglion of the second cervical nerve.[6] However, the time course of patient symptoms such as headache and cerebral vasoconstriction argues against a causal relationship. For example, although patients typically present acutely with thunderclap headache, cerebral vasoconstriction often does not become evident for a week or more following symptom onset. Furthermore, resolution of vasoconstriction may take weeks to months in some individuals, persisting long after the resolution of patient symptomatology.[56]

Other Clinical Presentations and Sequelae of RCVS

Other clinical presentations, or sequelae, of RCVS include generalized seizures, encephalopathy, focal neurologic deficits, altered mental status, transient ischemic attacks, ischemic stroke, intracranial hemorrhage, cerebral edema, and PRES (Table 3).[2,6,8,12,13,20,23,39,57-59] In her meta-analysis of 3 large case series of patients with RCVS, Ducros[19] found that focal neurologic deficits were present in 8%–43% of patients, seizures in 1%–17%, cortical subarachnoid hemorrhage in 30%–34% (1 study had hemorrhage as an exclusion criterion and was not included), cerebral infarction in 6%–39%, and concomitant PRES

Table 3: Potential triggers of RCVS

Triggers of Secondary RCVS
Vasoactive medications
Sympathomimetic drugs, bromocriptine, ergotamine, pseudoephedrine, selective serotonin-uptake inhibitors, interferon, triptans, diet pills, nonsteroidal anti-inflammatory drugs
Vasoactive recreational drugs
Alcohol, amphetamines, cannabis, cocaine, ecstasy, nicotine
Pregnancy and postpartum states
Blood products
Blood transfusions, erythropoietin, intravenous immunoglobulin
Headache disorders
Migraines
Tumors
Pheochromocytoma
Paraganglioma
Trauma
Carotid dissection, unruptured cerebral aneurysm
Head and neck surgery
Various medical conditions
Hemolysis, elevated liver enzymes, low platelets
Antiphospholipid antibody syndrome
Thrombotic thrombocytopenic purpura

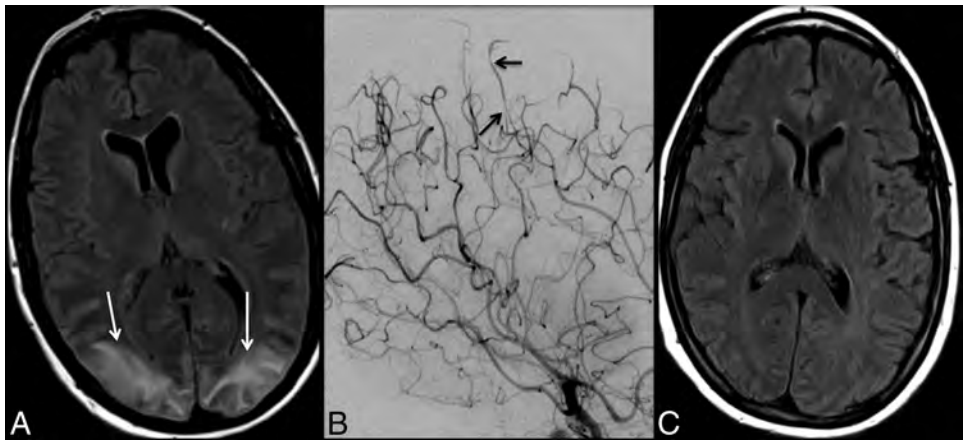

FIG 2. A 42-year-old woman who presented with altered mental status and lethargy. FLAIR imaging (*A*) demonstrates signal hyperintensity involving the cortex and underlying subcortical white matter in the parietal and occipital lobes (*white arrows*), consistent with PRES. There is no evidence of associated diffusion restriction. Trace sulcal subarachnoid hemorrhage was also noted overlying the right frontal lobe (not shown). Note subtle irregularity and multifocal narrowings involving distal cortical branches of the bilateral middle and anterior cerebral arteries (*black arrows*) on cerebral angiography (*B*), suggestive of RCVS. The patient made a full recovery, with complete resolution of cerebral areas of abnormal FLAIR hyperintensity (*C*) and cerebral vasoconstriction (not shown).

in 9%–38% (Fig 2). This wide range in reported incidence of various sequelae of RCVS may reflect recruitment bias, with more ill patients being more likely to present for medical care; selection criteria; and the clinical context in which patients were encountered.[19] For example, reported rates of ischemic infarct and intracranial hemorrhage in patients developing RCVS postpartum appear to be higher than those in series included by Ducros.[33,60]

Although patients with RCVS may initially present with generalized seizure, seizures rarely persist and long-term antiepileptic therapy is generally not indicated.[1,42] Hypertension is commonly encountered in patients with RCVS in the acute period; however, it is unclear whether high blood pressure is from pain associated with headache, a response to cerebral vasoconstriction, or some other manifestation of the syndrome.[5,13] As previously described, cervical arterial dissections may be encountered in patients with RCVS and should be excluded in patients who present with neck pain and/or territorial cerebral infract.[1,2,5,19,45,46]

Focal neurologic deficits encountered with RCVS include visual deficits, hemiplegia, dysarthria, aphasia, numbness, cortical blindness, or ataxia.[6,42,59] Focal deficits of vision, sensory, sensation, and motor function are encountered in decreasing frequency.[1,5] Focal neurologic deficits may be transient or permanent, often reflecting the sequelae of TIA or ischemic infarct resulting from severe segmental cerebral vasoconstriction, though some transient deficits may be due to a migraine-type aura phenomenon.[1,2,6] Neurologic deficits lasting >24 hours are unlikely to improve and likely reflect the sequelae of ischemic infarct, which typically occur in bilateral watershed zones of the cerebral hemispheres.[1,19] Cerebellar infarcts are also possible.[19]

Risk factors for the development of intracranial hemorrhage in patients with RCVS include a history of migraines, older age, and female sex.[11,61] Subarachnoid hemorrhage, the most common hemorrhagic complication of RCVS, is most often focal and localized in superficial cerebral sulci near the cerebral convexities.[1,5,8,11-13] Given this distribution, subarachnoid hemorrhage associated with RCVS may be missed on imaging and CSF analysis, and its incidence in the syndrome consequently is underestimated.[11] It has been postulated that vasoconstriction of small arterioles early in the course of RCVS, along with hypertension and breakdown of autoregulatory mechanisms, may precipitate the rupture of small pial vessels with resulting subarachnoid hemorrhage.[17,59,62] Other patterns of intracranial hemorrhage encountered in RCVS include intraparenchymal hemorrhage and subdural hematomas.[1,8,57,59,63] Intraparenchymal hemorrhage can be see in up to 6%–20% of patients and most often is unifocal and lobar in location.[1,8,19,57]

The various sequelae of RCVS tend to occur at different times during the course of the syndrome.[9] Hemorrhagic complications, such as subarachnoid and intraparenchymal hemorrhage and concomitant PRES and seizures, most often occur during the first week of illness.[1,8,9,56] In contradistinction, ischemic events and their resulting focal neurologic deficits often arise later in RCVS, peaking between 1 and 2 weeks following patient presentation.[9] Ischemic stroke can occur even later in the course of the syndrome, occasionally after resolution of symptoms such as headache, and presumably reflects the well-documented delay in resolution of cerebral vasoconstriction.[44] Overall, Ducros et al[9] found that ischemic events such as TIA and stroke occurred on average approximately 8 days later than hemorrhagic complications.[9]

Association with PRES

RCVS and PRES overlap significantly in their clinical and radiographic features, and the 2 entities are frequently encountered concurrently (Fig 2).[4,5,58,62,64,65] PRES is a clinical and radiographic syndrome characterized by headache, visual changes, seizure, and imaging findings, including cerebral edema affecting the cerebral cortex and underlying white matter, manifesting as areas of hyperintensity on T2 and FLAIR imaging, most often involving the occipital and posterior parietal lobes.[2,62,64] However, other distribution patterns can be encountered with PRES, including involvement of the frontal and temporal lobes, basal ganglia, deep white matter, and brain stem.[2,64] While the areas of cerebral edema encountered in PRES are

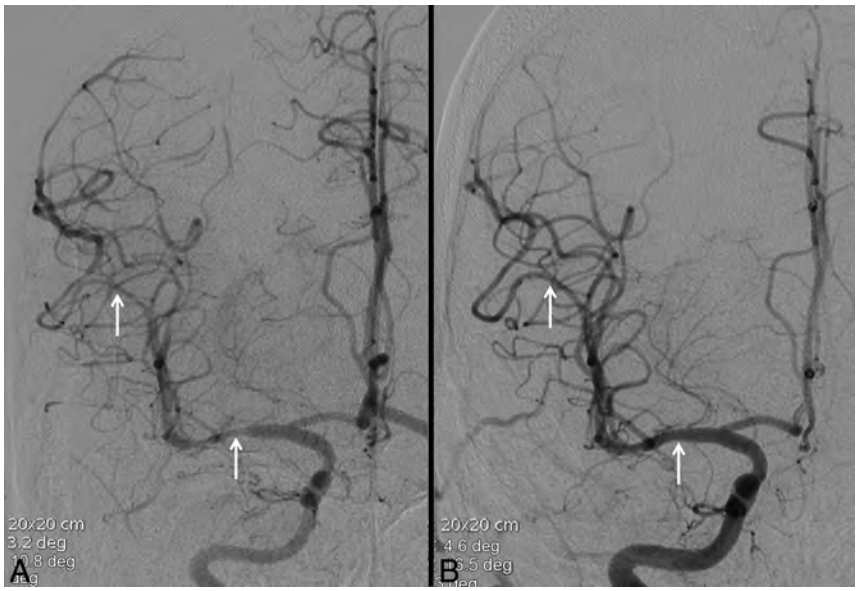

FIG 3. A 19-year-old man with a 2-day history of recurrent headaches and prior marijuana use. Noncontrast CT was negative for acute hemorrhage (not shown). Conventional angiography (*A*) reveals multifocal areas of moderate narrowing and irregularity involving the cerebral vasculature (*white arrows*, *A*). These areas resolved following intra-arterial administration of verapamil (*white arrows*, *B*). Clinical course and imaging findings are consistent with RCVS.

often reversible, progression to cytotoxic edema and infarct can occur.[2,62] Finally, like RCVS, the exact pathophysiologic etiology of PRES remains unknown, though a breakdown in autoregulation of the cerebral vasculature leading to hyperperfusion is 1 possible mechanism.[2,62]

PRES-like reversible cerebral edema is encountered in anywhere from 9% to 38% of patients with RCVS, while most patients with PRES (>85%) demonstrate some element of RCVS-like cerebral vasoconstriction when conventional angiography is performed.[19] When PRES-like features are encountered in cases of RCVS, the anatomic distribution of cerebral edema is similar to PRES encountered in other settings.[44] Furthermore, PRES and RCVS often arise concurrently as complications of various medical conditions, including intravenous immunoglobin therapy, Guillain-Barre syndrome, immunosuppression, stem cell transplantation, blood transfusions, and septic shock.[2,7,28,54,56,66,67] Finally, both PRES and RCVS demonstrate similar clinical features, including an acute, self-limited course and symptomatology, such as headache, confusion, seizure, and transient or permanent neurologic deficits.[1,2,54] Given the significant overlap between the 2 entities, it is possible that RCVS and PRES may represent a spectrum of potential clinical manifestations of a common underlying pathophysiology involving various degrees of altered cerebral vascular tone and endothelial dysfunction.

Treatment

The treatment of RCVS is based on observational data obtained from retrospective studies.[1,5,21] Current treatment recommendations for RCVS include withdrawal of any suspected exogenous triggers, including vasoactive medications, and intensive care unit–level care, symptom relief with analgesics, blood pressure control, and seizure prophylaxis.[1,2,5,34,68] Patients should avoid activities that are associated with the onset of symptoms/headache as much as possible. Calcium channel blockers, including nimodipine, have been administered to patients with RCVS via oral and intravenous routes and have been shown in prospective and retrospective studies to provide symptom relief, including headache.[2,3,17,24,44,69-72] However, calcium channel blockers have not been shown to influence the evolution of cerebral vasoconstriction or the possible complications of RCVS, including intracranial hemorrhage and ischemic stroke.[1,6,16,17]

Other vasodilators, such as phosphodiesterase inhibitors, have also been used with anecdotal success in case reports.[73] However, vasodilators, including calcium channel blockers, must be used with caution because drops in systolic blood pressure may impair cerebral perfusion in patients with RCVS with severe cerebral vasoconstriction.[2,44] Intra-arterial administration of vasodilators and balloon angioplasty have been performed in cases of severe RCVS-related vasoconstriction, though the indications and efficacy of these treatments remain unclear (Fig 3).[1,69,74,75] Although RCVS vasoconstriction has been shown to improve following intra-arterial vasodilator therapy, recurrence of arterial narrowing has been reported, sometimes necessitating multiple treatment sessions.[69,76] Glucocorticoid steroids have been administered to patients with RCVS, without improvement in either patient symptoms or sequelae of the disease. Some case series have even suggested that steroid therapy may be associated with worse outcomes in RCVS.[3,17,76]

Prognosis and Clinical Course

Fortunately, the prognosis for most patients with RCVS is very good. The syndrome typically follows a self-limiting, monophasic course, with resolution of symptoms by 3 weeks, and no new symptoms after 1 month.[1,13,17,23,39,57,77] By definition, resolution of vasoconstriction should occur by 3 months. However, a minority of patients will demonstrate delayed clinical worsening in the first few weeks following symptoms onset, most often due to the development of an ischemic infarct.[39,42,43,77] A more fulminant course of RCVS leading to permanent disability or death can be encountered in 5%–10% of patients.[1,2,6,12,43,60,77] Recurrence of RCVS appears to be rare, though some patients may have chronic mild headaches and fatigue on follow-up.[2,42,43,78]

RCVS encountered in the postpartum period deserves special attention because it has been reported to be more likely to follow a fulminant course, with multifocal infarct, intracranial hemorrhage, extensive vasogenic edema, and death.[1,39,60] When Fugate et al[33] evaluated patients with postpartum angiopathy in a small retrospective series ($n = 18$), they found focal neurologic deficits in 50%, visual disturbances in 44%, encephalopathy in 33%, sei-

zure in 28%, intracranial hemorrhage in 39%, vasogenic edema in 35%, and infarction in 35%. Somewhat unusual for RCVS, only slightly less than half of patients in this small series achieved a complete recovery, while the remaining patients either died or were left with significant neurologic deficits.[33]

CONCLUSIONS

RCVS is characterized by a thunderclap headache and reversible cerebral artery vasoconstriction on imaging. Alterations in cerebral vascular tone likely underlie development of the syndrome. Most patients with RCVS have a good outcome with no permanent sequelae, while a small minority will experience a more fulminant course culminating in permanent disability or death.

REFERENCES

1. Ducros A. **L37: reversible cerebral vasoconstriction syndrome—distinction from CNS vasculitis.** *Presse Med* 2013;42(4 pt 2):602–04
2. Ducros A, Bousser MG. **Reversible cerebral vasoconstriction syndrome.** *Pract Neurol* 2009;9:256–67
3. Gupta S, Zivadinov R, Ramasamy D, et al. **Reversible cerebral vasoconstriction syndrome (RCVS) in antiphospholipid antibody syndrome (APLA): the role of centrally acting vasodilators—case series and review of literature.** *Clin Rheumatol* 2014;33:1829–33
4. Marder CP, Donohue MM, Weinstein JR, et al. **Multimodal imaging of reversible cerebral vasoconstriction syndrome: a series of 6 cases.** *AJNR Am J Neuroradiol* 2012;33:1403–10
5. Sheikh HU, Mathew PG. **Reversible cerebral vasoconstriction syndrome: updates and new perspectives.** *Curr Pain Headache Rep* 2014;18:414
6. Calabrese LH, Dodick DW, Schwedt TJ, et al. **Narrative review: reversible cerebral vasoconstriction syndromes.** *Ann Intern Med* 2007;146:34–44
7. Chen SP, Fuh JL, Wang SJ. **Reversible cerebral vasoconstriction syndrome: current and future perspectives.** *Expert Rev Neurother* 2011;11:1265–76
8. Stary JM, Wang BH, Moon SJ, et al. **Dramatic intracerebral hemorrhagic presentations of reversible cerebral vasoconstriction syndrome: three cases and a literature review.** *Case Rep Neurol Med* 2014;2014:782028
9. Ducros A, Boukobza M, Porcher R, et al. **The clinical and radiological spectrum of reversible cerebral vasoconstriction syndrome: a prospective series of 67 patients.** *Brain* 2007;130(pt 12):3091–101
10. Alvaro LC, Iriondo I, Villaverde FJ. **Sexual headache and stroke in a heavy cannabis smoker.** *Headache* 2002;42:224–26
11. Ansari SA, Rath TJ, Gandhi D. **Reversible cerebral vasoconstriction syndromes presenting with subarachnoid hemorrhage: a case series.** *J Neurointerv Surg* 2011;3:272–78
12. Calic Z, Choong H, Schlaphoff G, et al. **Reversible cerebral vasoconstriction syndrome following indomethacin.** *Cephalalgia* 2014;34:1181–86
13. Edlow BL, Kasner SE, Hurst RW, et al. **Reversible cerebral vasoconstriction syndrome associated with subarachnoid hemorrhage.** *Neurocrit Care* 2007;7:203–10
14. Grooters GS, Sluzewski M, Tijssen CC. **How often is thunderclap headache caused by the reversible cerebral vasoconstriction syndrome?** *Headache* 2014;54:732–35
15. Hajj-Ali RA, Singhal AB, Benseler S, et al. **Primary angiitis of the CNS.** *Lancet Neurol* 2011;10:561–72
16. Hammad TA, Hajj-Ali RA. **Primary angiitis of the central nervous system and reversible cerebral vasoconstriction syndrome.** *Curr Atheroscler Rep* 2013;15:346
17. Singhal AB, Hajj-Ali RA, Topcuoglu MA, et al. **Reversible cerebral vasoconstriction syndromes: analysis of 139 cases.** *Arch Neurol* 2011;68:1005–12
18. Call GK, Fleming MC, Sealfon S, et al. **Reversible cerebral segmental vasoconstriction.** *Stroke* 1988;19:1159–70
19. Ducros A. **Reversible cerebral vasoconstriction syndrome.** *Lancet Neurol* 2012;11:906–17
20. Chen SP, Wang SJ. **Hyperintense vessels: an early MRI marker of reversible cerebral vasoconstriction syndrome?** *Cephalalgia* 2014;34:1038–39
21. Koopman K, Uyttenboogaart M, Luijckx GJ, et al. **Pitfalls in the diagnosis of reversible cerebral vasoconstriction syndrome and primary angiitis of the central nervous system.** *Eur J Neurol* 2007;14:1085–87
22. Wolff V, Lauer V, Rouyer O, et al. **Cannabis use, ischemic stroke, and multifocal intracranial vasoconstriction: a prospective study in 48 consecutive young patients.** *Stroke* 2011;42:1778–80
23. Bain J, Segal D, Amin R, et al. **Call-Fleming syndrome: headache in a 16-year-old girl.** *Pediatr Neurol* 2013;49:130–33.e1
24. Hajj-Ali RA, Furlan A, Abou-Chebel A, et al. **Benign angiopathy of the central nervous system: cohort of 16 patients with clinical course and long-term followup.** *Arthritis Rheum* 2002;47:662–69
25. Kirton A, Diggle J, Hu W, et al. **A pediatric case of reversible segmental cerebral vasoconstriction.** *Can J Neurol Sci* 2006;33:250–53
26. Liu HY, Fuh JL, Lirng JF, et al. **Three paediatric patients with reversible cerebral vasoconstriction syndromes.** *Cephalalgia* 2010;30:354–59
27. Probert R, Saunders DE, Ganesan V. **Reversible cerebral vasoconstriction syndrome: rare or underrecognized in children?** *Dev Med Child Neurol* 2013;55:385–89
28. Bayer-Karpinska A, Patzig M, Adamczyk C, et al. **Reversible cerebral vasoconstriction syndrome with concurrent bilateral carotid artery dissection.** *Cephalalgia* 2013;33:491–95
29. Boughammoura A, Touze E, Oppenheim C, et al. **Reversible angiopathy and encephalopathy after blood transfusion.** *J Neurol* 2013;250:116–18
30. Comabella M, Alvarez-Sabin J, Rovira A, et al. **Bromocriptine and postpartum cerebral angiopathy: a causal relationship?** *Neurology* 1996;46:1754–56
31. Cvetanovich GL, Ramakrishnan P, Klein JP, et al. **Reversible cerebral vasoconstriction syndrome in a patient taking citalopram and Hydroxycut: a case report.** *J Med Case Rep* 2011;5:548
32. Dou YH, Fuh JL, Chen SP, et al. **Reversible cerebral vasoconstriction syndrome after blood transfusion.** *Headache* 2014;54:736–44
33. Fugate JE, Ameriso SF, Ortiz G, et al. **Variable presentations of postpartum angiopathy.** *Stroke* 2012;43:670–76
34. Granier I, Garcia E, Geissler A, et al. **Postpartum cerebral angiopathy associated with the administration of sumatriptan and dehydroergotamine: a case report.** *Intensive Care Med* 1999;25:532–34
35. Lopez-Valdes E, Chang HM, Pessin MS, et al. **Cerebral vasoconstriction after carotid surgery.** *Neurology* 1997;49:303–04
36. Moussavi M, Korya D, Panezai S, et al. **Reversible cerebral vasoconstriction syndrome in a 35-year-old woman following hysterectomy and bilateral salpingo-oophorectomy.** *J Neurointerv Surg* 2012;4:e35
37. Paliwal PR, Teoh HL, Sharma VK. **Association between reversible cerebral vasoconstriction syndrome and thrombotic thrombocytopenic purpura.** *J Neurol Sci* 2014;338:223–25
38. Verillaud B, Ducros A, Massiou H, et al. **Reversible cerebral vasoconstriction syndrome in two patients with a carotid glomus tumour.** *Cephalalgia* 2010;30:1271–75
39. Katz BS, Fugate JE, Ameriso SF, et al. **Clinical worsening in reversible cerebral vasoconstriction syndrome.** *JAMA Neurol* 2014;71:68–73
40. Cantu C, Arauz A, Murillo-Bonilla LM, et al. **Stroke associated with sympathomimetics contained in over-the-counter cough and cold drugs.** *Stroke* 2003;34:1667–72
41. Nighoghossian N, Derex L, Trouillas P. **Multiple intracerebral hemorrhages and vasospasm following antimigrainous drug abuse.** *Headache* 1998;38:478–80
42. Singhal AB, Bernstein RA. **Postpartum angiopathy and other cerebral vasoconstriction syndromes.** *Neurocrit Care* 2005;3:91–97

43. Williams TL, Lukovits TG, Harris BT, et al. **A fatal case of postpartum cerebral angiopathy with literature review.** *Arch Gynecol Obstet* 2007;275:67–77
44. Chen SP, Fuh JL, Wang SJ, et al. **Magnetic resonance angiography in reversible cerebral vasoconstriction syndromes.** *Ann Neurol* 2010; 67:648–56
45. Mawet J, Boukobza M, Franc J, et al. **Reversible cerebral vasoconstriction syndrome and cervical artery dissection in 20 patients.** *Neurology* 2013;81:821–24
46. Mitchell LA, Santarelli JG, Singh IP, et al. **Reversible cerebral vasoconstriction syndrome and bilateral vertebral artery dissection presenting in a patient after cesarean section.** *J Neurointerv Surg* 2014;6:e5
47. Nouh A, Ruland S, Schneck MJ, et al. **Reversible cerebral vasoconstriction syndrome with multivessel cervical artery dissections and a double aortic arch.** *J Stroke Cerebrovasc Dis* 2014;23:e141–43
48. Chen SP, Chung YT, Liu TY, et al. **Oxidative stress and increased formation of vasoconstricting F2-isoprostanes in patients with reversible cerebral vasoconstriction syndrome.** *Free Radic Biol Med* 2013;61:243–48
49. Marra A, Vargas M, Striano P, et al. **Posterior reversible encephalopathy syndrome: the endothelial hypotheses.** *Med Hypotheses* 2014; 82:619–22
50. Chen SP, Fuh JL, Wang SJ, et al. **Brain-derived neurotrophic factor gene Val66Met polymorphism modulates reversible cerebral vasoconstriction syndromes.** *PLoS One* 2011;6:e18024
51. Cheng YC, Kuo KH, Lai TH. **A common cause of sudden and thunderclap headaches: reversible cerebral vasoconstriction syndrome.** *J Headache Pain* 2014;15:13
52. Koopman K, Teune LK, ter Laan M, et al. **An often unrecognized cause of thunderclap headache: reversible cerebral vasoconstriction syndrome.** *J Headache Pain* 2008;9:389–91
53. Schwedt TJ, Matharu MS, Dodick DW. **Thunderclap headache.** *Lancet Neurol* 2006;5:621–31
54. Dodick DW, Eross EJ, Drazkowski JF, et al. **Thunderclap headache associated with reversible vasospasm and posterior leukoencephalopathy syndrome.** *Cephalalgia* 2003;23:994–97
55. Wang SJ, Fuh JL, Wu ZA, et al. **Bath-related thunderclap headache: a study of 21 consecutive patients.** *Cephalalgia* 2008;28:524–30
56. Chen SP, Fuh JL, Chang FC, et al. **Transcranial color Doppler study for reversible cerebral vasoconstriction syndromes.** *Ann Neurol* 2008;63:751–57
57. Geocadin RG, Razumovsky AY, Wityk RJ, et al. **Intracerebral hemorrhage and postpartum cerebral vasculopathy.** *J Neurol Sci* 2002;205:29–34
58. Noda K, Fukae J, Fujishima K, et al. **Reversible cerebral vasoconstriction syndrome presenting as subarachnoid hemorrhage, reversible posterior leukoencephalopathy, and cerebral infarction.** *Intern Med* 2011;50:1227–33
59. Santos E, Zhang Y, Wilkins A, et al. **Reversible cerebral vasoconstriction syndrome presenting with haemorrhage.** *J Neurol Sci* 2009;276:189–92
60. Fugate JE, Wijdicks EF, Parisi JE, et al. **Fulminant postpartum cerebral vasoconstriction syndrome.** *Arch Neurol* 2012;69:111–17
61. Ducros A, Fiedler U, Porcher R, et al. **Hemorrhagic manifestations of reversible cerebral vasoconstriction syndrome: frequency, features, and risk factors.** *Stroke* 2010;41:2505–11
62. Singhal AB. **Postpartum angiopathy with reversible posterior leukoencephalopathy.** *Arch Neurol* 2004;61:411–16
63. Moskowitz SI, Calabrese LH, Weil RJ. **Benign angiopathy of the central nervous system presenting with intracerebral hemorrhage.** *Surg Neurol* 2007;67:522–27; discussion 527–28
64. Sadek AR, Waters RJ, Sparrow OC. **Posterior reversible encephalopathy syndrome: a case following reversible cerebral vasoconstriction syndrome masquerading as subarachnoid haemorrhage.** *Acta Neurochir (Wien)* 2012;154:413–16
65. Soo Y, Singhal AB, Leung T, et al. **Reversible cerebral vasoconstriction syndrome with posterior leucoencephalopathy after oral contraceptive pills.** *Cephalalgia* 2010;30:42–45
66. Agarwal R, Davis C, Altinok D, et al. **Posterior reversible encephalopathy and cerebral vasoconstriction in a patient with hemolytic uremic syndrome.** *Pediatr Neurol* 2014;50:518–21
67. Imataki O, Uemura M, Shintani T, et al. **Reversible cerebral vasoconstriction syndrome resulted in cerebral infarction after allogeneic stem cell transplantation: a case report.** *Ann Hematol* 2014;93: 895–96
68. Meschia JF, Malkoff MD, Biller J. **Reversible segmental cerebral arterial vasospasm and cerebral infarction: possible association with excessive use of sumatriptan and Midrin.** *Arch Neurol* 1998;55: 712–14
69. Elstner M, Linn J, Muller-Schunk S, et al. **Reversible cerebral vasoconstriction syndrome: a complicated clinical course treated with intra-arterial application of nimodipine.** *Cephalalgia* 2009;29:677–82
70. Grände PO, Lundgren A, Bjartmarz H, et al. **Segmental cerebral vasoconstriction: successful treatment of secondary cerebral ischaemia with intravenous prostacyclin.** *Cephalalgia* 2010;30:890–95
71. Lu SR, Liao YC, Fuh JL, et al. **Nimodipine for treatment of primary thunderclap headache.** *Neurology* 2004;62:1414–16
72. Zuber M, Touze E, Domigo V, et al. **Reversible cerebral angiopathy: efficacy of nimodipine.** *J Neurol* 2006;253:1585–88
73. Bouchard M, Verreault S, Gariepy JL, et al. **Intra-arterial milrinone for reversible cerebral vasoconstriction syndrome.** *Headache* 2009;49:142–45
74. John S, Donnelly M, Uchino K. **Catastrophic reversible cerebral vasoconstriction syndrome associated with serotonin syndrome.** *Headache* 2013;53:1482–87
75. Song JK, Fisher S, Seifert TD, et al. **Postpartum cerebral angiopathy: atypical features and treatment with intracranial balloon angioplasty.** *Neuroradiology* 2004;46:1022–26
76. French KF, Hoesch RE, Allred J, et al. **Repetitive use of intra-arterial verapamil in the treatment of reversible cerebral vasoconstriction syndrome.** *J Clin Neurosci* 2012;19:174–76
77. Robert T, Kawkabani Marchini A, Oumarou G, et al. **Reversible cerebral vasoconstriction syndrome identification of prognostic factors.** *Clin Neurol Neurosurg* 2013;115:2351–57
78. Ursell MR, Marras CL, Farb R, et al. **Recurrent intracranial hemorrhage due to postpartum cerebral angiopathy: implications for management.** *Stroke* 1998;29:1995–98

Mesial Temporal Sclerosis: Accuracy of NeuroQuant versus Neuroradiologist

M. Azab, M. Carone, S.H. Ying, and D.M. Yousem

ABSTRACT

BACKGROUND AND PURPOSE: We sought to compare the accuracy of a volumetric fully automated computer assessment of hippocampal volume asymmetry versus neuroradiologists' interpretations of the temporal lobes for mesial temporal sclerosis. Detecting mesial temporal sclerosis (MTS) is important for the evaluation of patients with temporal lobe epilepsy as it often guides surgical intervention. One feature of MTS is hippocampal volume loss.

MATERIALS AND METHODS: Electronic medical record and researcher reports of scans of patients with proved mesial temporal sclerosis were compared with volumetric assessment with an FDA-approved software package, NeuroQuant, for detection of mesial temporal sclerosis in 63 patients. The degree of volumetric asymmetry was analyzed to determine the neuroradiologists' threshold for detecting right-left asymmetry in temporal lobe volumes.

RESULTS: Thirty-six patients had left-lateralized MTS, 25 had right-lateralized MTS, and 2 had bilateral MTS. The estimated accuracy of the neuroradiologist was 72.6% with a κ statistic of 0.512 (95% CI, 0.315–0.710) [moderate agreement, $P < 3 \times 10^{-6}$]), whereas the estimated accuracy of NeuroQuant was 79.4% with a κ statistic of 0.588 (95% CI, 0.388–0.787) [moderate agreement, $P < 2 \times 10^{-6}$]). This discrepancy in accuracy was not statistically significant. When at least a 5%–10% volume discrepancy between temporal lobes was present, the neuroradiologists detected it 75%–80% of the time.

CONCLUSIONS: As a stand-alone fully automated software program that can process temporal lobe volume in 5–10 minutes, NeuroQuant compares favorably with trained neuroradiologists in predicting the side of mesial temporal sclerosis. Neuroradiologists can often detect even small temporal lobe volumetric changes visually.

ABBREVIATION: MTS = mesial temporal sclerosis

Temporal lobe epilepsy represents the most common type of partial complex epilepsy in adulthood.[1] There are 2 forms of temporal lobe epilepsy: a common form with mesial temporal lobe symptoms and a rarer form with lateral temporal lobe symptoms.[2]

Mesial temporal sclerosis (MTS) is the most common pathologic entity encountered in epilepsy surgery series.[1] Its histologic confirmation is a major predictive factor for postoperative seizure control.[3] Sclerosis of the hippocampus progresses with time as both a consequence and/or a cause of seizures.[4] It most commonly manifests pathologically as gliosis and volume loss. Clinically epileptiform electroencephalography activity lateralizes to the temporal lobe on the ipsilateral side of MTS.

Multiple structural and functional imaging modalities are available to diagnose MTS and to guide surgical treatment of medically intractable seizures.[5] Most clinical MR imaging studies are sufficient to detect gross hippocampal atrophy changes; however, early changes of hippocampal atrophy may be overlooked by even experienced radiologists because of their subtlety.[6]

According to Spencer et al,[7] computerized volumetric measurement of the hippocampus improves the assessment of patients with temporal lobe epilepsy and adds sensitivity and specificity to the clinical visual evaluation. Others believe that visual inspection alone is sufficient to accurately detect hippocampal sclerosis.[8] The degree of disproportionate hippocampal volume inequality required for visual detection of the hippocampal atro-

Received December 18, 2014; accepted after revision January 19, 2015.

From the Division of Neuroradiology (M.A., S.H.Y., D.M.Y.), The Russell H. Morgan Department of Radiology and Radiological Science, Johns Hopkins Medical Institutions, Baltimore, Maryland; Department of Radiology (M.A.), Suez Canal University, Ismailia, Ismailia Governorate; and Department of Biostatistics (M.C.), University of Washington, Seattle, Washington.

Please address correspondence to David M. Yousem, MD, MBA, Johns Hopkins Medical Institutions, 600 N Wolfe St, Phipps B100F, Baltimore, MD 21287; e-mail: dyousem1@jhu.edu

http://dx.doi.org/10.3174/ajnr.A4313

phy in MTS has not yet been determined. Because there are other nonvolumetric findings that suggest MTS (eg, signal-intensity changes, blurring of gray-white borders, malrotation), it would seem that merely assessing volume, even if highly reliable, would not be sufficient for adequately assessing patients with temporal lobe epilepsy.

Manual hippocampal volumetry has been the standard technique for assessing hippocampal volume loss in MTS, Alzheimer disease, and other disorders in the research realm.[9] However, such manual quantification of temporal lobe volume is cumbersome, time-consuming, not easily reimbursed, and requires extensive training. Until recently, there was no FDA-approved means for providing computer-based, semiautomated, or automated hippocampal volumetry. NeuroQuant (CorTechs Labs, San Diego, California) is a software package that is FDA-cleared for marketing (510[k]K061855) and is now commercially available. Its value in the clinical setting has not been extensively reviewed since FDA approval. The technique for parcellating brain regions and assessing volumetry has been previously outlined by Brewer et al[10] in 2009 in the *American Journal of Neuroradiology*. The steps involved include sequence-checking to ensure that appropriate high-resolution and contrast image parameters are performed, correction for field/gradient inhomogeneities, removal of the overlying calvaria, alignment to the probabilistic atlas of stereotypical anatomy, and segmented volumetry of predetermined anatomic areas derived from multiple subjects of multiple age groups (Brewer et al).[10-13]

We sought to assess the value of NeuroQuant volumetry of the temporal lobe in patients with MTS with the added goal of trying to determine the difference in right and left hippocampal volumes that can be detected by experienced neuroradiologists in the clinical assessment of patients with temporal lobe epilepsy. We hypothesized that because radiologists assess the hippocampi for other imaging findings above and beyond volume loss alone, the neuroradiologist's determination of the correct side of the MTS would be more accurate than basic NeuroQuant volumetry.

MATERIALS AND METHODS

This retrospective study was reviewed and approved by the institutional review board of the School of Medicine and the Committee for the Protection of Human Subjects. Due to the retrospective nature of the study, informed patient consent was not required for the review of medical records and radiographic examinations, and the study was deemed to be Health Insurance Portability and Accountability Act–compliant.

The radiology information system data base was surveyed for the term "mesial temporal sclerosis" during a 53-month period (between January 2009 and May 2013) to find patients who had MR imaging studies. We included 46 healthy control research subjects from the same period who had NeuroQuant-compatible equivalent MR pulse sequences to assess normal variations in hippocampal volumes. The search yielded an initial sample of 85 patients with MTS (mean age, 34.9 ± 15.9 years) matched with the 46 control subjects (mean age, 26.7 ± 15.7 years). Of the 85 subjects, 61 patients who had electroencephalography, clinical, or pathologic findings that localized to the right or left side and 2 patients who had them localized bilaterally had MR pulse sequences in a high-resolution 3D dataset that could be analyzed by NeuroQuant. The 63 patients for analysis included 35 women and 28 men with a mean age of 35.0 ± 16.2 years, similar to the initial cohort and control subjects (no statistical difference in age or sex). Because of the emphasis on asymmetry, the 2 patients with bilateral MTS were removed from a second analysis, leaving 61 subjects as a second dataset. The patients had symptoms of partial complex seizures in 56 cases, intractable seizures in 5 cases, and generalized seizures in 2 cases. Patients with temporal lobe seizures due to a cause other than MTS (eg, tumors, strokes, congenital anomalies) were excluded.

All patients had a dedicated epilepsy protocol that included sagittal T1-weighted images, axial diffusion-weighted images with ADC mapping, axial T2-weighted, axial T2 FLAIR, coronal T2-weighted, coronal T2 FLAIR, coronal 3D spoiled gradient-echo T1-weighted scans, and coronal thin-section T1-weighted scans obtained specifically through the temporal lobes to determine hippocampal volumes and identify any cortical dysplasia. Postcontrast T1 images were added in some cases. Thirty-seven patients were scanned on a 3T scanner, and 26, on a 1.5T scanner.

The NeuroQuant analysis was based on a sagittal 3D volumetric MPRAGE pulse sequence with the following parameters: TR, 2300–2400 ms; TI, 900-1000 ms; TE set to minimum; flip angle, 8°; FOV, 24 cm; section thicknesses, 1.2 mm, for 170 sections. The control subjects and patients with MTS were scanned with identical volumetric pulse sequences. Scans were sent via the PACS to an Apple Mac Mini computer (Cupertino, California) with NeuroQuant installed. NeuroQuant takes the high-resolution 3D T1-weighted, sagittal non-contrast-enhanced MR imaging data, autoroutes them as input with no user intervention, and returns a new full-volume spatially corrected and anatomically labeled dataset along with 2 printable patient reports containing the absolute and relative volumes of the hippocampus, temporal horn, and other structures in DICOM-compliant format (Fig 1). This process, from the time sent from the PACS to creation of the report, typically takes between 5 and 10 minutes, and the report appears in the PACS as 2 additional "Morphometry Results" series.

A clinical neuroradiologist reviewed all MR images at the time of the patient's initial assessment, and a study neuroradiologist reviewed them retrospectively. Twelve neuroradiologists with a range of experience between 2 and 30 years interpreted the clinical studies. The clinical reports were reviewed from the electronic medical record after the study neuroradiologist gave an opinion as to the side of the MTS. In instances in which the research neuroradiologist's interpretation differed from the clinical prospective reading in the electronic medical record, a third neuroradiologist with 25 years of experience provided a third opinion to break the impasse. This occurred in 5 of 63 cases. No attempt was made to parse the data on the basis of individual results of neuroradiology faculty members.

For the criterion standard, patients were classified as having left, right, or bilateral MTS on the basis of electroencephalography recordings, histopathologic findings of surgical specimens, and clinical determination reviewed in the electronic medical record. The proof of diagnosis included pathologic specimens in 25 (of

MORPHOMETRY RESULTS

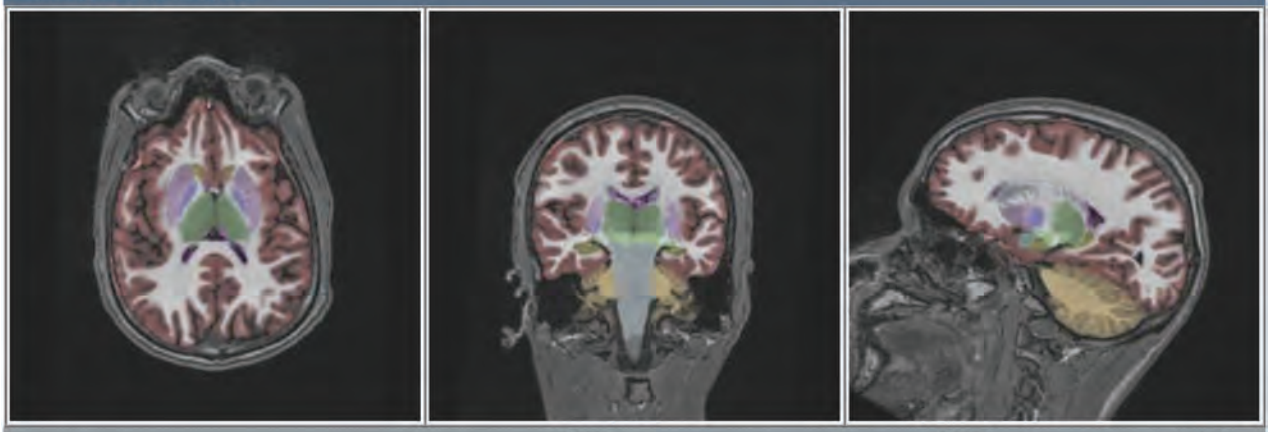

Brain Structure	LH Volume (cm³)	LH Volume (% of ICV)	RH Volume (cm³)	RH Volume (% of ICV)	Asymmetry Index (%)*
Forebrain Parenchyma	461.70	29.93	538.59	34.92	-15.37
Cortical Gray Matter	236.10	15.31	275.65	17.87	-15.46
Lateral Ventricle	7.04	0.46	6.01	0.39	15.69
Inferior Lateral Ventricle	1.05	0.07	1.35	0.09	-25.10
Hippocampus	2.50	0.16	4.22	0.27	-51.32
Amygdala	1.27	0.08	1.90	0.12	-39.29
Caudate	2.39	0.16	2.59	0.17	-7.95
Putamen	5.95	0.39	6.08	0.39	-2.16
Pallidum	0.88	0.06	1.15	0.07	-26.52
Thalamus	8.07	0.52	9.05	0.59	-11.44
Cerebellum	67.46	4.37	65.37	4.24	3.15

*The Asymmetry Index is defined as the difference between left and right volumes divided by their mean (in percent)

FIG 1. Output from NeuroQuant. The NeuroQuant output for this project included basic volumes of several structures. However, the hippocampal asymmetry index was the parameter used to determine MTS laterality.

63, 39.7%) cases and localizing electroencephalography in patients without an operation in 48 (of 63, 60.3%) cases.

The difference in volume between the right and left hippocampi also was assessed to determine the sensitivity of the clinical neuroradiologist's visual assessment of the hippocampal volume. We specifically looked at the electronic medical record reports to determine whether the neuroradiologist commented on one hippocampus being larger than the other. An attribution of hippocampal volume loss to one side in the electronic medical record was compared with the criterion standard for the side of abnormality and also the raw data analysis from the NeuroQuant assessment.

Because previous literature by Pedraza et al[14] had indicated that the left hippocampus tends to be slightly smaller than the right hippocampus in healthy adults by an average of 2.7% and Woolard and Heckers had shown a 4.4% difference in raw volumes of the hippocampus (mean left volume, 3352 mm^3; mean right volume, 3504 mm^3),[15] we performed our data analysis before and after adjustment of volumetry based on analysis of our 46 control subjects, to account for this natural asymmetry. Although Rogers et al[16] and Woolard and Heckers[15] had suggested that this was largely due to asymmetry in the anterior hippocampus (6.3% in the study of Rogers et al), we adjusted for overall hippocampal measures as produced by the NeuroQuant output.

Basic descriptive statistics were computed to summarize characteristics of our patient sample. Accuracy between 2 classifiers was estimated as the empiric proportion of cases on which the classifiers agreed, and the Wilson score interval was computed as a confidence set. The Cohen κ statistic was computed as an additional measure of classifier agreement, and a corresponding confidence interval was calculated. The R statistical computing software functions for medical statistics book (fmsb) (http://www.r-project.org) was used for this purpose. To test the null hypothesis that the neuroradiologist's accuracy is the same for each side of lateralization, we constructed bootstrap confidence intervals for the relative accuracy and inverted them to yield a *P* value. Comparisons between neuroradiologist and NeuroQuant accuracy were similarly performed.

RESULTS

Asymmetry in Healthy Controls

Using data from the 46 healthy controls in our study, we observed a very slight asymmetry in volumes between the 2 hippocampi (right larger than left), as reported in the literature.[10-12] Figure 2

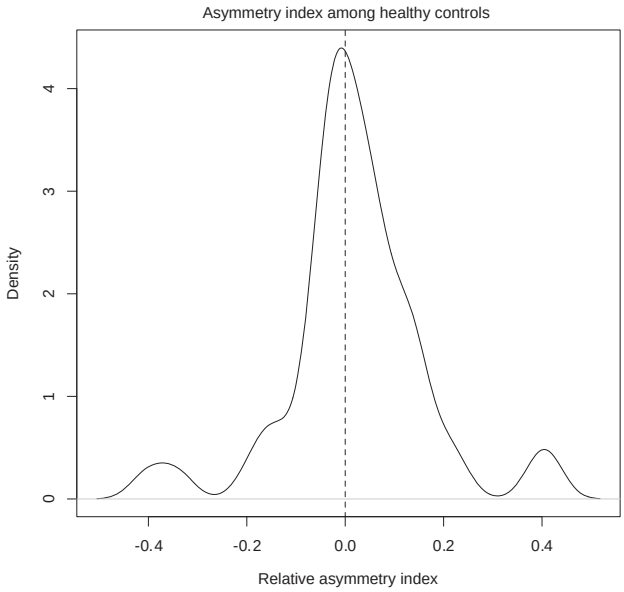

FIG 2. Control subjects' relative asymmetry indices (positive means the right hippocampus is larger than the left).

provides a depiction of the distribution of observed relative asymmetry indices, defined as right volume − left volume/left volume. The NeuroQuant mean asymmetry index among healthy patients was estimated to be 2.1% (95% CI, −2.1–6.2) in our study: This asymmetry was not significantly different from zero.

NeuroQuant Versus Neuroradiologist

On the basis of the criterion standard of pathologic specimens and definitive electroencephalography readings concurrent with clinical impressions, 36 patients had left-lateralized sclerosis, 25 had right-lateralized sclerosis, and 2 had bilateral sclerosis.

Using these 63 patients, the neuroradiologist had an estimated classification accuracy of 71.4% (95% CI, 58.5%–81.8%) with a κ statistic of 0.50 (95% CI, 0.30–0.69), suggesting moderate agreement with the criterion standard ($P < 3 \times 10^{-6}$). When only confirmed lateralized cases were used in the analysis (ie, excluding the 2 subjects with bilateral MTS), the radiologist was estimated to have an accuracy of 73.8% (95% CI, 60.7%–83.8%) with a κ statistic of 0.53 (95% CI, 0.34–0.73. This represented only very modest improvement. The estimates of accuracy for left-sided MTS (72.2%; 95% CI, 57.1%–86.2%) and right-sided MTS (76.0%; 95% CI, 58.1%–91.7%) were not significantly different.

For uncorrected hippocampus-based NeuroQuant analysis of all 63 subjects, the estimated classification accuracy of NeuroQuant was 79.4%, and the resulting κ statistic was 0.59 (95% CI, 0.39–0.79), again indicating moderate agreement with the criterion standard ($P < 2 \times 10^{-6}$). When only confirmed lateralized cases were used in the analysis, NeuroQuant had an estimated accuracy of 82.0% (95% CI, 72.1%–91.8%) and a κ statistic of 0.63 (95% CI, 0.43–0.83). This estimated accuracy was not significantly greater than that of the neuroradiologist ($P = .148$). The estimates of accuracy for left-sided MTS (83.3%; 95% CI, 70.6%–94.4%) and right-sided MTS (80.0%; 95% CI, 63.2%–95.0%) were also not significantly different.

In 12 of the 63 cases, the neuroradiologist rated the hippocampi as symmetric but based the MTS diagnosis on findings other than volumetry (signal intensity on FLAIR, morphology of hippocampus (HC), fornix-mammillary body asymmetry, and so forth). In 8/12 (66.7%) of these cases, the radiologist was correct. Three of the 4 incorrect cases were ones in which the MTS was incorrectly suggested as bilateral by the radiologist.

Of these 12 cases in which the hippocampuses were deemed to be symmetric but the radiologist identified MTS on a nonvolumetric basis, the radiologist agreed with NeuroQuant (which did quantitative hippocampus analysis) and correctly identified the side in 6 cases, agreed with NeuroQuant but both were incorrect in 2 cases, and disagreed with NeuroQuant in 4 cases. Of these 4 cases, the radiologist was correct in 2 and NeuroQuant was correct in 2. Overall accuracy when not using visual volumetric differences by the radiologist was 8/12 (66.7%). Of these 12 patients, NeuroQuant had a similar accuracy (8/12) however.

Classifications according to the neuroradiologist and NeuroQuant were discordant in 27.9% of all cases (17 of 61; 95% CI, 16.4%–39.3%). NeuroQuant was correct in 58.8% of such cases (10 of 17, 95% CI, 35.0%–82.4%). Of the 10 cases in which NeuroQuant was correct and the radiologist was wrong, we found that the radiologist relied on volume to pick the (wrong) side of MTS in 9 cases. Of the 7 cases in which NeuroQuant was wrong and the radiologist was correct, the radiologist based his or her determination on findings other than the visual assessment of volume in 2/7 cases.

Because of the slight asymmetry demonstrated in our control subjects, we re-evaluated the data after they were reclassified as showing left-sided MTS if the relative asymmetry index was <2.1% and as right-sided MTS if it was >2.1%. Under this classification rule, NeuroQuant had an estimated accuracy of 77.8% (95% CI, 65.2%–86.9%) and a κ statistic of 0.56 (95% CI, 0.35–0.76), indicating moderate agreement with the criterion standard ($P < 3 \times 10^{-5}$). This finding suggests no added benefit for correcting for the left-to-right inherent volume asymmetry in the brain. When we repeated this analysis excluding the 2 bilateral MTS cases, the accuracy of NeuroQuant was only marginally improved but was still worse than the performance assessments, not accounting for a natural asymmetry.

Neuroradiologist Threshold for Detecting Volumetric Differences

To better understand whether there is a threshold in asymmetry in delineating cases in which an experienced radiologist might be able to detect a volumetric difference between one hippocampus versus another, we performed a visual inspection of the available data, including classifications according to the criterion standard and the volumes calculated by the neuroradiologist and NeuroQuant (Fig 3). No such threshold was identified. In cases in which NeuroQuant yielded an index of asymmetry of at least 5%, 10%, or 20%, the neuroradiologist had an estimated accuracy of 75.0%, 78.9%, and 84.2%, respectively.

DISCUSSION

Despite the logic that would suggest that quantitative assessment of hippocampal volumes allows a more accurate assessment of

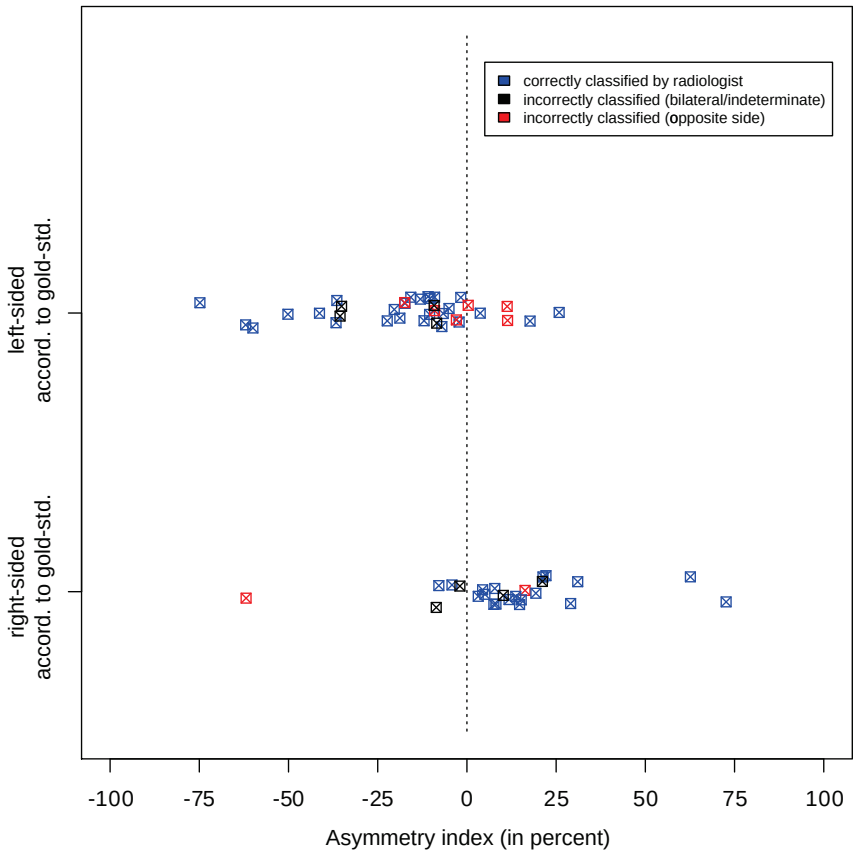

FIG 3. The relationship between the degree of asymmetry and the radiologist's classification. This plot suggests that there is no hard threshold below which the radiologist is unable to appropriately identify a case of unilateral mesial temporal sclerosis. In fact, in those cases for which the hippocampal volumes differed by >5%, 10%, and 20%, the radiologist's classification had an estimate accuracy of 75.0%, 78.9%, and 84.2%, respectively.

patients with temporal lobe epilepsy, several limitations have prevented its widespread implementation.[17,18] The anatomy of the hippocampus is quite intricate, with curved surfaces and layers of gray and white matter that render parcellation of the cortex from subcortical content a difficult task. The plane of orientation also does not lend itself to easy assessment in the axial plane: This is the plane in which neuroradiologists are often most comfortable. Additionally, because the overall volume of the hippocampus is quite small, minor manual or automated errors in calculation can lead to wide relative error bars.

Manual segmentation of hippocampi has been performed for decades both for the evaluation of MTS but also for assessing patients at risk for or with probable Alzheimer disease. The process is time-consuming and requires training as to the relevant anatomy. It is not necessarily conducive to the rapid workflow required of practicing neuroradiologists focused on efficiency and accuracy. Hippocampal volumetric accuracy is difficult to assess in vivo with live subjects, so most authors focus on reproducibility. To that end, Gonçalves Pereira et al[19] noted inter- and intraobserver error rates of approximately 6%–8% in the amygdala and piriform cortex. The volumes of these areas differed between controls and patients with MTS by 15%–20%. Achten et al, [20] by using a manual ray-tracing methodology, reported inter- and intraobserver variabilities that ranged between 3.6%–7.3% and 3.4%–5.6%, respectively, for various structures, suggesting good reproducibility.

Neuroradiologists may suggest a diagnosis of MTS even in the face of absent volumetric changes. The following findings may also suggest MTS: 1) hippocampal T2-weighted/FLAIR signal-intensity abnormalities, 2) loss of the crenated margin of the upper surface of the hippocampus, 3) gray matter–white matter blurring, 4) malrotation of the hippocampus, 5) ipsilateral mammillary body and fornical column volume loss, and 6) unilateral temporal horn dilation (sometimes as secondary findings of volume loss in the limbic system).[21-23] The ability to detect changes suggestive of MTS has been shown to be significantly correlated with the experience of the reader and the quality of the study. For example, Von Oertzen et al[24] have shown that the sensitivity for detection of MTS varies between 39% and 50% when comparing nonexpert and dedicated epilepsy expert readers of standard brain MRI, respectively. However, when given an epilepsy-specific MR imaging with appropriate sequences and protocols, the sensitivity of dedicated epilepsy expert readers increased to 91%, with a 4-fold improvement in accuracy when an epilepsy-specific protocol was performed and interpreted by expert readers over standard protocols read by general readers.[24]

Automated methods for the analysis of hippocampal volumetry have recently been published in clinical journals.[13,25] However, there have been few reports using an FDA-approved solution that could be practical in a busy clinical practice. Brewer et al[10] and Brewer[11] published results using NeuroQuant for temporal lobe volumetry in 2009. Intraclass correlations for the NeuroQuant-derived hippocampal volumes compared with manual segmentation were 0.93 (outstanding), and the intraclass correlation coefficients for 10 of 15 brain structures were >0.90 with the lowest value (still excellent at intraclass correlation coefficients of 0.61) for the nucleus accumbens.

Most recently Farid et al[13] examined the ability of NeuroQuant to predict MTS: The right-left classification accuracy was 94% for hippocampal volumes. Our dataset differs from that of Farid et al in the following manner: 1) Two patients who had bilateral MTS were initially included; 2) while Farid et al relied on video-electroencephalography for localization, nearly 40% of our cases had histopathologically proved MTS; 3) our case number ($n = 63$) is larger than the 37 cases of that group; 4) Farid et al scanned their patients on a 1.5T scanner, whereas 37 (of 63) of our patients were scanned by using a 3T scanner; and 5) we used electronic medical record reports from a wide variety of neuroradiologists with 2–30 years' experience as the clinical reports. Farid

et al confirmed the existence of a natural asymmetry, with the right hippocampus found to be larger than the left hippocampus (4.00 versus 3.82 mL, 4.6% difference): The level of asymmetry they observed differed slightly from ours. Farid et al also showed that visual inspection by radiologists was concordant with the NeuroQuant assessment in 85% of cases, whereas we had a lower agreement rate of 72.1%.[13] While NeuroQuant was correct in <60% of our discordant cases, they found quantitative analysis to be correct in 80% of their discordant cases.[13]

How good are neuroradiologists at detecting volumetric changes in the hippocampi? What is the threshold for an experienced physician? We did not detect a threshold clearly delineating scenarios in which a neuroradiologist would or would not be able to detect a volumetric change. In going from a 5%–20% difference in hippocampal volume, ranging from 1.59 to 4.7 mL overall, the radiologist's estimated accuracy ranged from 75.0% to 84.2%. However, in 9 of the 10 cases in which NeuroQuant was correct and the neuroradiologists were incorrect over lateralizing the MTS, the radiologists selected the wrong hippocampus as being the smaller one. By the same token, when the neuroradiologists used findings other than volumetry to select a side of MTS, they were correct 67% (8/12) of the time, but this was dominated by misclassifications of bilateral MTS.

Coan et al[26] have suggested that adding T2 relaxometry to automated T1-weighted-based volumetry of the hippocampus can increase interpretation accuracy. They found that the use of combined hippocampal volumetry and T2 relaxometry increased the sensitivity to detect MR imaging signs of MTS, notably reclassifying 28% of patients read as having normal findings on visual inspection alone. While automated volumetry detected atrophy in 119 of 125 (95%) patients who were identified by radiologists as having MTS, it identified an additional 10 of 78 patients (12.8%) initially read as having normal findings by the radiologists. T2 relaxometry analysis detected hyperintense T2 signal in 103 of the 125 cases (82.4%) of radiologist-detected MTS and in 15 of 78 subjects (19.2%) whom the radiologist classified as having normal findings. Coan et al used an automatic volumetric analysis with FreeSurfer software (Version 5.1.0; http://surfer.nmr.mgh.harvard.edu) from a T1-weighted dataset. As of this publication, FreeSurfer has not been FDA-approved and is not being used clinically in our setting. While both NeuroQuant and FreeSurfer use a probabilistic atlas for labeling, the adaptation of this approach for clinical use and FDA clearance required adaptation of the probabilistic atlas and complete rebuilding of the code by using Good Manufacturing Practices by NeuroQuant. Indeed FreeSurfer and NeuroQuant often do not return identical volumetry values, despite both using a similar underlying algorithm.

Given the report that epilepsy expert readers have a sensitivity for MTS of 91%,[20] why is the accuracy reported in the current study only 71.4%? Some factors are the following: Many cases of MTS are bilateral; the cases that get sent to a quarternary care hospital in academia are often not straightforward and are the ones that are confounding the outside physicians; our study was stricter in making sure the cases were "proved" (requiring pathology for more cases); and our experience is more the "norm" for a neuroradiology academic practice.

Although the use of both 1.5T and 3T datasets in this cohort may seem to be a limitation of the study, hippocampal volume measures obtained by using 1.5T and 3T scanners have not been found to differ.[27,28] The limitations of this study include the limited percentage of cases that had histologic confirmation; nevertheless, our rate of pathologic proof is greater than that of most other published series. We also struggled with the inclusion of bilateral MTS cases in the analysis, given that we were using an asymmetry index and not an absolute classification of individual hippocampal volumes. We used the radiologist's interpretation of the MR images that not only included volumetry but also an assessment of signal intensity and morphology.

CONCLUSIONS

In assessing asymmetry in hippocampal sizes and thereby predicting the side of MTS, an automated FDA-approved volumetric analysis software package performed as well as experienced neuroradiologists who reviewed the scans for all MTS MR imaging findings. In those cases in which the radiologist and the computer analysis disagreed, NeuroQuant performed slightly better (10 versus 7 of 17). Implementing this quantitative analysis may assist neuroradiologists in their assessment of hippocampal asymmetry, even though small changes in right-to-left hippocampal volumes can be detected by the neuroradiologists.

Disclosures: Sarah H. Ying—*UNRELATED*: *Employment*: Johns Hopkins University, Pfizer, Inc; *Grants/Grants Pending*: National Institutes of Health. David M. Yousem—*UNRELATED*: *Consultancy*: medicolegal; *Expert Testimony*: medicolegal expert witness; *Payment for Lectures (including service on Speakers Bureaus)*: American College of Radiology Education Center, *Comments*: revenue shared with Johns Hopkins School of Medicine; *Royalties*: 3 Elsevier books; *Payment for Development of Educational Presentations*: CMEInfo.com, *Comments*: revenue to Johns Hopkins.* *Money paid to the institution.

REFERENCES

1. Manford M, Hart YM, Sander JW, et al. **National General Practice Study of Epilepsy (NGPSE): partial seizure patterns in a general population.** *Neurology* 1992;42:1911–17
2. Labate A, Gambardella A, Andermann E, et al. **Benign mesial temporal lobe epilepsy.** *Nat Rev Neurol* 2011;7:237–40
3. Falconer MA, Serafetinides EA, Corsellis JA. **Etiology and pathogenesis of temporal lobe epilepsy.** *Arch Neurol* 1964;10:233–48
4. Theodore WH, Bhatia S, Hatta J, et al. **Hippocampal atrophy, epilepsy duration, and febrile seizures in patients with partial seizures.** *Neurology* 1999;52:132–36
5. Knowlton RC. **Multimodality imaging in partial epilepsies.** *Curr Opin Neurol* 2004;17:165–72
6. Reutens DC, Stevens JM, Kingsley D, et al. **Reliability of visual inspection for detection of volumetric hippocampal asymmetry.** *Neuroradiology* 1996;38:221–25
7. Spencer SS, McCarthy G, Spencer DD. **Diagnosis of medial temporal lobe seizure onset: relative specificity and sensitivity of quantitative MRI.** *Neurology* 1993;43:2117–24
8. Jackson GD, Berkovic SF, Duncan JS, et al. **Optimizing the diagnosis of hippocampal sclerosis using MR imaging.** *AJNR Am J Neuroradiol* 1993;14:753–62
9. Cendes F, Andermann F, Gloor P, et al. **Atrophy of mesial structures in patients with temporal lobe epilepsy: cause or consequence of repeated seizures?** *Ann Neurol* 1993;34:795–801
10. Brewer JB, Magda S, Airriess C, et al. **Fully-automated quantification of regional brain volumes for improved detection of focal atrophy in Alzheimer disease.** *AJNR Am J Neuroradiol* 2009;30:578–80
11. Brewer JB. **Fully-automated volumetric MRI with normative ranges: translation to clinical practice.** *Behav Neurol* 2009;21:21–28
12. Kovacevic S, Rafii MS, Brewer JB; Alzheimer's Disease Neuroimaging

Inititative. **High-throughput, fully-automated volumetry for prediction of MMSE and CDR decline in mild cognitive impairment.** *Alzheimer Dis Assoc Disord* 2009;23:139–45
13. Farid N, Girard HM, Kemmotsu N, et al. **Temporal lobe epilepsy: quantitative MR volumetry in detection of hippocampal atrophy.** *Radiology* 2012;264:542–50
14. Pedraza O, Bowers D, Gilmore R. **Asymmetry of the hippocampus and amygdala in MRI volumetric measurements of normal adults.** *J Int Neuropsychol Soc* 2004;10:664–78
15. Woolard AA, Heckers S. **Anatomical and functional correlates of human hippocampal volume asymmetry.** *Psychiatry Res* 2012;201:48–53
16. Rogers BP, Sheffield JM, Luksik AS, et al. **Systematic error in hippocampal volume asymmetry measurement is minimal with a manual segmentation protocol.** *Front Neurosci* 2012;6:179
17. Cendes F, Leproux F, Melanson D, et al. **MRI of amygdala and hippocampus in temporal lobe epilepsy.** *J Comput Assist Tomogr* 1993;17:206–10
18. Van Paesschen W, Sisodiya S, Connelly A, et al. **Quantitative hippocampal MRI and intractable temporal lobe epilepsy.** *Neurology* 1995;45:2233–40
19. Gonçalves Pereira PM, Insausti R, Artacho-Pérula E, et al. **MR volumetric analysis of the piriform cortex and cortical amygdala in drug-refractory temporal lobe epilepsy.** *AJNR Am J Neuroradiol* 2005;26:319–32
20. Achten E, Deblaere K, De Wagter C, et al. **Intra- and interobserver variability of MRI-based volume measurements of the hippocampus and amygdala using the manual ray-tracing method.** *Neuroradiology* 1998;40:558–66
21. Jackson GD, Berkovic SF, Tress BM, et al. **Hippocampal sclerosis can be reliably detected by magnetic resonance imaging.** *Neurology* 1990;40:1869–75
22. Berkovic SF, Andermann F, Olivier A, et al. **Hippocampal sclerosis in temporal lobe epilepsy demonstrated by magnetic resonance imaging.** *Ann Neurol* 1991;29:175–82
23. Ozturk AO, Yousem DM, Mahmood A, et al. **Prevalence of asymmetry of mamillary body and fornix size on MR imaging.** *AJNR Am J Neuroradiol* 2008;29:384–87
24. Von Oertzen J, Urbach H, Jungbluth S, et al. **Standard magnetic resonance imaging is inadequate for patients with refractory focal epilepsy.** *J Neurol Neurosurg Psychiatry* 2002;73:643–47
25. Hammers A, Heckemann R, Koepp MJ, et al. **Automatic detection and quantification of hippocampal atrophy on MRI in temporal lobe epilepsy: a proof-of-principle study.** *Neuroimage* 2007;36:38–47
26. Coan AC, Kubota B, Bergo FP, et al. **3T MRI quantification of hippocampal volume and signal in mesial temporal lobe epilepsy improves detection of hippocampal sclerosis.** *AJNR Am J Neuroradiol* 2014;35:77–83
27. Briellmann RS, Syngeniotis A, Jackson GD. **Comparison of hippocampal volumetry at 1.5 T and at 3 T.** *Epilepsia* 2001;42:1021–24
28. Scorzin JE, Kaaden S, Quesada CM, et al. **Volume determination of amygdala and hippocampus at 1.5 and 3.0 T MRI in temporal lobe epilepsy.** *Epilepsy Res* 2008;82:29–37

Perfusion Deficits and Mismatch in Patients with Acute Lacunar Infarcts Studied with Whole-Brain CT Perfusion

S. Rudilosso, X. Urra, L. San Román, C. Laredo, A. López-Rueda, S. Amaro, L. Oleaga, and Á. Chamorro

ABSTRACT

BACKGROUND AND PURPOSE: The incidence and significance of perfusion abnormalities on brain imaging in patients with lacunar infarct are controversial. We studied the diagnostic yield of CTP and the type of perfusion abnormalities in patients presenting with a lacunar syndrome and in those with MR imaging–confirmed lacunar infarcts.

MATERIALS AND METHODS: A cohort of 33 patients with lacunar syndrome underwent whole-brain CTP on admission. Twenty-eight patients had an acute ischemic lesion at follow-up MR imaging; 16 were classified as lacunar infarcts. Two independent readers evaluated NCCT and CTP to compare their diagnostic yield. In patients with DWI-confirmed lacunar infarcts and visible deficits on CTP, the presence of mismatch tissue was measured by using different perfusion thresholds.

RESULTS: The symptomatic acute lesion was seen on CTP in 50% of patients presenting with a lacunar syndrome compared with only 17% on NCCT, and in 62% on CTP compared with 19% on NCCT, respectively, in patients with DWI-confirmed lacunar infarcts. CTP was more sensitive in supratentorial than in infratentorial lesions. In the nonblinded analysis, a perfusion deficit was observed in 12/16 patients with DWI-confirmed lacunar infarcts. The proportion of mismatch tissue was similar in patients with lacunar infarcts or nonlacunar strokes (32% versus 36%, $P = .734$).

CONCLUSIONS: Whole-brain CTP is superior to NCCT in identifying small ischemic lesions, including lacunar infarcts, in patients presenting with a lacunar syndrome. Perfusion deficits and mismatch are frequent in lacunar infarcts, but larger studies are warranted to elucidate the clinical significance of these CTP findings.

ABBREVIATIONS: LI = lacunar infarct; TOAST = Trial of Org 10172 in Acute Stroke Treatment; TTD = time to drain

Small-vessel disease is common and causes cognitive, psychiatric, and physical disability.[1] Lacunar infarcts (LIs) are one of the main manifestations of small-vessel disease, accounting for 10%–20% of all ischemic strokes, and they often present with the characteristic classic lacunar syndromes: pure motor hemiparesis, pure sensory stroke, sensorimotor stroke, ataxic hemiparesis, and dysarthria–clumsy hand syndrome. LIs are usually <1.5 cm wide and are often located in the territory of deep perforating arteries such as lenticulostriate, thalamoperforant, or paramedian territories. However, LIs can also result from in situ occlusion of single superficial perforators from pial arteries. LIs are thought to be related to arteriopathy of small blood vessels in the brain, either because of lipohyalinosis or microatheroma.[2] Less frequent causes are stenosis of a large vessel or microembolization.

The sensitivity of neuroimaging techniques in acute LI is variable, ranging from 40% for NCCT scans,[3,4] 80% for MR imaging,[5] and up to 94% for DWI.[6] Conflicting results have been reported regarding the presence of perfusion deficits in patients with LI,[7-11] with sensitivities varying from 0% to 68% in studies using MR imaging[12-14] and from 17% to 47% with CTP.[15,16] In fact, LI is considered one of the causes of false-negative CTP findings.[10,11] Some reports suggest that the presence of a perfusion deficit is associated with worse outcome in patients with LIs.[8,13] Regarding the presence of mismatch, a study using perfusion MR imaging did not find a mismatch between perfusion and diffusion sequences in strokes involving perforating arteries, but these results could be explained by the low resolution of their imaging methods.[12]

In this study, we first assessed the clinical utility of CTP in the

Received November 18, 2014; accepted after revision December 22.

From the Functional Unit of Cerebrovascular Diseases (S.R., X.U., L.S.R., C.L., A.L.-R., S.A., L.O., Á.C.) and Department of Radiology (L.S.R., A.L.-R., L.O.), Hospital Clínic, Barcelona, Spain; Institut d'Investigacions Biomèdiques August Pi i Sunyer (X.U., S.A., Á.C.), Barcelona, Spain; and Department of Medicine (Á.C.), School of Medicine, University of Barcelona, Barcelona. Spain.

Please address correspondence to Xabier Urra, MD, PhD, Institute of Neurosciences, 170 Villarroel, 08036 Barcelona, Spain; e-mail: xurra@clinic.cat; @xabierurra

Indicates article with supplemental on-line table.

Indicates article with supplemental on-line photo.

http://dx.doi.org/10.3174/ajnr.A4303

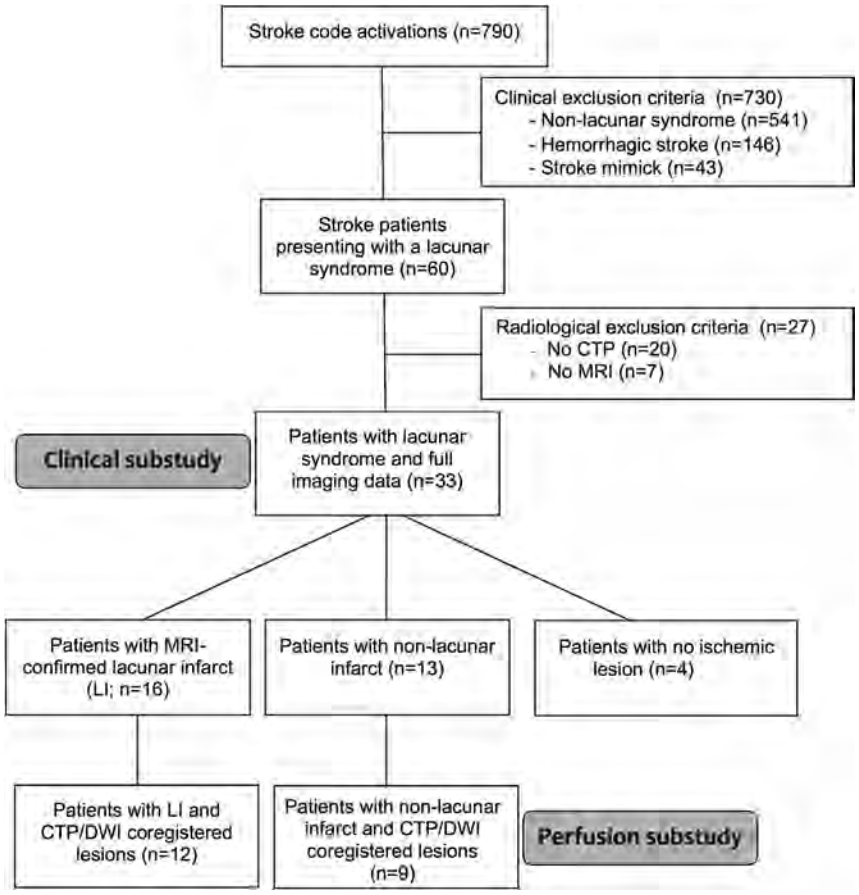

FIG 1. Flow chart describing the patients in the study.

real-life scenario of patients presenting to the emergency department with a lacunar syndrome. Then, we studied the details of the perfusion abnormalities in a subgroup of patients with MR imaging–confirmed LIs and compared them with those of patients with nonlacunar infarcts.

MATERIALS AND METHODS

Patients

Because CTP is routinely used in our institution in the work-up of patients arriving in the first hours after stroke, we studied all patients in the Stroke Unit registry of the Hospital Clínic, Barcelona, admitted from January 2009 to December 2012, in whom the Stroke Code was activated (patients within 8 hours of stroke onset and wake-up strokes). The description of the study population is summarized in Fig 1.

Twenty-four patients (73%) received treatment with tPA within 4.5 hours after a head NCCT ruled out intracranial hemorrhage, and CTP was performed just before ($n = 4$) or during tPA perfusion ($n = 20$). Stroke etiology was assigned by using the Trial of Org 10172 in Acute Stroke Treatment (TOAST) criteria[17] after a complete diagnostic work-up. All patients were admitted to an intermediate care Stroke Unit and were treated by stroke neurologists certified in the use of the NIHSS. The demographics, risk factors, clinical course, imaging data, concomitant therapies, and functional outcome were prospectively collected and stored in the Hospital Clínic Stroke Unit data base. The neurologic course was assessed at arrival, at day 1 after admission, at day 7 or discharge, and at day 90. Functional outcome was assessed by using the mRS at a follow-up visit at 3 months. Because many of the patients were expected to have mild strokes, favorable recovery was defined as an mRS score of ≤ 1.

The study protocol was approved by the institutional review board of the center, and the patients or their legal representatives signed a written informed consent if they were treated with tPA and were older than 80 years of age.

Neuroimaging

NCCT and CTP were performed at admission at a median (interquartile range) delay of 245 minutes (range, 175–344 minutes) after stroke onset on a Somatom Definition Flash 128-section dual-source CT system (Siemens, Erlangen, Germany) with a 98-mm z-coverage and 26 time points acquired at each 1.5 seconds (total acquisition time, 39 seconds). Fifty milliliters of nonionic iodinated contrast was administered intravenously at 5 mL/s by using a power injector. CT perfusion imaging parameters were 80 kV(peak), 250 mAs, 1.5-second rotation, and 2-mm thickness, and color maps were reformatted at 4-mm thickness. CTP maps were calculated with syngo CT Neuro Perfusion VA20 (Siemens), which uses singular-value decomposition without delay correction and automatically performs motion correction and selects an arterial input function from an unaffected artery and venous output function from a large draining vein. The perfusion maps generated were the following: CBF, CBV, MTT, time to maximum of residue function maps, TTP, time to drain (TTD), and MIP. Ischemic lesions usually show decreased CBV and CBF and prolonged measures of time maps (Fig 2*A*).

Two experienced physicians (a neurologist and a neuroradiologist) evaluated the NCCT and the CTP maps and were only aware of the side of the clinical symptoms but were blinded to the follow-up MR imaging data and clinical outcome. They described the presence of perfusion deficits (with lacunar or nonlacunar appearance) and their location. A consensus reading was achieved in cases of differences in the individual readings.

MR imaging was performed on a 1.5T scanner at a median delay of 26 hours (interquartile range, 18–43 hours) after stroke onset. The stroke MR imaging protocol included a DWI sequence, obtained with b-values of 1000, 5-mm section thickness, and 128×128 matrix. DWI hyperintensities were analyzed in isotropic images. A vascular neurologist (X.U.) confirmed the final diagnosis by reviewing the patient's clinical course and DWI findings and by using Amira software (www.amira.com) segmented the infarct in DWI by a semiautomatic procedure, selecting DWI

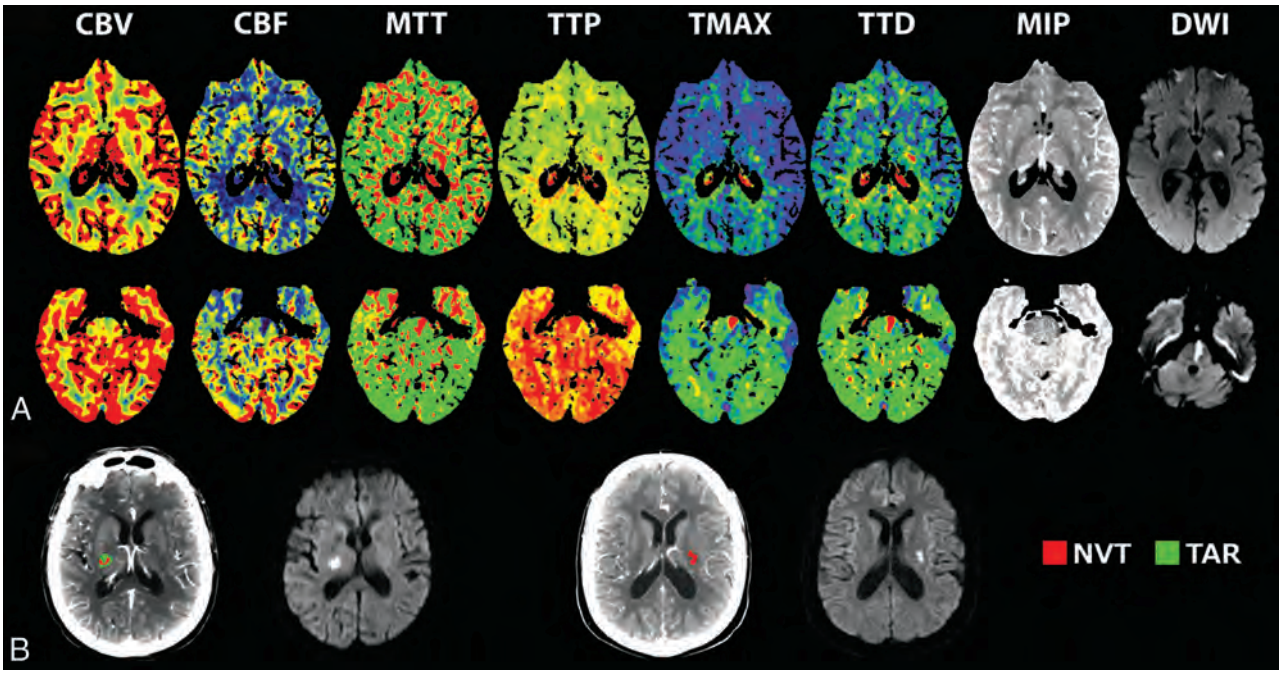

FIG 2. Neuroimaging methods. *A*, CTP maps and DWI lesions in a patient with a supratentorial lacunar infarct (*upper row*) and in a patient with a brain stem paramedian infarct (*lower row*). *B*, Representative examples of the quantification of NVT and TAR and the final DWI lesion in a patient with mismatch (*left*) and a patient with no mismatch (*right*). NVT indicates nonviable tissue; TAR, tissue at risk.

ROIs with a signal intensity exceeding by >3 SDs the intensity of the contralateral hemisphere. The volume of the DWI lesion was calculated, and the lesion shape was categorized as previously described.[18] To be categorized as LI on DWI, the infarcts had to be located within the territories of the lenticulostriate, thalamoperforant, paramedian, or white matter long medullary arteries, and they had to be <1.767 cm^3 (the volume of a sphere with a diameter of 1.5 cm).[19] This strict definition was chosen to describe the perfusion characteristics of a homogeneous group of patients with typical LIs.

For the analysis of the perfusion abnormalities, an image-processing pipeline was developed by using in-house fully automated software running in Matlab (Version 2013a; MathWorks, Natick, Massachusetts) to implement a comprehensive analysis of the perfusion maps. A neurologist (X.U.) evaluated time maps (MTT, time to maximum of residue function maps) and semiautomatically delineated the regions defining perfusion abnormalities. This ROI was then registered to perfusion maps generated by using MIStar (Apollo Medical Imaging Technology, Melbourne, Australia), a software that uses singular-value decomposition with a delay correction.[20] Within this ROI, we used a range of relative and absolute thresholds in the CBF and time maps to define infarct core or nonviable tissue and critically hypoperfused or tissue at risk, respectively (Fig 2*B*). "Mismatch" was defined as a greater extent of tissue at risk than nonviable tissue.[21] In an effort not to underestimate the size of the lesion defined in time maps, we applied a dilation filter to the ROI. Nonviable tissue or infarct core was segmented on the basis of a relative CBF threshold of 30% of the value in the contralateral hemisphere, and tissue at risk, on the basis of a delay time of 2 seconds.[22] Additionally, we explored the presence of mismatch by using various combinations of CBF (relative CBF of <20%–40%) and delay time thresholds (>2 or 3 seconds).

For the coregistration of the infarct, each perfusion CT map was coregistered to the corresponding 24- to 48-hour DWI. Using Statistical Parametric Mapping (SPM8; http://www.fil.ion.ucl.ac.uk/spm/software/spm8), we automatically subjected the DWI to a sequence of two 3D registration procedures to match the CTP map by using TOF as an intermediary. The first step was a 6-*df* coregistration of the DWI to the TOF. Following this step, we performed another rigid coregistration of the TOF to the CTP, and we finally applied the obtained transformation matrix to the DWI, placing CTP maps, DWI, and TOF in the register. Once CTP and DWI were in the register, we checked that the lesions defined in DWI and CTP were at the same anatomic and spatial locations.

Statistics

Normal distribution of all studied variables was assessed. Continuous variables were compared with Student *t*, Mann-Whitney, or Kruskal-Wallis tests as appropriate. Correlations were assessed with Spearman coefficients, and categoric variables were compared with the Fisher exact test. Interrater agreement was assessed with the κ statistic. The level of significance was established at a 2-tailed value of $P < .05$. All tests were performed by using SPSS, Version 20.0 (IBM, Armonk, New York).

RESULTS

Clinical and MR Imaging Characteristics of Patients Presenting with Lacunar Syndrome

The main clinical characteristics of the study patients are summarized in the Table. Most patients presented with a sensory motor syndrome (34%) or a pure motor syndrome (30%). According to

Clinical characteristics of the study population

Patients	Lacunar Syndrome (*n* = 33)	MRI-Confirmed LI (*n* = 16)
Age (yr) (mean) (SD)	65.5 (11)	62.6 (10)
Sex (%) (male/female)	70:30	62.5:37.5
tPA (%)	73	62.5
NIHSS score (median) (IQR)		
Admission	4 (3–5.5)	3.5 (3–4.5)
24 Hours	3 (1–5)	3 (2–4.5)
Discharge	2 (1–4)	2.5 (1.5–4)
Day 90	1 (0–2)	1 (0–2)
Excellent outcome (%)	48	44
TOAST (%)		
Lacunar	64	81
Large-artery atherosclerosis	12	0
Cardioembolic	3	0
Undetermined	21	19

Note:—IQR indicates interquartile range.

the TOAST criteria, most of the strokes were related to small-artery occlusions; only 3 patients had brain MR imaging findings consistent with LI but diagnosed as infarcts of undetermined origin due to the coexistence of ipsilateral carotid stenosis of >50% ($n = 2$) or atrial fibrillation ($n = 1$). Only 5 patients (2 with MR imaging–confirmed LIs) experienced neurologic deterioration.

On MR imaging, 29 of 33 patients (88%) had an ischemic lesion on DWI and 4 patients had negative findings on MRI, despite the presence of focal symptoms or signs for >24 hours (1 pure sensory, 1 pure motor, 1 ataxic hemiparesis, and 1 sensorimotor syndrome). Thirteen patients had non-LIs, and 16 had LIs (additional information can be found in On-line Fig 1 and On-line Table 1). These involved the thalamoperforator arteries in 7 patients, the territory of paramedian arteries in 6, the lenticulostriate territory in 2, and the white matter long medullary arteries in 1 patient. The median volume of LIs was 0.62 cm^3, and most had a tubular (56%) or nodular (37.5%) shape.

Diagnostic Yield of CTP in Patients with Lacunar Syndrome and MR Imaging–Confirmed LIs

CTP results matched those of the follow-up MR imaging in 17/33 cases, while NCCT did so in only 6/33 cases. Both the sensitivity and positive predictive value for the symptomatic acute lesions were higher for CTP compared with NCCT (50% versus 18%, $P = .023$%, and 54% versus 20%, $P = .05$, respectively). The negative predictive value was similar for CTP and CT (43% versus 37.5%, $P = 1.0$), and specificity was the same (20%). Interrater agreement was also equal for NCCT and CTP ($\kappa = 0.61$). CTP was more sensitive for supratentorial lesions compared with infratentorial lesions (65% versus 16%, $P = .011$). Among the 12 false-positive cases, in 6 cases, the CTP actually showed small perfusion deficits, but they were greater than the 1.767-cm^3 limit defined for LIs. In 5 cases, the perfusion maps showed a small hypoperfusion, but the stroke was found to be in another territory on the DWI; and in 1 case, a CTP hypoperfusion had negative findings on follow-up DWI. In the subgroup of 16 cases with MR imaging–confirmed LI, CTP also had superior sensitivity and positive predictive value to NCCT (62.5% versus 19%, $P = .029$%, and 83% versus 43%, $P = .129$, respectively). The proportion of CTP studies with negative findings was not significantly different between patients with lacunar syndrome treated and not treated with tPA

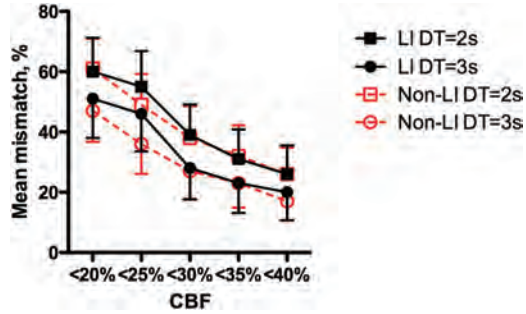

FIG 3. Rates of mismatch tissue according to different definitions of nonviable tissue and tissue at risk in patients with LI and nonlacunar infarcts. Values are mean and standard error of the mean. DT indicates delay time.

(39.4% and 12.1%, $P = .59$) or in the LI group (37.5% and 18.8%, $P = .55$).

Although the evaluators assessed all perfusion maps together, the infarcts were best seen on TTD maps, which often showed the LIs as small red dots that were easy to distinguish from the background (On-line Fig 2). Among the 16 cases with MR imaging–confirmed LI, CTP with negative findings was due to movement artifacts in 2 patients and to lesions located in the brain stem in 4 patients. In 2 of them, small perfusion deficits could be seen after reviewing the DWI, but the lesions were either too small or poorly differentiated from the background.

Perfusion Deficits in Patients with MR Imaging–Confirmed LIs and in Other Strokes

In the nonblinded analysis, a clear perfusion abnormality to be segmented was identified in 12/16 of LIs and in 8/12 of nonlacunar infarcts within the ROIs of lesions on DWI. Mismatch was found in 5 (42%) of the patients with measurable perfusion deficits by using the standard thresholds, and the mean percentage of mismatch volume ranged from 20% by using the strictest thresholds to 65% in both patients with MR imaging–confirmed LI and those with nonlacunar strokes (Fig 3). The proportion of mismatch patients ranged from 17% to 50% in patients with LIs and from 11% to 56% in patients with nonlacunar strokes.

Although clinical progression was more frequent in patients without mismatch (43% versus 0%, $P = .205$), the rate of improvement after thrombolysis and functional outcome at 3 months and the rest of the clinical features were similar between patients with and without mismatch (data not shown).

DISCUSSION

Previous studies have reported conflicting results regarding perfusion abnormalities in patients with lacunar infarcts, probably reflecting differences in available technology. The results of this study by using whole-brain-coverage CTP are very similar to those of a recent study by using perfusion MR imaging in patients with LI that reported perfusion deficits in 10/16 patients.[14] The sensitivity of whole-brain CTP was much higher than that of NCCT for acute stroke and in particular for LI, and the greater sensitivity of CTP in this study may reflect both whole-brain coverage of perfusion maps and the refinement of current parameters to assess perfusion maps. Studies with negative findings were due to very small lesions that were poorly differentiated from the

background, especially in the brain stem; and in a few cases, they were due to poor image quality from movement artifacts. In studies with no movement artifacts and after reviewing the results of the DWI, we could identify a clear perfusion deficit in most patients with LIs.

The rate of clinical deterioration was rather low in patients with LIs, and all patients with clinical deterioration had a no-mismatch profile. However, the number of patients with MR imaging–confirmed LIs was too low to draw definite conclusions on the clinical consequences of the perfusion deficits in these patients. Larger studies will be required to establish whether the presence of mismatch in LIs represents a predictor of clinical recovery as it did for nonlacunar strokes,[23] particularly after the administration of thrombolytic therapy.[24] The specificity of CTP to show MR imaging–confirmed lacunar stroke was low because some small hypoperfused lesions were not confirmed to be true LIs by using a strict DWI volume limit, but sensitivity was higher and a whole-brain-coverage CTP in the first hours after symptom onset may be helpful in evaluating patients in whom the diagnosis is not clear, even when the symptoms are mild.

TTD maps provided high-contrast images that were most useful in identifying small perfusion deficits. TTD is a recently introduced time-related perfusion parameter defined as the sum of the time from arterial enhancement to tissue enhancement and MTT.[25] Condensing both pathologic changes in contrast bolus delay time from arterial enhancement to tissue enhancement and tissue transit time, TTD describes the time of contrast medium washout and is very sensitive to all kinds of hemodynamic disturbances.[26]

It has been argued that patients with true LIs should not have detectable perfusion deficits and/or that they should have no mismatch between infarcted tissue and hypoperfused tissue.[12] This study suggests that the hemodynamic abnormalities of LIs, though small, are very similar to those described in infarcts resulting from occlusion of greater vessels (it has been claimed that lacunes are just small strokes).[27] The hypoperfusion in LIs may reflect the fact that occlusions of small arterioles are not compensated by dilation of neighboring arterioles.[28] Although there are contradictory statements in the literature regarding intraparenchymal arteriolar-to-arteriolar anastomoses,[29] the capillary bed of the brain comprises an attenuated network of intercommunicating vessels, and dilation in capillaries after penetrating arteriole occlusion in the rat brain allows some collateral flow from one arteriolar territory to neighbor territories.[28] This could result in less severely hypoperfused areas with mismatch in CTP maps.

In addition to hypoperfusion, other mechanisms may contribute to the final infarct after occlusion of small vessels. In experimental models, these lesions are accompanied by activation of inflammatory cells,[30] and extensive increases in vascular permeability have been described in patients with small-vessel disease and in particular LI.[31] Although we have seen patients in whom the final infarct was greater than the initial hypoperfused area, we were not able to accurately measure the initial ischemic volume, and therefore lesion expansion, because the segmentation of the perfusion abnormalities was focused on delineating the hypoperfusion within the DWI lesion.

The main limitation of this study is its small sample size, despite studying all consecutive patients arriving at our center for the 3 years in which the Stroke Code was activated. The low percentage of patients with a lacunar syndrome among them is probably due to the lower clinical severity of these strokes. CTP was not performed in 20 patients because acute revascularization therapies were not considered in patients with milder symptoms. Therefore, these findings cannot be extrapolated to patients with other clinical presentations or to LIs assessed more protractedly after the onset of symptoms, given the dynamic nature of perfusion data after acute stroke. The small size of LIs is also challenging for CTP-DWI coregistration, but its accuracy was manually confirmed. Thus, we do not think that the results are less accurate than those in nonlacunar infarcts.

CONCLUSIONS

These results suggest that whole-brain CTP technology can identify abnormal perfusion maps in 62.5% of patients with DWI-confirmed LI, mostly in supratentorial lesions. The rate of mismatch in patients with perfusion deficits was similar to that in patients with other strokes, suggesting that some collateral flow exists in human microcirculation after the occlusion of small penetrating vessels. However, further study is warranted to elucidate whether the presence of mismatch in patients with LI predicts a better clinical outcome and might even be used to select candidates for new therapies, for example, to receive thrombolytic therapy after the established 4.5-hour window.

ACKNOWLEDGMENTS

We thank Dr Martha Vargas for her assistance in developing the patient data base.

REFERENCES

1. Wardlaw JM, Smith C, Dichgans M. **Mechanisms of sporadic cerebral small vessel disease: insights from neuroimaging.** *Lancet Neurol* 2013;12:483–97
2. Arboix A, Martí-Vilalta JL. **Lacunar stroke.** *Expert Rev Neurother* 2009;9:179–96
3. Chamorro A, Sacco RL, Mohr JP, et al. **Clinical-computed tomographic correlations of lacunar infarction in the Stroke Data Bank.** *Stroke* 1991;22:175–81
4. Arboix A, Martí-Vilalta JL, García JH. **Clinical study of 227 patients with lacunar infarcts.** *Stroke* 1990;21:842–47
5. Hommel M, Besson G, Le Bas JF, et al. **Prospective study of lacunar infarction using magnetic resonance imaging.** *Stroke* 1990;21:546–54
6. Schonewille WJ, Tuhrim S, Singer MB, et al. **Diffusion-weighted MRI in acute lacunar syndromes: a clinical-radiological correlation study.** *Stroke* 1999;30:2066–69
7. Reichenbach JR, Röther J, Jonetz-Mentzel L, et al. **Acute stroke evaluated by time-to-peak mapping during initial and early follow-up perfusion CT studies.** *AJNR Am J Neuroradiol* 1999;20:1842–50
8. Yamada M, Yoshimura S, Kaku Y, et al. **Prediction of neurologic deterioration in patients with lacunar infarction in the territory of the lenticulostriate artery using perfusion CT.** *AJNR Am J Neuroradiol* 2004;25:402–08
9. Kane I, Hand PJ, Rivers C, et al. **A practical assessment of magnetic resonance diffusion-perfusion mismatch in acute stroke: observer variation and outcome.** *J Neurol* 2009;256:1832–38
10. Campbell BC, Weir L, Desmond PM, et al. **CT perfusion improves diagnostic accuracy and confidence in acute ischaemic stroke.** *J Neurol Neurosurg Psychiatry* 2013;84:613–18
11. Biesbroek JM, Niesten JM, Dankbaar JW, et al. **Diagnostic accuracy**

of CT perfusion imaging for detecting acute ischemic stroke: a systematic review and meta-analysis. *Cerebrovasc Dis* 2013;35:493–501
12. Gerraty RP, Parsons MW, Barber PA, et al. **Examining the lacunar hypothesis with diffusion and perfusion magnetic resonance imaging.** *Stroke* 2002;33:2019–24
13. Poppe AY, Coutts SB, Kosior J, et al. **Normal magnetic resonance perfusion-weighted imaging in lacunar infarcts predicts a low risk of early deterioration.** *Cerebrovasc Dis* 2009;28:151–56
14. Förster A, Kerl HU, Wenz H, et al. **Diffusion- and perfusion-weighted imaging in acute lacunar infarction: is there a mismatch?** *PLoS One* 2013;8:e77428
15. Mayer TE, Hamann GF, Baranczyk J, et al. **Dynamic CT perfusion imaging of acute stroke.** *AJNR Am J Neuroradiol* 2000;21:1441–49
16. Maruya J, Yamamoto K, Ozawa T, et al. **Simultaneous multi-section perfusion CT and CT angiography for the assessment of acute ischemic stroke.** *Acta Neurochir (Wien)* 2005;147:383–91; discussion 391–92
17. Adams HP Jr, Bendixen BH, Kappelle LJ, et al; TOAST Investigators. **Classification of subtype of acute ischemic stroke: definitions for use in a multicenter clinical trial.** *Stroke* 1993;24:35–41
18. Hervé D, Mangin JF, Molko N, et al. **Shape and volume of lacunar infarcts: a 3D MRI study in cerebral autosomal dominant arteriopathy with subcortical infarcts and leukoencephalopathy.** *Stroke* 2005;36:2384–88
19. Gerraty RP, Parsons MW, Alan Barber P, et al. **The volume of lacunes.** *Stroke* 2001;32:1937–38
20. Bivard A, Levi C, Spratt N, et al. **Perfusion CT in acute stroke: a comprehensive analysis of infarct and penumbra.** *Radiology* 2013;267:543–50
21. Obach V, Oleaga L, Urra X, et al. **Multimodal CT-assisted thrombolysis in patients with acute stroke: a cohort study.** *Stroke* 2011; 42:1129–31
22. Campbell BC, Christensen S, Levi CR, et al. **Cerebral blood flow is the optimal CT perfusion parameter for assessing infarct core.** *Stroke* 2011;42:3435–40
23. Wechsler LR. **Imaging evaluation of acute ischemic stroke.** *Stroke* 2011;42:S12–15
24. Kidwell CS, Alger JR, Saver JL. **Evolving paradigms in neuroimaging of the ischemic penumbra.** *Stroke* 2004;35(11 suppl 1):2662–65
25. Thierfelder KM, Sommer WH, Baumann AB, et al. **Whole-brain CT perfusion: reliability and reproducibility of volumetric perfusion deficit assessment in patients with acute ischemic stroke.** *Neuroradiology* 2013;55:827–35
26. Abels B, Klotz E, Tomandl BF, et al. **Perfusion CT in acute ischemic stroke: a qualitative and quantitative comparison of deconvolution and maximum slope approach.** *AJNR Am J Neuroradiol* 2010;31:1690–98
27. Millikan C, Futrell N. **The fallacy of the lacune hypothesis.** *Stroke* 1990;21:1251–57
28. Nishimura N, Rosidi NL, Iadecola C, et al. **Limitations of collateral flow after occlusion of a single cortical penetrating arteriole.** *J Cereb Blood Flow Metab* 2010;30:1914–27
29. Moody DM, Bell MA, Challa VR. **Features of the cerebral vascular pattern that predict vulnerability to perfusion or oxygenation deficiency: an anatomic study.** *AJNR Am J Neuroradiol* 1990;11:431–39
30. Nishimura N, Schaffer CB. **Big effects from tiny vessels: imaging the impact of microvascular clots and hemorrhages on the brain.** *Stroke* 2013;44:S90–92
31. Wardlaw JM, Doubal FN, Valdes-Hernandez M, et al. **Blood-brain barrier permeability and long-term clinical and imaging outcomes in cerebral small vessel disease.** *Stroke* 2013;44:525–27

Residual Thromboembolic Material in Cerebral Arteries after Endovascular Stroke Therapy Can Be Identified by Dual-Energy CT

A.E. Grams, M. Knoflach, R. Rehwald, J. Willeit, M. Sojer, E.R. Gizewski, and B. Glodny

ABSTRACT

BACKGROUND AND PURPOSE: Dual-energy CT features the opportunity to differentiate among up to 3 different materials because the absorption of x-rays depends on the applied tube voltage and the atomic number of the material. For example, it is possible to distinguish between blood-brain barrier disruption and an intracerebral hemorrhage following treatment for a stroke. The aim of this study was to evaluate whether dual-energy CT is capable of distinguishing intra-arterial contrast agent from residually clotted vessels immediately after endovascular stroke therapy.

MATERIALS AND METHODS: Sixteen patients (9 women, 7 men; mean age, 63.6 ± 13.09 years) were examined. Measurements were made on the postinterventional dual-energy CT virtual noncontrast, iodine map, and "weighted" brain window (weighted dual-energy) series. Postinterventional conventional angiography was used as the criterion standard method.

RESULTS: A residual clot was found in 10 patients. On the virtual noncontrast series, the Hounsfield attenuation of the clotted arteries was higher than that in the corresponding perfused contralateral arteries (53.72 ± 9.42 HU versus 41.64 ± 7.87 HU; $P < .05$). The latter had higher absorption values on the weighted dual-energy series than on the virtual noncontrast series (49.37 ± 7.44 HU versus 41.64 ± 7.87 HU; $P < .05$). The sensitivity for the detection of a residual clot was 90%; the specificity was 83.3%, and the accuracy was 87.5%. Interrater agreement was good ($\kappa = 0.733$).

CONCLUSIONS: Dual-energy CT may be valuable in the detection of clot persistence or early re-thrombosis without the necessity of additional contrast administration. However, its relevance for the prediction of outcomes remains to be determined in further studies.

ABBREVIATIONS: CI = confidence interval; DECT = dual-energy CT; DEw = weighted dual-energy series; IM = iodine map series; VNC = virtual noncontrast series

In specialized centers, endovascular stroke therapy is a method frequently used in addition to or instead of intravenous thrombolysis. In recent decades, various intra-arterial treatment methods such as intra-arterial thrombolysis, clot aspiration, and stent retrievers have been introduced.[1,2] During the intervention, a contrast agent must be administered; the diagnostic value of a postinterventional CT is therefore limited because hyperattenuated hemorrhage cannot always be differentiated from hyperattenuated intraparenchymal contrast staining due to blood-brain barrier disruption. It has been shown that this dilemma can be overcome with dual-energy CT (DECT). DECT is a quite recent innovation in CT imaging, in which datasets are acquired with 2 different tube voltages, typically with 80 kV or 100 and 140 kV.[3-5] Individual tube settings are adapted so that the overall dose does not exceed the dose of a comparable conventional CT acquired with 1 tube voltage. Some studies even suggest that a dose reduction can be achieved with DECT compared with conventional CT.[6,7] In principle, the absorption of x-rays depends on the tube voltage and the atomic number of a tissue.[8-11] While for low or medium voltages, the photoelectric effect is more likely to be responsible for the absorption of radiation, for medium voltages Compton scattering is more often responsible.[12,13] The photoelectric effect and Compton scattering are related in different ways to the energy of the radiation and the mass of the material radiated. While the probability of the occurrence of a photoelectric effect increases with the fourth power of the atomic number and decreases with the third power of the energy, the probability of the occurrence of Compton scattering increases only linearly with the atomic number of the radiated element and decreases linearly with radiation energy.[12] These phenomena allow up to 3 different materials to be distinguished.[12] The main application is

Received November 29, 2014; accepted after revision January 26, 2015.

From the Departments of Neuroradiology (A.E.G., E.R.G.), Neurology (M.K., J.W., M.S.), and Radiology (R.R., B.G.), Medical University of Innsbruck, Innsbruck, Austria.

Please address correspondence to Astrid Ellen Grams, MD, Department of Neuroradiology, Medical University of Innsbruck, Anichstr 35, 6020 Innsbruck, Austria; e-mail: astrid.grams@googlemail.com, astrid.grams@i-med.ac.at

http://dx.doi.org/10.3174/ajnr.A4350

Table 1: Relevant information about the included patients

No.	Sex	Age (yr)	Clot	Intravenous Thrombolysis	Residual Clot	Intra-Arterial Thrombolysis	Hematocrit (l/l)
1	Female	79	BA	Yes	Right P1	Yes	0.276
2	Male	79	BA	No	Left P2	Yes	0.346
3	Male	50	Right MCA	Yes	M2	Yes	0.441
4	Female	73	Left MCA	No	M2	Yes	0.401
5	Female	58	Right MCA	No	M3	No	0.429
6	Male	63	Left MCA	Yes	M3	Yes	0.438
7	Female	77	Right MCA	Yes	M2	Yes	0.419
8	Female	51	Right MCA	Yes	M3	Yes	0.413
9	Female	62	Left MCA	No	M3	Yes	0.354
10	Female	48	Right MCA	Yes	M3	No	0.4
11	Female	73	Right MCA	Yes	No	Yes	0.315
12	Male	58	Right MCA	Yes	No	Yes	0.41
13	Female	48	BA	Yes	No	Yes	0.36
14	Male	50	BA	Yes	No	No	0.401
15	Male	60	Right MCA	No	No	Yes	0.384
16	Male	89	Right MCA	Yes	No	Yes	0.431

Note:—BA indicates basilar artery.

for the differentiation between hemorrhagic transformation and contrast staining in the brain after recent intravascular contrast application.[13-19] After neuroendovascular therapy, important questions regarding possible hemorrhage, swelling, or infarction can be answered reliably with this method.[18] However, this method is also widely applied to differentiate various tissues in other regions of the body.[20-23]

The hyperattenuated artery sign is an accepted tool for detecting a clotted vessel in the diagnostic management of acute stroke on unenhanced CT scans.[24,25] However, other factors that influence vascular attenuation, mainly an increased hematocrit level, must be taken into account when interpreting vascular attenuation.[26,27] Postinterventionally, residual contrast agent remaining in the vessel is the greatest factor affecting vascular attenuation. It can prevent the correct diagnosis of residual or new clots on a CT scan because the increased vascular attenuation due to contrast agent cannot be distinguished from genuine clots that usually appear hyperattenuated.[14] However, DECT could, theoretically at least, make this distinction possible because the iodine still remaining in the vessel could be quantified and, by using voxels, subtracted from the absorption values found.[14,18] However, this technique has never been investigated with the focus on small residual clots following endovascular stroke therapy. Therefore, the aim of the present study was to discover whether residual intra-arterial clots after endovascular stroke therapy can be detected with DECT by using conventional angiography as the criterion standard.

MATERIALS AND METHODS

This study was approved by the local ethics review board. From October 2013 to October 2014, 16 patients (9 women and 7 men) with a mean age of 63.6 ± 13.09 years (range, 48–89 years) who received endovascular therapy after an ischemic stroke due to intracranial vascular occlusion from an intra-arterial clot were examined. A preinterventional conventional CT scan ($n = 15$) had been performed by using different scanners because the patients were transferred from other hospitals or from different locations of the hospital campus. Twelve patients had an occlusion of the middle cerebral artery; and 4 had an occlusion of the basilar artery. Most patients received intravenous thrombolysis with recombinant tissue plasminogen activator before endovascular therapy. The reasons for the others not receiving thrombolysis were due to therapy with anticoagulants ($n = 3$), recent stroke ($n = 1$), or a recent surgical procedure ($n = 1$). Endovascular therapy was performed with the patient under either general or local anesthesia. In all patients, recanalization was performed by using a stent retriever. Some patients (Table 1) received additional intra-arterial thrombolysis. Demographic data of the 16 patients, sex, age, initial clot location, information about performed intravenous or intra-arterial thrombolysis, residual clot localization, and hematocrit values, are presented in Table 1.

After endovascular therapy, patients were immediately transferred to the DECT scanner (Somatom Definition Flash; Siemens, Erlangen, Germany). The postinterventional unenhanced DECT scan was performed within no more than 1 hour after finalization of the endovascular therapy, in most cases earlier, to rule out hemorrhage or infarct demarcation requiring further treatment such as decompressive craniectomy. The DECT datasets were acquired with both tubes in parallel. The tube parameters of the first tube were 100 kV and 360 mA; the second tube was operated at 140 kV and 360 mA. The other parameters were the same for both tubes: Pitch was 0.45, the acquisition mode was incremental with 32 × 0.6 mm collimation, section thickness was 4 mm, and scan FOV was 200 mm in each. The following datasets were reconstructed secondarily: brain window weighted dual-energy series (DEw) in axial planes with a weighting of 50% for the 100 kV and 50% for the 140 kV series (section thickness, 4 mm; increment, 4 mm; kernel, H30f medium smooth; window, base orbit; FOV, 200 mm). From the data from each of the 2 tubes, series were calculated with the following parameters: 1-mm section thickness, 0.8-mm increment, H40f medium kernel, base orbit window, 200-mm FOV. Using the Brain Hemorrhage postprocessing software (Siemens), we constructed virtual noncontrast (VNC) and iodine map (IM) series on a dedicated workstation (syngo.CT Workplace 2012B; Siemens).

Attenuation measurements were performed by using ROIs, after maximum magnification in PACS software on a dedicated

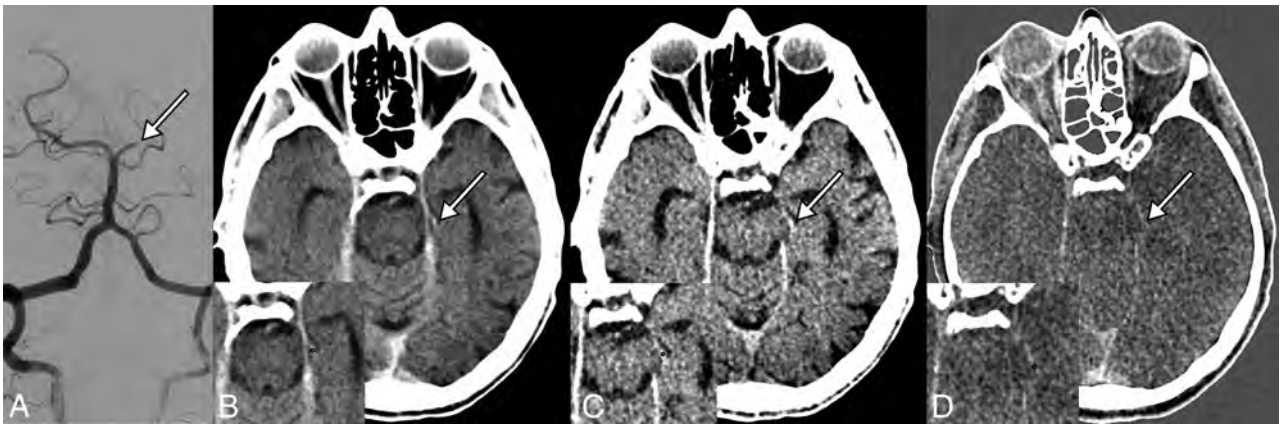

FIG 1. Residual clot (*arrow*) in the left P2 segment on conventional angiography (*A*) and in the different dual-energy series: weighted dual-energy (*B*), virtual noncontrast (*C*), and iodine map (*D*). The *arrows* indicate the hyperattenuated residual clots in the DEw and the VNC series. No clot is visible in the IM series. Note demonstration of ROI measurements in the residual clots after magnification in the left lower image sections.

Table 2: Attenuation measurements on the different series with mean values, SDs, upper/lower 95% CIs of rater 1, and results from Wilcoxon tests between residual clots and perfused vessels in the 10 patients with residual clots

	Hounsfield Attenuation (Mean)			
	CT	DEw	VNC	IM
Clots	58.88 ± 10.98	50.50 ± 10.08	53.72 ± 9.42	16.02 ± 12.07
Lower/upper 95% CI of mean	55.05/70.66	43.29/57.71	46.98/60.46	7.39/24.65
Vessels	43.35 ± 5.54	49.37 ± 7.44	41.64 ± 7.87	10.88 ± 11.35
Lower/upper 95% CI of mean	39.5/47.72	42.37/53.71	33.17/44.79	10.55/15.13
P values (Wilcoxon)	.0091[a]	.4316	.0020[a]	.8457

[a] Significant difference.

workstation (Impax EE R20 XIV v20140703_1249; Agfa-Gevaert, Mortsel, Belgium) by an experienced board-certified neuroradiologist (A.E.G.) and an experienced board-certified radiologist (B.G.).

In the preinterventional CT series, measurements were performed in the clotted vessels on the basis of the data from CT or conventional angiography and in the corresponding perfused segment of the MCA (M1 segment) on the contralateral side. If the basilar artery was occluded, the right middle cerebral artery was used for comparison. The same datasets were then blinded by removing all patient data including information on the clinical symptoms. Four months later, they were shown to the 2 raters in random order for identification of clot positions.

In the postinterventional DECT examination, measurements were performed within the residual clots known from a conventional angiogram only in the patients with residual clots (Fig 1*A*) and in the perfused contralateral MCA (M1 segment) in all patients on the different DEw (Fig 1*B*), VNC (Fig 1*C*), and IM (Fig 1*D*) series. If residual clots were no longer present, measurements were made only in the contralateral MCA.

The postinterventional DECT datasets were also blinded as described above and were presented to the 2 raters 4 months later in random order for identification of the positions of residual clots.

Descriptive statistics such as mean values and SDs were compiled with the Excel software (Microsoft Office 2013; Microsoft, Redmond, Washington). Due to the small sample size, only nonparametric tests not requiring normal distribution were used. The Wilcoxon signed rank test was applied for matched-pairs group comparisons. Correlation analyses were performed by using the Spearman method. Sensitivity, specificity, and positive and negative predictive values regarding the detection of clots in the preinterventional CT and of residual clots in the postinterventional CT were calculated by using the data collected by the neuroradiologist (A.E.G.). To evaluate the interrater variability with respect to the correct localization of clots or residual clots, we determined a Cohen κ for each.[28] All these calculations were made with the statistics software GraphPad Prism, Version 6 (GraphPad Software, San Diego, California) and GraphPad on-line (www.graphpad.com). The interrater variability with respect to the agreement of the measured absorption values was evaluated by using the intraclass correlation coefficient as proposed by Shrout and Fleiss.[29] A $P < .05$ was significant.

RESULTS

Descriptive data, mean attenuation, SDs, and *P* values for the preinterventional CT and the different postinterventional DECT series and vascular segments are given in Table 2.

In the preinterventional conventional CT scan, the clotted arteries were significantly more attenuated than the perfused arteries. In 8 of 9 cases (88.9%), clotted arteries could be identified by the blinded reader due to pronounced hyperattenuation of the vessel.

On the postinterventional VNC series, significantly higher attenuation was found in clotted than in perfused arteries, but not on the DEw series. In 9 of 10 cases (90.0%), residual clots could be identified by the blinded rater due to pronounced hyperattenuation of the vessel. On the IM series, no significant difference was found between clotted and perfused arteries. Whereas between the DEw and VNC series, no significant difference in attenuation was found in the clotted arteries, significantly lower attenuation was found on the DEw series than on the VNC series in perfused arteries (Table 3 and Fig 2).

There was a weak, not statistically significant positive correlation between hematocrit values and perfused arteries on the VNC

series (Spearman ρ, 0.24; 95% confidence interval [CI], 0.31–0.66; $P > .05$), but not on the other series.

On the VNC series, residually clotted vessels were identified in 9 of 10 arteries (90%) due to vascular hyperattenuation, with a false-negative evaluation in 1 case. In the 6 patients with no residual clot, the absence of a residual clot was correctly detected in 5 cases, with 1 false-positive evaluation. The sensitivity for the detection of residual clots was thus 90% (95% CI, 54.1%–99.5%), specificity was 83.3% (95% CI, 36.5%–99.1%), positive predictive value was 63.5% (95% CI, 35.9%–83.7%), and the negative predictive value was 37.5% (95% CI, 16.2%–64.1%). The accuracy was 87.5%.

The Cohen κ for the evaluation of the interrater agreement for the localization of initial clots was 0.762 (95% CI, 0.324–1.0), and for the localization of residual clots, 0.733 (95% CI, 38.9–1.0). The intraclass correlation coefficient regarding the measurements (Table 4) of the initial clots was 0.8196 ($P < .05$), and for the measurements of residual clots in the VNC map, 0.9133 ($P < .05$).

DISCUSSION

This study demonstrated that it is possible to detect intra-arterial clots shortly after the administration of intra-arterial contrast agent by DECT with quantitative measurements and subjective clot detections. Sensitivity and specificity were high, and the interrater agreement was good. On the DEw series, clotted and perfused vessels displayed a similar attenuation, but on the VNC series, clotted arteries were more attenuated than perfused arteries.

In various earlier studies, DECT in combination with the Brain Hemorrhage software has been described as a useful tool for differentiating intracranial hemorrhage and contrast staining after prior intravenous contrast application[13,14,17] or neuroendovascular therapy.[15,18,19]

It has been shown that by using a combined evaluation of the VNC and IM series from DECT, sensitivity and specificity for the detection of an underlying contrast-enhancing mass within a cerebral hemorrhage was as high as 94.4% and 97.4%,[17] with positive or negative predictive values up to 95.7% and 94.1%.[30] With regard to the differentiation between hemorrhage and contrast staining in different intracranial compartments, another study even described a sensitivity of 100%, specificity between 84.4% and 100%, and accuracy between 87.2% and 100%, with some limitations in calcified areas.[14] For the differentiation between hemorrhage and contrast staining after endovascular stroke therapy, it has been suggested that sensitivity, specificity, and accuracy are 100%, 91%, and 93%, respectively,[13] with positive and negative predictive values of up to 100% and 89%.[18,19] In the present study, a sensitivity of 90%, specificity of 83%, a positive predictive value of 63%, and a negative predictive value of 38% were reached. The accuracy was 87.5%. These values for sensitivity, specificity, and accuracy are of the same magnitude as those reported for the differentiation between intraparenchymal hematomas and intraparenchymal contrast staining[13,18,19] or for the differentiation between these features at other locations.[31] However, the positive and negative predictive values are clearly lower than those for the differentiation between intraparenchymal hematomas and intraparenchymal contrast staining, for example. The reason for this difference is most likely the small size of clots detected in this study. In contrast to intraparenchymal space-occupying hematomas, partial volume effects that lower the attenuation of the clots and make them more difficult to detect could play a role in the evaluation of residual intra-arterial clots. In this study, angiography as the criterion standard method was used for comparison, but in the other studies, only follow-up tests were available as the standard of reference.[13,14,18,19]

Table 3: Results from Wilcoxon tests between the different DECT series in clotted and perfused vessels of the 10 patients with residual clots

	P Values (Wilcoxon)	
	Clots	Vessels
DEw and VNC	.5703	.0020[a]
DEw and IM	.0020[a]	.0020[a]
VNC and IM	.0020[a]	.0020[a]

[a] Significant difference.

Table 4: Results from attenuation measurements of raters 1 and 2 and intraclass correlation on the different series

	Rater 1 (Mean)	Rater 2 (Mean)	Intraclass Correlation
Clot			
CT	58.88 ± 10.98	56.57 ± 9.49	0.8244
DEw	50.50 ± 10.08	54.53 ± 25.30	0.7599
VNC	53.72 ± 9.42	54.43 ± 8.33	0.9133
IM	16.02 ± 12.07	19.60 ± 36.08	0.65
Vessel			
CT	43.35 ± 5.54	43.99 ± 5.74	0.8779
DEw	49.37 ± 7.44	50.68 ± 10.05	0.7687
VNC	41.64 ± 7.87	46.23 ± 5.63	0.6277
IM	11.22 ± 6.90	10.88 ± 11.35	0.6682

Note:—CT indicates preinterventional CT.

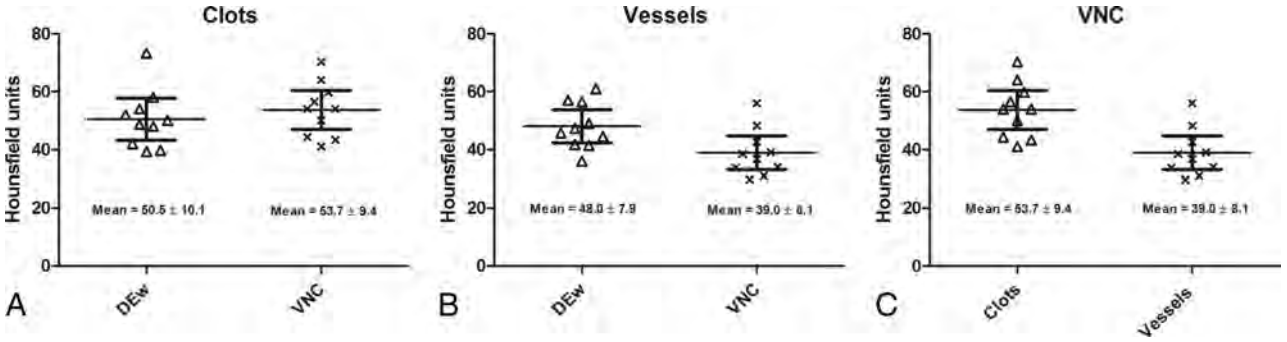

FIG 2. Mean values with upper/lower 95% confidence intervals and SDs of Hounsfield attenuation measured in clotted (*A*) and perfused (*B*) vessels in the weighted dual-energy and virtual noncontrast series and as a comparison of clotted and perfused vessels in the VNC series (*C*).

The κ value of 0.733 for interrater agreement with respect to the detection of residual clots was of the same magnitude as the κ value for the preinterventional detection of the initial clots (κ = 0.762). The interrater agreement can thus be considered good.[28] The intraclass correlation coefficient for the preinterventional and residual clot attenuation (Table 3) can be considered strong.[29] The good detectability of residual clots may be due to the difference between the attenuation of the clots and the perfused vessels with only a small overlap (Fig 2). Both indicate that the method can be readily reproduced.

Only 1 existing study describes the application of DECT for the differentiation between intra-arterial contrast agent and intra-arterial cerebral clots in 10 patients as a co-result.[14] However, no information about the location of or the reason for the investigated clots was given in this study, and no ROI measurements were performed as in our study. Moreover, in the study mentioned, the lumens of branches involved were not visualized and the respective lesions were not associated with reported clinical symptoms, so the observation must be considered unverified or anecdotal.

Thus far, no studies are available that describe the use of DECT to detect residual peripheral intra-arterial clots after endovascular therapy, to our knowledge.

The described method of clot detection after intravascular contrast administration has various potential clinical applications. After endovascular stroke therapy with angiographically proved residual clots, DECT could be used to demonstrate delayed recanalization or early reclotting of initially recanalized arteries. Early postinterventional DECT could therefore lead to consequences for treatment, such as modification of medication or transfer to an intensive care unit.

In addition to this application, the described technique could be applied to detect early thromboembolic complications after other neurointerventional procedures with persistent contrast staining such as intracranial stent placement or coiling. In addition, it could be useful in cases with cerebral thromboembolic complications after interventional procedures of other regions such as the heart or the aortic arch. Another potential application could be in patients with suspected arterial or even venous intracerebral clots after intravenous contrast application for various reasons without the requirement of additional contrast agent application.

In this study, there was a low but not significant correlation between hematocrit values and perfused arteries on the VNC series. However, in general, the hematocrit levels seem to have only little impact on vascular attenuation before or after endovascular therapy, in contrast to the findings in other studies.[26,27] One reason for this phenomenon might be that some of the hematocrit levels were determined before endovascular therapy, and others, immediately afterward. Therefore a dilution effect due to catheter flushing or intravenous fluid application might play a role. In addition, the relatively small population in this study might inadvertently mask the effect of hematocrit on arterial attenuation.

Several limitations of this study must be mentioned. Due to the occasionally small size of the peripheral, residually clotted, hyperattenuated arteries, it was not always easy to distinguish them from image noise. As discussed above, it has to be assumed that the size of a structure has a relevant impact on the applicability of the method to distinguish tissues, with better distinguishability between tissues in larger hemorrhages or clots, though no publication is available regarding this topic now. Complementary studies with larger patient populations must be conducted to elucidate not only the influencing factors vessel size, clot volume, and vessel direction on the sensitivity, specificity, and positive or negative predictive value of DECT but also the effect of technical factors such as mode of acquisition (axial or helical), signal-to-noise ratio, section thickness, or postprocessing of smaller FOVs and thinner sections. Furthermore, an estimation of the degree of a stenosis or the differentiation between stenosis and occlusion, such as might be possible with contrast-enhanced imaging, is not feasible with the described method. Due to the small number of patients, the CIs for sensitivity, specificity, positive predictive value, negative predictive value, and accuracy are relatively wide. They must be determined more precisely in further studies.

CONCLUSIONS

The described technique makes it possible to accelerate standardized stroke management of patients with previous contrast administration in whom intracranial clot detection with nonenhanced CT would be otherwise difficult. The application of DECT after contrast administration described here can make additional time-consuming imaging studies such as MR imaging or the application of additional contrast agent unnecessary.

Disclosures: Elke R. Gizewski—*UNRELATED*: *Payment for Lectures (including service on Speakers Bureaus)*: Bracco Imaging, lecture for radiologists-in-training.

REFERENCES

1. Novakovic RL, Toth G, Narayanan S, et al. **Retrievable stents, "stentrievers," for endovascular acute ischemic stroke therapy.** *Neurology* 2012;79:S148–57
2. Przybylowski CJ, Ding D, Starke RM, et al. **Evolution of endovascular mechanical thrombectomy for acute ischemic stroke.** *World J Clin Cases* 2014;2:614–22
3. Chiro GD, Brooks RA, Kessler RM, et al. **Tissue signatures with dual-energy computed tomography.** *Radiology* 1979;131:521–23
4. Millner MR, McDavid WD, Waggener RG, et al. **Extraction of information from CT scans at different energies.** *Med Phys* 1979;6:70–71
5. Genant HK, Boyd D. **Quantitative bone mineral analysis using dual energy computed tomography.** *Invest Radiol* 1977;12:545–51
6. Johnson TR. **Dual-energy CT: general principles.** *AJR Am J Roentgenol* 2012;199:S3–8
7. Kamiya K, Kunimatsu A, Mori H, et al. **Preliminary report on virtual monochromatic spectral imaging with fast kVp switching dual energy head CT: comparable image quality to that of 120-kVp CT without increasing the radiation dose.** *Jpn J Radiol* 2013;31:293–98
8. Thomas C, Krauss B, Ketelsen D, et al. **Differentiation of urinary calculi with dual energy CT: effect of spectral shaping by high energy tin filtration.** *Invest Radiol* 2010;45:393–98
9. Zhang LJ, Peng J, Wu SY, et al. **Dual source dual-energy computed tomography of acute myocardial infarction: correlation with histopathologic findings in a canine model.** *Invest Radiol* 2010;45:290–97
10. Chae EJ, Seo JB, Lee J, et al. **Xenon ventilation imaging using dual-energy computed tomography in asthmatics: initial experience.** *Invest Radiol* 2010;45:354–61
11. Kalender WA. *Computertomographie.* Erlangen: Publicis; 2006
12. Simpkin DJ. **Radiation interactions and internal dosimetry in nuclear medicine.** *Radiographics* 1999;19:155–67; quiz 153–54
13. Gupta R, Phan CM, Leidecker C, et al. **Evaluation of dual-energy CT**

for differentiating intracerebral hemorrhage from iodinated contrast material staining. *Radiology* 2010;257:205–11
14. Phan CM, Yoo AJ, Hirsch JA, et al. **Differentiation of hemorrhage from iodinated contrast in different intracranial compartments using dual-energy head CT.** *AJNR Am J Neuroradiol* 2012;33:1088–94
15. Brockmann C, Scharf J, Nolte IS, et al. **Dual-energy CT after perinterventional subarachnoid haemorrhage: a feasibility study.** *Clin Neuroradiol* 2010;20:231–35
16. Postma AA, Hofman PA, Stadler AA, et al. **Dual-energy CT of the brain and intracranial vessels.** *AJR Am J Roentgenol* 2012;199: S26–33
17. Kim SJ, Lim HK, Lee HY, et al. **Dual-energy CT in the evaluation of intracerebral hemorrhage of unknown origin: differentiation between tumor bleeding and pure hemorrhage.** *AJNR Am J Neuroradiol* 2012;33:865–72
18. Morhard D, Ertl L, Gerdsmeier-Petz W, et al. **Dual-energy CT immediately after endovascular stroke intervention: prognostic implications.** *Cardiovasc Intervent Radiol* 2014;37:1171–78
19. Tijssen MP, Hofman PA, Stadler AA, et al. **The role of dual energy CT in differentiating between brain haemorrhage and contrast medium after mechanical revascularisation in acute ischaemic stroke.** *Eur Radiol* 2014;24:834–40
20. Kraśnicki T, Podgórski P, Guziński M, et al. **Novel clinical applications of dual energy computed tomography.** *Adv Clin Exp Med* 2012;21:831–41
21. Karçaaltıncaba M, Aktas A. **Dual-energy CT revisited with multidetector CT: review of principles and clinical applications.** *Diagn Interv Radiol* 2011;17:181–94
22. De Cecco CN, Darnell A, Rengo M, et al. **Dual-energy CT: oncologic applications.** *AJR Am J Roentgenol* 2012;199:S98–105
23. Nicolaou S, Liang T, Murphy DT, et al. **Dual-energy CT: a promising new technique for assessment of the musculoskeletal system.** *AJR Am J Roentgenol* 2012;199:S78–86
24. Rutgers DR, van der Grond J, Jansen GH, et al. **Radiologic-pathologic correlation of the hyperdense middle cerebral artery sign: a case report.** *Acta Radiol* 2001;42:467–69
25. Leary MC, Kidwell CS, Villablanca JP, et al. **Validation of computed tomographic middle cerebral artery "dot"sign: an angiographic correlation study.** *Stroke* 2003;34:2636–40
26. Rauch RA, Bazan C, 3rd, Larsson EM, et al. **Hyperdense middle cerebral arteries identified on CT as a false sign of vascular occlusion.** *AJNR Am J Neuroradiol* 1993;14:669–73
27. Black DF, Rad AE, Gray LA, et al. **Cerebral venous sinus density on noncontrast CT correlates with hematocrit.** *AJNR Am J Neuroradiol* 2011;32:1354–57
28. Landis JR, Koch GG. **The measurement of observer agreement for categorical data.** *Biometrics* 1977;33:159–74
29. Shrout PE, Fleiss JL. **Intraclass correlations: uses in assessing rater reliability.** *Psychol Bull* 1979;86:420–28
30. Watanabe Y, Tsukabe A, Kunitomi Y, et al. **Dual-energy CT for detection of contrast enhancement or leakage within high-density haematomas in patients with intracranial haemorrhage.** *Neuroradiology* 2014;56:291–95
31. Flors L, Leiva-Salinas C, Norton PT, et al. **Imaging follow-up of endovascular repair of type B aortic dissection with dual-source, dual-energy CT and late delayed-phase scans.** *J Vasc Interv Radiol* 2014;25:435–42

Performance and Predictive Value of a User-Independent Platform for CT Perfusion Analysis: Threshold-Derived Automated Systems Outperform Examiner-Driven Approaches in Outcome Prediction of Acute Ischemic Stroke

S. Dehkharghani, R. Bammer, M. Straka, L.S. Albin, O. Kass-Hout, J.W. Allen, S. Rangaraju, D. Qiu, M.J. Winningham, and F. Nahab

ABSTRACT

BACKGROUND AND PURPOSE: Treatment strategies in acute ischemic stroke aim to curtail ischemic progression. Emerging paradigms propose patient subselection using imaging biomarkers derived from CT, CTA, and CT perfusion. We evaluated the performance of a fully-automated computational tool, hypothesizing enhancements compared with qualitative approaches. The correlation between imaging variables and clinical outcomes in a cohort of patients with acute ischemic stroke is reported.

MATERIALS AND METHODS: Sixty-two patients with acute ischemic stroke and MCA or ICA occlusion undergoing multidetector CT, CTA, and CTP were retrospectively evaluated. CTP was processed on a fully operator-independent platform (RApid processing of PerfusIon and Diffusion [RAPID]) computing automated core estimates based on relative cerebral blood flow and relative cerebral blood volume and hypoperfused tissue volumes at varying thresholds of time-to-maximum. Qualitative analysis was assigned by 2 independent reviewers for each variable, including CT-ASPECTS, CBV-ASPECTS, CBF-ASPECTS, CTA collateral score, and CTA clot burden score. Performance as predictors of favorable clinical outcome and final infarct volume was established for each variable.

RESULTS: Both RAPID core estimates, CT-ASPECTS, CBV-ASPECTS, and clot burden score correlated with favorable clinical outcome ($P < .05$); CBF-ASPECTS and collateral score were not significantly associated with favorable outcome, while hypoperfusion estimates were variably associated, depending on the selected time-to-maximum thresholds. Receiver operating characteristic analysis demonstrated disparities among tested variables, with RAPID core and hypoperfusion estimates outperforming all qualitative approaches (area under the curve, relative CBV = 0.86, relative CBF = 0.81; $P < .001$).

CONCLUSIONS: Qualitative approaches to acute ischemic stroke imaging are subject to limitations due to their subjective nature and lack of physiologic information. These findings support the benefits of high-speed automated analysis, outperforming conventional methodologies while limiting delays in clinical management.

ABBREVIATIONS: AIS = acute ischemic stroke; AUC = area under the curve; CBS = clot burden score; CS = collateral score; RAPID = RApid processing of PerfusIon and Diffusion; rCBF = relative CBF; rCBV = relative CBV; ROC = receiver operating characteristic; Tmax = time-to-maximum of the tissue residue function

Primary goals in the management of acute ischemic stroke (AIS) include timely pharmacologic or mechanical intervention, while avoiding untoward risks related to complications of treatment. Appropriate patient selection may thus prove paramount, and identification of a subpopulation most likely to benefit has been the subject of extensive inquiry.[1,2] While the precise profile of this target population remains to be conclusively defined, recent work has highlighted the potential strengths of stratification by using the ischemic penumbra formalism defining an irreversibly injured infarct core and putative penumbra of at-risk tissues.[1,3]

Despite promising results, penumbral imaging has met with skepticism and inconsistent outcomes, particularly because the broad array of imaging and computational approaches and interpretive parameters has precluded formulation of generalizable

Received December 9, 2014; accepted after revision January 20, 2015.

From the Departments of Radiology and Imaging Sciences (S.D., L.S.A., J.W.A., D.Q.) and Neurology (S.R., M.J.W., F.N.), Emory University Hospital, Atlanta, Georgia; Department of Radiology (R.B.), Stanford University Hospital, Stanford, California; Institut für Radiologie und Nuklearmedizin (M.S.), Kantonsspital Winterthur, Winterthur, Switzerland; and Department of Neurology (O.K.-H.), Catholic Health System, Buffalo, New York.

S. Dehkharghani and R. Bammer were co-lead authors.

Paper previously presented in part at: American Society of Neuroradiology Annual Meeting and the Foundation of the ASNR Symposium, May 17–22, 2014, Montreal, Quebec, Canada, as follows: "Reliability and Performance of a User-Independent Platform for Computed Tomography-Perfusion Analysis: Threshold-Derived Automated Systems Outperform Examiner-Driven Approaches to Prognosis and Outcome Prediction in Acute Ischemic Stroke." Control #2162, Presentation #0–559.

Please address correspondence to Roland Bammer, PhD, Radiologic Sciences Lab, Department of Radiology, Stanford University Hospital, Lucas Center P271, 1201 Welch Rd, Stanford, CA 94305; e-mail: rbammer@stanford.edu; and Seena Dehkharghani, MD, Neuroradiology Division; Attention: Mary Davis, Department of Radiology and Imaging Sciences, Emory University Hospital, 1364 Clifton Rd NE, Atlanta, GA 30322; e-mail: seena.dehkharghani@emory.edu

http://dx.doi.org/10.3174/ajnr.A4363

conclusions.[4-7] With studies further complicated by the time, materials, and expertise requisite to successfully undertake perfusion imaging, some investigators have focused on triage algorithms examining more readily attainable biomarkers derived from noncontrast CT (eg, Alberta Stroke Program Early CT Score) or CT angiography (eg, collateral score [CS], clot burden score [CBS]) common to stroke protocols.[8-11] While quickly attainable, the performance of ASPECTS in triaging patients to therapy or predicting outcome has been variable, and its use in prognostication of individual outcomes has been questioned.[12-14] Similarly, CS and CBS have shown promise as rapid approaches to assessment but may underperform when compared with perfusion imaging metrics.[9-11] Recently, the ASPECTS methodology was applied to CTP parametric maps in an effort to impart standardization and mitigate subjective elements of perfusion analysis; however, even in this context, the strengths of perfusion imaging may be attenuated by variability in postprocessing, computational analysis, selection of parametric maps, and the generally qualitative nature of such approaches.[10,11]

Expert consensus has emphasized the demand for standardization in the acquisition, processing, and analysis of perfusion imaging.[15,16] The potential for disparate results and the variability in accuracy among competing software platforms have been the subject of recent studies and were thoroughly expounded in a comparative analysis by Kudo et al.[17] In light of recent reports, the primary objective of this study were to examine the predictive performance of several user-defined approaches to NCCT, CTA, and CTP analysis, by comparison with a fast, vendor- and operator-independent computational tool using fully automated lesion segmentation and pixel-wise parametric thresholding for semiquantitation (RApid processing of PerfusIon and Diffusion [RAPID]).[18] The objective of our study was to evaluate these tools to determine their ability to predict 90-day favorable clinical outcome in patients with AIS.

MATERIALS AND METHODS

We retrospectively identified patients with AIS presenting within 12 hours of symptom onset found to have intracranial ICA or MCA occlusion as part of a prospectively collected registry of patients undergoing acute comprehensive stroke imaging with NCCT, CTA, and CTP at Emory University Hospital from February 2011 to December 2013. All patients were initially evaluated by vascular neurology in the emergency setting, with initiation of an institutional stroke protocol facilitating expedited triage, imaging, interpretation, and treatment when appropriate. Patients were excluded from this analysis if they did not successfully complete the comprehensive imaging protocol, had motion or other artifacts rendering imaging nondiagnostic, or lacked data on 90-day clinical outcome. Exclusion criteria further included patients in whom large symptomatic intracerebral hemorrhage developed, among whom measurement of final infarct volumes may be confounded or hindered by resultant mass effect. Retrospective analysis was supported under the guidelines of the institutional review board, and written informed consent was waived for this study.

Medical records were reviewed for a clinical history of atrial fibrillation, type 2 diabetes, hypertension, dyslipidemia, and congestive heart failure. Any pre-existing disability (modified Rankin Scale >0) was determined on initial questioning and during review of the electronic medical record. Initial neurologic screening at presentation included determination of National Institutes of Health Stroke Scale score recorded by a vascular neurologist with NIHSS certification. A subset of patients received intravenous and/or intra-arterial thrombolytic therapy per institutional protocol and at the discretion of the vascular neurologist. The modified Rankin Scale was established at discharge and 90 days. A favorable clinical outcome was defined as mRS ≤2 at 3 months.

Imaging Protocol

All patients underwent an institutional stroke imaging protocol to include NCCT, CTA, and CTP. CT was performed on a 40-mm, 64–detector row clinical system (LightSpeed VCT; GE Healthcare, Milwaukee, Wisconsin). Helical NCCT (120 kV; 100–350 auto-mA; CT dose index, ~43.15) was performed from the foramen magnum through the vertex at a 5.0-mm section thickness. In the absence of visible intracranial hemorrhage during real-time evaluation by a radiologist and vascular neurologist, 2 contiguous CTP slabs were obtained for 8-cm combined coverage of the supratentorial brain, obtained at eight 5-mm sections per slab. Cine mode acquisition (80 kV; 100 mA; CT dose index, ~293.48) permitting high-temporal-resolution (1-second sampling interval) dynamic bolus passage imaging was obtained following the administration of 35-mL iodinated contrast (iopamidol, Isovue 370; Bracco, Princeton, New Jersey) power injected at 5 mL/s through an 18-ga or larger antecubital IV access. Contrast administration was followed by a 25-mL saline flush at the same rate. Last, helical CTA (120 kV; 200–350 auto-mA; CT dose index, ~38.08) was performed from the carina to the vertex (section thickness/interval, 0.625/0.375 mm) following IV administration of 70-mL iodinated contrast injected at 5 mL/s and followed by a 25-mL saline flush. Follow-up in all patients included either MR imaging and/or NCCT, documenting final infarct size before discharge. All images were transferred to a separate workstation for analysis (Mac Pro; Apple, Cupertino, California) by using a third-party DICOM viewer (Osirix 64-bit; http://www.osirix-viewer.com).

Image Analysis

NCCT-ASPECTS. All NCCTs were assigned an ASPECTS by 2 experienced vascular neurologists blinded to patient clinical information, other imaging, and clinical outcome. ASPECTS used a 10-point visual inspection scale assessing the early ischemic burden in the supratentorial brain as detailed previously by Barber et al.[8]

CTA Collateral Score and Clot Burden Score. Tan et al[9] proposed a rapid, qualitative visual inspection methodology for brain CTA, emphasizing the importance of both the extent of vascular clot (CBS) and the adequacy of surface vascular enhancement, ostensibly reflecting collateral flow response (CS). Two experienced neuroradiologists with subspecialty certification applied visual inspection CTA scores, blinded to clinical and outcome data and all other imaging, specifically as follows: CBS defining clot extent for anterior circulation disease was assigned a score of 0–10, whereby 2 points are deducted for thrombus within each of the supraclinoid ICAs, the proximal 50% of the horizontal (M1)

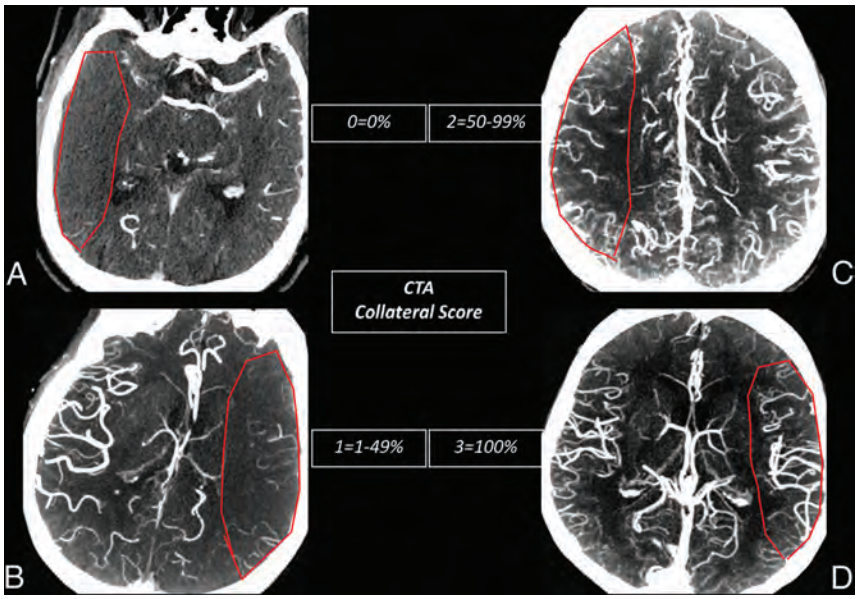

FIG 1. CTA CS. CTA CS methodology as proposed by Tan et al.[9] Axial 20-mm maximum-intensity-projection images demonstrate the extent and asymmetry in the peripheral leptomeningeal collateral supply graded as relative to the contralateral normal hemisphere (pathologic MCA territory indicated by a red ROI). *A*, A score of zero suggests near-complete absence of surface collateralization. *B*, A score of 1 indicates greater than zero but <50% collateral flow. *C*, A score of 2 suggests >50% but <100% of normal leptomeningeal collaterals. *D*, A score of 3 suggests normal or, when present, greater than normal surface collaterals.

MCA trunk, or the distal 50% of the M1; a single point was then deducted for thrombus within the infraclinoid ICA and the anterior cerebral artery and for each individual vertical (M2) MCA branch.[9] As per the original methodology proposed by Tan et al, the thrombus may be partial or complete, with a minimum potential score of zero reflecting extensive anterior circulation occlusion. CTA CS (Fig 1) was described as an ordinal, visual grading system for collateral flow, scored 0–3; collateral flow was assigned a score of zero for absent surface collateralization, 1 for >0 but <50% collateral supply, 2 for 50–99% collateral supply, and 3 for normal or supranormal surface vasculature of the MCA territory. CTA analysis was performed by using 20-mm axial maximum-intensity-projection and 0.625-mm axial source images, as well as orthogonal and curved multiplanar reformats as needed.

CT Perfusion. All perfusion imaging was postprocessed by using a vendor-independent software platform (RAPID). RAPID is an operator-independent image processing and visualization tool operating on standardized DICOM data and configured for entirely automated image processing.[18] As an extension of earlier iterations compiled for analysis of MRI diffusion and perfusion imaging, the current implementation further permits CTP postprocessing carried through a computational pipeline similar to that initially described. Briefly, following preprocessing steps correcting rigid-body motion, arterial input function selection is performed and deconvolved from the voxel time-attenuation course using a delay-insensitive algorithm for isolation of the tissue residue function. Time-to-maximum of the tissue residue function (Tmax) is determined on a voxelwise basis, with Tmax maps incrementally thresholded between 4–10 seconds at 2-second intervals, and overlaid upon source CTP data for analysis.

Cerebral blood volume maps were computed as outlined elsewhere, and cerebral blood flow was determined in milliliter/100 g/minute.[18] Both CBV and CBF have been proposed as estimates of irreversibly infarcted (core) tissues, with past investigations describing both absolute and relative (rCBV, rCBF) thresholds for the detection of infarct core.[19] For the purposes of this study, separate estimates were supplied for each, thresholded at relative rCBF or rCBV <30% normal. Color-coded core maps for both parameters were automatically generated and overlaid on source images for review purposes (Fig 2). Processing time from the transfer of perfusion data to the RAPID suite to production of processed maps was approximately 3 minutes.

CTP analysis lastly included examiner-driven qualitative evaluation of perfusion parametric maps. Recent studies have extended ASPECTS methodology to perfusion imaging, reporting both improvements in predictive performance relative to clinical outcome and stronger interrater agreement.[10,20] As detailed by Aviv et al,[20] CBV and CBF maps were assigned CTP-ASPECTS by the same 2 neuroradiologists, again blinded to clinical and other radiographic data, in separate scoring sessions spaced approximately 7 days from the prior analyses. CTP-ASPECTS again ranged from 0 to 10, with a single point deducted for any of 10 supratentorial regions exhibiting apparent hypoperfusion.

Radiographic Outcome

The correlation between the RAPID core infarct estimates, CBV and CBF, and final infarct volume was determined independently. Final infarct volumes were measured following export of raw DICOM data to the Fiji release of the ImageJ software platform (http://imagej.nih.gov/ij/). Analysis included a series of postprocessing steps (Fig 3), beginning with optimization of image contrast for detection of hyperintense regions on follow-up trace DWI or CT images. Binary images were generated following application of intensity thresholds permitting voxelwise measures of final infarct volume in milliliters, cross-referenced with original DWI to exclude regions of EPI-related artifacts, such as those near the skull base or air-tissue interfaces.

Statistical Analysis

Statistical analysis was performed in SAS software, Version 9.3 (SAS Institute, Cary, North Carolina). Pearson correlation coefficients were calculated to assess the relationship between continuous variables (predicted infarct core and final infarct volume). Ordinal (ASPECTS, CS, CBS) and continuous (predicted infarct core volume, at-risk tissue volume, and final infarct volume)

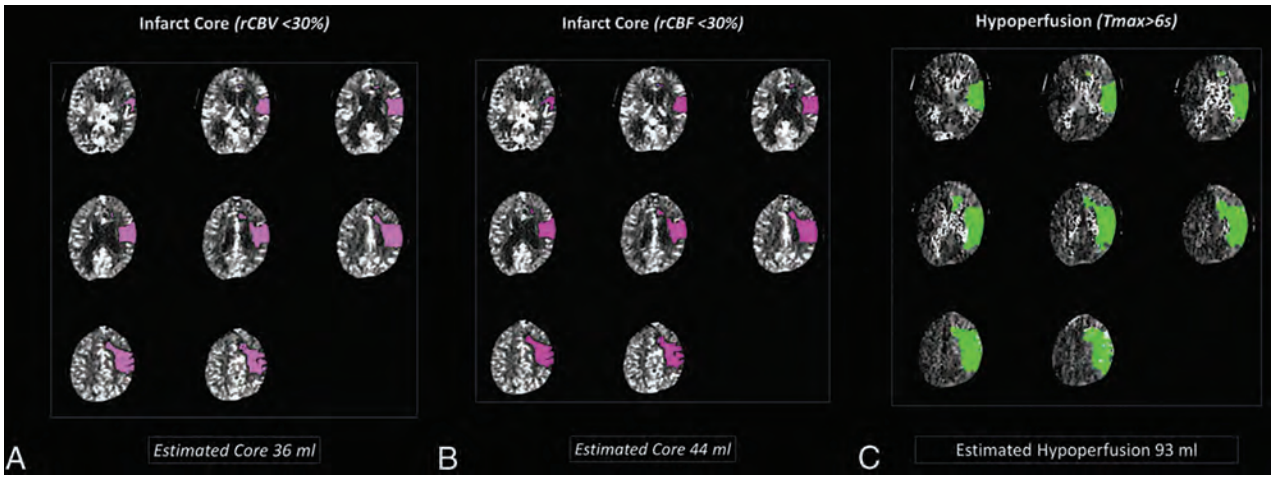

FIG 2. RAPID CTP core-penumbra mismatch. Sample output from RAPID perfusion module. The upper of 2 perfusion slabs (4-cm supratentorial coverage across 8 contiguous 5-mm sections) underwent delay-insensitive deconvolution, normalization and lesion segmentation, and thresholding for the production of infarct core and hypoperfused tissue estimates. Similar analysis was undertaken for the inferior perfusion slab (not shown) and cumulative predicted core and penumbral volumes established for each patient. Default output parameters for infarct core (rCBV <30%, *A*), infarct core (rCBF <30%, *B*), and hypoperfused tissues (Tmax >6 seconds, *C*) are shown. The final infarct volume (not shown) measured 97 mL.

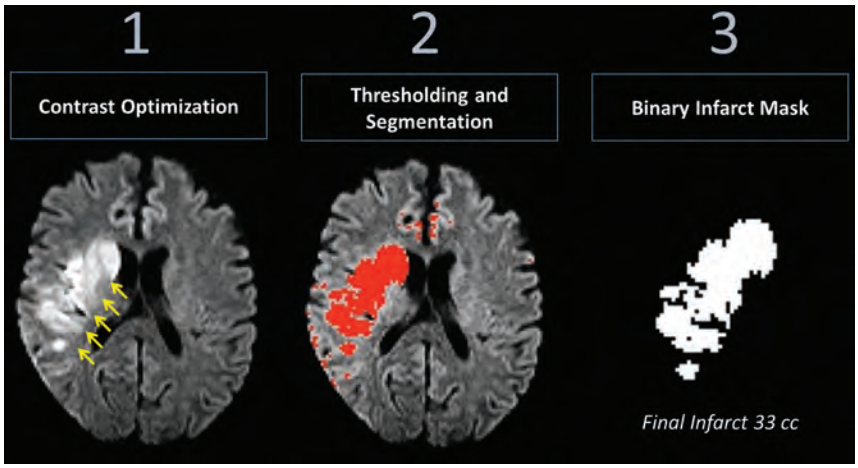

FIG 3. Analysis pipeline, final infarct volume. Postprocessing steps for determination of final infarction volume on follow-up. Optimization of image contrast for intensity-wise lesion segmentation was performed with manual thresholding toward production of a binary image, with cross-reference to the original DWI data to exclude spurious areas related to susceptibility or EPI distortions.

variables were considered for the input model of univariate and multivariate logistic regression, against dichotomized outcomes (mRS ≤2) for all patients at 90-day follow-up. Receiver operating characteristics (ROCs) were computed; optimal operating values were established for each variable of interest as discriminators of favorable clinical outcome; and sensitivity, specificity, and confidence intervals were determined. Statistical significance among tested variables as predictors of final infarct volume was determined at $P < .05$. Interobserver agreement for NCCT-ASPECTS, CBV-ASPECTS, CBF-ASPECTS, CBS, and CS was established by Pearson correlation coefficients. Intraobserver agreement for binary determination of ASPECTS >7 was established separately by κ statistics.

RESULTS

Sixty-two patients (36 women; median age, 70 years; range years, 33–94 years) with AIS (<12 hours) and MCA or intracranial ICA occlusion constituted the study population. Among these, 15 were excluded due to severe, unrecoverable motion artifacts ($n = 5$) or lack of 90-day clinical outcome data ($n = 10$), leaving 47 patients for analysis. No patients were observed to harbor bilateral arterial occlusions.

Median NIHSS at admission was 15 (interquartile range, 16); the mean duration from the time of onset/last known healthy to imaging was 210 minutes. Twenty-three (52%) patients received IV tPA, and 10 (23%) underwent endovascular treatment for intra-arterial clot lysis or retrieval. The mean mRS at both discharge and at 90 days was 3; favorable outcome (mRS ≤2) at 90 days was recorded in 16 patients (34%). An ICA or M1 occlusion was present in 41 (72%) patients, with MCA M2 segment occlusion observed in the remainder. Final infarct volume was measured by DWI in 77% of patients with the remainder established by NCCT; median final infarct volume was 34 mL (interquartile range, 94 mL).

Results of adjusted multivariable logistic regression analysis and odds ratios for dichotomized favorable outcome (mRS, ≤2) are presented in Table 1. Patients with favorable clinical outcome at 90 days exhibited higher baseline NCCT-ASPECTS ($P = .03$). Similarly, significant interactions were observed relative to 90-day favorable clinical outcome for CBV-ASPECTS ($P = .01$), CBF-ASPECTS ($P = .04$), and CTA clot burden score ($P = .02$), but not for CTA CS ($P = .09$).

Among RAPID parameters interrogated, predicted core infarct determined both by CBV and CBF demonstrated significant correlations with favorable clinical outcome at 90 days ($P = .01$). Estimates of hypoperfusion at thresholded values of Tmax

exhibited variable results; statistical significance was observed for the default threshold Tmax of >6 seconds ($P = .03$) as well as Tmax of >4 seconds ($P = .01$), but not for the remaining Tmax thresholds.

ROC analysis (Table 2) demonstrated the strongest predictors of favorable outcome with RAPID-derived core infarct volumes (rCBV core area under the curve [AUC], 0.86, $P < .001$; rCBF core AUC, 0.81, $P < .001$). Among the predicted measures of hypoperfusion and overall at-risk tissues by using thresholded Tmax of ≥4, 6, 8, and 10 seconds, predictive performance for dichotomized favorable outcome was similar (respectively, AUC = 0.80, 0.77, 0.76, 0.74; $P < .01$); the highest combinations of sensitivity and specificity were observed for Tmax of ≥6 seconds (sensitivity, 77%; specificity, 72%). For both rCBV and rCBF core measures, the threshold with optimized sensitivity (100%) for favorable outcome was 9.2 mL, while the threshold with greatest specificity (100%) was 43 mL.

Among qualitative, reader-defined measures, CBV-ASPECTS exhibited the strongest performance (AUC, 0.75; $P < .01$). Among CTA-derived parameters, CBS was superior to CS; however, sensitivity for predicting favorable outcome was lowest among all measures for CBS, shared only by CBF-ASPECTS (CBS AUC, 0.74; 95% CI, 0.59–0.89; optimal cutoff, 5; sensitivity, 58%; specificity, 77%; $P < .01$). Performance for NCCT-ASPECTS (AUC, 0.72; sensitivity, 68%; specificity, 68%; $P = .01$) was comparable with CBF-ASPECTS and CS, but inferior to all automated perfusion metrics.

The strongest overall predictive performance toward favorable clinical outcome was observed with final, follow-up infarct volume (AUC, 0.96; 95% CI, 0.91–1.0; optimal cutoff, 29.1 mL; sensitivity, 91%; specificity, 88%; $P < .001$).

Analysis of interrater agreement yielded superior results for CTP- and CTA-derived measures compared with NCCT ASPECTS (Pearson correlation: NCCT-ASPECTS, 0.52, $P < .001$; CBV-ASPECTS, 0.94, $P < .001$; CBF-ASPECTS, 0.93, $P < .001$; CS, 0.85, $P < .001$; CBS, 0.94, $P < .001$). Interrater agreement for determination of NCCT-ASPECTS >7 improved (κ coefficient = 0.93, $P < .001$).

Table 1: Ninety-day adjusted odds ratios: favorable clinical outcome (mRS ≤2)[a]

Variable	Odds Ratio	95% CI	*P* Value
Final infarct volume	0.84	0.72–0.98	.03
NCCT-ASPECTS	3.23	1.09–9.54	003
CBV-ASPECTS	1.78	1.13–2.80	.01
CBF-ASPECTS	1.46	1.01–2.11	.05
Collateral score	2.27	0.88–5.83	.09[b]
Clot burden score	1.66	1.07–2.59	.02
RAPID rCBV core	0.92	0.86–0.98	.01
RAPID rCBF core	0.92	0.85–0.99	.02
RAPID Tmax >4 sec	0.98	0.96–0.99	.03
RAPID Tmax >6 sec	0.98	0.97–0.99	.01
RAPID Tmax >8 sec	0.98	0.96–1.00	.06[b]
RAPID Tmax >10 sec	0.98	0.96–1.00	.06[b]

[a] NCCT-ASPECTS, CBV-ASPECTS, and CBF-ASPECTS represent ASPECTS applied respectively to noncontrast CT, cerebral blood volume maps, or cerebral blood flow maps.
[b] Statistical significance in logistic regression observed with all tested variables with the exception of RAPID-derived Tmax of >8 seconds and >10 seconds and the CTA collateral score ($P > .05$).

Table 2: ROC analysis: dichotomized favorable outcome (mRS ≤2)[a]

Variable	AUC	*P* Value	95% CI	OOP	Sensitivity	Specificity
Final infarct (mL)	0.96	<.001	0.91–1.00	29.1	91%	88%
RAPID rCBV core	0.86	.001	0.74–0.96	10.4	85%	78%
RAPID rCBF core	0.81	<.001	0.68–0.93	5.6	73%	72%
RAPID Tmax >4 sec	0.80	<.01	0.65–0.93	146.6	73%	67%
RAPID Tmax >6 sec	0.77	<.01	0.63–0.92	81.9	77%	72%
RAPID Tmax >8 sec	0.76	<.01	0.60–0.91	53.1	77%	72%
RAPID Tmax >10 sec	0.74	<.01	0.58–0.89	26.6	73%	72%
NCCT-ASPECTS	0.72	.01	0.57–0.87	9.5	68%	68%
CBV-ASPECTS	0.75	.01	0.61–0.89	5.0	76%	62%
CBF-ASPECTS	0.72	.02	0.57–0.87	5.0	58%	66%
Clot burden score	0.74	.01	0.59–0.89	6.5	58%	77%
Collateral score[b]	.72	.20	0.56–0.89	1.5	70%	70%

Note:—OOP indicates optimal operating point, optimal cut-off from ROC analysis for the variable of interest.
[a] Results of ROC analysis relative to dichotomized favorable clinical outcome (90-day mRS ≤2). Performance indicated by ROC AUC in descending-order performance.
[b] Significant relationships were observed for all tested variables, with the exception of the CTA collateral score.

Radiographic Outcome

Correlation between variables of interest and final infarct volume (Table 3) demonstrated similar results, with the highest correlations among RAPID-derived estimates of infarct core (CBV core $r^2 = 0.77$, $P < .001$; CBF core $r^2 = 0.75$, $P < .001$); adjusted logistic regression analyses comparing the odds ratios for final infarct volumes of ≤29 mL (optimal cutoff defining favorable clinical outcomes, above) were similar between the 2 measures (CBV core OR, 1.10; 95% CI, 1.05–1.15; CBF core OR, 1.12; 95% CI, 1.04–1.20; $P < .05$). Significant correlations were observed between all tested variables and final infarct, with the exception of CBS ($r^2 = -0.23$, $P = .11$).

DISCUSSION

The results herein support the feasibility of integrating a semiquantitative analytic and visualization tool for advanced CT triage in the time-sensitive domain of AIS. The findings highlight the potential benefits of advanced image processing in this context, whereby enhancements to typically qualitative and sometimes subjective interpretive algorithms were shown to augment the predictive value of acute stroke imaging as it relates to clinical outcome.

Among the variables tested, the semiquantitative predictors of irreversible ischemia, CBV core and CBF core, exhibited the strongest performance by ROC. By comparison with qualitative approaches to core estimation, relying on visual inspection and subjective definition of lesion extent, core estimates derived from the RAPID suite were produced following a series of normalization and quantitation steps, with automated lesion segmentation and determination of lesion volumes at predefined thresholds. Past reports and expert consensus have proposed the benefits of streamlined and reproducible approaches to postprocessing and analysis; however, rigorous postprocessing may be impractical in the clinical setting.[15,16] Accordingly, diagnostic paradigms in

Table 3: Parameter correlation with final infarct volume[a]

Variable	Correlation	*P* Value
RAPID rCBV core	0.77	<.001
RAPID rCBF core	0.75	<.001
RAPID Tmax >4 sec	0.38	<.01
RAPID Tmax >6 sec	0.44	<.001
RAPID Tmax >8 sec	0.49	<.001
RAPID Tmax >10 sec	0.54	<.001
NCCT-ASPECTS	−0.40	<.01
CBV-ASPECTS	−0.50	<.001
CBF-ASPECTS	−0.48	<.001
Clot burden score[b]	−0.23	.11
Collateral score	−0.41	<.01

[a] Correlational analysis between tested variables and final infarct volume (MRI or CT, in milliliters). The strongest overall correlations were observed with RAPID-derived core estimates (rCBF core and rCBV core). Negative correlations were observed between all ASPECTS and CTA-derived measures relative to the final infarct volume.
[b] Significant relationships were observed for all tested variables with the exception of the CTA clot burden score.

multiparametric CTP commonly involve the subjective determination of relative mismatch between putative infarct core and the remaining at-risk tissues. With regions of irreversibly injured, at-risk, and modestly hypoperfused tissues potentially overlapping by visual inspection alone, voxelwise thresholding may provide some immunity to incorrect tissue classification. Heterogeneity in reperfusion of the study population precludes conclusive judgments as to a singular, ideal Tmax threshold for outcome prediction, for which past reports have documented variability in performance between a 4- and 6-second delay, depending on reperfusion status, in line with the best performing Tmax thresholds above.[6]

NCCT-ASPECTS, while providing a rapid algorithm for determination of the extent of infarcted tissues, may have insensitivity to infarction in the early stages of injury, before the bulk water shift detection on noncontrast imaging.[10,12,14,20] We suspect that the clustering of abnormal brain regions in ASPECTS methodology, while providing for some uniformity in analysis, may have further limited the dynamic range for discriminating between lesions with similar ASPECTS but differing in actual extent or size. The inability of ASPECTS to provide an estimate of the extent or severity of tissues at ongoing ischemic risk may additionally limit its utility in patient selection. Application of ASPECTS methodology to CTP imaging aims to leverage some benefits of physiologic and flow imaging, while providing uniformity in analysis and reporting as in NCCT-ASPECTS. While showing improvements compared with NCCT-ASPECTS in prior reports, the analysis remains fundamentally subjective and again lacks in its ability to subclassify tissues within ASPECTS regions.[10,20]

Two previously proposed CTA-derived measures, the clot burden score and collateral score, were investigated among triage variables in this study.[9,11,21] While previously having shown promise as outcome predictors, their ability to supplant tissue-level information provided by perfusion imaging may be limited by uncertainty as to the nutritive capacity of surface-level collaterals vis-à-vis the tissue perfusion approximated by dynamic bolus passage deconvolution with an arterial input function. The importance of leptomeningeal collateral flow in preserving ischemic neuronal substrate and potentially protecting against hemorrhage has been discussed, and numerous multimodal collateral scoring methodologies have been proposed but may lack in their ability to characterize the dynamic nature of collateral flow or discriminate nonperfusion from flow delayed at the moment of acquisition.[22] Such vulnerabilities may, in combination, have contributed to the lack of statistical significance observed with CS relative to dichotomized favorable clinical outcome.

Stroke imaging protocols commonly include some combination of CT or MR imaging to exclude the presence of acute hemorrhage and for characterization of infarct core, as well as CT or MR imaging hemodynamic-sensitized techniques to identify the presence/extent of tissue at ongoing ischemic risk.[4,23,24] Several studies have aimed to apply such methodology to imaging triage; however, no consensus has emerged regarding the optimal combination of qualitative and quantitative metrics to accurately identify the ischemic penumbra.[15,16]

Image-based patient selection has shown success in some recent multicenter trials favoring interrogation with perfusion parameters.[1,2] Variability among vendor-based and locally developed perfusion analysis tools is known to produce considerable differences in results from perfusion data and may engender variable conclusions from common datasets.[17] The relative performance of several tools was compared in a digital phantom in a recent work by Kudo et al[17]; with this in mind, a study of predictive performance against commonly used qualitative approaches was conducted, suggesting enhancement to performance with the use of a standardized, user-independent platform. The disparate outcomes following re-analysis of data from the Echoplanar Imaging Thrombolytic Evaluation Trial support the idea that such differences in analysis may not be purely trivial.[25]

We acknowledge several study limitations. The relatively small sample population may have impacted the ability to identify significant relationships among some tested variables; however, significant trends among most tested parameters in our study are consistent with the generally strong performance of such approaches in past reports. Within the statistical limits of the study, we believe the findings offer generalizable support for the strengths of advanced, automated computational tools for clinical use. We acknowledge that ROC results in this study may suggest generally stricter and more conservative thresholds for favorable outcome compared with past studies. We suspect that the small sample size and heterogeneity in treatment and revascularization status account substantially for such differences; however, because the primary study aim was establishing the feasibility, utility, and superiority of an automated platform by comparison with user-driven approaches, we do not suspect that these observations have significantly affected the study conclusions. The aims in this study included principally the characterization of varying approaches to predicting clinical outcome. The design and statistical limits did not permit assessment of interactions between study variables and revascularization or tPA administration among patients and, in this respect, cannot specifically be assumed as generalizable to the merits of treatment in such patients. We, however, maintain that within the study aims, specifically to highlight the advantages of robust automation over qualitative analysis regimens in AIS imaging triage, the interaction term relating reperfusion to outcomes is not likely to have influenced the reported

results. A larger scale study permitting dichotomization between treated and untreated patients is necessary and is underway for the assessment of such diagnostic approaches as predictors of a beneficial therapeutic effect in AIS.

CONCLUSIONS

Automated approaches to imaging in AIS may offer some immunity to limitations inherent in qualitative methodologies. These findings support the benefits of high-speed automated analysis in AIS, outperforming conventional methodologies while avoiding delays in management.

Disclosures: Roland Bammer—*UNRELATED*: *Grants/Grants Pending*: National Institutes of Health*; *Stock/Stock Options*: I am a board member and hold equity in iSchemaView. Matus Straka—*UNRELATED*: *Employment*: iSchemaView; *Stock/Stock Options*: iSchemaView (minor, <5%). *Money paid to the institution.

REFERENCES

1. Albers GW, Thijs VN, Wechsler L, et al. **Magnetic resonance imaging profiles predict clinical response to early reperfusion: the diffusion and perfusion imaging evaluation for understanding stroke evolution (DEFUSE) study.** *Ann Neurol* 2006;60:508–17
2. Lansberg MG, Straka M, Kemp S, et al. **MRI profile and response to endovascular reperfusion after stroke (DEFUSE 2): a prospective cohort study.** *Lancet Neurol* 2012;11:860–67
3. Davis SM, Donnan GA, Parsons MW, et al. **Effects of alteplase beyond 3 h after stroke in the Echoplanar Imaging Thrombolytic Evaluation Trial (EPITHET): a placebo-controlled randomised trial.** *Lancet Neurol* 2008;7:299–309
4. Astrup J, Siesjo BK, Symon L. **Thresholds in cerebral ischemia: the ischemic penumbra.** *Stroke* 1981;12:723–25
5. Kamalian S, Kamalian S, Maas MB, et al. **CT cerebral blood flow maps optimally correlate with admission diffusion-weighted imaging in acute stroke but thresholds vary by postprocessing platform.** *Stroke* 2011;42:1923–28
6. Olivot JM, Mlynash M, Thijs VN, et al. **Optimal Tmax threshold for predicting penumbral tissue in acute stroke.** *Stroke* 2009;40:469–75
7. Sobesky J, Zaro Weber O, Lehnhardt FG, et al. **Does the mismatch match the penumbra? Magnetic resonance imaging and positron emission tomography in early ischemic stroke.** *Stroke* 2005; 36:980–85
8. Barber PA, Demchuk AM, Zhang J, et al. **Validity and reliability of a quantitative computed tomography score in predicting outcome of hyperacute stroke before thrombolytic therapy: ASPECTS Study Group—Alberta Stroke Programme Early CT Score.** *Lancet* 2000;355:1670–74
9. Tan IY, Demchuk AM, Hopyan J, et al. **CT angiography clot burden score and collateral score: correlation with clinical and radiologic outcomes in acute middle cerebral artery infarct.** *AJNR Am J Neuroradiol* 2009;30:525–31
10. Sillanpaa N, Saarinen JT, Rusanen H, et al. **CT perfusion ASPECTS in the evaluation of acute ischemic stroke: thrombolytic therapy perspective.** *Cerebrovasc Dis Extra* 2011;1:6–16
11. Sillanpaa N, Saarinen JT, Rusanen H, et al. **The clot burden score, the Boston Acute Stroke Imaging Scale, the cerebral blood volume ASPECTS, and two novel imaging parameters in the prediction of clinical outcome of ischemic stroke patients receiving intravenous thrombolytic therapy.** *Neuroradiology* 2012;54:663–72
12. Weir NU, Pexman JH, Hill MD, et al. **How well does ASPECTS predict the outcome of acute stroke treated with IV tPA?** *Neurology* 2006;67:516–18
13. Puetz V, Dzialowski I, Hill MD, et al. **The Alberta Stroke Program Early CT Score in clinical practice: what have we learned?** *Int J Stroke* 2009;4:354–64
14. Dzialowski I, Hill MD, Coutts SB, et al. **Extent of early ischemic changes on computed tomography (CT) before thrombolysis: prognostic value of the Alberta Stroke Program Early CT Score in ECASS II.** *Stroke* 2006;37:973–78
15. Wintermark M, Albers GW, Broderick JP, et al. **Acute Stroke Imaging Research Roadmap II.** *Stroke* 2013;44:2628–39
16. Wintermark M, Albers GW, Alexandrov AV, et al. **Acute stroke imaging research roadmap.** *Stroke* 2008;39:1621–28
17. Kudo K, Christensen S, Sasaki M, et al. **Accuracy and reliability assessment of CT and MR perfusion analysis software using a digital phantom.** *Radiology* 2013;267:201–11
18. Straka M, Albers GW, Bammer R. **Real-time diffusion-perfusion mismatch analysis in acute stroke.** *J Magn Reson Imaging* 2010; 32:1024–37
19. Campbell BC, Christensen S, Levi CR, et al. **Cerebral blood flow is the optimal CT perfusion parameter for assessing infarct core.** *Stroke* 2011;42:3435–40
20. Aviv RI, Mandelcorn J, Chakraborty S, et al. **Alberta Stroke Program Early CT Scoring of CT perfusion in early stroke visualization and assessment.** *AJNR Am J Neuroradiol* 2007;28:1975–80
21. Tan JC, Dillon WP, Liu S, et al. **Systematic comparison of perfusion-CT and CT-angiography in acute stroke patients.** *Ann Neurol* 2007;61:533–43
22. McVerry F, Liebeskind DS, Muir KW. **Systematic review of methods for assessing leptomeningeal collateral flow.** *AJNR Am J Neuroradiol* 2012;33:576–82
23. Heiss WD. **The concept of the penumbra: can it be translated to stroke management?** *Int J Stroke* 2010;5:290–95
24. Heiss WD. **Ischemic penumbra: evidence from functional imaging in man.** *J Cereb Blood Flow Metab* 2000;20:1276–93
25. Lansberg MG, Lee J, Christensen S, et al. **RAPID automated patient selection for reperfusion therapy: a pooled analysis of the Echoplanar Imaging Thrombolytic Evaluation Trial (EPITHET) and the Diffusion and Perfusion Imaging Evaluation for Understanding Stroke Evolution (DEFUSE) Study.** *Stroke* 2011;42:1608–14

Hyperintense Vessels on FLAIR: Hemodynamic Correlates and Response to Thrombolysis

A. Kufner, I. Galinovic, V. Ambrosi, C.H. Nolte, M. Endres, J.B. Fiebach, and M. Ebinger

ABSTRACT

BACKGROUND AND PURPOSE: Hyperintense vessels on baseline FLAIR MR imaging of patients with ischemic stroke have been linked to leptomeningeal collateralization, yet the ability of these to maintain viable ischemic tissue remains unclear. We investigated whether hyperintense vessels on FLAIR are associated with the severity of hypoperfusion and response to thrombolysis in patients treated with intravenous tissue-plasminogen activator.

MATERIALS AND METHODS: Consecutive patients with ischemic stroke with an MR imaging before and within 24 hours of treatment, with proved vessel occlusion and available time-to-maximum maps were included ($n = 62$). The severity of hypoperfusion was characterized on the basis of the hypoperfusion intensity ratio (volume with severe/mild hypoperfusion [time-to-maximum $\geq$ 8 seconds / time-to-maximum $\geq$ 2 seconds]). The hypoperfusion intensity ratio was dichotomized at the median to differentiate moderate (hypoperfusion intensity ratio $\leq$ 0.447) and severe (hypoperfusion intensity ratio $>$ 0.447) hypoperfusion. Good outcome was defined as a modified Rankin Scale score of $\leq$2.

RESULTS: Hyperintense vessels on FLAIR were identified in 54 patients (87%). Patients with extensive hyperintense vessels on FLAIR (>4 sections) had higher NIHSS scores, larger baseline lesion volumes, higher rates of perfusion-diffusion mismatch, and more severe hypoperfusion (hypoperfusion intensity ratio). In stepwise backward multivariate regression analysis for the dichotomized hypoperfusion intensity ratio (including stroke etiology, age, perfusion deficit, baseline lesion volume, smoking, and extent of hyperintense vessels on FLAIR), extensive hyperintense vessels on FLAIR were independently associated with severe hypoperfusion (OR, 6.8; 95% CI, 1.1–42.7; $P = .04$). The hypoperfusion intensity ratio was an independent predictor of a worse functional outcome at 3 months poststroke (OR, 0.2; 95% CI, 0.5–0.6; $P < .01$).

CONCLUSIONS: Hyperintense vessels on FLAIR are associated with larger perfusion deficits, larger infarct growth, and more severe hypoperfusion, suggesting that hyperintense vessels on FLAIR most likely indicate severe ischemia as a result of insufficient collateralization.

ABBREVIATIONS: FHV = hyperintense vessels on FLAIR; HIR = hypoperfusion intensity ratio; IQR = interquartile range; Tmax = time-to-maximum; TOAST = Trial of Org 10172 in Acute Stroke Treatment

While most studies agree that hyperintense vessels on FLAIR (FHV) are highly associated with large-vessel occlusion, results on the underlying pathophysiology are seemingly split.[1] Several studies suggest FHV to be indicative of hemodynamic stress, inadequate collateralization, and poor functional recovery.[2-5] Conversely, others attributed FHV to increased leptomeningeal collateralization and found an association with smaller lesions, slower infarct progression, and better prognosis.[6-10]

The apparent contradiction of these studies may stem from the use of different methodologies and the diversity of populations studied, making the plethora of results challenging to analyze. Nevertheless, 2 critical questions remain due to lack of comprehensive imaging data and long-term clinical follow-up: Do FHV represent good collateralization or indicate the insufficiency of established collaterals to maintain ischemic tissue? Second, does FHV have clinical relevance in terms of functional recovery?

Received September 23, 2014; accepted after revision January 8, 2015.

From the Klinik und Hochschulambulanz für Neurologie (A.K., C.H.N., M. Endres, M. Ebinger), International Graduate Program Medical Neurosciences (A.K., V.A.), and Cluster of Excellence NeuroCure (M. Endres), Charité–Universitätsmedizin Berlin, Berlin, Germany; and Center for Stroke Research Berlin (I.G., C.H.N., M. Endres, J.B.F., M. Ebinger), Berlin, Germany.

This work was funded by the Federal Ministry of Education and Research via the grant Center for Stroke Research Berlin (01 EO 0801), the Volkswagen Foundation (Lichtenberg program to Matthias Endres), the EU (EUSTROKE, ARISE), and the German Research Foundation (NeuroCure, SFB-TR 43).

Please address correspondence to Anna Kufner, MSc, Klinik und Hochschulambulanz für Neurologie, Charité–Universitätsmedizin Berlin, Charitéplatz 1, Berlin-10117, Germany; e-mail: anna.kufner@charite.de

Indicates open access to non-subscribers at www.ajnr.org

http://dx.doi.org/10.3174/ajnr.A4320

The difficulty in determining collateral status poses a major challenge in answering these questions because digital subtraction angiography is not always readily available and associated risks may not be justified in most cases. Bang et al[11] used a hypoperfusion intensity ratio (HIR: time-to-maximum [Tmax] ≥ 8 seconds/Tmax ≥ 2 seconds) on baseline MR perfusion imaging as a surrogate marker of collateral status and found that excellent and intermediate collateral grades were highly associated with lower HIRs.

In the PRE-FLAIR study, patients with FHV had larger initial lesion volumes and more severe clinical impairment[12]; therefore, we hypothesized that patients with FHV would have more severe hypoperfusion, suggesting the insufficiency of established collaterals to maintain ischemic tissue before reperfusion is achieved. In this study, we investigated whether the extent of FHV is correlated with the severity of hypoperfusion by using Tmax perfusion maps and whether this plays a role in response to thrombolysis in patients with arterial occlusion treated with intravenous recombinant tissue plasminogen activator.

MATERIALS AND METHODS

This was a retrospective study conducted at the Center for Stroke Research Berlin at Charité University Hospital. Consecutive patients with acute stroke recruited between March 2008 and December 2012 (1000Plus study registered with clinicaltrials.gov; NCT 00715533) were selected for analysis on the basis of the following criteria: received IV-tPA within 4.5 hours of symptom onset, had MR imaging before and within 24 hours after treatment, and had proved vessel occlusion and acute perfusion maps of sufficient quality to postprocess into Tmax maps. MR imaging (3T, Tim Trio; Siemens, Erlangen, Germany) protocol included T2*, FLAIR (TE = 100 ms, TR = 8000 ms, TI = 2370.5 ms, FOV = 220 mm, matrix = 256 × 232, 5-mm section thickness with a 0.5-mm intersection gap), diffusion-weighted imaging (TE = 93.1 ms, TR = 7600 ms, FOV = 230 mm, matrix = 192 × 192, 2.5-mm section thickness with no intersection gap), MR angiography (TE = 3.86 ms, TR = 22.0 ms, FOV = 200 mm, matrix = 384 × 268, 0.65-mm section thickness with a 7.2 mm intersection gap), and perfusion imaging (TE = 29 ms, TR = 1390 ms, FOV = 230 mm, matrix = 128 × 128, 5-mm section thickness with a 0.5-mm intersection gap).

The following cerebrovascular risk factors were evaluated on admission by using previously published definitions[13]: smoking, arterial hypertension, diabetes mellitus, hypolipoproteinemia, and atrial fibrillation. Stroke severity was assessed by using the National Institutes of Health Stroke Scale. Stroke etiology was determined by using the Trial of Org 10172 in Acute Stroke Treatment (TOAST) criteria.[14] Functional outcome was assessed 3 months poststroke by using the modified Rankin Scale score; favorable outcome was defined as mRS of ≤2.

Blinded to acute perfusion imaging, 2 raters (A.K., I.G.) independently counted the number of FLAIR sections with FHV, defined as focal, linear, or serpentine hyperintensities distal to the main occluded artery. In case of disagreement, raters met for consensus. The number of sections with FHV was dichotomized at the median (≤ or >4 sections) to distinguish between less pronounced versus more extensive FHV.

Postprocessing of DWI was performed by using MRIcro (Advanced Brain Imaging; McCausland Center for Brain Imaging, Columbia, South Carolina) to assess lesion volumes on acute and second-scan images to determine infarct growth (DWI lesion volume after thrombolysis − DWI baseline lesion volume). Stroketool (Digital Image Solutions; Frechen, Germany) was used to assess acute perfusion deficit volume (MTT > 6 seconds). Perfusion-diffusion mismatch was assessed as a binary variable defined as follows: (perfusion deficit − DWI lesion volume)/DWI lesion volume × 100 > 20%. Tmax maps of acute perfusion imaging images were created in Stroketool. The severity of the hypoperfusion was characterized on the basis of HIR (Fig 1), defined as tissue volume with severe hypoperfusion (Tmax ≥ 8 seconds) divided by volume with mild hypoperfusion (Tmax ≥ 2 seconds). HIR was dichotomized at the median to differentiate moderate (HIR ≤ 0.447) and severe (HIR > 0.447) hypoperfusion.

Arterial occlusion was evaluated on time-of-flight MRA. Arterial occlusions were categorized on the basis of the size of the occluded vessel: large-vessel occlusions (internal carotid artery and carotid-T occlusions), medium-vessel occlusions (ie, M1, M2, P1, P2, and vertebral occlusions), and small-vessel occlusions (ie, occlusion in distal arterial branches).[15] Recanalization was defined as an increase in at least 2 Thrombolysis in Myocardial Infarction points within 24 hours of treatment based on acute and follow-up MRA.

For all 2-group analyses, we used the Fisher exact test and Mann-Whitney *U* test as appropriate. We chose a stepwise backward regression model with a binary dependent variable (dichotomized HIR and outcome) for multivariate regression analyses; all parameters that reached a significance of <.1 in univariate analysis based on the dependent variable were included for analysis.

Stepwise backward multivariate regression analysis was performed to determine independent predictors of the severity of hypoperfusion. We included the following parameters: TOAST criteria, the size of the vessel occlusion, smoking, baseline perfusion deficit, baseline lesion volume, and extent of FHV. Analogously, stepwise backward regression analysis was performed for favorable outcome, with the only change being that age was also dichotomized at older than 70 years to increase external comparability[13] (age [older than 70 years], smoking, atrial fibrillation, HIR [>0.447], NIHSS score on admission, baseline lesion volume, and extent of FHV [>4 sections]). All statistical analyses were performed by using SPSS, Version 19 (IBM, Armonk, New York).

RESULTS

Sixty-two patients were included for final analysis (mean age, 71.4 ± 13.9 years; 48.4% female; median NIHSS score on admission, 11; interquartile range [IQR], 4.8–16); 87% had visible FHV on acute FLAIR ($n = 54$). Interrater reliability for the presence of FHV was high ($\kappa = 0.86$; $P < .01$); in 9 cases, raters differed in >2 sections when counting the number of sections with FHV.

Patients with extensive FHV (>4 sections) had higher NIHSS scores on admission, larger baseline lesion volumes, higher rates of perfusion-diffusion mismatch, and more severe hypoperfusion (ie, HIR) (Table 1). Patient groups also differed in terms of stroke

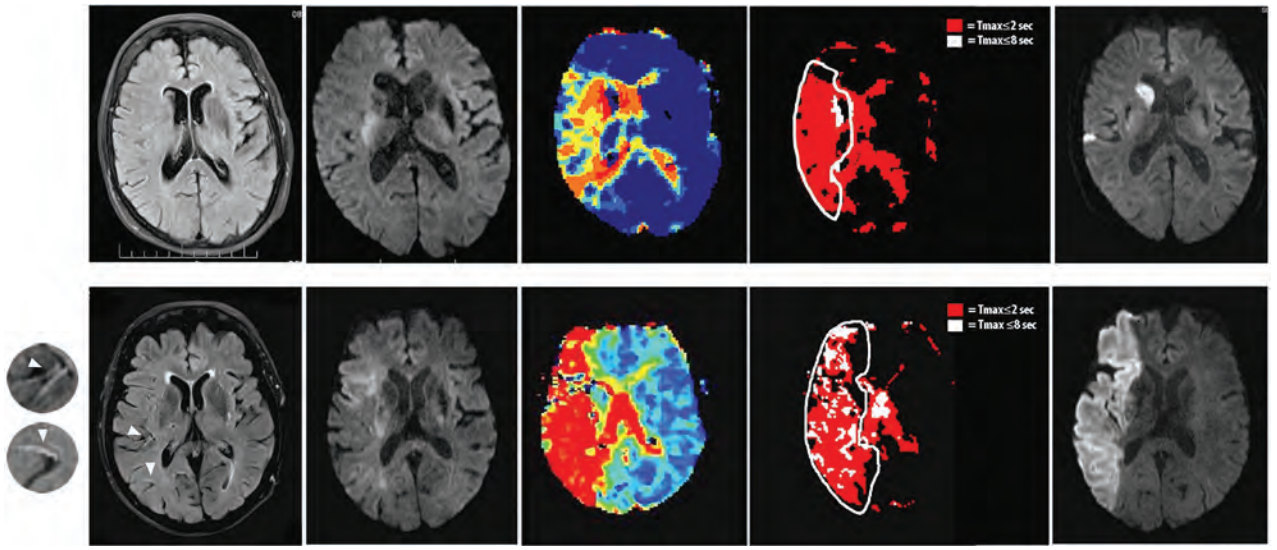

FIG 1. MR imaging (left-to-right: acute FLAIR, acute DWI, acute Tmax, dichotomized Tmax, follow-up DWI) of patients with middle cerebral artery occlusions (M1). Patient A (82 years of age; baseline NIHSS score, 13; baseline lesion volume, 1.4 mL; HIR, 0.031; recanalization to Thrombolysis in Myocardial Infarction 2 following treatment; absolute infarct growth, 3.3 mL) had FLAIR hyperintense vessels on 3 sections (FHV ≤ 4; not visible on the depicted section) and patient B (76 years of age; baseline NIHSS score, 23; baseline lesion volume, 63.8 mL; HIR, 0.53; no recanalization following treatment [Thrombolysis in Myocardial Infarction, 0]; absolute infarct growth, 80.2 mL) had FHV on 8 sections (*arrows*; FHV > 4).

Table 1: Comparison of baseline parameters and response to thrombolysis based on the number of sections with FLAIR hyperintense vessels[a]

	Visible FHV on ≤4 Sections	Visible FHV on >4 Sections	*P* Value
No.	30	32	
Age (yr) (mean) (SD)	71 (10.8)	71.9 (16.5)	.42
Time to MRI in min (median) (IQR)	88.5 (72–103)	93.5 (61–121)	.98
NIHSS score on admission (median) (IQR)	5 (4–13)	14.5 (11–18)	<.001
NIHSS score on day 2 (median) (IQR)	3 (1–5)	5 (2–17)	.03
TOAST			.05
Cardioembolic (%) (No.)	40.7 (11)	36.7 (11)	
Macroangiopathic (%) (No.)	37 (10)	63.3 (19)	
Microangiopathic (%) (No.)	0 (0)	0 (0)	
Other (%) (No.)	7.4 (2)	0 (0)	
Competing causes (%) (No.)	14.8 (4)	0 (0)	
Baseline lesion volume (mL) (median) (IQR)	1.6 (.3–4.9)	8.1 (2.4–20.6)	<.01
Infarct growth (median) (IQR)	1.2 (0.2–12.7)	12.8 (2.5–43.9)	<.01
Perfusion-diffusion mismatch (%) (No.)	67.7 (21)	96.9 (31)	<.01
Baseline perfusion deficit (mL) (median) (IQR)	24.8 (14.5–54.6)	118 (82–175)	<.001
Tmax ≥2 sec	30 (16.7–97.1)	155 (115.7–191.2)	<.001
Tmax ≥8 sec	10.3 (3.7–27.2)	87.2 (62.5–123.7)	<.001
HIR	0.28 (0.07–0.47)	0.61 (0.44–0.73)	<.01
Vessel occlusion size:			.29
Large (%) (No.)	20 (6)	9.4 (3)	
Medium (%) (No.)	80 (24)	90.6 (29)	
Small (%) (No.)	0 (0)	0 (0)	
Recanalization (%) (No.)	53.3 (16)	74.2 (23)	.11
Favorable outcome at 3 months (%) (No.)	66.7 (20)	38.7 (12)	.02

[a] A Fisher exact test and Mann-Whitney *U* test were used for categoric and continuous variables, respectively.

etiology, in which patients with extensive FHV more often had macroangiopathic strokes. Despite the similarity of vessel-occlusion size and recanalization rates, patients with extensive FHV had larger infarct growth and a worse functional recovery 3 months poststroke.

Patients with severe hypoperfusion were significantly older and less often smokers and had higher NIHSS scores on admission, more sections with FHV, larger perfusion deficits, higher baseline lesion volumes, and lower rates of a favorable outcome (Table 2). Stroke etiology based on the TOAST criteria did not differ between groups.

In multivariate regression analysis for HIR, the extent of FHV was associated with severe hypoperfusion (OR, 6.8; 95% CI, 1.1–42.7; $P = .04$; Table 3). In multivariate regression analysis for outcome, only baseline lesion volume (OR, 0.95; 95% CI, 0.9–1.0; $P = .05$) and dichotomized HIR (OR, 0.17; 95% CI, 0.05–0.57; $P < .01$) remained in the model (Table 4). Last-step multivariate r^2 increased from 0.42 to 0.49 when age was included in the model as a continuous variable.

DISCUSSION

The extent of FHV is not only associated with larger perfusion deficits[1,16] but is also an independent predictor of more severe hypoperfusion, resulting in larger infarct growth. Although we found no independent association between the extent of FHV and functional recovery, the severity of hypoperfusion was independently associated with a worse functional recovery 3 months poststroke (Table 2).

Similar to results from a multicenter observational study,[12] approximately 87% of patients with proved vessel occlusion had at least 1 section with FHV on acute examination. Patients with extensive FHV (>4 sections) had comparatively higher NIHSS scores on admission, more severe hypoperfusion, larger infarct growth, and a worse functional outcome 3 months poststroke. While patient

Table 2: Univariate analysis comparing patients with moderate hypoperfusion (HIR ≤ 0.447) with patients with severe hypoperfusion (HIR > 0.447)[a]

	Low HIR (≤0.447)	High HIR (>0.447)	*P* Value
No.	31	31	
Age (yr) (mean) (SD)	67.5 (13.2)	75.4 (13.7)	.02
Female (%) (No.)	51.6 (16)	45.2 (14)	.8
Arterial hypertension (%) (No.)	80.6 (25)	87.1 (27)	.73
Diabetes mellitus (%) (No.)	16.1 (5)	25.8 (8)	.53
Smoking (%) (No.)	38.7 (12)	9.7 (3)	.02
Hypolipoproteinemia (%) (No.)	54.8 (17)	46.4 (15)	.9
Atrial fibrillation (%) (No.)	35.5 (11)	45.2 (14)	.6
No. of sections with FHV (median) (IQR)	3 (1–7)	7 (4–10)	<.01
NIHSS score on admission (median) (IQR)	5 (4–13)	15 (11–18)	<.001
Baseline lesion volume (mL) (median) (IQR)	1.5 (0.27–5.8)	6.7 (2.3–28.2)	<.01
Infarct growth (median) (IQR)	1.6 (0.2–10.6)	6.2 (1.4–39.0)	<.01
Baseline perfusion deficit (mL) (median) (IQR)	41.2 (15.8–101.7)	117.1 (56.0–171.6)	<.01
Tmax ≥ 2 sec	75.6 (24.7–179.4)	143.1 (70.5–170.2)	.08
Tmax ≥ 8 sec	10.5 (3.7–61.9)	88.2 (43.7–122.6)	<.001
Vessel-occlusion size:			.47
Large (%) (No.)	19.4 (6)	9.7 (3)	
Medium (%) (No.)	80.6 (25)	90.3 (28)	
Small (%) (No.)	0 (0)	0 (0)	
Recanalization (%) (No.)	70 (21)	58.1 (18)	.43
Favorable outcome at 3 months (%) (No.)	75.9 (22)	32.3 (10)	<.01

[a] A Fisher exact test and Mann-Whitney *U* test were used for categoric and continuous variables, respectively.

Table 3: Stepwise multivariate regression analysis for severity of hypoperfusion (dichotomized at median)

	Odds Ratio	95% CI	*P* Value	Univariate r^2
First step (multivariate $r^2 = 0.68$)				
Age	1.2	1.0–1.3	.01	0.12
TOAST	0.76	0.15–4.2	.77	0.004
Baseline lesion volume	1.1	1.0–1.2	.04	0.12
Baseline perfusion deficit	1.0	0.99–1.0	.06	0.12
Sections with FHV (>4)	6.7	1.0–41.9	.04	0.26
Smoking	0.04	0.001–0.99	.05	0.14
Last step (multivariate $r^2 = 0.68$)				
Age	1.2	1.0–1.3	.01	
Baseline lesion volume	1.1	1.0–1.2	.05	
Baseline perfusion deficit	1.01	0.9–1.0	.06	
Smoking	0.04	0.001–0.96	.05	
Sections with FHV (>4)	6.8	1.1–42.7	.04	

Table 4: Stepwise multivariate regression analysis for favorable outcome (mRS ≤2)

	Odds Ratio	95% CI	*P* Value	Univariate r^2
First step (multivariate $r^2 = 0.42$)				
Age (older than 70 years)	1.0	0.23–5.8	.95	0.0
Smoking	0.84	0.20–4.5	.83	0.02
Atrial fibrillation	0.41	0.10–1.6	.21	0.14
Sections with FHV (>4)	0.89	0.2–3.9	.88	0.12
HIR (>0.447)	0.24	0.05–1.1	.07	0.24
NIHSS score on admission	0.93	0.83–1.0	.12	0.25
Baseline lesion volume	0.96	0.90–1.0	.12	0.21
Last step (multivariate $r^2 = 0.36$)				
HIR (>0.447)	0.17	0.05–0.57	< .01	
Baseline lesion volume	0.95	0.90–1.0	.05	

groups based on FHV differed in terms of stroke etiology, TOAST criteria showed neither association with the severity of hypoperfusion nor functional recovery in univariate analysis.

Bang et al[11] used the same Tmax HIR ratio to determine the severity of the perfusion deficit and found similar results in terms of NIHSS scores on admission and infarct volume. Most interesting, this study found that low HIR (moderate hypoperfusion) was highly associated with good collateral grades. This finding is in line with our hypothesis that FHV are indicative of severe hypoperfusion and insufficient collateralization. These results stand in contrast to previous studies suggesting that FHV represent increased leptomeningeal collateralization[6,7,10,17]; these studies, however, did not report perfusion status or clinical follow-up.

Peripheral collateralization is an inherent defense mechanism following proximal vessel occlusion; collaterals can prolong tissue viability if blood flow is sufficient to keep hypoperfusion moderate until reperfusion is achieved. Vessels become hyperintense on FLAIR when blood flow is so slow that there is a loss of the flow-void phenomenon. Here, we observe an independent association between the extent of FHV and severe hypoperfusion (Table 3); however, the link to collateral flow is not yet clear. On the one hand, one might imagine that slow flow in collaterals directly causes arterial hyperintensities on FLAIR, suggesting that FHV directly depict insufficient or sluggish flow in collateral pathways.[7,8] On the other hand, vessel occlusion and subsequent ischemia cause cerebral swelling, which likely compresses distal collateral vessels, slowing blood flow. Regardless, FHV most likely reflect slow flow in distal collateral pathways distributed over a large ischemic area, resulting in larger ischemic lesions. Hence, this frequently observed MR imaging feature may be useful as a tool to assess the severity of hypoperfusion over an ischemic area as a result of poor collateralization.

Of note, patients with large-vessel occlusion had less pronounced FHV (<4) and more moderate hypoperfusion (low HIR), though these did not reach the level of significance (Tables 1 and 2). Carotid occlusions are frequently the end result of chronic occlusive disease, and the recruitment of collaterals often happens before acute stroke takes place. Thus, one might imagine that the longer large-vessel disease has been in existence before the index event, the greater the likelihood of excellent flow in collaterals. These collaterals might maintain good flow without visible FHV; however, this is mere speculation.

Although HIR was an independent predictor of functional recovery, we observed no independent associations of the extent of FHV and outcome (Table 4). A possible explanation may lie in the heterogeneity of vessel occlusion size observed in this cohort; an independent analysis including only patients with middle cerebral artery occlusions is suggested.

In multivariate analysis for outcome, baseline lesion volume remained in the model, accounting for 21% of the variance; this is to be expected because initial infarct volume may reflect collateral status. While FHV may be indicative of insufficient collateral flow, the clinical relevance of this MR imaging sign in terms of predicting response to treatment remains unclear. A study by Olindo et al[9] found extensive FHV associated with smaller infarcts pre- and posttreatment, as well as a better prognosis in patients with MCA occlusion. The discordance of these results may lie in the use of different MR imaging units (1T versus 3T), the characteristics of populations studied, and the question at hand. In this study, we focused primarily on the acute hemodynamic correlates of FHV, which show a clear independent association with more severe hypoperfusion; the prognostic value of FHV remains unresolved.

Most interesting, smoking was independently associated with moderate hypoperfusion, suggesting better collateralization in patients with this risk factor. Bang et al[11] also found an association between smoking status and low HIR. Studies have suggested that long-term smoking-induced atherosclerosis leads to increased collateralization,[18] which may explain this observed phenomenon.

This study has limitations. Most important, it is a retrospective observational study. Furthermore, lack of DSA did not allow direct assessment of collateral grade; the use of HIR only partially compensated for this limitation. Finally, due to small numbers, this study runs the risk of type 2 errors, and multivariable regression analyses may lead to overfitting.

CONCLUSIONS

The extent of FHV on baseline MR imaging is an independent predictor of severe hypoperfusion in patients with acute ischemic stroke. FHV were highly associated with more severe strokes and larger infarct growth, suggesting that this frequently observed MR imaging feature most likely indicates severe ischemia due to the insufficiency of established collaterals to maintain ischemic tissue before recanalization is achieved.

Disclosures: Christian H. Nolte—*UNRELATED*: *Consultancy*: Bristol-Myers Squibb, Pfizer, Bayer Pharma; *Payment for Lectures (including service on Speakers Bureaus)*: Pfizer, Boehringer Ingelheim; *OTHER*: payment for lectures and travel grants from Boeheringer-Ingelheim and Takeda-Pharma. Matthia Endres—*RELATED*: *Grant*: DFG: Excellence Cluster NeuroCure,* Federal Ministry of Education and Research: Center for Stroke Research,* EU: WakeUp,* Volkswagen Foundation: Lichtenberg-Program*; *UNRELATED*: *Board Membership*: Bayer, Boehringer Ingelheim, Pfizer, BMS, MSD, Sanofi, *Comments*: Advisory Board; *Grants/Grants Pending*: DFG,* EU,* AstraZeneca,* Roche,* Sanofi,* *Comments*: DFG: SFB TR43, KFO 247, KFO 213, EU: ESN, Counterstroke (an EU-funded research project in which specialists collaborate to develop novel therapies to treat stroke); *Payment for Lectures (including service on Speakers Bureaus)*: Astra Zeneca, Bayer, Boston Scientific, Bristol-Myers Squibb, Boehringer-Ingelheim, Ever, Glaxo Smith Kline, MSD, Novartis, Pfizer, Sanofi; *OTHER*: He reports the following consultancies, grants and/or payments for lectures including service on speakers bureaus: Astra Zeneca, Bayer, Berlin Chemie, BMS, Boehringer-Ingelheim, Glaxo Smith Kline, Novartis, Pfizer, Sanofi-Aventis, Trommsdorff; he holds a patent for the upregulation of type III endothelial cell nitric oxide synthase by HMG-CoA reductase inhibitors (US patent number 6,147,109). Jochen B. Fiebach—*RELATED*: *Consulting Fee or Honorarium*: Boehringer; *UNRELATED*: *Board Membership*: Lundbeck, Sygnis, Synarc, *Comments*: Head of Imaging Board of the Desmotoplase in Acute Ischemic Stroke Trial (DIAS) 3&4 and Imaging Board DIAS J; central reader AXIS 2 trial; central reader i.a. Thrombolysis trial; *Consultancy*: Lundbeck, *Comments*: DIAS 3&4; *Payment for Lectures (including service on Speakers Bureaus)*: Boehringer Ingelheim, Siemens, *Comments*: stroke imaging; *OTHER*: He reports the following board memberships, consultancies and/or payments for lectures including service on speakers bureaus: Boehringer-Ingelheim, Lundbeck, Siemens, Sygnis, Synarc. *Money paid to the institution.

REFERENCES

1. Azizyan A, Sanossian N, Mogensen MA, et al. **Fluid-attenuated inversion recovery vascular hyperintensities: an important imaging marker for cerebrovascular disease.** *AJNR Am J Neuroradiol* 2011;32:1771–75
2. Ebinger M, Kufner A, Galinovic I, et al. **Fluid-attenuated inversion recovery images and stroke outcome after thrombolysis.** *Stroke* 2012;43:539–42
3. Girot M, Gauvrit JY, Cordonnier C, et al. **Prognostic value of hyperintense vessel signals on fluid-attenuated inversion recovery sequences in acute cerebral ischemia.** *Eur Neurol* 2007;57:75–79
4. Hohenhaus M, Schmidt WU, Brunecker P, et al. **FLAIR vascular hyperintensities in acute ICA and MCA infarction: a marker for mismatch and stroke severity?** *Cerebrovasc Dis* 2012;34:63–69
5. Kamran S, Bates V, Bakshi R, et al. **Significance of hyperintense vessels on FLAIR MRI in acute stroke.** *Neurology* 2000;55:265–69
6. Huang X, Liu W, Zhu W, et al. **Distal hyperintense vessels on FLAIR: a prognostic indicator of acute ischemic stroke.** *Eur Neurol* 2012;68:214–20
7. Lee KY, Latour LL, Luby M, et al. **Distal hyperintense vessels on FLAIR: an MRI marker for collateral circulation in acute stroke?** *Neurology* 2009;72:1134–39
8. Liu W, Xu G, Yue X, et al. **Hyperintense vessels on FLAIR: a useful non-invasive method for assessing intracerebral collaterals.** *Eur J Radiol* 2011;80:786–91
9. Olindo S, Chausson N, Joux J, et al. **Fluid-attenuated inversion recovery vascular hyperintensity: an early predictor of clinical outcome in proximal middle cerebral artery occlusion.** *Arch Neurol* 2012;69:1462–68
10. Pérez de la Ossa N, Hernandez-Perez M, Domenech S, et al. **Hyperintensity of distal vessels on FLAIR is associated with slow progression of the infarction in acute ischemic stroke.** *Cerebrovasc Dis* 2012;34:376–84
11. Bang OY, Saver JL, Alger JR, et al. **Determinants of the distribution and severity of hypoperfusion in patients with ischemic stroke.** *Neurology* 2008;71:1804–11
12. Cheng B, Ebinger M, Kufner A, et al. **Hyperintense vessels on acute stroke fluid-attenuated inversion recovery imaging: associations with clinical and other MRI findings.** *Stroke* 2012;43:2957–61
13. Kufner A, Nolte CH, Galinovic I, et al. **Smoking-thrombolysis paradox: recanalization and reperfusion rates after intravenous tissue plasminogen activator in smokers with ischemic stroke.** *Stroke* 2013;44:407–13
14. Adams HP Jr, Bendixen BH, Kappelle LJ, et al; TOAST Investigators. **Classification of subtype of acute ischemic stroke: definitions for use in a multicenter clinical trial.** *Stroke* 1993;24:35–41
15. TIMI Study Group. **The Thrombolysis in Myocardial Infarction (TIMI) trial—phase I findings.** *N Engl J Med* 1985;312:932–36
16. Schellinger PD. **Diagnostic accuracy and relevance of early MRI vessel signs are highly overrated.** *Cerebrovasc Dis* 2006;21:215; author reply 215–16
17. Liu W, Xu G, Yue X, et al. **Hyperintense vessels on FLAIR: a useful non-invasive method for assessing intracerebral collaterals.** *Eur J Radiol* 2011;80:786–91
18. Koerselman J, de Jaegere PP, Verhaar MC, et al. **Coronary collateral circulation: the effects of smoking and alcohol.** *Atherosclerosis* 2007;191:191–98

Evaluating CT Perfusion Deficits in Global Cerebral Edema after Aneurysmal Subarachnoid Hemorrhage

H. Baradaran, V. Fodera, D. Mir, K. Kesavobhotla, J. Ivanidze, U. Ozbek, A. Gupta, J. Claassen, and P.C. Sanelli

ABSTRACT

BACKGROUND AND PURPOSE: Global cerebral edema is an independent predictor of mortality and poor outcomes after aneurysmal SAH. Global cerebral edema, a complex disease process, is thought to be associated with an altered cerebral autoregulatory response. We studied the association between cerebral hemodynamics and early global cerebral edema by using CTP.

MATERIALS AND METHODS: We retrospectively studied consecutive patients with aneurysmal SAH with admission CTP performed at days 0–3. Two neuroradiologists classified global cerebral edema and hydrocephalus on NCCT performed concurrently with CTP. Global cerebral edema was defined as diffuse effacement of the sulci and/or basal cisterns or diffuse disruption of the cerebral gray-white matter junction. CTP was postprocessed into CBF and MTT maps by using a standardized method. Quantitative analysis of CTP was performed by using standard protocol with ROI sampling of the cerebral cortex. The Fisher exact test, Mann-Whitney test, and independent-samples *t* test were used to determine statistical associations.

RESULTS: Of the 45 patients included, 42% (19/45) had global cerebral edema and 58% (26/45) did not. Patient groups with and without global cerebral edema were well-matched for demographic and clinical data. Patients with global cerebral edema were more likely to have qualitative global CTP deficits than those without global cerebral edema ($P = .001$) with an OR = 13.3 (95% CI, 2.09–138.63). Patients with global cerebral edema also had a very strong trend toward statistical significance, with reduced quantitative CBF compared with patients without global cerebral edema ($P = .064$).

CONCLUSIONS: Global perfusion deficits are significantly associated with global cerebral edema in the early phase after aneurysmal SAH, supporting the theory that hemodynamic disturbances occur in global cerebral edema.

ABBREVIATIONS: GCE = global cerebral edema; aSAH = aneurysmal subarachnoid hemorrhage; DCI = delayed cerebral ischemia

Aneurysmal subarachnoid hemorrhage (aSAH) is a devastating disease with serious complications and lasting impairment in patients who survive. It has a mortality rate ranging from 32% to 67%[1-3] and accounts for up to 7% of all strokes.[4] While there has been some minimal improvement in the mortality rate since the 1960s, the persistently poor outcomes make aSAH a serious disease. Poor outcomes occur after survival from the initial aneurysm rupture, with long-term functional disability in more than half of patients, of whom 26% have persistent dependence.[5] Additionally, as many as 20% of patients have global cognitive impairment contributing to poor functional status.[6] Thus, aSAH is associated with a substantial burden on health care resources, most of which are related to long-term care for functional and cognitive disability.[7]

After aneurysm rupture, early global cerebral edema (GCE) contributes significantly to functional and cognitive disability as a secondary complication.[7-12] GCE typically occurs in the early phase (days 0–3) after SAH[10-12] and has been shown to be an independent predictor of morbidity and mortality.[10] Currently, detection of GCE is limited to qualitative assessment of subtle findings on NCCT.[10] While this finding is fairly common, it is

Received September 3, 2014; accepted after revision January 18, 2015.

From the Departments of Radiology (H.B., V.F., D.M., K.K., J.I., A.G.) and Public Health (U.O.), NewYork-Presbyterian Hospital, Weill Cornell Medical College, New York, New York; Department of Neurology (J.C.), NewYork-Presbyterian Hospital, Columbia University Medical Center, New York, New York; and Department of Radiology (P.C.S.), North-Shore–Long Island Jewish Health System, Great Neck, New York.

This work was supported by Grant 5K23NS058387 from the National Institute of Neurological Disorders and Stroke, a component of the National Institutes of Health.

Paper previously presented at: Annual Meeting of the American Society of Neuroradiology and the Foundation of the ASNR Symposium, May 18–23, 2013; San Diego, California.

Please address correspondence to H. Baradaran, MD, Department of Radiology, NewYork-Presbyterian Hospital, Weill Cornell Medical College, 525 East 68th St, Starr 8A, NY, NY 10065; e-mail: heb2017@nyp.org

Indicates open access to non-subscribers at www.ajnr.org

http://dx.doi.org/10.3174/ajnr.A4328

often difficult to appreciate and quantify, so the true incidence of GCE is likely underreported.[10] The lack of quantitative markers is a major limitation for accurate detection and monitoring of GCE to guide management. Although little is known about the mechanisms underlying GCE, microvascular dysfunction from diffuse ischemic injury has been implicated in the initial circulatory arrest at the time of aneurysm rupture.[10] The neurotoxic effects from the breakdown of blood products after the initial circulatory arrest may lead to hemodynamic disturbances in autoregulatory response and neuronal dysfunction,[10] which may be involved in the pathophysiology of GCE.[13-16]

GCE is a complex and poorly understood disease process with many contributing factors. Understanding the mechanisms underpinning the development of GCE can aid in prevention and treatment of this disease process. Because of the potential role of hemodynamic disturbance in GCE, we evaluated cerebral perfusion parameters, including CBF and MTT by using CTP in patients with early GCE after aSAH.

MATERIALS AND METHODS

Study Population

This was an institutional review board–approved retrospective study of consecutive patients with aSAH with CTP examinations performed on admission (days 0–3) between October 2008 to March 2011 at New York-Presbyterian Hospital–Weill Cornell. A total of 105 patients were admitted with aneurysmal subarachnoid hemorrhage; however, patients were only included if they had a baseline CTP examination on days 0–3 of admission according to our standard scanning protocol. The presence of GCE and the degree of hydrocephalus were determined on NCCT performed concurrently with CTP by 2 neuroradiologists by consensus. They interpreted the NCCT and CTP findings at separate time points, blinded to all other clinical and imaging data. We used a 2-part definition for GCE that was similar to that in published criteria: 1) complete or near-complete effacement of the hemispheric sulci and basal cisterns, and 2) bilateral and extensive disruption of the cerebral gray-white matter junction at the level of the centrum semiovale.[10] Patients were classified as having GCE if either diffuse effacement of the sulci and basal cisterns or diffuse disruption of the cerebral gray-white matter junction was present on the admission NCCT scan. Hydrocephalus was classified as none, mild, moderate, or severe by 2 neuroradiologists by consensus on the basis of the admission NCCT. All demographic and clinical data, including Glasgow Coma Scale scores, Hunt and Hess scores, smoking history, and history of hypertension, were obtained from retrospective chart review.

CTP Scanning, Postprocessing, and Data Collection

CTP was performed on admission (days 0–3) in all patients with aSAH before aneurysm treatment. We performed initial noncontrast CT of the head from the foramen magnum to the vertex, using 5.0-mm-thick sections with 120 kV(peak), 250 mAs, and 1.0 rotation time. A standard scanning protocol for CTP at our institution uses the HD750 scanner (GE Healthcare, Milwaukee, Wisconsin) with a cine 4i scanning mode and a 45-second acquisition at 1 rotation per second with 80 kVp and 190 mA. A scanning volume of 2.0 cm was used, consisting of 4 sections at 5.0-mm thickness with its inferior extent selected at the level of the basal ganglia, above the orbits, to minimize radiation exposure to the lenses. Approximately 45 mL of nonionic iodinated contrast was administered intravenously at 5 mL/s by using a power injector with a 5-second delay.

Postprocessing of the acquired images into CBF, MTT, and CBV maps was performed on an Advantage Workstation by using CTP software, Version 3.0 (GE Healthcare). This software uses a deconvolution method, which is considered most accurate for low-contrast injection rates.[17] The postprocessing technique was standardized for all patients according to recommended guidelines,[18] with the arterial input function as the A2 segment of the anterior cerebral artery[19] and the venous function as the superior sagittal sinus. In the deconvolution method, selection of the arterial input function has been shown to not significantly affect the quantitative perfusion values.[18,20,21]

The perfusion maps were qualitatively evaluated by 2 neuroradiologists (with 7 and 10 years' experience) blinded to clinical and imaging data, to determine the presence of global perfusion deficits, defined as diffusely decreased CBF and/or elevated MTT. Focal perfusion abnormalities due to the primary hemorrhagic event, surgical intervention, hematoma, or vasospasm as identified on the acquired images from the CTP dataset were not included as perfusion deficits related to early global cerebral ischemia. After the images were reviewed independently, consensus judgment was determined.

Quantitative analysis was conducted by using a standardized method with contiguous ROI placement, measuring 157 mm^2, sampling the cerebral cortex. Each CTP section had up to 24 ROIs distributed along the cortical surfaces to include mostly gray matter in the following territories: approximately 6 ROIs in the anterior cerebral artery, 12 in the MCA, and 6 in the posterior cerebral artery (Fig 1). CTP studies were analyzed with readers blinded to all clinical and imaging data to limit test-review bias.

Statistical Analysis

The incidence of qualitative diffuse CTP deficits was calculated for each outcome group (GCE and non-GCE). Two-tailed *P* values were calculated by using the Fisher exact test to determine statistical significance. The OR was also calculated to determine the strength of association between GCE and CTP deficits. The Mann-Whitney test was used to determine the statistical difference between patient groups for demographic characteristics.

Quantitative CTP data were analyzed by calculating the mean CBF, CBV, and MTT and their SDs for each outcome group by using all ROIs for all 4 section locations included in the arithmetic means. To minimize the contribution of vascular pixels from large vessels, we excluded CBF values of >100 mL/100 g/min from the statistical analysis and did not use these in calculating the mean CBF, CBV, and MTT because this method has been published in the evaluation of ischemia.[22] The ROIs in the perfusion abnormalities due to the primary hemorrhagic event and/or surgical intervention were not included in the statistical analysis. A Student 2-tailed *t* test was used to determine statistical significance, accepted at $P < .05$.

Interobserver reliability for the detection of GCE between the 2 neuroradiologists was calculated by using the Cohen κ statistic

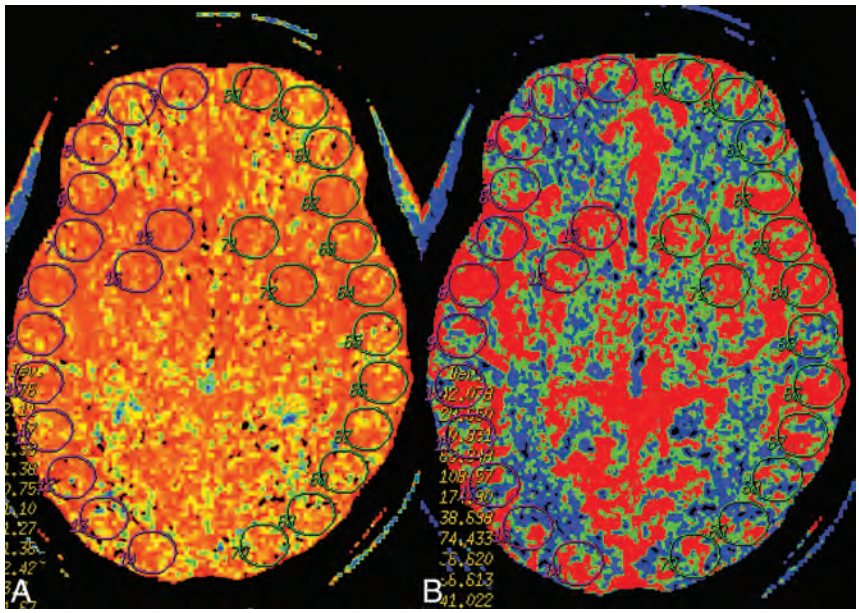

FIG 1. Example of ROI placement on the MTT (*A*) and CBF (*B*) maps in a representative patient.

Demographic, clinical, and imaging characteristics[a]

	No GCE	GCE	Statistical Comparison
Age (yr)	55.4 ± 13.5	49.7 ± 12.56	$Z = 0.36$
Sex	76.9% (female)	73.7% (female)	$P = 1$
Smoking history	50% (13/26)	42% (8/19)	$P = .76$
History of hypertension	42% (11/26)	63% (12/19)	$P = .23$
Admission Hunt and Hess score	2.58 ± 1.00	2.95 ± 1.10	$P = .64$
Admission GCS	13–14	13–14	$P = .67$
Hydrocephalus	1.77 ± 0.80 (mild)	2.00 ± 0.65 (mild)	$P = .368$
Global CBF	40.3 ± 11.0	34.8 ± 7.6	$P = .06$
Global MTT	5.6 ± 1.56	6.38 ± 2.02	$P = .15$

Note:—GCS indicates Glasgow Coma Scale.

[a] Mean values are given for age, admission Hunt and Hess score, admission GCS, hydrocephalus, global CBF, and global MTT.

with separate analyses for each criterion of sulcal effacement and gray-white matter differentiation.

RESULTS

Forty-five patients with aSAH and admission CTP studies were included in the statistical analysis. Of these 45 patients, 42.2% (19/45) were classified as having GCE, and 57.8% (26/45), without GCE. Patient groups with and without GCE were well-matched for basic demographic characteristics including age, sex, admission Hunt and Hess and Glasgow Coma Scale scores, and hydrocephalus (Table). Qualitative global perfusion deficits were seen in 53% (10/19) of patients with GCE and 7.7% (2/26) of patients without GCE. No evidence of vasospasm was seen on either the CTA or CTP examinations for the patients included in the study. The Fisher exact test revealed that patients with GCE had significantly higher rates of global perfusion deficits ($P = .001$) compared with patients without GCE (Fig 2) with an OR = 13.3 (95% CI, 2.09–138.63). The mean global CBF in patients without GCE was 40.31 mL/100 g/min compared with 34.75 mL/100 g/min in patients with GCE ($P = .064$). The mean global MTT in patients with GCE was 6.38 seconds compared with 5.60 seconds in patients without GCE ($P = .153$). The mean global CBV in patients with GCE was 2.29 mL/100 g compared with 2.16 mL/100 g in patients without GCE ($P = .78$). The Cohen κ statistic for interobserver reliability for classification of sulcal effacement was high, with a value of 0.86 ($P < .0001$), and the Cohen κ statistic for classification of gray-white matter differentiation showed a medium association, with a value of 0.73 ($P < .0001$).

DISCUSSION

GCE is fairly commonly encountered after aSAH and has been shown to have associated devastating consequences.[10] The presence of GCE on initial head NCCT is an independent predictor of poor outcome and mortality.[10] Despite its relatively common occurrence, GCE is an incompletely understood, complex multifactorial process with several proposed contributing etiologies including metabolic disturbances, increased intracranial pressure, and global ischemia.[13,15] Additionally, GCE is associated with breakdown of the blood-brain barrier, leading to disturbances in the autoregulatory response, which may manifest as hemodynamic alterations in perfusion.[13,14]

Our results support global perfusion deficits on CTP occurring more frequently in patients with GCE compared with patients without GCE. Furthermore, the patient groups with and without GCE did not have significant differences in key demographic features, such as age and sex or history of smoking or hypertension. Increased disease severity cannot be attributed to increased perfusion deficits because our patients were also well-matched for measures of disease severity, including Glasgow Coma Scale scores and Hunt and Hess scores. Additionally, even though hydrocephalus has been shown to cause global perfusion deficits[23] and could potentially confound our analysis, most important, we found no statistical difference in the severity of hydrocephalus between the GCE and non-GCE groups. Also, although vasospasm is a common complication of aSAH and could potentially confound perfusion deficits, our patients were imaged within the first 3 days after initial presentation when vasospasm is less likely to occur. Typically, development of vasospasm after aSAH is thought to peak at 7 days.[24,25] Additionally, focal perfusion deficits of any kind were excluded, and only global deficits were considered true perfusion deficits suggestive of global cerebral edema.

The exact mechanism underlying GCE and its role in patients with aSAH developing serious neurologic complications are not clearly understood. Some studies have suggested that the initial bleeding insult causes high intracranial pressure leading to

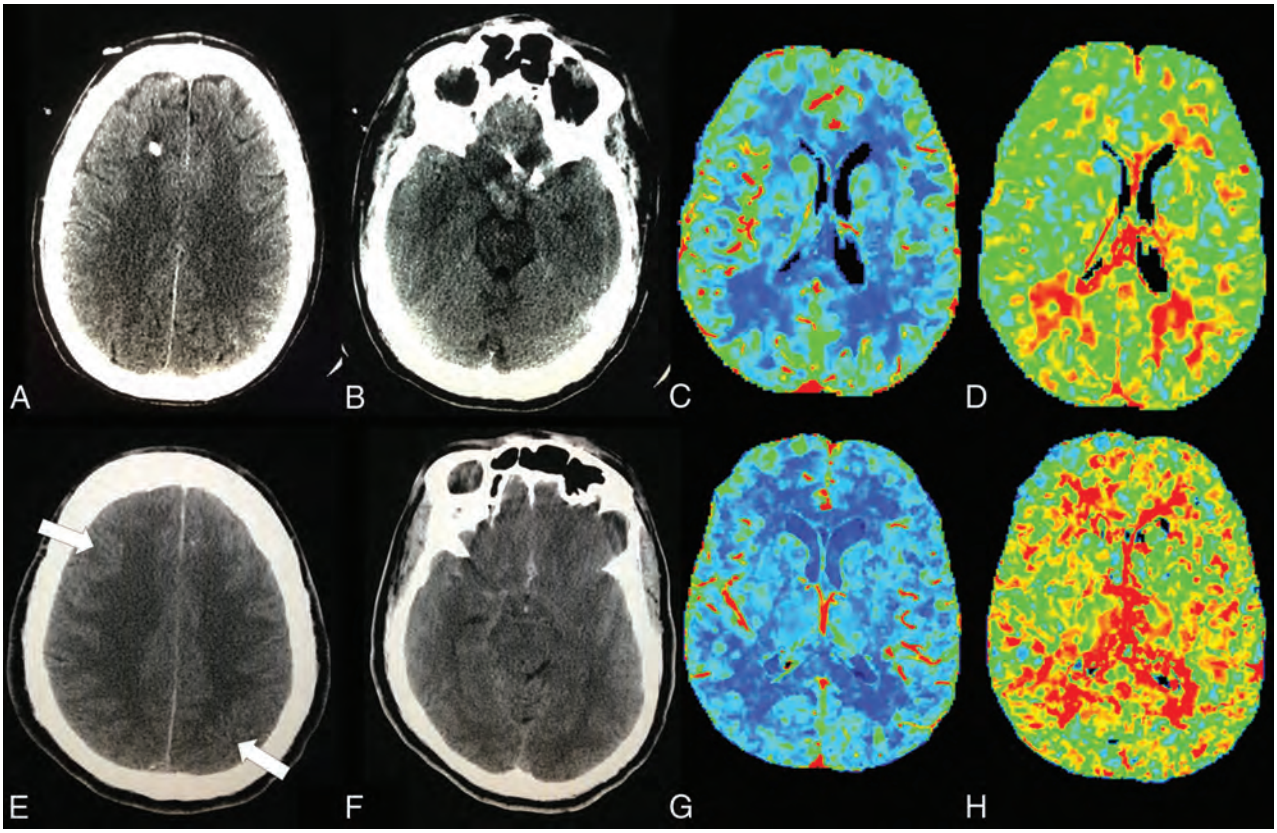

FIG 2. Patient 1 is an 87-year-old woman with acute aSAH from a right posterior communicating artery aneurysm who presented with Hunt and Hess grade 4 and a Glasgow Coma Scale score of 7–12. No GCE is seen on NCCT (*A* and *B*). Normal findings on CBF (*C*) and MTT (*D*) maps are seen in this patient. Patient 2 is a 53-year-old man with right middle cerebral artery aneurysmal rupture who presented with Hunt and Hess grade 2 and a Glasgow Coma Scale score of 15. GCE is seen on NCCT with a loss of gray-white differentiation at the level of the centrum semiovale as demonstrated by fingerlike projections of white matter extending to the cortex[10] (*E*, *arrows*) and diffuse effacement of the basal cisterns and cerebral sulci (*F*). Globally decreased CBF (*G*) and increased MTT (*H*) are seen in this patient.

cerebral circulatory arrest causing ischemic brain injury. This may lead to cytotoxic edema and breakdown of the blood-brain barrier with disturbances in the autoregulatory response from inflammatory and neurotoxic effects on the vasomotor centers of the brain.[13,14] Recently, microarterial constriction and microthrombosis have been shown to contribute to the early damage leading to delayed cerebral ischemia (DCI).[26] Although the relationship between the vascular pathology in DCI and GCE is not well-understand, microvascular dysfunction represents a plausible mechanistic link between DCI and GCE, which warrants further investigation.

Our study demonstrates that patients with GCE are more likely to have global perfusion deficits with reduced CBF and/or elevated MTT compared with patients without GCE, confirming that disturbances in the autoregulatory response occur in patients with GCE. Further investigation is needed to fully elucidate the underlying pathophysiologic mechanism leading to GCE.

Our study has some limitations. First, our sample size was relatively small, and though our results achieved statistical significance, the wide confidence interval in our OR suggests that additional work is needed to more precisely determine the strength of the association of global perfusion deficits with GCE. Second, the diagnosis of GCE on NCCT can be prone to subjective assessment. The proportion of patients with GCE in our aSAH cohort was 42.2%, which is in the 6%–62% range of previously published studies.[10,15,27] Additionally, we had medium-to-high interobserver reliability between our neuroradiologists for the 2-part definition of global cerebral edema used. While the interobserver reliability was high for sulcal effacement, indicating that it may be a more important factor in the definition of GCE than loss of gray-white differentiation, other imaging markers, such as perfusion metrics, might aid in the definition of GCE. Although our study was adequately powered to assess our primary outcome of qualitative global perfusion deficits, we were not able to demonstrate the statistical significance in quantitative CBF between the 2 groups, despite a strong trend. Further work should be done with larger sample sizes to evaluate the quantitative assessment of CBF.

In summary, our study reveals that patients with aSAH with GCE have a statistically increased incidence of global perfusion deficits on CTP in the early phase (days 0–3) compared with those without GCE, supporting the theory that GCE is associated with altered cerebral hemodynamics. However, further work is needed to understand the pathologic mechanisms leading to altered hemodynamics in GCE and to assess the clinical implications of global perfusion deficits in contributing to poor outcomes after aSAH.

CONCLUSIONS

Patients with aSAH who have GCE on early-phase (days 0–3) NCCT are significantly more likely to have global perfusion deficits on CTP compared with patients without GCE. GCE and its

relationship with poor clinical outcomes in patients with aSAH are complex, but our study supports the theory that GCE is associated with altered cerebral hemodynamics.

Disclosures: Jana Ivanidze—*UNRELATED*: *Grants/Grants Pending*: Radiological Society of North America,* *Comments*: Radiological Society of North America Resident Research Grant. Umut Ozbek—*UNRELATED*: *Grants/Grants Pending*: Clinical and Translational Science Center at Weill Cornell Medical College (UL1-TR000457-06); Ajay Gupta—*UNRELATED*: *Grants/Grants Pending*: Foundation of the American Society of Neuroradiology Scholar Award,* Association of University Radiologists GE Radiology Research Academic Fellowship Grant.* Jan Claassen—*UNRELATED*: *Board Membership*: Actelion (Advisory Board).* *Money paid to the institution.

REFERENCES

1. Hop JW, Rinkel GJ, Algra A, et al. **Case-fatality rates and functional outcome after subarachnoid hemorrhage: a systematic review.** *Stroke* 1997;28:660–64
2. Ingall T, Asplund K, Mähönen M, et al. **Project for the WHOM: a multinational comparison of subarachnoid hemorrhage epidemiology in the WHO MONICA stroke study.** *Stroke* 2000;31:1054–61
3. Longstreth WT, Nelson LM, Koepsell TD, et al. **Clinical course of spontaneous subarachnoid hemorrhage: a population-based study in King County, Washington.** *Neurology* 1993;43:712
4. Feigin VL, Lawes CM, Bennett DA, et al. **Stroke epidemiology: a review of population-based studies of incidence, prevalence, and case-fatality in the late 20th century.** *Lancet Neurol* 2003;2:43–53
5. Molyneux AJ, Kerr RSC, Birks J, et al. **Risk of recurrent subarachnoid haemorrhage, death, or dependence and standardised mortality ratios after clipping or coiling of an intracranial aneurysm in the International Subarachnoid Aneurysm Trial (ISAT): long-term follow-up.** *Lancet Neurol* 2009;8:427–33
6. Springer MV, Schmidt JM, Wartenberg KE, et al. **Predictors of global cognitive impairment 1 year after subarachnoid hemorrhage.** *Neurosurgery* 2009;65:1041–43
7. Roos YB, Dijkgraaf MG, Albrecht KW, et al. **Direct costs of modern treatment of aneurysmal subarachnoid hemorrhage in the first year after diagnosis.** *Stroke* 2002;33:1595–99
8. Mayer SA, Kreiter KT, Copeland D, et al. **Global and domain-specific cognitive impairment and outcome after subarachnoid hemorrhage.** *Neurology* 2002;59:1750–58
9. Hackett ML, Anderson CS. **Health outcomes 1 year after subarachnoid hemorrhage: an international population-based study—the Australian Cooperative Research on Subarachnoid Hemorrhage Study Group.** *Neurology* 2000;55:658–62
10. Claassen J, Carhuapoma JR, Kreiter KT, et al. **Global cerebral edema after subarachnoid hemorrhage: frequency, predictors, and impact on outcome.** *Stroke* 2002;33:1225–32
11. Kreiter KT, Copeland D, Bernardini GL, et al. **Predictors of cognitive dysfunction after subarachnoid hemorrhage.** *Stroke* 2002; 33:200–08
12. Lagares A, Gómez PA, Lobato RD, et al. **Prognostic factors on hospital admission after spontaneous subarachnoid haemorrhage.** *Acta Neurochir (Wien)* 2001;143:665–72
13. Mocco J, Prickett CS, Komotar RJ, et al. **Potential mechanisms and clinical significance of global cerebral edema following aneurysmal subarachnoid hemorrhage.** *Neurosurg Focus* 2007;22:E7
14. Zetterling M, Hallberg L, Hillered L, et al. **Brain energy metabolism in patients with spontaneous subarachnoid hemorrhage and global cerebral edema.** *Neurosurgery* 2010;66:1102–10
15. Helbok R, Ko SB, Schmidt JM, et al. **Global cerebral edema and brain metabolism after subarachnoid hemorrhage.** *Stroke* 2011; 42:1534–39
16. Grote E, Hassler W. **The critical first minutes after subarachnoid hemorrhage.** *Neurosurgery* 1988;22: 654–61
17. Wintermark M, Maeder P, Thiran JP, et al. **Quantitative assessment of regional cerebral blood flows by perfusion CT studies at low injection rates: a critical review of the underlying theoretical models.** *Eur Radiol* 2001;11:1220–30
18. Sanelli PC, Lev MH, Eastwood JD, et al. **The effect of varying user-selected input parameters on quantitative values in CT perfusion maps.** *Acad Radiol* 2004;11:1085–92
19. Wintermark M, Lau BC, Chien J, et al. **The anterior cerebral artery is an appropriate arterial input function for perfusion-CT processing in patients with acute stroke.** *Neuroradiology* 2008;50:227–36
20. Shin BJ, Anumula N, Hurtado-Rúa S, et al. **Does the location of the arterial input function affect quantitative CTP in patients with vasospasm?** *AJNR Am J Neuroradiol* 2014;35:49–54
21. Ferreira RM, Lev MH, Goldmakher G V, et al. **Arterial input function placement for accurate CT perfusion map construction in acute stroke.** *AJR Am J Roentgenol* 2010;194:1330–36
22. Murphy BD, Fox AJ, Lee DH, et al. **Identification of penumbra and infarct in acute ischemic stroke using computed tomography perfusion–derived blood flow and blood volume measurements.** *Stroke* 2006;37:1771–77
23. van Asch CJ, van der Schaaf IC, Rinkel GJ. **Acute hydrocephalus and cerebral perfusion after aneurysmal subarachnoid hemorrhage.** *AJNR Am J Neuroradiol* 2010;31:67–70
24. Aralasmak A, Akyuz M, Ozkaynak C, et al. **CT angiography and perfusion imaging in patients with subarachnoid hemorrhage: correlation of vasospasm to perfusion abnormality.** *Neuroradiology* 2009;51:85–93
25. Weidauer S, Lanfermann H, Raabe A, et al. **Impairment of cerebral perfusion and infarct patterns attributable to vasospasm after aneurysmal subarachnoid hemorrhage: a prospective MRI and DSA study.** *Stroke* 2007;38:1831–36
26. Vergouwen MD, Vermeulen M, Coert BA, et al. **Microthrombosis after aneurysmal subarachnoid hemorrhage: an additional explanation for delayed cerebral ischemia.** *J Cereb Blood Flow Metab* 2008;28:1761–70
27. Kassell NF, Torner JC, Haley EC, et al. **The International Cooperative Study on the Timing of Aneurysm surgery. Part 1: overall management results.** *J Neurosurg* 1990;73:18–36

Constrained Source Space MR Spectroscopy: Multiple Voxels, No Gradient Readout

K. Landheer, A. Sahgal, S. Das, and S.J. Graham

ABSTRACT

BACKGROUND AND PURPOSE: Our goal was to develop a novel technique for measuring a small number of localized spectra simultaneously and in a time-efficient manner.

MATERIALS AND METHODS: Using appropriate radiofrequency pulses, the magnetization from multiple voxels is excited simultaneously and then separated (reconstructed) by using the individual coil-sensitivity profiles from a multichannel receiver coil. Because no gradients are used for *k*-space encoding, constrained source space MR spectroscopy provides a time advantage over conventional spectroscopic imaging and an improved signal-to-noise ratio per square root of unit time over single-voxel spectroscopy applied at each successive location. In the present work, we considered prototype application of constrained source space MR spectroscopy for 2 voxels.

RESULTS: Experimental data from healthy volunteers and simulation results showed that constrained source space MR spectroscopy is effective at extracting 2 independent spectra even in the challenging scenario of the voxels being closely spaced. Also, from 6 patients with various types of brain cancer we obtained 2-voxel constrained source space MR spectroscopy data, which showed spectra of clinical quality in half the time required to perform successive single-voxel MR spectroscopy.

CONCLUSIONS: Constrained source space MR spectroscopy provides clinical quality spectra and could be used to probe multiple voxels simultaneously in combination with Hadamard encoding for further scan-time reductions.

ABBREVIATIONS: CSSMRS = constrained source space MR spectroscopy; PRESS = point-resolved spectroscopy sequence; SVS = single-voxel spectroscopy

There are 2 major categories of MR spectroscopy pulse sequences on current clinical MR imaging systems: single-voxel spectroscopy (SVS), which measures one voxel, and MR spectroscopic imaging, which measures many spectra simultaneously over a Cartesian grid of voxels. Both SVS and MR spectroscopic imaging are widely applied in humans to detect certain molecular constituents of normal and abnormal tissues, especially those associated with cellular metabolism, and to monitor therapeutic response.[1-3] Each MR spectroscopy category has its application niche, because SVS and MR spectroscopic imaging exploit different spatial and temporal resolution trade-offs. SVS is attractive when anatomic MR imaging provides a precise indication of where spectral information should be collected. When pathology is more diffuse, widely distributed, or not detectable on anatomic MR imaging, MR spectroscopic imaging is the technique of choice for generating spectra from many voxels by using multiple repetitions for *k*-space encoding.[4,5] To reduce spectroscopic scan times, various "parallel imaging" approaches have been applied to reduce the amount of *k*-space data acquired. These techniques exploit the spatial sensitivity of individual elements in multichannel receiver coils[6-9] and can substantially reduce scan times.

The spatial limitations of SVS are well recognized; it is usually the case that SVS spectra are required at more than one location, either to compare spectra from diseased and normal tissue or in the case of multifocal disease. This limitation naturally leads to execution of SVS pulse sequences successively for each voxel location. There have been some attempts to modify spectroscopy acquisition to extend the volume of SVS coverage, such as with line-scan echo-planar spectroscopic imaging,[10] which provides spectra from a column of voxels. However, for clinical applica-

Received September 26, 2014; accepted after revision January 19, 2015.

From the Departments of Medical Biophysics (K.L., S.J.G.), Surgery (S.D.), and Radiation Oncology, Sunnybrook Odette Cancer Centre (A.S.), University of Toronto, Ontario, Canada; Physical Sciences (K.L., S.J.G.), Sunnybrook Research Institute, Toronto, Ontario, Canada; and Keenan Research Centre (S.D.), St. Michael's Hospital, Toronto, Ontario, Canada.

K. Landeer was supported by scholarships from the Natural Sciences Research Council of Canada, the Ontario Graduate Scholarship program, and the Walter C. Sumner foundation.

Please address correspondence to Karl Landheer, MSc, Sunnybrook Research Institute, 2075 Bayview Ave, Room S605, Toronto, Ontario M4N 3M5, Canada; e-mail: landheer@sri.utoronto.ca

http://dx.doi.org/10.3174/ajnr.A4319

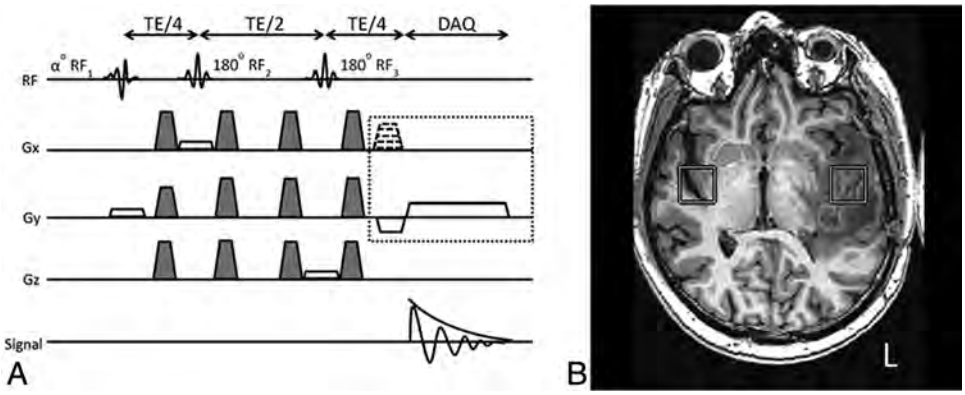

FIG 1. *A*, Pulse diagram for CSSMRS. The first radiofrequency pulse has a flip angle of α (where α is $<90°$) and is cosine modulated, such that the subsequent spin echo after the third radiofrequency pulse excites 2 voxels. Shaded gradients are crusher gradients. The section-select rephasing lobe for the *y* gradient is added directly to the first crusher. The gradient-echo readout in the dotted box is optional for voxel localization verification. RF indicates radiofrequency; DAQ, data acquisition. *B*, An anatomic T1-weighted image of patient 6 with the nominal voxel locations overlaid and a brain tumor evident in the left middle temporal gyrus. The 2 spectra for this patient are displayed in the bottom row of Fig 2.

Table 1: Summary of patients with brain tumor studied in experiment 2

Patient No.	Age (yr)	Sex	Disease	Radiation Treatment Status	Tumor Location	Tumor Size (vs Voxel Size)
1	36	F	Grade II oligodendroglioma	None	Right cingulate gyrus	Larger
2	84	M	Grade IV glioblastoma	Currently undergoing focused radiation	Left middle temporal gyrus	Comparable
3	79	M	Grade IV glioblastoma	Currently undergoing focused radiation	Left superior temporal gyrus	Larger
4	61	F	Brain metastases from breast cancer	60 days since completion of focused radiation	Left middle temporal gyrus	Smaller
5	79	M	Brain metastases from colon cancer	70 days since completion of focused radiation	Right superior temporal gyrus	Smaller
6	61	M	Grade IV glioblastoma	Currently undergoing focused radiation	Left middle temporal gyrus	Larger

Note:—F indicates female; M, male.

tions, standard SVS methods, notably point-resolved spectroscopy (PRESS)[11] and stimulated echo acquisition mode,[12] remain entrenched.

Previously, a technique that uses radiofrequency localization and sensitivity encoding[13] was developed for fast functional MR imaging.[14] It is reasonable that this "constrained source space" approach, appropriately modified for MR spectroscopy applications, should be investigated more to determine whether it usefully augments existing SVS capabilities. In the present work, in which we used constrained source space MR spectroscopy (CSSMRS), a prototype pulse sequence was developed and analyzed for its ability to acquire and separate spectra from 2 voxels simultaneously with no *k*-space encoding. The efficacy of spectral separation was investigated for a variety of distances between the 2 voxels in a healthy volunteer. In addition, numeric simulations were performed to assess the validity of certain assumptions made in the reconstruction and to predict CSSMRS performance in cases in which lengthy experimentation was impractical. Last, 2-voxel CSSMRS data were reported in relation to conventional SVS data acquired successively at each voxel location for patients with a variety of different brain cancers ranging from low grade to high grade.

MATERIALS AND METHODS

CSSMRS Implementation and Spectral Analysis

All experimental data were collected by using a Discovery MR750 3T imaging system (GE Healthcare, Milwaukee, Wisconsin) with a standard 8-channel head coil receiver. To achieve CSSMRS for proof-of-principle demonstrations, a standard PRESS sequence was modified to excite 2 voxels (instead of 1) arbitrarily in space (Fig 1*A*). Illustrative voxel locations are shown overlaid on the anatomic image of a patient with brain cancer in Fig 1*B* (see patient 6 data in Table 1). The 2 user inputs were the voxel size, chosen throughout as 20 mm × 20 mm × 20 mm, and the x, y, and z coordinates of each voxel location. In this approach, 2 arbitrarily positioned voxels were excited via cosine modulation of the first radiofrequency pulse, which resulted in the excitation of 2 parallel sections, followed by the standard spin-echo formation process thereafter. Arbitrary localization was obtained by modifying the offset frequencies of the radiofrequency pulses and changing the rotation array between logical and physical gradients. The 3 radiofrequency pulses were Shinnar-Le Roux pulses[15] with durations of 3600, 5200, and 5200 milliseconds and bandwidths of 2366.67, 1384.62, and 1384.62 Hz for the first, second, and third pulses, respectively.

The additional pulse sequence parameters for this initial work included a TR and TE of 1500 milliseconds and 288 milliseconds (unless otherwise stated), respectively, a flip angle of 63° (approximately the Ernst angle), a readout bandwidth of 2500 Hz, and 1024 points of data acquisition (total acquisition time, 409.6 milliseconds). A TE value of 288 milliseconds was chosen because it has been shown to have high MR spectroscopy reproducibility,[16] an important clinical factor compared with the other common TE values of 30 and 144 milliseconds, despite the associated reduction in SNR. Water suppression was implemented by us-

ing chemical shift selective saturation.[17] Before each data acquisition, first- and second-order shimming was applied to encompass most of the brain to decrease spectral linewidths. The typical linewidth of the water peak was approximately 8 Hz. The total number of excitations was 128, and the total scan time was 3.2 minutes.

Regarding spatial reconstruction of CSSMRS data to separate spectra from the 2 voxels, the governing equation can be expressed in matrix form as follows[13,14]:

$$y(t) = Sx(t) + \epsilon(t), \quad (1)$$

where the sensitivity matrix S relates how the magnetization signals $x(t)$ from each voxel result in the acquired signals $y(t)$ from each element in the receiver coil, and $\epsilon(t)$ represents coil element-dependent noise. As can be seen from Equation 1, the reconstruction of CSSMRS requires a calibration scan for the measurement of the coil sensitivity. The sensitivity matrix is generated by assuming that the spatial sensitivity C of each coil element varies slowly over the extent of each voxel. For each of the l coils and n sections,

$$S_{l,n} = \frac{1}{N_p} \sum_{i=i_{\min}}^{i_{\max}} \sum_{j=j_{\min}}^{j_{\max}} C_{l,n}(i,j), \quad (2)$$

where N_p is the number of pixels within the specified region inside the voxel, $i_{\min}$ and $i_{\max}$ are the minimum and maximum, respectively, row pixel limits on the voxel, and $j_{\min}$ and $j_{\max}$ are the minimum and maximum, respectively, column pixel limits on the voxel. Equation 1 can be solved by the sensitivity encoding formalism by using weak reconstruction with SNR optimization[13]:

$$\hat{x}(TR_p;t) = (S^H \Psi^{-1} S)^{-1} S^H \Psi^{-1} y(TR_p;t), \quad (3)$$

where $\hat{x}$ is the estimated magnetization signal for each voxel, TR_p denotes the pth repetition, and Ψ represents the noise covariance matrix between the coils. For example,

$$\Psi_{l_1,l_2} = \frac{1}{N_E} \sum_{i=1}^{N_E} (\epsilon_{l_1}^*(i) - \overline{\epsilon_{l_1}^*})(\epsilon_{l_2}(i) - \overline{\epsilon_{l_2}}), \quad (4)$$

where the complex noise samples can be taken from the last datum of each acquisition, and the covariance is calculated over the total number of excitations, N_E.

The C matrices can be estimated by various approaches,[18-20] though previous CSS work has shown that a simple procedure is sufficient for proof-of-concept implementation.[14] Two sets of fast gradient-echo images were acquired with the same pulse sequence parameters (TE, 1.3 milliseconds; TR, 34 milliseconds; flip angle, 5°; field of view, 30 cm; 64 × 64 acquisition matrix; section thickness, 5 mm): 1 set with the body coil and 1 set with the multichannel head coil receiver. These images were then interpolated to produce 256 × 256 images with an isotropic in-plane resolution of 1.17 mm. For each of the l coils and n sections, the coil-sensitivity map at each in-plane x,y coordinate, $C_{l,n}(x,y)$, was estimated by dividing each of the individual head coil images by the analogous body coil image and then thresholding by using an "object indicator" to set the coil sensitivity to 0 in regions in which noise dominated the object signal.

The CSSMRS reconstruction was performed by using specially written scripts in Matlab (MathWorks, Natick, Massachusetts). The 2 separated signals were first zero-filled by a factor of 2 and then transformed to the spectral domain by fast Fourier transformation. The spectra were then phase corrected including zero- and first-order correction terms by using an automated algorithm based on minimizing entropy.[21] The spectra were then shifted in frequency to place the peak for NAA at 2.04 ppm, normalized by their L2 norm, and subjected to Hankel-Lanczos singular value decomposition[22] for the removal of residual spectral content arising from water. Spectral components were then quantified automatically by using the freeware SPID (http://homes.esat.kuleuven.be/~biomed/software.php), which uses a separable nonlinear least-squares fitting algorithm known as automated quantitation of the short echo time MR spectroscopy spectra.[22] The automated quantitation of short echo time MR spectroscopy spectra algorithm provides Cramer-Rao lower-bound estimates of the standard deviation of each quantified spectral component. The basis set used was simulated by using Java Magnetic Resonance User Interface (jMRUI) and the scan parameters. The values obtained from the quantification algorithm for NAA, Cho, and Cr were then scaled by attenuation factors to account for transverse and longitudinal relaxation effects by using relaxation constants obtained in a normal brain.[23] According to common practice, the values for lactate were not adjusted for attenuation.

Experimental Validation

Bloch equation simulations confirmed that cosine modulation had negligible effects on the integrity of the spatial profile. A water-fat phantom was used to measure the signal bleed between voxels. One voxel was placed inside a stationary fat container, and another voxel was placed inside a surrounding water bath. Typical scan parameters, except a TE of 30 milliseconds for increased SNR, were used. This scan was repeated for center-to-center distances of 30–70 mm. The bleed was defined to be the amplitude of the contaminating spectrum divided by the amplitude of the main spectrum in the other voxel multiplied by 100%. Two validation experiments were subsequently conducted on healthy volunteers and patients with brain cancer to assess CSSMRS capabilities in practical scenarios. Each volunteer participated with free and informed consent and with the approval of the hospital research ethics board.

Experiment 1 was performed to investigate how CSSMRS results are affected by voxel placement in relation to coil-sensitivity profiles. Because CSSMRS involves sensitivity encoding reconstruction, overall performance depends on the condition number of the reconstruction matrix, as quantified by the g factor[13]:

$$g(k) = \sqrt{(S^* \Psi^{-1} S)^{-1}_{k,k} (S^* \Psi^{-1} S)_{k,k}}, \quad (5)$$

where the integer k is used to denote the different voxels that are reconstructed (ie, $k = [1,2]$ in this case). To assess CSSMRS results for various g factors, one voxel was placed in a fixed central location in the brain, and the other was placed to achieve center-to-center separations between voxels varying from 20 mm (ie, adjacent voxels) to 70 mm in the radial direction toward the head coil. SVS PRESS data were acquired in each successive location for comparison. These CSSMRS and PRESS data were collected for one healthy adult male (23 years old). Equation 2 was then used to calculate the sensitivity ma-

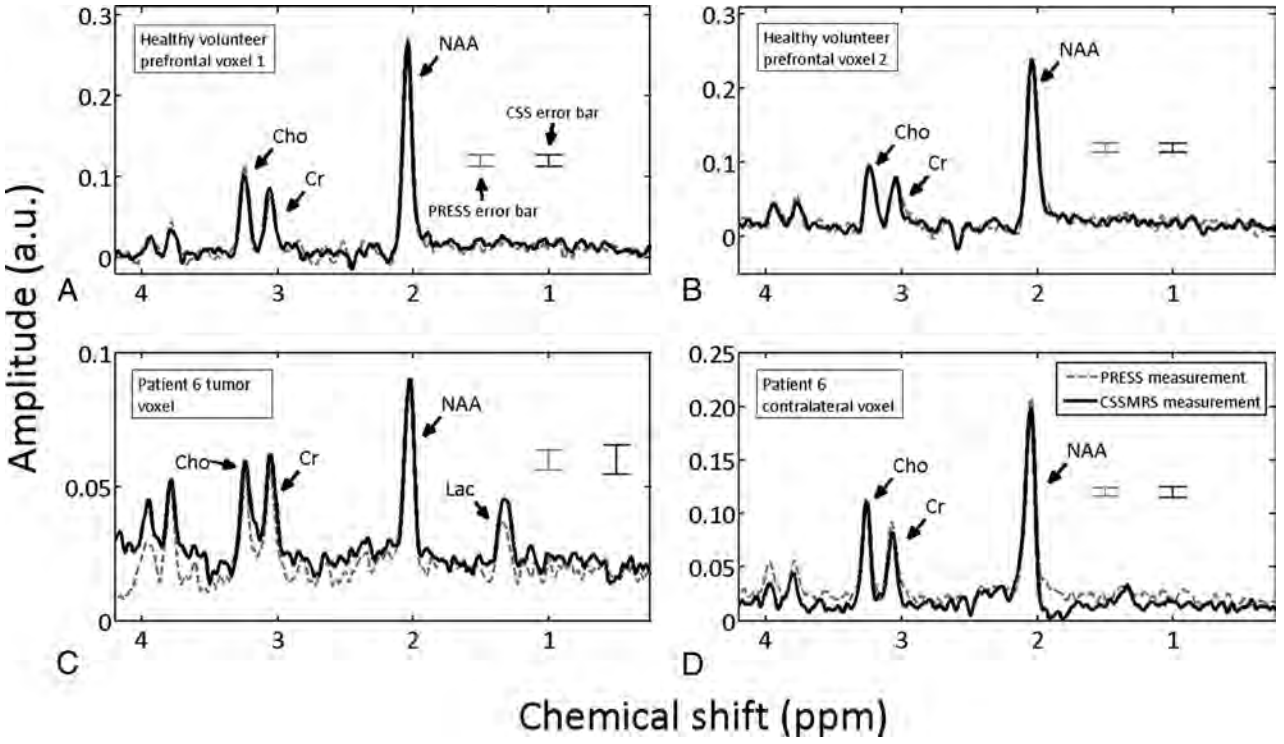

FIG 2. Spectra from a healthy volunteer (*A* and *B*) and a patient with brain cancer (*C* and *D*) measured with both CSSMRS and PRESS. Spectra from patient 6 are shown, because this patient exhibited the median g-factor, typifying CSSMRS reconstruction quality. Errors represent the standard deviation over 128 excitations. a.u. indicates arbitrary units.

trix from the measured coil sensitivities at each individual voxel location, which, along with the noise covariance matrix (Equation 4), can be used to calculate the g factor by using Equation 5. In addition to these experiments, a single scan was performed on a healthy volunteer with a TE of 30 milliseconds to investigate the short echo time regimen.

Experiment 2 was performed to investigate how well CSSMRS distinguishes spectra from cancerous and normal tissue over a representative range of clinical presentations. Six patients with brain cancer were recruited from the Sunnybrook Odette Cancer Centre during the course of their treatment (see Table 1 for tumor characteristics). Patients were included if they presented with a tumor volume approximately the same size as the prescribed voxel, or slightly larger or smaller. Tumor location was verified by using a high-resolution fast-spoiled gradient-echo with an anatomic inversion recovery preparation (acquisition parameters are shown below). For each patient, one voxel was placed at the center of the tumor, and the other was placed on the contralateral side in the analogous neuroanatomic region within normal-appearing brain tissue. PRESS data were also acquired successively in these 2 locations for comparison purposes.

In both experiments, PRESS was performed with the identical acquisition parameters used in CSSMRS and with the same spectral analysis pipeline. The total examination time for comparing CSSMRS and PRESS data from 2 voxels was approximately 20 min, which included scout images, anatomic MR imaging (fast-spoiled gradient-echo with an anatomic inversion recovery; 256 × 256 pixels; pixel size, 0.86 × 0.86 mm; TR, 8.2 milliseconds; TE, 3.2 milliseconds; flip angle, 8°), and 2 fast gradient-echo scans (for measuring coil sensitivity, as already described) and high-order shim, CSSMRS, and PRESS acquisitions.

Numeric Simulation

A simple numeric simulation was also written in Matlab for additional insight into the results of experiments 1 and 2. The simulation assessed the impact on spatial reconstruction of the important assumption underlying Equation 1, namely that coil sensitivity could be reasonably approximated as a constant over each voxel. Given good agreement between experimental results and simulations for experiment 1 (see "Results"), the simulation also was used to predict CSSMRS performance under conditions that were not possible to measure experimentally during experiment 2 because of the inherent time restrictions for collecting MR spectroscopy data in patients.

The simulation used measured coil-sensitivity and PRESS data from 2 voxels as initial inputs. In the context of the simulation, the PRESS data (obtained according to the experimental parameters already given, averaged over 128 excitations) were considered to represent a situation in which signal components were concentrated uniformly over each voxel volume. Simulated signals were then generated for each coil element, while accounting for nonuniform coil sensitivity, by performing the appropriate spatial integral. Complex Gaussian noise was added to each simulated signal to approximate the levels observed experimentally for each coil. These simulated coil signals were then used for spatial reconstruction of 2 voxel signals according to Equations 1–4 for subsequent comparison with the PRESS data that were input originally. Spatial recon-

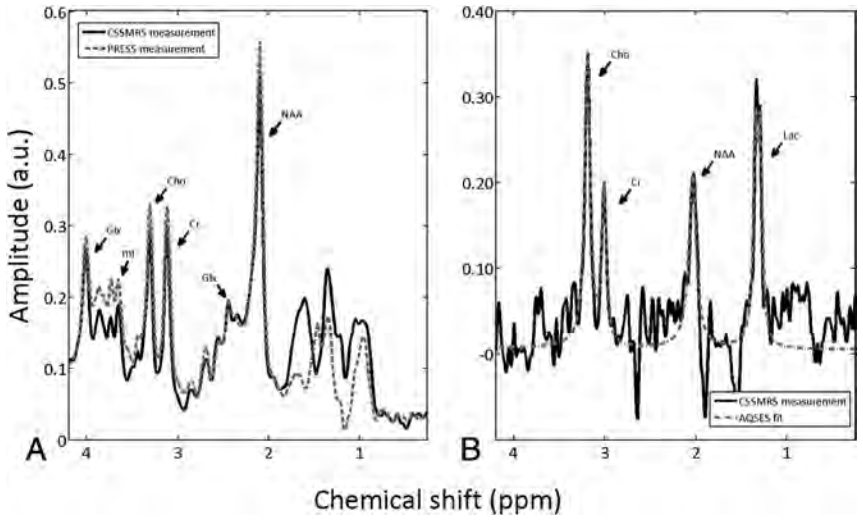

FIG 3. *A*, Spectra from a healthy volunteer at 30-millisecond echo time, obtained by using both CSSMRS and PRESS. The labeled metabolites are myo-inositol (mI), Cho, Cr, Glx, and NAA. *B*, The unapodized spectrum obtained from CSSMRS from patient 1 (highest g-factor) along with the automated quantitation of short echo time MR spectroscopy spectra (AQSES) fit.

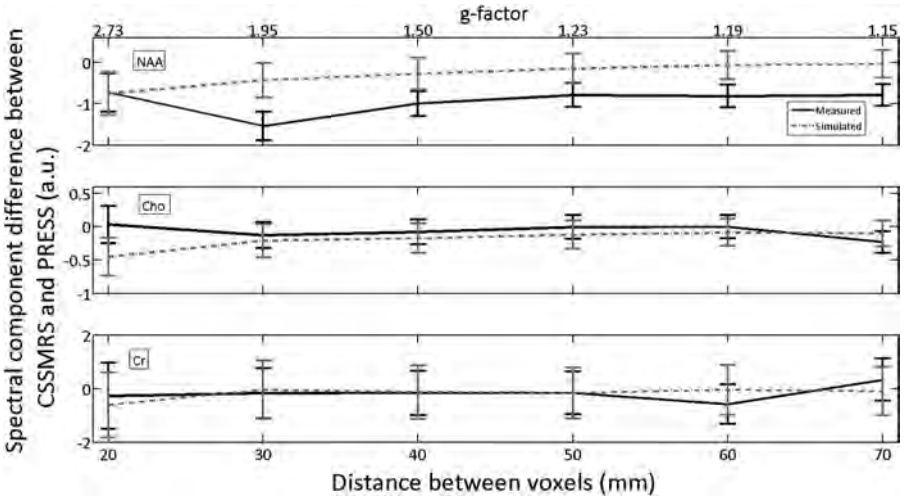

FIG 4. Measured and simulated differences between the CSSMRS and PRESS measurement for 6 different voxel separations for the 3 main metabolites within a healthy adult brain: NAA, Cho, and Cr. The signal from the CSSMRS voxel that was kept in a fixed position was reconstructed and compared with the PRESS measurement obtained from the same location. The black and gray lines represent the measured and simulated values, respectively. The g factors are also displayed for reference above the top x-axis, though there is a nonlinear relationship between g factor and voxel separation. Error bars represent Cramer-Rao bounds.

struction, spectral processing, and analysis were conducted as outlined above for experimental data.

RESULTS

For center-to-center spacings of 30, 40, 50, 60, and 70 mm, the observed bleeds of water into the fat voxel were 6.2%, 6.3%, 3.5%, 0.4%, and 1.7%, respectively, and the observed bleeds of fat into the water voxel were 3.0%, 0.2%, 0.1%, 5.2%, and 2.4%, respectively.

For visual comparison, Fig 2 displays 4 representative spectra obtained by CSSMRS (solid black lines) and PRESS (dashed gray lines). As commonly performed for display purposes, all spectra were apodized by a Gaussian filter with 2 Hz full-width at half-maximum. The spectra shown in Fig 2*A*, -*B* are qualitatively similar and were obtained from a healthy volunteer with both voxels placed inside the prefrontal cortex. The spectra shown in Fig 2*C*, -*D* were obtained from patient 6 (Table 1) and are substantially different for the 2 voxels, with the spectra in Fig 2*C* obtained from tumor tissue inside the left middle temporal gyrus and those in Fig 2*D* obtained from contralateral homologous tissue, as shown in Fig 1*B*. Spectra from patient 6 were chosen for display in Fig 2 because CSSMRS results were obtained in this case with the median g factor observed over the patient cohort. Figure 3*A* displays spectra obtained from both CSSMRS and PRESS for the minimum achievable TE of this pulse sequence (30 milliseconds). Figure 3*B* shows the tumor spectrum obtained from CSSMRS for patient 1 and the fit obtained from automated quantitation of short echo time MR spectroscopy spectra.

The results of experiment 1 and related numeric simulations are shown in Fig 4, in which are plotted the difference between quantified spectral components measured by CSSMRS and PRESS for 6 different voxel separations (one voxel held fixed, one moved radially) and the 3 main metabolites observed in Fig 2*A*, -*B*: NAA, Cr, and Cho. The difference values (CSSMRS minus PRESS) reported are specifically for the voxel that was maintained in a fixed position. For both the experimental and simulated results, the difference between CSSMRS and PRESS remained constant within experimental error over all the voxel separations. Furthermore, the difference values for experimental and simulation results also agreed within error, with the only exception being a slight bias in NAA quantification when voxels were separated by more than 20 mm.

Given the good level of agreement between experiment and simulation observed in Fig 4, numeric simulations were then extended to assess CSSMRS reconstruction quality as a function of voxel separation with spectra that were substantially different in the 2 voxels. Figure 5 shows plots of the difference between quantified spectral components measured by CSSMRS and PRESS in a manner analogous to that shown in Fig 4; however, in this case, the inputs to the simulation were provided from patient 6 with the difference values relating to quantification of the tumor spectral components: NAA, Cho, Cr, and lactate. For additional

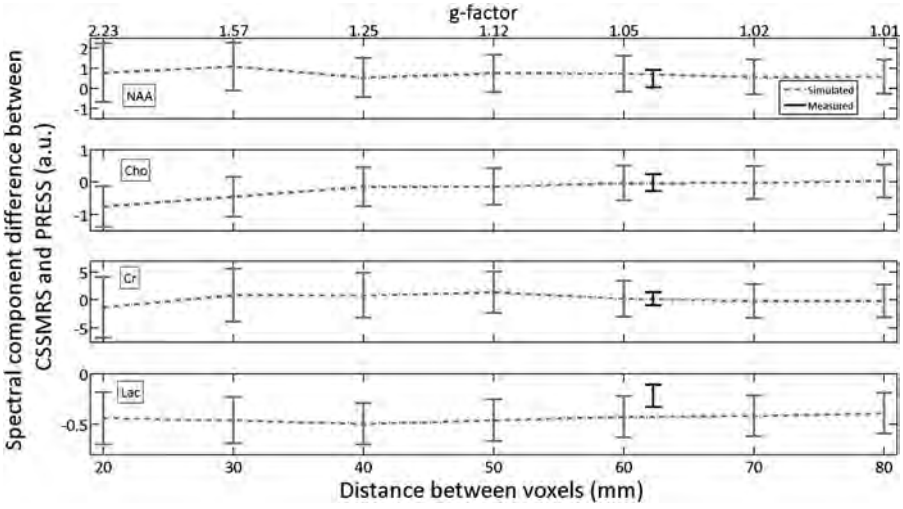

FIG 5. Simulated metabolite quantification values for 7 different voxel separations for the 4 main metabolites within the tumor spectra for patient 6: NAA, Cho, Cr, and lactate (Lac). The quantified values were from the stationary voxel placed within the tumor and are plotted in gray. The black data points located at 62 cm in each plot are the experimental results for this patient, corresponding to the first difference column values listed in Tables 2–5 for patient 6. The estimated g factors are also displayed above the top x-axis for reference, though there is a nonlinear relationship between the g factor and voxel separation.

context, the difference values obtained experimentally for patient 6 are also indicated as single data points in Fig 5. Similar to Fig 4, Fig 5 shows difference values of 0 within error for all voxel separations and metabolites (except Cho for adjacent voxels), indicating that good CSSMRS reconstruction quality was maintained even when the 2 voxels were located in close proximity to one another. In addition, the reconstruction tends to improve as the distance between the voxels increases for all metabolites. The simulation results and experimental results also agree within error for the single experimental data point.

To summarize the results of experiment 2, CSSMRS and PRESS results are quantified in Tables 2–5 for patients 1–6 across tumor and normal tissue voxels for NAA, Cr, Cho,

Table 2: Quantified NAA values from PRESS and CSSMRS for both voxels[a]

Patient No.	CSSMRS Tumor Voxel (a.u.)	PRESS Tumor Voxel (a.u.)	Difference (a.u.)	CSSMRS Healthy Voxel (a.u.)	PRESS Healthy Voxel (a.u.)	Difference (a.u.)
1	5.70 ± 0.65	4.86 ± 0.58	0.83 ± 0.87	9.73 ± 0.28	9.88 ± 0.20	−0.15 ± 0.35
2	2.70 ± 0.44	2.08 ± 0.40	0.62 ± 0.59	9.34 ± 0.35	8.84 ± 0.35	0.50 ± 0.49
3	1.70 ± 0.19	1.60 ± 0.20	0.10 ± 0.28	9.14 ± 0.12	9.42 ± 0.14	−0.28 ± 0.18
4	3.33 ± 0.54	0.14 ± 0.25	3.19 ± 0.59	8.09 ± 0.38	8.89 ± 0.36	−0.81 ± 0.52
5	5.27 ± 0.29	4.22 ± 0.21	1.05 ± 0.35	8.87 ± 0.38	10.93 ± 0.55	−2.06 ± 0.66
6	5.89 ± 0.27	5.41 ± 0.33	0.48 ± 0.43	6.81 ± 0.21	6.98 ± 0.20	−0.17 ± 0.29

Note:—a.u. indicates arbitrary units.

[a] Shown are means and standard deviations (Cramer-Rao bounds).

Table 3: Quantified Cho values from PRESS and CSSMRS for both voxels[a]

Patient No.	CSSMRS Tumor Voxel (a.u.)	PRESS Tumor Voxel (a.u.)	Difference (a.u.)	CSSMRS Healthy Voxel (a.u.)	PRESS Healthy Voxel (a.u.)	Difference (a.u.)
1	2.93 ± 0.39	2.89 ± 0.24	0.04 ± 0.45	1.72 ± 0.18	1.73 ± 0.13	−0.01 ± 0.22
2	1.86 ± 0.27	1.67 ± 0.17	0.19 ± 0.32	1.89 ± 0.20	2.22 ± 0.22	−0.33 ± 0.30
3	0.67 ± 0.12	0.96 ± 0.17	−0.28 ± 0.21	2.06 ± 0.07	2.31 ± 0.08	−0.25 ± 0.11
4	0.97 ± 0.93	0.83 ± 0.33	0.15 ± 0.99	1.36 ± 0.18	2.05 ± 0.21	−0.69 ± 0.75
5	1.66 ± 0.12	1.81 ± 0.11	−0.15 ± 0.16	1.56 ± 0.26	3.02 ± 0.66	−1.46 ± 0.71
6	1.56 ± 0.17	1.59 ± 0.20	−0.02 ± 0.26	1.75 ± 0.13	1.80 ± 0.12	−0.05 ± 0.17

Note:—a.u. indicates arbitrary units.

[a] Shown are means and standard deviations (Cramer-Rao bounds).

Table 4: Quantified Cr values from PRESS and CSSMRS for both voxels[a]

Patient No.	CSSMRS Tumor Voxel (a.u.)	PRESS Tumor Voxel (a.u.)	Difference (a.u.)	CSSMRS Healthy Voxel (a.u.)	PRESS Healthy Voxel (a.u.)	Difference (a.u.)
1	10.62 ± 2.44	7.77 ± 1.07	2.85 ± 2.66	6.34 ± 0.77	6.50 ± 0.61	−0.16 ± 0.98
2	3.82 ± 1.68	1.66 ± 0.55	2.16 ± 1.77	9.09 ± 0.89	10.40 ± 1.07	−1.32 ± 1.39
3	2.41 ± 0.77	1.56 ± 0.67	0.85 ± 1.02	8.73 ± 0.32	8.37 ± 0.35	0.36 ± 0.48
4	4.66 ± 4.17	0.42 ± 0.63	4.24 ± 4.22	8.94 ± 1.03	8.60 ± 0.95	−0.25 ± 1.40
5	6.19 ± 0.61	5.98 ± 0.48	0.21 ± 0.77	10.44 ± 1.76	10.58 ± 2.97	−0.15 ± 3.45
6	8.21 ± 0.74	8.00 ± 0.88	0.22 ± 1.15	6.13 ± 0.56	6.19 ± 0.52	−0.05 ± 0.77

Note:—a.u. indicates arbitrary units.

[a] Shown are means and standard deviations (Cramer-Rao bounds).

Table 5: Quantified lactate values from PRESS and CSSMRS for both voxels[a]

Patient No.	CSSMRS Tumor Voxel (a.u.)	PRESS Tumor Voxel (a.u.)	Difference (a.u.)	CSSMRS Healthy Voxel (a.u.)	PRESS Healthy Voxel (a.u.)	Difference (a.u.)
1	1.31 ± 0.09	1.46 ± 0.08	−0.16 ± 0.12	0.03 ± 0.04	0.23 ± 0.07	−0.20 ± 0.08
2	3.36 ± 0.11	3.16 ± 0.10	0.20 ± 0.15	0.60 ± 0.11	0.51 ± 0.11	0.09 ± 0.16
3	2.83 ± 0.04	2.77 ± 0.04	0.06 ± 0.05	0.25 ± 0.04	0.28 ± 0.05	0.03 ± 0.06
4[b]	3.22 ± 0.14	2.76 ± 0.13	0.46 ± 0.19	1.84 ± 0.10	1.59 ± 0.10	0.25 ± 0.14
5	2.26 ± 0.08	2.32 ± 0.07	−0.06 ± 0.10	0.73 ± 0.13	0.87 ± 0.17	−0.14 ± 0.21
6	0.54 ± 0.07	0.76 ± 0.08	−0.22 ± 0.11	0.22 ± 0.05	0.29 ± 0.05	−0.08 ± 0.07

Note:—a.u. indicates arbitrary units.

[a] Shown are means and standard deviations (Cramer-Rao bounds).

[b] Lipid contamination from scalp mislabeled as lactate in healthy voxel.

and lactate, including the differences in spectral quantification. The CSSMRS g factors for patients 1–6 were 1.39, 1.00, 1.00, 1.13, 1.17, and 1.01, respectively, which indicates that there should be a SNR per square root of unit time benefit for CSSMRS over PRESS in all cases. Overall, large decreases in NAA and increases in lactate and Cho were observed for tumor voxels in relation to normal tissue voxels for CSSMRS and PRESS for most patients, consistent with results from previous studies.[24] Tables 2–5 also show large variability in the tumor spectra across patients. A Mann-Whitney *U* test on the pooled values from all metabolites obtained from CSSMRS versus PRESS yielded a *P* value of .86, indicating no significant difference. There was no evidence of significant voxel bleed in the in vivo experiments, because no systematic increase in lactate was observed in normal tissue CSSMRS voxels (Table 5), except that a large lactate value was obtained from CSSMRS and PRESS spectra in the healthy tissue of patient 4. Voxel placement was close to the scalp in this particular patient, which produced contaminating lipid signals that were subsequently misinterpreted as lactate by the automated quantitation of short echo time MR spectroscopy spectra software. Thus, this specific result should be discounted. In addition there was a significant increase observed for this patient in NAA in the CSSMRS tumor voxel, which is likely because of motion that exacerbated the bleed effects (this particular patient had difficulty remaining still).

DISCUSSION

This work has introduced a prototype pulse sequence for CSSMRS, a novel spectroscopy technique that measures spectra from multiple voxels simultaneously without the need for *k*-space encoding. Instead, spatial encoding is achieved by multivoxel radiofrequency selective excitation, signal readouts from a multichannel receiver coil, and sensitivity encoding[14] reconstruction to separate the signals from each voxel. The CSSMRS method is important from the perspective of SNR per square root of acquisition time, potentially providing efficiency in comparison to the standard clinical practice of performing successive SVS acquisitions at different voxel locations.

Careful experiments and simulations were undertaken to investigate the capabilities of CSSMRS for simultaneous measurement of 2 voxels. In particular, considerable attention was paid to whether CSSMRS provides adequate spatial localization in relation to the standard SVS PRESS method. In a water-fat experiment, it was shown that the bleed rate was up to 6% for very closely spaced voxels and less for further spaced voxels. This amount of bleed is acceptable for spectroscopic applications. Experiments 1 and 2, conducted with healthy volunteers and a diverse group of 6 patients with a brain tumor (4 different types of cancer were represented), showed overall that CSSMRS and successive PRESS spectra agreed within experimental error. Furthermore, CSSMRS spatial reconstruction was shown to be robust over a range of voxel prescriptions (with one voxel held fixed and the voxel separation varied) by both experiments and numeric simulations. The experiment and simulation were in agreement for a healthy volunteer, indicating excellent reconstruction even when the 2 voxels were placed adjacent to one another. The only additional feature of note in this regard was a systematic decrease in the measured value of NAA in CSS (as shown in Fig 4), which was not predicted by simulation. This feature is likely a result of either motion or the relatively simplistic nature of the simulations, which did not account for various experimental factors. However, given that the overall level of agreement between experiment and simulation was very good, these factors evidently have a small influence. The simulation, therefore, helped to support the assumption made in CSSMRS reconstruction that coil-sensitivity variations can be neglected within the voxels.

The agreement between these experiments and the simulation provides rationale for using simulations to further predict CSSMRS capabilities in a patient with brain cancer . As expected, slightly larger variations were observed as a function of voxel separation in this case, likely because of the larger spectral differences between the 2 voxels. However, with the exception of NAA for voxels separated by greater than 20 mm, all CSSMRS results were predicted to be consistent with PRESS results within error.

Given that CCSMRS has been demonstrated to provide robust high-quality results, discussion can turn productively to the potential efficiency of this pulse sequence in terms of SNR per square root of acquisition time. In the 2-voxel implementation investigated in the present work, spectra were obtained in half the time of successive application of PRESS. The quality of the CSSMRS results may have been affected by noise amplification in the sensitivity encoding reconstruction, however, as parameterized by the g factor. Therefore, the appropriate context for by using CSSMRS advantageously over PRESS is when the g factor is less than $\sqrt{2}$, which corresponds to a minimum center-to-center separation in voxels of approximately 35 mm near the center of the 8-channel head receiver coil used in this work. All patients had a g factor below this threshold.

CSSMRS performed similarly with a short echo time, though a notable increase in the lipid peaks was observed. This increase is likely a result of the slight modification of the pulse profile and

will be corrected for in the future by using outer-volume suppression.

It is also interesting to note that CSSMRS is compatible with another approach that avoids using *k* space for spatially encoding spectral information. In principle, if the flip angles assigned to each voxel can be modulated appropriately, then simple algebraic combinations of the successive spectroscopic readouts can be used to localize each voxel without sensitivity encoding reconstruction, as achieved in Hadamard spectroscopic imaging.[24] The Hadamard spectroscopic imaging approach is independent of g factor and also provides improvements in SNR per square root of time but traditionally has required excellent radiofrequency fidelity and is sensitive to how spatial radiofrequency nonuniformity and patient motion influence algebraic combination and the subsequent leakage of signals between voxels. In addition, the algebraic combination of multiple recordings reduces the minimum temporal resolution that is achievable with Hadamard spectroscopic imaging, whereas CSSMRS provides spectral separation in as little as a single TR value. CSSMRS and Hadamard spectroscopic imaging are not mutually exclusive, however, and it is possible that a robust hybrid technique can be developed in the future for further scan-time reductions.

Irrespective of developing such a hybrid technique, the method discussed here has potential applications in any in vivo spectroscopy experiment in which there are 2 regions of interest and the lengthy acquisition times of MR spectroscopic imaging are impractical. CSSMRS may also be beneficial in a research setting in which sophisticated 2D MR spectroscopy experiments have inherently long acquisition times, such as J-resolved MR spectroscopy.[25] Another promising application of CSSMRS is in functional spectroscopy, in which real-time changes in metabolic information can be measured from multiple points within the brain simultaneously with high temporal resolution. Further development and applications of CSSMRS should be explored in the future.

CONCLUSIONS

CSSMRS has been developed to extract signals from 2 localized regions simultaneously and reliably. Utility was demonstrated in a clinical setting, though the technique also has promising applications in research settings.

Disclosures: Karl Landheer—*RELATED*: *Support for Travel to Meetings for the Study or Other Purposes*: University of Toronto SGS Travel Award; *UNRELATED: Grant:* NSERC Canadian Graduate Scholarship. Sunit Das—*RELATED*: *Grant*: Canadian Cancer Society Research Institute.* *Money paid to institution.

REFERENCES

1. Frahm J, Bruhn H, Gyngell ML, et al. **Localized proton NMR spectroscopy in different regions of the human brain in vivo: relaxation times and concentrations of cerebral metabolites.** *Magn Reson Med* 1989;11:47–63
2. Spielman D, Pauly J, Macovski A, et al. **Spectroscopic imaging with multidimensional pulses for excitation: SIMPLE.** *Magn Reson Med* 1991;19:67–84
3. Segebarth CM, Balériaux DF, Luyten PR, et al. **Detection of metabolic heterogeneity of human intracranial tumors in vivo by ^{1}H NMR spectroscopic imaging.** *Magn Reson Med* 1990;13:62–76
4. Brown TR, Kincaid BM, Ugurbil K. **NMR chemical shift imaging in three dimensions.** *Proc Natl Acad Sci U S A* 1982;79:3523–26
5. Maudsley AA, Hilal SK, Perman WH, et al. **Spatially resolved high resolution spectroscopy by "four-dimensional" NMR.** *J Magn Reson* 1983;51:147–52
6. Lin FH, Tsai SY, Otazo R, et al. **Sensitivity-encoded (SENSE) proton echo-planar spectroscopic imaging (PEPSI) in the human brain.** *Magn Reson Med* 2007;57:249–57
7. Gu M, Liu C, Spielman DM. **Parallel spectroscopic imaging reconstruction with arbitrary trajectories using k-space sparse matrices.** *Magn Reson Med* 2009;61:267–72
8. Posse S, Otazo R, Tsai SY, et al. **Single-shot magnetic resonance spectroscopic imaging with partial parallel imaging.** *Magn Reson Med* 2009;61:541–47
9. Bonekamp D, Smith MA, Zhu H, et al. **Quantitative SENSE-MRSI of the human brain.** *Magn Reson Imaging* 2010;28:305–13
10. Oshio K, Kyriakos W, Mulkern RV. **Line scan echo planar spectroscopic imaging.** *Magn Reson Med* 2000;44:521–24
11. Bottomley PA. **Spatial localization in NMR spectroscopy in vivo.** *Ann NY Acad Sci* 1987;508:333–48
12. Frahm J, Merboldt KD, Hänicke W. **Localized proton spectroscopy using stimulated echoes.** *J Magn Reson* 1987;72:502–08
13. Chiew M, Graham SJ. **Constrained source space imaging: application to fast, region-based functional MRI.** *Magn Reson Med* 2013;70:1058–69
14. Pruessmann KP, Weiger M, Scheidegger MB, et al. **SENSE: sensitivity encoding for fast MRI.** *Magn Reson Med* 1999;42:952–62
15. Pauly J, Le Roux P, Nishimura D, et al. **Parameter relations for the Shinnar-Le Roux selective excitation pulse design algorithm [NMR imaging].** *IEEE Trans Med Imaging* 1991;10:53–65
16. Inglese M, Spindler M, Babb JS, et al. **Field, coil, and echo-time influence on sensitivity and reproducibility of brain proton MR spectroscopy.** *AJNR Am J Neuroradiol* 2006;27:684–88
17. Haase A, Frahm J, Hänicke W, et al. **^{1}H NMR chemical shift selective (CHESS) imaging.** *Phys Med Biol* 1985;30:341–44
18. Jin J, Liu F, Weber E, et al. **An electromagnetic reverse method of coil sensitivity mapping for parallel MRI—theoretical framework.** *J Magn Reson* 2010;207:59–68
19. Allison MJ, Ramani S, Fessler JA. **Regularized MR coil sensitivity estimation using augmented Lagrangian methods.** *Proc IEEE Int Symp Biomed Imaging* 2012;32:394–97
20. Allison MJ, Ramani S, Fessler JA. **Accelerated regularized estimation of MR coil sensitivities using augmented Lagrangian methods.** *IEEE Trans Med Imaging* 2013;32:556–64
21. Chen L, Weng Z, Goh L, et al. **An efficient algorithm for automatic phase correction of NMR spectra based on entropy minimization.** *J Magn Reson* 2002;158:164–68
22. Poullet JB, Sima DM, Simonetti AW, et al. **An automated quantitation of short echo time MRS spectra in an open source software environment: AQSES.** *NMR Biomed* 2007;20:493–504
23. Li Y, Xu D, Ozturk-Isik E, et al. **T1 and T2 metabolite relaxation times in normal brain at 3T and 7T.** *J Mol Imaging Dyn* 2012;1:1–5
24. Horská A, Barker PB. **Imaging of brain tumors: MR spectroscopy and metabolic imaging.** *Neuroimaging Clin N Am* 2010;20:293–310
25. Ryner LN, Sorenson JA, Thomas MA. **Localized 2D J-resolved ^{1}H MR spectroscopy: strong coupling effects in vitro and in vivo.** *Magn Reson Imaging* 1995;13:853–69

High-Resolution DCE-MRI of the Pituitary Gland Using Radial *k*-Space Acquisition with Compressed Sensing Reconstruction

M.C. Rossi Espagnet, L. Bangiyev, M. Haber, K.T. Block, J. Babb, V. Ruggiero, F. Boada, O. Gonen, and G.M. Fatterpekar

ABSTRACT

BACKGROUND AND PURPOSE: The pituitary gland is located outside of the blood-brain barrier. Dynamic T1 weighted contrast enhanced sequence is considered to be the gold standard to evaluate this region. However, it does not allow assessment of intrinsic permeability properties of the gland. Our aim was to demonstrate the utility of radial volumetric interpolated brain examination with the golden-angle radial sparse parallel technique to evaluate permeability characteristics of the individual components (anterior and posterior gland and the median eminence) of the pituitary gland and areas of differential enhancement and to optimize the study acquisition time.

MATERIALS AND METHODS: A retrospective study was performed in 52 patients (group 1, 25 patients with normal pituitary glands; and group 2, 27 patients with a known diagnosis of microadenoma). Radial volumetric interpolated brain examination sequences with golden-angle radial sparse parallel technique were evaluated with an ROI-based method to obtain signal-time curves and permeability measures of individual normal structures within the pituitary gland and areas of differential enhancement. Statistical analyses were performed to assess differences in the permeability parameters of these individual regions and optimize the study acquisition time.

RESULTS: Signal-time curves from the posterior pituitary gland and median eminence demonstrated a faster wash-in and time of maximum enhancement with a lower peak of enhancement compared with the anterior pituitary gland ($P < .005$). Time-optimization analysis demonstrated that 120 seconds is ideal for dynamic pituitary gland evaluation. In the absence of a clinical history, differences in the signal-time curves allow easy distinction between a simple cyst and a microadenoma.

CONCLUSIONS: This retrospective study confirms the ability of the golden-angle radial sparse parallel technique to evaluate the permeability characteristics of the pituitary gland and establishes 120 seconds as the ideal acquisition time for dynamic pituitary gland imaging.

ABBREVIATIONS: GRASP = golden-angle radial sparse parallel; STC = signal-time curve; VIBE = volumetric interpolated brain examination

The pituitary gland is a highly perfused gland located within the sella turcica and outside the blood-brain barrier. Pathologies intrinsic to this region, listed from most common to least common, include benign micro- and macroadenomas, invasive adenomas, and carcinomas. Of these, benign pituitary adenomas represent 10%–25% of all intracranial neoplasms, with an estimated prevalence rate of 17% within the general population.[1]

MR imaging is the criterion standard for the evaluation of the pituitary gland. Imaging is performed in a dynamic manner by using section-selective T1-weighted TSE sequences before and at multiple time points after the injection of a gadolinium-based contrast agent.[2,3] Such dynamic scanning allows assessment of underlying pathology, especially microadenomas, by evaluating any focal area of differential enhancement within the pituitary gland. However, such a dynamic scanning technique has certain limitations. Enhancement within the posterior pituitary gland cannot be appreciated due to its inherently bright T1 signal. Evaluation of very small-sized (1–3 mm) microadenomas can be challenging, depending on the underlying section thickness. Distinction between a simple cyst and a microadenoma can sometimes be difficult, especially without a good history. Furthermore, there is not a standard dynamic image-acquisition timeframe. Literature suggests that the acquisition time for the dynamic sequence varies among different institutions, ranging from 150 to 240 seconds.[4-6]

Received November 20, 2014; accepted after revision January 6, 2015.

From the Department of Radiology, New York University Langone Medical Center, New York, New York.

Paper previously presented in part at: Annual Meeting of the American Society of Neuroradiology and the Foundation of the ASNR Symposium, May 17–22, 2014; Montreal, Quebec, Canada.

Please address correspondence to M.C. Rossi Espagnet, MD, Department of Radiology, New York University Langone Medical Center, 550 First Ave, New York, NY 10016; e-mail: camilla.rossiespagnet@gmail.com

http://dx.doi.org/10.3174/ajnr.A4324

Standardization of this image acquisition time is especially important in today's economic imaging scenario, where we strive for the best possible information in the most appropriate time.

Golden-angle radial sparse parallel MR imaging (GRASP) is a new volumetric dynamic imaging technique based on a 3D gradient-echo sequence with radial "stack-of-stars" *k*-space sampling[7] and golden-angle ordering.[8] As opposed to the conventional dynamic MR imaging techniques that perform multiple separate examinations, the GRASP technique acquires all dynamic information in a single continuous scan during which the contrast agent is injected. Image reconstruction is then achieved by binning the data into sequential timeframes and reconstructing the frames with an iterative method that combines parallel imaging and compressed sensing.[9] By using a total-variation constraint along time, the GRASP technique can reconstruct images from highly undersampled data, offering simultaneously high submillimeter spatial and excellent temporal resolution. In addition, a unique feature of GRASP imaging is that the desired temporal resolution can be selected retrospectively and can be designated as high as approximately 2.5 seconds per frame. Thus, compared with conventional 2D TSE examinations, GRASP provides greater through-plane resolution, improved sensitivity to motion and flow, and improved fat suppression.[10]

The purpose of our study was, therefore, to evaluate the role of GRASP for assessing the pituitary gland. More specifically, the study proposed to do the following: 1) establish normal enhancement patterns and signal-time curves (STCs) for the anterior and posterior pituitary gland and median eminence, 2) optimize the acquisition time for dynamic pituitary gland imaging, and 3) evaluate differences in the STCs to distinguish a simple cyst from a microadenoma.

MATERIALS AND METHODS

Patients

This study was approved by the institutional review board and is Health Insurance Portability and Accountability Act–compliant. We retrospectively evaluated MR imaging data of 52 patients who underwent dynamic imaging of the pituitary gland by using the GRASP technique between July 2013 and November 2013. For our study, these patients were divided into 2 groups: group 1 patients ($n = 25$; male/female ratio, 9:16; age range, 10–74 years; mean age, 39 years) included healthy volunteers ($n = 8$) or patients undergoing brain studies for the evaluation of headache ($n = 13$) and patients who had undergone pituitary gland studies for incidentally noted suspicious sellar lesions on prior conventional brain studies ($n = 4$). Group 2 consisted of 27 patients (male/female ratio, 12:15; age range, 26–63 years; mean age, 37 years) with a known microadenoma. Specifically, patients were included in group 2 if they had the following: 1) a history of endocrinologic disturbances favoring a central cause, and 2) previous MR imaging studies demonstrating a focus of "reduced" differential enhancement within the pituitary gland compatible with a microadenoma. Patients with susceptibility artifacts at the skull base resulting from dental hardware ($n = 2$) and aneurysm clips ($n = 1$) were excluded from the study. Patients with hemorrhagic ($n = 1$) or cystic lesions ($n = 2$) within the pituitary gland were also excluded.

MR Imaging

All patients underwent MR imaging with a 3T system (Magnetom Skyra; Siemens, Erlangen, Germany). A 20-channel head/neck coil was used. Imaging protocol included a coronal radial volumetric interpolated brain examination (VIBE) with a GRASP acquisition (TR/TE, 6.4/2.4 ms; in-plane resolution, 0.7 mm; section thickness, 0.8 mm; 32 sections; FOV, 180 mm; flip angle, 9.5°; bandwidth, 391 Hz/pixel; pixel base resolution, 256; 800 spokes; acquisition time, 180 seconds), precontrast sagittal T1 (TR/TE, 440/2.66 ms; section thickness, 3 mm; 25 sections; FOV, 160 mm; flip angle, 90°; bandwidth, 380 Hz/pixel; pixel base resolution, 320), coronal T2 (TR/TE, 4000/97 ms; section thickness, 2 mm; 15 sections; FOV, 140 mm; flip angle, 150°; bandwidth, 260 Hz/pixel; pixel base resolution, 320), and axial FLAIR (TR/TE, 9000/90 ms; TI, 2500; section thickness, 5 mm; 15 sections; FOV, 220 mm; flip angle, 150°; bandwidth, 290 Hz/pixel; pixel base resolution, 320). Contrast material, 0.01-mmol gadopentetate dimeglumine (Magnevist; Bayer HealthCare Pharmaceuticals, Wayne, New Jersey) per kilogram of body weight, was administered at 3 mL/s on initiation of the GRASP sequence.

Image Data Analysis and Processing

Images were evaluated by 1 neuroradiologist (G.M.F., with 15 years of experience), who was blinded to the study population. The acquired data from the GRASP scans were exported and reconstructed off-line by using a C++ implementation of the GRASP algorithm, creating 9 dynamic image frames with a temporal resolution of 20.00 seconds each. Reconstructed images were sent to the PACS and analyzed by using the software Olea Sphere, Version 2.2 (Olea Medical, La Ciotat, France) to obtain signal-time curves and generate permeability measurements, including wash-in, washout, peak, time to maximum enhancement, and area under the curve (Fig 1).

Evaluation of the normal-appearing pituitary gland was performed in group 1 by placing ROIs on the GRASP images of the anterior and posterior pituitary gland and the median eminence. Sagittal reconstructions confirmed the placement of ROIs within their respective locations (Fig 2*A*–*C*). The ROIs were used to generate STCs for each of these individual regions (Fig 2*D*). In addition, ROIs were placed within incidentally noted cysts ($n = 3$) in group 1 to compare the generated STCs with microadenomas in group 2.

To optimize image acquisition times, we generated STCs and permeability measurements for group 2, placing the ROIs in the normal-appearing pituitary gland and in the microadenoma (Fig 3).

Statistical Analysis

Statistical analysis was performed with SAS 9.3 software (SAS Institute, Cary, North Carolina). The analysis was divided into 2 parts. The first part was using the paired-sample Wilcoxon signed rank test to evaluated differences in normal STCs and permeability parameters of the anterior and posterior pituitary gland and

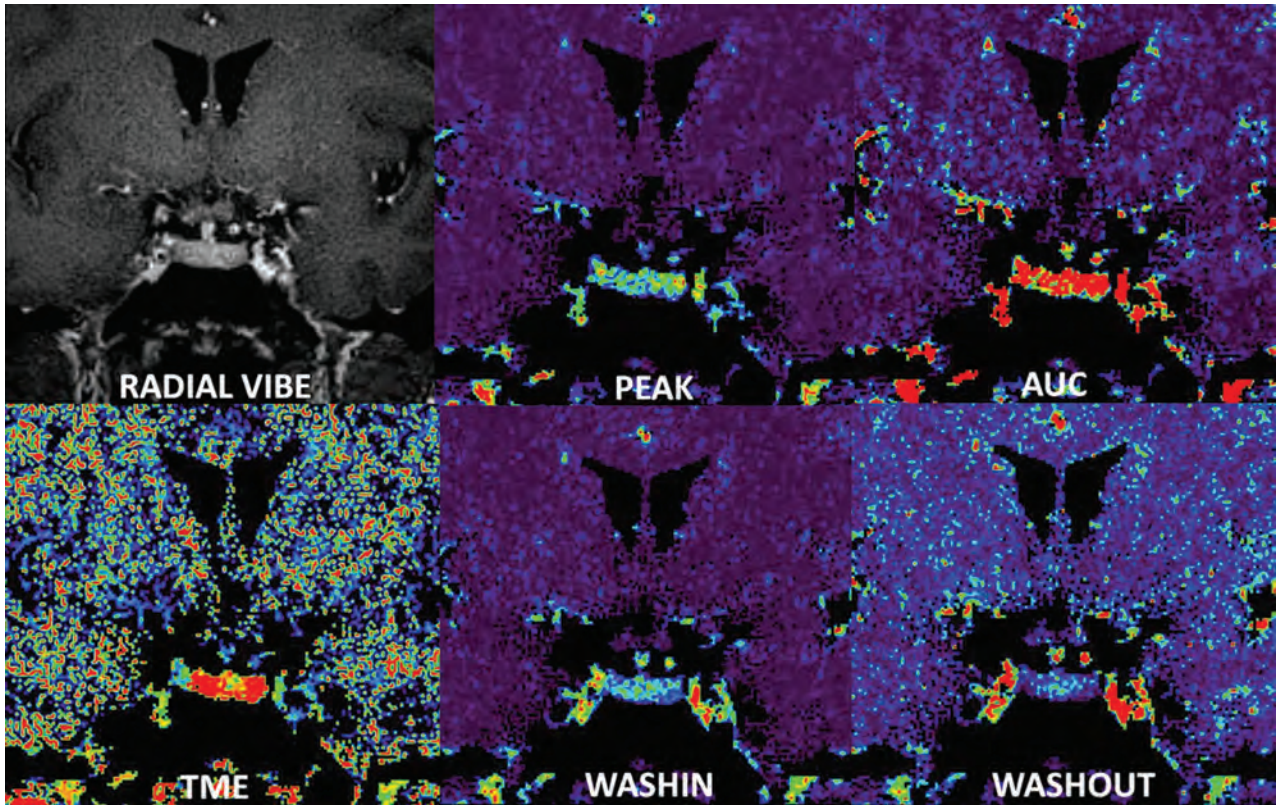

FIG 1. Analysis of radial VIBE images provide maps of different permeability parameters: peak, area under the curve, time of maximum enhancement, wash-in, and washout.

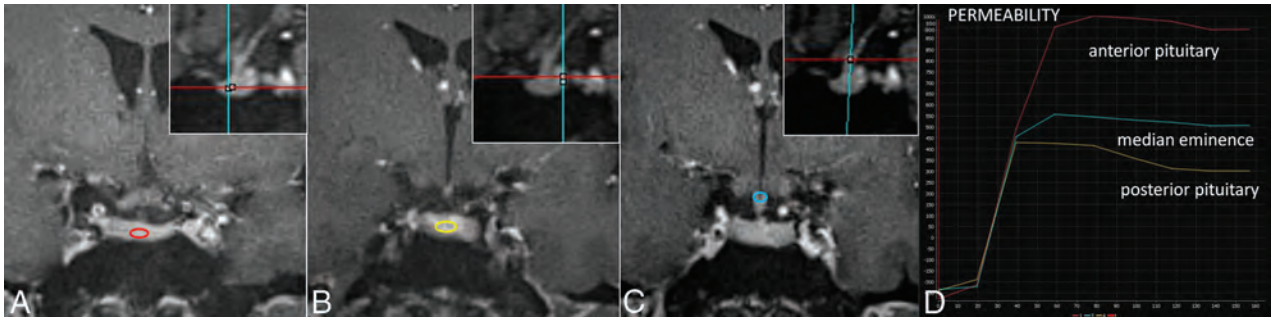

FIG 2. GRASP images in a healthy volunteer show the ROIs in the anterior pituitary gland (*A*), posterior pituitary gland (*B*), and median eminence (*C*). Sagittal reference planes are shown *top right*. Corresponding signal-time curves from the ROIs (*D*) demonstrate a different pattern of enhancement in the anterior (red) and posterior pituitary gland (yellow) and the median eminence (light blue).

the median eminence from group 1 subjects. The mean significance level was set up at $P < .005$. The second part of the analysis used the Student *t* test and focused on optimizing the acquisition time for dynamic pituitary gland imaging. This was performed by comparing peak enhancement values between the anterior pituitary gland and the microadenoma in group 2 patients at 10-second time intervals beginning at 60 seconds (when the maximum enhancement was almost reached) to 140 seconds. This allowed us to estimate a total of 8 mean, minimum, and maximum percentage-change values beginning at T1 (from 60 to 70 seconds) until T8 (from 130 to 140 seconds) (Table 1). A Student *t* test was used to demonstrate any significant difference in peak enhancement values between the normal-appearing anterior pituitary gland and the microadenoma in this time (60–140 seconds). The mean significance level was set at $P < .001$.

Table 1: Mean, SD, median, maximum, and lower and upper limits of a 95% confidence interval of the mean for the percentage change in the peak enhancement estimate from time T0 = 60 seconds to time T8 = 140 seconds in the normal-appearing anterior pituitary gland of group 2 patients

Time	Mean	SD	Median	Maximum	Lower	Upper
1	9.82	9.97	5.25	30.99	5.16	14.49
2	6.11	6.65	4.52	21.69	3.00	9.23
3	2.00	2.52	1.05	8.53	0.82	3.18
4	2.17	2.55	1.18	8.98	0.97	3.36
5	1.41	0.87	1.06	2.76	1.01	1.82
6	1.38	0.87	1.04	3.82	0.98	1.79
7	0.94	0.87	0.71	3.28	0.53	1.35
8	0.57	0.33	0.62	1.30	0.42	0.73

Table 2: Values of perfusion parameters obtained from ROI analysis in different regions of the normal-appearing pituitary gland[a]

	Anterior		Posterior		Median Eminence	
Parameter	Mean	SD	Mean	SD	Mean	SD
AUC	69980.65	20169.32	37500.10	17701.73	40246.39	16626.70
Peak	754.94	242.04	439.61	205.67	446.62	192.66
TME (sec)	86.55	19.23	58.96	16.23	62.60	18.70
Wash-in	10.92	3.89	9.14	4.20	8.54	3.71
Washout	1.52	1.34	1.90	1.48	1.56	1.27

Note:—TME indicates time of maximum enhancement.
[a] All parameters other than TME are dimensionless.

Table 3: Mean, minimum, and maximum peak enhancement values measured at different times in the microadenoma of group 2 patients

Time (sec)	Mean PE	Min PE	Max PE
60	327	90	500
70	365	120	600
80	400	170	630
90	420	200	660
100	417	180	650
110	342	165	625
120	345	172	620
130	346	171	613
140	344	170	613

Note:—PE indicates peak enhancement; Min, minimum; Max, maximum.

RESULTS

Region Analysis (Group 1)

An evaluation of the STCs derived from the anterior and posterior pituitary gland and the median eminence demonstrated differential patterns of enhancement for each of these individual regions. STCs from the posterior pituitary gland and the median eminence demonstrated a faster wash-in (9.14 and 8.54, respectively) compared with the anterior pituitary gland (10.92), a faster time of maximum enhancement (58.96 and 62.60 seconds, respectively) compared with that of the anterior pituitary gland (86.55 seconds), and a lower peak of enhancement (439.61 and 446.62, respectively) compared with the anterior pituitary gland (754.94). The anterior pituitary gland and median eminence showed a faster washout compared with the posterior pituitary gland (1.52 and 1.56 versus 1.90, respectively). The results of the statistical analysis of the preceding data are summarized in Table 2. These findings are consistent across patients in group 1, with a mean significance level of $P < .005$.

Time Analysis (Group 2)

The mean peak enhancement for the anterior pituitary gland was reached at 80 ± 10 seconds. There was no significant change in the enhancement values for the anterior pituitary gland after 90 seconds (Table 1). The mean peak enhancement value for the microadenoma was reached at 90 ± 10 seconds. There was a relative plateau to mild washout noted in the enhancement values measured subsequent to the peak enhancement time (Table 3). A statistically significant difference ($P < .001$) in the enhancement values between the normal pituitary gland and the microadenoma could be consistently noted throughout all the time points measured from 60 seconds (T1) to 140 seconds (T8) (Fig 3).

Microadenomas

Of the 27 microadenomas, 7 were 6–9 mm, 19 were 3–5 mm, and 1 was <3 mm.

DISCUSSION

In this study, we have successfully demonstrated the role of a radial 3D gradient-echo acquisition with GRASP reconstruction to provide a quantitative assessment of permeability characteristics and enhancement patterns of the normal pituitary gland and microadenomas.

Golden-angle radial sparse parallel MR imaging is a volumetric dynamic imaging technique based on a 3D gradient-echo sequence with radial "stack-of-stars" *k*-space sampling and golden-angle ordering. Such an image acquisition allows excellent spatial and temporal resolution. The current study exploited the potential of this technique in evaluating the pituitary gland with an in-plane resolution of 0.7 mm, a contiguous section thickness of 0.8 mm, and a temporal resolution of 20 seconds.

Our ROI-based analysis of STCs demonstrates a greater maximum and mean enhancement in the anterior pituitary gland compared with the posterior pituitary gland and median eminence. Furthermore, we found faster wash-in in the median eminence and posterior pituitary gland compared with the anterior pituitary gland (Fig 2). These findings may reflect differences in the underlying vascular anatomy and perfusion characteristics of these regions. The superior hypophyseal artery is a branch of the supraclinoid segment of the internal carotid artery. The inferior hypophyseal artery is a branch of the meningohypophyseal trunk that arises from the cavernous segment of the internal carotid artery. Both the superior and inferior hypophyseal arteries anastomose with each other and their counterparts at the level of the median eminence to form the primary plexus. This primary plexus of capillaries gives rise to a series of short and long portal hypophyseal veins, which pass down the stalk to form a secondary plexus to supply the anterior pituitary gland. In contrast, the posterior pituitary gland is supplied directly by the inferior hypophyseal arteries. It is likely that the differences in the blood supply to the anterior and posterior pituitary gland reflect the variation in their enhancement patterns. Specifically, the posterior pituitary gland, due to the direct vascular supply from the inferior hypophyseal artery, enhances earlier than the anterior pituitary gland.[11] Similarly, the anterior pituitary gland receives blood supply from both the superior and inferior hypophyseal arteries via the portal plexus. The anterior pituitary gland, therefore, exhibits delayed wash-in, likely due to the additional time taken for the blood to course through the portal plexus of veins. Likewise, the greater maximum enhancement within the anterior pituitary gland results from an intrinsic attenuated and complex capillary network contributed by the dual vascular supply of the superior and inferior hypophyseal arteries.[12,13]

Our findings are supported by a previous study by Tien,[13] which obtained STCs from 1.5T sagittal dynamic contrast-enhanced T1-weighted gradient-echo sequences, similarly demonstrating slightly delayed enhancement of the anterior pituitary

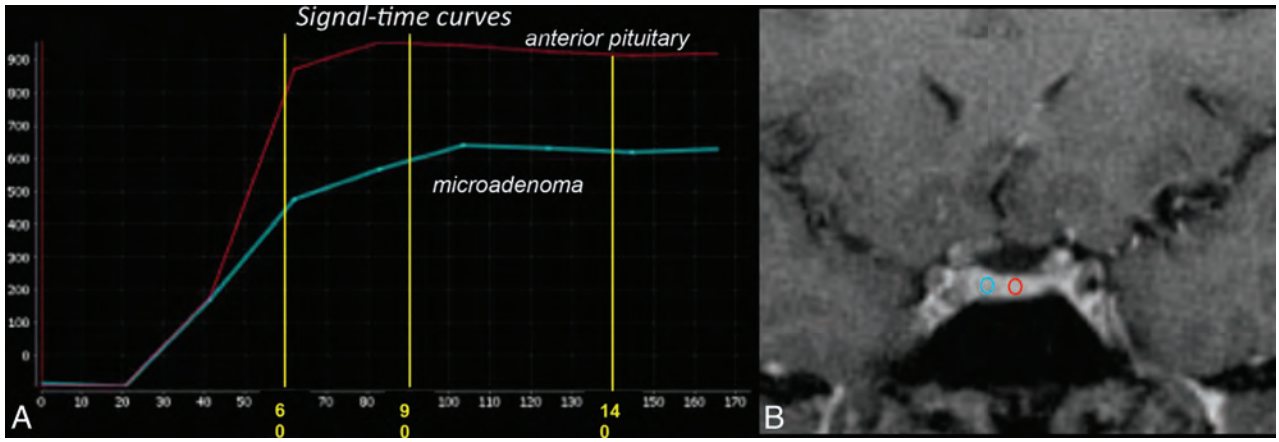

FIG 3. *A*, GRASP image demonstrates placement of ROIs within the normal-appearing pituitary gland and microadenoma. *B*, Corresponding signal-time curves are shown. Peak enhancement from the anterior pituitary gland is seen at approximately 80 seconds with subsequent gradual washout. Peak enhancement from the microadenoma is seen at approximately 100 seconds with a subsequent plateau. There is a significant difference in the enhancement between the anterior pituitary gland and the microadenoma from 60 seconds onward.

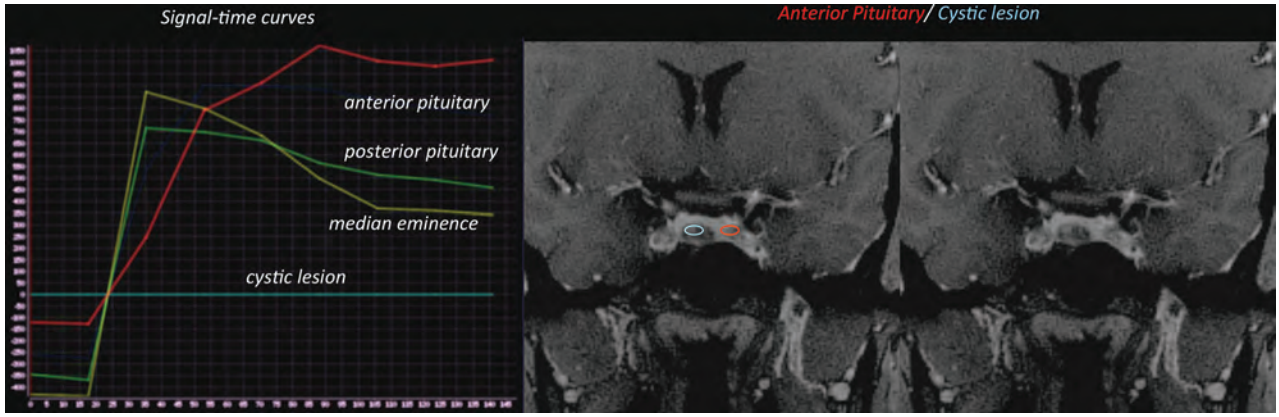

FIG 4. Signal-time curve derived from an ROI applied to a cyst demonstrates a flat STC compared with the normal STCs from the anterior pituitary gland, posterior pituitary gland, and median eminence evaluated in the same patient.

gland compared with the posterior pituitary gland and median eminence.

There is a large variation in the acquisition time (150–240 seconds) for dynamic imaging of the pituitary gland among imaging centers.[4-6] Our study based on the STCs sought to establish a more defined acquisition time for dynamic pituitary gland imaging. Our results demonstrate that maximum enhancement of the anterior pituitary gland occurs at approximately 80 ± 10 seconds, subsequent to which there is no significant change in enhancement for a measured time period up to 140 seconds. In contrast, the microadenomas demonstrate maximum enhancement at 90 ± 10 seconds, subsequent to which there is no significant change in the enhancement for a total measured time of 140 seconds. Furthermore, statistical analysis demonstrated that a significant difference in the enhancement curves between the anterior pituitary gland and the microadenoma is seen beginning 60 seconds postinjection of contrast and continuing for the entire remaining duration of the study. Our results therefore suggest that 120 seconds (2 minutes) is a reasonably appropriate dynamic acquisition time to evaluate the pituitary gland following contrast administration. According to our literature search, ours is the first imaging study that has looked into the signal-time curves to establish a defined acquisition imaging time for pituitary studies. This has significant bearing in the current economic imaging scenario, allowing appropriate use of magnet scanning time to achieve optimum patient throughput without compromising patient care. By establishing a 120-second acquisition time, we save 30–120 seconds of imaging time from that quoted in the literature.[4-6]

The study also demonstrated that the signal-time curves for microadenomas are distinctly different from those of cysts. The STC from a microadenoma demonstrated some uptake of contrast in the initial 60 seconds following contrast administration before plateauing off. In contrast, the simple cyst did not pick up any contrast and is represented by a flat STC (Fig 4).

The retrospective nature of the study, the small sample size, and lack of surgical confirmation for microadenomas are the major limitations of our study. We excluded cystic and hemorrhagic adenomas from our study population; this exclusion can be considered a relative limitation as well. However, we did this to have a homogeneous patient-microadenoma population, keeping in mind that this was a proof-of-concept study.

CONCLUSIONS

We have demonstrated that dynamic imaging of the pituitary gland by using a radial VIBE with GRASP is feasible in clinical

practice and enables both quantitative and qualitative assessment of temporal variance in signal-enhancement patterns of the anterior and posterior pituitary gland and the median eminence. Moreover, we have shown that an acquisition time of 120 seconds following contrast administration is sufficient to provide adequate dynamic evaluation of the pituitary gland, allowing optimal use of magnet scanning time.

Disclosures: Kai Tobias Block—*UNRELATED*: *Patents (planned, pending or issued)*: Patent application for GRASP technique submitted by New York University.* Fernando Boada—*RELATED*: *Grant*: National Institutes of Health.* *Money paid to the institution.

REFERENCES

1. Ezzat S, Asa SL, Couldwell WT, et al. **The prevalence of pituitary adenomas: a systematic review.** *Cancer* 2004;101:613–19
2. Rand T, Lippitz P, Kink E, et al. **Evaluation of pituitary microadenomas with dynamic MR imaging.** *Eur J Radiol* 2002;41:131–35
3. Kucharczyk W, Bishop JE, Plewes DB, et al. **Detection of pituitary microadenomas: comparison of dynamic keyhole fast spin-echo, unenhanced, and conventional contrast-enhanced MR imaging.** *AJR Am J Roentgenol* 1994;163:671–79
4. Gao R, Isoda H, Tanaka T, et al. **Dynamic gadolinium-enhanced MR imaging of pituitary adenomas: usefulness of sequential sagittal and coronal plane images.** *Eur J Radiol* 2001;39:139–46
5. Bartynski WS, Lin L. **Dynamic and conventional spin-echo MR of pituitary microlesions.** *AJNR Am J Neuroradiol* 1997;18:965–72
6. Lee HB, Kim ST, Kim HJ, et al. **Usefulness of the dynamic gadolinium-enhanced magnetic resonance imaging with simultaneous acquisition of coronal and sagittal planes for detection of pituitary microadenomas.** *Eur Radiol* 2012;22:514–18
7. Chadarana H, Block TK, Rosenkrantz AB, et al. **Free-breathing radial 3D fat-suppressed T1-weighted gradient-echo sequence: a viable alternative for contrast-enhanced liver imaging in patients unable to suspend respiration.** *Invest Radiol* 2011;46:648–53
8. Winkelmann S, Schaeffter T, Koehler T, et al. **An optimal radial profile order based on the golden ratio for time-resolved MRI.** *IEEE Trans Med Imaging* 2007;26:68–76
9. Chandarana H, Feng L, Block TK, et al. **Free-breathing contrast-enhanced multiphase MRI of the liver using a combination of compressed sensing, parallel imaging, and golden-angle radial sampling.** *Invest Radiol* 2013;48:10–16
10. Feng L, Grimm R, Tobias Block K, et al. **Golden-angle radial sparse parallel MRI: combination of compressed sensing, parallel imaging, and golden-angle radial sampling for fast and flexible dynamic volumetric MRI.** *Magn Reson Med* 2014;72:707–17
11. Castillo M. **Pituitary gland: development, normal appearances, and magnetic resonance imaging protocols.** *Top Magn Reson Imaging* 2005;16:259–68
12. Aron DC, Findling JW, Tyrrell JB. **Hypothalamus and pituitary.** In: Greenspan FS, Strewler GJ, eds. *Basic & Clinical Endocrinology*. 5th ed. Stamford, Connecticut: Appleton & Lange; 1997:95–156.
13. Tien RD. **Sequence of enhancement of various portions of the pituitary gland on gadolinium-enhanced MR images: correlation with regional blood supply.** *AJR Am J Roentgenol* 1992;158:651–54

How Does the Accuracy of Intracranial Volume Measurements Affect Normalized Brain Volumes? Sample Size Estimates Based on 966 Subjects from the HUNT MRI Cohort

T.I. Hansen, V. Brezova, L. Eikenes, A. Håberg, and T.R. Vangberg

ABSTRACT

BACKGROUND AND PURPOSE: The intracranial volume is commonly used for correcting regional brain volume measurements for variations in head size. Accurate intracranial volume measurements are important because errors will be propagated to the corrected regional brain volume measurements, possibly leading to biased data or decreased power. Our aims were to describe a fully automatic SPM-based method for estimating the intracranial volume and to explore the practical implications of different methods for obtaining the intracranial volume and normalization methods on statistical power.

MATERIALS AND METHODS: We describe a method for calculating the intracranial volume that can use either T1-weighted or both T1- and T2-weighted MR images. The accuracy of the method was compared with manual measurements and automatic estimates by FreeSurfer and SPM-based methods. Sample size calculations on intracranial volume–corrected regional brain volumes with intracranial volume estimates from FreeSurfer, SPM, and our proposed method were used to explore the benefits of accurate intracranial volume estimates.

RESULTS: The proposed method for estimating the intracranial volume compared favorably with the other methods evaluated here, with mean and absolute differences in manual measurements of −0.1% and 2.2%, respectively, and an intraclass correlation coefficient of 0.97 when using T1-weighted images. Using both T1- and T2-weighted images for estimating the intracranial volume slightly improved the accuracy. Sample size calculations showed that both the accuracy of intracranial volume estimates and the method for correcting the regional volume measurements affected the sample size.

CONCLUSIONS: Accurate intracranial volume estimates are most important for ratio-corrected regional brain volumes, for which our proposed method can provide increased power in intracranial volume–corrected regional brain volume data.

ABBREVIATIONS: ARBM = automatic reverse brain mask; HUNT = Nord-Trøndelag Health Study; ICC = intraclass correlation coefficient; ICV = intracranial volume; RBM = reverse brain mask; SPM = Statistical Parameteric Mapping

A large part of the variability in regional brain volume measurements can be explained by differences in head size because individuals with larger heads tend to have larger brain structures than people with smaller heads. Thus, regional brain volumes are usually normalized by some measure of the head size to reduce this variability. The most commonly used measure is intracranial volume (ICV),[1] which is defined as the volume inside the cranium, including the brain, meninges, and CSF. The ICV is often preferred over the brain volume because it is a good measure of premorbid brain size.[2]

Manual delineation is considered the criterion standard for measuring ICV on MR images, but it is labor-intensive; therefore, a number of automatic methods have been developed. Two of the most popular are one by Buckner et al[3] implemented in FreeSurfer (http://surfer.nmr.mgh.harvard.edu/) and another based on the Statistical Parameteric Mapping (SPM) program package (www.fil.ion.ucl.ac.uk/spm/software/spm8).

Several of the automatic methods for estimating the ICV report good accuracy, with volume estimates close to those of manual measurements.[3,4] However, because the ICV is seldom used directly but instead is used for reducing the variability due to head

Received September 29, 2014; accepted after revision January 28, 2015.

From the Departments of Neuroscience (T.I.H., V.B., A.H.) and Circulation and Medical Imaging (L.E.), Norwegian University of Science and Technology, Trondheim, Norway; Department of Medical Imaging (T.I.H., V.B., A.H.), St. Olavs Hospital Trondheim University Hospital, Trondheim, Norway; Medical Imaging Research Group (T.R.V.), Department of Clinical Medicine, UiT The Arctic University of Norway, Tromsø, Norway; and Department of Radiology (T.R.V.), University Hospital North Norway, Tromsø, Norway.

T.I.H. and V.B. contributed equally (shared first authorship).

This study was funded by the Norwegian Ministry of Education and Research.

Please address correspondence to Torgil Riise Vangberg, PhD, Department of Clinical Medicine, Faculty of Health Sciences, UiT The Arctic University of Norway, 9037 Tromsø, Norway; e-mail: torgil.vangberg@uit.no

Indicates open access to non-subscribers at www.ajnr.org

Indicates article with supplemental on-line tables.

http://dx.doi.org/10.3174/ajnr.A4299

size in other regional brain volume measurements, it may be more relevant to consider how the accuracy of the ICV estimates affects the normalized regional brain volumes. This detail is important because the method for estimating the ICV can change the outcome of statistics on ICV-normalized regional brain volumes. This difference was shown in a recent study that compared statistics on normalized hippocampal volumes by using ICV estimates from FreeSurfer and SPM.[5]

The method for normalizing the regional brain volumes with the ICV will affect how errors in the ICV measurements are propagated to the normalized volumes. Two of the most common normalization methods are the "ratio" method, which amounts to dividing the regional brain volumes by the ICV, and the "residual" method, which uses residuals from a linear regression between the volume of interest and the ICV,[6] but other techniques are also used.[1,7,8] Studies have shown that the ratio method is more sensitive to errors in ICV than the residual method.[1,9]

In this study, we describe a fully automatic SPM-based method for estimating the ICV, which improves on previous SPM-based methods in 2 important ways; First, there is no need to define an empiric threshold for estimating the ICV; and second, our method can estimate the ICV by using both T1- and T2-weighted images, which might be more accurate than using only T1-weighted images. We assessed the accuracy of our method against manually traced ICV measurements and ICV estimates from FreeSurfer and an accurate SPM-based method, called the "reverse brain mask" (RBM).[4] To explore the practical implications of both methods for obtaining the ICV and the normalization method (residual-versus-ratio correction), we estimated the sample sizes needed to detect significant differences in ICV-normalized regional brain volumes between 2 groups with ICV estimates from FreeSurfer, the RBM method, and our proposed method.

MATERIALS AND METHODS

Subjects

The MR images in this study were from The Nord-Trøndelag Health Study (HUNT Study), which is a collaboration between the HUNT Research Centre (Faculty of Medicine, Norwegian University of Science and Technology), the Nord-Trøndelag County Council, the Central Norway Health Authority, and the Norwegian Institute of Public Health. The MR images in the HUNT MR imaging cohort (n = 1006) represent subjects (n = 14,033) who participated in the 3 public health surveys in Nord-Trøndelag County (HUNT 1, 1985–1987; HUNT 2, 1995–1997; HUNT 3, 2006–2008) in Norway. MR imaging examinations were performed from 2007 to 2009. The mean age for the subjects was 59 ± 4.2 years (range, 50.5–66.8 years) at the time of scanning. Of the 1006 MR imaging datasets, 40 had to be discarded because of motion or image artifacts (n = 34), missing T2-weighted images (n = 5), and failed FreeSurfer processing (n = 1), leaving 966 for analysis.

This study was approved by the Regional Committee for Ethics in Medical Research (REK-Midt #2011/456). All participants gave written informed consent before participation.

Subjects Selected for Manual Segmentation. Images from 30 healthy individuals (15 men) were selected for manual segmentation. To avoid biasing the sample toward any particular age, we divided the sample into 3 age groups, 50–55 years, 55–60 years, and 60–67 years, and randomly selected 5 men and 5 women from each age group. The mean age for the subjects selected for manual segmentation was 58 ± 4.4 years (range, 51–65 years).

Image Acquisition

Examinations were performed on a 1.5T Signa HDx MR imaging scanner (GE Healthcare, Milwaukee, Wisconsin) with an 8-channel head coil at Levanger Hospital, Nord-Trøndelag. T1-weighted 3D MPRAGE images were acquired sagittally by using the following parameters: TE = 4 ms, TR = 10 ms, flip angle = 10°, matrix size = 256 × 256, FOV = 240 × 240 mm, 166 sections of 1.2-mm thickness. T2-weighted images were acquired axially by using the following parameters: TE = 7.8 ms, TR = 95.3 ms, flip angle = 90°, matrix size = 512 × 512, FOV = 230 × 230 mm, 27 sections, 4-mm section thickness, 1-mm gap.

ICV Measurements

Manual Tracing. ICV was traced on the T1-weighted images by a single rater (V.B.) by using the ITK-SNAP software (Version 2.2.0, www.itksnap.org),[10] by drawing along the outer surface of the dura using the lowest point of the cerebellum as the most inferior point.[11] There was no active exclusion of sinuses or large veins. The pituitary gland was excluded by drawing a straight line from the anterior-to-posterior upper pituitary stalk. Drawings were made on each section in the axial plane. Intrarater accuracy was assessed by re-segmenting 10 randomly selected images from the previously segmented data after at least 2 months.

Automatic Methods

Standard FreeSurfer Method. We used FreeSurfer, Version 4.5.0. FreeSurfer differs from the other methods evaluated here in that it does not produce an ICV mask but estimates the ICV from the scaling factor of the affine transform of the anatomic images to the Talairach template.[3] This scaling factor is approximately proportional to the ICV, and by linearly fitting the scaling factor from a set of images in which the ICV also has been determined by manual tracing, one can use the slope from the fit to estimate the ICV, yielding ICV estimates with an accuracy equivalent that of manual segmentation.[3]

Optimized FreeSurfer Method. Differences in image quality or subject composition could render the default scaling factor in FreeSurfer suboptimal for our data. Therefore, we optimized the scaling factor to the manual ICV estimates in our dataset. We refer to these results as "optimized FreeSurfer."

Reverse Brain Mask Method. The reverse brain mask method[4] uses the unified segmentation algorithm[12] in SPM to derive a nonlinear transform from template space to the subject's native image space. An ICV mask based on the tissue probability maps in SPM is transformed to native space, and by using an empirically derived threshold, one can obtain an estimate of the ICV.[4] The RBM method was implemented in SPM8 with an improved unified segmentation algorithm called "new segment"[13] and default settings for nonuniformity correction (bias full width at half maximum = 60-mm cutoff, and bias regularization = 0.0001 "very light

regularization"). The threshold on the ICV probability mask was determined by least-squares, minimizing the volume difference between the ICV mask and the manually traced ICV volumes.

Automatic Reverse Brain Mask Method. The RBM method needs a threshold to calculate the ICV. This can be obtained empirically as in the original implementation[4] or by optimization against a manually segmented dataset as in this work. Both methods have disadvantages, however, and we implemented an alternative SPM-based method that avoided the use of a threshold. This "automatic reverse brain mask method" (ARBM) uses a manually drawn ICV mask in template space, which is transformed to native space by using the nonlinear transform from the "new segment" in SPM and nearest neighbor interpolation, thus avoiding any need for a threshold. The ICV mask in template space was traced on the 1-mm^3 T1-weighted Montreal Neurological Institute template by using the same segmentation protocol as described previously and the same rater (V.B.) used for the manual segmentation.

ICV Estimates by Using Multispectral Data

T2-weighted images provide better contrast between the dura and skull. Our implementation of the RBM and ARBM methods allows multispectral input to the segmentation algorithm, and by using both the T1- and T2-weighted images, a more accurate estimate of the ICV might be achieved. We made additional ICV estimates with both the RBM and ARBM methods, by using T1- and T2-weighted images as input, which we refer to as "RBM multi" and "ARBM multi."

Assessing the Accuracy of ICV Estimates

The accuracy of the automatic ICV estimates relative to manual tracing was assessed by the accuracy of the volume estimates, by the overlap of the ICV masks, and by the agreement between the measurements as quantified by the intraclass correlation coefficient (ICC).

The accuracy of the volume estimates was quantified by the mean of the relative volume difference (RDIFF) and absolute volume difference (ADIFF), both expressed as percentages. These metrics capture slightly different aspects: RDIFF is sensitive to systematic differences in the ICV, but not random errors that may cancel out over the whole sample, while ADIFF is sensitive to random errors.

$$1) \qquad RDIFF = \left(\frac{V_{\text{manual}} - V_{\text{calculated}}}{0.5 \cdot (V_{\text{manual}} + V_{\text{calculated}})} \right) \times 100,$$

$$2) \qquad ADIFF = \left(\frac{|V_{\text{manual}} - V_{\text{calculated}}|}{0.5 \cdot (V_{\text{manual}} + V_{\text{calculated}})} \right) \times 100.$$

We also quantified the overlap between the calculated ICV mask and the manually traced ICV mask by using the Dice coefficient,[14] a unitless quantity ranging from 0 (no overlap) to 1 (perfect overlap). It is defined as the overlap between 2 binary images A and B, divided by the mean size of the 2 images.

$$3) \qquad Dice = \frac{(A \cap B)}{0.5 \cdot (A + B)}.$$

The Dice coefficient was only calculated for the SPM-based methods because FreeSurfer does not produce an explicit mask of the ICV.

The agreement between the manual ICV measurements and the ICV estimates was quantified with a 2-way mixed single-measures ICC.[15]

Power Analysis

To explore how the different ICV estimates affect the statistical power in ICV-normalized regional brain volume measurements, we estimated the minimum sample size needed to detect a hypothetic volume difference between 2 groups by using the whole dataset of 966 subjects. We reported sample size estimates on 4 ICV measurements, the original FreeSurfer method, the optimized FreeSurfer method, and the 2 ARBM estimates. Results from the RBM method were omitted because they were almost identical to those of the ARBM method.

Regional brain volume measurements of subcortical gray matter structures, total cortical volume, and total white matter volume of the cerebrum and cerebellum were obtained with FreeSurfer (version 4.5.0) by using methods described in Fischl et al,[16,17] and the volumes for the right and left hemispheres were added. The ICV was calculated with FreeSurfer, RBM, and ARBM methods as previously described. For the RBM method, we used the threshold optimized on the manually segmented images, and for the optimized FreeSurfer method, we used the scaling factor fitted to the manually segmented images.

ICV Normalized Volumes

The regional brain volumes were normalized with the ratio and residual methods. The ratio-corrected volumes were calculated as the ratio of the regional brain volume to the ICV. For the residual method, we expressed the ICV-corrected measurements as

$$4) \qquad Vol_{\text{adj}} = Vol - b(ICV - \overline{ICV}),$$

where Vol_{adj} is the ICV-corrected regional brain volume, Vol is the original uncorrected volume, b is slope from the linear regression of Vol on ICV, ICV is the intracranial volume for a particular subject, and $\overline{ICV}$ is the mean ICV over all subjects. Note that ratio- and residual-corrected volumes must be interpreted differently[18] and that the residual-corrected regional volumes have a zero correlation with the ICV, whereas the ratio-corrected volumes will usually correlate to some degree with the ICV.[19]

Estimating the Sample Size

For each regional brain volume measure, we calculated the minimum sample size required to detect a specified difference in the means between 2 groups when testing for a 2-sided difference with a power set to 0.8 and a type I error rate of 0.05. This calculation was performed for the raw volumes, the residual-, and ratio-corrected volumes.

We varied the effect size from 1% to 5% of the mean of the hippocampus volumes to determine how the sample size varied as a function of the effect size as an illustration of the general behavior. We also computed sample size estimates for all regional brain volume measurements for detecting a 2% difference from the mean, which amounts to approximately a "small effect size."[20]

Table 1: Accuracy of the automatic methods for estimating ICV compared with manual delineation[a]

	FreeSurfer	Opt FreeSurfer	RBM	RBM Multi	ARBM	ARBM Multi
Volume difference (mL)						
Mean (SD)	111.25 (53.62)	0.21 (53.02)	−9.17 (42.34)	2.49 (26.72)	−0.07 (41.64)	30.29 (26.75)
Absolute mean (SD)	111.25 (53.62)	40.11 (33.86)	34.38 (25.63)	20.66 (16.69)	34.57 (22.31)	33.71 (22.12)
Volume difference (%)						
DIFF (SD)	7.3 (3.7)	−0.1 (3.5)	−0.6 (2.7)	0.1 (1.7)	−0.1 (2.6)	1.9 (1.7)
ADIFF (SD)	7.3 (3.7)	2.6 (2.3)	2.2 (1.6)	1.3 (1.1)	2.2 (1.4)	2.1 (1.3)
ICC	0.96	0.96	0.97	0.99	0.97	0.99
Dice overlap (mean) (SD)	NA[b]	NA[b]	0.96 (0.01)	0.97 (0.01)	0.96 (0.01)	0.97 (0.00)

Note:—DIFF indicates volume difference; ADIFF, absolute volume difference; NA, not applicable.

[a] Positive differences indicate that the manual measurements were larger.

[b] Calculation not possible because FreeSurfer does not produce an ICV mask.

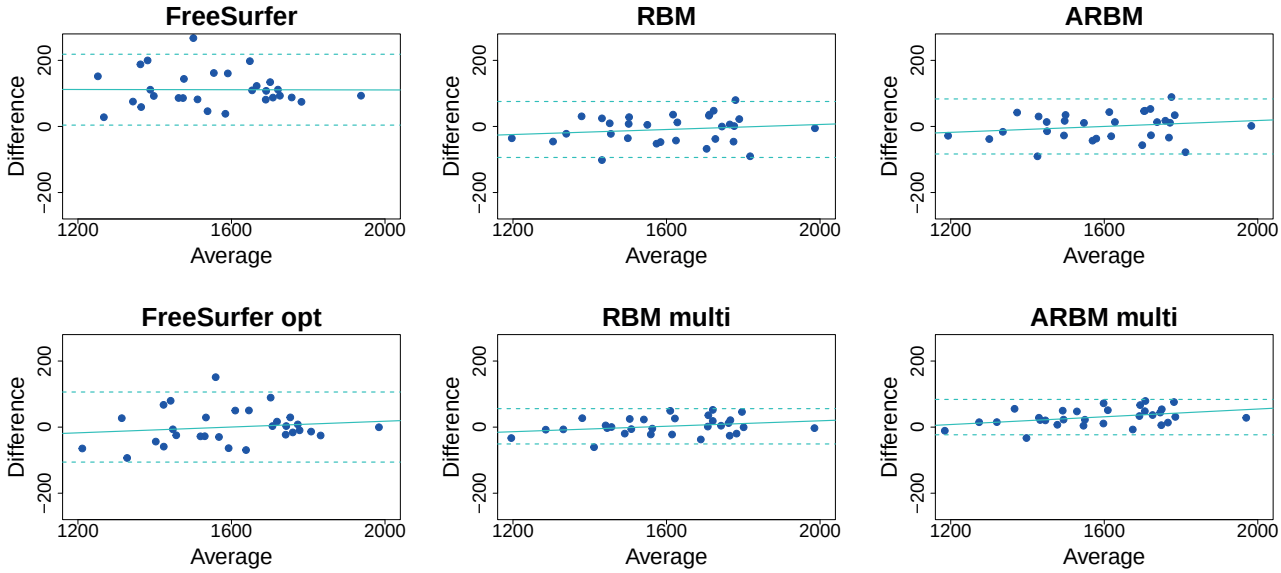

FIG 1. Bland-Altman plots show the ICV difference (manual-automatic) plotted against the mean of the 2 measurements. Units are in milliliters. The *dotted horizontal lines* are 2 SDs above and below the mean, and the *solid line* is the best-fit line from the regression of the difference on the mean.

The effect was calculated on the uncorrected volumes as a percentage from the mean and transformed to the corrected volumes. The SD was calculated directly on the raw volumes and ICV-corrected volumes. For power calculations, we used the "power.t.test" part of the "stats" package in the R statistical computing software, Version 3.0.2 (http://www.r-project.org).

RESULTS

Interrater Accuracy of Manual ICV Estimates

The intraclass correlation (2-way random, absolute agreement, single measures) was 0.99, indicating good agreement between the 2 manual segmentations.

Accuracy of ICV Estimates

The accuracy of the automatic ICV estimates compared with manual delineation is summarized in Table 1. (See On-line Table 1 for mean ICV values for each method.) The FreeSurfer measurements were the least accurate in terms of relative agreement, absolute agreement, and ICC. All ICV estimates by FreeSurfer were lower than the manual measurements, with a mean underestimate of 111 mL. The SDs in the volume differences were also the largest. The optimized FreeSurfer estimates were considerably better than the standard FreeSurfer estimates as seen by the mean and absolute mean of the volume differences, but the SD of the difference was still among the highest. The RBM and RBM multi methods had the lowest absolute mean differences. Table 1 also shows that the multispectral RBM method, by using both T1- and T2-weighted images, was slightly more accurate than the RBM method by using only T1-weighted images. The ARBM method performed in a manner comparable with the RBM method, but the absolute mean difference was slightly larger for the ARBM and ARBM multi methods compared with the RBM counterparts. The Dice and ICC values were very similar for the RBM and ARBM methods but also indicated a slightly better agreement when using multispectral data.

There was good agreement between the automatic methods and manual segmentation (Fig 1). The linear fit between the difference and average had a slightly positive slope for all methods except for the standard FreeSurfer ICV estimates (Fig 1) but was nonsignificant (all $P > .14$, $r^2 < 0.08$) except for the ARBM multi method, in which the difference and average correlated significantly ($P = .03$, $r^2 = 0.15$). This result indicates that the errors increased with increasing ICV. A potential consequence of such a biased error could be that a sex-related bias was introduced in the ICV estimates because men, on average, have a larger ICV than women. We did not, however, find significant differences be-

tween men and women in the errors of the ICV estimates (all $P > .1$; $t < 1.7$).

The use of T1 and T2 images as input improved the accuracy of the RBM method. Table 1 shows that all accuracy metrics are improved for RBM multi over RBM. For the ARBM multi method, the benefits of using multispectral data are less evident. Although the ARBM multi method improves the ICC, Dice overlap, and SD of the volume differences over the ARBM method, the ARBM multi method underestimates, on average, the ICV by 1.9%, compared with only −0.1% for the ARBM method (Table 1).

Sample Size Calculations

Figure 2 shows how the sample size varied over a range of effect sizes for hippocampal volumes normalized with ICV estimates from the FreeSurfer and ARBM methods. The differences in the required sample sizes were most pronounced for small effect sizes, whereas for larger effect sizes, the differences between both ICV estimates and correction methods diminished. Figure 2 also shows that in terms of increasing power, the residual correction was more effective than the ratio correction.

The minimum sample sizes per group required to detect a 2% difference in regional brain volume measurements are shown in Table 2. Compared with the uncorrected volume measurements, both the ratio and residual corrections reduced the required sample size considerably. With residual correction, the differences in the estimated sample size were small and generally in favor of the FreeSurfer methods. The largest difference was for normalized caudate volumes, in which the ICV derived from the ARBM method would require 32 more subjects per group than using the ICV from FreeSurfer. With ratio correction, the differences were larger, as expected. Comparing the standard FreeSurfer estimates with the ARBM estimate showed that the ARBM estimate reduced the sample size considerably for some structures. For the hippocampus volumes, sample size was reduced by 44, and for nucleus accumbens, by 52 subjects per group when using the ARBM ICV estimate compared with the FreeSurfer ICV values. The difference was even larger with the ARBM multi method, with a reduction in the sample size of 51 and 61 per group for the hippocampus and nucleus accumbens, respectively.

There was considerable variation in the required sample size for the different regional volume measurements (Table 2), with cerebral cortex and cerebral white matter volumes requiring the lowest sample sizes, whereas nucleus accumbens measurements required a sample of >800 subjects to reach sufficient power. We found that the sample size was associated with the strength of the correlation between the regional volume measurements and the ICV. This result is expected for the ratio-normalized volumes because there is a linear dependence between the variance of ratio-corrected volumes and the correlation between the ICV and raw volume.[19] However, a similar relationship was also found for the residual-corrected volumes. The association between the Pearson correlation coefficient and sample size estimates for both the residual- and ratio-correction methods is plotted in Fig 3. (See On-line Table 2 for correlation coefficients between the regional brain volumes and the different ICV estimates.)

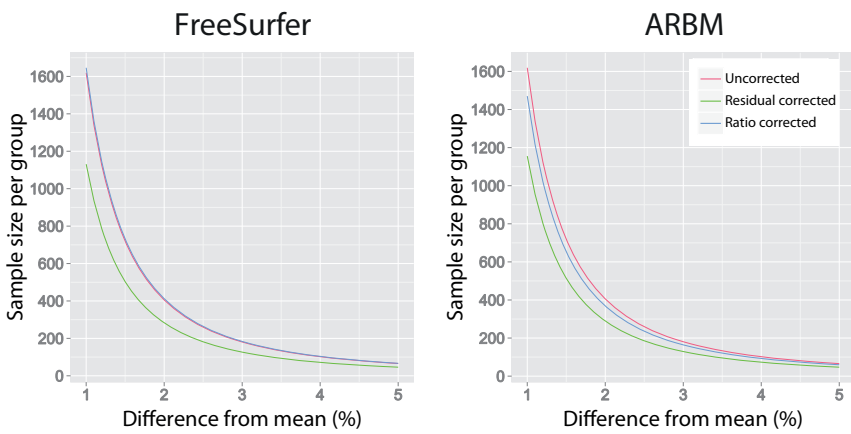

FIG 2. Effect size in percentage difference from the mean plotted against the sample size per group for uncorrected hippocampal volumes and ICV-corrected hippocampal volumes by using FreeSurfer and ARBM ICV estimates.

DISCUSSION

Accuracy of the Automated Methods versus Manual Segmentation

The automatic methods for estimating the ICV, which we evaluated, produced

Table 2: Required sample size per group for detecting a 2% difference in raw and ICV-normalized regional brain volumes between 2 groups, with a power of 0.8 and a type I error rate of 0.05

		Residual Method			Ratio Method			
Brain Volumes	Raw	FreeSurfer[a]	ARBM	ARBM Multi	FreeSurfer	Opt FreeSurfer	ARBM	ARBM Multi
Cerebral white matter	771	195	213	186	195	211	227	202
Cerebral cortex	377	143	143	129	194	164	159	147
Cerebellum white matter	748	441	453	446	459	441	454	452
Cerebellum cortex	450	252	257	255	321	285	287	293
Thalamus proper	490	236	254	243	276	249	272	264
Caudate	738	486	518	511	526	498	532	533
Putamen	504	354	365	359	453	407	423	422
Hippocampus	406	284	290	280	412	360	368	361
Pallidum	669	498	527	520	592	549	596	595
Amygdala	772	536	531	526	570	543	536	534
Nucleus accumbens	1042	849	844	834	933	891	881	872

Note:—Opt indicates optimized.

[a] The FreeSurfer and optimized FreeSurfer sample size estimates are identical when using residual correction because these 2 measurements are linearly related.

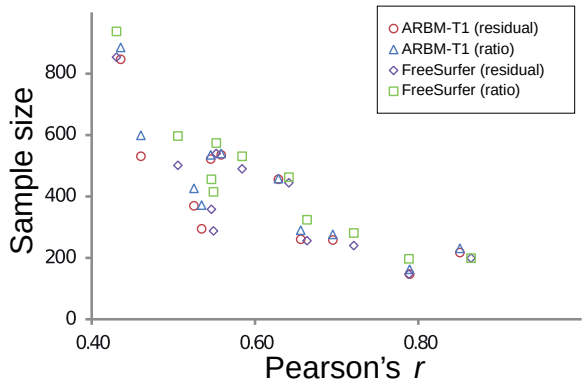

FIG 3. The relationship between sample size estimates for detecting a 2% difference from the mean and Pearson's *r* between uncorrected regional volumes and ICV estimates.

ICV estimates that closely matched those of manual segmentation. The ICV FreeSurfer estimates had a bias that was larger than the other methods, and FreeSurfer consistently underestimated the ICV. A possible cause is that the default scaling factor in FreeSurfer is not optimal for the present study, or that differences between the segmentation protocol for the images on which the scaling factor was optimized and that of the present study could account for the bias.

Optimizing the FreeSurfer scaling factor improved the ICV estimates. A drawback is that one must have a sufficiently large set of images with manually derived ICV measurements to compute an optimized scale factor. Future studies could determine whether the variation in the optimal scaling parameter is primarily determined by the scanner parameters or by the study population.

The RBM method was the most accurate for estimating the ICV. We also found that in comparison with the original implementation of the RBM method, the "new segment" algorithm in SPM improved the accuracy of the RBM method. (See On-line Table 3 for a summary of the accuracy of the original RBM method.) A disadvantage of the RBM method, however, is that one must set an empiric threshold for calculating the ICV. Therefore, the accuracy of the RBM method is dependent on the threshold. This dependency is illustrated in On-line Table 3 showing the accuracy of the RBM method with the optimized threshold and with the threshold recommended by the authors of the RBM method.[4] Using the nonoptimized threshold renders the RBM method less accurate than the ARBM method. We also found that a visual determination of the threshold was difficult because it varied among different raters. Optimizing the threshold against the manual segmentation result avoided this problem but is impractical in many instances because it necessitates manual measurements.

The ARBM method attempts to alleviate the drawback of using a threshold. An ICV mask must still be drawn in template space, but it needs to be done only once. The ARBM approach was, however, less accurate than the RBM method but more accurate than the FreeSurfer methods. The ICV estimates with the ARBM method may be robust over different field strengths, similar to those with the RBM method,[4] because the 2 methods only differ in how the brain masks are thresholded.

Multispectral input clearly improved the accuracy of the RBM method, suggesting that the transformation from template space to native space is more accurate when using T1 and T2 images as input compared with using only T1 images. For the ARBM method, however, multispectral input resulted in a slight underestimation of the ICV. This discrepancy in accuracy between these methods can appear puzzling because they rely on the same transformation from template space to native space. The underlying cause is that the multispectral segmentation, on average, generates a slightly smaller volume in native space than the segmentation based on T1 images only. The bias is adjusted during the optimization of the threshold in the RBM method because the optimized threshold for RBM multi is 0.29 compared with 0.34 for the RBM method (a lower threshold results in a larger ICV mask). For the ARBM method, the ICV is fully determined by the transformation to native space; therefore, there is an increase in the mean volume difference for the ARBM multi method. The bias in the ARBM multi estimates is mainly a concern when using ratio correction. For residual correction, the ARBM multi method would still be preferable over the ARBM method because the multispectral segmentation reduces the variance in the volume estimates compared with the T1-only ARBM. This outcome is reflected in the slight decrease in sample size estimates for the ARBM multi method over the ARBM method (Table 2).

Sample Size Estimates

The ICV is often used for correcting variations in regional brain volume measurements due to differences in head size. Several studies have compared the accuracy of various ICV-estimation methods,[3,4,21,22] but surprisingly few have examined the practical benefits of an accurate ICV measurement. Naively, one would expect that accurate ICV estimates would increase the statistical power of ICV-corrected regional volume measurements. Our results demonstrate that not only the choice of ICV estimate, but also the method of ICV correction can affect the statistical power. We found that residual correction resulted in only minor differences between the FreeSurfer and ARBM methods (Table 2). In fact, the FreeSurfer ICV correction generally required a smaller sample size than the ARBM-corrected volumes. This is surprising considering that the ARBM method had higher accuracy than FreeSurfer compared with manual segmentation (Table 1). However, the differences in the required sample sizes for the volume estimates can largely be explained by the strength of the correlation between the ICV and the volume measurements (Fig 3).

We found that accurate ICV estimates were more crucial for the ratio-corrected volumes, a finding that is in agreement with previous studies,[9,19] and that the ratio-correction method, unlike the residual-correction method, requires absolute agreement in the ICV estimates. When using ratio correction, we found that the more accurate ARBM ICV estimates can provide increased power compared with the FreeSurfer ICV estimates. For example, to detect a 2% difference in the hippocampus volumes requires 44 fewer subjects per group when using ARBM ICV estimates compared with FreeSurfer ICV estimates. However, the difference in the required sample size becomes smaller for larger effects (Fig 2); for medium-sized or larger effects, there are only minor differences among the methods we evaluated.

CONCLUSIONS

In this article, we described an SPM-based method for calculating the ICV, which compared favorably against other available methods. Sample size estimates showed that ICV estimates from the ARBM method could increase the statistical power in ICV-corrected regional brain volume data compared with using ICV estimates from FreeSurfer, but only when using ratio correction and for small effect sizes. For detecting larger effects or when using residual correction, the choice of method for estimating the ICV became less critical. The ARBM method can serve as a robust and efficient method for obtaining accurate ICV estimates in large datasets and in datasets in which application of FreeSurfer or other software is not possible or needed. The Matlab (MathWorks, Natick, Massachusetts) source code for the ARBM method can be obtained from the corresponding author.

ACKNOWLEDGMENTS

The authors thank Lars Jacob Stovner (Norwegian University of Science and Technology) and the HUNT administration for organizing and the MR imaging technologists at the Department of Radiology at Levanger Hospital for collecting the HUNT MR imaging data.

REFERENCES

1. Barnes J, Ridgway GR, Bartlett J, et al. **Head size, age and gender adjustment in MRI studies: a necessary nuisance?** *Neuroimage* 2010;53:1244–55
2. Davis PJ, Wright EA. **A new method for measuring cranial cavity volume and its application to the assessment of cerebral atrophy at autopsy.** *Neuropathol Appl Neurobiol* 1977;3:341–58
3. Buckner RL, Head D, Parker J, et al. **A unified approach for morphometric and functional data analysis in young, old, and demented adults using automated atlas-based head size normalization: reliability and validation against manual measurement of total intracranial volume.** *Neuroimage* 2004;23:724–38
4. Keihaninejad S, Heckemann RA, Fagiolo G, et al. **A robust method to estimate the intracranial volume across MRI field strengths (1.5T and 3T).** *Neuroimage* 2010;50:1427–37
5. Nordenskjöld R, Malmberg F, Larsson EM, et al. **Intracranial volume estimated with commonly used methods could introduce bias in studies including brain volume measurements.** *Neuroimage* 2013; 83:355–60
6. Jack R, Twomey K, Sharbrough FW, et al. **Anterior temporal lobes and hippocampal formations: normative volumetric measurements from MR images in young adults.** *Radiology* 1989;172:549–54
7. Lehmann M, Douiri A, Kim LG, et al. **Atrophy patterns in Alzheimer's disease and semantic dementia: a comparison of FreeSurfer and manual volumetric measurements.** *Neuroimage* 2010; 49:2264–74
8. O'Brien LM, Ziegler DA, Deutsch CK, et al. **Statistical adjustments for brain size in volumetric neuroimaging studies: some practical implications in methods.** *Psychiatry Res* 2011;193:113–22
9. Sanfilipo MP, Benedict RHB, Zivadinov R, et al. **Correction for intracranial volume in analysis of whole brain atrophy in multiple sclerosis: the proportion vs. residual method.** *Neuroimage* 2004; 22:1732–43
10. Yushkevich PA, Piven J, Hazlett HC, et al. **User-guided 3D active contour segmentation of anatomical structures: significantly improved efficiency and reliability.** *Neuroimage* 2006;31:1116–28
11. Whitwell JL, Crum WR, Watt HC, et al. **Normalization of cerebral volumes by use of intracranial volume: implications for longitudinal quantitative MR imaging.** *AJNR Am J Neuroradiol* 2001;22: 1483–89
12. Ashburner J, Friston KJ. **Unified segmentation.** *Neuroimage* 2005; 26:839–51
13. Weiskopf N, Lutti A, Helms G, et al. **Unified segmentation based correction of R1 brain maps for RF transmit field inhomogeneities (UNICORT).** *Neuroimage* 2011;54:2116–24
14. Dice LR. **Measures of the amount of ecologic association between species.** *Ecology* 1945;26:297–302
15. Shrout PE, Fleiss JL. **Intraclass correlations: uses in assessing rater reliability.** *Psychol Bull* 1979;86:420–28
16. Fischl B, Salat DH, Busa E, et al. **Whole brain segmentation: automated labeling of neuroanatomical structures in the human brain.** *Neuron* 2002;33:341–55
17. Fischl B, Salat DH, van der Kouwe AJW, et al. **Sequence-independent segmentation of magnetic resonance images.** *Neuroimage* 2004; 23(suppl 1):S69–84
18. Smith RJ. **Relative size versus controlling for size: interpretation of ratios in research on sexual dimorphism in the human corpus callosum.** *Current Anthropology* 2005;46:249–73
19. Mathalon DH, Sullivan EV, Rawles JM, et al. **Correction for head size in brain-imaging measurements.** *Psychiatry Res* 1993;50:121–39
20. Cohen J. **A power primer.** *Psychol Bull* 1992;112:155–59
21. Fein G, Di Sclafani V, Taylor C, et al. **Controlling for premorbid brain size in imaging studies: T1-derived cranium scaling factor vs. T2-derived intracranial vault volume.** *Psychiatry Res* 2004;131: 169–76
22. Pengas G, Pereira JM, Williams GB, et al. **Comparative reliability of total intracranial volume estimation methods and the influence of atrophy in a longitudinal semantic dementia cohort.** *J Neuroimaging* 2009;19:37–46

Longitudinal Mixed-Effect Model Analysis of the Association between Global and Tissue-Specific Brain Atrophy and Lesion Accumulation in Patients with Clinically Isolated Syndrome

M. Varosanec, T. Uher, D. Horakova, J. Hagemeier, N. Bergsland, M. Tyblova, Z. Seidl, M. Vaneckova, J. Krasensky, M.G. Dwyer, E. Havrdova, and R. Zivadinov

ABSTRACT

BACKGROUND AND PURPOSE: The relationship between lesion formation and brain atrophy development in the early phase of multiple sclerosis is unclear. We investigated the association between new lesion accumulation and brain atrophy progression in patients with clinically isolated syndrome over 48 months.

MATERIALS AND METHODS: Patients with clinically isolated syndrome ($n = 210$) were evaluated with 1.5T MR imaging at baseline and at 6, 12, 24, 36, and 48 months as part of a multicenter observational study of early administration of intramuscular interferon β-1a. Mixed-effect model analyses, adjusted for age, sex, and treatment status, investigated the association between accumulation of contrast-enhancing and T2 lesions and brain-volume percent changes in a 48-month period.

RESULTS: In patients with clinically isolated syndrome, the average whole-brain volume decreased 2.5%, the mean lateral ventricle volume increased 16.9%, and a mean of 7.7 new/enlarging T2 lesions accumulated over the follow-up period. Patients with clinically isolated syndrome who showed greater percentages of change in whole-brain, white and gray matter, cortical, and lateral ventricle volumes over the follow-up period had more severe lesion outcomes at baseline (all $P < .007$). There were significant associations between decreased individual brain-volume measures at baseline and greater percentages of change during follow-up ($P < .05$). We found a significant association between the total cumulative number of new/enlarging T2 lesions and the evolution of whole-brain ($P < .001$), lateral ventricle ($P = .007$), gray matter and thalamic ($P = .013$), subcortical deep gray matter ($P = .015$), and cortical ($P = .036$) volumes over the follow-up period.

CONCLUSIONS: Lesion accumulation and brain-volume changes occur simultaneously in the early phase of clinically isolated syndrome. More severe lesion and brain-volume outcomes at baseline were associated with greater development of brain atrophy over the follow-up period in patients with clinically isolated syndrome.

ABBREVIATIONS: CIS = clinically isolated syndrome; CE = contrast-enhancing; EDSS = Expanded Disability Status Scale; LV = lesion volume; SDGM = subcortical deep gray matter

Multiple sclerosis is a chronic inflammatory demyelinating disease that affects the central nervous system. Approximately 85% of patients with MS begin with the relapsing-remitting form.[1] This event consists of an episode of neurologic disturbance known as a clinically isolated syndrome (CIS). The risk of progression to clinically definite MS is highest within the first 5 years of the initial event.

The development of brain atrophy is a well-known feature of MS.[2] The general loss of brain tissue in MS derives from focal and diffuse damage, including loss of myelin and axons and Wallerian neurodegeneration.[3] In recent years, there has been an increased focus on GM pathology in MS. This surge has been triggered by new histochemical and MR imaging techniques that enable improved detection of GM pathology.[4] Recent studies have shown that global and regional GM atrophy at the first clinical event in patients with CIS is associated with conversion to clinically definite MS.[5-8]

GM pathology in MS has become a focal point of research

Received October 31, 2014; accepted after revision December 26.

From the Buffalo Neuroimaging Analysis Center (M.V., T.U., J.H., N.B., M.G.D., R.Z.), Department of Neurology, University at Buffalo SUNY, Buffalo, New York; Department of Neurology and Center of Clinical Neuroscience (T.U., D.H., M.T., E.H.) and Department of Radiology (Z.S., M.V., J.K.), Charles University in Prague, First Faculty of Medicine and General University Hospital, Prague, Czech Republic; and IRCCS "Santa Maria Nascente" (N.B.), Don Gnocchi Foundation, Milan, Italy.

The Observational Study of Early Interferon β-1a Treatment in High Risk Subjects after CIS (SET) study was supported by Czech Ministries of Education and Health (NT13237-4/2012, PRVOUK-P26/LF1/4, RVO-VFN64165/2012) and Biogen Idec.

Please address correspondence to Robert Zivadinov, MD, PhD, FAAN, Buffalo Neuroimaging Analysis Center, MRI Clinical Translational Research Center, Department of Neurology, School of Medicine and Biomedical Sciences, University at Buffalo, 100 High St, Buffalo, NY 14203; e-mail: rzivadinov@bnac.net

http://dx.doi.org/10.3174/ajnr.A4330

since the discovery that GM atrophy can predict clinical outcomes better than WM pathology.[9-11] Weak-to-modest associations between the development of regional brain atrophy and changes in lesion number and lesion volume (LV) suggest that newly detected lesions, as well as progressive tissue damage in pre-existing lesions, contribute only partially to the loss of overall brain tissue.[12,13] At this time, the importance of lesion formation in relation to brain atrophy development is unclear, especially at the earliest clinical stages of MS.

Against this background, the aim of the present study was to investigate the relationship between new/enlarging lesion formation and brain atrophy progression over 48 months in patients with CIS who presented with their first clinical event.

MATERIALS AND METHODS

Study Population

This was an investigator-initiated, multicenter, prospective, observational clinical study in patients with CIS in which we investigated the evolution of clinical and MR imaging outcomes over 24 and 48 months.[5,14-17]

Inclusion criteria were age between 18 and 55 years and enrollment into the study within 4 months of the first clinical event. Criteria included diagnostic MR imaging showing ≥2 T2-hyperintense lesions, an Expanded Disability Status Scale (EDSS) score of ≤3.5, and ≥2 oligoclonal bands in the CSF at the screening visit before the start of treatment. Exclusion criteria were a second relapse before the baseline examination, missing or invalid clinical or MR imaging follow-up information after the baseline examination, and pregnancy. Clinical visits were performed every 3 months, and disability, as measured by the EDSS, was assessed every 6 months. MR imaging was performed at baseline and at 6, 12, 24, 36, and 48 months.

All patients received the same treatment at baseline, which included 30 μg of intramuscular interferon β-1a once per week. Necessary adjustments were made in the treatment for patients who presented with no or limited treatment effects, including the development of 2 relapses, a 6-month sustained EDSS progression of 1 point, or other clinical reasons. Each study subject was treated with 3–5 g of methylprednisolone after the first symptom before study entry, and a baseline MR imaging examination was performed at least 30 days after administration of the steroid. During the study, relapses were treated with 3–5 g of methylprednisolone.

The local ethics committees approved the study protocol, and each study subject gave written informed consent.

MR Imaging Acquisition and Analysis

MR imaging was performed at baseline and at 6, 12, 24, 36, and 48 months with a standardized protocol using the same 1.5T MR imaging scanner (Gyroscan; Philips Healthcare, Best, the Netherlands). Axial brain images were obtained by using FLAIR with a section thickness of 1.5 mm (TR, 11,000 ms; TE, 140 ms; TI, 2600 ms; matrix size, 256 × 181; flip angle, 90°). Axial T1-weighted 3D T1 images were acquired with a section thickness of 1 mm (TR, 25 ms; TE, 5 ms; matrix size, 256 × 204; flip angle, 30°). The FLAIR and 3D T1 images were contiguous. In addition, each patient underwent a postcontrast T1 spin-echo scan with a section thickness of 3 mm, 5 minutes after contrast injection of a single dose of 0.1 mmol/kg of Gd-DTPA (TE, 12 ms; TR, 450 ms).

The image analysis included the cumulative number of new and enlarging T2 lesions, defined as the overall number of new and enlarging T2 lesions, and the cumulative number of contrast-enhancing (CE) lesions between all time points from baseline to 48 months. All lesion measures were performed by a single analyst (M.G.D.) who was blinded to the disease status of the patients. T2 and CE LVs were calculated by applying a semiautomated contouring-thresholding technique in Jim software (http://www.xinapse.com).[18]

Baseline whole-brain, GM, WM, cortical, and lateral ventricle volumes were calculated by using FSL Structural Imaging Evaluation of Normalized Atrophy Cross-sectional (SIENA/X; http://fsl.fmrib.ox.ac.uk/fsl/fslwiki/SIENA).[19] Subcortical deep gray matter (SDGM)—defined as the thalamus, globus pallidus, putamen, caudate, nucleus accumbens, hippocampus, and amygdala—volume was calculated by using the FMRIB Integrated Registration and Segmentation Tool (FIRST; http://fsl.fmrib.ox.ac.uk/fsl/fslwiki/FIRST).[20] All brain-volume measures were performed by a single analyst (N.B.) who was blinded to the disease status of the patients. Each baseline tissue volume was normalized for head size by using a skull-constrained registration to the standard MNI 152 template. Longitudinal percent changes in whole-brain, GM, WM, cortical, and lateral ventricle volumes were obtained by using direct methods of atrophy measurement. Briefly, whole-brain volume changes were measured by using the SIENA technique,[21] whereas GM, WM, and lateral ventricle changes were calculated by using a longitudinal regularization of a hidden Markov random field model.[22] Absolute and percent volume changes for the SDGM and thalamus at each time point were calculated.

Statistical Analysis

SPSS (version 21; IBM, Armonk, NY) and Statistica (version 10; StatSoft, Tulsa, Oklahoma) were used for all analyses. Because of non-normal distribution of the data, as assessed by using the Kolmogorov–Smirnov method, T2 and CE LVs and lesion numbers were logarithmically transformed.

Longitudinal linear mixed-effect models were used with random intercept for patients and adjusted for age, sex, and treatment status to describe temporal associations between baseline and follow-up MR imaging measures. Separate longitudinal linear mixed-effect models with a random intercept for patients, with interaction with time, were used to describe temporal associations between changes in individual MR imaging measures over the 48 months. The analyses included percent change values for whole-brain, GM, WM, lateral ventricle, cortical, SDGM, and thalamic volumes for each time point.

Mixed-effect model analyses investigated the association between MR imaging lesion outcomes, including the cumulative T2 and CE lesion activity, absolute T2 and CE LV changes, CE positivity (general occurrence of CE lesions during the study period), and the evolution of MR imaging brain volumetric percentage measures of global and tissue-specific volumes over 48 months.

The first mixed-effect model explored the association between the number of T2 and CE lesions, T2 and CE LVs, and CE positivity at baseline as the independent predictor variables with re-

spect to the dependent outcome variables, which were global and tissue-specific brain-volume percent changes over the 48 months. To minimize the potential confounding effect of baseline brain volumes, we performed an additional confirmatory analysis adjusted also for baseline brain volumes.

After this analysis, we investigated the relationship between baseline MR imaging brain volumetric measures (independent variables) and the evolution of global and tissue-specific brain-volume percent changes over the 48 months (dependent variables).

Finally, we analyzed the association between lesion activity and brain-volume changes over the whole study period by comparing the total cumulative T2 and CE lesion activity and absolute T2 and CE LV changes over the 48 months with global and tissue-specific brain-volume percent changes over the same time period. To minimize the potential effect of baseline brain volume and LV, we performed an additional confirmatory analysis adjusted also for baseline brain volume and LV.

The results of the mixed-effect model analyses are presented for the whole study population. The Benjamini–Hochberg correction was used to minimize the false-discovery rate, and *P* values of <.05 are considered significant.[23]

Table 1: Demographic, clinical, and MRI lesion and brain volumetric measures in patients with CIS over a 48-month period (*n* = 210)[a]

Measure	Patient Data
No. (%) female	139 (66)
Age at onset, y	28.7 ± 7.9
Time to baseline, days	81.9 ± 23.7
EDSS at baseline[b]	1.7 ± 0.7; 1.5 (0.0–3.5)
EDSS at 48 mo[b]	1.8 ± 0.9; 1.5 (0.0–6.5)
Cumulative no. of	
Total new T2 lesions	7.7 ± 14.4; 3.0
New T2 lesions	5.8 ± 10.7; 2.0
Newly enlarging T2 lesions	1.9 ± 4.6; 0.0
Cumulative no. of new CE lesions	1.5 ± 6.1; 0.0
T2 lesion volume absolute change, mL	−0.08 ± 3.6; −0.1
CE lesion volume absolute change, mL	−0.07 ± 0.3; 0.0
WB volume, % change	−2.5 ± 2.1; −2.0
GM volume, % change	−2.3 ± 2.3; −2.0
WM volume, % change	−1.7 ± 2.1; −1.4
Cortical volume, % change	−2.8 ± 2.2; −2.6
Lateral ventricle volume, % change	16.9 ± 14.2; 14.3
Total normalized SDGM volume, % change	−3.6 ± 3.6; −3.1
Thalamic volume, % change	−4.6 ± 4.2; −4.0

Note:—WB indicates whole brain.
[a] Unless otherwise indicated, all data are reported as mean ± standard deviation; median.
[b] Data in parentheses are ranges.

RESULTS

Demographic, Clinical, and MR Imaging Characteristics

Overall, 210 patients with CIS underwent clinical and MR imaging assessments and were included in the analysis over the 48 months of this study. Demographic, clinical, and MR imaging global and tissue-specific volumes and lesion characteristics over the 48 months are shown in Table 1. The mean age at onset was 28.7 years, and the median baseline EDSS score was 1.5. An average total of 7.7 new T2 lesions were accumulated over 48 months. Global and tissue-specific brain-volume percent changes showed average decreases of 2.5% in whole-brain, 2.8% in cortical, and 4.6% in thalamic volumes and an average increase of 16.9% in lateral ventricle volumes.

Mixed-Effect Model Analysis Using Baseline Lesion Measures as Independent Outcome Variables and Brain-Volume Evolution Measures as Dependent Outcome Variables

Table 2 shows the relationship between baseline lesion measures and the evolution of brain-volume percent changes over the 48 months. Patients with CIS who showed greater percent changes in whole-brain, WM, GM, cortical, and lateral ventricle volumes over the 48 months had a greater lesion activity at baseline (all $P <$ .007). The percent change in thalamic volume over the 48 months was associated with greater baseline T2 LV and lesion number ($P \leq .001$) and baseline CE lesion number ($P = .018$), whereas the percent change in SDGM volume was associated only with greater baseline CE lesion number ($P = .029$).

Patients with CIS with the highest number of CE lesions at baseline progressed the most in whole-brain, cortical, and lateral ventricle volume changes over the 48 months (all $P < .0001$) (Fig 1). The association was somewhat less pronounced for thalamic volume ($P = .018$).

Similarly, patients with CIS with the highest number of T2 lesions at baseline progressed the most in cortical, thalamic, and lateral ventricle volume changes (all $P < .0001$), and there was also an association with the whole-brain volume progression ($P = .01$) (Fig 2).

The effects of baseline T2 and CE lesion numbers and T2 LV on whole-brain, WM, GM, cortical, and lateral ventricle volume changes persisted (all $P < .008$) even when adjusting the analyses for baseline brain volumes. In this confirmatory analysis, the percent change in thalamic volume over the 48 months was associated with greater baseline T2 LV and lesion number ($P < .001$) and baseline CE lesion number ($P = .004$), whereas the percent

Table 2: Relationship between MRI lesions at baseline and evolution of MRI brain volumetric measures in patients with CIS over a 48-month period[a]

	MRI Brain Volume % Changes Over 48 mo						
MRI Lesions at Baseline	WB	WM	GM	Cortical	Lateral Ventricle	SDGM	Thalamus
T2 LV	0.001[b]	.001[b]	<.001[b]	.004[b]	<.001[b]	.133	<.001[b]
T2 LN	.010[b]	.001[b]	<.001[b]	<.001[b]	<.001[b]	.243	<.001[b]
CE positivity	<.001[b]	.007[b]	.004[b]	.002[b]	<.001[b]	.292	.517
CE LN	<.001[b]	<.001[b]	<.001[b]	<.001[b]	<.001[b]	.029[b]	.018[b]
CE LV	<.001[b]	.001[b]	<.001[b]	<.001[b]	<.001[b]	.101	.234

Note:—WB indicates whole brain; LN, lesion number.
[a] All data are reported as *P* values corrected by the Benjamini–Hochberg procedure. Associations between MRI measures were tested by using mixed-model analysis.
[b] $P < .05$.

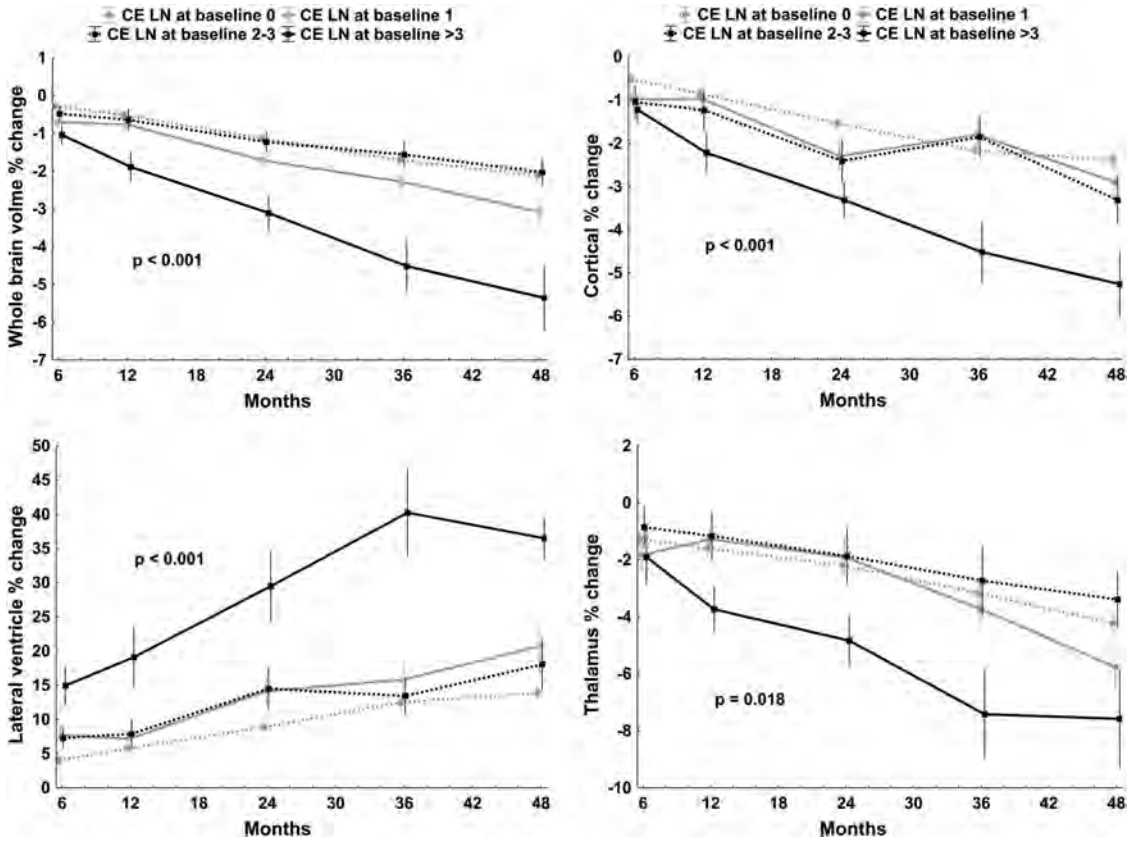

FIG 1. Mixed-effect model analysis of global and tissue-specific brain-volume percent changes over 48 months (dependent variables) and number of CE lesions at baseline (independent variable). For better visualization, the CE lesions were categorized into different baseline number groups, including 0, 1, 2–3, and >3 lesions. The Benjamini–Hochberg method was used to minimize the false-discovery rate, and *P* values of <.05 were considered significant.[23]

change in SDGM volume was associated with greater baseline T2 LV ($P = .01$) and baseline CE lesion number ($P = .013$).

Mixed-Effect Model Analysis Using Baseline Brain Volumetric Measures as Independent Outcome Variables and Brain-Volume Evolution Measures as Dependent Outcome Variables

Table 3 shows the relationship between normalized baseline brain-volume measures and associations with their percent changes over 48 months. There were significant associations between decreased individual brain-volume measures at baseline and their greater percent changes over the follow-up period ($P < .05$). Of all the explored brain-volume measures, only greater enlargement of lateral ventricles showed a consistent association with a decrease in most of the brain-volume measures at baseline ($P < .013$).

Mixed-Effect Model Analysis Using Evolution of Lesion Measures as Independent Outcome Variables and Brain-Volume Measures as Dependent Outcome Variables

We performed a mixed-effect model analysis to evaluate the associations between longitudinal changes of lesion variables with respect to brain-volume percent changes over 48 months. The results revealed a significant association between the total cumulative number of new/enlarging T2 lesions and the evolution of whole-brain ($P < .001$), lateral ventricle ($P = .007$), GM and thalamic ($P = .013$), SDGM ($P = .015$), and cortical ($P = .036$) volumes (Table 4 and On-line Fig 1). No significant differences were found between absolute changes in T2 LV (On-line Fig 2), cumulative CE lesion number, or absolute CE LV changes and the evolution of global and tissue-specific brain-volume measures over the 48 months.

The relationship between total cumulative number of new/enlarging T2 lesions and whole-brain, GM, cortical, lateral ventricle, subcortical deep GM, and thalamic volume changes persisted (all $P < .016$), even when adjusting analyses for the baseline brain volume and LV. In this confirmatory analysis, no significant differences were found between absolute changes in T2 LV and the evolution of global and tissue-specific brain-volume measures over the 48 months.

DISCUSSION

In this prospective, longitudinal, observational study of high-risk patients with CIS for development of clinically definite MS treated with interferon β-1a,[5,14-17] we investigated the association of brain-volume changes in relation to the formation of new T2 and CE lesions and their volumes over the 48-month study period.

Using mixed-effect model analysis in which global and tissue-specific volumes changes were used as dependent outcome variables and MR imaging lesions at baseline as independent predictors, the progression of brain-volume measures was significantly associated with higher CE and T2 lesion numbers,

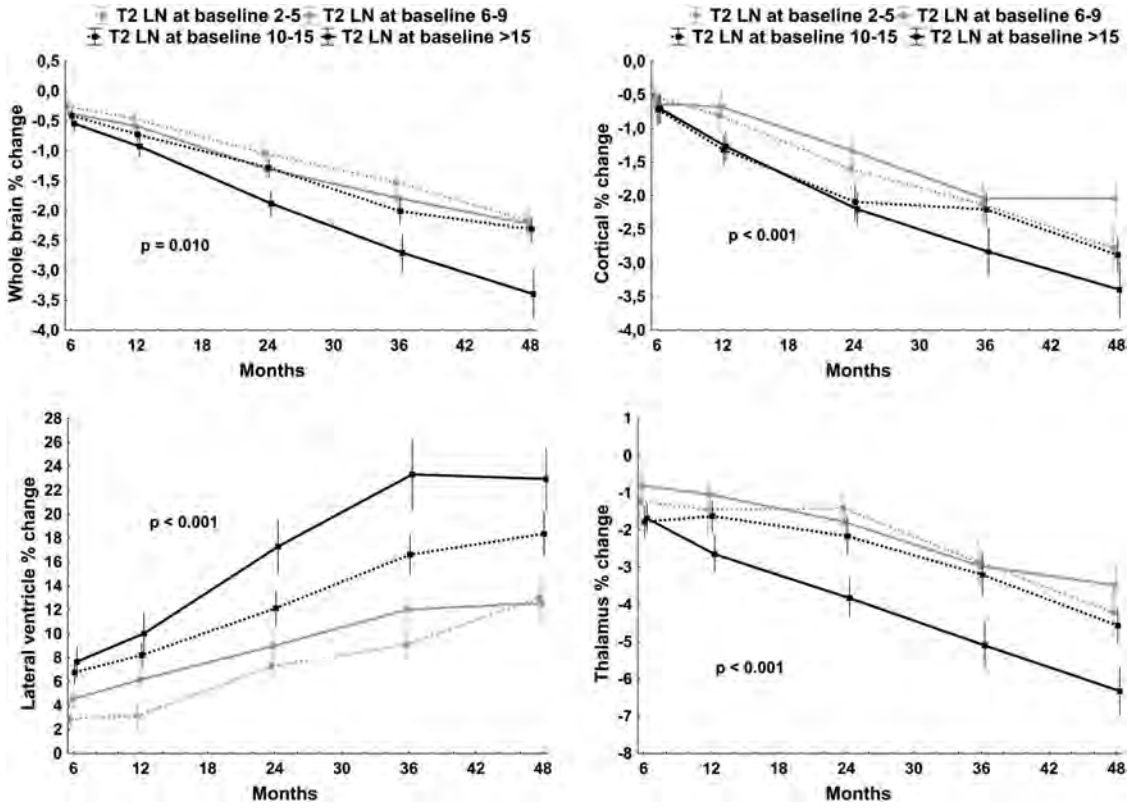

FIG 2. Mixed-effect model analysis of global and tissue-specific brain-volume percent changes over 48 months (dependent variables) and number of T2 lesions at baseline. For better visualization, the T2 lesions were categorized into different baseline number groups, including 1–5, 6–9, 10–15, and >15 lesions. The Benjamini–Hochberg method was used to minimize the false-discovery rate, and *P* values of <.05 are considered significant.[23]

Table 3: Relationship between MRI brain volumetric measures at baseline and evolution of changes over a 48-month period in patients with CIS[a]

MRI Brain Volumetric Measures at Baseline	MRI Brain Volume % Changes Over 48 mo						
	WB	WM	GM	Cortical	Lateral Ventricle	SDGM	Thalamus
Normalized WB volume	.712	.004[b]	.426	.299	<.001[b]	.182	.174
Normalized WM volume	.591	<.001[b]	.711	.904	.001[b]	.588	.254
Normalized GM volume	.881	.794	.049[b]	.075	.004[b]	.069	.248
Normalized cortical volume	.847	.774	.075	.040[b]	.007[b]	.192	.343
Normalized lateral ventricle volume	.066	.156	.935	.587	.013[b]	.342	.769
Total normalized SDGM volume	.032[b]	.710	.177	.291	.394	.042[b]	.457
Normalized thalamic volume	.115	.578	.243	.291	.343	.038[b]	<.001[b]

Note:—WB indicates whole brain.

[a] All data are reported as *P* values corrected by the Benjamini-Hochberg procedure. Associations between MRI measures were tested by using mixed-model analysis.

[b] $P < .05$.

Table 4: Relationship between evolution of MRI lesion and brain volumetric measures over a 48-month period[a]

Longitudinal MRI Lesion Measures	MRI Brain Volume % Changes Over 48 mo						
	WB	WM	GM	Cortical	Lateral Ventricle	SDGM	Thalamus
Total cumulative T2 LN	<.001[b]	.517	.013[b]	.036[b]	.007[b]	.015[b]	.013[b]
T2 LV absolute change	.115	.444	.234	.456	.861	.717	.659
Total cumulative CE LN	.394	.182	.489	.795	.341	.193	.489
CE LV absolute change	.360	.936	.399	.802	.160	.769	.843

Note:—WB indicates whole brain; LN, lesion number.

[a] All data are reported as *P* values corrected by the Benjamini-Hochberg procedure. Associations between MRI measures were tested by using mixed-model analysis with interaction with time.

[b] $P < .05$.

CE and T2 LVs, and CE positivity. The impact of baseline lesion number and LV on global and tissue-specific brain-volume changes persisted, even when adjusting the analyses for baseline brain volumes. These findings suggest that more severe lesion outcomes at baseline are associated with greater development of brain atrophy over the follow-up period in patients with CIS. A possible explanation for these findings is that diffuse inflammation in the WM and GM is responsible

for accelerated tissue loss that occurs from the earliest disease stages.[9,11,13,24]

Exploring the relationship between accumulation of new/enlarging CE and T2 lesions and global and tissue-specific volumetric changes over 48 months, we found a significant association between the total cumulative number of new/enlarging T2 lesions and the evolution of whole-brain, lateral ventricle, GM, thalamic, SDGM, and cortical volumes. The relationship between lesion accumulation and brain-volume changes over 48 months persisted, even when adjusting the analyses for baseline brain volume and LV. These results suggest that lesion accumulation and brain-volume changes occur simultaneously in the early phase of the disease. Other studies showed an additional correlation between T2 LV and brain-volume changes during early treatment phases.[25] In our study, however, absolute change of T2 LV was not associated with the progression of brain atrophy measures over the follow-up period, but this finding has to be interpreted with caution, given that over the 48 months of our study, the T2 LV remained stable. Overall, these results suggest that measurement of cumulative accumulation of new/enlarging T2 lesions may be a more sensitive marker of disease activity in patients with CIS than the accumulation of T2 LV.

While the CE lesion number and LV at baseline showed significant associations with the evolution of brain-volume changes over the 48 months, no significant associations between cumulative CE lesions or CE LV absolute changes and the evolution of brain-volume measures over the follow-up period were found in this study. The impact of acute inflammation on the evolution of brain-volume changes remains unclear at this time.[26-30] The transient nature of CE lesions can be better captured by using frequent serial scanning, which may not be feasible in long-term studies.[26,27] The findings from this study support the notion that brain atrophy and active inflammation may occur simultaneously, and that monitoring the accumulation of new/enlarging T2 lesions can better reflect this relationship than monitoring CE lesions.

Patients with CIS who presented with lower individual brain-volume measures at baseline showed greater percent changes over the follow-up period. This is an interesting result, because it suggests that, along with the predictive value of baseline lesion burden, the baseline brain volume is also a reliable predictor of future brain-volume changes and therefore of disease progression.[31] Lower baseline brain volumes found in this study can reflect more aggressive disease ongoing even before the first clinical manifestation.[32]

The results from this study indicate that the association between accumulation of new/enlarging T2 lesions and development of whole-brain atrophy and enlargement of lateral ventricles was stronger than the association with the GM volume measures. The close association between lateral ventricular enlargement and accumulation of T2 lesions in patients with CIS was previously reported.[33] Other mechanisms at work, including an effect of altered CSF flow pulsatility, may be considered when interpreting these findings.[34]

There is evidence that approximately 40% of patients with CIS have cortical lesions according to histopathologic examination.[35] They occur early in patients with CIS and increase in number and size over time.[36] These lesions are characterized pathologically by demyelination and microglial activation.[37,38] Therefore, compared with WM lesions, inflammation is not as prominent and breakdown of the blood-brain barrier occurs less frequently with GM lesions.[38] Assessment of cortical atrophy was proposed as an indirect marker of cortical pathologic assessment over time.[4] The use of advanced MR imaging sequences, such as double inversion recovery,[39] can enhance the detection of the number and volume of cortical lesions. We did not apply this sequence; therefore, a somewhat weaker association between accumulation of T2 lesions and the evolution of cortical volume changes in the current study should be interpreted in light of the technical limitations of the MR imaging study protocol.

A strength of this study is the use of a mixed-effect model, which provides the ability to assess the interaction of 2 variables at multiple time points while including covariates. However, there are also several limitations to the present study. It is well known that high-dose intravenous corticosteroid,[40] interferon β,[41] or natalizumab[42] treatment leads to a temporary reduction in brain volume, mainly from WM volume loss,[42] a phenomenon described as pseudoatrophy.[43] Because all the patients in this study were treated with interferon β-1a, the rate of brain-volume changes could have been influenced by the anti-inflammatory effect of the drug over the first 6 months of the study period. However, it is less likely that these medications would have impacted significantly on brain-volume changes over the 48 months in the present study. In addition, MR imaging scans were performed at least 30 days after high-dose intravenous corticosteroid administration.

Even though this was a longitudinal serial MR imaging study, it is difficult to establish causality between lesion formation and atrophy progression without using more sophisticated microstructural imaging methods or histopathology; therefore, only inferences about an association are presented. Another approach for determining causes and effects would be to investigate pathologic processes in specific regions, and experimental animal model studies may be more suited for investigation of this relationship. More frequent MR imaging could also provide greater ability to investigate the relationship between lesion accumulation and brain atrophy progression at the earliest clinical stages of MS.

CONCLUSIONS

We have demonstrated the utility of longitudinal mixed-effect model analysis approaches in the study of patients with CIS, and we have shown that lesion accumulation and brain-volume changes occur simultaneously in the early phase of the disease. More severe LV and lower brain volume at baseline are associated with greater development of brain atrophy over the follow-up period in patients with CIS.

Disclosures: Mihael Varosanec—*RELATED*: *Grant*: The SET study was supported by Czech Ministries of Education and Health (NT13237-4/2012, PRVOUK-P26/LF1/4, RVO-VFN64165/2012) and Biogen Idec.* Thomas Uher—*UNRELATED*: *Grants/Grants Pending*: Biogen Idec*; *Payment for Lectures (including service on speakers bureaus)*: Biogen Idec; *Travel/Accommodations/Meeting Expenses Unrelated to Activities Listed*: Biogen Idec,* Genzyme*; *Other*: Received financial support for conference travel and honoraria from Biogen Idec. Dana Horakova—*RELATED: Grant:* The SET study was supported by Czech Ministries of Education and Health (NT13237-4/2012, PRVOUK-P26/LF1/4, RVO-VFN64165/2012) and Biogen Idec*; *UNRELATED*: Received compensation for travel, speaker honoraria, and consultant fees from Biogen Idec, Novartis, Merck Serono, Bayer Schering, and Teva and support for research activities from Biogen Idec. Michaela Tyblova—*RELATED: Grant:* The SET study was supported by Czech Ministries of Education and Health (NT13237-4/2012, PRVOUK-P26/LF1/4, RVO-VFN64165/2012) and Biogen Idec*; *UNRELATED*: received compensation for travel and honoraria from Biogen Idec, Sanofi Aventis,

Teva, Novartis, and Merck Serono. Zdenek Seidl—*RELATED*: *Grant*: Biogen Idec. Manuela Vaneckova—*RELATED*: *Grant*: RVO-VFN64165/2012*; *Fees for Participation in Review Activities such as Data Monitoring Boards, Statistical Analysis, Endpoint Committees, and the Like*: Biogen Idec; *Consultancy*: Biogen Idec, Novartis, Merck Serono, and Teva; *Grants/Grants Pending*: RVO-VFN64165/2012*; *Payment for Development of Educational Presentations*: Biogen Idec, Novartis, Merck Serono, and Teva; *Other*: Received compensation for speaker honoraria and consultant fees from Biogen Idec, Novartis, Merck Serono, and Teva and support for research activities from Biogen Idec. Jan Krasensky—*RELATED*: *Support for Travel to Meetings for the Study or Other Purposes*: Biogen Idec; *Other*: Received financial support for research activities from Biogen Idec. Michael Dwyer—*UNRELATED*: *Consultancy*: Claret Medical, EMD Serono, *Comments*: Study consulting by Claret Medical, and served on scientific advisory board for EMD Serono; *Grants/Grants Pending*: Novartis International,* *Comments*: Grant support for new software development. Eva Havrdova—*RELATED*: *Grant*: Biogen Idec*; *UNRELATED*: *Consultancy*: Biogen Idec, Genzyme, Novartis, Roche, Teva, Merck, and Receptos; *Payment for Lectures (including service on speakers bureaus)*: Biogen Idec, Genzyme, Novartis, Teva, and Merck; *Other*: Received speaker honoraria and consultant fees from Biogen Idec, Merck Serono, Novartis, Genzyme, and Teva and support for research activities from Biogen Idec and Merck Serono. Robert Zivadinov—*RELATED*: *Grant*: Biogen Idec*; *UNRELATED*: *Consultancy*: Novartis, Claret Medical, Genzyme, and Teva; *Grants/Grants Pending*: Novartis,* Claret Medical,* Genzyme,* and Teva*; *Payment for Development of Educational Presentations*: Genzyme; *Other*: Received financial support for research activities from Teva Pharmaceuticals, Biogen Idec, Claret Medical, Genzyme, Novartis, and Greatbatch and received personal compensation from Biogen Idec, Novartis, Genzyme, Claret Medical, and EMD Serono for speaking and consultant services. *Money paid to the institution.

REFERENCES

1. Confavreux C, Vukusic S. **Natural history of multiple sclerosis: a unifying concept.** *Brain* 2006;129:606–16
2. Zivadinov R, Bakshi R. **Role of MRI in multiple sclerosis II: brain and spinal cord atrophy.** *Front Biosci* 2004;9:647–64
3. Miller DH, Barkhof F, Frank JA, et al. **Measurement of atrophy in multiple sclerosis: pathological basis, methodological aspects and clinical relevance.** *Brain* 2002;125:1676–95
4. Geurts JJ, Stys PK, Minagar A, et al. **Gray matter pathology in (chronic) MS: modern views on an early observation.** *J Neurol Sci* 2009;282:12–20
5. Zivadinov R, Havrdová E, Bergsland N, et al. **Thalamic atrophy is associated with development of clinically definite multiple sclerosis.** *Radiology* 2013;268:831–41
6. Calabrese M, Rinaldi F, Mattisi I, et al. **The predictive value of gray matter atrophy in clinically isolated syndromes.** *Neurology* 2011;77:257–63
7. Dalton CM, Chard DT, Davies GR, et al. **Early development of multiple sclerosis is associated with progressive grey matter atrophy in patients presenting with clinically isolated syndromes.** *Brain* 2004;127:1101–07
8. Raz E, Cercignani M, Sbardella E, et al. **Gray- and white-matter changes 1 year after first clinical episode of multiple sclerosis: MR imaging.** *Radiology* 2010;257:448–54
9. Fisniku LK, Chard DT, Jackson JS, et al. **Gray matter atrophy is related to long-term disability in multiple sclerosis.** *Ann Neurol* 2008;64:247–54
10. Zivadinov R, Bergsland N, Dolezal O, et al. **Evolution of cortical and thalamus atrophy and disability progression in early relapsing-remitting MS during 5 years.** *AJNR Am J Neuroradiol* 2013;34:1931–39
11. Fisher E, Lee JC, Nakamura K, et al. **Gray matter atrophy in multiple sclerosis: a longitudinal study.** *Ann Neurol* 2008;64:255–65
12. Cappellani R, Bergsland N, Weinstock-Guttman B, et al. **Subcortical deep gray matter pathology in patients with multiple sclerosis is associated with white matter lesion burden and atrophy but not with cortical atrophy: a diffusion tensor MRI study.** *AJNR Am J Neuroradiol* 2014;35:912–19
13. Roosendaal SD, Bendfeldt K, Vrenken H, et al. **Grey matter volume in a large cohort of MS patients: relation to MRI parameters and disability.** *Mult Scler* 2011;17:1098–106
14. Kalincik T, Vaneckova M, Tyblova M, et al. **Volumetric MRI markers and predictors of disease activity in early multiple sclerosis: a longitudinal cohort study.** *PLoS ONE* 2012;7:e50101
15. Uher T, Benedict RH, Horakova D, et al. **Relationship between gray matter volume and cognitive learning in CIS patients on disease-modifying treatment.** *J Neurol Sci* 2014;347:229–34
16. Uher T, Blahova-Dusankova J, Horakova D, et al. **Longitudinal MRI and neuropsychological assessment of patients with clinically isolated syndrome.** *J Neurol* 2014;261:1735–44
17. Uher T, Horakova D, Bergsland N, et al. **MRI correlates of disability progression in patients with CIS over 48 months.** *Neuroimage Clin* 2014;6:312–19
18. Zivadinov R, Heininen-Brown M, Schirda CV, et al. **Abnormal subcortical deep-gray matter susceptibility-weighted imaging filtered phase measurements in patients with multiple sclerosis: a case-control study.** *Neuroimage* 2012;59:331–39
19. Smith SM, Zhang Y, Jenkinson M, et al. **Accurate, robust, and automated longitudinal and cross-sectional brain change analysis.** *Neuroimage* 2002;17:479–89
20. Patenaude B, Smith SM, Kennedy DN, et al. **A Bayesian model of shape and appearance for subcortical brain segmentation.** *Neuroimage* 2011;56:907–22
21. Smith SM, De Stefano N, Jenkinson M, et al. **Normalized accurate measurement of longitudinal brain change.** *J Comput Assist Tomogr* 2001;25:466–75
22. Dwyer MG, Bergsland N, Zivadinov R. **Improved longitudinal gray and white matter atrophy assessment via application of a 4-dimensional hidden Markov random field model.** *Neuroimage* 2014;90:207–17
23. Benjamini Y, Drai D, Elmer G, et al. **Controlling the false discovery rate in behavior genetics research.** *Behav Brain Res* 2001;125:279–84
24. Calabrese M, Atzori M, Bernardi V, et al. **Cortical atrophy is relevant in multiple sclerosis at clinical onset.** *J Neurol* 2007;254:1212–20
25. Comi G, Martinelli V, Rodegher M, et al. **Effects of early treatment with glatiramer acetate in patients with clinically isolated syndrome.** *Mult Scler* 2013;19:1074–83
26. Zivadinov R, Zorzon M. **Is gadolinium enhancement predictive of the development of brain atrophy in multiple sclerosis? A review of the literature.** *J Neuroimaging* 2002;12:302–09
27. Zivadinov R, Bagnato F, Nasuelli D, et al. **Short-term brain atrophy changes in relapsing-remitting multiple sclerosis.** *J Neurol Sci* 2004;223:185–93
28. Rashid W, Davies GR, Chard DT, et al. **Relationship of triple dose contrast enhanced lesions with clinical measures and brain atrophy in early relapsing-remitting multiple sclerosis: a two-year longitudinal study.** *Mult Scler* 2007;13:178–85
29. Inglese M, Mancardi GL, Pagani E, et al. **Brain tissue loss occurs after suppression of enhancement in patients with multiple sclerosis treated with autologous haematopoietic stem cell transplantation.** *J Neurol Neurosurg Psychiatry* 2004;75:643–44
30. Paolillo A, Piattella MC, Pantano P, et al. **The relationship between inflammation and atrophy in clinically isolated syndromes suggestive of multiple sclerosis: a monthly MRI study after triple-dose gadolinium-DTPA.** *J Neurol* 2004;251:432–39
31. De Stefano N, Giorgio A, Battaglini M, et al. **Assessing brain atrophy rates in a large population of untreated multiple sclerosis subtypes.** *Neurology* 2010;74:1868–76
32. Rojas JI, Patrucco L, Míguez J, et al. **Brain atrophy in radiologically isolated syndromes.** *J Neuroimaging* 2015;25:68–71
33. Dalton CM, Brex PA, Jenkins R, et al. **Progressive ventricular enlargement in patients with clinically isolated syndromes is associated with the early development of multiple sclerosis.** *J Neurol Neurosurg Psychiatry* 2002;73:141–47
34. Magnano C, Schirda C, Weinstock-Guttman B, et al. **Cine cerebrospinal fluid imaging in multiple sclerosis.** *J Magn Reson Imaging* 2012;36:825–34
35. Lucchinetti CF, Popescu BF, Bunyan RF, et al. **Inflammatory cortical demyelination in early multiple sclerosis.** *N Engl J Med* 2011;365:2188–97

36. Calabrese M, Rocca MA, Atzori M, et al. **Cortical lesions in primary progressive multiple sclerosis: a 2-year longitudinal MR study.** *Neurology* 2009;72:1330–36
37. Bø L, Vedeler CA, Nyland H, et al. **Intracortical multiple sclerosis lesions are not associated with increased lymphocyte infiltration.** *Mult Scler* 2003;9:323–31
38. van Horssen J, Brink BP, de Vries HE, et al. **The blood-brain barrier in cortical multiple sclerosis lesions.** *J Neuropathol Exp Neurol* 2007;66:321–28
39. Geurts JJ, Pouwels PJ, Uitdehaag BM, et al. **Intracortical lesions in multiple sclerosis: improved detection with 3D double inversion-recovery MR imaging.** *Radiology* 2005;236:254–60
40. Fox RJ, Fisher E, Tkach J, et al. **Brain atrophy and magnetization transfer ratio following methylprednisolone in multiple sclerosis: short-term changes and long-term implications.** *Mult Scler* 2005;11:140–45
41. Hardmeier M, Wagenpfeil S, Freitag P, et al. **Rate of brain atrophy in relapsing MS decreases during treatment with IFNbeta-1a.** *Neurology* 2005;64:236–40
42. Vidal-Jordana A, Sastre-Garriga J, Pérez-Miralles F, et al. **Early brain pseudoatrophy while on natalizumab therapy is due to white matter volume changes.** *Mult Scler* 2013;19:1175–81
43. Zivadinov R, Reder AT, Filippi M, et al. **Mechanisms of action of disease-modifying agents and brain volume changes in multiple sclerosis.** *Neurology* 2008;71:136–44

Improving Multiple Sclerosis Plaque Detection Using a Semiautomated Assistive Approach

J. van Heerden, D. Rawlinson, A.M. Zhang, R. Chakravorty, M.A. Tacey, P.M. Desmond, and F. Gaillard

ABSTRACT

BACKGROUND AND PURPOSE: Treating MS with disease-modifying drugs relies on accurate MR imaging follow-up to determine the treatment effect. We aimed to develop and validate a semiautomated software platform to facilitate detection of new lesions and improved lesions.

MATERIALS AND METHODS: We developed VisTarsier to assist manual comparison of volumetric FLAIR sequences by using interstudy registration, resectioning, and color-map overlays that highlight new lesions and improved lesions. Using the software, 2 neuroradiologists retrospectively assessed MR imaging MS comparison study pairs acquired between 2009 and 2011 (161 comparison study pairs met the study inclusion criteria). Lesion detection and reading times were recorded. We tested inter- and intraobserver agreement and comparison with original clinical reports. Feedback was obtained from referring neurologists to assess the potential clinical impact.

RESULTS: More comparison study pairs with new lesions (reader 1, $n = 60$; reader 2, $n = 62$) and improved lesions (reader 1, $n = 28$; reader 2, $n = 39$) were recorded by using the software compared with original radiology reports (new lesions, $n = 20$; improved lesions, $n = 5$); the difference reached statistical significance ($P < .001$). Interobserver lesion number agreement was substantial (≥1 new lesion: $\kappa = 0.87$; 95% CI, 0.79–0.95; ≥1 improved lesion: $\kappa = 0.72$; 95% CI, 0.59–0.85), and overall interobserver lesion number correlation was good (Spearman ρ: new lesion = 0.910, improved lesion = 0.774). Intraobserver agreement was very good (new lesion: $\kappa = 1.0$, improved lesion: $\kappa = 0.94$; 95% CI, 0.82–1.00). Mean reporting times were <3 minutes. Neurologists indicated retrospective management alterations in 79% of comparative study pairs with newly detected lesion changes.

CONCLUSIONS: Using software that highlights changes between study pairs can improve lesion detection. Neurologist feedback indicated a likely impact on management.

ABBREVIATIONS: CSP = comparative study pairs; CSSC = conventional side-by-side comparison; IL = improved lesion; NL = new lesion; VTS = VisTarsier software

Multiple sclerosis affects approximately 2 million people worldwide, predominantly young adults.[1] During the past decade, a number of novel disease-modifying drugs have emerged that are effective during the early phases of the disease; reducing the frequency of relapses, potentially halting disease progression, and even reversing early neurologic deficits.[2] This choice in therapeutic options allows treating neurologists to alter management strategies when progression is detected.[2]

Because most demyelinating events are asymptomatic, MR imaging has been the primary biomarker for disease progression, and both physical disability and cognitive function have been shown to have a nonplateauing association with white matter demyelinating lesion burden, as seen on FLAIR and T2-weighted sequences.[2-6]

Recent advances in imaging, including 3T 3D volumetric T2 FLAIR sequences, allow better resolution of small demyelinating lesions, resulting in better clinicoradiologic correlation.[7,8] Despite advances in imaging techniques, conventional side-by-side comparison (CSSC) is often subject to a reader's expertise.[9] The sensitivity of detecting new lesions is also likely to be reduced when the section number is increased and scan planes are un-

Received November 30, 2014; accepted after revision February 3, 2015.

From the Department of Radiology (J.v.H., P.M.D., F.G.), The Royal Melbourne Hospital and University of Melbourne, Parkville, Victoria, Australia; Department of Electrical and Electronic Engineering (D.R., A.M.Z.), School of Engineering, University of Melbourne, Parkville, Victoria, Australia; IBM Research (R.C.), Melbourne, Victoria, Australia; and Melbourne EpiCentre (M.A.T.), The Royal Melbourne Hospital and Department of Medicine, University of Melbourne, Parkville, Victoria, Australia.

Please address correspondence to Jolandi van Heerden, MD, Department of Radiology, The Royal Melbourne Hospital, 300 Grattan St, Parkville, Victoria, Australia 3050; e-mail: jolandivh@hotmail.com

Indicates article with supplemental on-line tables.

Indicates article with supplemental on-line photo.

http://dx.doi.org/10.3174/ajnr.A4375

matched; however, to our knowledge, this reduction has not yet been investigated. In an attempt to facilitate accurate lesion-load and lesion-volume detection, much research has been devoted to fully automated computational approaches with unsatisfactory results. Robust lesion segmentation has been identified as a critical obstacle to widespread clinical adoption for several reasons: difficulties specific to MS, problems inherent to segmentation, and data variability.[10]

A review of fully automated MS segmentation techniques concluded that basic data-driven methods are inherently inaccurate; supervised learning methods (such as artificial neural networks) require costly and extensive training on representative data; deformable models are better; and statistical models are most promising, though these also require training on representative data.[3]

An alternative to total automation is to assist manual reporting with partial automation. A few semiautomated lesion-subtraction strategies have been used in the research setting on small patient populations with good lesion detection and interreader correlation.[11,12]

Semiautomation without segmentation is inherently easier, more robust, and less affected by data variability because the lesion count is judged manually. The software can present a number of false-positives without a negative impact on accuracy.

Our aim was to design a nonsegmentation semiautomated assistive software platform that can be integrated into vendor-agnostic PACS and validated by application to a large number of existing routine clinical scans in patients with an established diagnosis of multiples sclerosis. The approach is to merely draw the attention of the radiologist to potentially new or improved lesions rather than automate the entire process, thus preserving the expertise of neuroradiologists in determining whether a finding is real.

Our hypothesis was that CSSCs of volumetric FLAIR studies in patients with MS were prone to false-negative errors in the perception of both new and improved lesions and that more lesions would be identified by using the assistive software with improved inter- and intrareader reliability. Secondly, we hypothesized that presenting this information to clinicians would likely have changed patient management.

MATERIALS AND METHODS

Software Development

Detecting lesion change in studies obtained at 2 time points, "old" and "new," requires numerous steps including the following: 1) brain-surface extraction and masking (to remove skull and soft tissues of the head and neck), 2) coregistration and resectioning (to accurately align the 2 scans in all axes), 3) normalization of the FLAIR signal intensity (to remove global signal differences), and 4) calculating the difference in signal intensity between the old and new study at each point (to identify new T2 bright plaques and previously abnormal areas that have regained normal white matter signal). Changes between scans were presented as a color map superimposed on conventional FLAIR sequences (Fig 1). This was accomplished by bespoke code (given the trademark VisTarsier, henceforth VTS or "the software") with the inclusion of a number of open-source components (Fig 2).

Step 1: Brain surface was identified by conforming a reference model (by using BrainSuite from the University of Southern California, http://brainsuite.org/)[13] to the FLAIR images. This brain surface was then used to mask out the skull and extracranial soft tissues.

Step 2: The "new" study was coregistered with the "old" study by performing a 6 *df* (axis of movement) rigid-body transformation, recovered by using mutual information as the distance metric.[14] Both the resulting transformation and the brain surface mask were stored in a separate PACS data base (by using DCM4CHE, http://sourceforge.net/projects/dcm4che/).[15] Both the old and new volumetric FLAIR datasets were resectioned into orthogonal axial, sagittal, and coronal planes, allowing exact comparison of any individual pixel regardless of the orientations at which the original scans were obtained. Trilinear interpolation (by using the ImageJ library; National Institutes of Health, Bethesda, Maryland)[16] was used to preserve image quality and minimize artifacts during these transformations.

Step 3: Image signal intensity was normalized by using histogram equalization to eliminate global differences.

Step 4: Using the now masked, coregistered, and normalized volumetric new and old FLAIR sequences, we computed a volumetric image containing signed pixel differences. We used both color and transparency to encode the changes between the 2 studies, transparency to encode the magnitude of change, and color to indicate the type of change, with red indicating new lesions (NLs) and green indicating improved lesions (ILs).

The resultant images were then viewed in a bespoke DICOM viewer, with the reader able to view all 3 planes for both old and new studies, and each point could be correlated in all view panes (Fig 1). The total processing time for steps 1–4 is approximately 1 minute on a typical desktop computer (1.6 GHz), including data retrieval and storage time. Rendering of the 3D and 2D perspectives requires approximately 10 ms per viewpoint, allowing rapid scrolling through the data. Most rendering time consists of trilinear interpolation.

Validation

Institutional ethics approval was obtained for this study. The hospital PACS was queried for MR imaging brain demyelination-protocol studies performed on a single 3T magnet (Tim Trio, 12-channel head coil; Siemens, Erlangen, German) between 2009 and 2011 inclusive, for patients who had ≥2 studies during that period, yielding 367 studies. Eligibility criteria were the following: consecutive studies in patients with a confirmed diagnosis of multiple sclerosis (based on information provided on requisition forms) and availability of a diagnostic-quality MR imaging volumetric FLAIR sequence (FOV = 250, 160 sections, section thickness = 0.98 mm, matrix =258 × 258, TR = 5000 ms, TE = 350 ms, TI = 1800 ms, 72 sel inversion recovery magnetic preparation). One hundred sixty-six comparison pairs (332 studies) met the above inclusion criteria. Of these, 5 comparative study pairs (CSP) had to be excluded due to a lack of exact lesion quantification in the issued radiology reports. A final total of 161 CSP (median time between scans, 343 ± 174 days) of 153 individual patients (women = 116, men = 37; median age, 41.5 ±10.2 years) with accompanying reports were thus included in the study. MR imaging–trained radiologists at our institution reported all studies. Of the 161 CSP, 43 had initial clinical reports by 1 of the authors (reader 1).

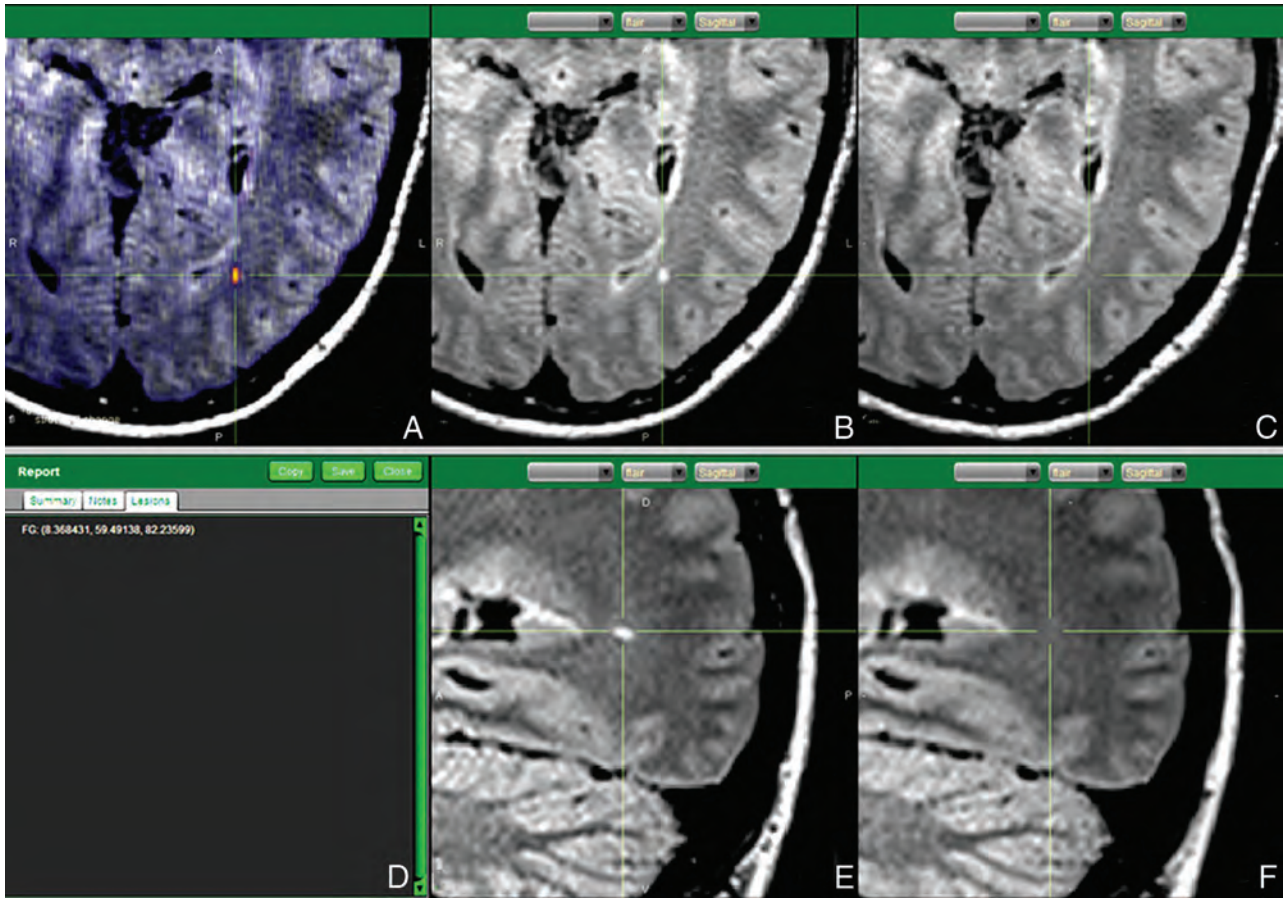

FIG 1. Annotated capture of the software reporting screen. *A*, Axial FLAIR with superimposed change map shows the new occipital white matter lesion in orange. Coregistered and resectioned FLAIR sequences comparing axial of new study (*B*) with axial of old study (*C*); and sagittal of new study (*E*) with sagittal old study (*F*)—thus confirming that the lesion is real and consistent with a new demyelinating plaque. *D*, Each lesion is marked with 3D coordinates.

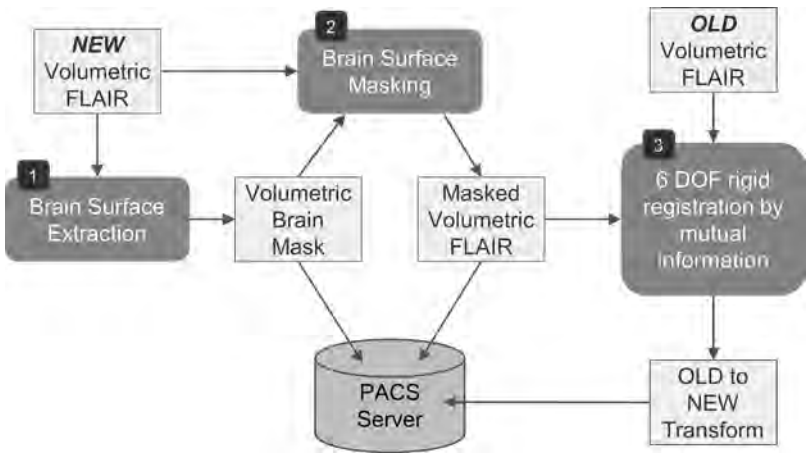

FIG 2. Preprocessing for change-detection on receipt of a new study. A pair of old and new studies are required, each containing a volumetric series used for change detection. In our case, this series uses the FLAIR protocol. Due to significant deformation in soft tissues outside the cranium, it is preferable to register the studies by using only the brain tissue. To this end, a brain-surface extraction tool (BrainSuite from the University of Southern California)[13] is fitted (1) and then used to mask the brain in the new study (2). Next, the equivalent series in the old study is retrieved and coregistered to the new study (3) by using the Mutual Information algorithm. The recovered transformation is stored in the PACS data base. Note that it is only necessary to mask the new study during registration and that rigid registration yielded sufficient accuracy after exclusion of the masked areas. DOF indicates degrees of freedom.

To assess interobserver characteristics and validate the detection ability of the software, 2 fellowship-trained neuroradiologists (readers 1 and 2) with 6 and 3 years' clinical experience, respectively, retrospectively assessed all CSP by using the software. The readers were blinded to each other's findings and to the existing radiology reports (median time between clinical report being issued and assessment with the software was 449 ± 159.7 days). The time required to read a study by using the software was assessed in real-time, by using a digital stopwatch.

The CSP initially clinically read by reader 1 were reread using the PACS a second time, 12 months later, to assess intraobserver characteristics. These same CSP were also again read by reader 1 three months later, still using the software, with all images left-right reversed to reduce the risk of recalling individual

Table 1: Demonstrating the number of study pairs showing a change in lesion load as identified using conventional side-by-side comparison and the software

Change in Lesion Load	Issued Radiology Report	Reader 1	Reader 2
Study pairs with new lesions (No.)	20	60 ($P < .001$)	62 ($P < .001$)
Study pairs with improved lesions (No.)	5	28 ($P < .001$)	39 ($P < .001$)

Table 2: Interreader agreement demonstrated with binary groupings of new and improved lesions when using the software

Change in Lesion Load, Binary Grouping	κ	95% CI
New lesions (0, 1+)	0.87	0.79–0.95
New lesions (0–1, 2+)	0.81	0.71–0.91
New lesions (0–2, 3+)	0.96	0.90–1.00
Improved lesions (0, 1+)	0.72	0.59–0.85
Improved lesions (0–1, 2+)	0.79	0.64–0.94
Improved lesions (0–2, 3+)	0.70	0.49–0.91

lesions. The time taken to reread the studies by reader 1 was also recorded in real-time by using a digital stopwatch.

Lesion Assessment

NLs were defined as those with new focal regions of increased T2 FLAIR signal in previously normal white matter. Due to the time interval between studies, no concentrically enlarging (worsening) plaques were identified.

ILs were defined as those with either concentric reduction in lesion size or global reduction in abnormal T2 FLAIR signal.

When using the software to assess NLs, the reader scrolled through axial colored change maps, with areas of increased FLAIR signal highlighted in red. Each time a candidate lesion was identified, the area was correlated to coregistered resectioned but otherwise conventional source FLAIR images in all 3 orthogonal planes of both new and old studies. The reader assessed the lesion as one would during conventional reporting (without the aid of any assistive software), judging whether the lesion represented a new demyelinating lesion, other pathology, or artifact. When the reader was satisfied that the lesion was indeed a true finding and represented a new demyelinating plaque, it was marked with 3D Cartesian coordinates.

This process was repeated for all lesions and was similarly repeated when examining the decreased FLAIR signal maps to identify ILs (highlighted in green).

When subsequently analyzing these marked lesions, the recorded coordinates for each read were automatically compared to ensure that the same lesions were being identified. Lesions with coordinates <2 mm apart were considered as 1 lesion. For lesions with coordinates >2 mm apart, both readers performed manual review of each lesion to determine whether both coordinates belonged to 1 large lesion marked in different locations or to 2 separately detected but adjacent lesions.

Statistical Analysis

The Cohen κ interrater reliability was used to measure and compare the agreement between the 2 readers and between the readers and the originally issued radiology reports. The Spearman correlation coefficient was also used to assess interreader correlation of overall lesion load. Three sets of binary subgroups were considered (≥1 lesion, ≥2 lesions, and ≥3 lesions) when assessing interreader κ agreement. Univariate χ^2 and 2-group proportion analyses were conducted to compare the number of new or improved lesions identified by the clinical report and by the readers when using the assistive software. The time taken to complete the assessment was recorded for each reader and reported as averages. The Mann-Whitney rank sum test was used to compare the time taken to read the scan data when using the side-by-side comparison with that when using the software. For all statistical tests, a 2-sided α value of .05 was used to indicate significance. Data were analyzed with STATA (Version 12.1; StataCorp, College Station, Texas).

Potential Clinical Impact

Questionnaires were sent to the referring neurologists concerning CSP if there was a change in lesion load when comparing the originally issued radiology report and the report of the readers using the software. Neurologists were asked to indicate whether their management strategies would have been changed retrospectively in regard to medication regimens, clinical follow-up interval, or MR imaging follow-up interval.

RESULTS

Using the software, readers were able to detect changes in a greater proportion of CSP than had been detected with conventional assessment for both NL (reader 1, 37%; reader 2, 39%; CSSC, 12%) and IL (reader 1, 17%; reader 2, 24%; CSSC, 3%). In both instances, statistical significance was reached (NL, $P < .001$; IL, $P < .001$) (Table 1). Lesions were located widely throughout the brain (On-line Fig 1).

To substratify the comparison pairs with NL and IL, we considered 3 sets of dichotomized subgroups (CSP with ≥1 lesion, ≥2 lesions, and ≥3 lesions). For CSP with detected NL and IL, κ statistics indicating substantial interreader agreement were observed (Table 2). These κ values were reduced slightly due to reader 2 identifying slightly higher numbers of both NLs and ILs in each subgroup, resulting from an interreader difference in the interpretation of lobulated lesions as either 2 confluent lesions or 1 irregular lesion. The Spearman correlation coefficient demonstrated good overall interreader correlation (Spearman ρ: NL = 0.910, IL = 0.774).

Comparing the subgroups of both NL and IL, readers detected a higher number of CSP with a changed lesion load compared to the original radiology reports (Fig 3*A*, -*B*), despite a wide variation of total background lesion load (On-line Fig 2).

Three false-negatives occurred by using the software; 2 NLs and 1 IL were described in 3 respective radiology reports, not detected by the readers.

Assessment of lesion location accuracy was calculated by using the total agreed base lesion load (defined as the lowest number of NLs or ILs that both readers agreed on per CSP) and showed good interreader location accuracy (NL location accuracy = 94%, 313/333; IL location accuracy = 96%, 70/73).

Despite identifying more NLs and ILs in a greater proportion of CSP when using the software, intraobserver agreement between

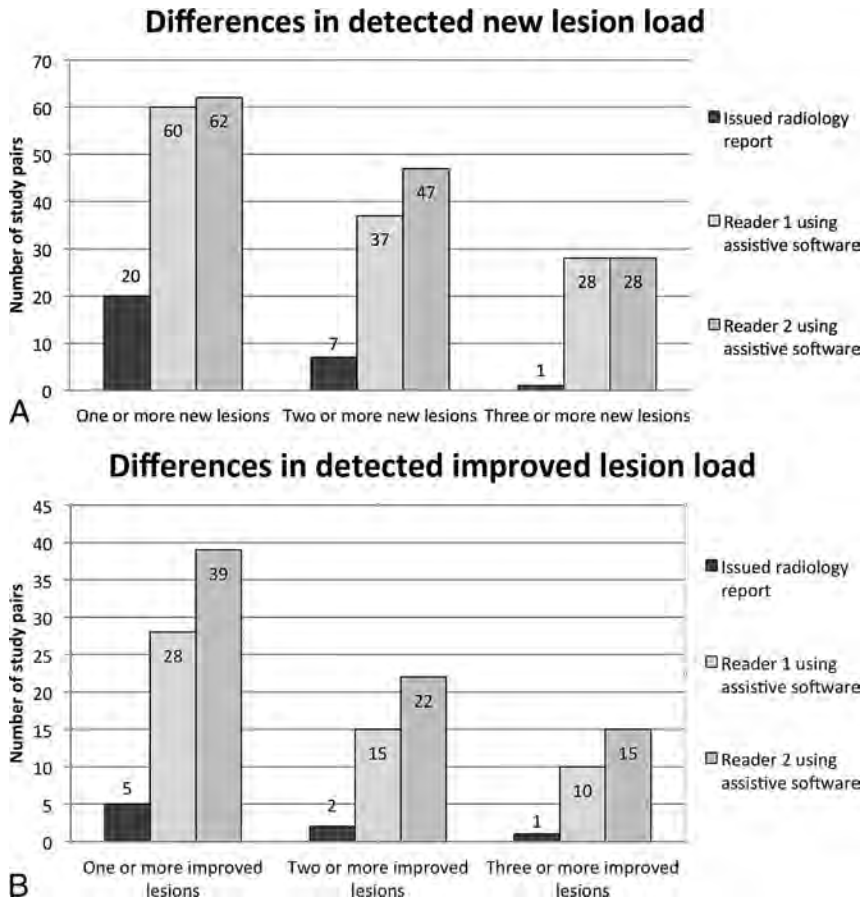

FIG 3. *A*, Comparative graphic representation of the number of study pairs with new lesions detected by both readers when using the software compared to the issued radiology report. *B*, Comparing the number of study pairs improved with demyelinating lesions detected by both readers when using the newly developed assistive software to the issued radiology report.

Table 3: Intrareader agreement demonstrated with binary groupings of new and improved lesions using both conventional side-by-side comparison and the software[a]

	New Lesions (κ) (95% CI)	Improved Lesions (κ) (95% CI)
One or more lesions		
VTS 1st vs VTS 2nd read	1.000	0.937 (0.815–1.000)
CSSC 1st vs CSSC 2nd read	0.941 (0.826–1.000)	0.462 (0.039–0.886)
Two or more lesions		
VTS 1st vs VTS 2nd read	1.000	0.731 (0.448–1.000)
CSSC 1st vs CSSC 2nd read	0.846 (0.640–1.000)	0.482 (−0.118–1.000)
Three or more lesions		
VTS 1st vs VTS 2nd read	1.000	0.774 (0.472–1.000)
CSSC 1st vs CSSC 2nd read	0.724 (0.361–1.000)	0.482 (−0.118–1.000)

[a] Correlations demonstrated substantial intrareader agreement. The software generally outperformed conventional side-by-side comparison without, however, reaching statistical significance.

the first and second read of the "reader 1 subgroup" applying the software was very good and better than that with CSSC, though this did not reach statistical significance with the sample size limited to 43 CSP (Table 3 and On-line Table 1).

Mean reporting times per CSP were <3 minutes (reader 1 = 2 minutes 15 seconds ± 1 minute 5 seconds and reader 2 = 2 minutes 45 seconds ± 1 minute 44 seconds), and there was an overall reduction in study reading times as the readers became more familiar with the software (mean read time of the first 25 studies: reader 1 = 3 minutes 9 seconds, reader 2 = 4 minutes 30 seconds versus a mean read time of the last 25 studies: reader 1 = 1 minute 36 seconds, reader 2 = 1 minute 49 seconds).

When we compared VTS with CSSC, there was a significant difference in read times (median interquartile range): VTS = 1 minute 58 seconds (range, 1 minute 37 seconds to 2 minutes 52 seconds) compared with CSSC = 3 minutes 41 seconds (range, 51 seconds to 4 minutes 12 seconds; $P < .001$).

Feedback forms were drafted for the 60 CSP that showed interval lesion load change when comparing the originally issued radiology reports and the lesion load detected by using VTS. A total of 47/60 completed feedback forms were returned (respondent rate of 78%). In 79% (37/47) of cases, neurologists reported that they would have been likely to change management strategies if the altered lesion load had been known at the time, prompting a change in either MR imaging follow-up interval, clinical follow-up interval, or therapeutic management (On-line Table 2).

DISCUSSION

Management strategy considerations for MS are based on clinical, biochemical, and imaging findings and are aimed at treating acute attacks, preventing relapses and progression, managing symptoms, and rehabilitation.[2,17]

In recent years, a number of new agents have become available, targeting various multiple sclerosis disease pathways.[1,2] MR imaging plays an important role in detecting not only the total demyelinating lesion load but also, possibly more important, interval change in the number of demyelinating lesions, reflecting disease activity and potentially resulting in changes to treatment.[2]

Conventional comparative image assessment is subjective, dependent on the skill and consistency of the reviewer.[9] To facilitate time-efficient, reproducible, and accurate lesion-load detection, many algorithms have been proposed for fully automated computer-assistive solutions.[3,18] These methods use different principles, including intensity-gradient features,[19] intensity thresholding,[20] intensity-histogram modeling of expected tissue classes,[21-23] fuzzy connectedness,[24] identification of nearest neighbors in a feature space,[25,26] or a combination of these. Methods such as Bayesian inference, expectation maximization, support-vector machines, k-nearest neighbor majority voting, and artificial neural networks are algorithmic approaches used to op-

timize segmentation.[18] All of these approaches tend to show promising results; however, the results are usually on small samples, often nonreproducible and unreliable, and have not entered into routine clinical use.[18]

In smaller study populations, semiautomated assistive approaches have been investigated with promising results by using both MR imaging subtraction techniques and coregistered comparative volumetric FLAIR color-map overlays.[11,12]

Our semiautomated radiology assistive platform is computationally fast and robust, successfully processing all 322 included studies. The software allows color maps superimposed on anatomic FLAIR sequences and direct comparison between old and new studies in exactly aligned axes as well as accurate localization of any given point in all 3 planes.

In our study population, the largest reported of its kind (161 CSP; 322 individual studies), a statistically significant number of increased CSP with NLs and ILs were detected when using the assistive software compared with the originally issued MR imaging reports generated with CSSC. On the basis of responses by referring neurologists, at least 79% of CSP with changes in detected lesion loads (VTS versus CSSC) were likely to have undergone a change in management if the altered lesion load had been appreciated at the time. This represents 22% (37/161) of the whole cohort; studies reported as "stable" that actually had sufficient change in disease burden to potentially alter management.

In addition to detecting NLs, our approach demonstrates a statistically significant improvement in detecting ILs. There is, however, a larger disparity between readers when assessing ILs. After we reviewed the discrepant lesions, this does not appear to stem from software failure but from intrinsic heterogeneity in lesions that appear to be reducing in size or signal intensity. Some lesions demonstrated an unequivocal concentric reduction in size. Many lesions, however, demonstrated diffuse or ill-defined signal normalization. It was these lesions that resulted in most interreader discordance. This difficulty in clearly defining the nature of improving demyelinating lesions is echoed in studies correlating the MR imaging appearances of demyelinating lesions with lesion pathology, highlighting the heterogeneity that also exists in radiologic-pathologic correlation.[27] Although the significance of new demyelinating lesions on MR imaging has been well established in the literature,[1,2,4-7] the clinical significance of "improved" demyelinating lesions is less clear.

Limitations

Our study has a number of limitations. One is the single-scanner/single-sequence nature of the dataset. The software platform has been designed to be vendor-agnostic and should be able to accept any volumetric FLAIR sequence; however, this has not yet been tested, and likely, performance will vary depending on the quality of the source data. Indeed, vascular flow-induced artifacts through the anterior pons and inferior temporal lobes seen in our FLAIR sequence resulted in some difficulty in interpreting signal change in these regions, and improved sequence design may allow even greater lesion detection. Additionally, there is likely to be decreased performance if the 2 volumetric FLAIR sequences compared are from different MR imaging scanners or differ in their specifications, though again transformation, coregistration, and normalization are not dependent on identical sequences. Although not tested in this study, other volumetric sequences such as double inversion recovery should fulfill the criteria to be used with the software.

Other limitations of our study include the inability to comment on interobserver agreement on the original radiology reports because these were single-read by various MR imaging–trained radiologists in our department and a reread of all CSP by both readers was beyond the scope of this study.

Although we can also not comment on the time it took to read the original MR imaging studies in clinical practice (at our institution, we do not routinely record reporting times), we tried to address this, in part, by measuring the time taken to perform conventional interpretation by using CSSC on the PACS during the second reread by reader 1. Having done so, we nonetheless acknowledge that applying the software clinically may result in unforeseen program-related and user-related time delays. We are hoping to minimize these by incorporating the platform directly into a PACS workflow and by familiarizing MR imaging readers with the program; these changes will be explored in future work.

Although intrareader correlation was shown to be very good in the subset of cases that reader 1 reread (Table 3), the accuracy of the other radiology reports may have been influenced by factors related to the daily demands of a busy radiology department, such as time pressures and interruptions (factors not simulated when testing the software). All MR imaging readers in our department are experienced; thus, radiologic expertise is unlikely to present a limitation. If anything, it is likely that the lesion-detection improvement would be larger for radiologists with less neuroradiology experience.

We also acknowledge that we did not directly assess the clinical impact of a second read without the software; however, we believe we have, in part, explored this by having reader 1 additionally reread all the studies he originally assessed ($n = 43$) by using CSSC. The agreement between the 2 reads was high (Table 3). More important, in only a single patient did the reads differ in categorization (On-line Table 1). The reports of a second read by using CSSC would have been, in all except 1 case, indistinguishable from the initial clinical reports; thus, no change in management would be expected. As such, retrospective changes to management reported by treating clinicians are attributable to the software, rather than to merely a second read.

Future Work

Our current development work is focused on deploying the software to the live clinical PACS workflow at our institution, which will allow us to carry out prospective research and ensure that the findings of this study are replicated in terms of improved lesion detection without the burden of false-positives. We are also hoping to make the software available to other institutions for further validation by introducing additional readers and by using a variety of FLAIR sequences. The functionality of the software can also be extended in the future by adding semiautomated segmentation for quantification of lesion volume.

CONCLUSIONS

We have developed a semiautomated software platform to assist the radiologist reading comparative MR imaging MS follow-up study pairs with accurate and timely reporting. We have shown that it significantly outperforms CSSC in the identification of NLs and ILs, while maintaining high intra- and interobserver reliability. On the basis of neurologists' feedback, it is likely that identifying new lesions would result in some management change. Given the availability and efficacy of numerous disease-modifying drugs, even a small change in prescribing practices could result in sizable effects on the long-term patient disability.

ACKNOWLEDGMENTS

The authors acknowledge Andy Le, Suria Barelds, Irene Ngui, and Alex Stern for their assistance with data gathering and integration. The National Information and Communications Technology of Australia Research Centre of Excellence (NICTA) contribution to this work was supported by the Australian Research Council and by the NICTA Victorian Research Laboratory.

Disclosures: Frank Gaillard—*UNRELATED*: *Employment*: Founder/CEO Radiopaedia.org, Radiopaedia Australia Pty Ltd; *Grants/Grants Pending*: multiple grants in progress for this and related projects, through the National Health and Medical Research Council development grants,* Business Development Initiative Victoria Government (successful first round),* and Royal Melbourne Hospital Foundation*; *Payment for Lectures (including service on Speakers Bureaus)*: Medtronic Australia, *Comments*: travel and payment to give talks on MRI safety; *Other*: technical consultant, Medtronic Australasia Pty Ltd. David Rawlinson—*RELATED*: *Other*: Our institute, NICTA/University of Melbourne, was funded by state and federal governments, which paid our wages.* Patricia M. Desmond—*UNRELATED*: *Grants/Grants Pending*: National Health and Medical Research Council.* *Money paid to the institution.

REFERENCES

1. Jones JL, Coles AJ. **New treatment strategies in multiple sclerosis.** *Exp Neurol* 2010;225:34–39
2. Weiner HL. **The challenge of multiple sclerosis: how do we cure a chronic heterogeneous disease?** *Ann Neurol* 2009;65:239–48
3. Mortazavi D, Kouzani AZ, Soltanian-Zadeh H. **Segmentation of multiple sclerosis lesions in MR images: a review.** *Neuroradiology* 2012;54:299–320
4. Caramanos Z, Francis SJ, Narayanan S, et al. **Large, nonplateauing relationship between clinical disability and cerebral white matter lesion load in patients with multiple sclerosis.** *Arch Neurol* 2012;69:89–95
5. Sormani MP, Rovaris M, Comi G, et al. **A reassessment of the plateauing relationship between T2 lesion load and disability in MS.** *Neurology* 2009;73:1538–42
6. Fisniku LK, Brex PA, Altmann DR, et al. **Disability and T2 MRI lesions: a 20-year follow-up of patients with relapse onset of multiple sclerosis.** *Brain* 2008;131:808–17
7. Stankiewicz JM, Glanz BI, Healy BC, et al. **Brain MRI lesion load at 1.5T and 3T versus clinical status in multiple sclerosis.** *J Neuroimaging* 2011;21:e50–e56
8. Bink A, Schmitt M, Gaa J, et al. **Detection of lesions in multiple sclerosis by 2D FLAIR and single-slab 3D FLAIR sequences at 3.0 T: initial results.** *Eur Radiol* 2006;16:1104–10
9. Abraham AG, Duncan DD, Gange SJ, et al. **Computer-aided assessment of diagnostic images for epidemiological research.** *BMC Med Res Methodol* 2009;9:74
10. García-Lorenzo D, Francis S, Narayanan S, et al. **Review of automatic segmentation methods of multiple sclerosis white matter lesions on conventional magnetic resonance imaging.** *Med Image Anal* 2013;17:1–18
11. Moraal B, Meier DS, Poppe PA, et al. **Subtraction MR images in a multiple sclerosis multicenter clinical trial setting.** *Radiology* 2009;250:506–14
12. Bilello M, Arkuszewski M, Nasrallah I, et al. **Multiple sclerosis lesions in the brain: computer-assisted assessment of lesion load dynamics on 3D FLAIR MR images.** *Neuroradiol J* 2012;25:17–21
13. Shattuck DW, Leahy RM. **BrainSuite: an automated cortical surface identification tool.** *Med Image Anal* 2002;6:129–42
14. Cover TM, Thomas JA. *Elements of Information Theory*. New York: John Wiley & Sons; 1991
15. Warnock MJ, Toland C, Evans D, et al. **Benefits of using the DCM4CHE DICOM archive.** *J Digit Imaging* 2007;20:125–29
16. Rasband WS. ImageJ. Bethesda; National Institutes of Health; 1997–2014. http://imagej.nih.gov/ij/. Accessed April 1, 2013
17. Murray TJ. **Diagnosis and treatment of multiple sclerosis.** *BMJ* 2006;332:525–27
18. Vrenken H, Jenkinson M, Horsfield MA, et al; MAGNIMS Study Group. **Recommendations to improve imaging and analysis of brain lesion load and atrophy in longitudinal studies of multiple sclerosis.** *J Neurol* 2013;260:2458–71
19. Pachai C, Zhu YM, Grimaud J, et al. **A pyramidal approach for automatic segmentation of multiple sclerosis lesions in brain MRI.** *Comput Med Imaging Graph* 1998;22:399–408
20. Goldberg-Zimring D, Achiron A, Miron S, et al. **Automated detection and characterization of multiple sclerosis lesions in brain MR images.** *Magn Reson Imaging* 1998;16:311–18
21. Shiee N, Bazin PL, Ozturk A, et al. **A topology-preserving approach to the segmentation of brain images with multiple sclerosis lesions.** *Neuroimage* 2010;49:1524–35
22. Khayati R, Vafadust M, Towhidkhah F, et al. **Fully automatic segmentation of multiple sclerosis lesions in brain MR FLAIR images using adaptive mixtures method and Markov random field model.** *Comput Biol Med* 2008;38:379–90
23. Freifeld O, Greenspan H, Goldberger J. **Multiple sclerosis lesion detection using constrained GMM and curve evolution.** *Int J Biomed Imaging* 2009;2009:715124
24. Horsfield MA, Bakshi R, Rovaris M, et al. **Incorporating domain knowledge into the fuzzy connectedness framework: application to brain lesion volume estimation in multiple sclerosis.** *IEEE Trans Med Imaging* 2007;26:1670–80
25. Anbeek P, Vincken KL, van Osch MJ, et al. **Automatic segmentation of different-sized white matter lesions by voxel probability estimation.** *Med Image Anal* 2004;8:205–15
26. Mohamed FB, Vinitski S, Gonzalez CF, et al. **Increased differentiation of intracranial white matter lesions by multispectral 3D-tissue segmentation: preliminary results.** *Magn Reson Imaging* 2001;19:207–18
27. Filippi M, Rocca MA, Barkhof F, et al; Attendees of the Correlation between Pathological MRI Findings in MS workshop. **Association between pathological and MRI findings in multiple sclerosis.** *Lancet Neurol* 2012;11:349–60

Mean Diffusional Kurtosis in Patients with Glioma: Initial Results with a Fast Imaging Method in a Clinical Setting

A. Tietze, M.B. Hansen, L. Østergaard, S.N. Jespersen, R. Sangill, T.E. Lund, M. Geneser, M. Hjelm, and B. Hansen

ABSTRACT

BACKGROUND AND PURPOSE: Diffusional kurtosis imaging is an MR imaging technique that provides microstructural information in biologic systems. Its application in clinical studies, however, is hampered by long acquisition and postprocessing times. We evaluated a new and fast (2 minutes 46 seconds) diffusional kurtosis imaging method with regard to glioma grading, compared it with conventional diffusional kurtosis imaging, and compared the diagnostic accuracy of fast mean kurtosis (MK′) to that of the widely used mean diffusivity.

MATERIALS AND METHODS: MK′ and mean diffusivity were measured in the contrast-enhancing tumor core, the perifocal hyperintensity (indicated on T2 FLAIR images), and the contralateral normal-appearing white and gray matter of 34 patients (22 with high-grade and 12 with low-grade gliomas). MK′ and mean diffusivity in the different tumor grades were compared by using a Wilcoxon rank sum test. Receiver operating characteristic curves and the areas under the curve were calculated to determine the diagnostic accuracy of MK′ and mean diffusivity.

RESULTS: MK′ in the tumor core, but not mean diffusivity, differentiated high-grade from low-grade gliomas, and MK′ differentiated glioblastomas from the remaining gliomas with high accuracy (area under the $\text{curve}_{MK'} = 0.842$; $P_{MK'} < .001$). MK′ and mean diffusivity identified glioblastomas in the group of high-grade gliomas with similar significance and accuracy (area under the $\text{curve}_{MK'} = 0.886$; area under the $\text{curve}_{\text{mean diffusivity}} = 0.876$; $P_{MK'} = .003$; $P_{\text{mean diffusivity}} = .004$). The mean MK′ in all tissue types was comparable to that obtained by conventional diffusional kurtosis imaging.

CONCLUSIONS: The diffusional kurtosis imaging approach used here is considerably faster than conventional diffusional kurtosis imaging methods but yields comparable results. It can be accommodated in clinical protocols and enables exploration of the role of MK′ as a biomarker in determining glioma subtypes or response evaluation.

ABBREVIATIONS: AC = astrocytoma; DKI = diffusional kurtosis imaging; GBM = glioblastoma multiforme; HGG = high-grade glioma; LGG = low-grade glioma; MD = mean diffusivity; MK = mean kurtosis; MK′ = fast mean kurtosis; NAGM = normal-appearing gray matter; NAWM = normal-appearing white matter

Diffusion-weighted and diffusion tensor imaging are currently used in patients with cerebral glioma as presurgical imaging tools for the World Health Organization grading system, neuronavigation, and response evaluation during radiochemotherapy or antiangiogenic treatment.[1] DTI and DWI approximate the displacements of diffusing water molecules by a Gaussian distribution as if water molecules were moving unrestricted in all directions. However, it is well established that the diffusion signal from cerebral water molecules for moderate-to-high values of the magnetic gradient field is not described accurately by the standard monoexponential decay as a function of the diffusion weighting (b-value).[2]

Diffusional kurtosis imaging (DKI) is a recently described MR imaging technique that aims to provide additional microstructural information by extending the DTI model to incorporate fourth-order gradient field terms in the diffusion signal.[2] In this higher-order description of diffusion signal decay, the dimensionless kurtosis term describes the degree of deviation from the Gaussian distribution of spin displacements along the axis of observation. When averaged over all directions, the mean kurtosis (MK) is obtained.[2] The deviation from free (Gaussian) diffusion

Received November 18, 2014; accepted after revision January 24, 2015.

From the Department of Neuroradiology (A.T., L.Ø., M.G., M.H.), Aarhus University Hospital, Aarhus, Denmark; Center of Functionally Integrative Neuroscience and MINDLab, Institute of Clinical Medicine (A.T., M.B.H., L.Ø., S.N.J., R.S., T.E.L., M.G., B.H.) and Department of Physics and Astronomy (S.N.J.), Aarhus University, Aarhus, Denmark.

This work was supported by the Danish Ministry of Science, Technology and Innovation's University Investment Grant (MINDLab). B.H. acknowledges support from NIH 1R01EB012874-01.

Please address correspondence to Anna Tietze, MD, Department of Neuroradiology, Aarhus University Hospital, Nørrebrogade, DK-8000 Aarhus, Denmark; e-mail: annatietze@gmail.com

Indicates open access to non-subscribers at www.ajnr.org

Indicates article with supplemental on-line table

http://dx.doi.org/10.3174/ajnr.A4311

is generally assumed to be caused by tissue microstructure, and MK is therefore interpreted as a general microstructural marker.[3] Use of the DKI model may be beneficial in 2 ways: 1) the diffusion tensor is indirectly corrected through the higher-order terms,[4] and 2) the additional microscopic diffusion characteristics may be used for clinical purposes. Compared with gray matter or edematous tissue, white matter and malignant tumors are characterized by higher architectural complexity that results from cell membranes, organelles, axons, or vascular structures impeding proton diffusion and leading to higher non-Gaussianity and increased MK.[5]

Gliomas are a heterogeneous group, categorized as low-grade glioma (LGG) and a high-grade glioma (HGG) with different histopathologic features, such as cellularity or the presence or absence of necrosis and neoangiogenesis. This heterogeneity is likely to be reflected in MK alterations, and promising first studies have reported MK as an imaging-based means of presurgical glioma grading.[6,7] Larger studies and the more widespread use of DKI, however, have been held back by relatively long acquisition times that result from a model requirement for data to be obtained along several directions at each of many b-values.[8] Such protocols are clearly incompatible with the daily routines in busy clinical imaging departments and are often not tolerable by critically ill patients.

We recently proposed a kurtosis method[9,10] that is much faster than traditional kurtosis-acquisition schemes,[2,4] in terms of both acquisition and postprocessing times, and on the basis of this method we present here our first clinical results in 34 patients with glioma. We correlated MK values with histopathologic grades and compared them with those from the literature. Moreover, we compared the diagnostic accuracy of MK with that of the widely used mean diffusivity (MD), calculated in our case as part of the fast-MK method.

MATERIALS AND METHODS

Patients

Thirty-five patients with cerebral gliomas were included in this retrospective study. A waiver from the local ethics committee was granted, because DKI was acquired without increasing the scan time by modification of the diffusion-weighted sequence that is a part of our routine clinical protocol. Apart from steroids in some patients with glioblastoma multiforme (GBM), these patients did not receive any treatment at the time of imaging. One patient had to be excluded because of motion artifacts on conventional sequences so severe that reliable tumor outlining could not be performed. The diagnosis of glioma (22 HGGs, 12 LGGs) was determined by biopsy or resection in 30 cases. Three of the remaining 4 cases without histopathology results were considered to be LGG and 1 was considered to be GBM; these diagnoses were based on the clinical behavior and imaging characteristics on conventional MR imaging. Two of 34 patients, both with LGG, had undergone surgery many years before being included in this study and were re-imaged because of disease recurrence. Included were 15 patients with GBM, 5 with a grade III astrocytoma (AC), 2 with a grade III oligodendroglioma, and 12 with an LGG (3 with a proven grade II oligodendroglioma). One tumor was classified as a grade II oligodendroglioma with a minor astrocytic component and was subsequently included in the group of those with a grade II oligodendroglioma.

Imaging

MR imaging was performed on a Skyra 3T system (Siemens, Erlangen, Germany) with a standard 20-element head coil. The MR imaging protocol consisted of 3D T1-weighted images before and after intravenous contrast (0.1 mmol/kg gadoterate meglumine; TR, 2300 ms; TE, 3.8 ms; voxel size, $1 \times 1 \times 1$ mm^3; FOV, 256×256 mm^2; acquisition time, 349 s) and axial precontrast T2 FLAIR images (TR, 9000 ms; TE, 117 ms; TI, 2500 ms; voxel size, $0.7 \times 0.7 \times 3$ mm^3; FOV, 230×220 mm^2; acquisition time, 326 s). Axial DKI was performed before intravenous contrast (TR, 10,300 ms; TE, 100 ms; voxel size, $2 \times 2 \times 2$ mm^3; FOV, 196×196 mm^2; number of excitations, 1; sections, 60; acquisitions, 3 [one along each of the x-, y-, and z-directions] with $b=1000$ s/mm^2, 9 different directions [as specified in Hansen et al[9]] with $b=2500$ s/mm^2, and 1 acquisition with $b=0$ s/mm^2; 13 diffusion-weighted images in total). The acquisition time for DKI was 166 seconds.

MR Imaging Data Analysis

In the framework of the fast kurtosis sequence,[9] $\bar{W}$, the mean of the kurtosis tensor W, is computed, and it was shown to be very similar numerically to the traditional MK. Here, we refer to it as MK′ for convenience. MK′ is calculated from 13 diffusion-weighted images: 1 $b=0$ scan for normalization, 3 images at $b=1000$ s/mm^2 along each of the x-, y-, and z-directions, and 9 images at $b=2500$ s/mm^2 along the 9 directions defined in Hansen et al.[9] From these data, a robust estimate of MD can also be achieved with the kurtosis term taken into account in its calculation, which was shown to improve MD estimates[4] and implemented as proposed in Jensen et al.[11]

Postprocessing of the DKI data, including the reslicing and co-registration steps, were performed by running modules developed in-house in SPM8 (http://www.fil.ion.ucl.ac.uk/spm/software/spm8) and Matlab (MathWorks, Natick, Massachusetts).

Contrast-enhanced T1-weighted images were resliced to T2 FLAIR. A neuroradiologist, blinded for the histopathologic diagnosis (A.T., 5 years of experience), outlined the tumor core (contrast-enhancing part), the perifocal hyperintensity on T2 FLAIR (hereafter termed FLAIR mask), and regions of normal-appearing white and gray matter (NAWM and NAGM, respectively) in the contralateral centrum semiovale and thalamus (Fig 1). In cases of a nonenhancing lesion, only T2 FLAIR was used to define the tumor. Normal vessel structures, necrotic areas, and potential blood products were avoided, guided by conventional sequences. Tumor core, FLAIR masks, contralateral NAWM masks, contrast-enhanced T1, and T2 FLAIR images were subsequently co-registered and resliced to the localization of the DKI data. The co-registration step was checked visually by using SPM8.

The duration of the DKI sequence is quite short (166 seconds); hence, it was deemed unnecessary to perform motion correction of the individual volumes. The validity of this strategy was verified

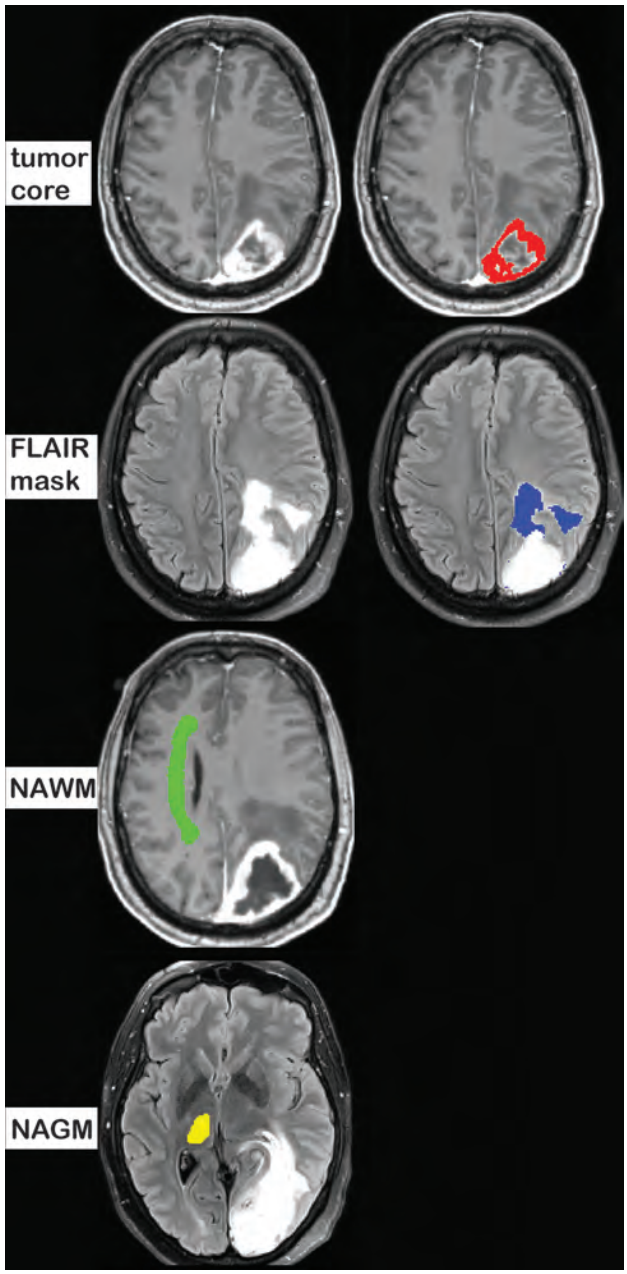

FIG 1. The tumor core was defined as the contrast-enhancing part on postcontrast T1-weighted images, and the FLAIR masks were defined as hyperintense regions on T2 FLAIR images (minus the tumor core and necrosis, if present). In cases of nonenhancing tumors, hyperintensity areas on T2 FLAIR images were defined as the tumor core (the tumor core and edema were identical regions). The NAWM was outlined in the centrum semiovale of the contralateral hemisphere (on ≥4 consecutive sections). The NAGM was defined in the contralateral thalamus (on ≥3 sections).

in all cases by visual inspection of all diffusion images. To remove possible spurious voxels, the DKI data were up-sampled by a factor of 2 in all directions by using linear interpolation and subsequently smoothed by a $2 \times 2 \times 2$–mm^3 kernel. The spatial distortions introduced in the images by eddy currents were compensated to some extent by using a double spin-echo sequence, which is currently the best clinically viable solution (it does not add additional time to the scan sequence). The postprocessing of a single DKI dataset took 3–5 seconds.

Statistical Analysis

Statistical analysis was performed by using R Studio (http://rstudio.org/download/desktop) and Matlab. Voxelwise values of MD and MK′ values were extracted from the 4 regions. The MK′ and MD values were normalized by calculating the ratio of tumor core values and the individual mean values obtained in the contralateral NAWM (termed nMK′ and nMD, respectively). The same was done for values in the FLAIR masks. The mean values in all the regions were computed. To evaluate data variations of MK′ and MD, we calculated the coefficient of variation in pathologic tissue in contralateral normal-appearing tissue (NAWM and NAGM). A paired *t* test was performed to assess whether variations of MK′ and MD were significantly different. A Wilcoxon rank sum test was used to compare mean MK′ and MD values between tumor types and grades. The statistical threshold for significant discrimination was set to a *P* value of ≤ .05. Receiver operating characteristic curves were constructed to determine the diagnostic performance of MK′, MD, nMK′, and nMD. The area under the receiver operating characteristic curve was used to measure the accuracy, and *P* values were used to measure strength. Moreover, logistic regression was performed to investigate whether the combination of MK′ and MD increased the area under the curve and thereby the diagnostic performance. Finally, the sensitivity and specificity for discriminating HGG, LGG, and specific tumor grades were determined.

RESULTS

Typical examples of an LGG (grade II AC, upper panel *A*) and an HGG (GBM, lower panel *B*) are shown in Fig 2. Note the areas with increased MK′ and decreased MD in the GBM, whereas MK′ is low and MD is high in the grade II AC case.

Nonnormalized and normalized mean values of MK′ and MD in the contrast-enhancing tumor core (or the hyperintense area on T2 FLAIR, for nonenhancing tumors) for the different tumor types and grades are shown in Fig 3. Median values for tumor types and grades along with measurements in the contralateral NAWM and NAGM are given in the On-line Table. The data variation in NAWM was significantly larger ($P < .001$) for MD (coefficient of variation = 0.122 ± 0.019) than for MK′ (coefficient of variation = 0.093 ± 0.013), and MD values varied slightly less (coefficient of variation = 0.163 ± 0.058) than the MK′ values (coefficient of variation = 0.189 ± 0.043) in NAGM ($P = .036$).

The mean value of MK′ in the tumor core was significantly higher in HGGs than in LGGs. nMK′ was increased in HGGs, but it was with a *P* value of .058, which is above the threshold for statistical significance. MD and nMD were not significantly different between the HGGs and LGGs. MK′ and nMK′ were increased, and MD and nMD were decreased in GBMs when comparing them with the remaining HGGs or with the entire study group consisting of HGGs and LGGs (all $P < .05$). In the group of HGGs, grade III AC cases were identified by MK′, MD, nMK′, and nMD. It was not possible to discriminate groups by values in the FLAIR masks. All *P* values are reported in Table 1.

The receiver operating characteristic curves for the discrimination between HGGs and LGGs showed higher areas under the curve for MK′ and nMK′ than for MD and nMD in the tumor core. The areas under the curve for the differentiation between

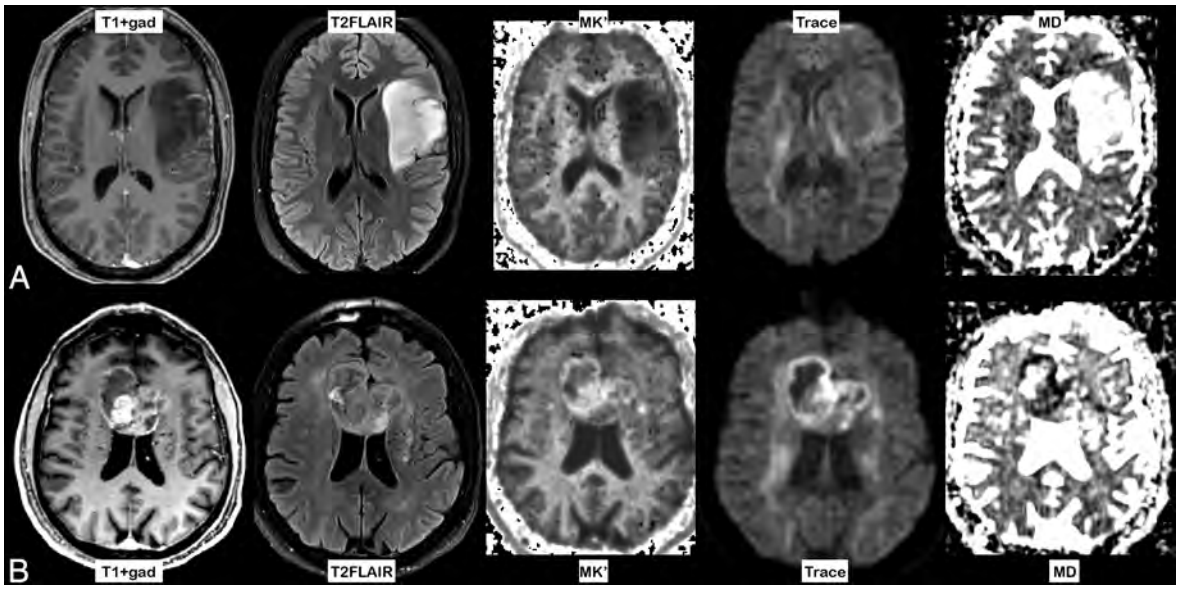

FIG 2. *A*, Contrast-enhanced T1-weighted and T2 FLAIR images of a grade II astrocytoma grade in the left hemisphere. The map of MK′ demonstrates low MK′, whereas the trace image and the MD map show high diffusivity (high signal changes on MD). *B*, Typical example of a glioblastoma, with contrast enhancement on postcontrast T1-weighted and complex signal changes on T2 FLAIR images. Increased MK′ is noted in most of the tumor. The trace image and MD show restricted diffusion, primarily in the periphery of the lesion.

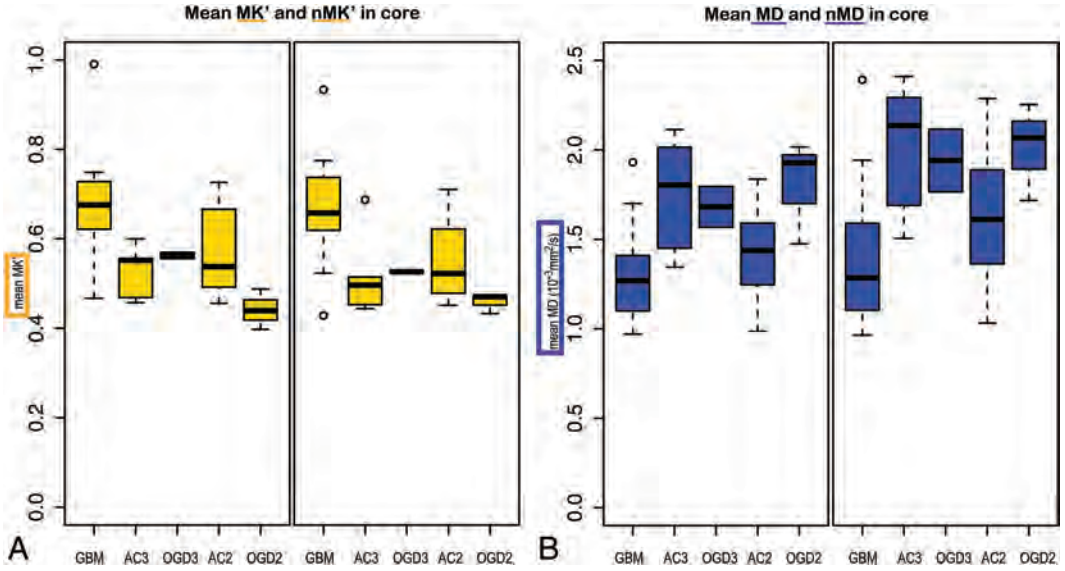

FIG 3. Boxplots of average MK′ and normalized MK′ (in yellow) (*A*) and MD and normalized MD (in blue) (*B*) in the contrast-enhancing tumor core of all patients, grouped according to tumor types and grades, are shown. The horizontal lines in the boxes are the median values, the upper and lower box edges are the 25th and 75th percentiles, respectively, and the upper and lower whiskers represent the minimums and maximums, respectively. AC indicates grade III astrocytoma; ODG3, grade III oligodendroglioma; AC2, grade II astrocytoma; ODG2, grade II oligodendroglioma.

Table 1: Significance of mean MK′, nMK′, MD, and nMD values in different tumor grades[a]

Tumor Type	MK′	nMK′	MD	nMD
HGG/LGG	.028[b]	.058	.383	.511
GBM/all	<.001[b]	.002[b]	.006[b]	.006[b]
GBM/HGG	.003[b]	.011[b]	.004[b]	.004[b]
AC3/all	.135	.135	.063	.033[b]
AC3/HGG	.011[b]	.031[b]	.024[b]	.019[b]

Note:—AC3 indicates grade III astrocytoma.

[a] Mean MK′, nMK′, MD, and nMD values in the tumor core were compared between different tumor grades, and the resulting *P* values are listed.

[b] A *P* value of <.05 indicates a significant difference between groups.

GBMs and the remaining gliomas were higher for MK′ and nMK′ than for the corresponding MD values. When identifying grade III AC cases, MK′ and MD performed similarly. Areas under the curve calculated from values in the FLAIR masks were either low or not statistically significant. Combining MK′ and MD or nMK′ and nMD could increase accuracy, but only MK′ and nMK′ contributed to the logistic regression model differentiating HGGs from LGGs or identifying GBMs in the entire glioma group. Area under the curve values are given in Table 2. GBMs were diagnosed with 87% sensitivity and 74% specificity with a cutoff MK′ value of 0.58 (87% sensitivity and 74% specificity for an nMK′ value of

Table 2: Results of regression analysis[a]

Tumor Type	MK′	*P*	nMK′	*P*	MD	*P*	nMD	*P*	MK′ + MD	*P*[b]	nMK′ + nMD	*P*[b]
HGG/LGG	0.731	.045[c]	0.701	.056	0.595	.512	0.572	.456	0.754	.032[c] .220	0.746	.041[c] .213
GBM/all	0.842	.004[c]	0.811	.004[c]	0.775	.017[c]	0.772	.014[c]	0.842	.045[c] .796	0.807	.047[c] .835
GBM/HGG	0.886	.027[c]	0.838	.022[c]	0.876	.018[c]	0.876	.019[c]	0.895	.127 .204	0.905	.181 .184
AC3/all	0.717	.146	0.717	.170	0.766	.052	0.800	.060	0.793	.744 .165	0.779	.885 .155
AC3/HGG	0.871	.039[c]	0.824	.055	0.835	.038[c]	0.847	.042[c]	0.882	.127 .328	0.871	.301 .265

Note:—AC3 indicates grade III astrocytoma.

[a] The areas under the receiver operating characteristic curves as a measure for diagnostic accuracy are reported.

[b] Two *P* values occur when two values (MK′ and MD) are tested at the same time.

[c] The variable contributes significantly to the regression model if the corresponding *P* value is $<.05$.

0.60), whereas the corresponding sensitivity and specificity for an MD value of 1.460 were 80% and 63%, respectively (80% sensitivity and 63% specificity for an nMD value of 1.683).

DISCUSSION

In this study, we investigated MK′ in the tumor core and the perifocal hyperintensity on T2 FLAIR images in different glioma grades. Our data were acquired with a new and rapid DKI method[9] that is easily implemented and provides fast acquisition and postprocessing times, which make it potentially useful in clinical departments and for larger studies. The discrimination between HGGs and LGGs was possible only by means of MK′, and the MK′ and MD values allowed us to identify cases of GBM in the HGG group and in the entire study population. Our receiver operating characteristic analyses revealed high accuracy for MK′ and nMK′, represented by high areas under the curve. Although we chose to correct MD for the non-Gaussian phenomena (described in "Materials and Methods") to obtain more accurate measurements, we found that MK′ was still superior to MD in diagnosing GBMs when evaluating a group of mixed glioma types, whereas MD and MK′ perform similarly when analyzing only HGGs. Moreover, we showed that MK′ data variation was significantly smaller in NAWM and larger in NAGM. The high b-values, used for DKI, dampen the signal considerably, and with noise being constant, the signal-to-noise ratio decreases. Because MD is higher in NAGM than in NAWM, the decrease in signal-to-noise ratio is expected to be more distinct in NAGM, negatively impacting parameter estimates and causing larger variation.

Currently, few studies in which DKI parameters in patients with glioma were investigated have been published. Van Cauter et al[7] examined 28 patients (17 with an HGG and 11 with an LGG, both oligodendroglial and astrocytic types) with a conventional DKI sequence taking 17 minutes 29 seconds and showed a significant difference in MK, nMK, and nMD values between HGGs and LGGs, with areas under the curve of >0.8 for all 3 values. Median values in the tumor core, the perifocal hyperintensity on T2 FLAIR images, and the contralateral NAGM were similar to ours, but the median value for the contralateral NAWM was considerably lower than ours.[7] The higher MK values for NAWM measured in our study corresponds better, however, to values reported earlier.[2,9] Values for single tumor grades (eg, GBM or grade III AC) were not reported by these studies. Raab et al[6] evaluated 33 patients with an astrocytoma only (AC grade 2, AC grade 3, or GBM) by using a DKI sequence that took 11 minutes 57 seconds. Mean MK values in the core of grade II ACs, grade III ACs, and GBMs were somewhat higher in their study (between 0.09 higher for nMK in grade III ACs and 0.14 for MK in GBMs), and their ability to separate tumor grades was slightly better than ours. Several possible causes for these discrepancies are conceivable, including unconfirmed histopathology in 4 of our cases, previous surgery,[3] the risk of misdiagnosis caused by imprecise sampling in cases of biopsy, the inclusion of gliomas with both oligodendroglial and astrocytic histology results, differences between the MR imaging systems used for data acquisition (particularly gradient performance and its influence on diffusion times and achievable echo times), different technical and postprocessing approaches, and the distinct physical nature of MK and MK′.

We were able to differentiate HGGs from LGGs by means of MK′, but our separation of GBMs and AC3s from the remaining gliomas might be clinically even more critical than the rough classification of HGGs and LGGs that in most cases is accomplished by conventional or perfusion-weighted MR imaging.[12] Even more detailed subtyping of gliomas in those with a relatively favorable outcome and those with a poor outcome are becoming increasingly relevant, because different therapeutic approaches can be considered. The prediction of patient outcome by means of imaging biomarkers correlating them with genomic subtypes is an expanding field, and MK should be included in the future.[13] We also suggest that DKI might be an important diagnostic tool for assessing tumor progression and treatment response. It is well known that LGGs progress to higher grades with time, a process that is essential to monitor for accurately timed treatment adjustment, and gradually increasing MK might be a valuable tool for detecting these subtle changes in dedifferentiation. Therefore, visualization of aggressive regions within a lesion by detailed MK mapping could have important implications on the neurosurgical approach or radiation treatment planning. A promising additional application area for DKI is response evaluation of patients during antiangiogenic treatment, which is currently a diagnostic challenge.[14] Our fast DKI protocol with very short postprocessing times enables real-time image reconstruction on the scanner and is therefore a promising tool for integrating multimodal evaluation of patients with glioma.

Only a small number of patients were included in this study, which might limit its power but can also be regarded as a strength,

because we still showed a significant difference between tumor grades. We aimed to compare our new method with that of 2 previously published studies in which a data volume of approximately the same scale was investigated, and we could reproduce most of their results with a fast sequence that maps MK′ on the basis of only 13 images (2 minutes 46 seconds in our case) and a DKI postprocessing time of just a few seconds. Other metrics that evaluate directional non-Gaussianity, such as axial or radial kurtosis, have been described and may be of interest, because they are likely to reveal different and supplemental information about microstructure.[15] These kurtosis metrics cannot be estimated from the data, because they are derived from the full kurtosis tensor, and reliable estimation of the tensor would require the measurement of additional diffusion directions and the nonlinear fitting of the results to a diffusion model. These requirements would add considerably to the scanning and postprocessing times, which would be particularly inexpedient in clinical applications. As a result, the significance of these measures for tumor grading was not evaluated in this study. Axial and radial kurtosis were assessed by Van Cauter et al,[7] but the diagnostic impact of these parameters did not differ considerably from the MK in their study. A limitation of our study is that some of the patients with GBM received steroid treatment at the time of imaging. Steroids might have an influence on MK, MK′, and MD values by reducing the amount of edema. We are not able to correct for this effect. Finally, potential partial volume effects caused by co-registration steps might have influenced the results. We inspected our data for co-registration errors closely and adjusted them thoroughly to avoid the inclusion of CSF and necrosis, but inexactness was still possible.

The increasing MK in GBM is interesting with regard to the underlying microstructural characteristics of these tumors. Little is known about what might cause MK alterations, but it has been postulated that changes in the quantity of cell membranes and the amount of intracellular and extracellular protein are likely to influence the degree of non-Gaussianity.[16] The chaotic vascular architecture of and micronecrosis in GBMs might contribute further to the microstructural complexity causing an increase in MK. The association between increased cellularity and restricted water diffusion, estimated by MD, was investigated in several previous studies,[17-19] but the utility of this parameter was not always reconfirmed.[20,21] A weak correlation can be a result of concomitant MD increases caused by edema and micronecrosis in HGGs, and it remains to be shown if MK can add important diagnostic information. MK calculated from a conventional DKI sequence and MK′ obtained by our fast method are distinct quantities, because they are estimated in a different way. However, it was shown that they are highly correlated both in normal brain[9] and in acute stroke tissue.[22] We are not able to compare both approaches, because only the rapid version was acquired, but we expect this correlation to be the same in our patients and avail ourselves of the comparison with literature values.

CONCLUSIONS

We have shown that MK′ is a valuable tool for glioma grading and that our fast DKI method provides robust measurements comparable to those from the literature. These results enable larger-scale implementation of DKI in clinical studies and allow for the investigation of its significance in treatment evaluation, diagnosis of LGG dedifferentiation, and detection of recurrent disease. Moreover, imaging with a rapid DKI technique in clinically unstable patients, such as those after a stroke or trauma, has the potential to provide new insights into the pathophysiology and longitudinal progression of these diseases.[22-25]

ACKNOWLEDGMENTS

We thank Kim Mouridsen for his advice on the statistical analysis. B.H. acknowledges support from NIH 1R01EB012874–01 and Aarhus University's nanomedicine center (LUNA).

Disclosures: Anna Tietze—*RELATED*: *Grant*: Danish Ministry of Science, Technology and Innovation's University Investment Grant (MINDLab).* Mikkel Hansen—*RELATED*: *Grant*: Danish Ministry of Science, Technology and Innovation*; *UNRELATED*: *Stock/Stock Options*: Combat Stroke, *Comments*: co-founder, shareholder, and member of the board (unpaid) of the spin-out company named "Combat Stroke." Lief Østergaard—*RELATED*: *Grant*: Danish Ministry for Research and Innovation.* Sune Nørhøj Jespersen—*UNRELATED*: *Grants/Grants Pending*: The Lundbeck Foundation, *Comments*: 2,000,000 DKK to a project on biological interpretations of diffusion imaging (mainly postdoctoral salary); *Patents (planned, pending, or issued)*: patent pending on the fast-diffusion kurtosis method used in the study and 2 related to measurements of capillary blood flow heterogeneity. Siemens has shown limited interest in the first patent. Torben E. Lund—*RELATED*: *Grant*: Danish Agency for Science, Technology and Innovation,* *Comments*: Aarhus University received 120,000,000 DKK to the UNIK project MINDLab. B. Hansen—*RELATED*: *Grant*: salary and work supported by the Danish Ministry of Science, Technology and Innovation's University Investment Grant (MINDLab).* My work was also supported by National Institutes of Health 1R01EB012874-01.* *Money paid to the institution.

REFERENCES

1. Gerstner ER, Sorensen AG. **Diffusion and diffusion tensor imaging in brain cancer.** *Semin Radiat Oncol* 2011;21:141–46
2. Jensen JH, Helpern JA, Ramani A, et al. **Diffusional kurtosis imaging: the quantification of non-Gaussian water diffusion by means of magnetic resonance imaging.** *Magn Reson Med* 2005;53:1432–40
3. Zhuo J, Xu S, Proctor JL, et al. **Diffusion kurtosis as an in vivo imaging marker for reactive astrogliosis in traumatic brain injury.** *Neuroimage* 2012;59:467–77
4. Veraart J, Poot DH, Van Hecke W, et al. **More accurate estimation of diffusion tensor parameters using diffusion kurtosis imaging.** *Magn Reson Med* 2011;65:138–45
5. Steven AJ, Zhuo J, Melhem ER. **Diffusion kurtosis imaging: an emerging technique for evaluating the microstructural environment of the brain.** *AJR Am J Roentgenol* 2014;202:W26–33
6. Raab P, Hattingen E, Franz K, et al. **Cerebral gliomas: diffusional kurtosis imaging analysis of microstructural differences.** *Radiology* 2010;254:876–81
7. Van Cauter S, Veraart J, Sijbers J, et al. **Gliomas: diffusion kurtosis MR imaging in grading.** *Radiology* 2012;263:492–501
8. Lu H, Jensen JH, Ramani A, et al. **Three-dimensional characterization of non-Gaussian water diffusion in humans using diffusion kurtosis imaging.** *NMR Biomed* 2006;19:236–47
9. Hansen B, Lund TE, Sangill R, et al. **Experimentally and computationally fast method for estimation of a mean kurtosis.** *Magn Reson Med* 2013;69:1754–60
10. Hansen B, Lund TE, Sangill R, et al. **Erratum: Experimentally and Computationally Fast Method for Estimation of a Mean Kurtosis.** *Magn Reson Med* 2014;71:2250
11. Jensen JH, Hu C, Helpern JA. **Rapid data acquisition and postprocessing for diffusional kurtosis imaging.** In: *17th Annual Meeting of ISMRM*, Honolulu, Hawaii. April 18–24, 2009
12. Lev MH, Ozsunar Y, Henson JW, et al. **Glial tumor grading and outcome prediction using dynamic spin-echo MR susceptibility mapping compared with conventional contrast-enhanced MR:**

confounding effect of elevated rCBV of oligodendrogliomas [corrected]. *AJNR Am J Neuroradiol* 2004;25:214–21
13. Jain R, Poisson LM, Gutman D, et al. **Outcome prediction in patients with glioblastoma by using imaging, clinical, and genomic biomarkers: focus on the nonenhancing component of the tumor.** *Radiology* 2014;272:484–93
14. Ellingson BM, Cloughesy TF, Lai A, et al. **Quantitative volumetric analysis of conventional MRI response in recurrent glioblastoma treated with bevacizumab.** *Neuro Oncol* 2011;13:401–09
15. Carmeliet P, De Smet F, Loges S, et al. **Branching morphogenesis and antiangiogenesis candidates: tip cells lead the way.** *Nat Rev Clin Oncol* 2009;6:315–26
16. Maier SE, Sun Y, Mulkern RV. **Diffusion imaging of brain tumors.** *NMR Biomed* 2010;23:849–64
17. Hilario A, Ramos A, Perez-Nunez A, et al. **The added value of apparent diffusion coefficient to cerebral blood volume in the preoperative grading of diffuse gliomas.** *AJNR Am J Neuroradiol* 2012;33:701–07
18. Khayal IS, Polley MY, Jalbert L, et al. **Evaluation of diffusion parameters as early biomarkers of disease progression in glioblastoma multiforme.** *Neuro Oncol* 2010;12:908–16
19. Moffat BA, Chenevert TL, Lawrence TS, et al. **Functional diffusion map: a noninvasive MRI biomarker for early stratification of clinical brain tumor response.** *Proc Natl Acad Sci U S A* 2005;102:5524–29
20. Castillo M, Smith JK, Kwock L, et al. **Apparent diffusion coefficients in the evaluation of high-grade cerebral gliomas.** *AJNR Am J Neuroradiol* 2001;22:60–64
21. Rose S, Fay M, Thomas P, et al. **Correlation of MRI-derived apparent diffusion coefficients in newly diagnosed gliomas with [^{18}F]-fluoro-L-dopa PET: what are we really measuring with minimum ADC?** *AJNR Am J Neuroradiol* 2013;34:758–64
22. Sun PZ, Wang Y, Mandeville E, et al. **Validation of fast diffusion kurtosis MRI for imaging acute ischemia in a rodent model of stroke.** *NMR Biomed* 2014;27:1413–18
23. Taoka T, Fujioka M, Sakamoto M, et al. **Time course of axial and radial diffusion kurtosis of white matter infarctions: period of pseudonormalization.** *AJNR Am J Neuroradiol* 2014;35:1509–14
24. Hori M, Fukunaga I, Masutani Y, et al. **Visualizing non-Gaussian diffusion: clinical application of q-space imaging and diffusional kurtosis imaging of the brain and spine.** *Magn Reson Med Sci* 2012;11:221–33
25. Jensen JH, Falangola MF, Hu C, et al. **Preliminary observations of increased diffusional kurtosis in human brain following recent cerebral infarction.** *NMR Biomed* 2011;24:452–57

Influence of Resting-State Network on Lateralization of Functional Connectivity in Mesial Temporal Lobe Epilepsy

L. Su, J. An, Q. Ma, S. Qiu, and D. Hu

ABSTRACT

BACKGROUND AND PURPOSE: Although most studies on epilepsy have focused on the epileptogenic zone, epilepsy is a system-level disease characterized by aberrant neuronal synchronization among groups of neurons. Increasingly, studies have indicated that mesial temporal lobe epilepsy may be a network-level disease; however, few investigations have examined resting-state functional connectivity of the entire brain, particularly in patients with mesial temporal lobe epilepsy and hippocampal sclerosis. This study primarily investigated whole-brain resting-state functional connectivity abnormality in patients with mesial temporal lobe epilepsy and right hippocampal sclerosis during the interictal period.

MATERIALS AND METHODS: We investigated resting-state functional connectivity of 21 patients with mesial temporal lobe epilepsy with right hippocampal sclerosis and 21 neurologically healthy controls. A multivariate pattern analysis was used to identify the functional connections that most clearly differentiated patients with mesial temporal lobe epilepsy with right hippocampal sclerosis from controls.

RESULTS: Discriminative analysis of functional connections indicated that the patients with mesial temporal lobe epilepsy with right hippocampal sclerosis exhibited decreased resting-state functional connectivity within the right hemisphere and increased resting-state functional connectivity within the left hemisphere. Resting-state network analysis suggested that the internetwork connections typically obey the hemispheric lateralization trend and most of the functional connections that disturb the lateralization trend are the intranetwork ones.

CONCLUSIONS: The current findings suggest that weakening of the resting-state functional connectivity associated with the right hemisphere appears to strengthen resting-state functional connectivity on the contralateral side, which may be related to the seizure-induced damage and underlying compensatory mechanisms. Resting-state network–based analysis indicated that the compensatory mechanism among different resting-state networks may disturb the hemispheric lateralization.

ABBREVIATIONS: DMN = default-mode network; FC = functional connectivity or connection; HS = hippocampal sclerosis; mTLE = mesial temporal lobe epilepsy; R-mTLE = mesial temporal lobe epilepsy with right hippocampal sclerosis; RS = resting-state; RSN = resting-state network; TLE = temporal lobe epilepsy

Up to 0.1% of the human population worldwide has temporal lobe epilepsy (TLE), and 60%–70% of these cases are classified as mesial temporal lobe epilepsy (mTLE).[1] mTLE is a drug-refractory form of human epilepsy that is typically characterized by hippocampal sclerosis (HS). Surgical intervention can prevent temporal lobe seizure recurrence in patients with mTLE.[2] Aberrant neuronal synchronization is believed to be as important as abnormal excitability with respect to epileptic seizure occurrences,[3,4] and resting-state functional connectivity (RS-FC) analysis is an effective approach for examining neural synchronization.

Debilitating mTLE seizures are believed to originate primarily from specific anatomic divisions of the temporal lobe.[2]

Received October 1, 2014; accepted after revision January 25, 2015.

From the College of Mechatronics and Automation (L.S., Q.M., D.H.), National University of Defense Technology, Changsha, Hunan, People's Republic of China; Department of Medical Imaging (J.A., S.Q.), First Affiliated Hospital of Guangzhou University of Chinese Medicine, Guangzhou, Guangdong, People's Republic of China; and Department of Information Engineering (L.S.), Officers College of Chinese Armed Police Force, Chengdu, Sichuan, China.

This study was supported by the National Basic Research Program of China (2011CB707802, 81271389, 81471251, 91420302, and 61420106001).

Drs Longfei Su and Jie An contributed equally to this work.

Please address correspondence to Dewen Hu, PhD, No. 109, Deya Rd, Kaifu District, Changsha City, Hunan Province, People's Republic of China; e-mail: dwhu@nudt.edu.cn; and Shijun Qiu, PhD, First Affiliated Hospital of Guangzhou University of Chinese Medicine, 16 Airport Rd, Guangzhou, Guangdong, 510405, People's Republic of China; e-mail: qiu-sj@163.com

Indicates open access to non-subscribers at www.ajnr.org
Indicates article with supplemental on-line appendix and table.
Indicates article with supplemental on-line photo.
Evidence-Based Medicine Level 2.
http://dx.doi.org/10.3174/ajnr.A4346

Demographic and clinical data

	Mean (Range)		
	R-mTLE	Control	*P* Value
Sample size	21	21	–
Sex (M/F)	9:12	9:12	1.000[a]
Age (yr)	28.5 ± 7.9 (18–43)	25.1 ± 5.7 (17–37)	.187[b]
Education (yr)	11.6 ± 2.3 (9–16)	11.5 ± 2.7 (6–16)	.891[b]
Onset (yr)	15.7 ± 9.8 (2–34)	–	–
Duration (yr)	12.9 ± 7.4 (3–33)	–	–

[a] Pearson χ^2 test.
[b] Two-sample *t* test.

However, investigations involving large-scale network analysis have challenged this traditional conceptualization.[3,5-7] Furthermore, several studies have reported an mTLE-related decrease in basal RS-FC in the epileptogenic hemisphere in brains of patients with mTLE, accompanied by contralateral compensatory mechanisms.[8,9]

Many mTLE studies have focused on the epileptogenic zone, and most analyses that have investigated regions outside the hippocampus have focused on structural imaging technology.[1,10,11] In contrast, few whole-brain functional network analyses of mTLE have been conducted. Structural MRI or electroencephalography or both incompletely measure temporal changes during the disease process,[5] while resting-state fMRI takes serial images during a time period that can capture the dynamic and evolving changes related to epilepsy.[12] The RS-FC derived from the fMRI images reflects functional aberrations and offers a network perspective on the psychiatric and cognitive complications of mTLE.[7,13] We hypothesized that mesial temporal lobe epilepsy with right hippocampal sclerosis (R-mTLE) is a functional disease involving disturbances of RS-FC over the entire brain rather than a local disease that is confined to the temporal lobe. To test this hypothesis, we applied the multivariate pattern analysis method in this study.[14]

MATERIALS AND METHODS

Participants

We studied 21 consecutive right-handed patients with R-mTLE who underwent presurgical evaluation at Guangdong 999 Brain Hospital. Diagnoses of R-mTLE and the lateralization of the seizure foci of this disease were determined via comprehensive evaluations that included examinations of the patients' detailed medical histories, video-electroencephalography telemetry, and neuroimaging. The presence of abnormally elevated T2 fluid-attenuated inversion recovery signals in the hippocampus was used as the diagnostic criterion for HS. In all patients, the HS site corresponded to the epileptogenic site. None of the patients with R-mTLE had mass lesions (tumor, vascular malformation, or malformations of cortical development) or traumatic brain injury. HS was detected in all patients following qualitative histopathologic analysis.[15] Twenty-one healthy right-handed subjects were recruited as controls; these controls were matched to the examined patients with R-mTLE with respect to age, sex, and years of education (Table). All controls were medically healthy and free of any neurologic or psychiatric disorders at the time of the study.

Standard Protocol Approvals, Registrations, and Patient Consents

This study was approved by the Research Ethics Review Board of the Institute of Mental Health of Southern Medical University. Informed consent was obtained from each subject.

Imaging Protocol

During the experiments, subjects were instructed to keep their eyes closed, relax, and remain awake. Subjects were asked not to perform any specific cognitive exercises. After each session, the subjects were asked whether they had fallen asleep during the preceding session, and all subjects confirmed that they had remained awake throughout the experiment. Functional MR images were acquired by using an Intera 1.5T MR scanner (Philips Healthcare, Best, the Netherlands) with a gradient-echo EPI sequence. We used the following imaging parameters: TR/TE = 3000/50 ms; thickness/gap = 4.5/0 mm; FOV = 230 × 230 cm; flip angle = 90°; matrix = 128 × 128; sections = 31. The duration of each functional resting-state session was approximately 8 minutes, and 160 volumes were obtained for each patient.

Data Preprocessing

Data preprocessing was performed by using the Statistical Parametric Mapping software package (SPM8; http://www.fil.ion.ucl.ac.uk/spm/software/spm12). For each subject, the first 10 volumes of scanning data were discarded to reduce magnetic saturation effects. The remaining 150 volumes of data were corrected by registering and reslicing for head motion. Subsequently, these volumes were normalized to standard echo-planar imaging templates in Montreal Neurological Institute space. The resulting images were spatially smoothed with a Gaussian filter with an 8-mm full width at half maximum kernel, detrended to remove linear trends, and temporally filtered with a Chebyshev bandpass filter (0.01–0.08 Hz) to reduce artifacts caused by respiration or cardiac action. All fMRI volumes were registered to a Montreal Neurological Institute template before further time-series extraction for ROIs. The Montreal Neurological Institute coordinates for the ROIs in this template are shown in the On-line Table. Each regional mean time-series was further corrected for the effects of WM, CSF, and head movement by regression on the time-series of WM, CSF signal and translations, and rotations of the head estimated in the course of initial movement correction by image realignment. The residuals of these regressions constituted the set of regional mean time-series used for functional connectivity analysis.[16]

The center coordinates were defined as the areas of peak activity identified in 5 meta-analyses that focused on error processing, default-mode network (DMN), memory, language, and sensorimotor functions. Although these functional networks were identified in task-related studies, they have been confirmed by many previous resting-state fMRI studies and were further used as resting-state networks (RSNs).[17-20] Inevitably, using this pre-existing localization of ROIs can introduce bias; however, using a priori ROIs also offers a substantial increase in power.[4]

We used the Pearson correlation coefficient to evaluate the functional connectivity between each pair of ROIs. This approach allowed us to obtain symmetric 160 × 160 matrices that captured

the resting-state functional network activity of each subject. After removing the 160 diagonal elements of each functional connectivity matrix, we extracted the upper triangle elements of these connection matrices as classification features; therefore, the feature space for classification was spanned by the remaining $(160 \times 159) / 2 = 12{,}720$ dimensional feature vectors. In this article, the functional connections (FCs) for classification are referred to as "features."

Alternatively, an unsampled version of the automatic anatomic labeling template was introduced for ROI definition, which segmented the cerebrum into 600 ROIs. Further analysis by using this template and selection of ROI radii are displayed in "ROI Definition for the Entire Brain" in the On-Line Appendix.

Identification of Features with High Discriminative Power

The support vector machine recursive feature elimination algorithm was originally proposed for gene selection[21] and has been applied in fMRI studies for the identification of multiple active voxels.[22] The support vector machine recursive feature elimination algorithm combines the support vector machine and recursive feature elimination approaches to produce a multivariate feature-selection algorithm. In the support vector machine classification procedure, all samples are categorized into 2 parts. One portion of the samples with class labels was used to train the classifier, called "training samples." The training samples can be used to identify the parameters of the classifier. All training samples constructed the training set. The other portion of the samples without class labels was used to test the effectiveness of the classifier called "testing samples." The classifier can predict the class labels of the testing samples. The support vector machine classification was applied to the training set, and the discriminative weight $w(f_i)$ of feature f_i was obtained for each training sample. The scoring function was defined as follows:

$$Score\ (f_i) = \frac{\sum_{k=1}^{n} |w_k(f_i)|}{n}$$

In the equation above, f_i represents the ith feature, $w_k(f_i)$ represents the discriminative weight of feature f_i in the kth sample, and n is the number of training samples. The features $f_i, i = 1,2,\cdots, n$ were then ranked by $Score\ (f_i), i = 1,2,\cdots, n$, and the feature with the smallest score was eliminated. This procedure was repeated on the retained features until all features were eliminated. To accelerate the computational process, we eliminated the half of the remaining features with the smallest scores in each iteration of the algorithm.

The details of identification of discriminative FCs are displayed in "Cross-Validation and Consensus Functional Connections" in the On-line Appendix.

Support Vector Classification and Performance Evaluation

Support Vector Classification. After the dataset of features had been prepared, linear support vector machines were used to solve the classification problem.[23] All pattern analyses were implemented by using the LIBSVM software package (http://www.csie.ntu.edu.tw/~cjlin/libsvm/).

Performance Evaluation. Based on the cross-validation results, the performance of a classifier was quantified in terms of the generalization rate, sensitivity, and specificity.[24] Notably, "sensitivity" represents the proportion of patients who were correctly classified, and "specificity" represents the proportion of controls who were correctly classified. The overall proportion of correctly classified samples was evaluated by using the generalization rate.

RESULTS

Classification Results

The network analysis was based on the classification results. The classification accuracy rates relative to the number of selected FCs are indicated in Fig 1. Classification accuracies (expressed in terms of the generalization rate) of >90% were achieved in classification approaches that used relatively few (approximately 10–50) FCs.

In particular, when the first 8 FCs were used, a sensitivity of 95.2% and a specificity of 95.2% were obtained (only 1 patient and 1 control participant were not successfully identified). Furthermore, if the support vector machine classification boundary was replaced with the optimal classification boundary, a sensitivity of 95.2% and a specificity of 100% were obtained (only 1 patient was not successfully identified), which are reflected in Fig 2*B*. When the first 23 connections were used, a sensitivity of 90.5% and a specificity of 100% were obtained (only 2 patients were not successfully classified). Furthermore, if the optimal classification boundary was used, a sensitivity of 100% and a specificity of 100% were obtained (all subjects were correctly classified), which were also reflected by the receiver operating characteristic in Fig 2*D*.

Using the generalization rate as the applicable statistic, we determined the permutation distribution of estimates, which are shown in Fig 2*A*, -*C*; the results indicated that the classifier learned the relationship between the data and the labels with a <.0001 probability of being incorrect.

Because a leave-one-out cross-validation approach was used, the results represent estimations of the classification accuracy for the scanning results for a new subject; thus, these findings have a direct diagnostic relevance. The receiver operating characteristic curves of the classifiers, which were determined by using a leave-one-out cross-validation approach, are depicted in Fig 2*B*, -*D*. The area under the receiver operating characteristic curve for the classification method was 99.6% when 8 FCs were used and 100% when 23 FCs were used.

In the present study, each ROI was defined as a sphere with a given center coordinate and a radius of 5 mm. Radii of 4 and 7.5 mm were also used for ROI definitions, but the classification results were not better than those of the radius of 5 mm, which are displayed in On-line Fig 1.

Functional Connectivity Changes

The RS-FC analysis in this study primarily focused on R-mTLE-related alterations in the strengths of FCs. The first finding of this study was the hemispheric lateralization of the changes in RS-FC. In summary, weaker connections in patients with R-mTLE relative to healthy controls were mainly located in the right hemi-

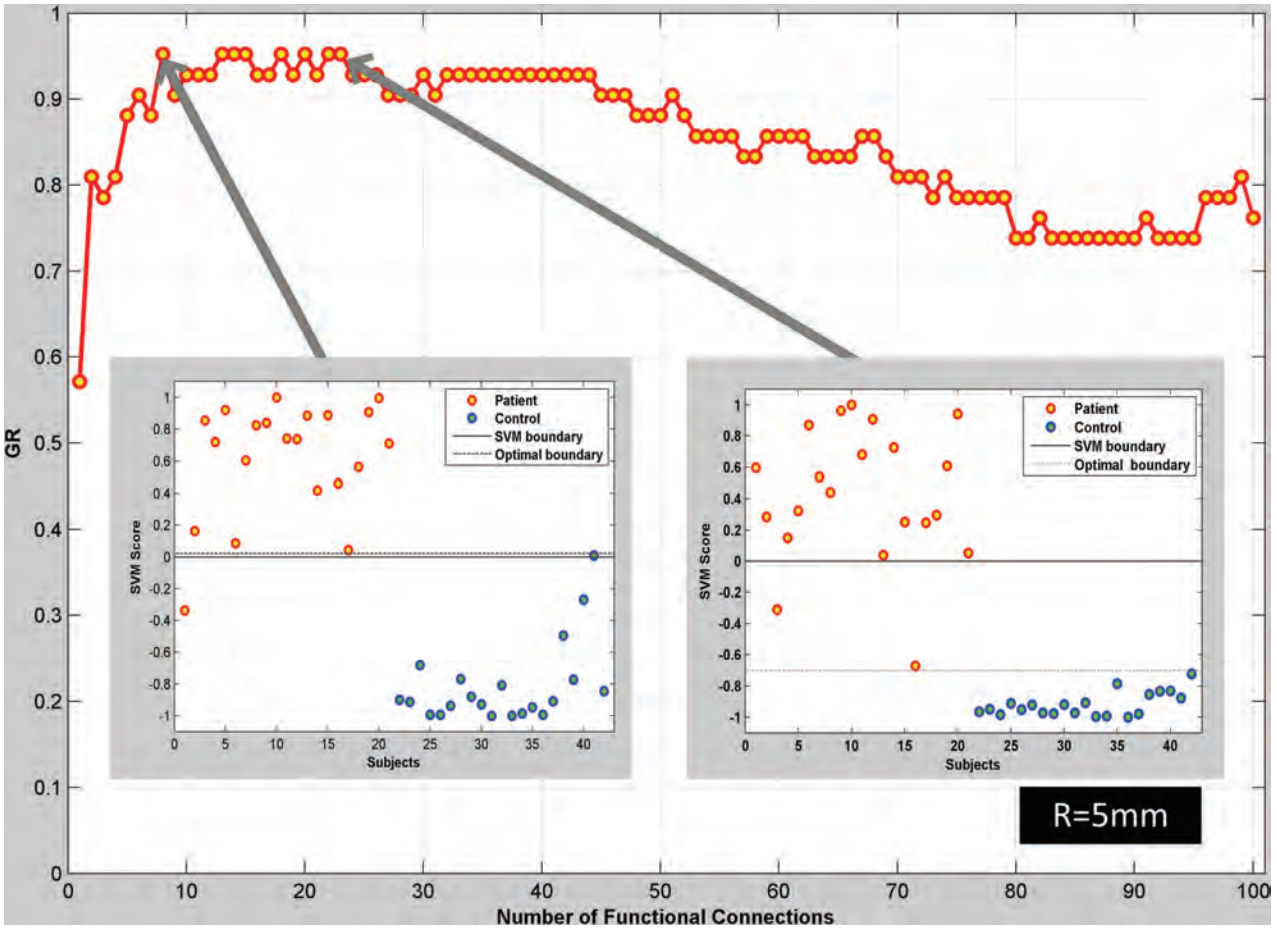

FIG 1. Classification results for patients with R-mTLE and healthy controls via leave-one-out cross-validation. The x-axis indicates the number of connections involved in the classification; the y-axis indicates classification accuracy (as represented by the generalization rate). The subplot illustrates the prediction results of all subjects with the highest accuracy, which used the first 8 and the first 23 most discriminative connections.

sphere (Fig 3*A*), and stronger connections in patients with R-mTLE relative to healthy controls were mainly distributed in the left hemisphere (Fig 3*B*).

These altered FCs may be categorized as either intranetwork connections, connecting nodes within the same functional network; or internetwork connections, connecting nodes from 2 different functional networks. The second finding of this study was that compared with healthy controls, patients with R-mTLE showed a different internetwork pattern compared with the intranetwork connectivity changes.

Most intranetwork FCs were weaker, while more internetwork FCs were stronger in the patients with R-mTLE compared with controls (Fig 4*A*, -*B*).

DISCUSSION

In this study, we sought to validate the hypothesis that R-mTLE is a disease with RSN disturbances. Multivariate pattern analysis results indicated that R-mTLE-related changes in functional connectivity predominantly follow this pattern: Weaker connections were primarily distributed in the right hemisphere, while most of the stronger connections were in the left hemisphere. Additional RSN analysis demonstrated that most of the altered FCs—not strictly associated with hemispheric lateralization—were intranetwork FCs; most of the FCs—which primarily obeyed the hemispheric lateralization—were internetwork FCs. Specifically, weaker connections were localized within the DMN, cingulo-opercular network, and frontoparietal network, whereas stronger connections were localized within the sensorimotor network.

RSN Analysis of Brain Regions beyond the Hippocampus

To validate the hypothesis that mTLE is a network disease, some studies have investigated abnormalities in brain regions other than the hippocampus.[1,6,10,11,25,26] In addition, the support vector classification accuracy of structural MRI and DTI datasets that exclude the hippocampus can reach approximately 90%.[10] Given that resting-state fMRI can capture dynamic and evolving changes related to epilepsy,[12] we applied RS-FC on the basis of fMRI data. Although the hippocampus is particularly important for the identification of R-mTLE, this study sought to demonstrate that R-mTLE is a disease affecting the RSN of the entire brain rather than a local disease that is limited to hippocampal aberrations. The ROI template used in this investigation, which facilitated the RSN analysis and excluded the hippocampus, achieved classification accuracies up to 95%. This result provides important evidence that R-mTLE is a network disease characterized by functional aberrations distributed across the entire brain. In addition, we defined the epileptogenic zone through the use of a 2-sample *t* test, which compared patients with R-mTLE with healthy con-

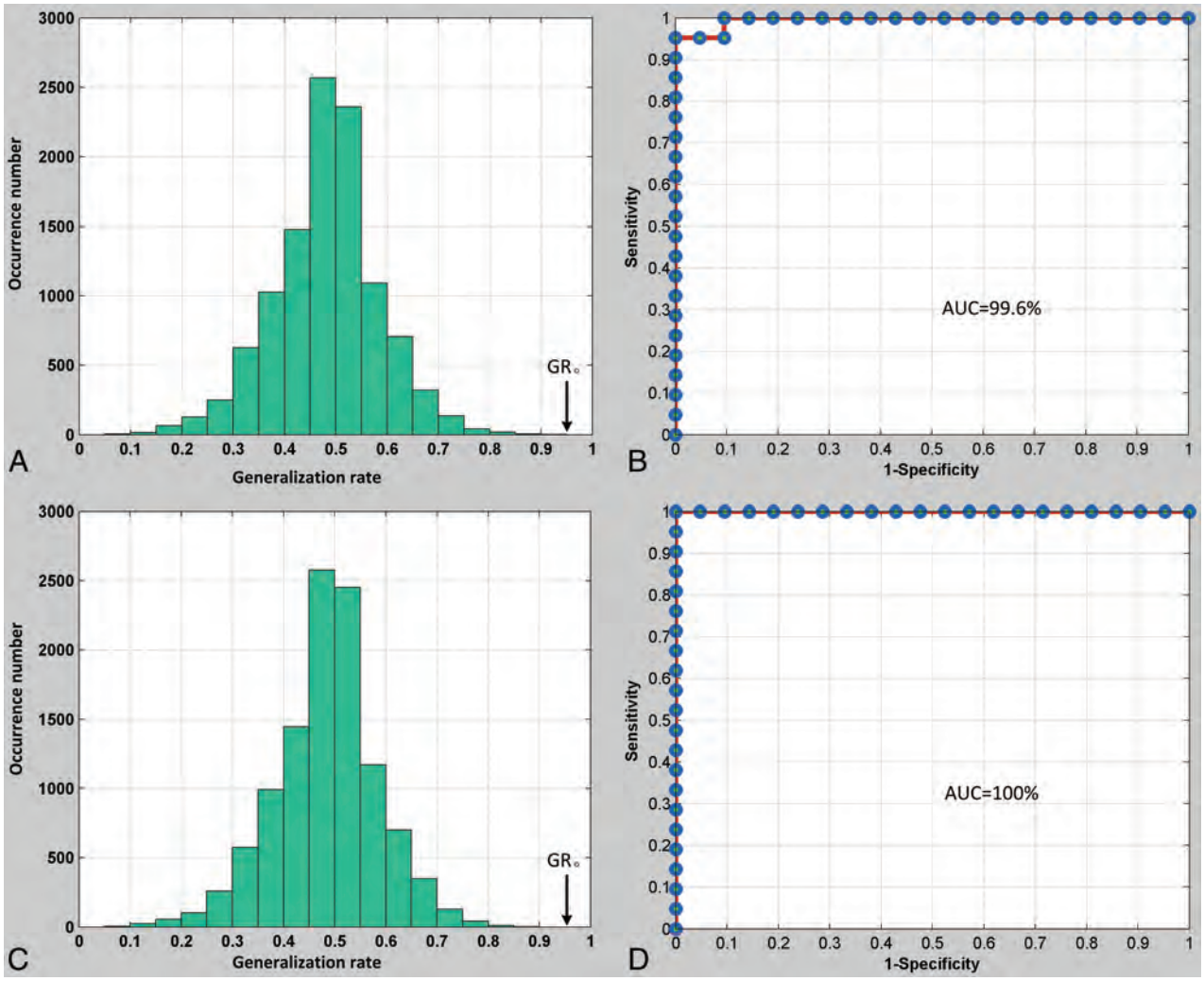

FIG 2. Classification evaluation. *A*, The permutation distribution of estimates produced by the linear support vector machine classifier (with 10,000 repetitions) if the first 8 most discriminating features are used. The x- and y-axes indicate the generalization rate and occurrence number; GR_0, is the generalization rate obtained by the classifier trained on the actual class labels. Using the generalization rate as the test statistic, this figure demonstrates that the classifier learned the relationship between the data and the labels with a probability of being incorrect of <.0001. *B*, Receiver operating characteristic curves indicate the overall classification performance of the functional connectivity–based classification of patients with R-mTLE and healthy controls. The area under the receiver operating characteristic curve (AUC) was 99.6% when the first 8 connections were used for classification. *C*, The permutation distribution of estimates produced by the linear support vector machine classifier (with 10,000 repetitions) if the first 23 most discriminating features are used. *D*, Receiver operating characteristic curves indicate the overall classification performance of the functional connectivity–based classification of patients with R-mTLE and healthy controls. The area under the receiver operating characteristic curve was 100% when the first 23 connections were involved in the classification.

trols, and this zone was added to the ROI template. Whole-brain functional connectivity was determined on the basis of the 160 + 1 ROIs mentioned above. The resulting classification accuracy was not improved, and the identified discriminative connections were identical to the results presented in this article.

Identification of FCs

From a functional integration perspective, RS-FC analysis exhibits advantages relative to other modalities,[27] particularly when multivariate pattern analysis methods are used.[28] The support vector machine recursive feature elimination method can predict group membership at an individual subject level, and the results obtained by using this method may be clinically useful[29] because the results can include unique information that may be overlooked by univariate voxel-based morphometry approaches.[30,31] As indicated in Fig 1, maximal classification accuracy (generalization rate = 95.2%, area under the receiver operating characteristic curve = 100%) was obtained by using only 23 features. We assigned connection strengths on the basis of the occurrence of these connections in the leave-one-out cross-validation results (Fig 3). As the number of features increased beyond 23, the classification accuracy generally decreased. This result suggests that only a few of the 12,720 examined connections were highly discriminative.

Different R-mTLE-Related RS-FC Changes in the Epileptogenic and Contralateral Sides of the Brain

An initial finding of this study was that changes in RS-FC in patients with R-mTLE demonstrate hemispheric lateralization. Weaker FCs in patients with R-mTLE were primarily distributed in the right hemisphere (Fig 3*A*). However, most of the stronger FCs in the patients with R-mTLE were located in the left hemi-

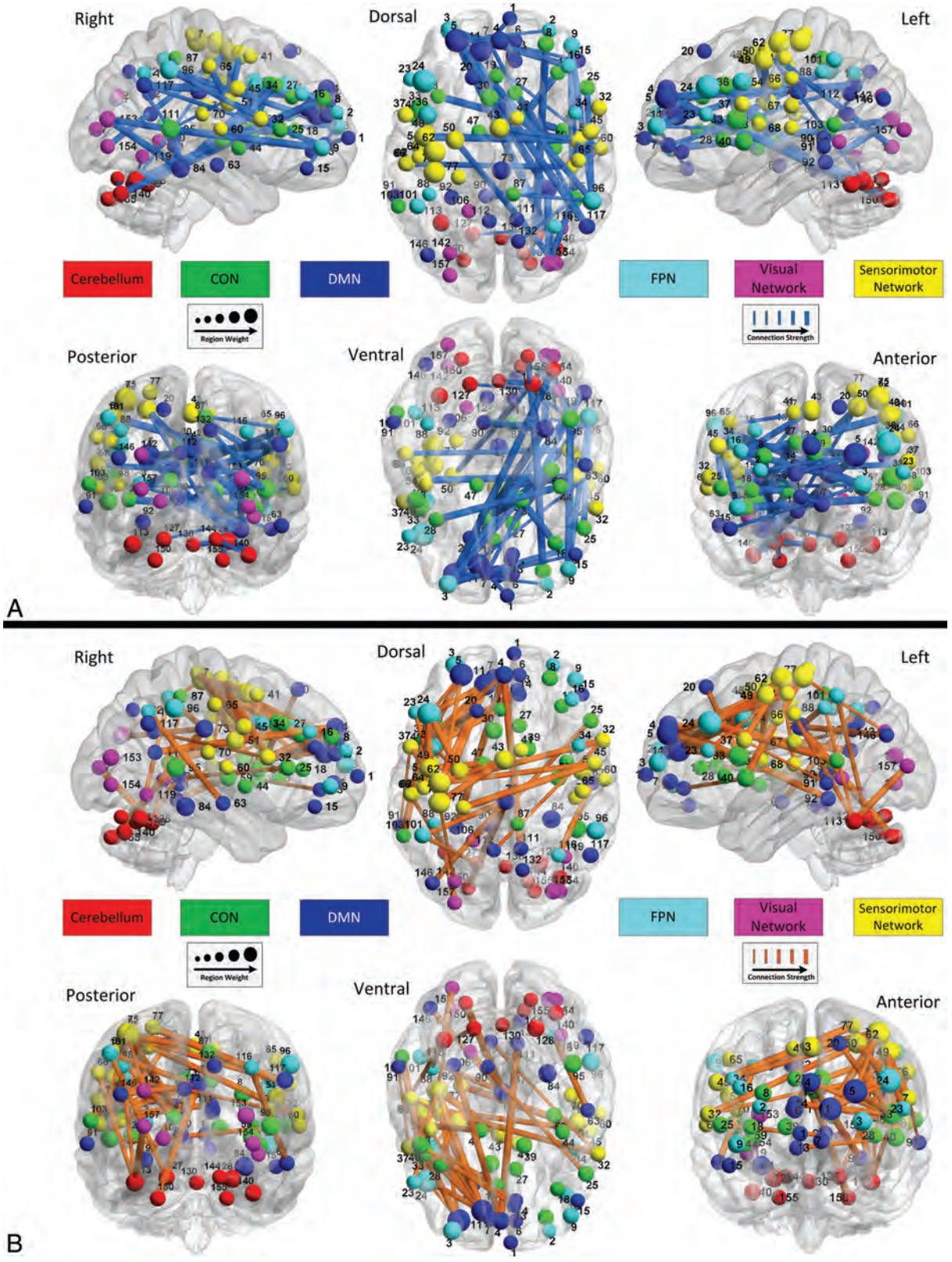

FIG 3. Region weights and connection strengths categorized by hemisphere. The connections are displayed in a surface rendering of a human brain. The thicknesses of the consensus connections in the leave-one-out cross-validation are scaled by their strengths (which were the normalized occurrences of the first 23 connections during all iterations of the leave-one-out cross-validation). *A*, Connections with lower strengths in patients with R-mTLE than in controls are depicted in light blue. *B*, Connections with greater strengths in patients with R-mTLE than in controls are displayed in orange. The ROIs related to the selected consensus connections are also scaled by their weights (calculated as the sum of the weights of all connections to and from the ROI) and are displayed. The ROIs are color-coded by functional network (cerebellum, red; cingulo-opercular network, green; DMN, blue; frontoparietal network, cyan; visual network, rose; and sensorimotor network, yellow). The numeric labels for the ROIs in this figure are provided in the On-line Table.

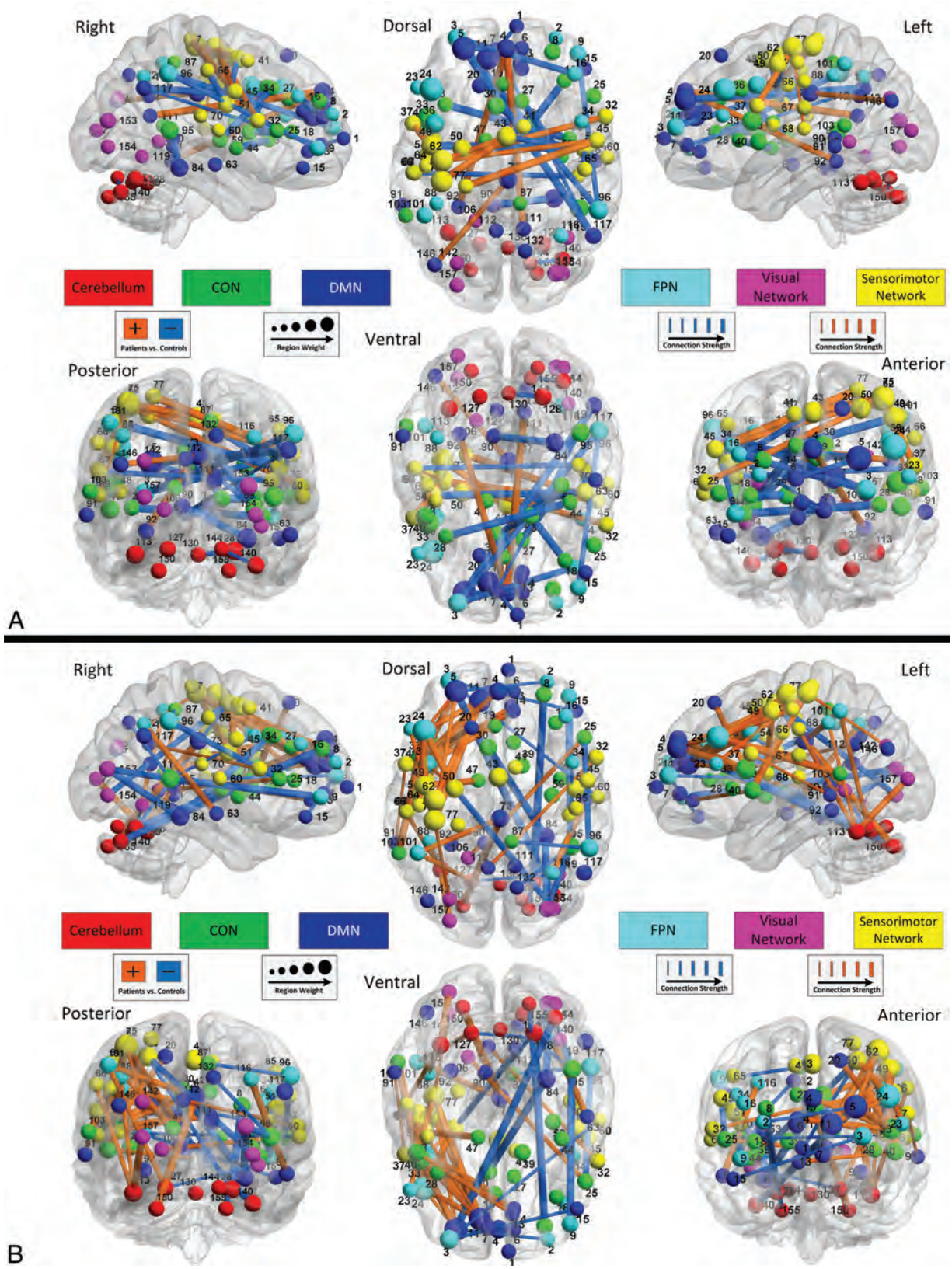

FIG 4. Region weights and connection strengths viewed from inter- and intranetwork perspectives. The connections are displayed in a surface rendering of a human brain. The thicknesses of the consensus connections in the leave-one-out cross-validation are scaled by their strengths (which were the normalized occurrences of the first 23 connections during all iterations of the leave-one-out cross-validation). *A*, Internetwork connections. *B*, Intranetwork connections. Connections with greater strengths in patients with R-mTLE than in controls are displayed in orange. Connections with lower strengths in patients with R-mTLE than in controls are depicted in light blue. The ROIs related to the selected consensus connections are also scaled by their weights (calculated as the sum of the weights of all connections to and from the ROI of interest) and are displayed. The ROIs are color-coded as in Fig 3.

sphere (Fig 3*B*). Previous studies have attributed the lateralization of RS-FC in mTLE to compensatory mechanisms in the human brain.[8,9] However, this conclusion was derived from RS-FC analyses that were restricted to the hippocampus and several other brain regions that are closely related to mTLE. Furthermore, only a small sample of patients with mTLE and even fewer patients with R-mTLE were examined in the prior studies. Our study provides further support for the hypothesis that patients with mTLE demonstrate decreased functional connectivity in the epileptogenic sides of their brains but exhibit contralateral compensatory mechanisms. First, our study focused on brain regions outside the hippocampus, thereby suggesting that the pathophysiology may be more widely distributed than previously recognized,. The weaker RS-FC in the contralateral hemisphere suggests a compensatory mechanism that involves the entire brain. Second, previous studies have examined only a small number of patients with R-mTLE. Relative to these prior studies, our investigation included a larger number of participants with R-mTLE.

Further evidence is needed to validate the hemispheric lateralization of the RS-FC in mTLE. To validate this hemispheric lateralization, we also investigated GM and WM concentrations and the GM and WM presenting with similar hemispheric lateralizations, which are detailed in "Voxel-Based Morphometric Analysis" in the Appendix and On-line Fig 2.

RSN Analysis of R-mTLE

The second finding of the current study is that the intranetwork FCs were weakened, while the internetwork RS-FC was increased. It is generally believed that the decrease in RS-FC reflects an impairment in the functional network related to the corresponding RSN, while an increased RS-FC may indicate enhanced function due to the compensatory mechanism.[32,33] Furthermore, most of the FCs that did not conform to the observed pattern of hemispheric lateralization were intranetwork FCs. In contrast, most internetwork FCs followed the observed laterality patterns. This result may indicate that as functional units, the RSN and the hemisphere influence each other.

Intranetwork FCs that were weakened in patients with R-mTLE relative to control subjects were mainly localized to the DMN cingulo-opercular network and frontoparietal network. In contrast, intranetwork FCs that were strengthened in patients with R-mTLE relative to control subjects were localized to the sensorimotor network. The DMN is characterized by task-induced deactivation, which is essential for maintaining baseline levels of brain activities related to self-awareness, episodic memory, and environmental monitoring.[34] In recent years, the DMN has been reported to be decreased in RS-FC and has attracted considerable attention in mTLE research.[35-37] Previous studies also found that the RS-FC in the frontoparietal network was decreased in mTLE.[37,38] The strength of most intranetwork connections in the DMN, cingulo-opercular network, and frontoparietal network was reduced in patients with R-mTLE relative to healthy controls in this study, consistent with a previous independent component analysis–based study.[38] This result may indicate that R-mTLE produces disturbances in executive control functions for the DMN, cingulo-opercular network, and fronto-parietal network, which are believed to be closely related to executive control tasks.[39-41] Patients with mTLE demonstrate apparent executive deficits.[42-44] In previous studies, the sensorimotor network had abnormal RS-FC and the patients with mTLE displayed cognitive impairments.[38,43,45] The increased RS-FC in the sensorimotor network in the current study may be a compensatory mechanism between the left and the right sensorimotor cortex as shown in Fig 3*B*.

In contrast, internetwork connections between the aforementioned RSNs were generally stronger in patients with R-mTLE than in control subjects. This phenomenon may have been produced by compensatory mechanisms. The increased RS-FC strength reflects increased spontaneous synchronization among brain regions, and previous studies have attributed increased RS-FC in mTLE to underlying compensatory mechanisms.[35] Several age-related studies have reported that the weakening of short-range connectivity and the strengthening of long-range connectivity during aging are driven by functional segregation and integration, respectively.[14,46,47] In addition, a published article reported that patients with mTLE demonstrated decreased local functional connectivity and increased intrahemispheric functional connectivity.[33] However, the results obtained in our study suggest that R-mTLE induces impairments in specific functional networks and that the functional networks become more integrated to compensate for deficits caused by these impairments. We propose that the compensatory mechanism involves interactions between distinct functional units and cannot simply be assessed in terms of anatomic distance.

Finally, comparing Figs 3 and 4, we found that most intranetwork FCs were interhemispheric FCs, which indicates that the compensatory mechanism among different RSNs may disturb the hemispheric lateralization.

Limitations and Future Work

There were several limitations in our study. First, it examined a small sample. Our findings must be replicated with larger datasets before the findings of this investigation can be broadly generalized to patient populations with R-mTLE. Second, mesial temporal lobe epilepsy with left HS was not considered in our study. In future studies, we plan to address these limitations by conducting multimodal network analyses to investigate patients with mesial temporal lobe epilepsy with left HS and R-mTLE.

CONCLUSIONS

Based on the classification results, we found that compared with connections of the healthy controls, weakened connections of the patients with R-mTLE were primarily distributed in the right hemisphere, whereas the majority of strengthened connections were located in the left hemisphere. Additional RSN analyses demonstrated that most of the altered FCs—not strictly associated with hemispheric laterality—were intranetwork FCs; most of the FCs—which tended to obey the hemispheric laterality—were internetwork FCs.

ACKNOWLEDGMENTS

The authors thank the anonymous reviewers for their constructive suggestions and Ann M. Hermundstad for providing us the unsampled version of the automatic anatomic labeling template.

Disclosures: Longfei Su—*RELATED*: *Grant*: National Natural Science Foundation of China,* *Comments*: National Basic Research Program of China (2011CB707802) and the National Natural Science Foundation of China (61003202, 61005084). *Money paid to the institution.

REFERENCES

1. Mueller SG, Laxer KD, Barakos J, et al. **Widespread neocortical abnormalities in temporal lobe epilepsy with and without mesial sclerosis.** *Neuroimage* 2009;46:353–59
2. Engel J Jr. **Mesial temporal lobe epilepsy: what have we learned?** *Neuroscientist* 2001;7:340–52
3. Spencer SS. **Neural networks in human epilepsy: evidence of and applications for treatment.** *Epilepsia* 2002;43:219–27
4. Engel J, Thompson PM, Stern JM, et al. **Connectomics and epilepsy.** *Curr Opin Neurol* 2013;26:186–94
5. Maccotta L, He BJ, Snyder AZ, et al. **Impaired and facilitated functional networks in temporal lobe epilepsy.** *Neuroimage Clin* 2013;2:862–72
6. Voets NL, Beckmann CF, Cole DM, et al. **Structural substrates for resting network disruption in temporal lobe epilepsy.** *Brain* 2012;135:2350–57
7. Cataldi M, Avoli M, de Villers-Sidani E. **Resting state networks in temporal lobe epilepsy.** *Epilepsia* 2013;54:2048–59
8. Bettus G, Bartolomei F, Confort-Gouny S, et al. **Role of resting state functional connectivity MRI in presurgical investigation of mesial temporal lobe epilepsy.** *J Neurol Neurosurg Psychiatry* 2010;81:1147–54
9. Bettus G, Guedj E, Joyeux F, et al. **Decreased basal fMRI functional connectivity in epileptogenic networks and contralateral compensatory mechanisms.** *Hum Brain Mapp* 2009;30:1580–91
10. Focke NK, Yogarajah M, Symms MR, et al. **Automated MR image classification in temporal lobe epilepsy.** *Neuroimage* 2012;59:356–62
11. Mueller SG, Laxer KD, Cashdollar N, et al. **Voxel-based optimized morphometry (VBM) of gray and white matter in temporal lobe epilepsy (TLE) with and without mesial temporal sclerosis.** *Epilepsia* 2006;47:900–07
12. Richardson M. **Current themes in neuroimaging of epilepsy: brain networks, dynamic phenomena, and clinical relevance.** *Clin Neurophysiol* 2010;121:1153–75
13. Zhang Z, Liao W, Chen H, et al. **Altered functional-structural coupling of large-scale brain networks in idiopathic generalized epilepsy.** *Brain* 2011;134:2912–28
14. Dosenbach NU, Nardos B, Cohen AL, et al. **Prediction of individual brain maturity using fMRI.** *Science* 2010;329:1358–61
15. Meencke H, Veith G. **Hippocampal sclerosis in epilepsy.** In: Lüders H, ed. *Epilepsy Surgery.* New York: Raven; 1991:705–15
16. Achard S, Salvador R, Whitcher B, et al. **A resilient, low-frequency, small-world human brain functional network with highly connected association cortical hubs.** *J Neurosci* 2006;26:63–72
17. Lee MH, Smyser CD, Shimony JS. **Resting-state fMRI: a review of methods and clinical applications.** *AJNR Am J Neuroradiol* 2013;34:1866–72
18. van den Heuvel MP, Hulshoff Pol HE. **Exploring the brain network: a review on resting-state fMRI functional connectivity.** *Eur Neuropsychopharmacol* 2010;20:519–34
19. Repovs G, Csernansky JG, Barch DM. **Brain network connectivity in individuals with schizophrenia and their siblings.** *Biol Psychiatry* 2011;69:967–73
20. Tedeschi G, Esposito F. **Neuronal networks observed with resting state functional magnetic resonance imaging in clinical populations.** In: Bright P. *Neuroimaging Cognitive and Clinical Neuroscience.* North Logan: InTech; 2012:3
21. Guyon I. **Gene selection for cancer classification using support vector machines.** *Mach Learn* 2002;46:389–422
22. De Martino FD, Valente G, Staeren N, et al. **Combining multivariate voxel selection and support vector machines for mapping and classification of fMRI spatial patterns.** *Neuroimage* 2008;43:44–58
23. Vapnik V. *The Nature of Statistical Learning Theory.* New York: Springer-Verlag; 1995
24. Fawcett T. **An introduction to ROC analysis.** *Pattern Recognition Letters* 2006;27:861–74
25. Focke NK, Yogarajah M, Bonelli SB, et al. **Voxel-based diffusion tensor imaging in patients with mesial temporal lobe epilepsy and hippocampal sclerosis.** *Neuroimage* 2008;40:728–37
26. Bernhardt BC, Chen Z, He Y, et al. **Graph-theoretical analysis reveals disrupted small-world organization of cortical thickness correlation networks in temporal lobe epilepsy.** *Cereb Cortex* 2011;21:2147–57
27. Friston KJ, Frith CD. **Schizophrenia: a disconnection syndrome?** *Clin Neurosci* 1995;3:89–97
28. Shen H, Wang L, Liu Y, et al. **Discriminative analysis of resting-state functional connectivity patterns of schizophrenia using low dimensional embedding of fMRI.** *Neuroimage* 2010;49:3110–21
29. Gong Q, Wu Q, Scarpazz C, et al. **Prognostic prediction of therapeutic response in depression using high-field MR imaging.** *Neuroimage* 2011;55:1497–503
30. Haynes JD, Rees G. **Decoding mental states from brain activity in humans.** *Nat Rev Neurosci* 2006;7:523–34
31. Su L, Wang L, Chen F, et al. **Sparse representation of brain aging: extracting covariance patterns from structural MRI.** *PloS One* 2012;7:e36147
32. Zhang Z, Lu G, Zhong Y, et al. **Impaired attention network in temporal lobe epilepsy: a resting FMRI study.** *Neurosci Lett* 2009;458:97–101
33. Greicius MD, Flores BH, Menon V, et al. **Resting-state functional connectivity in major depression: abnormally increased contributions from subgenual cingulate cortex and thalamus.** *Biol Psychiatry* 2007;62:429–37
34. Buckner RL, Andrews-Hanna JR, Schacter DL. **The brain's default network: anatomy, function, and relevance to disease.** *Ann N Y Acad Sci* 2008;1124:1–38
35. Zhang Z, Lu G, Zhong Y, et al. **Altered spontaneous neuronal activity of the default-mode network in mesial temporal lobe epilepsy.** *Brain Res* 2010;1323:152–60
36. Liao W, Zhang Z, Pan Z, et al. **Default mode network abnormalities in mesial temporal lobe epilepsy: a study combining fMRI and DTI.** *Hum Brain Mapp* 2011;32:883–95
37. Zeng H, Pizarro R, Nair VA, et al. **Alterations in regional homogeneity of resting-state brain activity in mesial temporal lobe epilepsy.** *Epilepsia* 2013;54:658–66
38. Luo C, Qiu C, Guo Z, et al. **Disrupted functional brain connectivity in partial epilepsy: a resting-state fMRI study.** *PLoS One* 2011;7:e28196
39. Dosenbach NU, Fair DA, Cohen AL, et al. **A dual-networks architecture of top-down control.** *Trends Cogn Sci* 2008;12:99–105
40. De Pisapia N, Turatto M, Lin P, et al. **Unconscious priming instructions modulate activity in default and executive networks of the human brain.** *Cereb Cortex* 2012;22:639–49
41. Corbetta M, Shulman GL. **Control of goal-directed and stimulus-driven attention in the brain.** *Nat Rev Neurosci* 2002;3:201–15
42. Zamarian L, Trinka E, Bonatti E, et al. **Executive functions in chronic mesial temporal lobe epilepsy.** *Epilepsy Res Treat* 2011;2011:596174
43. Bell B, Lin JJ, Seidenberg M, et al. **The neurobiology of cognitive disorders in temporal lobe epilepsy.** *Nat Rev Neurol* 2011;7:154–64
44. Keller SS, Baker G, Downes JJ, et al. **Quantitative MRI of the prefrontal cortex and executive function in patients with temporal lobe epilepsy.** *Epilepsy Behav* 2009;15:186–95
45. Hermann BP, Lin JJ, Jones JE, et al. **The emerging architecture of neuropsychological impairment in epilepsy.** *Neurol Clin* 2009;27:881–907
46. Zuo XN, Ehmke R, Mennes M, et al. **Network centrality in the human functional connectome.** *Cereb Cortex* 2012;22:1862–75
47. Fair DA, Cohen AL, Power JD, et al. **Functional brain networks develop from a "local to distributed" organization.** *PLoS Comput Biol* 2009;5:e1000381

Challenges in Identifying the Foot Motor Region in Patients with Brain Tumor on Routine MRI: Advantages of fMRI

R.A. Fisicaro, R.X. Jiao, C. Stathopoulos, N.M. Petrovich Brennan, K.K. Peck, and A.I. Holodny

ABSTRACT

BACKGROUND AND PURPOSE: Accurate localization of the foot/leg motor homunculus is essential because iatrogenic damage can render a patient wheelchair- or bed-bound. We hypothesized the following: 1) Readers would identify the foot motor homunculus <100% of the time on routine MR imaging, 2) neuroradiologists would perform better than nonradiologists, and 3) those with fMRI experience would perform better than those without it.

MATERIALS AND METHODS: Thirty-five attending-level raters (24 neuroradiologists, 11 nonradiologists) evaluated 14 brain tumors involving the frontoparietal convexity. Raters were asked to identify the location of the foot motor homunculus and determine whether the tumor involved the foot motor area and/or motor cortex by using anatomic MR imaging. Results were compared on the basis of prior fMRI experience and medical specialty by using Mann-Whitney *U* test statistics.

RESULTS: No rater was 100% correct. Raters correctly identified whether the tumor was in the foot motor cortex 77% of the time. Raters with fMRI experience were significantly better than raters without experience at foot motor fMRI centroid predictions (13 $\pm$ 6 mm versus 20 $\pm$ 13 mm from the foot motor cortex center, $P = 2 \times 10^{-6}$) and arrow placement in the motor gyrus (67% versus 47%, $P = 7 \times 10^{-5}$). Neuroradiologists were significantly better than nonradiologists at foot motor fMRI centroid predictions (15 $\pm$ 8 mm versus 20 $\pm$ 14 mm, $P = .005$) and arrow placement in the motor gyrus (61% versus 46%, $P = .008$).

CONCLUSIONS: The inability of experienced readers to consistently identify the location of the foot motor homunculus on routine MR imaging argues for using fMRI in the preoperative setting. Experience with fMRI leads to improved accuracy in identifying anatomic structures, even on routine MR imaging.

Localization of the precentral (motor) gyrus by using functional MR imaging before neurosurgical resection of brain tumors has gained acceptance clinically and is a routine procedure.[1-3] Two motor areas commonly mapped by using fMRI are the hand and face.[4] The localization of these areas by fMRI is often validated intraoperatively by using direct cortical stimulation.[2,3,5] However, localization of the foot motor homunculus in the preoperative setting in patients with brain tumor is uniquely important. First, iatrogenic damage to the foot motor homunculus and the resultant paresis of the leg can render a patient wheelchair- or bed-bound, conditions that may be more debilitating than paresis of the nondominant hand or arm. By contrast, iatrogenic compromise of the face and tongue homunculus is often compensated for by corticobulbar fibers from the contralateral hemisphere. Second, the localization of the foot motor homunculus lacks a discernible anatomic landmark such as the "reverse Ω sign" for the hand motor area.[6] Anatomic localization is also rendered more difficult because the central sulcus often does not reach the hemispheric fissure.[4,7] Third, the foot motor homunculus is tucked under the sagittal sinus along the interhemispheric fissure, making its localization difficult to confirm by intraoperative direct cortical stimulation.[8,9] Last, there is no sulcus between the foot motor homunculus and the supplementary motor area, making distinction of the foot motor area from the supplementary motor area more difficult on routine MR imaging.[4,10]

Due to the importance of foot motor function preservation and the difficulties with identifying the foot motor homunculus on routine MR images, we aimed to assess the utility of fMRI of the foot in the preoperative setting. To test the utility of obtaining fMRI in cases in which the brain tumor involved the medial aspect of the high frontoparietal convexity, we asked a group of clinicians to identify the foot motor homunculus on preoperative anatomic

Received November 20, 2014; accepted after revision January 13, 2015.

From the Functional MRI Laboratory, Department of Radiology (R.A.F., R.X.J., C.S., N.M.P.B., K.K.P, A.I.H.), Department of Medical Physics (K.K.P.), and the Brain Tumor Center (A.I.H.), Memorial Sloan-Kettering Cancer Center, New York, New York.

Please address correspondence to Andrei I. Holodny, MD, Functional MRI Laboratory, Department of Radiology, Memorial Sloan-Kettering Cancer Center, 1275 York Ave, New York, NY 10065; e-mail: holodnya@mskcc.org

http://dx.doi.org/10.3174/ajnr.A4292

Table 1: Summary of patient characteristics

Patient	Sex	Age (yr)	Tumor Location	Pathology	Previous Surgery
1	M	64	L	Grade IV GBM	No
2	F	56	R	Grade IV GBM	No
3	M	36	R	Low-grade astrocytoma	No
4	M	38	L	High-grade glioma	No
5	M	66	R	Grade II meningioma	Yes
6	F	48	L	Glioma with astrocytic and oligodendroglial features	No
7	F	26	R	Glioma with astrocytic and oligodendroglial features	No
8	F	59	L	Metastatic adenocarcinoma	No
9	F	64	R	Grade IV GBM	Yes
10	F	65	R	Metastatic breast carcinoma	Yes
11	F	58	R	Metastatic adenocarcinoma	No
12	M	58	L	Grade IV GBM	Yes
13	F	51	R	Meningioma	No
14	F	53	L	Grade IV GBM	No

Note:—GBM indicates glioblastoma multiforme; R, right; L, left.

(non-fMRI) MR images. These results were compared with those of the fMRI study performed simultaneously, to which the respondents were blinded. We hypothesized the following: 1) The respondents would identify the foot motor homunculus <100% of the time, 2) neuroradiologists would perform better than nonradiologists, and 3) those with fMRI experience would perform better than those without fMRI experience.

MATERIALS AND METHODS

This study was approved by the institutional review board. The raters reviewed MR imaging data acquired previously; therefore, obtaining informed consent was waived by the institutional review board.

Rater Groups

Thirty-five raters, all at the attending level, were recruited for this study and included 24 neuroradiologists (attending-level experience, 1–27 years; mean, 9 years) and 11 nonradiologists (attending-level experience, 1–26 years; mean, 10 years). Each nonradiologist was board-certified, with most of their practices devoted to patients with brain tumors. All radiologists were board-certified. Each rater was given a PowerPoint file (Microsoft, Bothell, Washington) with a questionnaire asking the rater to identify their specialty, length of practice at the attending level, and number of fMRI cases viewed per month (never, ≤1, 2–5, or ≥6). The file consisted of 14 consecutive patients with brain tumors involving the high frontoparietal convexity. Each case was represented by 6 contiguous axial MR imaging sections from the most relevant diagnostic series. The patients included 5 men and 9 women (26–66 years of age; mean age, 53 years) (Table 1). The pathology of the tumors was determined through histologic evaluation of surgical biopsies. For each case, the raters were to perform or respond to the following:

1) Please move the "arrow" sign to indicate your estimate of the foot motor region location on the side of pathology. (The tip of the arrow sign should be in the center of the foot motor area.)
2) Does the tumor involve the foot motor area? (Yes/No)
3) Does the tumor involve the motor cortex? (Yes/No)

Additional instructions were provided regarding the definition of the anatomic borders of the tumor:

- On gadolinium-enhanced images, tumor is defined as enhancing lesions; the surrounding T1 hypointensity representing edema is not considered tumor for the purpose of this study.
- On the FLAIR sequence, tumor is defined as FLAIR signal abnormality.
- For case 4 (T2), tumor is defined as the discrete lesion with rim hypointensity; the surrounding T2 hyperintensity representing edema is not considered tumor for the purpose of this study.

Returned responses were anonymized so that each rater was identified by his or her specialty and a number only.

MR Imaging Data Acquisition

All images were acquired with either a 3T or 1.5T Signa LX scanner (GE Healthcare, Milwaukee, Wisconsin) with an 8-channel head coil. For fMRI data acquisition, we used the following imaging sequence: gradient-echo echo-planar (TR, 4000 ms; TE, 30 ms [for 3T] and 40 ms [for 1.5T]; matrix, 128 × 128; flip angle, 90°; 4.5-mm section thickness with no gap; FOV, 240-mm; 32–36 axial sections covering whole brain). T1-weighted spin-echo (TR/TE, 600/8 ms; matrix, 256 × 256; flip angle, 90°; 4.5-mm section thickness with no gap; FOV, 240 mm up to 36 sections) and axial FLAIR images (TR/TE/TI, 9000/125/2250 ms; matrix, 512 × 512; flip angle, 90°; 4.5-mm section thickness with no gap; FOV, 240 mm; up to 36 axial sections) were obtained in the same axial orientation as the fMRI data. 3D T1-weighted anatomic images were also acquired with a spoiled gradient-recalled sequence (TR/TE, 22/4 ms; matrix, 256 × 256 matrix; flip angle, 30°; 1.5-mm thickness; FOV, 240 mm). Head motion was minimized in a standard head coil by using straps and foam padding. Gadopentetate dimeglumine (Magnevist; Bayer HealthCare Pharmaceuticals, Wayne, New Jersey) was injected through a peripheral angiocatheter (18–21 ga) at a standard dose (0.2 mL/kg body weight; maximum, 20 mL).

fMRI Paradigm and Task

We used a block motor paradigm (20 seconds for the task period and 40 seconds for rest) in which each patient performed self-paced toe movement on both feet while avoiding ankle and leg motion in response to an aural cue. The task consisted of 90 images for 6 cycles. The patient's compliance with fMRI paradigms, functional brain activity, and head motion were monitored in real-time by using available software (Brainwave; Medical Numerics, Germantown, Maryland).

fMRI Data Analysis

Image processing and analysis were performed by using Analysis of Functional Neuro Images (http://afni.nimh.nih.gov). Head-motion correction was performed by using 3D rigid-body registration. Spatial smoothing (Gaussian filter with 4-mm full width at half maximum) was applied to improve the signal-to-noise ratio. Functional activity was generated by using cross-correlation analysis. Signal changes with time were correlated with a mathematic model of the hemodynamic response to neural activation. To reduce false-positive activity from large venous structures or

head motion, we set to zero the voxels in which the SD of the acquired time-series exceeded 8% of the mean signal intensity. A board-certified neuroradiologist read each case for foot motor area and tumor localization.

Scoring Method and Statistical Analysis

For question 1, we measured the distance from the arrow placement to the centroid of fMRI activation in the foot motor area (defined as the 10 most statistically activated pixels) and recorded whether the arrow was in the motor gyrus binarily (on the basis of the fMRI data). Distance measurements were made by using the PACS Web system. Rater responses and patient fMRI reports for arrow and foot activation centers were made for placement on corresponding images in the PACS Web system. Intrinsic rulers were used for the measurements. For questions 2 and 3, responses were scored as correct/incorrect on the basis of the fMRI data. The ground truth locations of the foot motor homunculi were defined as the centroid of fMRI foot motor activation. Scores and distances were recorded for each rater and case, and summary statistics were calculated and compared by using the Mann-Whitney *U* test. Statistical significance was defined as $P = .05$. Comparisons were made across rater groups according to fMRI usage and specialty.

RESULTS

All Rater Results

No single rater scored 100% correct for the criteria used in this study. The average arrow placement was 17 ± 11 mm from the centroid of foot motor fMRI activation; 57% of the raters correctly placed the arrow in the motor gyrus. Raters correctly identified whether the tumor was in the foot motor cortex 77% of the time and whether the tumor was in the motor gyrus 71% of the time.

Distance Measurements

fMRI Experience. Raters were split into 2 groups: those without fMRI experience (18 raters; 11 neuroradiologists, 7 nonradiologists) and those with fMRI experience (17 raters; 13 neuroradiologists, 4 nonradiologists) (Table 2). If we considered all cases, the group with fMRI experience was significantly closer to the foot motor cortex center with their arrow placements than the group without fMRI experience (13 ± 6 mm versus 20 ± 13 mm, $P = 2 \times 10^{-6}$).

Experience Gradient. Raters were categorized on the basis of fMRI experience along a gradient into 3 groups: no experience (18 raters), ≤1 per month (14 raters; 10 neuroradiologists, 4 nonradiologists), and 2–5 per month (3 raters; 3 neuroradiologists) (Table 3). Both the ≤1 per month (13 ± 6 mm from the foot motor cortex center) and 2–5 per month (12 ± 7 mm) rater groups scored significantly better than those without experience ($P = 2 \times 10^{-6}$ and $P = 2 \times 10^{-5}$, respectively). The groups with experience did not differ significantly ($P = .204$).

Specialties. As a whole, neuroradiologists scored significantly better than nonradiologists (15 ± 8 mm versus 20 ± 14 mm from the foot motor cortex center, $P = .005$) (Table 4). We then compared within and across specialties on the basis of fMRI experience (no experience versus any experience). In the raters without experience, neuroradiologists were significantly closer than nonradiologists (18 ± 10 mm versus 23 ± 16 mm, $P = .036$). In raters with experience, there was no significant difference between neuroradiologists (13 ± 6 mm) and nonradiologists (14 ± 6 mm, $P = .565$). Within specialties, both neuroradiologists and nonradiologists with experience were significantly closer than those without experience ($P = 2 \times 10^{-6}$ and $P = 2 \times 10^{-4}$, respectively). When we crossed both experience and specialties, neuroradiologists with experience were significantly closer than nonradiologists without experience ($P = 1.4 \times 10^{-5}$) and nonradiologists with experience were significantly closer than neuroradiologists without experience ($P = .01$).

Table 2: Rater comparisons: no versus any fMRI experience[a]

	No fMRI Experience	Any fMRI Experience	*P* Value
Distance from foot motor centroid	20 ± 13 mm	13 ± 6 mm	2×10^{-6}[b]
Arrow in motor gyrus	47% (118/252)	67% (160/238)	7×10^{-5}[b]
Tumor in foot motor cortex	73% (183/252)	81% (192/238)	.121
Tumor in motor gyrus	66% (167/252)	76% (181/238)	.06

[a] Numbers in parentheses indicate the number of correct responses over the total number of responses (eg, in the no fMRI group, there were 18 raters for each of the 14 cases, making 252 total responses).
[b] Significant ($P \leq .05$).

Table 3: Rater comparisons by fMRI experience[a]

	0 Per Month	≤1 Per Month	2–5 Per Month	Significant Comparisons
Distance from foot motor centroid	20 ± 13 mm	13 ± 6 mm	12 ± 7 mm	0 vs <1, 0 vs 2–5
Arrow in motor gyrus	47% (118/252)	68% (133/196)	64% (27/42)	0 vs <1
Tumor in foot motor cortex	73% (183/252)	80% (156/196)	86% (36/42)	
Tumor in motor gyrus	66% (167/252)	74% (146/196)	83% (35/42)	

[a] Numbers in the parentheses indicate the number of correct responses over the total number of responses (eg, in the no fMRI group, there were 18 raters for each of the 14 cases, making 252 total responses).

Arrow Placement in the Motor Gyrus

Raters with fMRI experience correctly placed the arrow in the motor gyrus significantly more often than raters without fMRI experience (67% versus 47%, $P = 7 \times 10^{-5}$). On a gradient, raters in the ≤1 per month group (68%) were correct significantly more often than those without experience ($P = 1.1 \times 10^{-4}$). There were no significant differences between the 2–5 per month (64%) and no experience groups ($P = .067$) or the 2–5 per month and the ≤1 per month groups ($P = .717$).

Neuroradiologists were correct significantly more often than nonradiologists (61% versus 46%, $P = .008$). In raters without fMRI experience, neuroradiologists were correct significantly more often than nonradiologists (54% versus 35%, $P = .012$). In raters with experience, there was no significant difference between the specialties (neuroradiologists = 68%, nonradiologists = 66%, $P = .87$). Within specialties, both neuroradiologists and nonradiologists with experience were correct significantly more often ($P = .031$ and $P = .001$, respectively). When we crossed both expe-

Table 4: Rater comparisons by specialty[a]

	Neuroradiologist	Nonradiologist	*P* Value
Distance from foot motor centroid	15 ± 8 mm	20 ± 14 mm	.005[b]
Arrow in motor gyrus	61% (206/336)	46% (71/154)	.008[b]
Tumor in foot motor cortex	78% (261/336)	74% (114/154)	.515
Tumor in motor gyrus	72% (242/336)	69% (106/154)	.569

[a] Numbers in the parentheses indicate the number of correct responses over the total number of responses (eg, in the neuroradiologist group, there were 24 raters for each of the 14 cases, making 336 total responses).
[b] Significant ($P \leq .05$).

rience and specialties, neuroradiologists with experience were correct significantly more often than nonradiologists without experience ($P = 7.68 \times 10^{-6}$). Nonradiologists with experience did not differ significantly from neuroradiologists without experience ($P = .176$).

Tumor in the Foot Motor Cortex

In determining whether the tumor was located in the foot motor cortex, there was no significant difference in correct responses based on fMRI experience (no experience = 73%, fMRI experience = 81%, $P = .121$). Likewise, there was no significant difference among any of the groups along a gradient (0 per month = 73%, ≤1 per month = 80%, 2–5 per month = 86%, $P > .174$). As a whole, there was no significant difference between the specialties (neuroradiologists = 78%, nonradiologists = 74%, $P = .515$). Additionally, there was no significant difference between the specialties in those without experience (neuroradiologists = 72%, nonradiologists = 73%, $P = .852$) or with experience (neuroradiologists = 82%, nonradiologists = 75%, $P = .401$) or within specialties (neuroradiologists, $P = .102$; nonradiologists, $P = .876$). There were no significant differences between neuroradiologists with experience and nonradiologists without experience ($P = .217$) or nonradiologists with experience and neuroradiologists without experience ($P = .746$).

Tumor in the Motor Gyrus

In determining whether the tumor was located in the motor gyrus generally, while trending toward significance, there was no significant difference in correct responses based on fMRI experience (no experience = 66%, fMRI experience = 76%, $P = .06$). Likewise, there was no significant difference among any group along a gradient (0 per month = 66%, ≤1 per month = 74%, 2–5 per month = 83%, $P > .076$). As a whole, there was no significant difference between the specialties (neuroradiologists = 72%, nonradiologists = 69%, $P = .569$). Additionally, there was no significant difference between the specialties in those without experience (neuroradiologists = 68%, nonradiologists = 64%, $P = .664$) or with experience (neuroradiologists = 76%, nonradiologists = 77%, $P = .913$) or within specialties (neuroradiologists: $P = .190$, nonradiologists: $P = .197$). There were no significant differences between neuroradiologists with experience and nonradiologists without experience ($P = .111$) or nonradiologists with experience and neuroradiologists without experience ($P = .304$).

Case Example

One of the more difficult cases for the raters was patient 13 (Figure). The average distance from the foot motor center in arrow placement was 16 mm in those with fMRI experience and 23 mm in those without experience. Sixty-five percent of raters with fMRI experience and 50% of raters without fMRI experience placed the arrow in the correct gyrus. Eighteen percent and 33% of raters with and without fMRI experience respectively, correctly identified the tumor as not being located in the foot motor cortex. Last, 35% and 39% of raters with and without fMRI experience, respectively, correctly identified the tumor as not being located in the motor gyrus.

DISCUSSION

Accurate preoperative identification of eloquent cortices adjacent to brain tumors is essential and has been demonstrated to improve outcomes.[8,11] Localization of the foot motor homunculus presents a number of unique challenges because this structure lacks a discernible anatomic landmark on MR imaging such as the "reverse Ω sign" for the hand motor area[6] and is difficult to approach and confirm intraoperatively by direct cortical stimulation.[8,9] However, accurate localization of the foot motor homunculus is essential because iatrogenic damage and the resultant paresis of the leg can render a patient wheelchair- or bed-bound. In this study, we assessed the ability of physicians from different specialties and with varying fMRI experience to accurately identify the foot motor homunculus on routine MR images.

In this cohort of specialists, we found that experience with fMRI confers a positive effect on reading routine MR imaging examinations in terms of locating the relationship of a tumor to the foot motor homunculus. This effect was seen in those with fMRI experience performing significantly better in foot motor cortex center predictions and arrow placement in the motor gyrus than raters without fMRI experience. This advantage may be linearly related to the degree of fMRI experience, but we did not have the statistical power to show this relationship. There was no significant difference between the 2–5 cases per month group (64% correct) and the ≤1 case per month group (68%). The probable reason that there was no statistically significant difference between the 2–5 cases per month group (64% correct) and the no fMRI experience group (47% correct) was that the 2–5 cases per month group was underpowered: There were 3 raters in the 2–5 cases per month group versus 18 raters in the no experience group and 14 raters in the ≤1 case per month group. Additionally, at the specialist level, neuroradiologists performed significantly better than nonradiologists in foot motor cortex predictions and arrow placement in the motor gyrus. In our study, only 4 nonradiologists had fMRI experience, so how their results would compare with neuroradiologists without fMRI experience in a larger sample size is not known.

In our study, none of the raters, including highly experienced individuals, were 100% correct in identifying the foot motor homunculus on the anatomic MR imaging. Even in healthy volunteers, interobserver agreement on the location of the central sulcus by using MR imaging has been reported to be as low as 76%.[12] Therefore, the inability of even expert readers to correctly identify the location of the foot motor homunculus by anatomy alone

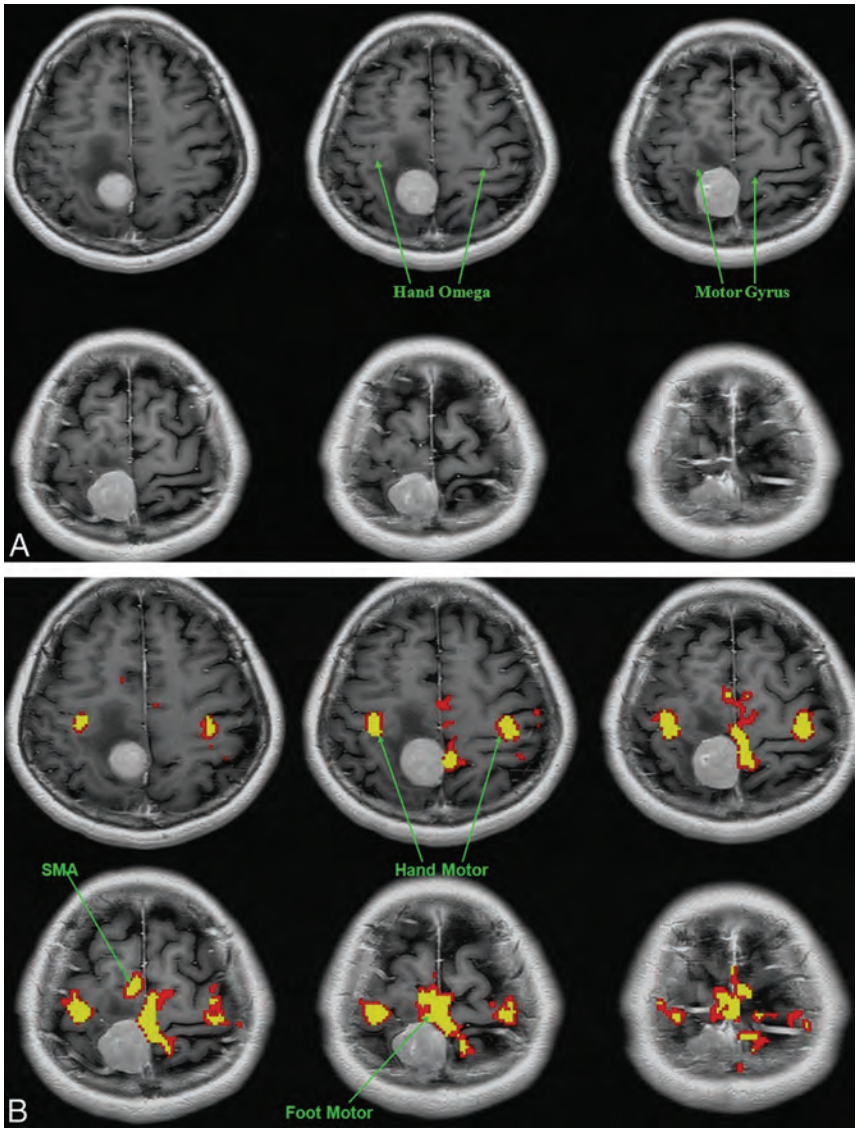

FIGURE. Axial T1-weighted without (*A*) or with (*B*) coregistered functional MR images obtained during a bilateral finger-tapping and foot motor paradigm. The raters were asked to identify the foot motor homunculus solely on the basis of the anatomic images (*A*) without the benefit of fMRI (*B*). fMRI places the extra-axial lesion just posterior to the primary motor gyrus, including the foot motor portion of the motor homunculus. Edema extends to involve both the precentral and postcentral gyri. The average arrow placement from the foot motor center was 16 mm in those with fMRI experience and 23 mm in those without it. A higher percentage of raters with fMRI experience than those without it placed the arrow in the motor gyrus (65% versus 50%). Eighteen percent of raters with fMRI experience correctly identified the tumor as not being located in the foot motor cortex, while 33% of raters without fMRI experience did so. Last, 35% and 39% of raters with and without fMRI experience, respectively, correctly identified the tumor as not being located in the motor gyrus. Most of the incorrect arrow placements were due to the arrow being placed in a gyrus posterior to the motor gyrus.

appears to encourage the use of fMRI in such cases. Localization of the foot motor cortex is of particular importance in preoperative planning in the medial frontoparietal region of the brain.[13] If we took the results of previous studies showing comparable motor mapping between fMRI and intraoperative corticography and direct cortical stimulation, fMRI appears to have both validity and utility.[11,14]

One finding is that the raters did not perform as well in placing the arrow in the motor gyrus as they did in nominally determining whether the tumor was in the motor cortex or in the foot motor area. One reason may be that tumors can span >1 gyrus, thus making it easier to determine whether the motor cortex or foot motor area is affected rather than placing an arrow in the correct gyrus. Another reason for the discrepancy may be that the edema accompanying the tumors increased the difficulty by blurring sulcal boundaries.

The current study has limitations and provides for future directions. One limitation is the sample size of specialists. Future studies might look at a larger number of specialists, include more specialties, and have a wider range of fMRI usage among the cohort to elucidate these comparisons further and inform training programs as to the extent of necessary fMRI training in anatomic determinations such as the foot motor region. Additionally, with the raters given 1 series of axial images for each case, whether additional imaging series might have facilitated foot motor localization is not known. Another consideration would be to see whether the addition of fMRI data actually influenced the surgical decision-making process as in Petrella et al.[11] A possible additional limitation is that some of the patients underwent previous surgery. Posttreatment changes, especially involving infiltrative tumors, may limit the determination of the tumor margin, which could affect the results. In addition, a study limitation may be that different tumor types were included, which could have affected the results. However, the current study supports the utility of fMRI for foot motor localization in preoperative planning.

CONCLUSIONS

In the current study, we evaluated the ability of neuroradiologists and nonradiologists to identify the foot motor homunculus on MR imaging in patients with brain tumors. None of the 35 raters scored 100% correct. Notwithstanding the expertise of the raters, they were only able to correctly identify whether the tumor was in the foot motor cortex 77% of the time. The inability of experienced readers to consistently identify the location of the foot motor homunculus on routine MR images argues for the use of fMRI in the preoperative setting. In addition, raters with prior fMRI experience were significantly better than raters without experience at foot motor fMRI centroid predictions and arrow placement in the motor gyrus. Therefore, experience in fMRI leads to improved accuracy in identifying anatomic structures even on routine MR imaging. Neuroradiologists were significantly better than nonradiologists

at foot motor fMRI centroid predictions and arrow placement in the motor gyrus.

Disclosures: Andrei Holodny—*UNRELATED*: *Other*: fMRI Consultants, LLC (a purely educational enterprise).

REFERENCES

1. Wood JM, Kundu B, Utter A, et al. **Impact of brain tumor location on morbidity and mortality: a retrospective functional MR imaging study.** *AJNR Am J Neuroradiol* 2011;32:1420–25
2. Bizzi A, Blasi V, Falini A, et al. **Presurgical functional MR imaging of language and motor functions: validation with intraoperative electrocortical mapping.** *Radiology* 2008;248:579–89
3. Stippich C. **Presurgical functional magnetic resonance imaging.** [in German]. *Radiologe* 2010;50:110–22
4. Lehéricy S, Duffau H, Cornu P, et al. **Correspondence between functional magnetic resonance imaging somatotopy and individual brain anatomy of the central region: comparison with intraoperative stimulation in patients with brain tumors.** *J Neurosurg* 2000;92:589–98
5. Puce A, Constable RT, Luby ML, et al. **Functional magnetic resonance imaging of sensory and motor cortex: comparison with electrophysiological localization.** *J Neurosurg* 1995;83:262–70
6. Yousry TA, Schmid UD, Alkhadhi H, et al. **Localization of the motor hand area to a knob on the precentral gyrus: a new landmark.** *Brain* 1997;120:141–57
7. Kido DK, LeMay M, Levinson AW, et al. **Computed tomographic localization of the precentral gyrus.** *Radiology* 1980;135:373–77
8. Wengenroth M, Blatow M, Guenther J, et al. **Diagnostic benefits of presurgical fMRI in patients with brain tumours in the primary sensorimotor cortex.** *Eur Radiol* 2011;21:1517–25
9. Holodny AI, Shevzov-Zebruna N, Brennan N, et al. **Motor and sensory mapping.** *Neurosurg Clin N Am* 2011;22:207–18, viii
10. Vincent DJ, Bloomer CJ, Hinson VK, et al. **The range of motor activation in the normal human cortex using BOLD fMRI.** *Brain Topogr* 2006;18:273–80
11. Petrella JR, Shah LM, Harris KM, et al. **Preoperative functional MR imaging localization of language and motor areas: effect on therapeutic decision making in patients with potentially resectable brain tumors.** *Radiology* 2006;240:793–802
12. Sobel DF, Gallen CC, Schwartz BJ, et al. **Locating the central sulcus: comparison of MR anatomic and magnetoencephalographic functional methods.** *AJNR Am J Neuroradiol* 1993;14:915–25
13. Brennan CW, Brennan NP. **Functional image-guided neurosurgery.** In: Holodny AI, ed. *Functional Neuroimaging: A Clinical Approach*. New York: Informa Healthcare USA; 2008:91–106
14. Jack CR Jr, Thompson RM, Butts RK, et al. **Sensory motor cortex: correlation of presurgical mapping with functional MR imaging and invasive cortical mapping.** *Radiology* 1994;190:85–92

Identifying Corticothalamic Network Epicenters in Patients with Idiopathic Generalized Epilepsy

G.-J. Ji, Z. Zhang, Q. Xu, Z. Wang, J. Wang, Q. Jiao, F. Yang, Q. Tan, G. Chen, Y.-F. Zang, W. Liao, and G. Lu

ABSTRACT

BACKGROUND AND PURPOSE: Corticothalamic networks are considered core pathologic substrates for idiopathic generalized epilepsy; however, the predominant epileptogenic epicenters within these networks are still largely unknown. The current study aims to identify these epicenters by resting-state functional connectivity.

MATERIALS AND METHODS: To identify epicenters within the corticothalamic networks in idiopathic generalized epilepsy, we retrospectively studied a large cohort of patients with this condition ($n = 97$) along with healthy controls ($n = 123$) by resting-state functional MR imaging. The thalamus was functionally divided into subregions corresponding to distinct cortical lobes for 5 parallel corticothalamic networks. The functional connectivity between each voxel in the cortical lobe and the corresponding thalamic subregion was calculated, and functional connectivity strength was used to evaluate the interconnectivity of voxels in the cortex and thalamus.

RESULTS: The projection of 5 cortical lobes to the thalamus is consistent with previous histologic findings in humans. Compared with controls, patients with idiopathic generalized epilepsy showed increased functional connectivity strength in 4 corticothalamic networks: 1) the supplementary motor area, pulvinar, and ventral anterior nucleus in the prefrontal-thalamic network; 2) the premotor cortex and ventrolateral nucleus in motor/premotor-thalamic networks; 3) the visual cortex, posterior default mode regions, and pulvinar in parietal/occipital-thalamic networks; and 4) the middle temporal gyrus in the temporal-thalamic network.

CONCLUSIONS: Several key nodes were distinguished in 4 corticothalamic networks. The identification of these epicenters refines the corticothalamic network theory and provides insight into the pathophysiology of idiopathic generalized epilepsy.

ABBREVIATIONS: FCS = functional connectivity strength; GSWD = generalized spike-wave discharge; IGE = idiopathic generalized epilepsy; SMA = supplementary motor area

Idiopathic generalized epilepsy (IGE) is a common subtype of epilepsy involving abnormally synchronized generalized spike-wave discharges (GSWDs) rapidly propagating to distributed networks.[1] Various theories have been proposed to explain the origin and mechanism of generalized seizures[2]; the corticothalamic network has been suggested as a preferred target for the modification or elimination of seizure discharges.[3,4]

There is substantial evidence that dysfunction in the corticothalamic circuitry contributes to the pathogenesis of generalized seizures.[3,4] Hemodynamic changes associated with GSWDs have been consistently observed in the thalamus and default mode areas.[5] Recently, corticothalamic interactions in generalized epilepsy have been characterized by morphometric covariance,[6] functional and anatomic connectivity,[7,8] and causal influence.[9] In particular, corticothalamic connections (parcellated through probabilistic tractography) showed abnormal functional connectivity in juvenile myoclonic epilepsy.[7] However, little attention

Received August 28, 2014; accepted after revision January 17, 2015.

From the Center for Cognition and Brain Disorders and the Affiliated Hospital (G.-J.J., J.W., Y.-F.Z., W.L.), Hangzhou Normal University, Hangzhou, China; Zhejiang Key Laboratory for Research in Assessment of Cognitive Impairments (G.-J.J., J.W., Y.-F.Z., W.L.), Hangzhou, China; Departments of Medical Imaging (Z.Z., Q.X., W.L., G.L.), Neurology (F.Y., G.C.), and Neurosurgery (Q.T.), Jinling Hospital, Nanjing University School of Medicine, Nanjing, China; Department of Medical Imaging (Z.W.), Nanjing Drum Tower Hospital, the Affiliated Hospital of Nanjing University Medical School, Nanjing, China; and Department of Radiology (Q.J.), Taishan Medical University, Tai'an, China.

G.-J. Ji and Z. Zhang contributed equally to the article.

This research was supported by the Natural Science Foundation of China (grants 81401400, Gong-Jun Ji; 81401402, Qiang Xu; 81201155, 81471653, Wei Liao; 81301198, Zhengge Wang; 81171328, Qing Jiao; 81201078, Fang Yang; 81271553, 81422022, Zhiqiang Zhang; 81020108022, 31471084, Yu-Feng Zang), China Postdoctoral Science Foundation (grant 2013M532229, Wei Liao), and Qian Jiang Distinguished Professor program (Yu-Feng Zang).

Please address correspondence to Wei Liao, PhD, Center for Cognition and Brain Disorders and the Affiliated Hospital, Hangzhou Normal University, Hangzhou 310015, China; e-mail: weiliao.wl@gmail.com; and Guangming Lu, MD, Department of Medical Imaging, Nanjing Jinling Hospital, 305, Eastern Zhongshan Rd, Nanjing 210002, China; e-mail: cjr.luguangming@vip.163.com

http://dx.doi.org/10.3174/ajnr.A4308

Table 1: Characteristics of patients and normal controls

Characteristic	IGE (n = 86)	NC (n = 123)	χ^2/t Value	P Value
Sex (male/female)	31/55	56/67	1.87	.17[a]
Age (yr)	25.77 ± 6.31[b]	25.49 ± 7.15[b]	1.22	.22[c]
Handedness (right/left)	86/0	123/0	–	–
Duration (yr)	8.93 ± 8.41[b]	–	–	–
Onset age (yr)	16.84 ± 7.93[b]	–	–	–
Frequency (times/yr)	19.02 ± 58.11[b]	–	–	–

Note:—NC, normal controls; –, not applicable.
[a] χ^2 test.
[b] Data represent mean ± SD.
[c] Two-sample t test.

has been paid to the functional topographic pathways linking distinct cortical areas and specific thalamic nuclei.[10,11] These projections likely have distinct roles in the mechanism of GSWDs,[12] so it is essential to investigate corticothalamic functional networks in generalized epilepsy. More precisely, characterizing epicenters within each network may facilitate the development of targeted surgical interventions (eg, deep brain stimulation) that selectively disrupt seizures and ultimately improve the clinical treatment of IGE.[4]

It was recently demonstrated that resting-state functional connectivity can reveal distinct corticothalamic networks[13] analogous to classic histologic parcellation.[10] As in previous investigations,[14-16] a similar approach was adopted here to identify corticothalamic networks. We hypothesized that the functional synchronization of corticothalamic networks is altered in patients with IGE. To localize epicenters within these networks, we conducted a voxelwise comparison of network functional connectivity between patients and controls.

MATERIALS AND METHODS

Participants

Patients were consecutively enrolled at Jinling Hospital, Nanjing, China. Patients were diagnosed according to International League Against Epilepsy criteria (2001). The inclusion criteria for patients were as follows: 1) manifestation of typical clinical symptoms of idiopathic generalized tonic-clonic seizures, including tonic extension of the limbs, followed by a clonic phase of rhythmic jerking of the extremities, loss of consciousness during seizures without precursory symptoms of partial epilepsy and aura; 2) no evidence of secondary generalized seizures, such as trauma, tumor, intracranial infection; 3) no abnormality on structural MR imaging; 4) presence of GSWDs on the video-electroencephalogram; and 5) right-handedness. Ninety-seven patients fulfilled these inclusion criteria. The exclusion criteria were as follows: 1) history of addictions or neurologic diseases other than epilepsy; 2) history of partial seizures; 3) self-reported falling asleep during resting-state fMRI scanning; and 4) head translation or rotation parameters exceeding ±1.5 mm or ±1.5°. After excluding 11 patients due to excessive head motion, we included 86 patients in the final dataset (Table 1). All 86 patients had generalized tonic-clonic seizures, and 17 had additional myoclonic jerks and absences. All 86 patients were taking antiepileptic drugs, including valproic acid, topiramate, lamotrigine, phenobarbitone, or some combination, and 34 had taken other medications, including carbamazepine, phenytoin, traditional Chinese herbal medicines, oxcarbazepine, or clonazepam.

Healthy controls (n = 123) were recruited from the staff of Jinling Hospital. They had no history of neurologic disorders or psychiatric illnesses and no gross abnormalities in brain MRI.

Written informed consent was obtained from all participants. The study was approved by the local medical ethics committee at Jinling Hospital.

Data Acquisition

Data were acquired by using a Magnetom Trio (Siemens, Erlangen, Germany) MR imaging scanner at Jinling Hospital. Functional images were acquired during the interictal period. Scalp electroencephalograms were not recorded during scanning. All patients were assumed to be in the interictal state during scanning because there were no apparent seizure symptoms observed by video monitoring. Foam padding was used to minimize subject head motion. Functional images were acquired by using a single-shot, gradient-recalled echo-planar imaging sequence (TR = 2000 ms, TE = 30 ms, flip angle = 90°). Thirty transverse sections (FOV = 240 × 240 mm^2, section thickness/intersection gap = 4 /0.4 mm) were acquired. A total of 250 volumes were acquired for each subject. Subjects were instructed to rest with their eyes closed, without thinking of anything in particular or falling asleep. After scanning, subjects were asked whether they had fallen asleep during the scan.

Data Processing

Preprocessing. Functional images were preprocessed by using the Data Processing Assistant for Resting-State fMRI (http://rfmri.org/DPARSF) and SPM8 software (http://www.fil.ion.ucl.ac.uk/spm/software/spm8) toolkits. Functional images were section-timing-corrected, then registered to correct for head motion during the scan. On the basis of the known impact of head motion, the frame-wise displacement was calculated for each time point.[17] If the frame-wise displacement exceeded 0.5 mm, the value of the signal at that point was interpolated by using piecewise cubic Hermite. Functional images were normalized to the EPI template in Montreal Neurological Institute space and resampled to an isotropic 2-mm^3 voxel. Next, linear trends were removed and temporal bandpass filtering (0.01–0.08 Hz) was performed. Finally, several sources of spurious variance were removed by regression of the following variables: 6 head-motion parameters, signals averaged over CSF, and white matter.[13,14] As previously proposed,[13] data were neither smoothed nor regressed out of the averaged global mean signal.

Identification of Functional Corticothalamic Networks. To identify functional corticothalamic networks, we divided bilateral hemispheres into 5 nonoverlapping cortical lobes based on anatomic templates[13]: 1) prefrontal cortex, 2) motor/premotor cortex, 3) somatosensory cortex, 4) parietal/occipital cortex, and 5) temporal cortex. We calculated the functional connectivity between the averaged signal within each lobe and each voxel of the thalamus by using partial correlation for each subject.[13] The thalamus mask was acquired from an automated anatomic labeling

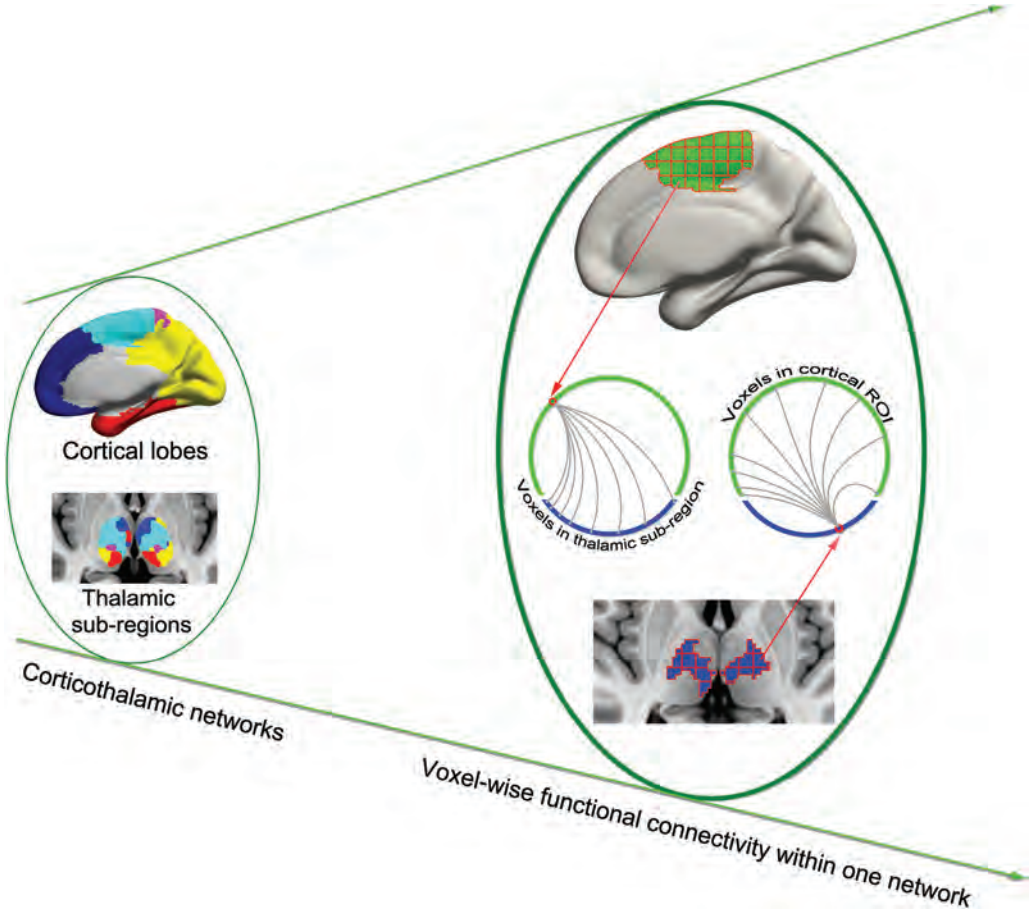

FIG 1. Schematic of data analysis. From the left to right planes, 5 corticothalamic networks were first identified; FCS was then calculated for each voxel within the corresponding corticothalamic network. For example, 1 voxel in the cortical lobe was correlated with all voxels in the corresponding thalamic subregion. All superthreshold coefficient values were averaged to obtain the FCS of the cortical voxel.

template. On the basis of previous studies,[14] positive correlations were included in further analyses and transformed to *z* scores by using the Fisher r-to-z transformation. *Z* score maps were combined across subjects in each group by using a 1-sample *t* test. Finally, each thalamic voxel was labeled according to the cortical lobe with the highest *t* value (ie, "winner take all").[13-16] Thus, the thalamus was separately divided into 5 subregions in each group. To compute the functional connectivity strength (FCS) and compare this value between groups, we applied the winner-take-all approach to all participants ($n = 209$) to limit group bias during thalamic subregion creation.[18]

Voxelwise Functional Connectivity in Corticothalamic Networks. Because generalized epileptic seizures may originate at specific regions or epicenters rather than throughout the brain simultaneously,[1] we sought to identify these epicenters in corticothalamic networks by using a voxelwise functional connectivity approach (Fig 1).[19] Specifically, given *N* voxels in a cortical lobe and *M* voxels in the corresponding thalamic subregion, Pearson correlation analysis generated an $N \times M$ matrix for each participant—that is, for a given voxel in the cortical lobe, there were *M* correlation values representing its functional synchronization with each voxel in the thalamic subregion. Only values above a predefined threshold (corresponding to $P = .05/M$) were transformed to *z* values and summed as the FCS value of cortical or thalamic subregion voxels. The FCS value is referred to as the "degree centrality" of weighted networks[20]; voxels with higher FCS values indicate a greater role in the heterogeneity of the capacity and intensity of connections.[19]

Statistical Analysis

FCS maps of 5 parallel corticothalamic networks were separately compared between groups by using the 2-sample *t* test. The corrected statistical threshold ($P < .05$) was accomplished by 2 steps: First, the comparison result was corrected ($P < .01$) by the AlphaSim program (http://afni.nimh.nih.gov/pub/dist/doc/program_help/AlphaSim.html) within each network (with a height threshold of $P < .001$ for all cortical and thalamic subregions, and extent thresholds for each cortical region and the corresponding thalamic subregion of >480 and 24 mm^3 [prefrontal cortex and thalamus], 160 and 32 mm^3 [motor/premotor and thalamus], 720 and 24 mm^3 [parietal/occipital cortex and thalamus], and 480 and 24 mm^3 [temporal cortex and thalamus]). This step was followed by a Bonferroni correction for the 5 corticothalamic network comparisons. The clinical variables (disease duration, seizure frequency, and onset age) were correlated with regions showing abnormal FCS. Spearman correlation analysis was used because none of the clinical variables showed a Gaussian distribution.

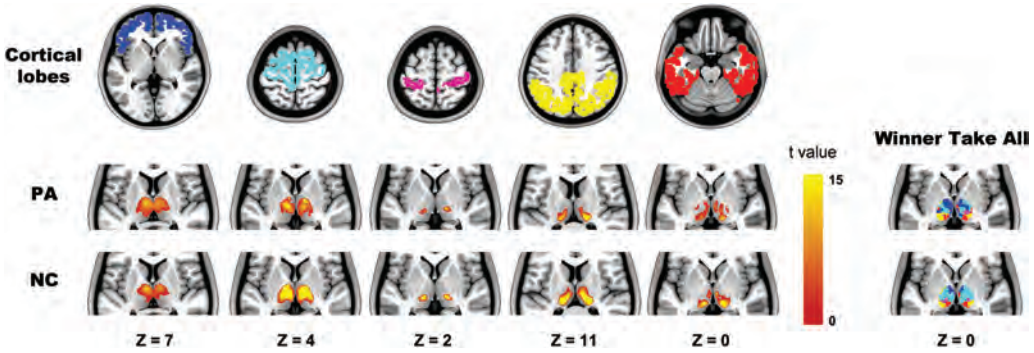

FIG 2. Highly specific connections between the cortical lobe and thalamus. The 5 columns on the left show the cortical lobe and highly correlated thalamic regions in patients with IGE and healthy controls. In the winner-take-all map, each thalamic voxel is labeled according to the cortical lobe with the highest *t* value. The *z* plane coordinates indicate the Montreal Neurological Institute space.

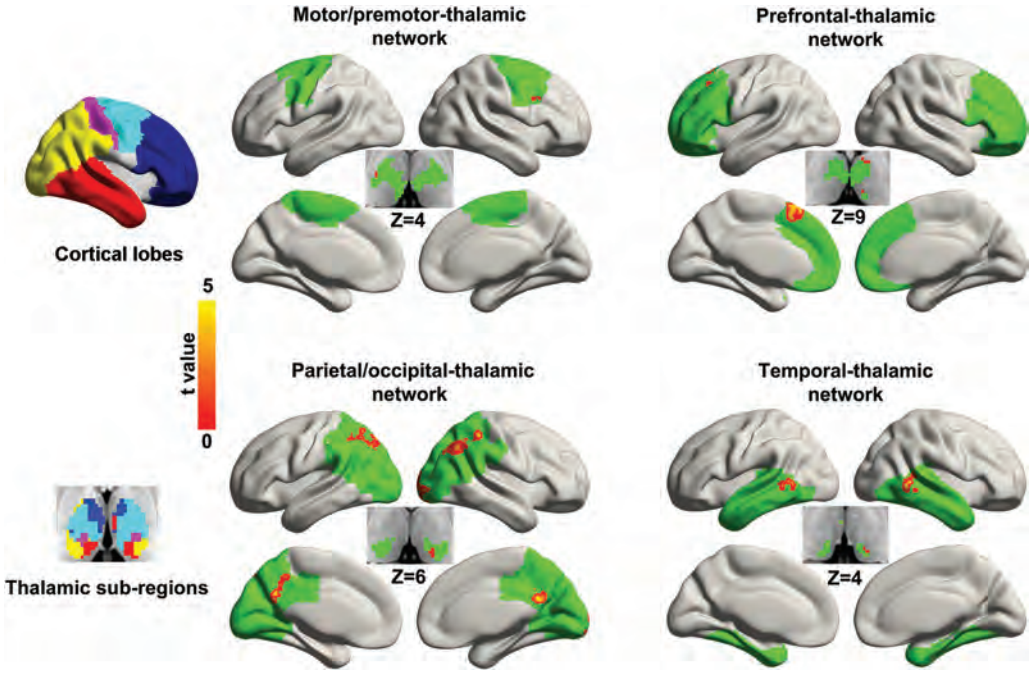

FIG 3. Comparison of voxelwise functional connectivity between groups. The left column shows cortical lobes and corresponding thalamic subregions obtained by using the winner-take-all approach. The right column shows the between-group difference in FCS. Abnormal voxels are labeled by warm colors and rendered on cortical lobe and thalamic subregions (green). The color scale represents *t* values by using 2-sample *t* tests ($P < .05$, corrected). The *z* plane coordinates indicate the Montreal Neurological Institute space.

RESULTS

Identification of Functional Corticothalamic Networks

In control subjects, each cortical lobe was connected to distinct, largely nonoverlapping parts of the thalamus (Fig 2), consistent with previous findings.[13] Specifically, the prefrontal lobe showed maximal correlation with the mediodorsal and anterior nuclear areas; the motor/premotor cortex corresponded most strongly to the ventral anterior, lateral dorsal, and part of the medial nucleus; the somatosensory cortex corresponded to the ventral posterior nucleus; and the parietal/occipital and temporal cortices corresponded to the lateral and medial part of the pulvinar. Similar patterns were observed in patients. However, qualitative differences were observed between the groups. Compared with controls, the thalamic subregions connected to the prefrontal and motor/premotor cortices were expanded and shrunken, respectively, in patients. The changes may simply relate to the different sample sizes of each group, rather than pathologic alteration.

Differences in Functional Connectivity Strength

A between-group comparison indicated that FCS was increased in patients (Fig 3 and Table 2). In the prefrontal-thalamic network, the regions of increase were located in the left middle frontal gyrus, left supplementary motor area (SMA), left pulvinar, and left ventral anterior nucleus. The motor/premotor-thalamic network showed increased FCS in the right premotor cortex and right ventrolateral nucleus. The parietal/occipital-thalamic network showed increased FCS in the bilateral inferior parietal lobule, left precuneus, right middle occipital gyrus, and left pulvinar. The FCS in the sensory-thalamic network did not differ between groups. The temporal-thalamic network showed increased FCS in the bilateral middle temporal gyrus and left pulvinar.

No significant correlation was found between the FCS in any abnormal region and disease duration, onset age, or seizure frequency, even when the age at time of the scan was controlled by regression.

Table 2: Regions in corticothalamic networks with abnormal FCS in patients with IGE

Brain Regions	MNI (*X*, *Y*, *Z*)	Brodmann Area	Volume (mm^3)	Peak *t* Value
Prefrontal-thalamic network				
SMA/middle frontal gyrus (L)	−30, 20, 60	8/6	2136	4.25
Pulvinar (L)	−8, −24, 8	–	48	3.54
Ventral anterior nucleus (L)	−8, −4, 10	–	24	3.47
Motor/premotor-thalamic network				
Premotor cortex (R)	46, 14, 34	6	184	4.26
Ventrolateral nucleus (R)	20, −14, 10	–	48	3.76
Parieto/occipital-thalamic network				
Middle occipital gyrus (R)	18, −102, −10	18	880	4.38
Precuneus (R)	6, −52, 24	31	888	4.88
Inferior parietal lobule (R)	42, −66, 46	40/7	2712	4.87
Inferior parietal lobule (L)	−36, −62, 50	40/7	2424	4.95
Pulvinar (L)	−14, −28, 6	–	48	4.08
Temporal-thalamic network				
Middle temporal gyrus (R)	62, −48, 4	22/21	560	4.88
Middle temporal gyrus (L)	−66, −50, −2	21	432	4.76
Pulvinar (L)	−8, −24, 2	–	48	3.41

Note:—L, left hemisphere; MNI, Montreal Neurological Institute; R, right hemisphere; –, not applicable.

DISCUSSION

By measuring brain synchronization by using resting-state fMRI, we characterized corticothalamic networks in patients with IGE. We replicated the 5 corticothalamic networks described previously in both patients and controls, indicating highly organized patterns of coherent activity in the thalamus and cerebral cortex. Most important, voxelwise functional connectivity analysis revealed epicenters within corticothalamic networks in patients. The results suggest that components of the corticothalamic network are not uniformly involved in IGE but that specific epicenters may be crucial to understanding the pathophysiology of this disorder.

IGE is regarded as a network disorder[1] involving abnormal corticothalamic connectivity.[4] Wang et al[8] identified abnormal thalamic nuclei in a group of patients with IGE by morphologic analysis, which provided the foundation for seed-based functional connectivity analysis. This revealed decreased connectivity between the medial dorsal nucleus and bilateral orbital frontal cortices, caudate nucleus, putamen, and amygdala. However, another study found a different pattern of connectivity by using a similar analytic strategy.[21] This inconsistency is at least partly due to the different locations of seed regions in these studies. To avoid the bias of a predefined seed region in the present study, we performed a voxelwise functional connectivity analysis (expressed as FCS) between the thalamus and cortex.[19] More important, the analysis was not restricted to any single corticothalamic network but considered each one independently. Brain regions with high FCS are network hubs that facilitate the integration and propagation of neural processing.[19] Increased FCS in patients with IGE is consistent with a high excitatory state or neuronal synchronization[22] and suggests that certain brain regions may be responsible for rapidly spreading the generalized spike-waves to all areas.

The original corticothalamic theory of seizure generalization was largely based on evidence from animal studies on absence seizures.[2-4] Recent neuroimaging studies have implicated prefrontal areas such as the SMA, medial prefrontal cortex, and orbital frontal cortex in the generation of generalized seizures.[22-24] The present findings also identified the SMA in a cohort of patients with IGE. In an fMRI study using an executive frontal lobe paradigm, patients with juvenile myoclonic epilepsy showed increased functional connectivity between the motor system and the frontoparietal cognitive networks, providing an explanation for how cognitive effects can cause myoclonic jerks in juvenile myoclonic epilepsy.[24]

It was suggested that the SMA, as a connector linking prefrontal cognitive areas and the motor system, may facilitate the occurrence of generalized seizures, a notion supported by alterations in anatomic connectivity of the SMA in juvenile myoclonic epilepsy.[25] To estimate the corticothalamic connectivity in juvenile myoclonic epilepsy, we parcellated the thalamus into several nuclei connected to different cortices by using probabilistic tractography.[7] A decreased probability of a connection between the anterior thalamus and SMA was found in patients. A psychophysiologic interaction analysis of fMRI data found greater task-dependent functional connectivity between these anterior nuclei and the superior frontal cortex. Accordingly, we observed increased FCS in the anterior nuclei. Similar altered prefrontal-thalamic connectivity in different IGE subtypes suggests that these network changes may be a common feature of IGE. The identification of these key regions—especially the SMA—provides putative epicenters that can be targeted by clinical treatment strategies. Research across disciplines on these epicenters can advance our understanding of the pathophysiology of IGE. Because specific changes in functional connectivity may respond best to particular clinical treatments,[26] our identification of aberrant corticothalamic epicenters may help in the development of improved therapies with fewer side effects.[4]

Because most patients experience sustained muscle rigidity and rapid muscle contractions/relaxations during seizures, it is reasonable to expect abnormalities in the motor-/sensory-thalamic system. The premotor cortex and specific nuclei (pulvinar and ventrolateral nucleus) showed increased FCS within the motor-thalamic but not the sensory-thalamic network. This is analogous to the disruption of functional integrity in the sensorimotor network of the neocortex[27] and may reflect the higher excitability of the motor system of patients with IGE compared with controls.[28] Thus, the motor system of these patients may be more susceptible to behavioral symptoms driven by the SMA during cognitive tasks.[24] Brain regions showing increased FCS in the parietal cortex (precuneus and inferior parietal lobule) belong to the posterior part of the default mode network.[29] Structural and functional abnormalities have been reported by diffusion-weighted imaging,[30] cortical thickness,[6] and resting-state fMRI studies.[27] The posterior default mode network and related subcortical structures have been associated with the loss of consciousness during seizures.[31] The increased default mode network–pulvinar FCS

in the current study is in accord with findings that default mode network activity increases several seconds before seizure onset.[32] Given that the default mode network–pulvinar network is associated with the default state of the human brain,[31] increased synchrony with thalamic nuclei in the interictal or preictal state may facilitate seizures.[33] In the temporal-thalamic network, the morphometric features of the posterior part of the middle temporal gyrus showed stronger correlation with those of the thalamus in patients with IGE than in controls.[6]

Our results provide additional evidence for abnormalities in this network at the functional level. Because the posterior part of the middle temporal gyrus has been suggested as a semantic hub,[34] our findings help explain abnormal semantic processing observed in many patients with IGE. In addition to corticothalamic involvement in the pathophysiology of IGE, increasing evidence underscores the importance of the striatal system.[7,8,30] The striatum exerts an inhibitory effect on motor systems,[35] and its interaction with the motor and premotor cortices enables the smooth execution of voluntary movements.[36] Decreased control over the highly excitable network may also underlie the behavioral symptoms of seizures such as myoclonic jerks.

There were several limitations to this study. First, simultaneous electroencephalograms were not acquired to exclude fMRI data with GSWDs; thus, we did not know whether the abnormalities in corticothalamic networks were caused by epileptic discharges. In addition, the mono-/polytherapy undertaken by some patients may have confounded the results. Furthermore, epileptic activity is dynamic, and it is therefore difficult to determine its origin by using a static method. Finally, cognitive data and the socioeconomic status of patients and controls were not taken into account; however, it is unlikely that these factors contributed to the between-group differences because most of the participants were from middle-class families.

CONCLUSIONS

Key regions within corticothalamic networks were identified with abnormal FCS in patients with IGE through a resting-state functional connectivity analysis. The identification of these epicenters (the SMA, premotor cortex, pulvinar, ventrolateral nucleus, and default mode network–pulvinar network) provides support for the corticothalamic network theory of IGE pathophysiology.

Disclosures: Gong-Jun Ji, Zhiqiang Zhang, Qing Jiao, Yu-Feng Zang, Wei Liao—*RELATED*: *Grants*: National Natural Science Foundation of China.

REFERENCES

1. Berg AT, Berkovic SF, Brodie MJ, et al. **Revised terminology and concepts for organization of seizures and epilepsies: report of the ILAE Commission on Classification and Terminology, 2005–2009.** *Epilepsia* 2010;51:676–85
2. Meeren H, van Luijtelaar G, Lopes da Silva F, et al. **Evolving concepts on the pathophysiology of absence seizures: the cortical focus theory.** *Arch Neurol* 2005;62:371–76
3. Avoli M. **A brief history on the oscillating roles of thalamus and cortex in absence seizures.** *Epilepsia* 2012;53:779–89
4. Blumenfeld H. **From molecules to networks: cortical/subcortical interactions in the pathophysiology of idiopathic generalized epilepsy.** *Epilepsia* 2003;44(suppl 2):7–15
5. Gotman J, Grova C, Bagshaw A, et al. **Generalized epileptic discharges show thalamocortical activation and suspension of the default state of the brain.** *Proc Natl Acad Sci U S A* 2005;102:15236–40
6. Bernhardt BC, Rozen DA, Worsley KJ, et al. **Thalamo-cortical network pathology in idiopathic generalized epilepsy: insights from MRI-based morphometric correlation analysis.** *Neuroimage* 2009;46:373–81
7. O'Muircheartaigh J, Vollmar C, Barker GJ, et al. **Abnormal thalamocortical structural and functional connectivity in juvenile myoclonic epilepsy.** *Brain* 2012;135:3635–44
8. Wang Z, Zhang Z, Jiao Q, et al. **Impairments of thalamic nuclei in idiopathic generalized epilepsy revealed by a study combining morphological and functional connectivity MRI.** *PLoS One* 2012;7:e39701
9. Szaflarski JP, DiFrancesco M, Hirschauer T, et al. **Cortical and subcortical contributions to absence seizure onset examined with EEG/fMRI.** *Epilepsy Behav* 2010;18:404–13
10. Morel A, Magnin M, Jeanmonod D. **Multiarchitectonic and stereotactic atlas of the human thalamus.** *J Comp Neurol* 1997;387:588–630
11. Metzger CD, van der Werf YD, Walter M. **Functional mapping of thalamic nuclei and their integration into cortico-striatal-thalamo-cortical loops via ultra-high resolution imaging: from animal anatomy to in vivo imaging in humans.** *Front Neurosci* 2013;7:24
12. Tyvaert L, Chassagnon S, Sadikot A, et al. **Thalamic nuclei activity in idiopathic generalized epilepsy: an EEG-fMRI study.** *Neurology* 2009;73:2018–22
13. Zhang D, Snyder AZ, Fox MD, et al. **Intrinsic functional relations between human cerebral cortex and thalamus.** *J Neurophysiol* 2008;100:1740–48
14. Woodward ND, Karbasforoushan H, Heckers S. **Thalamocortical dysconnectivity in schizophrenia.** *Am J Psychiatry* 2012;169:1092–99
15. Anticevic A, Cole MW, Repovs G, et al. **Characterizing thalamo-cortical disturbances in schizophrenia and bipolar illness.** *Cereb Cortex* 2014;24:3116–30
16. Nair A, Treiber JM, Shukla DK, et al. **Impaired thalamocortical connectivity in autism spectrum disorder: a study of functional and anatomical connectivity.** *Brain* 2013;136:1942–55
17. Power JD, Barnes KA, Snyder AZ, et al. **Spurious but systematic correlations in functional connectivity MRI networks arise from subject motion.** *Neuroimage* 2012;59:2142–54
18. Fair DA, Bathula D, Mills KL, et al. **Maturing thalamocortical functional connectivity across development.** *Front Syst Neurosci* 2010;4:10
19. Tomasi D, Volkow ND. **Functional connectivity density mapping.** *Proc Natl Acad Sci U S A* 2010;107:9885–90
20. Zhang Z, Liao W, Chen H, et al. **Altered functional-structural coupling of large-scale brain networks in idiopathic generalized epilepsy.** *Brain* 2011;134:2912–28
21. Kim JB, Suh SI, Seo WK, et al. **Altered thalamocortical functional connectivity in idiopathic generalized epilepsy.** *Epilepsia* 2014;55:592–600
22. Bai X, Guo J, Killory B, et al. **Resting functional connectivity between the hemispheres in childhood absence epilepsy.** *Neurology* 2011;76:1960–67
23. Holmes MD, Brown M, Tucker DM. **Are "generalized" seizures truly generalized? Evidence of localized mesial frontal and frontopolar discharges in absence.** *Epilepsia* 2004;45:1568–79
24. Vollmar C, O'Muircheartaigh J, Barker GJ, et al. **Motor system hyperconnectivity in juvenile myoclonic epilepsy: a cognitive functional magnetic resonance imaging study.** *Brain* 2011;134:1710–19
25. Vollmar C, O'Muircheartaigh J, Symms MR, et al. **Altered microstructural connectivity in juvenile myoclonic epilepsy: the missing link.** *Neurology* 2012;78:1555–59
26. Fox MD, Buckner RL, Liu H, et al. **Resting-state networks link invasive and noninvasive brain stimulation across diverse psychiatric and neurological diseases.** *Proc Natl Acad Sci U S A* 2014;111:E4367–75
27. Wang Z, Lu G, Zhang Z, et al. **Altered resting state networks in**

epileptic patients with generalized tonic-clonic seizures. *Brain Res* 2011;1374:134–41
28. Reutens DC, Berkovic SF, Macdonell RA, et al. **Magnetic stimulation of the brain in generalized epilepsy: reversal of cortical hyperexcitability by anticonvulsants.** *Ann Neurol* 1993;34:351–55
29. Raichle ME, MacLeod AM, Snyder AZ, et al. **A default mode of brain function.** *Proc Natl Acad Sci U S A* 2001;98:676–82
30. Yang T, Guo Z, Luo C, et al. **White matter impairment in the basal ganglia-thalamocortical circuit of drug-naive childhood absence epilepsy.** *Epilepsy Res* 2012;99:267–73
31. Blumenfeld H. **Impaired consciousness in epilepsy.** *Lancet Neurol* 2012;11:814–26
32. Benuzzi F, Mirandola L, Pugnaghi M, et al. **Increased cortical BOLD signal anticipates generalized spike and wave discharges in adolescents and adults with idiopathic generalized epilepsies.** *Epilepsia* 2012;53:622–30
33. Vaudano AE, Laufs H, Kiebel SJ, et al. **Causal hierarchy within the thalamo-cortical network in spike and wave discharges.** *PLoS One* 2009;4:e6475
34. Binder JR, Desai RH, Graves WW, et al. **Where is the semantic system? A critical review and meta-analysis of 120 functional neuroimaging studies.** *Cereb Cortex* 2009;19:2767–96
35. Stocco A, Lebiere C, Anderson JR. **Conditional routing of information to the cortex: a model of the basal ganglia's role in cognitive coordination.** *Psychol Rev* 2010;117:541–74
36. Nagano-Saito A, Martinu K, Monchi O. **Function of basal ganglia in bridging cognitive and motor modules to perform an action.** *Front Neurosci* 2014;8:187

Woven EndoBridge Intrasaccular Flow Disrupter for the Treatment of Ruptured and Unruptured Wide-Neck Cerebral Aneurysms: Report of 55 Cases

D. Behme, A. Berlis, and W. Weber

ABSTRACT

BACKGROUND AND PURPOSE: The safety and efficacy of the Woven EndoBridge (WEB) device for the treatment of cerebral aneurysms have been investigated in several studies. Most of these studies focused on specific aneurysms or a certain WEB device. Our objective was to report the experience of 2 German centers with the WEB device, including technical feasibility, safety, and short-term angiographic outcome.

MATERIALS AND METHODS: We performed a retrospective study of all ruptured and unruptured aneurysms that were treated with a WEB device (WEB Double-Layer, Single-Layer, and Single-Layer Sphere) between April 2012 and August 2014. Primary outcome measures included the feasibility of the implantation and the angiographic outcome at 3-month follow-up. Secondary outcome measures included the clinical outcome at discharge and procedural complications.

RESULTS: Fifty-five aneurysms in 52 patients, including 14 ruptured aneurysms, underwent treatment with the WEB device. The median age of patients was 55 years (range, 30–75 years); 19/55 (37%) were men. The device could be deployed in all patients and was implanted in 51/55 (93%) cases. Procedural complications occurred in 6/51 (12%), comprising 2 thromboembolic events, 2 thrombus formations, 1 high-grade posterior cerebral artery stenosis, and 1 aneurysm rupture. None of these had clinical sequelae. Angiographic follow-up at 3 months was available for 44/51 (86%) aneurysms. A favorable angiographic result at 3 months was achieved in 29/44 (66%) cases, whereas the percentage of good anatomic results increased from 40% in 2012 to 75% in 2014.

CONCLUSIONS: The WEB device proved to be safe. Acceptable occlusion rates can be achieved but seem to require wide experience with the device.

ABBREVIATIONS: ASA = acetylsalicylic acid; DL = Double-Layer; SL = Single-Layer; SLS = Single-Layer Sphere; WEB = Woven EndoBridge

Endovascular treatment has become a widely accepted therapeutic option for ruptured and unruptured cerebral aneurysms.[1-4] Wide-neck or large aneurysms are difficult to treat by coil embolization without the use of intraluminal support devices such as balloons or stents. When these devices are used for the treatment of complex cerebral aneurysms, promising results have been reported.[5,6] Nevertheless, there are several limitations in the use of intraluminal support devices, such as the risk of interventional complications or the need for dual anitplatelet therapy in the case of stent-assisted coil embolization.[7,8] The Woven EndoBridge (WEB; Sequent Medical, Aliso Viejo, California) is an intrasaccular flow-disruption device that modifies blood flow at the aneurysm neck.[9] Today the WEB is available in 3 different shapes: the WEB Double-Layer (DL), Single-Layer (SL) and Single-Layer Sphere (SLS).[10] So far, initial clinical results have mostly been published for the WEB-DL, comprising the results of a prospective, multicenter study and several case series. Additionally, there are only very limited data about the feasibility of the WEB device for the treatment of ruptured aneurysms.[10] Occlusion rates of 81%–92% have been reported when the WEB-DL was implanted.[11-13] In ruptured aneurysms, occlusion rates of 67% have been reported.[10] All studies reported high rates of neck remnants,

Received October 25, 2014; accepted after revision February 6, 2015.

From the Department of Neuroradiology (D.B.), Georg-August-University Göttingen, University Medical Center, Göttingen, Germany; Department of Neuroradiology (A.B.), Klinikum Augsburg, Augsburg, Germany; Departments of Radiology and Neuroradiology (W.W.), Ruhr-University-Bochum, University Medical Center, Bochum Langendreer, Departments of Radiology and Neuroradiology, Bochum, Germany.

D.B. and W.W. changed departments in July 2014. Treatment of the patients was performed at Recklinghausen and Augsburg.

Paper previously presented in part at: Annual Meeting of the Germany Society of Neurosurgeons, May 11–14, 2014; Dresden, Germany; and the Annual Meeting of the Workshop Interventional Neuroradiology (WIN), May 15–16, 2014; Hamburg, Germany.

Please address correspondence to Daniel Behme, MD, Georg-August-University Göttingen, University Medical Center, Department of Neuroradiology, 37099 Göttingen, Germany; e-mail: daniel.behme@med.uni-goettingen.de

http://dx.doi.org/10.3174/ajnr.A4323

which have been shown to represent an inflow into the recess of the WEB-DL in many cases.[11-13] To our knowledge, none of these studies reflect experience with ruptured and unruptured aneurysms that have been treated with all 3 types of WEB devices.

MATERIALS AND METHODS

We conducted a retrospective study of all patients who underwent endovascular therapy for the treatment of ruptured or unruptured cerebral aneurysms using the WEB device between April 2012 and August 2014 at 2 German centers. The indication for treatment and the technique chosen were decided for all aneurysms by a multidisciplinary team, consisting of neurosurgeons and interventional neuroradiologists in each center. All 3 types of the WEB device (DL, SL, and SLS) were used for treatment of the aneurysms. Each of the devices received a European Confirmatory Mark for the treatment of unruptured and ruptured aneurysms. According to the guidelines of the local ethics committee, no approval was necessary. The WEB device is a self-expanding, braided nitinol mesh. The Dual-Layer device is constructed with 2 compartments formed by inner and outer braids held together by proximal, middle, and distal radiopaque markers. The WEB-DL is braided with 216 or 288 nitinol wires, depending on the device size. The WEB-SL and the WEB-SLS devices were launched in 2013; these devices are braided like the dual-layer, but they form only a single-layer device that is oblate and either of globular or spheric geometry, facilitating a lower profile of the device. The WEB is fully retrievable before implantation, and it can be delivered through a 0.027-inch microcatheter. The device uses an electrothermal detachment system. Anitplatelet and anticoagulation regimens were the following: After the first patient had a thromboembolic complication at Center A, all patients with unruptured aneurysms received 100 mg acetylsalicylic acid (ASA) and 75 mg clopidogrel 5 days before treatment. ASA was continued for 6 weeks if no additional stent placement was performed. Clopidogrel was stopped after implantation of the WEB. If additional stent placement was performed, clopidogrel was continued for 6 weeks, and ASA, for 6 months. During the procedure, a bolus of 5000 IU heparin was administered, and systemic heparinization was continued for 48 hours. Heparin administration was then adjusted with activated clotting time, aiming for 2–3 times. At Center B, all patients with unruptured aneurysms received 100 mg ASA for 1 month of treatment; additionally, a bolus of 5000 IU heparin was administered during the endovascular procedure in general, before the detachment of the device. In cases of ruptured aneurysms, patients received 100 mg ASA for 6 weeks at Center A and no anitplatelet drugs at Center B if not required for other medical conditions.

All clinical data were taken from the electronic patient records. Clinical assessment at admission and discharge was performed by a consultant neurosurgeon. The angiographic and all other imaging data were re-evaluated by 2 senior neuroradiologists (W.W. and A.B.). Occlusion results were categorized into the following: complete, neck remnants with real inflow into the neck, neck remnants with inflow into the marker recess of the device, and aneurysm remnants. A favorable result was defined as complete occlusion or a neck remnant. Only DSA images were used for the evaluation of the occlusion results. Primary outcome measures were the technical feasibility of the WEB implantation and angiographic outcome at 3 months or at first angiographic control if the control was before 90 days of treatment. Secondary outcome measures were clinical outcome at discharge and procedural complications of the WEB implantation. Subgroups of interest were identified a priori, and statistical comparisons among these cohorts were performed by using contingency tables and the Fisher exact test. Statistical analyses were performed with GraphPad Prism Software, Version 6.01 (GraphPad Software, San Diego, California). A P value $\leq .05$ was considered statistically significant.

RESULTS

We identified 52 patients with 55 aneurysms who underwent an endovascular treatment using the WEB device between April 2012 and August 2014. Fourteen of 55 (25%) aneurysms were ruptured. Four of 52 (8%) patients in this series also participated in the Woven Endoluminal Bridge Clinical Assessment of intra-Saccular aneurysmal Therapy study.[14] The median age of patients was 50 years (range, 30–75 years); 19/55 (35%) were men. The WEB could be implanted in 51 aneurysms. In an additional 4 cases, the WEB was deployed but not implanted. The aneurysm locations in these were the following: the MCA in 2 cases, anterior communicating artery in 1 case, and the carotid-T in 1 case. The device was not implanted because of inappropriate sizing in all 4 cases. In 2 cases, the deployment led to a stenosis of an adjacent vessel, which was completely reversed after the WEB was removed. Neither vessel stenosis led to persistent impairment. Aneurysm location was the middle cerebral artery in 19/51(37%) (Fig 1); the anterior communicating in 9/51 (18%); the basilar artery in 10/51 (20%) (Fig 2); the posterior communicating artery in 4/51 (8%); the carotid-T in 4/51 (8%); and 4/51 (6%) internal carotid artery, anterior cerebral artery, and superior cerebellar artery in 1/51 each (2%). Aneurysm size was the following (median, range): neck, 5 mm (2–8 mm); dome, 7 mm (3.2–12 mm); and aneurysm height, 7 mm (4–15 mm). Forty-one of 51 (80%) aneurysms had a neck of ≥4 mm. In those patients with ruptured aneurysms, the location was the MCA in 6/14 (43%); the anterior communicating artery in 3/14 (21%); the posterior communicating artery in 2/14 (14%); the superior cerebellar artery in 1/14 (7%); the anterior cerebral artery, carotid-T 1/14 (7%) each, and posterior inferior cerebellar artery in 1/14 each (7%). The sizes of the ruptured aneurysms were the following: neck, 4.5 mm (range, 3.2–7.8 mm); dome, 6.7 mm (range, 3.4–9 mm); and height, 6.6 mm (range, 4–14 mm).

Clinical presentation of those patients with ruptured aneurysms was Hunt and Hess grades 1 and 2 in 4 cases each, Hunt and Hess 3 in 5 cases, and Hunt and Hess 4 in 1 case. Clinical outcome at discharge was favorable (mRS 0 + 1) in 11/14 (79%) ruptured aneurysms. Three of 14 (21%) patients died within the acute phase of the acute subarachnoid hemorrhage. In the cohort with unruptured aneurysms, 37/37 (100%) had a favorable outcome (mRS 0 + 1) at discharge. Of those patients with mRS 1 (5/37), 3 had been mRS 1 before treatment, 1 had a stroke caused by a thromboembolic complication, and the other had acute SAH after an accidental aneurysm rupture (Table).

Short-term angiographic results were available for 44/51

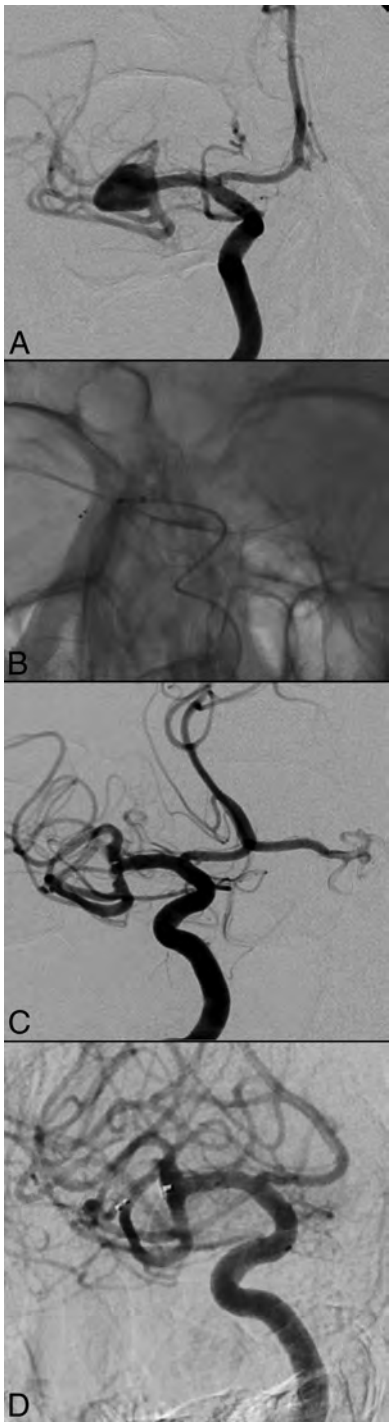

FIG 1. Unruptured MCA aneurysm of the right side, treated with a WEB-DL 9 × 6 mm. *A*, Initial angiogram of the aneurysm. *B*, Unsubtracted image after deployment of the WEB-DL 9 × 6 mm. *C*, Initial result after implantation of the WEB. *D*, Angiographic follow-up after 10 months, confirming stable occlusion of the aneurysm.

(86%) at 99 days (range, 8–471 days) after treatment. In 15/44 (34%) cases, a total occlusion was observed. In another 14/44 (32%) cases, a neck remnant was present, where 11/14 (79%) showed real inflow into the aneurysm neck and 3/14 (21%) were classified as inflow into the marker recess.

In the remaining 15 cases, an aneurysm remnant was observed. All of these 15 patients underwent endovascular retreatment. Y-stent placement with additional coil embolization was performed in 8/15 (53%) (Fig 2); additional stent placement without coil embolization, in 1; and coil embolization without the use of an intraluminal support device was used in the remaining 6 cases.

A favorable angiographic result (complete occlusion or neck remnant) was achieved in 23/35 (66%) unruptured aneurysms and in 6/9 (67%) ruptured aneurysms ($P = 1.0$). When the WEB-SL or -SLS was used, favorable results were achieved in 65% (15/23) compared with 14/21 (67%) when the WEB-DL was deployed ($P = 1.0$). Most interesting, we found a rate of 83% (5/6) favorable angiographic results when the WEB-SL was used in ruptured aneurysms. When analyzing the occlusion results according to the site of the aneurysms, we found favorable results to be the lowest in anterior communicating artery aneurysms, with 38% compared with 71% in the MCA and 71% in basilar artery aneurysms. Comparing the anatomic results at 3 months according to the year of treatment, we found that the percentage of favorable angiographic results increased from only 40% in 2012 to 68% in 2013 and reached 75% in 2014 (Fig 3). The number of treatments with follow-up available was 5 in 2012, 31 in 2013, and 8 in 2014.

For all patients (15/29) who had a second follow-up and who did not undergo retreatment after the initial implantation of the WEB, we could prove stable results compared with the first angiographic control at 360 days (range, 84–470 days) after treatment. Notably, all neck remnants (real and inflow into the marker recess) were stable at the time of the second control.

For those who received retreatment of an aneurysm remnant, we found aneurysms to be totally occluded or showing a neck remnant in only 5/10 (50%) cases.

In general, complications occurred in 6/51 (12%) cases (Table). In 4 cases, thrombus formation occurred in distal vessel branches; 2 resolved completely after therapy with abciximab (ReoPro); another resolved incompletely after administration of intra-arterial tissue plasminogen activator, leading to an incomplete infarction of the left posterior cerebral artery territory; and the remaining case resolved incompletely after treatment with tirofiban (Aggrastat), leading to a partial infarction of the right MCA territory. One of the patients who had a thromboembolic infarction did not develop any symptoms after the intervention. The other developed a weakness of the left arm after treatment that was completely resolved at discharge. In 1 case, the implantation of the WEB device into a basilar artery tip aneurysm led to a stenosis of the right posterior cerebral artery P1 segment, which had to be stented (Fig 2). In this case, eptifibatide (Integrilin) was administered for 24 hours and the patient was subsequently treated with ASA and clopidogrel. The patient did not develop any clinical symptoms. Additionally, 1 aneurysm rupture caused by the microcatheter occurred; the patient received additional treatment with a stent and coils. This patient developed a paresis of his left leg (mRS 1 at discharge).

The retreatment procedures were performed without complications. One patient had an in-stent thrombosis after Y-stent placement 10 days after the retreatment procedure because he had stopped the dual antiplatelet medication on his own.

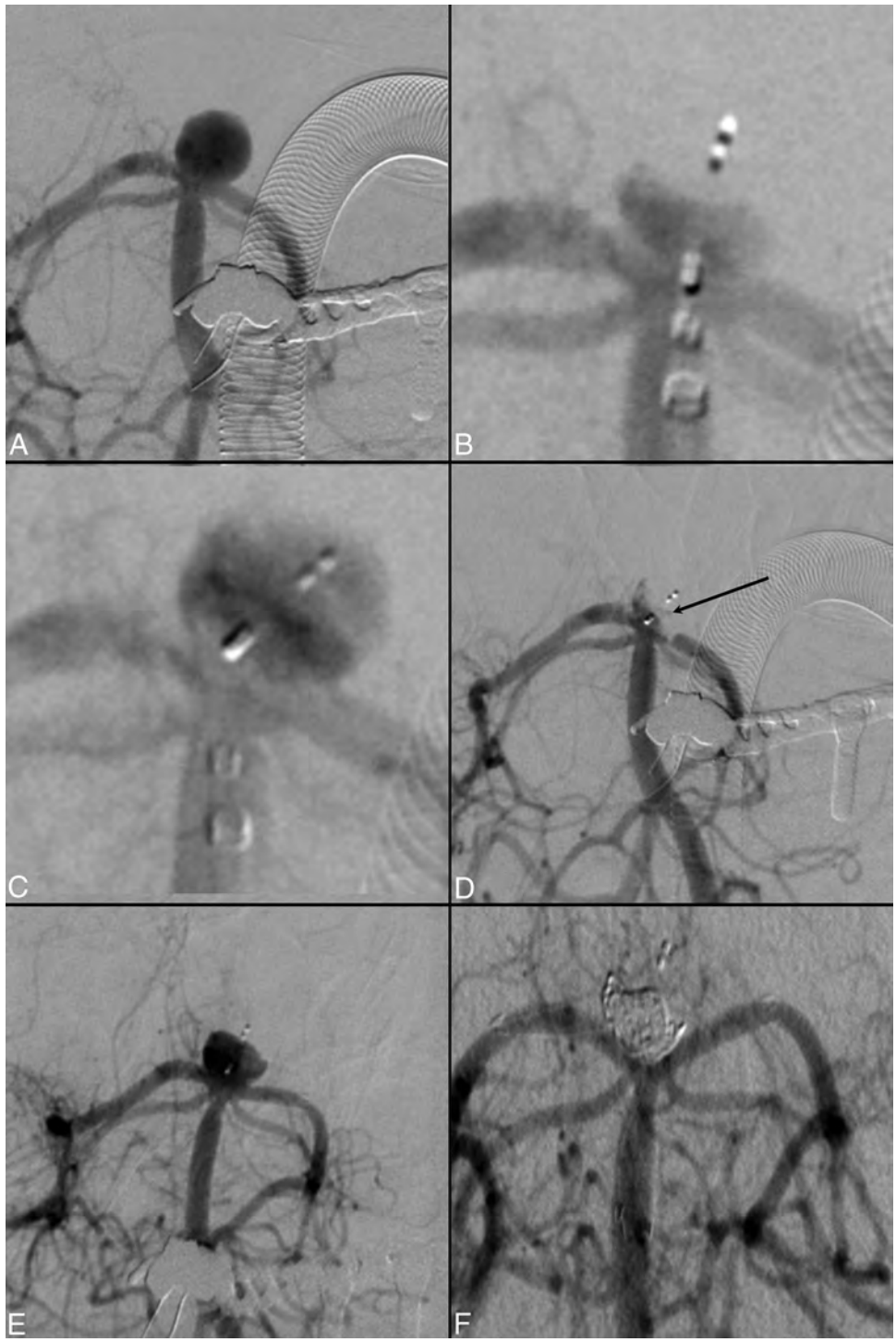

FIG 2. Unruptured basilar artery tip aneurysm and posterior cerebral artery stenosis after migration of the WEB and retreatment with stent and coils. *A*, Initial angiogram of the aneurysm. *B*, Deployment of the WEB-DL 7 × 4 mm. *C*, Migration of the device toward the left side of the aneurysm. *D*, High-grade stenosis of the left posterior cerebral artery P1 segment (*arrow*), which was stented subsequently with a Neuroform stent (Stryker Neurovascular, Fremont, California). *E*, Control angiogram at 3 months shows an aneurysm remnant. *F*, Aneurysm occlusion after Y-stent placement (Low-Profile Visualized Intraluminal Support Device; MicroVention, Tustin, California) and additional coil embolization.

DISCUSSION

Our findings confirm the results of the previously published case series and the preliminary results of the Woven Endoluminal Bridge Clinical Assessment of intraSaccular aneurysmal Therapy study regarding safety, technical feasibility, and high rates of favorable outcome of the device. The results do not confirm the very high rates of favorable occlusion results that have been reported previously.[11-15]

The deployment of the WEB device was feasible in all 55 aneurysms, and it was finally implanted in 51/55 (93%) cases, which is a rate of technical success comparable with that reported in the literature.[11,13] Complications occurred in 6/51 (12%) cases in our

Overview of complications

No.	Aneurysm Location	Neck Size (mm)	Device, Size	Status (Ruptured/Unruptured)	Complication	Outcome at Discharge (mRS)
1	BA tip	5.5	DL, 7 × 4	Unruptured	P1 stenosis	0
2	BA tip	8.0	DL, 10 × 7	Unruptured	Thromboembolic infarction left PCA territory	0
3	BA tip	4.5	DL, 5 × 3	Unruptured	Thrombus formation, no infarction	0
4	MCA	5.0	DL, 6 × 3	Unruptured	Thromboembolic with MCA infarction	0
5	MCA	5.5	DL, 7 × 6	Unruptured	Thromboembolic with MCA infarction	1
6	AcomA	4.1	SL, 6 × 4	Unruptured	Aneurysm rupture	1

Note:—BA indicates basilar artery; AcomA, anterior communicating artery; PCA, posterior cerebral artery.

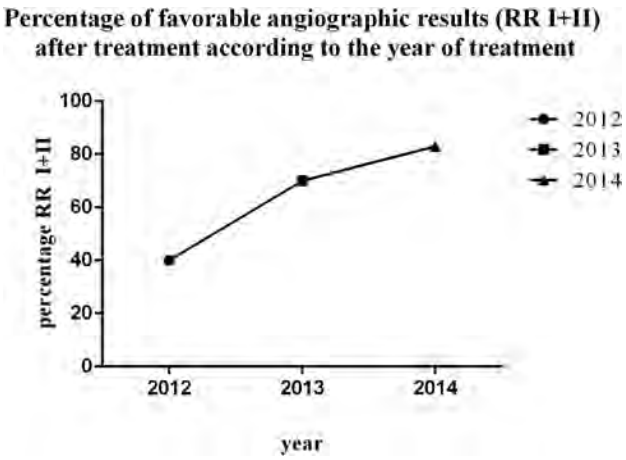

FIG 3. "Learning curve" showing the percentage of successful treatments from 2012 to 2014.

series, which is similar to those found by Papagiannaki et al[13] and Pierot et al [12] when the WEB was used for aneurysm embolization. In this study, thrombus formation occurred in 2 cases and was resolved completely after medical treatment; in 2 other cases, thromboembolic complications occurred that caused cerebral infarction. A rate of 2/51 (4%) thromboembolic complications, therefore, is very low compared with that published so far when the WEB was used.[11,13] When competing techniques such as stents or balloons have been deployed for the treatment of wide-neck cerebral aneurysms, much higher rates of thromboembolic complications were found.[16] A special concern of the treatment is the comparatively large microcatheter necessary for the delivery of the device, which might lead to higher rates of aneurysm rupture because of its rigidity. Nevertheless, this study found aneurysm rupture to be a rare event (2%), which was not more frequent than that reported in the Clinical and Anatomical Results in the Treatment of Ruptured Intracranial Aneurysms series or the Analysis of Treatment by Endovascular Approach of Nonruptured Aneurysms trial.[17,18] The overall complication rate in our series remains comparatively low when adding the complications of the 15 retreatment procedures, with only 1 thrombotic occlusion of a stent, which happened after the patient stopped his medication with ASA and clopidogrel autonomously.

Taking into account that one-third of the aneurysms in our series are MCA aneurysms that also could have been treated surgically, we compared the complication rates with those in large trials that investigated complications in the clipping of unruptured aneurysms. Barker et al[19] in 2004 reported about 7.8% neurologic complications and 6.4% occluded arteries after surgical clipping, whereas only 2/51 (4%) of the patients in our series had a neurologic complication or a thrombotic event that led to an infarction. Others found the rate of neurologic complications to be 7.4% and the occlusion of cerebral arteries to be 4.2%, also slightly higher rates compared with those in our series.[20]

The treatment with the WEB led to high rates of favorable clinical outcome at discharge in unruptured (100%, mRS 0 + 1) and ruptured (79%, mRS 0 + 1) aneurysms. Compared with what is known from the Analysis of Treatment by Endovascular Approach of Nonruptured Aneurysms trial (transient and permanent neurologic deficits in 5.4%) and the International Subarachnoid Aneurysm Trial (23.7% mortality and morbidity), these results are very promising and confirm what has been known about clinical outcome after treatment with the WEB.[1,18]

The rate of favorable angiographic results at 3 months was comparatively low, with 66% in this series. Others reported favorable occlusion results of 81%–92% when the WEB was used for aneurysm occlusion.[11-13] Caroff et al[10] found occlusion rates as low as 67% in ruptured wide-neck aneurysms when treated with the WEB device, which is comparable our findings.

In this series, the occlusion rate did not depend on the aneurysm location or the device used (SL versus DL) or on the aneurysm status (ruptured versus unruptured). Most interesting, we found that the rate of favorable angiographic results at 3 months was the highest in 2014 compared with 2012 and 2013, with 75% in 2014 versus only 40% in 2012, strongly indicating that experience is a prerequisite for successful use of the device, especially in terms of sizing, because feasibility was high and complication rates were low in all years. Furthermore, there was no rerupture when the WEB was used to treat patients with acute SAH. In addition, occlusion results were stable in those patients who underwent a midterm follow-up after treatment with a WEB alone but not in those with additional endovascular treatment, indicating that the WEB might lead to more stable anatomic results in wide-neck aneurysms compared with stent placement or balloon remodeling if the device was initially occluding the aneurysm.

Why occlusion rates are lower in this series remains uncertain; most likely the results are biased by the high rate of unfavorable occlusions in 2012 and the beginning of 2013, which were basically caused by undersizing the device.

The basic limitations of this study are the retrospective design and the low number of cases. Additionally, the adjudication of the

end points (eg, angiographic results, complications, and clinical outcome) was performed at the reporting site, without a core laboratory or requirement of an independent adjudicator. All statistical analyses might be underpowered due to the limited number of cases, and long-term controls are necessary to prove the efficacy of the device.

CONCLUSIONS

The deployment and implantation of the WEB device proved feasible and safe. Nevertheless, wide experience seems to be a prerequisite to achieve acceptable occlusion rates with the device. Larger studies are necessary to investigate the feasibility and results, especially with the recently introduced WEB-SL and WEB-SLS.

Disclosures: Daniel Behme—*UNRELATED*: *Support for Travel to Meetings for the Study or Other Purposes*: Sequent Medical (travel to German Society of Neurosurgery Meeting, Dresden, Germany); *Other*: minor speaking honoraria from Sequent Medical. Ansgar Berlis—*RELATED*: *Consulting Fee or Honorarium*: Sequent Medical (proctoring), MicroVention (proctoring), Covidien (proctoring); *Support for Travel to Meetings for the Study or Other Purposes*: Sequent Medical, MicroVention, Covidien, Stryker, Penumbra; *UNRELATED*: *Consultancy*: proctoring and consultancy agreements with Sequent Medical, Covidien, and Stryker; *Payment for Lectures (including service on Speakers Bureaus)*: Sequent Medical, Covidien, MicroVention, Stryker, Penumbra. Werner Weber—*RELATED*: *Consulting Fee or Honorarium*: proctor for the WEB device; *UNRELATED*: *Consultancy*: proctor for the WEB device in Europe; *Other*: participation in the Woven Endoluminal Bridge Clinical Assessment of Intrasaccular Aneurysmal Therapy I.

REFERENCES

1. Molyneux A, Kerr R, Stratton I, et al. **International Subarachnoid Aneurysm Trial (ISAT) of neurosurgical clipping versus endovascular coiling in 2143 patients with ruptured intracranial aneurysms: a randomised trial.** *Lancet* 2002;360:1267–74
2. Henkes H, Fischer S, Weber W, et al. **Endovascular coil occlusion of 1811 intracranial aneurysms: early angiographic and clinical results.** *Neurosurgery* 2004;54:268–80; discussion 280–85
3. Pierot L, Spelle L, Vitry F. **Immediate anatomic results after the endovascular treatment of unruptured intracranial aneurysms: analysis of the ATENA series.** *AJNR Am J Neuroradiol* 2010; 31:140–44
4. Pierot L, Cognard C, Ricolfi F, et al. **Immediate anatomic results after the endovascular treatment of ruptured intracranial aneurysms: analysis in the CLARITY series.** *AJNR Am J Neuroradiol* 2010;31:907–11
5. Biondi A, Janardhan V, Katz JM, et al. **Neuroform stent-assisted coil embolization of wide-neck intracranial aneurysms: strategies in stent deployment and midterm follow-up.** *Neurosurgery* 2007;61: 460–68; discussion 468–69
6. Behme D, Weber A, Kowoll A, et al. **Low-Profile Visualized Intraluminal Support Device (LVIS Jr) as a novel tool in the treatment of wide-necked intracranial aneurysms: initial experience in 32 cases.** *J Neurointerv Surg* 2015;7:281–85
7. Pierot L, Cognard C, Spelle L, et al. **Safety and efficacy of balloon remodeling technique during endovascular treatment of intracranial aneurysms: critical review of the literature.** *AJNR Am J Neuroradiol* 2012;33:12–15
8. Nishido H, Piotin M, Bartolini B, et al. **Analysis of complications and recurrences of aneurysm coiling with special emphasis on the stent-assisted technique.** *AJNR Am J Neuroradiol* 2014;35:339–44
9. Ding YH, Lewis DA, Kadirvel R, et al. **The Woven EndoBridge: a new aneurysm occlusion device.** *AJNR Am J Neuroradiol* 2011;32:607–11
10. Caroff J, Mihalea C, Dargento F, et al. **Woven EndoBridge (WEB) device for endovascular treatment of ruptured intracranial wide-neck aneurysms: a single-center experience.** *Neuroradiology* 2014; 56:755–61
11. Lubicz B, Klisch J, Gauvrit JY, et al. **WEB-DL endovascular treatment of wide-neck bifurcation aneurysms: short- and midterm results in a European study.** *AJNR Am J Neuroradiol* 2014;35:432–38
12. Pierot L, Klisch J, Cognard C, et al. **Endovascular WEB flow disruption in middle cerebral artery aneurysms: preliminary feasibility, clinical, and anatomical results in a multicenter study.** *Neurosurgery* 2013;73:27–34; discussion 34–35
13. Papagiannaki C, Spelle L, Januel AC, et al. **WEB intrasaccular flow disruptor—prospective, multicenter experience in 83 patients with 85 aneurysms.** *AJNR Am J Neuroradiol* 2014;35:2106–11
14. Pierot L, Spelle L, Costalat V, et al. **E-029 WEB Flow Disruption: Preliminary Results from WEBCAST trial.** *J Neurointerv Surgery* 2014;6(Suppl 1):A51
15. Pierot L, Liebig T, Sychra V, et al. **Intrasaccular flow-disruption treatment of intracranial aneurysms: preliminary results of a multicenter clinical study.** *AJNR Am J Neuroradiol* 2012;33:1232–38
16. Fargen KM, Mocco J, Neal D, et al. **A multicenter study of stent-assisted coiling of cerebral aneurysms with a Y-configuration.** *Neurosurgery* 2013;73:466–72
17. Cognard C, Pierot L, Anxionnat R, et al. **Results of embolization used as the first treatment choice in a consecutive nonselected population of ruptured aneurysms: clinical results of the CLARITY GDC study.** *Neurosurgery* 2011;69:837–41; discussion 842
18. Pierot L, Spelle L, Vitry F. **Immediate clinical outcome of patients harboring unruptured intracranial aneurysms treated by endovascular approach: results of the ATENA study.** *Stroke* 2008;39: 2497–504
19. Barker FG 2nd, Amin-Hanjani S, Butler WE, et al. **Age-dependent differences in short-term outcome after surgical or endovascular treatment of unruptured intracranial aneurysms in the United States, 1996–2000.** *Neurosurgery* 2004;54:18–28; discussion 28–30
20. Higashida RT, Lahue BJ, Torbey MT, et al. **Treatment of unruptured intracranial aneurysms: a nationwide assessment of effectiveness.** *AJNR Am J Neuroradiol* 2007;28:146–51

Vascular Wall Imaging of Unruptured Cerebral Aneurysms with a Hybrid of Opposite-Contrast MR Angiography

T. Matsushige, Y. Akiyama, T. Okazaki, K. Shinagawa, N. Ichinose, K. Awai, and K. Kurisu

ABSTRACT

BACKGROUND AND PURPOSE: Inflammation and degeneration of the intracranial saccular aneurysm wall play a major role in aneurysm formation, development and subsequent rupture. The aim of this study was to characterize the walls of unruptured intracranial aneurysms by using a hybrid of opposite-contrast MRA at 3T.

MATERIALS AND METHODS: Fourteen consecutive patients with 17 unruptured intracranial aneurysms who initially underwent clipping surgery were prospectively evaluated. All aneurysms were scanned preoperatively by using a hybrid of opposite-contrast MRA in 3T high-resolution MR imaging. We classified intraoperative findings of atherosclerotic plaques in the aneurysms into 3 grades: grade A (major plaques), grade B (minor plaques), and grade C (no plaques). The contrast ratio of the high-intensity area was also measured relative to the background low-intensity area inside the carotid artery.

RESULTS: Findings from preoperative plaque imaging of the aneurysm corresponded to the intraoperative findings in 15 of 16 aneurysms (excluding 1 that was impossible to visualize in its entirety due to anatomic reasons). Overall sensitivity and specificity of the hybrid of opposite-contrast MRA were 88.9% and 100%, respectively. During the operation, 4 aneurysms were classified as grade A; 5, as grade B; and 7, as grade C. The means of the contrast ratio for grades A, B, and C were 0.72 ± 0.03, 0.34 ± 0.30, and −0.02 ± 0.09, respectively.

CONCLUSIONS: The hybrid of opposite-contrast MRA can detect visible atherosclerotic plaques in the unruptured aneurysm wall, and the contrast ratio in intracranial aneurysms correlated with their presence and extent. A study including a larger series is needed to validate the diagnostic potential of this imaging technique.

ABBREVIATIONS: AcomA = anterior communicating artery; FSBB = flow-sensitive black-blood; HOP-MRA = hybrid of opposite-contrast MR angiography; WVCR = wall-vessel lumen contrast ratio

Intracranial aneurysms are common vascular lesions, often consisting of a saccular dilation of a cerebral artery vessel. The prevalence of intracranial aneurysms in the general population is estimated between 2.5% and 5%.[1,2] Aneurysmal rupture occurs with a 1% risk per year, depending on the size, location, and morphometry of the aneurysm, and leads to subarachnoid hemorrhage with associated high morbidity and mortality rates.[1,2] Intracranial aneurysms with an estimated high risk of rupture undergo management via a surgical or endovascular approach, depending on the specific risks of treatment.[3,4] Therefore, it is important to accurately assess the risk of aneurysmal rupture.

The pathogenesis of intracranial aneurysms and their natural history are not well-understood. Histopathologic studies have shown that the infiltration of inflammatory cells and the degeneration of the aneurysm wall with atherosclerosis correlates with the formation, development, and rupture risk of cerebral aneurysms.[5-9] However, characterization of the aneurysm wall is limited by imaging data quality and the need to harvest surgical specimens.

In this regard, the characteristics of high-field-strength MR imaging, which has a favorable SNR and changes in relaxation time and susceptibility, can depict the intracranial vessel walls and their pathologies, including small vessels with atherosclerosis.[10,11]

The hybrid of opposite-contrast MR angiography (HOP-MRA) used in this study is a modern technique that combines the advantages of 3D TOF MRA and flow-sensitive black-blood (FSBB) MRA.[12] The clinical efficacy of this technique was established to improve the visualization of peripheral vessels.[13,14] The-

Received September 17, 2014; accepted after revision January 9, 2015.

From the Department of Neurosurgery (T.M., T.O., K.S., N.I., K.K.), Graduate School of Biomedical and Health Sciences, Hiroshima University, Hiroshima, Japan; Department of Neurosurgery (T.M.), University Hospital Essen, Essen, Germany; and Department of Diagnostic Radiology (Y.A., K.A.), Institute of Biomedical and Health Sciences, Hiroshima University, Hiroshima, Japan.

Paper previously presented at: Annual Meeting of Radiological Society of North America, November 30–December 5, 2014; Chicago, Illinois.

Please address correspondence to Toshinori Matsushige, MD, PhD, Department of Neurosurgery, University Hospital Essen, Hufelandstr 55, 45147, Essen, Germany; e-mail: teruteru728@hiroshima-u.ac.jp

http://dx.doi.org/10.3174/ajnr.A4318

oretically, tissue with shorter T1 and T2* introduces high signal in FSBB of HOP-MRA, which demonstrates atherosclerotic plaques, including fat, as high-signal-intensity areas and demonstrates the blood space as low-signal-intensity areas in intracranial aneurysms.[12] The strength of this technique is the dual-echo 3D gradient-echo sequence, which enables a shorter imaging time and minimization of misregistration. The present study investigated the utility of HOP-MRA at 3T for the characterization of visible atherosclerotic plaques in intracranial aneurysms by using subtraction between TOF and FSBB imaging.

MATERIALS AND METHODS

Study Design

This study was approved by an institutional review committee, and the subjects gave informed consent to participate. It prospectively evaluated the diagnostic feasibility of delineating the aneurysm wall by using HOP-MRA at 3T in comparison with intraoperative findings of the aneurysm. Inclusion criteria were the following: 1) patients undergoing elective clipping surgery, 2) 18–80 years of age, and 3) the ability to give informed consent. Exclusion criteria were the following: 1) presence of cardiac pacemaker or any other electronic implants, 2) pregnancy or breast feeding, and 3) claustrophobia.

Preoperative Image Evaluation

Preoperative assessment of aneurysms in our institution includes routine cerebral DSA, CTA, and MR imaging. Calcification of the aneurysm was assessed by using CTA with sections of 1-mm thickness with a 0.5-mm overlap. The morphology, location, and size of the aneurysm were assessed by 3D rotational DSA by the operating neurosurgeon with 16 years of experience (T.O.). Additionally the presence of high signal intensity in the aneurysm wall was evaluated on multiplanar reconstruction (transverse, coronal, and sagittal) of HOP-MRA at 3T by a second neurosurgeon (T.M.) before the operation.

Intraoperative Assessment

The aneurysm was completely exposed via the trans-Sylvian or interhemispheric approach by craniotomy. Intraoperative evaluation of the aneurysm wall was performed in consensus by both neurosurgeons. In addition, a third neurosurgeon with 10 years of experience (K.S.), who was blinded to preoperative MR imaging data, evaluated the microscopic findings on all aneurysms by operative video. Microscopic surgical findings of the aneurysm wall were defined by visible atherosclerotic changes (yellowish) and classified into 3 grades by the neurosurgeons as grade A (major plaques), grade B (minor plaques), and grade C (no plaques).

HOP-MRA Sequence

All images were acquired on a commercially available 3T MR imaging scanner (Vantage Titan 3T; Toshiba Medical Systems, Tokyo, Japan) equipped with a 6-channel head coil. For HOP-MRA, we used a 3D gradient-echo, double-echo sequence. TEs were chosen for TOF-contrast with the first echo and FSBB contrast with the second echo. The 2 original images were subtracted and displayed by maximum intensity projection. The scan parameters were the following: acquisition time, 7:00 min; TR, 21 ms; TE 1, 3.3 ms (TOF); TE 2, 13.9 ms (FSBB); flow-dephasing gradient ($b = 0.3$ s/mm^2); flip angle, 20°; field of view, 240 mm; section thickness, 1 mm; number of partitions, 60; matrix, 192 × 256; and NEX, 2.

Image Evaluation

A radiologic technician (19 years of experience) measured the mean signal intensity of the highest intensity area in the aneurysm wall compared with the background low-intensity area inside the ipsilateral carotid artery. Imaging data were transferred to an Advantage Workstation (Version 3.1; GE Healthcare, Milwaukee, Wisconsin) with Virtual Place Office (Azemoto, Tokyo, Japan) software to perform postprocessing. Diameters for the ROIs in the aneurysm wall were 2 mm^2 without including voxels from adjacent structures. The ROI in the carotid artery was thought to be suitable for referring intensity very close to that of most aneurysms and was placed in the center of the ipsilateral carotid artery amounting to 2 mm^2. The wall-vessel lumen contrast ratio (WVCR = $\text{Signal}_{\text{wall}} - \text{Signal}_{\text{vessel lumen}}/\text{Signal}_{\text{wall}} + \text{Signal}_{\text{vessel lumen}}$) was also assessed.

Statistical analyses were performed by using the JMP statistical package (Version 10; SAS Institute, Cary, North Carolina). To compare differences between 2 groups, we used the Fisher exact test for categoric factors between 2 groups and the Mann-Whitney *U* test for quantitative variables. Statistical significance was indicated by $P < .05$.

RESULTS

All patients tolerated the examination well, and this prospective study included 14 patients (6 men, 8 women; median age, 60 years; age range, 24–76 years) with 17 aneurysms in total. Patient demographics including vascular atherosclerotic risk factors such as sex, age, hypertension, dyslipidemia, diabetes mellitus, and cigarette smoking are summarized in the Table. The evaluation by DSA showed that all aneurysms were located in the anterior circulation (ICA, $n = 3$; anterior cerebral artery, $n = 8$; and MCA, $n = 6$). The median maximum diameter of the aneurysms was 5.4 mm (range, 2.8–14.1 mm). There were no aneurysms with calcification on thin-section CTA.

The interobserver assessment between 2 neurosurgeons in consensus during the operation and another neurosurgeon was identical. Of 17 aneurysms, we delineated 9 aneurysms with thickened walls corresponding to high signal intensity. During the operation, 4 aneurysms were classified as grade A; 5, as grade B; and 7, as grade C. One aneurysm could not be completely characterized because it arose from the ICA terminal with posterior projection (case 5).

If we excluded this aneurysm, which was anatomically impossible to assess, 15 of 16 (93.8%) aneurysms showed excellent correlation between the surgical overview and the presence of high signal in the aneurysm wall. Overall sensitivity of HOP-MRA was 88.9%, and specificity was 100%. There was no correlation between the presence of atherosclerosis and vascular atherosclerotic risk factors: sex ($P = .70$), age ($P = .83$), hypertension ($P = .62$), dyslipidemia ($P = .64$), diabetes mellitus ($P = 1.00$), and cigarette smoking ($P = .64$). However, there was a statistically significant difference between the presence of atherosclerosis and aneurysm size ($P = .03$). The mean WVCR of the aneurysm wall with atherosclerotic plaques (grades A and B) was significantly higher than that in the aneurysm wall without plaques (grade C) ($P =$

Patient demographics and findings

Case No.	Aneurysm No.	Patients Sex	Patients Age (yr)	Aneurysms Location	Aneurysms Maximum Size (mm)	Aneurysms Intraoperative Plaque Findings[a]	Aneurysm Wall Findings at HOP-MRA High Signal Intensity	Aneurysm Wall Findings at HOP-MRA WVCR[b]	Atherosclerotic Risk Factors HT	Atherosclerotic Risk Factors DL	Atherosclerotic Risk Factors DM	Atherosclerotic Risk Factors CS
1	1	M	24	ICA Ach	4.2	A	+	0.73	+	−	−	−
2	2	M	35	ACA (A1)	2.8	C	−	−0.02	+	−	−	+
3	3	M	69	MCA	6.1	C	−	−0.22	−	+	−	+
4	4	M	76	MCA	14.1	A	+	0.70	+	−	−	+
5	5	F	71	ICA PcomA	5.9	C	−	0.01	−	+	−	+
	6	F	71	ICA terminal	3.5	NA[c]	+	0.64	−	+	−	+
6	7	F	53	dACA	7.2	A	+	0.68	+	+	−	+
	8	F	53	dACA	6.7	B	+	0.62	+	+	−	+
	9	F	53	AcomA	4.2	C	−	0.02	+	+	+	+
7	10	F	63	MCA	5.4	B	+	0.04	+	+	−	−
8	11	F	70	MCA	5.1	B	+	0.44	−	+	−	−
9	12	M	60	AcomA	4.7	C	−	0.00	+	−	−	−
10	13	F	63	AcomA	5.0	B	−	0.02	+	+	−	−
11	14	M	61	MCA	7.2	B	+	0.60	+	−	−	+
12	15	F	73	MCA	9.6	A	+	0.75	−	−	−	−
13	16	F	55	AcomA	4.0	C	−	0.04	+	−	−	+
14	17	F	69	AcomA	5.6	C	−	0.03	−	+	−	−

Note:—Ach indicates anterior choroidal artery; PcomA, posterior communicating artery; ACA (A1), anterior cerebral artery (A1 segment); dACA, distal anterior cerebral artery; HT, hypertension; DL, dyslipidemia; DM, diabetes mellitus; CS, cigarette smoking; NA, not assessed due to anatomic reasons; +, present; −, absent.

[a] Intraoperative plaque assessment in the aneurysm was demonstrated as the following: grade A, major plaques; grade B, minor plaques; grade C, no plaques.

[b] WVCR indicates a high-intensity area in the aneurysm wall to the background low-intensity area inside the aneurysm.

[c] Impossible to characterize the entire aneurysm due to anatomic reasons.

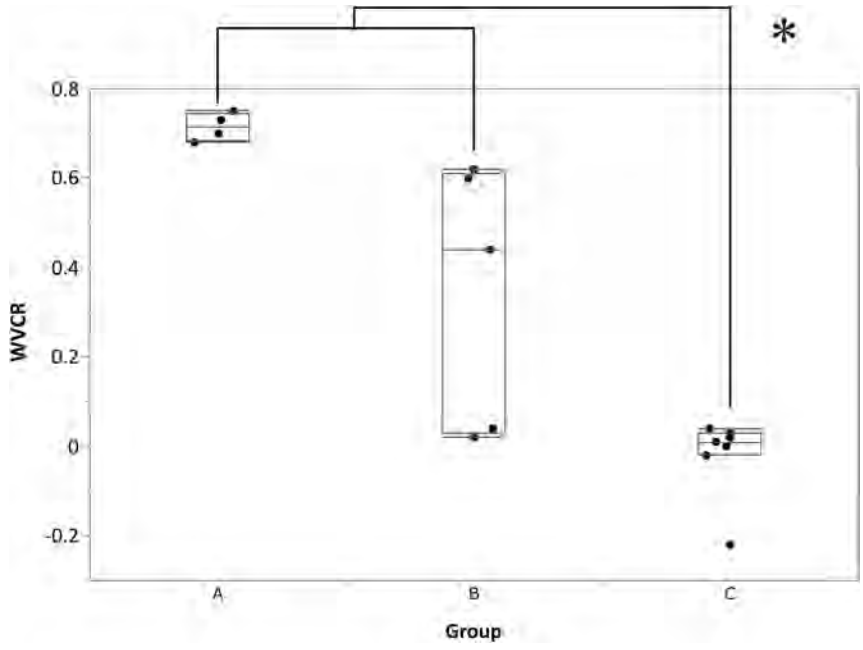

FIG 1. The distribution of WVCR in each plaque in the aneurysm wall. There is a significant difference in WVCR among A, B, and C ($P = .0011$). Group A indicates major plaques; group B, minor plaques; and group C, no plaques.

.0011). The means of the WVCRs for grades A, B, and C were 0.72 ± 0.03, 0.34 ± 0.30, and -0.02 ± 0.09, respectively. Details are illustrated in Fig 1.

Illustrative Cases

Case 1. A hypertensive 24-year-old man with a familial history of subarachnoid hemorrhage had an unruptured left ICA-anterior choroidal artery aneurysm of 4.2-mm maximum diameter (Fig 2*A-1*). Despite the patient's age, high signal intensity in the aneurysm wall was delineated by the presurgical FSBB. The lesion had a high contrast ratio (WVCR = 0.73) (Fig 2*A-2*). Atherosclerotic plaques in the aneurysm wall were evaluated as grade A intraoperatively (Fig 2*A-3*).

Case 8. A 70-year-old woman with an unruptured left MCA aneurysm of 5.1-mm maximum diameter was referred to our hospital (Fig 2*B-1*). Partial high signal intensity in the aneurysm wall was delineated by presurgical FSBB (Fig 2*B-2*). The lesion presented with mild elevation of contrast ratio (WVCR = 0.44). An intraoperative view via a trans-Sylvian approach showed the patchy atherosclerotic change on the wall, which was evaluated as grade B (Fig 2*B-3*).

Case 3. A 69-year-old man had an unruptured right MCA aneurysm of 6.1 mm maximum (Fig 2*C-1*). There was no high signal intensity in the aneurysm wall in the presurgical FSBB (Fig 2*C-2*). An intraoperative view via a trans-Sylvian approach showed no atherosclerosis in the aneurysm wall. The aneurysm wall was evaluated as grade C (Fig 2*C-3*).

Case 10. A 63-year-old woman with an unruptured anterior communicating artery (AcomA) aneurysm presented to our hospital (Fig 2*D-1*). FSBB failed to show high signal intensity that would have otherwise corresponded to atherosclerotic plaque in the aneurysm wall (Fig 2*D-2*). The actual intraoperative view showed

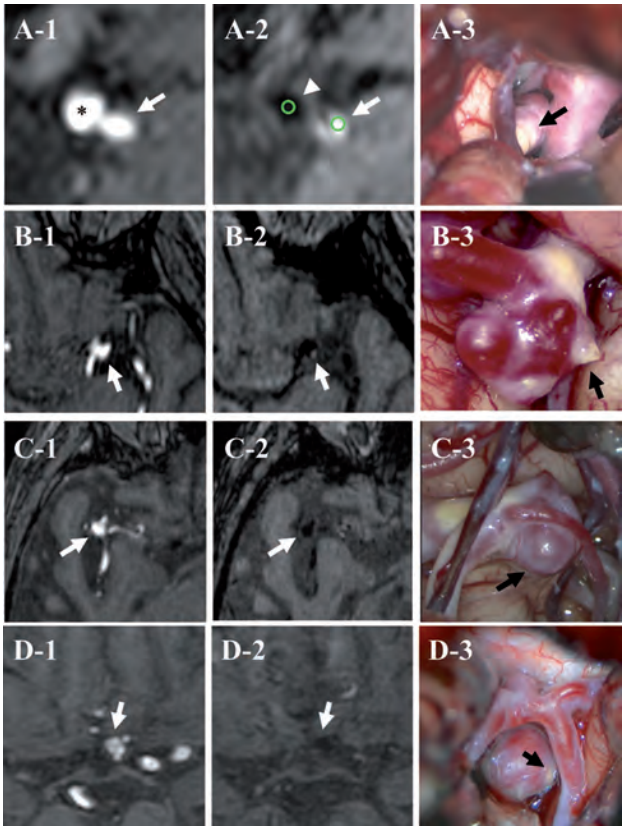

FIG 2. TOF-MRA (*first column*), FSBB (*second column*), and an intraoperative photomicrograph (*third column*) of 4 different patients with various degrees of atherosclerosis in the aneurysm wall. *A*, Left ICA–anterior choroidal artery unruptured aneurysm from case 1. TOF-MRA depicts the aneurysm (*A-1*, *arrow*) and left carotid artery (*A-1*, *asterisk*). FSBB shows high signal intensity in most of aneurysm wall with ROIs (*green circle*) in the wall (*A-2*, *arrow*) and at the center of the ipsilateral ICA for measuring the referring intensity (*A-2*, *arrowhead*). Intraoperative view showing abundant atherosclerotic plaques (grade A) in the aneurysm wall (*A-3*, *arrow*). *B*, Left MCA aneurysm from case 8. TOF-MRA shows the aneurysm (*B-1*, *arrow*). FSBB depicts focal high signal intensity in the aneurysm wall (*B-2*, *arrow*), corresponding to a patchy atherosclerotic plaque (grade B) in the intraoperative view (*B-3*, *arrow*). *C*, Right MCA aneurysm from case 3. TOF-MRA demonstrates the aneurysm (*C-1*, *arrow*). FSBB shows no high signal intensity in the wall (*C-2*, *arrow*), and the intraoperative view also shows no plaques (grade C) in the wall (*C-3*, *arrow*). *D*, Left AcomA aneurysm from case 10. TOF-MRA depicts the aneurysm (*D-1*, *arrow*), and FSBB shows no high signal intensity in the aneurysm wall (*D-2*, *arrow*). The operative view shows a small patchy atherosclerotic change on the right body of the aneurysm (*D-3*, *arrow*).

small atherosclerotic change on the right body of the aneurysm (Fig 2*D-3*).

DISCUSSION

This study showed that HOP-MRA at 3T can detect atherosclerotic plaques in the aneurysm wall preoperatively and that the WVCR in intracranial aneurysms correlated with the presence and extent of visible atherosclerotic plaques. This is the first report to show that high-resolution MR imaging, including the HOP-MRA technique at 3T, can delineate plaque in the aneurysm wall, though we found some studies on aneurysm wall imaging.[15-20]

In recent years, there is much evidence that inflammation and degeneration of the aneurysm wall play a major role in aneurysm formation, development, and rupture.[5-9] Along with elucidation of the histopathology of the aneurysm wall, it is expected vessel wall imaging will reveal biologic behavior of the aneurysm wall. Some authors reported the possibility of detecting unstable intracranial aneurysms by using contrast media, which in our opinion, corresponds to increased aneurysm wall permeability.[17,18] Aneurysm wall imaging can be performed with ultrasmall superparamagnetic particles of iron oxide (ferumoxytol) to reveal inflammation surrounding the aneurysm wall.[19] Recently, vessel wall imaging at 7T was reported to reveal variations of aneurysm wall thickness.[20] Ours is a novel study comparing the atherosclerotic changes of the aneurysm wall, which are presumably associated with one of the processes of degeneration, between HOP-MRA and the operative view.

Atherosclerotic change in the cerebral aneurysm wall is part of the pathologic degeneration underlying the development of inflammation.[5-9,21] The progression of the degeneration is considered to have a positive correlation with aneurysmal growth.[21] Although whether the presence of atherosclerosis correlates with the risk of aneurysm rupture is not yet well-known, we believe that the delineation of the aneurysm wall yields valuable information regarding intracranial cerebral aneurysms. As shown in our series, the signal intensity varied according to the degrees of atherosclerosis. The presence of high signal intensity on HOP-MRA may reflect the vulnerability of the plaque in the aneurysm wall.

In clinical practice, ischemic surgical complications are more likely if there is atherosclerotic change around the wall of the cerebral aneurysm.[22,23] It is possible that the fragile plaque migrates distally during the clipping procedure. We had a few patients who had silent ischemic lesions on diffusion-weighted imaging, as retrospectively proved by operative video. Some aneurysms that were surgically treated could not be completely observed for anatomic reasons. In such cases, preoperative imaging to determine the presence or absence of active atherosclerotic plaque around the neck of aneurysm is helpful for surgical planning and other treatment decisions.

High-resolution MR vessel wall imaging, including high-resolution black-blood imaging by presaturation pulse or a double inversion recovery black-blood sequence, yields information regarding the pathology of small cerebrovascular diseases.[10,11] Most vessel wall imaging techniques focus on steno-occlusive cerebrovascular disease with well-established atherosclerotic plaque imaging, though some imaging strategies can also yield information regarding the wall of cerebral aneurysms.[15-20] The strengths of the HOP technique include minimization of misregistration, among others. Because we performed TOF-MRA and FSBB simultaneously, we characterized the plaque clearly without the influence of pulse and flow in the aneurysm. To reduce the time and uncertain high signal by artifacts during FSBB imaging, we used a dual-echo 3D gradient-echo sequence and a high TE and b factor.

This study had several limitations. First, the comparison between the plaque imaging and the intraoperative view was subjective, though it was performed in a blinded manner by experienced neurosurgeons and radiologic technicians. Furthermore, because we routinely expose all parts of the aneurysm to mobilize it during microsurgical clipping, we were able investigate and record all these parts. Second, it is difficult to harvest a small aneurysm wall safely to compare the result of HOP-MRA and ex vivo pathologic

examination. Therefore, we could not determine why false-negative results on HOP-MRA occurred in the presence of patchy atherosclerotic plaque (case 10). We speculated that the degree of plaque containing vulnerable component might account for this phenomenon. High signal intensity in the aneurysm wall may include the presence of intraluminal thrombus, which is on the same degenerative pathway of the aneurysm wall.[6,7] Additionally, this study did not include calcified aneurysms. Vessel wall calcification is also a part of degeneration. Further study is needed to investigate whether HOP-MRA can characterize atherosclerosis with calcification and to characterize the precise spread, location, and the activity of atherosclerosis in relation to aneurysms.

Although HOP-MRA is a promising technique to determine the degree of atherosclerotic change in cerebral aneurysms, its clinical availability is limited. Although this study involved a small sample set, we believe that aneurysm wall imaging could become a standard examination to identify rupture-prone cerebral aneurysms.

CONCLUSIONS

The high signal intensity in intracranial aneurysms on HOP-MRA imaging correlated with the presence and extent of atherosclerotic plaques in the intracranial aneurysm wall.

ACKNOWLEDGMENTS

We thank Drs Ulrich Sure, Karsten H. Wrede, and Philipp Dammann of the University Hospital of Essen for their technical advice.

Disclosures: Kazuo Awai—*RELATED*: *Grant*: Toshiba Medical Systems (research grant)*; *Consulting Fee or Honorarium*: Toshiba Medical Systems (consultant); *Grants/Grants Pending*: Eizai,* Bayer,* Yakuhin*, Diichi Sankyo.* *Money paid to the institution.

REFERENCES

1. Wiebers DO, Whisnant JP, Huston J 3rd, et al. **Unruptured intracranial aneurysms: natural history, clinical outcome, and risks of surgical and endovascular treatment.** *Lancet* 2003;362:103–10
2. Morita A, Kirino T, Hashi K, et al. **The natural course of unruptured cerebral aneurysms in a Japanese cohort.** *N Engl J Med* 2012;366:2474–82
3. Naggara ON, Lecler A, Oppenheim C, et al. **Endovascular treatment of intracranial unruptured aneurysms: a systematic review of the literature on safety with emphasis on subgroup analyses.** *Radiology* 2012;263:828–35
4. Kotowski M, Naggara O, Darsaut TE, et al. **Safety and occlusion rates of surgical treatment of unruptured intracranial aneurysms: a systematic review and meta-analysis of the literature from 1990 to 2011.** *J Neurol Neurosurg Psychiatry* 2013;84:42–48
5. Kataoka K, Taneda M, Asai T, et al. **Structural fragility and inflammatory response of ruptured cerebral aneurysms: a comparative study between ruptured and unruptured cerebral aneurysms.** *Stroke* 1999;30:1396–401
6. Frosen J, Piippo A, Paetau A, et al. **Remodeling of saccular cerebral artery aneurysm wall is associated with rupture: histological analysis of 24 unruptured and 42 ruptured cases.** *Stroke* 2004;35:2287–93
7. Frosen J, Tulamo R, Paetau A, et al. **Saccular intracranial aneurysm: pathology and mechanisms.** *Acta Neuropathol* 2012;123:773–86
8. Chalouhi N, Ali MS, Jabbour PM, et al. **Biology of intracranial aneurysms: role of inflammation.** *J Cereb Blood Flow Metab* 2012;32:1659–76
9. Frosen J, Tulamo R, Heikula T, et al. **Lipid accumulation, lipid oxidation, and low plasma levels of acquired antibodies against oxidized lipids associate with degeneration and rupture of the intracranial aneurysm wall.** *Acta Neuropathol Comm* 2013;1:71
10. Klein IF, Lavallee PC, Mazighi M, et al. **Basilar artery atherosclerotic plaques in paramedian and lacunar pontine infarctions: a high-resolution MRI study.** *Stroke* 2010;41:1405–19
11. Song HK, Wright AC, Wolf RL, et al. **Multislice double inversion pulse sequence for efficient black-blood MRI.** *Magn Reson Med* 2002;47:616–20
12. Kimura T, Ikedo M, Takemoto S. **Hybrid of opposite-contrast MR angiography (HOP-MRA) combining time-of-flight and flow-sensitive black-blood contrasts.** *Magn Reson Med* 2009;62:450–58
13. Tsuchiya K, Kobayashi K, Nitatori T, et al. **Hybrid of opposite-contrast MRA of the brain by combining time-of-flight and black-blood sequences: initial experience in major trunk stenoocclusive diseases.** *J Magn Reson Imaging* 2010;31:56–60
14. Tsuchiya K, Yoshida M, Imai M, et al. **Hybrid of opposite-contrast magnetic resonance angiography of the brain by combining time-of-flight and black blood sequences: its value in Moyamoya disease.** *J Comput Assist Tomogr* 2010;34:242–46
15. Krings T, Piske RL, Lasjaunias PL. **Intracranial arterial aneurysm vasculopathies: targeting the outer vessel wall.** *Neuroradiology* 2005;47:931–37
16. Park JK, Lee CS, Sim KB, et al. **Imaging of the walls of saccular cerebral aneurysms with double inversion recovery black-blood sequence.** *J Magn Reson Imaging* 2009;30:1179–83
17. Matouk CC, Mandell DM, Gunel M, et al. **Vessel wall magnetic resonance imaging identifies the site of rupture in patients with multiple intracranial aneurysms: proof of principle.** *Neurosurgery* 2013;72:492–96
18. Edjlali M, Gentric JC, Regent-Rodriguez C, et al. **Does aneurysmal wall enhancement on vessel wall MRI help to distinguish stable from unstable intracranial aneurysms?** *Stroke* 2014;45:3704–06
19. Hasan DM, Mahaney KB, Magnotta VA, et al. **Macrophage imaging within human cerebral aneurysms wall using ferumoxytol-enhanced MRI: a pilot study.** *Arterioscler Thromb Vasc Biol* 2012;32:1032–38
20. Kleinloog R, Korkmaz E, Zwanenburg JJ, et al. **Visualization of the aneurysm wall: a 7.0 Tesla MRI study.** *Neurosurgery* 2014;75:614–22
21. Kosierkiewicz TA, Factor SM, Dickson DW. **Immunocytochemical studies of atherosclerotic lesions of cerebral berry aneurysms.** *J Neuropathol Exp Neurol* 1994;53:399–406
22. Grigorian AA, Marcovici A, Flamm ES. **Intraoperative factors associated with surgical outcome in patients with unruptured cerebral aneurysms: the experience of a single surgeon.** *J Neurosurg* 2003;99:452–57
23. Szelenyi A, Beck J, Sramet R, et al. **Is the surgical repair of unruptured atherosclerotic aneurysms at a higher risk of intraoperative ischemia?** *Clin Neurol Neurosurg* 2011;113:129–35

The Role of Core Needle Biopsy and Its Impact on Surgical Management in Patients with Medullary Thyroid Cancer: Clinical Experience at 3 Medical Institutions

E.J. Ha, J.H. Baek, D.G. Na, J.-h. Kim, J.K. Kim, H.S. Min, D.E. Song, K.E. Lee, and Y.K. Shong

ABSTRACT

BACKGROUND AND PURPOSE: Medullary thyroid carcinoma is an uncommon malignancy that is challenging to diagnose. Our aim was to present our experience using core needle biopsy for the diagnosis of medullary thyroid carcinoma compared with fine-needle aspiration.

MATERIALS AND METHODS: Between January 2000 and March 2012, 202 thyroid nodules in 191 patients were diagnosed as medullary thyroid cancer by using sonography-guided fine-needle aspiration, core needle biopsy, or surgery. One hundred eighty-three thyroid nodules in 172 patients were included on the basis of the final diagnosis. We evaluated the sensitivity and positive predictive value of fine-needle aspiration and core needle biopsy for the diagnosis of medullary thyroid cancer. We compared the rate of a delayed diagnosis, a diagnostic surgery, and surgery with an incorrect diagnosis for fine-needle aspiration and core needle biopsy and investigated the factors related to the fine-needle aspiration misdiagnosis of medullary thyroid cancer.

RESULTS: Fine-needle aspiration showed 43.8% sensitivity and 85.1% positive predictive value for the diagnosis of medullary thyroid cancer; 25.7% (44/171) of patients had a delayed diagnosis, while 18.7% (32/171) underwent an operation for accurate diagnosis, and 20.5% (35/171) underwent an operation with an incorrect diagnosis. Core needle biopsy achieved 100% sensitivity and positive predictive value without a delay in diagnosis (0/22), the need for a diagnostic operation (0/22), or an operation for an incorrect diagnosis (0/22). A calcitonin level of <100 pg/mL was the only significant factor for predicting the fine-needle aspiration misdiagnosis of medullary thyroid cancer ($P = .034$).

CONCLUSIONS: Core needle biopsy showed a superior sensitivity and positive predictive value to fine-needle aspiration and could optimize the surgical management in patients with medullary thyroid cancer. Because the ability of fine-needle aspiration to diagnose medullary thyroid cancer significantly decreases in patients with serum calcitonin levels of <100 pg/mL, core needle biopsy could be indicated for these patients to optimize their surgical management.

ABBREVIATIONS: AUS = atypia of undetermined significance or follicular lesion of undetermined significance; CNB = core needle biopsy; FNA= fine-needle aspiration; MTC = medullary thyroid carcinoma; PTC = papillary thyroid carcinoma; US = ultrasound

Medullary thyroid carcinoma (MTC) is an uncommon malignancy that is challenging to diagnose. Although it accounts for only 3%–5% of thyroid cancer diagnoses, it causes 15% of thyroid cancer–related deaths due to its aggressiveness.[1] Due to a lack of good treatment options other than surgery, early diagnosis of MTC and complete surgical resection comprising at least total thyroidectomy with central lymph node dissection offers the best chance for a cure.[2-5] In that respect, accurate and timely diagnosis of MTC is essential to ensure the appropriate surgical procedure.[6-9]

An early presurgical diagnosis of MTC remains a diagnostic challenge in clinical practice, however. Although fine-needle aspiration (FNA) cytology is an important diagnostic tool for evaluating thyroid nodules, its low sensitivity for diagnosing MTC limits an optimal preoperative evaluation and an operation in approximately half of the patients.[10,11] Serum calcitonin level measurement in patients with thyroid nodules is a sensitive and specific marker with even better diagnostic accuracy than cytology in unsuspected MTC, though the routine measurement of

Received June 18, 2014; accepted after revision January 4, 2015.

From the Department of Radiology and the Research Institute of Radiology (E.J.H., J.H.B), and Departments of Pathology (D.E.S.) and Metabolism and Endocrinology (Y.K.S.), University of Ulsan College of Medicine, Asan Medical Center, Seoul, Korea; Department of Radiology (E.J.H.), Ajou University School of Medicine, Suwon, Korea; Department of Radiology (D.G.N.), Human Medical Imaging and Intervention Center, Seoul, Korea; Healthcare System Gangnam Center (D.G.N.), Seoul National University Hospital, Seoul, Korea; Departments of Radiology (J.-h.K.), Pathology (H.S.M.), and Surgery (K.E.L.), Seoul National University Hospital, Seoul National University College of Medicine, Seoul, Korea; and Department of Radiology (J.K.K.), Chung-Ang University College of Medicine, Seoul, Korea.

Please address correspondence to Jung Hwan Baek, MD, Department of Radiology and the Research Institute of Radiology, University of Ulsan College of Medicine, Asan Medical Center, 86 Asanbyeongwon-Gil, Songpa-Gu, Seoul 138-736, Korea; e-mail: radbaek@naver.com

http://dx.doi.org/10.3174/ajnr.A4317

serum calcitonin levels in nodular thyroid disease and the cutoff value for a diagnosis of MTC are still debatable.[11-13] Due to these diagnostic difficulties, some MTC is still incidentally discovered after a diagnostic operation or after an operation with an incorrect presurgical diagnosis—this situation presents the risk of an incomplete therapeutic approach and a less favorable prognosis.[10,14,15] Therefore, early and accurate diagnosis of MTC is of crucial importance for optimal management.

We studied core needle biopsy (CNB) for the diagnosis of MTC at 3 medical institutions during a 10-year period. The study was designed to evaluate the following: 1) the diagnostic performance of CNB, 2) its impact on surgical management compared with FNA, and 3) factors related to the FNA misdiagnosis of MTC.

MATERIALS AND METHODS

The institutional review boards approved this retrospective study at the 3 participating sites and required neither patient approval nor informed consent for review of the images and medical records. However, informed consent for FNA or CNB was obtained from all patients before biopsy.

Patients

This retrospective analysis was based on patient data collected from 3 medical institutions (ie, Asan Medical Center, Seoul National University Hospital, and the Human Medical Imaging and Intervention Center). We reviewed the medical records of patients who were diagnosed with MTC between January 2000 and March 2012 at the 3 institutions. During this time, 202 thyroid nodules in 191 patients were initially diagnosed as MTC by using 1 of the following methods: ultrasound (US)-guided FNA, US-guided CNB, or surgery. Of these 191 patients, 19 were excluded because they were surgically treated at another hospital ($n = 5$) or were without FNA or CNB results before the operation ($n = 14$). This study finally included 183 thyroid nodules in 172 patients (112 women and 60 men; mean age, 49.6 years; range, 17–91 years).

Of the 183 nodules in 172 patients, FNA was initially used in 182 nodules in 171 patients. CNB was used in 22 nodules in 21 patients as the initial approach ($n = 1$), after the FNA results of non-MTC ($n = 13$), or simultaneously with FNA ($n = 8$). The final diagnosis was based on the pathology results obtained after surgery for all nodules except for 2 in 2 inoperable patients with high calcitonin levels of 1330 and 82,900, respectively.

US-Guided FNA and CNB Procedures

US examinations were performed by using 1 of 4 US systems: an iU22 U (Philips Healthcare, Best, the Netherlands), an EUB-7500 U (Hitachi Medical Systems, Tokyo, Japan), an Aplio XG (Toshiba Medical Systems, Tokyo, Japan), or an HDI 5000 (Philips Healthcare), equipped with a linear, high-frequency probe (5–14 MHz). All US examinations and US-guided FNA or CNB procedures were performed by 4 clinically experienced thyroid radiologists with 12–19 years of thyroid US experience or by residents and fellows under their supervision.

US-guided FNAs were performed with a combination of 25-, 23-, and 21-ga needles and a combination of capillary and aspiration FNA techniques according to the characteristics of the nodules. Each lesion was aspirated at least twice (range, 2–4 times). Materials obtained from the FNA were immediately placed in 95% alcohol for Papanicolaou staining.

US-guided CNBs were performed by using a disposable, 18-ga, double-action, spring-activated needle (1.1- or 1.6-cm excursion) (TSK Acecut; Create Medic, Yokohama, Japan) after local anesthesia with 1% lidocaine. Before the needle insertion, vessels along the approach route were carefully evaluated by power Doppler US to prevent procedure-related hemorrhage. Using a freehand technique, we advanced the core needle from the isthmus of the thyroid toward the target nodule by using the transisthmic approach. When the needle tip was advanced into the edge of the nodule, the stylet and cutting cannula of the needle were sequentially, carefully fired. The number of tissue cores obtained by CNB ranged from 1 to 3. A second or third CNB was performed when a lesion was considered inaccurately targeted, as in the case of small nodules or when an adequate tissue core was not obtained by visual inspection. Each patient was observed after firm, local compression of the biopsy site for 10–20 minutes after FNA or CNB. If a patient had pain or neck swelling, a repeat US examination was performed to evaluate possible complications.[16]

Cytologic and Histopathologic Analyses

The FNA, CNB, and surgical specimens were reviewed by experienced cytopathologists with 8–10 years of clinical experience in thyroid cytopathology; real-time cytology was not available during the biopsy procedure. FNA cytology diagnoses were categorized as nondiagnostic, benign, atypia of undetermined significance or follicular lesion of undetermined significance (AUS), follicular neoplasm/suspicious for follicular neoplasm, suspicious for malignancy, or malignant according to the Bethesda System for Reporting Thyroid Cytopathology.[17] Because the diagnostic criteria of CNB have not been standardized for thyroid nodules, the CNB histologic diagnoses were categorized into the same categories as those in the Bethesda System.[18-20] For evaluating the specific diagnostic performance for MTC on both the FNA and CNB, the "suspicious for malignancy" or "malignancy" reading was further categorized into subtypes suggesting papillary thyroid carcinoma (PTC), MTC, or other malignancy.

Additional special staining was performed on a case-by-case basis according to the cytopathologists' preferences and concerns. Calcitonin staining on FNA or CNB specimens was not routinely used for these readings, though it could be used as an additional requirement of the cytopathologists when the FNA or CNB findings were suspicious for MTC, to obtain a confirming diagnosis.

Statistical Analysis

Statistical analysis was performed by using the SPSS software package (Version 19.0 for Windows; IBM, Armonk, New York). Categoric data were summarized by using frequencies and percentages. The diagnostic performance of FNA and CNB for MTC was evaluated by using the sensitivity and positive predictive value. The χ^2 test, Student t test, and Mann-Whitney U test were used to evaluate the factors related to the FNA misdiagnosis of MTC. FNA misdiagnosis was defined as any FNA cytologic diagnosis except MTC. Binary logistic regression was used for multivariate analysis. The Spearman rank correlation was used to eval-

Table 1: Comparison of the initial FNA and CNB results with the final pathology results[a]

Final Diagnosis	Initial FNA Results (*n* = 182)							CNB (*n* = 22)[b]
	ND	Benign	AUS	FN	PTC	Malignancy, Others	MTC	MTC
MTC	6	13	44	12	5	15	74	22
PTC	–	–	–	–	–	–	7	–
Follicular adenoma	–	–	–	–	–	–	2	–
Follicular carcinoma	–	–	–	–	–	–	2	–
Hyalinizing trabecular tumor	–	–	–	–	–	–	1	–
Anaplastic carcinoma	–	–	–	–	–	–	1	–

Note:—ND indicates nondiagnostic; FN, follicular neoplasm or suspicious for follicular neoplasm.
[a] Data indicate the number of nodules.
[b] CNB was initially performed (*n* = 1) after the FNA results of non-MTC (*n* = 13) or with simultaneous FNA (*n* = 8).

Table 2: Relationship of the serum calcitonin level and the diagnosis of MTC after FNA or CNB procedures[a]

Calcitonin Level (pg/mL)	FNA Diagnosis (*n* = 158)		CNB Diagnosis (*n* = 18)	
	MTC	Non-MTC	MTC	Non-MTC
≥100	54 (54)	46 (46)	10 (10)	0 (0)
10–100	16 (16)	27 (27)	7 (7)	0 (0)
<10	11 (1)	4 (4)	1 (1)	0 (0)

[a] Data are number of nodules before the operation, with the number of MTCs after the operation in parentheses.

uate the relationship between the size and the calcitonin level. A *P* value < .05 was considered statistically significant.

To assess the clinical impact of FNA or CNB on the surgical management of MTC in current practice, we evaluated the rate of the delayed diagnosis, diagnostic surgery, and surgery by using an incorrect presurgical diagnosis as follows: "Delayed diagnosis" was defined as a nodule initially misdiagnosed as non-MTC but finally confirmed as MTC on the next FNA or CNB. "Diagnostic surgery" was defined as a nodule initially misdiagnosed as non-MTC (ie, nondiagnostic, benign, or AUS) but confirmed as MTC on subsequent surgery performed for a diagnostic purpose. "Surgery with an incorrect diagnosis" was defined as 1 of the following 2 categories: First, the nodule was initially misdiagnosed as non-MTC (ie, a follicular neoplasm/suspicious for follicular neoplasm, suspicious for or a definite diagnosis of PTC, or other types of malignancy) but was finally confirmed as MTC following the operation. Second, the nodule was initially misdiagnosed as MTC but was finally confirmed as non-MTC following the operation.

RESULTS

Demographic Data

Among the 183 nodules in 172 patients, 170 nodules in 159 patients were confirmed as MTCs and 13 nodules in 13 patients were confirmed as non-MTCs following surgery. The mean nodule size was 20.3 ± 15.7 mm (range, 3.0–85.0 mm). Of 170 confirmed MTCs, 26 nodules in 20 patients were hereditary MTCs and 144 nodules in 139 patients were sporadic MTCs.

The serum calcitonin level was measured before surgery in 148 patients with 159 nodules. The median serum calcitonin level was 389.0 pg/mL (range, 1.5–82,900.0 pg/mL), with a subclassification of ≥100 pg/mL (*n* = 92), ≥10 and <100 pg/mL (*n* = 41), or <10 pg/mL (*n* = 15).

Diagnostic Performance of FNA or CNB

Table 1 shows the comparison of the initial FNA and CNB results with the final pathology results. The sensitivity and positive predictive value for a diagnosis of MTC were 43.8% (74/169) and 85.1% (74/87), respectively, following the initial FNA, though they were both 100% (22/22) after CNB. MTCs were commonly misinterpreted as AUS (44/169, 26.0%) or other types of malignancy (15/169, 8.9%) after FNA. Thirteen false-positively diagnosed MTCs were actually PTC (7/13, 53.8%) follicular adenoma or carcinoma (4/13, 30.8%), hyalinizing trabecular tumor (1/13, 7.7%), or anaplastic carcinoma (1/13, 7.7%).

Table 2 shows the relationship between the serum calcitonin level and the diagnosis of MTC after FNA or CNB procedures. In patients with a serum calcitonin level of <10 pg/mL, 10 of 11 nodules with an FNA diagnosis of MTC were confirmed as non-MTC following the surgery. However, in this range, 5 nodules were finally confirmed as MTCs after surgery even though 4 were not diagnosed after FNA. One nodule with a CNB diagnosis of MTC was correct after surgery in this range.

Clinical Impact of FNA or CNB on Surgical Management

Delayed Diagnosis. Figure 1 shows the diagnostic flowchart for the patients following FNA. A delayed diagnosis was noted in 25.7% (44/171) of patients after FNA, while there was none in patients (0/22) after CNB. A delayed diagnosis continued in 22.2% (8/36) of these patients following the second FNA. Therefore, the delayed diagnosis rate differed significantly between FNA and CNB (*P* = .007) (Table 3).

Diagnostic Surgery. Diagnostic surgery was performed in 18.7% (32/171) of the patients after FNA, though it was not performed in any patients (0/22) after CNB. Of 32 patients, 24 with 28 nodules underwent diagnostic surgery after having initial FNA results of nondiagnostic (*n* = 2), benign (*n* = 7), and AUS (*n* = 19), and 7 patients with 7 nodules underwent diagnostic surgery after having second FNA results of nondiagnostic (*n* = 1) and AUS (*n* = 6). One patient underwent diagnostic surgery after 3 repetitive FNA results of AUS. The diagnostic surgery rate was significantly different between FNA and CNB (*P* = .028) (Table 3).

Surgery with an Incorrect Diagnosis. Surgery with an incorrect diagnosis was performed in 20.5% (35/171) of the patients after FNA, though it was not performed in any patients (0/22) after CNB. There were 2 types of surgery with an incorrect diagnosis: The first was surgery with a false-negative diagnosis of MTC; 12.9% (22/171) of the patients underwent surgery with a cytologic diagnosis of follicular neoplasm/suspicious for follicular neoplasm (*n* = 10), PTC (*n* = 4), or other types of malignancy (*n* = 8). The second was surgery with a false-positive diagnosis of MTC; 7.6% (13/171) of the patients underwent surgery with a cytologic diagnosis of MTC, which was, however, finally determined after surgery to be PTC (*n* = 7), follicular adenoma (*n* = 2), follicular carcinoma (*n* = 2), hyalinizing trabecular tumor (*n* = 1), or anaplastic carcinoma (*n* = 1). The rate of surgery with an incorrect diagnosis differed significantly between FNA and CNB (*P* = .016) (Table 3).

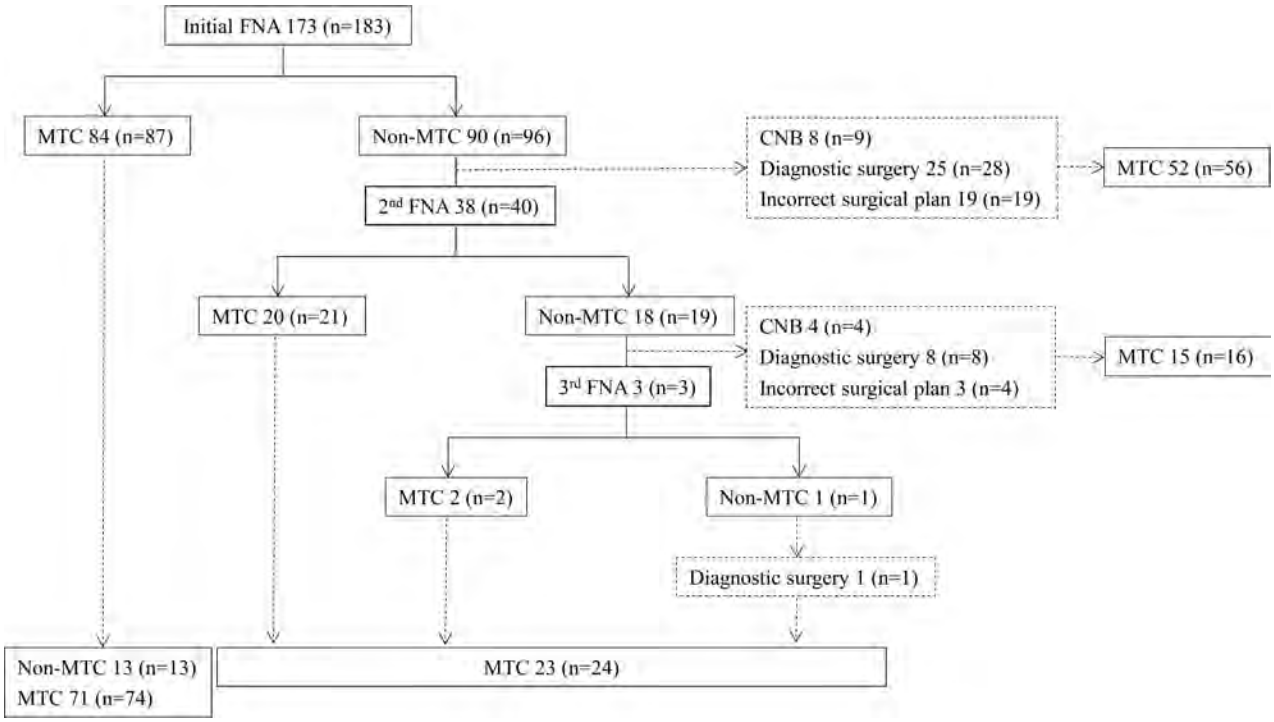

FIG 1. Diagnostic flowchart of patients following the initial FNA. Data indicate the number of patients, with the number of nodules in parentheses.

Table 3: Comparison of the FNA and CNB results with the factors regarding surgical decision-making of MTC[a]

Clinical Impact on Surgical Management	FNA (*n* = 171)	CNB (*n* = 22)	*P* Value
Delayed diagnosis	44 (25.7)	0 (0)	.007
Diagnostic operation	32 (18.7)	0 (0)	.028
Operation with an incorrect diagnosis	35 (20.5)	0 (0)	.016

[a] Data indicate the number of patients, with the percentages in parentheses.

Table 4: Factor analysis related to the FNA misdiagnosis of MTC[a]

	FNA Diagnosis (*n* = 74)	FNA Misdiagnosis (*n* = 95)[b]	*P* Value
Age (yr)			.914
Mean	49.0 ± 14.2	49.2 ± 13.4	
Range	18–81	17–81	
Sex			.786
Female	49 (66.2)	61 (64.2)	
Male	25 (33.8)	34 (35.8)	
Genetics			.869
Hereditary	11	15	
Sporadic	63	80	
Size			.258
<10 mm	14	25	
≥10 mm	60	70	
Serum calcitonin			.034
<100 pg/mL	17	31	
≥100 pg/mL	54	46	

[a] Data are the number of nodules, with percentages in parentheses.
[b] FNA misdiagnosis was defined as any cytologic diagnosis except MTC.

Factor Analysis Related to the FNA Misdiagnosis of MTC

Table 4 shows the factors related to the FNA misdiagnosis of MTC. On bivariate analyses, a serum calcitonin level of <100 pg/mL was the only significant factor for predicting the FNA misdiagnosis of MTC ($P = .034$). Mass size was not a significant factor ($P = .258$) despite the positive correlation with the serum calcitonin level ($\rho = 0.605$). A binary logistic regression analysis was performed to determine the independent factors for predicting the FNA misdiagnosis of MTC. A serum calcitonin level of <100 pg/mL showed a significant association with the FNA misdiagnosis ($P = .036$) (95% CI, 1.052–4.355; odds ratio, 2.141).

Complications

There were no complications leading to substantial morbidity or disability or resulting in a hospitalization after FNA or CNB. One patient after FNA had neck discomfort due to thyroid parenchymal edema. However, there were no major complications after FNA or CNB.

DISCUSSION

Our study confirms that FNA cytology has 43.8% sensitivity and 85.1% positive predictive value for the diagnosis of MTC, while the respective values for CNB were both 100.0%. FNA cytology caused a delayed diagnosis in 25.7% (44/171), required diagnostic surgery in 18.7% (32/171), and led to surgery with an incorrect diagnosis in 20.5% (35/171) of the study patients. Serum calcitonin levels of <100 pg/mL were the only significant factor related to the FNA misdiagnosis of MTC.

FNA cytology for a diagnosis of MTC has been proved to have a low sensitivity of 43.7% in recent multicenter and international studies.[10] It has been reported with a wide range from 30% to 89% in smaller series.[11,13,21,22] Its low sensitivity leads to the misdiagnosis of MTC and negatively impacts patient management in several ways. A delayed diagnosis can alter the MTC stage at the time of surgery and may thus influence both the surgical extent and the patient prognosis.[6-9] Diagnostic surgery or surgery with an incor-

rect diagnosis can overlook the evaluation for multiple endocrine neoplasia syndrome before surgery and can also be responsible for suboptimal surgery, which may require additional surgery for completion and may carry an increased risk of morbidity.[6-9] In our study, the low sensitivity of FNA for MTC was reconfirmed in 172 patients at 3 medical institutions during a 10-year period; 56.2% of the patients with MTC were initially misdiagnosed; therefore, proper surgical management was delayed or suboptimal after FNA.

Among the available diagnostic tools for MTC, serum calcitonin level measurement has been the most commonly used due to its higher sensitivity for MTC than FNA cytology.[11-13] Because the appropriate use of serum calcitonin level measurement is helpful for detecting unsuspected MTC, it is commonly used in patients with thyroid nodules to prevent the risk of a false-negative cytologic diagnosis. Patients with a serum calcitonin level of ≥100 pg/mL are strongly recommended for surgery, even though the cytologic diagnosis is not fulfilled for MTC under the current guidelines.[2,5,14,15] However, there is a diagnostic gray zone in patients with a serum calcitonin level between 10 and 100 pg/mL, and the cutoff value for a diagnosis of MTC is still debatable.[14] Our study results also showed 2 diagnostic dilemmas associated with the serum calcitonin level. First, MTC could not be completely excluded even in the normal range of serum calcitonin levels. Although most presurgical diagnoses of MTC after FNA were false-positive in this range, 5 nodules were proved to be MTCs following surgery. Second, a serum calcitonin level of <100 pg/mL, a diagnostic gray zone in the clinical setting, was also an independent factor related to the FNA misdiagnosis of MTC. Therefore, in these patients, CNB may have been a useful diagnostic tool for an accurate diagnosis and proper management of MTC in our study.

The diagnostic role of CNB for thyroid nodules is currently being investigated. Because US-guided CNB using a spring-activated biopsy needle has been reported safe and effective by Quinn et al,[23] several investigators have demonstrated the usefulness of CNB in diagnosing thyroid nodules with 90.3% (range, 78.5%–100%) sensitivity and 98.4% (range, 87%–100%) positive predictive value for thyroid malignancy.[18-20,24-26] Currently, the role of CNB has focused on the diagnosis of nodules with previously nondiagnostic results on FNA and, therefore, on preventing unnecessary diagnostic surgery.[19,24,25,27] For the diagnosis of a specific type of malignancy, however, CNB has also showed the possibility of superior diagnostic performance to that of FNA for thyroid lymphoma, anaplastic carcinoma, and metastasis in a small series of studies.[26,28-31] The complication rate was reported to be <1% and was considered to be similar to that of FNA if an experienced clinician performed the procedure.[18,19] In our study, all 22 patients who underwent CNB were correctly diagnosed with MTC without any major complications. Of these patients, the serum calcitonin levels were <100 pg/mL in 8 patients (36.4%), but the CNB diagnoses were consistent for MTC. CNB showed a precise histologic diagnosis in all cases regardless of the serum calcitonin levels.

Our study has several limitations. First, its retrospective design may have introduced a selection bias. Because the low incidence of MTC limits prospective study design, however, it may be the best method for retrospectively reviewing the clinical experience during long periods at many medical institutions. Second, FNA results before 2010 were re-interpreted according to the Bethesda System. Third, because the diagnostic categories of CNB specimens have not yet been standardized, this aspect requires further research. Fourth, a calcium stimulating test or calcitonin level measurement of aspiration needle washout fluids or both were not performed in our study. However, our experience using CNB provides useful information as a complementary diagnostic tool for MTC. Further studies are required for deciding a proper indication of each technique. Fifth, there is significant difference in size of the FNA and CNB group. Further studies are required.

CONCLUSIONS

A relatively small sample of CNBs showed a superior sensitivity and positive predictive value to those of FNA and could thus optimize the surgical management in patients with MTC. Because the FNA diagnosis of MTC significantly decreases in patients with serum calcitonin levels of <100 pg/mL, CNB could be a complementary diagnostic tool for these patients to optimize surgical management.

REFERENCES

1. Ahmed SR, Ball DW. **Clinical review: incidentally discovered medullary thyroid cancer—diagnostic strategies and treatment.** *J Clin Endocrinol Metab* 2011;96:1237–45
2. Kloos RT, Eng C, Evans DB, et al. **Medullary thyroid cancer: management guidelines of the American Thyroid Association.** *Thyroid* 2009;19:565–612
3. Wu LS, Roman SA, Sosa JA. **Medullary thyroid cancer: an update of new guidelines and recent developments.** *Curr Opin Oncol* 2011;23:22–27
4. Gimm O. **Extent of surgery in clinically evident but operable MTC: when is central and/or lateral lymphadenectomy indicated?** *Thyroid Res* 2013;6(suppl 1):S3
5. Sippel RS, Kunnimalaiyaan M, Chen H. **Current management of medullary thyroid cancer.** *Oncologist* 2008;13:539–47
6. Weber T, Schilling T, Frank-Raue K, et al. **Impact of modified radical neck dissection on biochemical cure in medullary thyroid carcinomas.** *Surgery* 2001;130:1044–49
7. Roman S, Lin R, Sosa JA. **Prognosis of medullary thyroid carcinoma: demographic, clinical, and pathologic predictors of survival in 1252 cases.** *Cancer* 2006;107:2134–42
8. Machens A, Dralle H. **Benefit-risk balance of reoperation for persistent medullary thyroid cancer.** *Ann Surg* 2013;257:751–57
9. Kebebew E, Ituarte PH, Siperstein AE, et al. **Medullary thyroid carcinoma: clinical characteristics, treatment, prognostic factors, and a comparison of staging systems.** *Cancer* 2000;88:1139–48
10. Essig GF Jr, Porter K, Schneider D, et al. **Fine needle aspiration and medullary thyroid carcinoma: the risk of inadequate preoperative evaluation and initial surgery when relying upon FNAB cytology alone.** *Endocr Pract* 2013;19:920–27
11. Niccoli P, Wion-Barbot N, Caron P, et al. **Interest of routine measurement of serum calcitonin: study in a large series of thyroidectomized patients—the French Medullary Study Group.** *J Clin Endocrinol Metab* 1997;82:338–41
12. Chambon G, Alovisetti C, Idoux-Louche C, et al. **The use of preoperative routine measurement of basal serum thyrocalcitonin in candidates for thyroidectomy due to nodular thyroid disorders: results from 2733 consecutive patients.** *J Clin Endocrinol Metab* 2011;96:75–81
13. Elisei R, Bottici V, Luchetti F, et al. **Impact of routine measurement of serum calcitonin on the diagnosis and outcome of medullary thy-**

roid cancer: experience in 10,864 patients with nodular thyroid disorders. *J Clin Endocrinol Metab* 2004;89:163–68
14. Trimboli P, Giovanella L, Crescenzi A, et al. **Medullary thyroid cancer diagnosis: an appraisal.** *Head Neck* 2014;36:1216–23
15. Roy M, Chen H, Sippel RS. **Current understanding and management of medullary thyroid cancer.** *Oncologist* 2013;18:1093–100
16. Ha EJ, Baek JH, Lee JH, et al. **Core needle biopsy can minimise the non-diagnostic results and need for diagnostic surgery in patients with calcified thyroid nodules.** *Eur Radiol* 2014;24:1403–09
17. Cibas ES, Ali SZ. **The Bethesda System for Reporting Thyroid Cytopathology.** *Thyroid* 2009;19:1159–65
18. Choi YJ, Baek JH, Ha EJ, et al. **Different risk of malignancy and management recommendations in subcategories of thyroid nodules with atypia of undetermined significance or follicular lesion of undetermined significance: the role of US-guided core-needle biopsy.** *Thyroid* 2014;24:494–501
19. Yeon JS, Baek JH, Lim HK, et al. **Thyroid nodules with initially nondiagnostic cytologic results: the role of core-needle biopsy.** *Radiology* 2013;268:274–80
20. Ha EJ, Baek JH, Lee JH, et al. **Sonographically suspicious thyroid nodules with initially benign cytologic results: the role of a core needle biopsy.** *Thyroid* 2013;23:703–08
21. Papaparaskeva K, Nagel H, Droese M. **Cytologic diagnosis of medullary carcinoma of the thyroid gland.** *Diagn Cytopathol* 2000;22:351–58
22. Bugalho MJ, Santos JR, Sobrinho L. **Preoperative diagnosis of medullary thyroid carcinoma: fine needle aspiration cytology as compared with serum calcitonin measurement.** *J Surg Oncol* 2005;91:56–60
23. Quinn SF, Nelson HA, Demlow TA. **Thyroid biopsies: fine-needle aspiration biopsy versus spring-activated core biopsy needle in 102 patients.** *J Vasc Interv Radiol* 1994;5:619–23
24. Na DG, Kim JH, Sung JY, et al. **Core-needle biopsy is more useful than repeat fine-needle aspiration in thyroid nodules read as nondiagnostic or atypia of undetermined significance by the Bethesda System for Reporting Thyroid Cytopathology.** *Thyroid* 2012;22:468–75
25. Samir AE, Vij A, Seale MK, et al. **Ultrasound-guided percutaneous thyroid nodule core biopsy: clinical utility in patients with prior nondiagnostic fine-needle aspirate.** *Thyroid* 2012;22:461–67
26. Hahn SY, Shin JH, Han BK, et al. **Ultrasonography-guided core needle biopsy for the thyroid nodule: does the procedure hold any benefit for the diagnosis when fine-needle aspiration cytology analysis shows inconclusive results?** *Br J Radiol* 2013;86:20130007
27. Lee SH, Kim MH, Bae JS, et al. **Clinical outcomes in patients with non-diagnostic thyroid fine needle aspiration cytology: usefulness of the thyroid core needle biopsy.** *Ann Surg Oncol* 2014;2:1870–77
28. Kwak JY, Kim EK, Ko KH, et al. **Primary thyroid lymphoma: role of ultrasound-guided needle biopsy.** *J Ultrasound Med* 2007;26:1761–65
29. Buxey K, Serpell J. **Importance of core biopsy in the diagnosis of thyroid lymphoma.** *ANZ J Surg* 2012;82:90
30. Ravinsky E, Morales C. **Diagnosis of lymphoma by image-guided needle biopsies: fine needle aspiration biopsy, core biopsy or both?** *Acta Cytol* 2005;49:51–57
31. Nam M, Shin JH, Han BK, et al. **Thyroid lymphoma: correlation of radiologic and pathologic features.** *J Ultrasound Med* 2012;31:589–94

Optimal Virtual Monochromatic Images for Evaluation of Normal Tissues and Head and Neck Cancer Using Dual-Energy CT

S. Lam, R. Gupta, M. Levental, E. Yu, H.D. Curtin, and R. Forghani

ABSTRACT

BACKGROUND AND PURPOSE: Dual-energy CT is not used routinely for evaluation of the head and neck, and there is no consensus on the optimal virtual monochromatic image energies for evaluating normal tissues or head and neck cancer. We performed a quantitative evaluation to determine the optimal virtual monochromatic images for visualization of normal tissues, head and neck squamous cell carcinoma, and lymphadenopathy.

MATERIALS AND METHODS: Dual-energy CT scans from 10 healthy patients and 30 patients with squamous cell carcinoma were evaluated at different virtual monochromatic energy levels ranging from 40 to 140 keV. The signal-to-noise ratios of muscles at 6 different levels, glands (parotid, sublingual, submandibular, and thyroid), 30 tumors, and 17 metastatic lymph nodes were determined as measures of optimal image quality. Lesion attenuation and contrast-to-noise ratios (compared with those of muscle) were evaluated to assess lesion conspicuity.

RESULTS: The optimal signal-to-noise ratio for all the tissues was at 65 keV ($P < .0001$). However, tumor attenuation ($P < .0001$), attenuation difference between tumor and muscles ($P = .03$), and lesion contrast-to-noise ratios ($P < .0001$) were highest at 40 keV.

CONCLUSIONS: The optimal image signal-to-noise ratio is at 65 keV, but tumor conspicuity compared with that of muscle is greatest at 40 keV. Optimal evaluation of the neck may be best achieved by a multiparametric approach, with 65-keV virtual monochromatic images providing the best overall image quality and targeted use of 40-keV virtual monochromatic images for tumor evaluation.

ABBREVIATIONS: CNR = contrast-to-noise ratio; DECT = dual-energy CT; HNSCC = head and neck squamous cell carcinoma; keV = kiloelectron volt; kVp = kilovoltage peak; VMI = virtual monochromatic image

There are emerging applications of dual-energy CT (DECT)[1] in all the major subspecialties of radiology.[2-8] Studies have increasingly been demonstrating potential advantages of DECT for the evaluation of head and neck pathologies.[8-18] Extrapolating from abdominal imaging, 70-keV virtual monochromatic image (VMI) reconstructions are believed to be those that most closely resemble a standard single-energy CT acquisition[19] and are usually the default setting for CT of the neck. On the other hand, enhancing tumors have increased attenuation on lower–kiloelectron volt (keV) VMIs, closer to the *k* edge of iodine,[20] albeit at the expense of other factors such as increased image noise. A recent study using a dual-source system (Somatom Definition Flash; Siemens, Erlangen, Germany) evaluated extrapolated monoenergetic datasets at 40, 60, 80, and 100 keV, and the authors concluded that image reconstructions at 60 keV improved lesion enhancement and the contrast-to-noise ratio (CNR), subjective overall image quality, and tumor delineation in head and neck squamous cell carcinoma (HNSCC).[10]

Most studies that evaluated HNSCC, other than a study that evaluated DECT for the differentiation of benign and malignant tumors,[14] were performed by using dual-source CT. The other major system currently in clinical use is a single-source single-detector DECT system. This system is based on rapid kilovoltage peak (kVp) switching that enables near-simultaneous acquisition of high- and low-energy projection data (GE Discovery

Received December 18, 2014; accepted after revision January 31, 2015.

From the Department of Radiology (S.L., M.L., R.F.), Jewish General Hospital, McGill University, Montreal, Quebec, Canada; Department of Radiology (R.G.), Massachusetts General Hospital, Harvard Medical School, Boston, Massachusetts; Joint Department of Medical Imaging (E.Y.), Princess Margaret Hospital, University Health Network, University of Toronto, Toronto, Ontario, Canada; and Department of Radiology (H.D.C.), Massachusetts Eye and Ear Infirmary, Harvard Medical School, Boston, Massachusetts.

Abstract previously presented at: Annual Meeting of the American Society of Head and Neck Radiology, September 10–14, 2014; Seattle, Washington. S.L. received the American Society of Head and Neck Radiology's Radiologist-in-Training award.

Please address correspondence to Reza Forghani, MD, PhD, Department of Radiology, Jewish General Hospital, Room C-212.1, 3755 Cote Ste-Catherine Rd, Montreal, Quebec H3T 1E2, Canada; e-mail: rforghani@jgh.mcgill.ca

http://dx.doi.org/10.3174/ajnr.A4314

Summary of primary HNSCC tumor sites evaluated

Tumor Type	No. of Patients
Untreated ($n = 22$), primary site	
Larynx	7
Hypopharynx	1
Retromolar trigone, anterior tonsillar pillar	3
Oral cavity–other	5
Oropharynx–other	3
Sinuses, nose	3
Recurrent or metastatic ($n = 8$)	
Oral cavity	2
Oropharynx	1
Other	5[a]

[a] Head and neck squamous cell carcinoma invading the parotid gland, $n = 2$; parapharyngeal space metastasis, $n = 1$; cheek, $n = 1$; and neopharynx, $n = 1$.

CT750HD; GE Healthcare, Milwaukee, Wisconsin). In this system, spectral separation is achieved on the basis of projection-based material decomposition by using the fast sampling capabilities of a proprietary scintillator detector with low afterglow.[5,21] Although the broad principles behind both DECT acquisition systems are similar, there are significant differences in hardware, acquisition, and postprocessing. As a result, any cross-platform application of observations made by using either system requires validation. Furthermore, there is currently no consensus on the optimal VMIs for the evaluation of HNSCC or the approach to incorporate DECT into routine clinical use.

The hypothesis behind our investigation was that VMIs acquired at energies other than 70 keV, either alone or in combination, can enhance the conspicuity of HNSCC. The objective of this investigation, therefore, was to determine the optimal VMI that provides the highest image quality and the VMI that enables optimal tumor visualization by using a single-source DECT scan with rapid kVp switching. This determination was made by objectively and quantitatively analyzing normal structures at different levels in the neck and tumors at different primary sites. Spectral evaluation was performed by using different VMI energy levels ranging from 40 to 140 keV in 5-keV increments, and mean attenuation, SNR, and CNR were used as end points for evaluation.

MATERIALS AND METHODS

Patients

This study was approved by the institutional review board at the Jewish General Hospital (Montreal, Quebec, Canada). A total of 40 patients who had undergone DECT between June 2013 and July 2014 were evaluated retrospectively. There were 10 consecutive healthy patients and 30 consecutive patients with histopathologically proven (by biopsy and/or surgery) HNSCC who met the selection criteria discussed below.[18] Normal cases consisted of normal or near-normal scan results with minor incidental findings (dental periapical lucencies, benign reactive lymph nodes or tonsillar enlargement, and incidental cutaneous lesions such as sebaceous cysts) in patients without known malignancy or major systemic disease. To have a broad and representative sample of HNSCC, patients with primary untreated or recurrent/metastatic tumors from different sites were included (Table). Exclusion criteria included suspected HNSCC not confirmed by biopsy or surgery and any tumor that was too small for sampling by the minimum preset ROI size and numbers (see below).

CT Technique

Each patient was scanned with the same 64-section dual-energy scanner (Discovery CT750HD; GE Healthcare). Examinations were performed after the administration of 80 mL of iopamidol (Isovue 300; Bracco Diagnostics, Princeton, New Jersey) injected at a rate of 2 mL/s and the patients were scanned after a delay of 65 sec. All scans were acquired in dual-energy rapid 80- to 140-kVp switching mode by using the following gemstone spectral imaging protocol: gemstone spectral imaging preset at 15, a large-scan field of view (up to 50 cm), a 40-mm beam collimation, a 0.6-second rotation time, and a 0.984:1 helical pitch. Images were reconstructed into 1.25-mm sections in a 25-cm display field of view and a 512 × 512 matrix. The average CT dose index volume for the main acquisition (entire neck to carina) was 17.3 mGy.

Postprocessing and Image Analysis

Postprocessing and General Analysis. A 70-keV reconstruction is generated automatically by the scanner for standard clinical use. Quantitative image analysis was performed at an Advantage 4.6 workstation (GE Healthcare). Normal structures or lesions were evaluated with circular ROIs, and CT attenuation (in Hounsfield units) and standard deviation were measured within the ROIs. In each case, quantitative spectral analysis was performed in identical ROIs at different VMI energy levels ranging from 40 to 140 keV, in 5-keV increments, for a total of 21 energy levels per ROI. Each normal structure or lesion was evaluated with multiple ROIs (described in greater detail below). For each patient, the mean attenuation of a given structure or lesion was determined on the basis of the average Hounsfield units of the respective ROIs in that structure or lesion. Image noise was based on the SD in an ROI, and the average noise for each structure or lesion was calculated by obtaining the average SD in their respective ROIs.[5] As described in greater detail below, because of different sizes of normal structures and lesions, different-sized ROIs had to be used. So that the results would not be biased toward larger structures (eg, larger tumors), the average ROI for a given normal structure or lesion for each patient was given equal weight when pooling data from multiple patients.

Spectral Evaluation of SNR in Normal Tissues. In the first part of the study, the SNR of muscles and major glands was evaluated. Because of changes in tissue composition and the shape of the neck in the craniocaudal plane, muscles were evaluated at 6 different levels in the neck. From cranial to caudal, the lateral pterygoid (level of fossa of Rosenmüller), masseter (level of parotid), genioglossus (oral cavity), sternocleidomastoid muscle at the level of the submandibular glands, sternocleidomastoid muscle at the level of true vocal cords, and sternocleidomastoid muscle at the level of the thyroid gland were evaluated. In addition, the parotid, submandibular, sublingual, and thyroid glands were evaluated. For consistency, the right side of the neck was evaluated, except for the sublingual gland and genioglossus muscle. In these cases, because of their relatively small sizes, the side with the larger gland or both sides were evaluated. Normal-structure ROIs were iden-

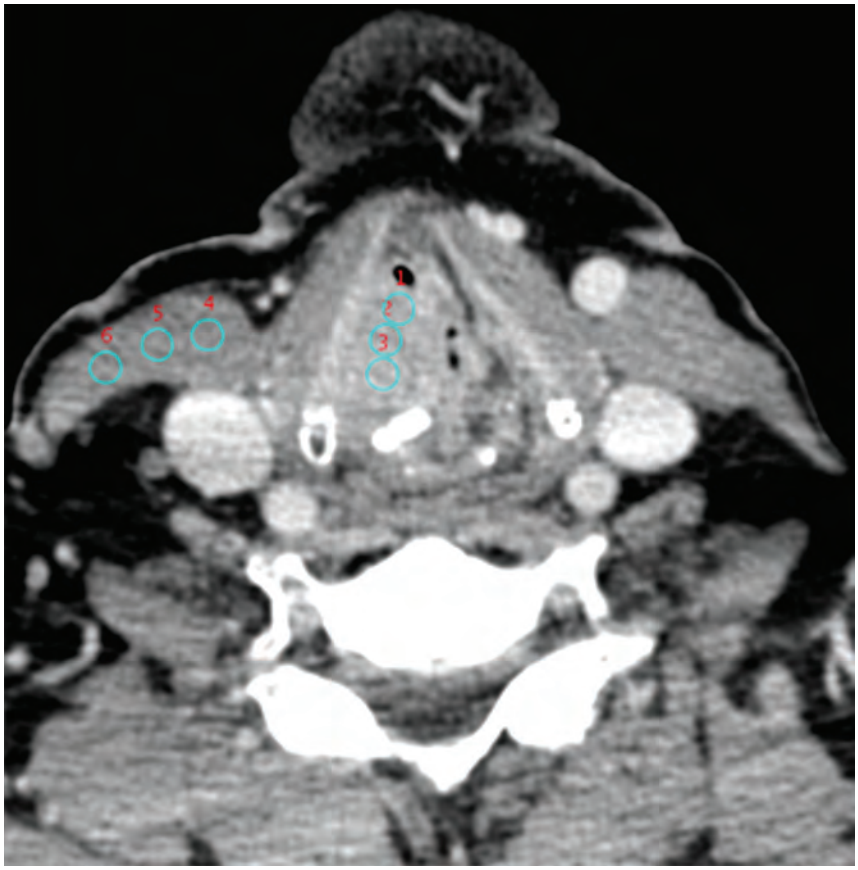

FIG 1. Example of a 5-mm ROI used for the assessment of laryngeal cancer and nearby sternocleidomastoid muscle. As described in detail in the text, in patients with head and neck squamous cell carcinoma, each lesion and a nearby structure were evaluated with 9 nonoverlapping ROIs on multiple sections.

tified by S.L. (diagnostic radiology resident with 3 years of training) and reviewed by R.F (attending physician with fellowship training and 4 years postfellowship experience in neuroradiology and head and neck radiology) before recording the data for further analysis. For each structure, 3 nonoverlapping ROIs were placed. When possible, all 3 ROIs were placed on the same section, except those for small structures (sublingual and genioglossus), for which the ROIs had to be placed on more than 1 section to obtain good coverage and avoid overlaps or artifacts. ROI sizes that enabled good sampling without overlapping or volume averaging with adjacent structures were used. Areas of visible artifacts, such as from dental amalgam, were avoided. For this part of the study, 30 ROIs per patient were evaluated. Depending on the size of the structure being evaluated, the minimum individual ROI diameter used was 3.3 mm (corresponding to a sampled area per ROI of 8.6 mm^2), and the maximum diameter used was 5.8 mm (corresponding to a sampled area per ROI of 26.4 mm^2). The SNR was calculated for each structure, in each patient, by dividing the mean CT attenuation for the 3 ROIs by the mean noise (SD) for the ROIs.

Spectral Evaluation of Tumors and Pathologic Lymph Nodes. For tumors, the mean attenuation and tumor–muscle CNR were calculated. In each patient, the tumor and a nearby normal muscle (completely separate from tumor without contact or invasion of any part of that muscle) were evaluated. Each tumor or normal muscle was evaluated with a total of 9 ROIs, placed on at least 3 separate sections (Fig 1). In addition, 17 pathologic lymph nodes in 9 of the patients were evaluated, and each node was evaluated with 9 ROIs. Only grossly pathologic nodes were evaluated on the basis of either 1) biopsy or neck dissection, when such results were available, or 2) an abnormal-appearing node in the primary or secondary drainage area of the primary tumor by at least 2 criteria among the following: abnormal short-axis diameter, internal necrosis/heterogeneity, rounded contour, or irregular contour.[22] For tumors and lymph nodes, the ROIs were placed in the homogeneous-appearing enhancing part of the lesion, avoiding areas of cystic change/necrosis or visible artifacts. For muscles, the ROIs were placed in areas without visible artifacts. For each normal-appearing structure or lesion, the mean attenuation was determined on the basis of the average Hounsfield units of the respective ROIs in that structure or lesion. Image noise was calculated as the SD in the ROI, and the average noise for each structure or lesion was calculated by obtaining the average SD in their respective ROIs.[5] For tumors, the minimum individual ROI diameter used was 1.7 mm (sampled area per ROI, 2.3 mm^2), and the maximum diameter used was 5.5 mm (sampled area per ROI, 23.8 mm^2). For lymph nodes, the ROI size range was 2.3–4.7 mm (area, 4.2–17.3 mm^2), and for muscles it was 2.3–4.8 mm (area, 4.2–18.1 mm^2). To select an ROI size that provided good sampling and could be applied to different structures in each patient, the size of the ROIs varied because of differences in lesion or muscle size, tumor or lymph node homogeneity, and presence of artifacts. All ROIs in this section were placed by the attending head and neck radiologist (R.F.). The CNR was calculated individually for tumor or lymph node in each patient by using the formula CNR = (average lesion attenuation − average muscle attenuation)/$\sqrt{}$(variance [lesion] + variance [muscle]).[5]

Statistical Analysis

The results are reported as mean ± SD. All comparisons between patients were performed by using the mean attenuation and/or noise from the structure or lesion of interest from each patient (and not by simply pooling all individual ROIs among all patients, which would have artificially inflated the statistical power of the study). Means from 2 different groups were compared by using a Student *t* test. For comparisons of multiple (>2) groups, 1-way ANOVA with the Dunnett multiple-comparisons test was used. Data from different ROI samples were compared by using an un-

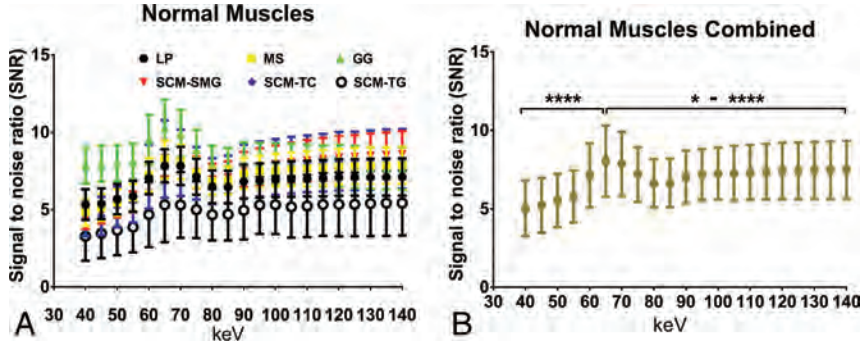

FIG 2. Quality index across the range of VMIs in muscles at different levels in the neck. Signal-to-noise ratios are shown for the lateral pterygoid (LP, level of fossa of Rosenmuller), masseter (MS, level of parotid and masticator space), genioglossus (GG, oral cavity), or sternocleidomastoid (SCM-SMG, level of submandibular glands; SCM-TC, level of true vocal cords; SCM-TG, level of thyroid gland) (*A*) and for all muscles combined (*B*). The highest SNR for the individual muscle curves (*A*) and data from all the muscles combined (*B*) was on VMIs reconstructed at 65 keV ($n = 10$; total ROIs evaluated, 180). * $P < .05$; **** $P < .0001$ (1-way ANOVA).

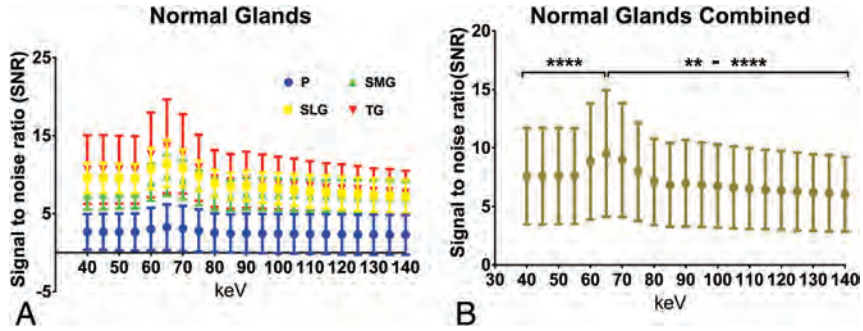

FIG 3. Quality index across the range of VMIs in glands at different levels in the neck. Signal-to-noise ratios are shown for the parotid gland (P), sublingual gland (SLG), submandibular gland (SMG), and thyroid gland (TG) (*A*) and all glands combined (*B*). The highest SNR for the individual muscle curves (*A*) and data from all the glands combined (*B*) was on VMIs reconstructed at 65 keV ($n = 10$; total ROIs evaluated, 120). ** $P < .01$; **** $P < .0001$ (1-way ANOVA).

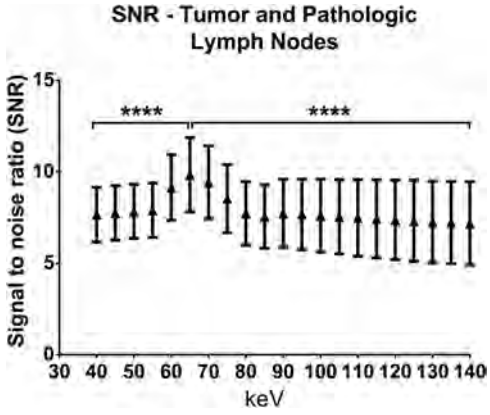

FIG 4. Quality index across the range of VMIs in HNSCC and metastatic lymph nodes. Combined SNRs from 30 tumors and 17 pathologic lymph nodes show that the highest SNR is at 65 keV. **** $P <$ .0001 (1-way ANOVA).

paired test. Spectral data at different keVs derived from the same ROIs were analyzed by using paired analysis. Variance was calculated by using the standard formula variance = SD^2. A *P* value of <.05 was considered statistically significant. We used GraphPad Prism software for statistical analysis (version 6.005; GraphPad Software, San Diego, California).

RESULTS

DECT scans from 10 healthy subjects and 30 subjects with HNSCC with a total of 993 ROIs were evaluated. The mean patient age was 66 years (range, 37–97 years; 20 women, 20 men). In healthy subjects, a total of 6 muscle levels and 4 glands per patient were evaluated, each with 3 ROIs, corresponding to a total of 300 ROIs. The average ROI area evaluated per structure was 62.7 mm^2 (range, 27.2–75.6 mm^2). In the HNSCC group, tumors, pathologic lymph nodes, and reference muscles were evaluated with a total of 270, 153, and 270 ROIs, respectively. The average ROI area evaluated was 105.7 mm^2 (range, 21.2–212.1 mm^2) for tumors, 71.0 mm^2 (range, 37.7–151.8 mm^2) for lymph nodes, and 126.3 mm^2 (range, 37.7–212.1 mm^2) for muscles.

Spectral Attenuation Characteristics and Optimal SNR of Muscles and Normal Glands

Muscle and gland attenuation progressively increased on lower-keV VMIs. However, the highest SNR for all the muscle groups and glands was at 65 keV. For all muscles combined, the mean SNR was 8.0, and for all glands combined the mean SNR was 9.5 at 65 keV. At this energy, the SNR was significantly greater than those at all other energies (1-way ANOVA with Dunnett multiple-comparisons test; Figs 2 and 3). This SNR was closely matched by the SNR at 70 keV (muscles, 7.9; glands, 9.0), followed by that at 60 keV (muscles, 7.1; glands, 8.8; Figs 2*B* and 3*B*). In addition to normal tissues, we also evaluated the SNRs of 30 tumors and 17 pathologic lymph nodes, and the optimal SNR was also at 65 keV (Fig 4).

Optimal VMIs and CNR for Evaluation of HNSCC

Similar to muscle, tumor attenuation increased at lower keVs. Tumor attenuation was highest on 40-keV VMIs, significantly different from those at all other energy levels (1-way ANOVA with Dunnett multiple-comparisons test; Fig 5). However, the slope of the increase in tumor attenuation was greater than that in muscles, resulting in greater attenuation separation in the low-keV range (Fig 5*A*). The greatest difference between tumor and muscle attenuation was at 40 keV. On VMIs reconstructed at this energy level, the mean tumor attenuation was 207.9 ± 46.8 and the mean muscle attenuation was 115.2 ± 31.3 ($P = .03$, unpaired 2-tailed *t* test; Fig 5). Because there is a progressive increase in image noise on lower-keV images, we also calculated tumor–muscle CNR as a quantitative index for lesion conspicuity. The tumor CNR was likewise highest at 40 keV, despite the increase in image noise, and significantly higher than those at other

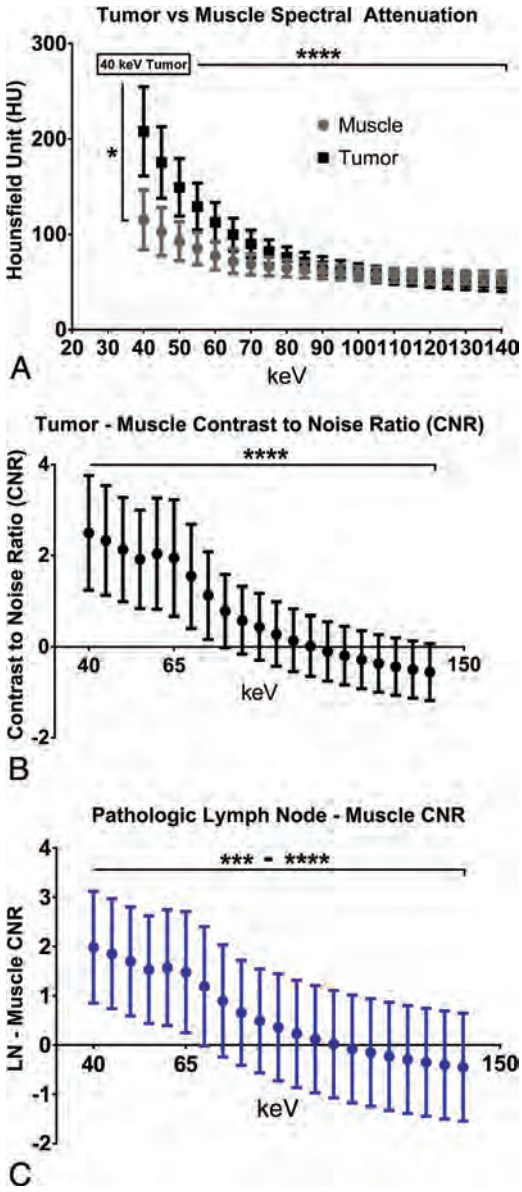

FIG 5. Optimal virtual monochromatic energy level for evaluation of HNSCC and pathologic lymph nodes. *A*, Spectral Hounsfield unit curves of HNSCC compared with those of muscle ($n = 30$). The highest tumor attenuation was at 40 keV, with a statistically significant difference compared with all other energy levels and with mean muscle attenuation at 40 keV. *B*, Tumor–muscle CNR ($n = 30$). The CNR was highest at 40 keV, significantly different from those at all other energy levels. *C*, Pathologic lymph node–muscle CNR ($n = 17$). The CNR was highest at 40 keV, significantly different from those of all other energy levels. ** $P < .01$; **** $P < .0001$ (1-way ANOVA).

energy levels (1-way ANOVA with Dunnett multiple-comparisons test; Fig 5).

Optimal VMI for Evaluation of Metastatic Lymphadenopathy

A total of 17 metastatic lymph nodes were evaluated, and lymph node–muscle CNRs were calculated as measures of conspicuity. Similar to those of tumors, the lymph node–muscle CNR was highest at 40 keV and significantly different from those at other energy levels (1-way ANOVA with Dunnett multiple-comparisons test; Fig 5). Although tumor–muscle and lymph node–muscle CNRs were highest at 40 keV, the optimal SNR was at 65 keV, similar to that of normal tissues (Fig 4).

Comparison of 40-keV VMIs with Other Key DECT VMIs

Mean tumor attenuation on 40-keV VMIs was significantly higher than that on 60-keV VMIs, 65-keV VMIs (optimal tissue SNR), and 70-keV VMIs (current standard reconstruction) ($P < .0001$; Fig 6*A*). Tumor–muscle CNRs were likewise significantly higher on 40-keV VMIs than on 60-, 65-, and 70-keV VMIs ($P < .0001$; Fig 6*B*). Qualitatively, the higher attenuation and CNR are result in increased tumor conspicuity at 40 keV (Fig 7).

DISCUSSION

In this investigation, we evaluated the optimal VMI energy levels for evaluation of the neck. Normal structures and lesions were evaluated by a general quality index, the SNR. In addition, the VMI energy level that provided optimal HNSCC and pathologic lymph node conspicuity was quantitatively evaluated by measuring lesion attenuation and calculating the CNR. Currently, the default reconstruction on the single-source dual-energy scanner with rapid kVp switching used in this study for neck CTs is 70 keV, the VMI believed to simulate the standard 120-kVp single-energy acquisition by extrapolation from abdominal CT studies. On the basis of our results, the 65-keV VMI has the optimal SNR and can be used as the default reconstruction for assessment of the neck. Similar observations have been made for head DECT scans by using this type of scanner.[5] By extrapolation, one would expect that the 65 keV VMI also provides the optimal SNR for evaluation of other normal soft-tissue structures in the neck, such as small normal-appearing lymph nodes, but this could be validated in future studies targeted at the evaluation of those structures.

Although the 65-keV VMIs yielded the best SNR, both absolute tumor attenuation and contrast (by using normal muscles as reference) were highest on 40-keV VMIs. The increase in attenuation on lower-keV VMIs is expected, because these energies approach the *k* edge of iodine. Although image noise increases with decreasing VMI energy levels, the tumor–muscle CNR was still highest on the 40-keV reconstructions. This observation is different from that in a recently published study in which 40-, 60-, 80-, and 100-keV VMIs were evaluated, and it was reported that the highest tumor–muscle CNR was achieved at 60 keV.[10] The reason for the difference is not entirely clear, but a number of explanations need to be considered. In the aforementioned study, a dual-source scanner was used. Apart from differences in acquisition, the methods of postprocessing for that scanner are different. Therefore, one possibility is that the differences are technical, related either to the different modes of acquisition and/or postprocessing algorithms. It is also noteworthy that noise was measured differently by using an ROI outside the patient, placed in air. We prefer using the SD within the tissues of interest as an indicator of noise and believe that it is more pertinent to clinical evaluation, similar to the method used by Pomerantz et al.[5] This represents another potential source of variation, though we believe that it is less likely to account for the differences between the 2 studies. Future studies using larger sample sizes and comparing both systems would be of interest.

In our study, we evaluated normal structures at multiple levels

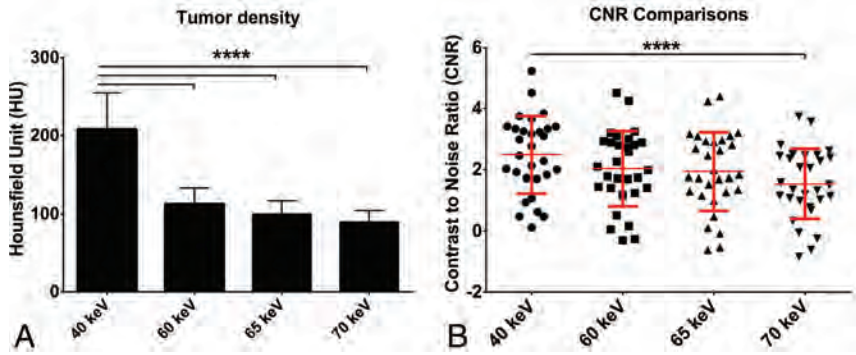

FIG 6. Optimal tumor attenuation and CNR comparisons. *A*, Tumor attenuation comparison of 40-keV VMIs with those on 60-, 65-, and 70-keV VMIs ($n = 30$). *B*, Scatterplot of CNRs comparing 40-keV VMIs with 60-, 65-, and 70-keV VMI reconstructions. **** $P < .0001$.

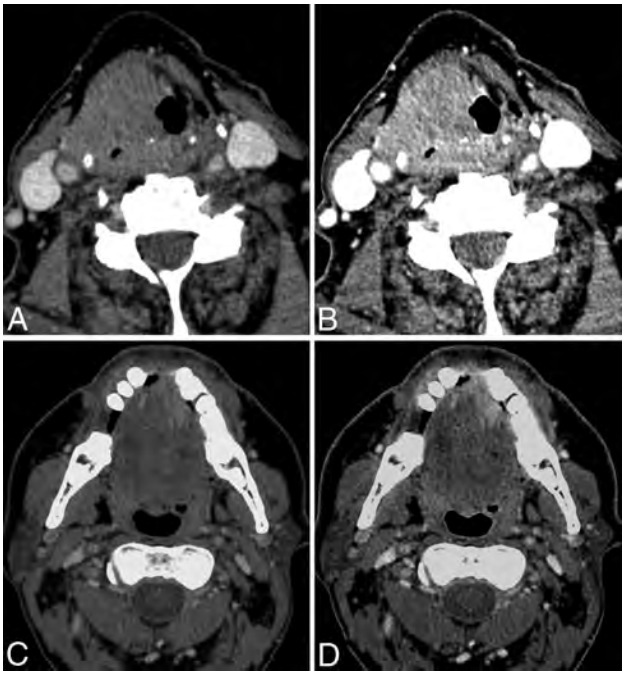

FIG 7. Case examples comparing the standard 70-keV VMI reconstructions with 40 keV VMIs. *A* and *B*, A 92-year-old man with supraglottic squamous cell carcinoma. The same VMIs reconstructed at 70 keV (*A*) and 40 keV (*B*) and with similar windowing (compare subcutaneous fat) are shown. There is increased tumor conspicuity and better visualization of the tumor interface with adjacent prelaryngeal strap muscle. *C* and *D*, A 60-year-old man with floor-of-mouth squamous cell carcinoma. VMIs reconstructed at 70 keV (*C*) and 40 keV (*D*) are shown. Note the increased tumor conspicuity on the 40-keV VMI reconstruction.

in the neck and tumors at different subsites to make sure that our conclusions can be applied generally to the evaluation of the neck. However, one limitation is that the number of HNSCC tumors for each specific subsite was small, and our study did not evaluate lesions centered at the skull base. Therefore, it is possible that additional adjustments may further improve evaluation at a given cancer subsite. Furthermore, we focused on the enhancing part of the tumor rather than the hypoenhancing core, which is pertinent for distinguishing the tumor–normal tissue interface. However, there are additional parameters of clinical interest that were not evaluated in this study, such as distinguishing enhancing and hypoenhancing parts of a lesion, which can potentially be relevant for the evaluation of lesions such as small pathologic lymph nodes. These topics are of interest for future research.

We also focused on quantitative objective evaluation, which we believe is more robust and reliable than subjective evaluation. It has been our experience that similarly windowed low-keV VMIs are clearly distinguishable from the standard-energy VMIs at 70 keV, which makes a blinded subjective comparison nearly impossible. Furthermore, we have found that user acceptance of noise levels changes with exposure and experience. Therefore, although subjective evaluation is an interesting topic of future investigation, any such study needs to be designed carefully with well-defined end points and by taking into account the above-mentioned considerations and pitfalls. Last, our study did not address the optimal assessment of areas obscured by artifacts. Artifact reduction is a complex topic that merits a separate dedicated investigation.

CONCLUSIONS

The optimal image SNR is at 65 keV, but tumor conspicuity, compared with that of other soft tissues, is greatest at 40 keV. Therefore, on the basis of our observations, we recommend that standard neck reconstructions using this type of scanner be made with a 65-keV VMI and in addition, a 40-keV VMI reconstruction generated for the evaluation of patients with HNSCC. We do not advocate replacing the 65-keV reconstruction with the 40-keV VMI. Instead, we recommend that both the standard 65-keV VMI reconstructions and the 40-keV VMIs be automatically generated and sent to the PACS for evaluation of patients with cancer. Optimal evaluation of the neck may then be performed by a multiparametric approach. Using the proposed approach, the 65-keV VMIs providing the best overall image quality are used for general evaluation of the neck, supplemented with the targeted use of 40-keV VMIs for tumor detection and optimal HNSCC–soft tissue boundary visualization.

ACKNOWLEDGMENTS

We thank Ms. Veronika Glyudza for her assistance in data preparation and processing.

Disclosures: Rajiv Gupta—*UNRELATED*: *Board Membership:* Actelion Corp, *Comments*: advising the company on imaging in their drug trials; *Grants/Grants Pending*: Siemens Medical Solutions,* *Comments*: research grant to Massachusetts General Hospital; the principal investigator on the grant (Udo Hoffman, MD) is not an author on this paper; *Travel/Accommodations/Meeting Expenses Unrelated to Activities Listed*: Siemens Medical Solutions, *Comments*: travel support for an educational symposium on photon-counting CT organized by Siemens Medical Solutions. Mark Levental—*UNRELATED*: *Consultancy*: Biogen Idec, *Comments*: honorarium for attending a training seminar; *Travel/Accommodations/Meeting Expenses Unrelated to Activities Listed*: Royal College Examiner, *Comments*: reimbursement of expenses. Hugh Curtin—*UNRELATED*: *Royalties*: Elsevier, *Comments*: royalties for textbook. Reza Forghani—*UNRELATED*: *Consultancy*: Biogen Idec, Collège des médecins du Québec, *Comments*: one-time honorarium for attending a training seminar; expert consultant for Collège des médecins du Québec (telemedicine committee, quality assurance); *Expert Testimony*: Collège des médecins du Québec, *Comments*: quality assurance and reviews; *Payment for Lectures (including service on Speakers Bu-*

reaus): Peer Review for Departmental QA and Audits: Essentials of a Successful Program, Benchmarks for Evaluation, and Challenges (Ontario Association of Radiologists CME course, 2014); Sinus Anatomy: Normal and Postoperative (Ontario Association of Radiologists CME course, 2014); Visiting Professor, McMaster University Health Sciences Center; Radiology Grand Rounds, St. Joseph's Healthcare Hamilton, 2013; *Stock/Stock Options*: Real Time Medical, *Comments*: member, medical and quality assurance committee. *Money paid to the institution.

REFERENCES

1. Johnson TRC, Kalender WA. **Physical background.** In: Johnson T, Fink C, Schönberg SO, et al, eds. *Dual Energy CT in Clinical Practice*. Berlin-Heidelberg: Springer-Verlag; 2011:3–9
2. De Cecco CN, Darnell A, Rengo M, et al. **Dual-energy CT: oncologic applications.** *AJR Am J Roentgenol* 2012;199:S98–105
3. Heye T, Nelson RC, Ho LM, et al. **Dual-energy CT applications in the abdomen.** *AJR Am J Roentgenol* 2012;199:S64–70
4. Lu GM, Zhao Y, Zhang LJ, et al. **Dual-energy CT of the lung.** *AJR Am J Roentgenol* 2012;199:S40–53
5. Pomerantz SR, Kamalian S, Zhang D, et al. **Virtual monochromatic reconstruction of dual-energy unenhanced head CT at 65–75 keV maximizes image quality compared with conventional polychromatic CT.** *Radiology* 2013;266:318–25
6. Postma AA, Hofman PA, Stadler AA, et al. **Dual-energy CT of the brain and intracranial vessels.** *AJR Am J Roentgenol* 2012;199:S26–33
7. Vliegenthart R, Pelgrim GJ, Ebersberger U, et al. **Dual-energy CT of the heart.** *AJR Am J Roentgenol* 2012;199:S54–63
8. Vogl TJ, Schulz B, Bauer RW, et al. **Dual-energy CT applications in head and neck imaging.** *AJR Am J Roentgenol* 2012;199:S34–39
9. Tawfik AM, Kerl JM, Bauer RW, et al. **Dual-energy CT of head and neck cancer: average weighting of low- and high-voltage acquisitions to improve lesion delineation and image quality-initial clinical experience.** *Invest Radiol* 2012;47:306–11
10. Wichmann JL, Nöske EM, Kraft J, et al. **Virtual monoenergetic dual-energy computed tomography: optimization of kiloelectron volt settings in head and neck cancer.** *Invest Radiol* 2014;49:735–41
11. Toepker M, Czerny C, Ringl H, et al. **Can dual-energy CT improve the assessment of tumor margins in oral cancer?** *Oral Oncol* 2014;50:221–27
12. Kuno H, Onaya H, Fujii S, et al. **Primary staging of laryngeal and hypopharyngeal cancer: CT, MR imaging and dual-energy CT.** *Eur J Radiol* 2014;83:e23–35
13. Kuno H, Onaya H, Iwata R, et al. **Evaluation of cartilage invasion by laryngeal and hypopharyngeal squamous cell carcinoma with dual-energy CT.** *Radiology* 2012;265:488–96
14. Srinivasan A, Parker RA, Manjunathan A, et al. **Differentiation of benign and malignant neck pathologies: preliminary experience using spectral computed tomography.** *J Comput Assist Tomogr* 2013;37:666–72
15. Stolzmann P, Winklhofer S, Schwendener N, et al. **Monoenergetic computed tomography reconstructions reduce beam hardening artifacts from dental restorations.** *Forensic Sci Med Pathol* 2013;9:327–32
16. Tawfik AM, Razek AA, Kerl JM, et al. **Comparison of dual-energy CT-derived iodine content and iodine overlay of normal, inflammatory and metastatic squamous cell carcinoma cervical lymph nodes.** *Eur Radiol* 2014;24:574–80
17. Tanaka R, Hayashi T, Ike M, et al. **Reduction of dark-band-like metal artifacts caused by dental implant bodies using hypothetical monoenergetic imaging after dual-energy computed tomography.** *Oral Surg Oral Med Oral Pathol Oral Radiol* 2013;115:833–38
18. Forghani R, Levental M, Gupta R, et al. **Different spectral Hounsfield unit curve and high-energy virtual monochromatic image characteristics of squamous cell carcinoma compared with nonossified thyroid cartilage.** *AJNR Am J Neuroradiol* 2015;36:1194–200
19. Patel BN, Thomas JV, Lockhart ME, et al. **Single-source dual-energy spectral multidetector CT of pancreatic adenocarcinoma: optimization of energy level viewing significantly increases lesion contrast.** *Clin Radiol* 2013;68:148–54
20. Krauss B, Schmidt B, Flohr TG. **Dual source CT.** In: Johnson T, Fink C, Schönberg SO, et al, eds. *Dual Energy CT in Clinical Practice*. Berlin-Heidelberg: Springer-Verlag; 2011:10–20
21. Chandra N, Langan DA. **Gemstone detector: dual energy imaging via fast kVp switching.** In: Johnson T, Fink C, Schönberg SO, et al, eds. *Dual Energy CT in Clinical Practice*. Berlin-Heidelberg: Springer-Verlag; 2011:35–41
22. Forghani R, Yu E, Levental M, et al. **Imaging evaluation of lymphadenopathy and patterns of lymph node spread in head and neck cancer.** *Expert Rev Anticancer Ther* 2015;15:207–24

Residual Cervical Thymus: A Normal CT Finding That May Be Present Throughout Patients' Lives

A.V. Prabhu, H.A. Kale, and B.F. Branstetter IV

ABSTRACT

BACKGROUND AND PURPOSE: Although the thymus is centered in the mediastinum, often a cervical component can be seen in children and young adults. The frequency of radiologically evident residual cervical thymus in older adults is not known. The purpose of our study was to determine the proportion of adults who have residual cervical thymus visible on contrast-enhanced neck CT.

MATERIALS AND METHODS: We retrospectively identified 700 patients who had undergone contrast-enhanced CT between February 2013 and August 2013. We categorized the patients by decade of life and calculated the proportion in which residual cervical thymic tissue could be detected. The location of the tissue focus, greatest axial diameter, and distance above the manubrium were recorded. A multivariate model was used to determine whether age or sex predicted the likelihood of identifiable cervical thymus, the size of residual thymus, or the distance of residual thymus above the sternum.

RESULTS: Of the 700 patients, 157 (22.4%) had residual cervical thymus. The mean distance of the residual thymus above the manubrium was 13.4 ± 7.26 mm. The mean size of the residual cervical thymus was 12.5 ± 4.11 mm. The frequency of residual thymus decreased exponentially with age. There was a statistically significant relationship between age and the size of the residual cervical thymus ($P = .02$). Most of the cervical thymic tissue was found in the left paratracheal region.

CONCLUSIONS: Residual cervical thymus may be present at any age, though the frequency decreases with increasing age.

Although the thymus is centered in the superior mediastinum, frequently a radiologically detectable cervical component of the gland can be seen in children and young adults.[1] This cervical extension can mimic a pathologic mass or enlarged lymph node, potentially leading to unnecessary surgery and increased medical costs. Radiologists are often unaware of residual cervical thymus tissue as a normal finding, not only in the pediatric population but also in the adult population, because no comprehensive study of residual cervical thymus has been conducted on adults, to our knowledge.

We hypothesized that radiologically detectable residual cervical thymus is present throughout patients' lives and that the frequency of detectable residual cervical thymus decreases with age. The purpose of this study was to determine the proportion of adults at various ages in whom residual thymic tissue can be detected superior to the level of the sternum on CT.

Received November 23, 2014; accepted after revision December 29.

From the Departments of Radiology (A.V.P., H.A.K., B.F.B.) and Otolaryngology (B.F.B.), University of Pittsburgh School of Medicine, Pittsburgh, Pennsylvania.

Please address correspondence to Barton F. Branstetter IV, MD, Department of Radiology, University of Pittsburgh School of Medicine, 200 Lothrop St, Pittsburgh, PA, 15213; e-mail: branbf@upmc.edu

http://dx.doi.org/10.3174/ajnr.A4304

MATERIALS AND METHODS

Subjects

The institutional review board at the University of Pittsburgh Medical Center approved this retrospective study of existing imaging data, and written consent was waived. We retrospectively searched our electronic medical records to identify contrast-enhanced CT scans of the neck obtained between February 2013 and August 2013, each performed on a different adult patient.

Patients were grouped into 10-year age intervals based on their age (in years) at the time of the examination. The 7 groups were 20–29 years, 30–39 years, 40–49 years, 50–59 years, 60–69 years, 70–79 years, and 80 years and older. Exactly 100 patients were included from each group; once 100 patients in a group were accumulated, no further patients from that group were evaluated. The criterion for inclusion was a contrast-enhanced CT that included the superiormost extent of the manubrium and the lower neck. Patients were excluded if they had undergone surgery or radiation to the lower neck, if the scans demonstrated malignancy within the lower neck or enlarged lower cervical lymph nodes, if there was edema in the lower neck soft tissues, if there was inad-

equate scan coverage of the neck, or if streak artifacts prevented clear evaluation of the lower neck.

Imaging

CT was performed on a 64-channel scanner (LightSpeed; GE Healthcare, Milwaukee, Wisconsin) with variable milliampere and kilovolt(peak) of 120. Display FOV varied with patient size but was approximately 25 mm; coronal and sagittal reformats were not used in this evaluation.

Each examination was evaluated by 1 of 2 Certificate of Added Qualification–certified dedicated head and neck radiologists (B.F.B. and H.A.K., with 12 and 8 years of experience, respectively) to determine whether residual cervical thymic tissue was present. Thymic tissue was defined as an oval focus of soft tissue interspersed with fat that had CT texture similar to that of the mediastinal thymus (Fig 1). The mass had to be discrete and well-defined (we chose this criterion to be conservative and avoid overcalling residual thymus). Only foci above the sternal notch were considered cervical. In patients with residual cervical thymus, the location of the tissue focus, size (greatest axial diameter), and distance between the midpoint of the tissue and the upper border of the manubrium were recorded.

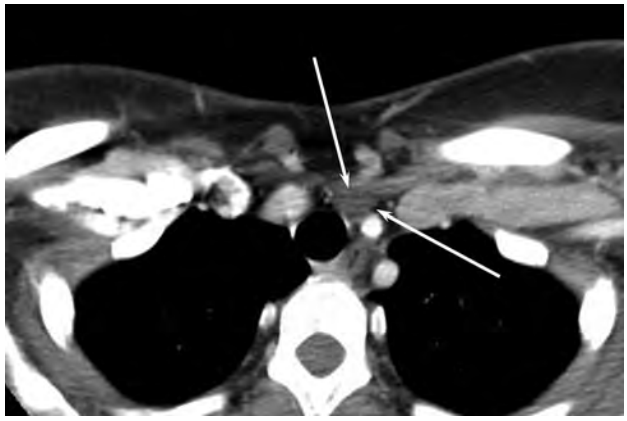

FIG 1. Axial contrast-enhanced CT image through the lower neck shows a uniform, well-defined ovoid mass (*arrows*) with mixed fat and soft-tissue elements deep to the sternal head of the sternocleidomastoid muscle. This is the characteristic location and appearance of residual cervical thymus.

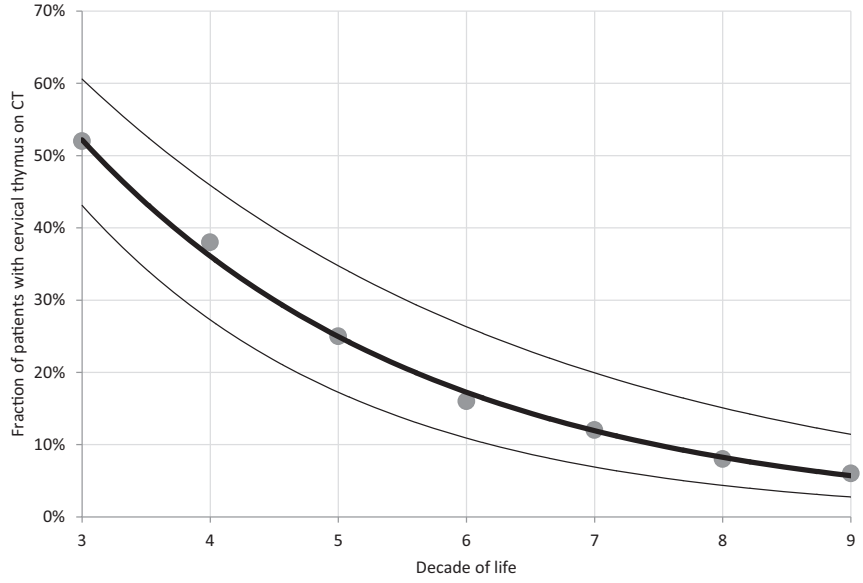

FIG 2. Graph demonstrating the relationship between the age decade and the presence of the cervical thymus on CT. *Circular markers* are raw data. The *dark line* is best-fit logistic regression. *Thin lines* are 95% confidence intervals. The third decade of life indicates patients 20–29 years of age.

Statistical Tests

Patients were grouped by decade of age. The percentage of patients with residual cervical thymus in each age group was tabulated and graphed, and a least-squares logistic regression curve was applied (Fig 2). A multivariate model was used to determine whether age or sex predicted the likelihood of identifiable cervical thymus, the size of the residual thymus, or the distance of the residual thymus above the sternum. All tests were 2-sided, and a P value of .05 was chosen as the threshold for statistical significance. SPSS, Version 22 (IBM, Armonk, New York) was used for all statistical calculations.

RESULTS

The 700 studied patients included 338 male (48.3%) and 362 female patients (51.7%). Of the 700 patients, 157 (22.4%) had residual cervical thymus. The mean distance of the residual thymus above the manubrium was 13.4 ± 7.26 mm. The mean size of the residual cervical thymus was 12.5 ± 4.11 mm.

The frequency of residual cervical thymus by 10-year age intervals is depicted in Table 1. Residual cervical thymus was seen in all decades of life. The frequency declined from 52% in the third decade of life to 25% in the fifth decade of life to 6% in the ninth decade of life. Residual cervical thymus was found in the left paratracheal region in 108 (69%) of 157 patients (Table 2).

Multivariate analysis demonstrated a statistically significant relationship between age and the size of the residual cervical thymus ($P = .02$, Table 1). There was no statistically significant relationship between sex and frequency or between sex and size of the residual cervical thymus. There was also no statistically significant relationship between age and the distance of the residual thymus above the manubrium or between sex and the distance of the residual thymus above the manubrium.

DISCUSSION

On CT in adults, the normal thymus can be seen as a triangular-shaped structure in the anterior mediastinum,[2-4] reflecting apposition of the 2 thymic primordia that arose from diverticula in the third branchial pouches. As age increases, the thymus undergoes normal involution in which mediastinal fat replaces glandular tissue.[5] Wide variability in thymic size and morphology, coupled with its association with diverse pathologic processes, allows the thymus to occasionally mimic pathology.[2-4,6]

Table 1: Frequency and size of residual cervical thymus visualized on neck CT[a]

Age (yr)	Frequency	Size (mm)
20–29	52% (42–62)	13.7
30–39	38% (29–48)	12.5
40–49	25% (18–34)	11.6
50–59	16% (10–24)	11.1
60–69	12% (7–20)	10.7
70–79	8% (4–15)	12.9
80 and older	6% (3–12)	12.5

[a] Frequency is reported with 95% confidence intervals in parentheses. Size is the mean of the maximal axial dimension, reported in millimeters. Both of these parameters were statistically significantly correlated with age.

Table 2: Location and frequency of residual cervical thymus[a]

Location	Frequency
Left paratracheal	108 (69)
Pretracheal	31 (20)
Right paratracheal	10 (6)
Left lower neck	8 (5)
Total	157 (100)

[a] Frequency is reported with percentage in parentheses. "Left lower neck" refers to a location at least 1 cm distant from the trachea.

Our study demonstrates that residual thymic tissue in the neck is a commonly occurring variant of the normal thymus, which should not be mistaken for pathology. In our study, residual cervical thymus was present throughout all decades of life. Of the 700 patients, 157 (22.4%) had residual cervical thymus, with approximately two-thirds of the thymus located in the left paratracheal region. Residual cervical thymus was evident in more than half of the patients in their 20s and showed an exponential decay in frequency with increasing patient age. Although the most common location for cervical thymic tissue is in the left paratracheal region, it can be seen anywhere in the lower neck.

This study builds on the work of Costa et al,[1] who determined the frequency of the residual cervical thymus in pediatric patients. They showed superior cervical extension of the thymus in 133 (66.5%) of 200 patients, ranging from zero to ≥20 years of age, with a mean age of 9.0 years.[1] Our results are consistent with the concept of cervical thymus as a frequent, normal anatomic finding. Together, these studies paint a complete picture of the presence and frequency of the cervical thymus in the pediatric and adult populations.

The differential diagnosis for a low-attenuation mass in the lower neck includes an enlarged Virchow node, thyroid mass, parathyroid mass, paratracheal lymphadenopathy, thymic cyst, and enlarged distal thoracic duct.[7] Cervical thymus may be distinguished from these entities by the CT texture (lobules of soft tissue interspersed with fat), which is similar to the texture of the native thymus.[6]

The decreased frequency of the residual cervical thymus with age is most likely the result of the natural involution of the gland.[5] However, other explanations could be offered. The distance between the thyroid gland and the sternum decreases with age, so that thymic tissue that was cervical in young adulthood could become retrosternal in later life. In addition, obesity can cause lower neck structures to shift into the thorax, potentially forcing the cervical thymus under the sternum. However, the consistent distance between the sternum and the cervical thymus across our patient population suggests that involution is the best explanation.

Residual cervical thymus should not be confused with ectopic cervical thymus.[8-12] Ectopic cervical thymus is the result of aberrant embryology. The thymus is derived from the paired third pharyngeal pouches in the upper neck. The thymic primordia descend via the thymopharyngeal ducts, which normally involute. Residual cells along this pathway may develop into ectopic foci of thymic tissue.[13,14] These ectopic foci can appear anywhere along the line from the angle of the mandible to the thyroid gland.[15] Ectopic thymic tissue is more common in males and is usually on the left side.[9,16,17] In contrast, the residual cervical thymus is continuous with the mediastinal thymus during childhood and becomes disconnected by selective atrophy of portions of the gland.

Our study has some important limitations. The study was retrospective, and all patients in the study were imaged for varying clinical reasons. Sick patients might have a higher rate of visible residual cervical thymus, but this is acceptable because it reflects the actual rate of cervical thymus that would be seen on medical imaging. The observers interpreting the images were blinded to patient age, but their clinical experience allowed them to gauge the approximate age of each patient on the basis of the images, which could have introduced bias. Finally, there was no histologic confirmation of the residual thymic tissue, but we think that the predictable decline in frequency of this finding with age reinforces our conclusion that this is indeed the thymus.

CONCLUSIONS

Residual cervical thymus may be present at any age and should not be mistaken for pathology. Residual cervical thymus is most frequently encountered in the left paratracheal region.

ACKNOWLEDGMENTS

The authors thank Rose Jarosz for her role as research coordinator for this study.

REFERENCES

1. Costa NS, Laor T, Donnelly LF. **Superior cervical extension of the thymus: a normal finding that should not be mistaken for a mass.** *Radiology* 2010;256:238–42
2. Nicolaou S, Muller NL, Li DK, et al. **Thymus in myasthenia gravis: comparison of CT and pathologic findings and clinical outcome after thymectomy.** *Radiology* 1996;201:471–74
3. Smith CS, Schoder H, Yeung HW. **Thymic extension in the superior mediastinum in patients with thymic hyperplasia: potential cause of false-positive findings on 18F-FDG PET/CT.** *AJR Am J Roentgenol* 2007;188:1716–21
4. Jacobs MT, Frush DP, Donnelly LF. **The right place at the wrong time: historical perspective of the relation of the thymus gland and pediatric radiology.** *Radiology* 1999;210:11–16
5. Francis IR, Glazer GM, Bookstein FL, et al. **The thymus: reexamination of age-related changes in size and shape.** *AJR Am J Roentgenol* 1985;145:249–54
6. Dua SG, Purandare NC, Shah S, et al. **Cervical extension of the thymus mimicking metastatic recurrence of Ewing sarcoma on PET/CT.** *Indian J Nucl Med* 2010;25:176–77
7. Liu ME, Branstetter BF 4th, Whetstone J, et al. **Normal CT appearance of the distal thoracic duct.** *AJR Am J Roentgenol* 2006;187:1615–20
8. Dano I, Dangoor E, Eliasher R, et al. **Thymic cyst mimicking a branchial cleft cyst.** *J Otolaryngol* 1998;27:236–37

9. Miller MB, De Vito MA. **Cervical thymic cyst.** *Otolaryngol Head Neck Surg* 1995;112:586–88
10. Millman B, Pransky S, Castillo J 3rd, et al. **Cervical thymic anomalies.** *Int J Pediatr Otorhinolaryngol* 1999;47:29–39
11. Nguyen Q, deTar M, Wells W, et al. **Cervical thymic cyst: case reports and review of the literature.** *Laryngoscope* 1996;106:247–52
12. Tunkel DE, Erozan YS, Weir EG. **Ectopic cervical thymic tissue: diagnosis by fine needle aspiration.** *Arch Pathol Lab Med* 2001; 125:278–81
13. Ahsan F, Allison R, White J. **Ectopic cervical thymus: case report and review of pathogenesis and management.** *J Laryngol Otol* 2010; 124:694–97
14. Tovi F, Mares AJ. **The aberrant cervical thymus. Embryology, pathology, and clinical implications.** *Am J Surg* 1978;136:631–37
15. Wu SL, Gupta D, Connelly J. **Adult ectopic thymus adjacent to thyroid and parathyroid.** *Arch Pathol Lab Med* 2001;125:842–43
16. Guba AM Jr, Adam AE, Jaques DA, et al. **Cervical presentation of thymic cysts.** *Am J Surg* 1978;136:430–36
17. Kiyosue H, Miyake H, Komatsu E, et al. **MRI of cervical masses of thymic origin.** *J Comput Assist Tomogr* 1994;18:206–08

Acute Invasive Fungal Rhinosinusitis: A Comprehensive Update of CT Findings and Design of an Effective Diagnostic Imaging Model

E.H. Middlebrooks, C.J. Frost, R.O. De Jesus, T.C. Massini, I.M. Schmalfuss, and A.A. Mancuso

ABSTRACT

BACKGROUND AND PURPOSE: Acute invasive fungal rhinosinusitis carries a high mortality rate. An easy-to-use and accurate predictive imaging model is currently lacking. We assessed the performance of various CT findings for the identification of acute invasive fungal rhinosinusitis and synthesized a simple and robust diagnostic model to serve as an easily applicable screening tool for at-risk patients.

MATERIALS AND METHODS: Two blinded neuroradiologists retrospectively graded 23 prespecified imaging abnormalities in the craniofacial region on craniofacial CT examinations from 42 patients with pathology-proven acute invasive fungal rhinosinusitis and 42 control patients proved negative for acute invasive fungal rhinosinusitis from the same high-risk population. A third blinded neuroradiologist decided discrepancies. Specificity, sensitivity, positive predictive value, and negative predictive value were determined for all individual variables. The 23 variables were evaluated for intercorrelations and univariate correlations and were interrogated by using stepwise linear regression.

RESULTS: Given the low predictive value of any individual variable, a 7-variable model (periantral fat, bone dehiscence, orbital invasion, septal ulceration, pterygopalatine fossa, nasolacrimal duct, and lacrimal sac) was synthesized on the basis of multivariate analysis. The presence of abnormality involving a single variable in the model has an 87% positive predictive value, 95% negative predictive value, 95% sensitivity, and 86% specificity ($R^2 = 0.661$). A positive outcome in any 2 of the model variables predicted acute invasive fungal rhinosinusitis with 100% specificity and 100% positive predictive value.

CONCLUSIONS: Our 7-variable CT-based model provides an easily applicable and robust screening tool to triage patients at risk for acute invasive fungal rhinosinusitis into a disease-positive or -negative category with a high degree of confidence.

ABBREVIATIONS: AIFR = acute invasive fungal rhinosinusitis; NPV = negative predictive value; PPV = positive predictive value

Fungal-related diseases of the nasal cavity and paranasal sinuses represent a broad spectrum of clinical entities, with acute invasive fungal rhinosinusitis (AIFR) being the most urgent and life-threatening.[1-3] The primary risk factors for acquiring AIFR are neutropenia or dysfunctional neutrophils, and the most commonly reported predisposing conditions are hematologic malignancies, poorly controlled diabetes mellitus, chemotherapy, or organ transplantation.[4-6] Although AIFR is a relatively rare disease, it carries a high mortality rate, with the largest published meta-analysis showing a mortality rate of approximately 50%.[7] The high mortality rate underscores the importance of a timely diagnosis. Patients with AIFR limited to the nasal cavity have lower mortality rates,[2] while intracranial extension is associated with twice the mortality.[7] Accurate and easy-to-use predictive screening models that could help diagnose AIFR in a timely manner are currently lacking.

CT has long been considered an integral part of screening at-risk patients, despite the reported low specificity.[8,9] The most commonly reported CT findings in early disease include severe unilateral nasal cavity mucosal thickening and soft-tissue infiltration of the maxillary periantral fat planes.[8,10] Involvement of the pterygopalatine fossa has also been described.[11] The most commonly affected areas are the middle turbinate, maxillary sinus, ethmoid air cells, and sphenoid sinus.[2] The frontal sinus has been reported as the least frequently affected.[2] Bone dehiscence, orbital invasion, and intracranial extension are more specific features of AIFR but are uncommon in early disease.[1,8,9,12] These findings have also been implicated as indicative of advanced disease.[10,11,13]

Received August 26, 2014; accepted after revision January 15, 2015.

From the Department of Radiology (E.H.M., R.O.D.J., T.C.M., I.M.S., A.A.M.), University of Florida College of Medicine, Gainesville, Florida; Medical Imaging Consultants, Inc (C.J.F.), Gainesville, Florida; and North Florida/South Georgia Veterans Administration (T.C.M., I.M.S.), Gainesville, Florida.

Paper previously presented at: Annual Meeting of the American Society of Head and Neck Radiology, September 10–14, 2014; Seattle, Washington.

Please address correspondence to Erik H. Middlebrooks, MD, PO Box 100374, Gainesville, FL 32610; e-mail: ehmiddlebrooks@gmail.com

Indicates open access to non-subscribers at www.ajnr.org

Indicates article with supplemental on-line table

http://dx.doi.org/10.3174/ajnr.A4298

A central purpose of this study was to characterize the imaging abnormalities of the nasal cavities, sinuses, and surrounding structures commonly associated with AIFR, as well as their incidence and predictive values. Previous institutional experience suggested that some features of AIFR are sparsely mentioned in or absent from the literature. This study was designed as a blinded retrospective study to comprehensively analyze the craniofacial region for changes on CT associated with AIFR. Because previous literature implicated the severity of the abnormality as a marker of AIFR,[7] we applied ordinal scales to capture the degrees of nasal and paranasal mucosal disease and regional disease involvement. A key goal of our multivariate analysis was the synthesis of a simple and robust CT-based diagnostic model that could be deployed as a routine screening tool for at-risk patients. Ideally, this model would allow the diagnosis or exclusion of AIFR with a higher degree of confidence than any model previously suggested.

MATERIALS AND METHODS

Patient Selection and Study Design

Requirement for informed consent was waived in this Health Insurance Portability and Accountability Act–compliant retrospective study, which was approved by the university institutional review board. In our attempt to locate all patients undergoing work-up for possible AIFR, we searched the hospital archive for the term "invasive fungal" appearing in reports dating from January 1, 2007 to October 31, 2013, to identify potential study enrollees. Inclusion criteria were the following: 1) histopathologically proved invasive fungal rhinosinusitis meeting the European Organization for Research and Treatment of Cancer/Invasive Fungal Infections Cooperative Group and the National Institute of Allergy and Infectious Diseases Mycoses Study Group Consensus Group criteria for "proven" invasive fungal sinonasal disease,[14] 2) a clinical time course of <4 weeks, and 3) CT imaging of the craniofacial region within the 5 days preceding biopsy or surgery. Forty-four patients met the inclusion criteria. Exclusion criteria were the following: 1) inadequate imaging by failure to cover the entirety of the craniofacial region (1 patient, 2%), or 2) severe motion or beam-hardening artifacts. Forty-two such patients were enrolled as positive for AIFR. Our standard for patients positive for AIFR was histopathology confirming mucosal fungal invasion, which is the criterion standard.[14]

To differentiate findings related specifically to AIFR, we selected an appropriate control group of at-risk patients. These control patients came from the same at-risk population and had undergone endoscopy or surgery for high clinical suspicion of AIFR. Patients underwent endoscopy for elevated serum galactomannan (19%, 8 of 42), suggestion based on imaging findings (33.3%, 14 of 42), or clinical suspicion in the absence of serologic or imaging findings (ie, sinonasal symptoms clinically and persistent fever of unknown source [47.6%, 20 of 42]). No patients were positive for β-D-glucan. Forty-two such patients were identified in reverse chronologic order with the inclusion criteria of having had an endoscopic visual survey of the nasal cavity with negative findings and/or negative histopathology results for invasive fungal disease, and CT imaging of the craniofacial region in the preceding 5 days. Exclusion criteria were the same as those for patients positive for AIFR. For the control group, all patients underwent, at minimum, a nasal endoscopic survey with negative findings. Biopsy or surgery was also performed in patients with suspicious lesions. All histopathology in the control group confirmed the absence of sinonasal fungal disease. Nasal endoscopy with biopsy of suspicious lesions has been validated as a screening tool[2] and served as the criterion standard for identification of control subjects in our study.

Clinical data were also collected from the medical record including surgical reports, histopathology reports, culture results, predisposing conditions, white blood cell count, absolute neutrophil count, and outcome. The absolute neutrophil count was tabulated only in patients with hematologic malignancy or bone marrow transplants. The cause of death was recorded as listed in the medical record.

Imaging Protocol

Eighty-one of the 84 studies were performed at the authors' hospital, using the institutional craniofacial CT protocol. According to our protocol, images were acquired as 1-mm-thick sections with spacing of 0.8 mm and an in-plane FOV from 170 to 190 mm. Reconstructions using a bone algorithm were also performed at a section thickness of 0.75 mm with 0.5-mm spacing. The scan was obtained in the axial plane from above the frontal sinuses through the hard palate. Multiplanar reformations were also completed in the coronal and sagittal plane. In 3 patients, only craniofacial studies performed at an outside institution were available for review. These studies were acquired with 2.5-mm thickness with coronal and sagittal reformations. Both bone and soft-tissue algorithm images were obtained, and only 1 used intravenous contrast. Patients with clinical suspicion of intraorbital or intracranial involvement received intravenous iodinated contrast (75-mL iohexol, Omnipaque 350; GE Healthcare, Piscataway, New Jersey) at 0.8 mL/s with imaging delayed 90 seconds after the injection of contrast. Contrast was administered in 11 of 42 patients with AIFR and 12 of 42 control patients.

Image Analysis

We used a blinded retrospective experimental design. Each study was completely anonymized before being loaded on an assigned PACS workstation. Two neuroradiologists independently interpreted the studies. Each reader had completed a 1-year Accreditation Council for Graduate Medical Education–approved neuroradiology fellowship and an additional dedicated 1-year fellowship in head and neck imaging. One reader (R.O.D.J.) had 3 years of experience interpreting head and neck imaging, and the second reader (T.C.M.) had 2 years of experience. A third reader (A.A.M.) with 35 years of experience in head and neck imaging was a tiebreaker for discrepancies by providing an ordinal value to replace the initial readers' results. The readers were blinded to all patient clinical information, histopathology results, and the number of AIFR cases versus controls. The studies were presented in randomized order to each reader.

The readers graded the amount of mucosal disease in each of the maxillary sinuses, frontal sinuses, sphenoid sinuses, anterior ethmoid air cells, posterior ethmoid air cells, anterior nasal cavity, posterior nasal cavity, and nasopharynx. Mucosal disease was

Table 1: Demographics and clinical characteristics of both groups

Characteristic	AIFR Group	Control Group	*P* Value
Age (yr)[a]	49.5 ± 21.2 (2–85)	46.7 ± 21.2 (2–75)	.54
Male	20	25	
Female	22	17	
White blood cell count (× 1000/mm^3)[a,b]	0.9 ± 1.5 (0–6)	4.5 ± 12.4 (0.1–65.6)	.3
Absolute neutrophil count (× 1000/mm^3)[a,b]	0.51 ± 1.2 (0–4.9)	1.8 ± 4.0 (0–20.3)	.66
No. of patients <500/mm^3[b]	60% (18/30)	57.1% (20/35)	
No. of patients <1000 mm^3[b]	83.3% (25/30)	68.6% (24/35)	
Time from CT to treatment (days)	0.95 ± 1.1	0.83 ± 0.82	.57
Follow-up time (days)[a]	412.9 ± 587.5 (2–2836)	346.7 ± 402.4 (18–2174)	.56
Deceased from AIFR	7[c]	0	
Deceased not from AIFR	14	9	
Not deceased	20	33	
Overall mortality	52% (22/42)	21% (9/42)	.003
AIFR-related mortality	17% (7/41)[a]	0% (0/42)	
Non-AIFR related mortality	34% (14/41)[a]	21% (9/42)	

[a] Data are reported as mean, with range in parentheses.
[b] Calculated only in patients with hematologic malignancy (including multiple myeloma) or bone marrow transplant.
[c] One patient was excluded because the cause of death was uncertain, reported as died with concomitant fulminant liver failure and AIFR.

Table 2: Prevalence of predisposing conditions for AIFR

Predisposing Condition	Prevalence in AIFR Group	Prevalence in Control Group
Acute myelogenous leukemia	42.9% (18/42)	38.1% (16/42)
Diabetes	28.6% (12/42)	9.5% (4/42)
Other leukemia (non-AML)	19.0% (8/42)	21.4% (9/42)
Multiple myeloma	7.1% (3/42)	7.1% (3/42)
Solid organ malignancy	7.1% (3/42)	0% (0/42)
Solid organ transplant	4.8% (2/42)	9.5% (4/42)
Myelodysplastic syndrome	2.4% (1/42)	7.1% (3/42)
Non-Hodgkin lymphoma	2.4% (1/42)	11.9% (5/42)
None	2.4% (1/42)	0% (0/42)

Note:—AML indicates acute myelogenous leukemia.

Table 3: Cultured fungal pathogens in patients with AIFR

Fungal Species	No. of Cases
Aspergillus sp	42.9% (18/42)
Mucor sp	23.8% (10/42)
Curvularia sp	7.1% (3/42)
Fusarium sp	2.4% (1/42)
Bipolaris sp	2.4% (1/42)
Alternaria sp	2.4% (1/42)
Unknown[a]	19.0% (8/42)

Note:—sp indicates species.
[a] Definitive speciation was not available in 8 cases.

graded on a scale of 0–5 (eg, 0 = normal, 1 = <25% opacified, 2 = 25%–50% opacified, 3 = 50%–75% opacified, 4 = 75%–100% opacified, 5 = mucocele [100% opacified with expansion]). The readers also recorded the presence of infiltration of the sphenopalatine foramen, pterygopalatine fossa, anterior periantral fat, posterior periantral fat, nasolacrimal duct, lacrimal sac, medial orbital fat, inferior orbital fat, and submucosa/bone of the hard palate on a 0–5 scale on the basis of the subjective severity of involvement for the left and right sides separately. The presence of nasal septal mucosal ulceration was assigned as either "present" or "absent." The presence of subdural, epidural, or brain parenchymal extension, along with cavernous sinus involvement, abscess formation, bone dehiscence, arterial thrombosis, and/or venous thrombosis, was similarly graded from 0 to 5. The purpose of using an expanded grading scale for extension beyond the sinus was to better elucidate minor discrepancies between readers. These values were analyzed as both graded variables and binary variables to ensure that no significant differences existed. The plane of the vertical process of the palatine bone defined the boundary between the sphenopalatine foramen and the pterygopalatine fossa.

There were 3 instances of disagreement (grading scale variation of >1) between the 2 primary readers that required reconciliation by the third reader. The specific disagreements included the presence of superior ophthalmic vein thrombosis (0 versus 2; final = 0), involvement of pterygopalatine fossa (0 versus 3, final = 3), and cavernous sinus involvement (1 versus 5, final = 5). All instances were in patients positive for AIFR.

Statistical Analysis

Basic data compilation and manipulation were performed in Excel (Microsoft, Bothell, Washington). Statistical analysis was performed by using JMP Software (SAS Institute, Cary, North Carolina). Specificity, sensitivity, positive predictive value, and negative predictive value were determined across ordinal ranges from binary (presence/absence) to the highest degree of opacity or disease involvement. Lateral data were used to assess lateral disease predominance. Otherwise, data from each measured region with laterality were consolidated to yield single ordinal estimates of disease prevalence or involvement. The resulting 23 variables were evaluated for intercorrelations and univariate correlations with AIFR and were further interrogated by using stepwise linear regression to elucidate the most salient predictors of AIFR. Variable entry into the regression required reducing Akaike Information Criterion, which is a measure of the relative quality of competing statistical models. ANOVA, *t* tests, and nonparametric χ^2 tests were used as appropriate to assess statistical differences between or among variables. The Cochran-Armitage Trend test was used as a modification to χ^2 for ordinal variables to assess the relationships between the degree of opacity (or degree of involvement) and AIFR.

RESULTS

There were few statistical differences of note for any of the demographic or clinical variables collected (Table 1). In particular, there was no significant difference in the absolute neutrophil count of the 2 groups ($P = .66$). The presence of blast crisis in 2 control patients increased the average absolute neutrophil count in the control group; however, this did not meet statistical significance. The control patients were all discharged and had a minimum of 18 days of follow-up (346.7 ± 402.4 days) after negative endoscopy findings. No evidence of fungal sinusitis was present at the time of the last follow-up. The most prevalent predisposing conditions were leukemia, particularly acute myelogenous leukemia, and diabetes (Table 2). As expected from our sampling regimen, these predisposing conditions were represented in statistically similar manners between control patients and those with AIFR.

Aspergillus species (42.9%) and *Mucor* species (23.8%) were the most commonly isolated fungal pathogens (Table 3). Because

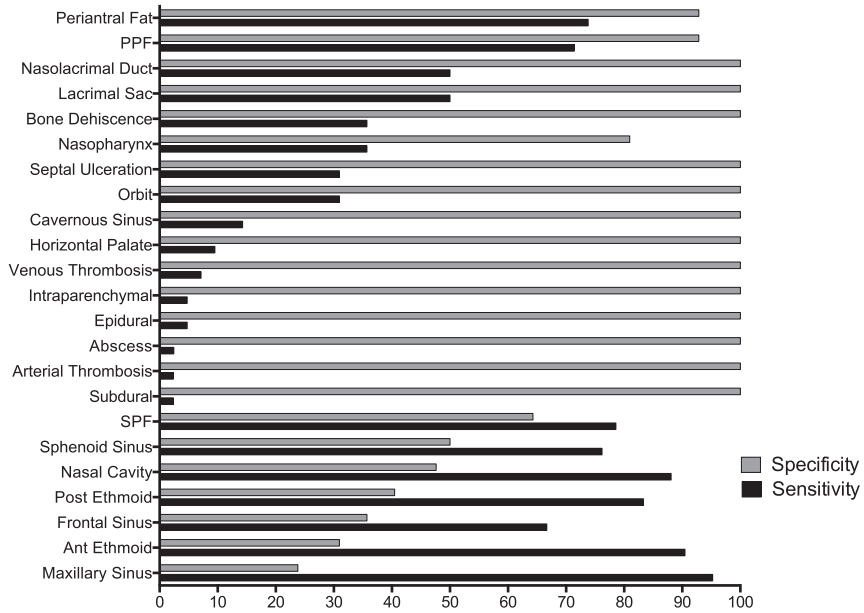

FIG 1. Sensitivity and specificity for all variables. PPF, pterygopalatine fossa; SPF, sphenopalatine foramen; Ant, anterior.

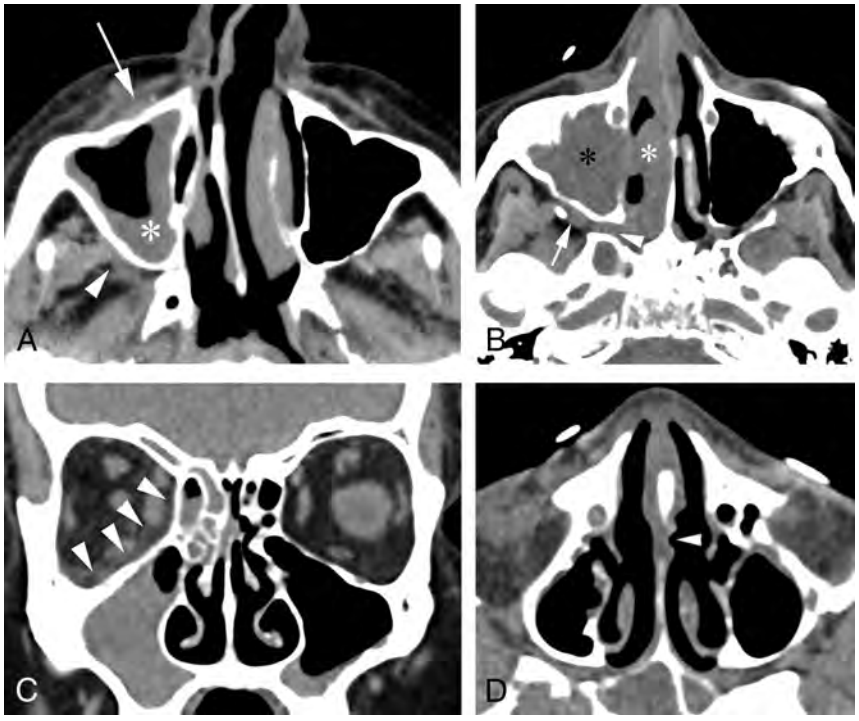

FIG 2. Examples of established findings in AIFR. *A*, Axial CT image shows unilateral mucosal thickening involving the right maxillary sinus (*asterisk*) with soft-tissue infiltration of the right anterior periantral fat (*arrow*) and the posterior periantral fat (*arrowhead*). *B*, Axial image in a different patient shows unilateral right nasal cavity (*white asterisk*) and maxillary sinus (*black asterisk*) mucosal thickening. Soft-tissue infiltration through the right sphenopalatine foramen and pterygopalatine fossa (*arrowhead*) is seen, as well as involvement of the right posterior periantral fat (*arrow*). *C*, Coronal CT in a third patient illustrates orbital involvement of AIFR with subtle infiltration of the right medial and inferior extraconal orbital fat (*arrowheads*), despite the absence of bone erosion. *D*, Axial CT shows a surgically proved subtle ulceration along the left side of the nasal septum (*arrowhead*) in a fourth patient.

fungal cultures commonly fail to have fungal growth,[15] no definitive speciation could be determined in 8 patients (19%). The overall mortality in the AIFR group was significantly higher than that in the control group (52% versus 21%, $\chi^2 = 8.845$, $P = .003$). The mortality related directly to AIFR was 17%.

AIFR correlated most strongly with disease involvement in the pterygopalatine fossa ($r = 0.64$), periantral fat ($r = 0.61$), nasolacrimal duct ($r = 0.52$), and the lacrimal sac ($r = 0.52$). When considered as binary variables (ie, absence [0]/presence [1–5]), these 4 variables displayed relatively high specificities (93%–100%) and sensitivities (50%–74%, Fig 1). A correlation of note is that sphenopalatine foramen involvement was present in 72% of patients positive for AIFR with pterygopalatine fossa involvement.

Thirteen variables had 100% specificity for AIFR, but only 5 of these had a sensitivity of >30% (nasolacrimal duct, lacrimal sac, septal ulceration, orbital involvement, and bone dehiscence; Figs 2 and 3). The remaining variables with 100% specificity represented late-stage disease findings (epidural, subdural, abscess, venous thrombosis, arterial thrombosis, cavernous sinus involvement, intraparenchymal extension, and horizontal palate involvement; Fig 4). Variables related to the degree of opacity had relatively poor sensitivity and specificity as binary variables.

AIFR specificity increased significantly as a function of the degree of opacity in 6 of the 8 measured regions (Fig 5)—that is, the number of AIFR-positive cases was proportionally greater with higher severity of mucosal disease in the anterior nasal cavity ($Z = -3.99$, $P < .001$), posterior nasal cavity ($Z = -4.51$, $P < .001$), nasopharynx ($Z = -2.72$, $P = .003$), sphenoid sinus ($Z = -2.89$, $P = .002$), anterior ethmoid air cells ($Z = -3.53$, $P < .001$), and posterior ethmoid air cells ($Z = -3.91$, $P < .001$). In particular, 93%–100% of the patients with ≥75% opacity (ordinal ranking, 3–5) in the nasal cavity or nasopharynx were positive for AIFR.

Laterality data were initially collected to determine whether a unilateral predominance existed. Unilateral AIFR was present in 78.6% of cases (33/42, $\chi^2 = 14.58$, $P < .001$) with strong predilection of the disease for the right side. Only the right side was affected in 69.7% of unilateral cases (23/33, $\chi^2 = 5.26$, $P = .022$). We did not find that laterality added additional predictive value to our models;

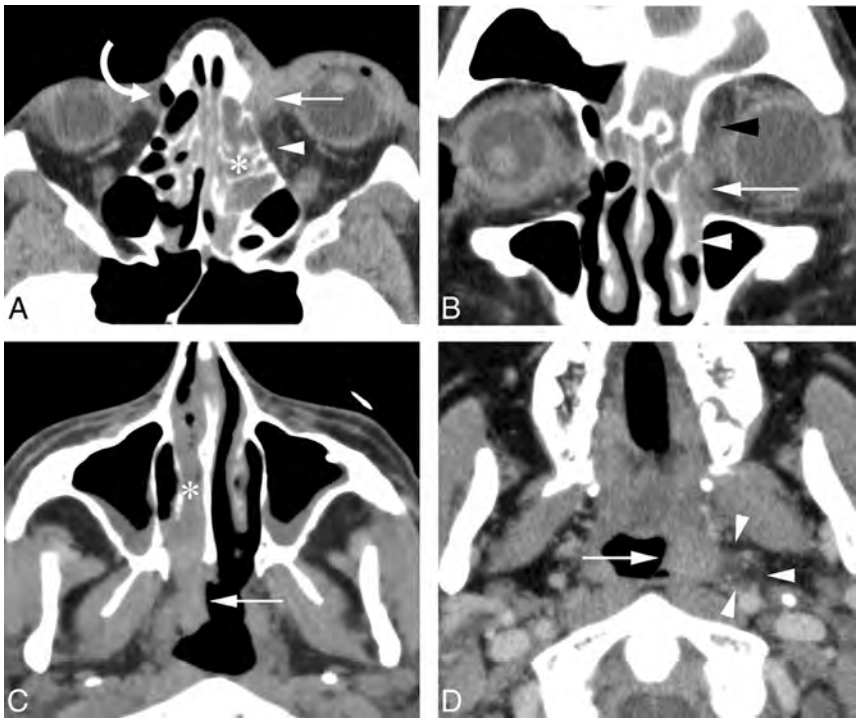

FIG 3. Illustration of less commonly described areas of AIFR, including the nasolacrimal duct, lacrimal sac, and nasopharynx. *A*, Contrast-enhanced axial CT image shows soft-tissue thickening and inflammatory stranding in the area of the left lacrimal sac (*white arrow*) and in the medial orbit (*white arrowhead*). The normal right nasolacrimal duct (*curved arrow*) is identified for comparison. Asymmetric unilateral mucosal disease is also seen in the left ethmoid air cells (*asterisk*). *B*, Coronal image again shows thickening and inflammatory change in the left lacrimal sac (*white arrow*) and medial orbit (*black arrowhead*). Similar inflammatory changes are seen in the left nasolacrimal duct (*white arrowhead*). *C*, Axial CT in a different patient with AIFR with marked asymmetric mucosal thickening of the right nasal cavity (*asterisk*) and right nasopharynx (*arrow*). *D*, Axial contrast-enhanced CT in a third patient with marked asymmetric mucosal thickening in the left nasopharynx (*arrow*) and subtle inflammatory stranding involving the left parapharyngeal fat (*arrowheads*).

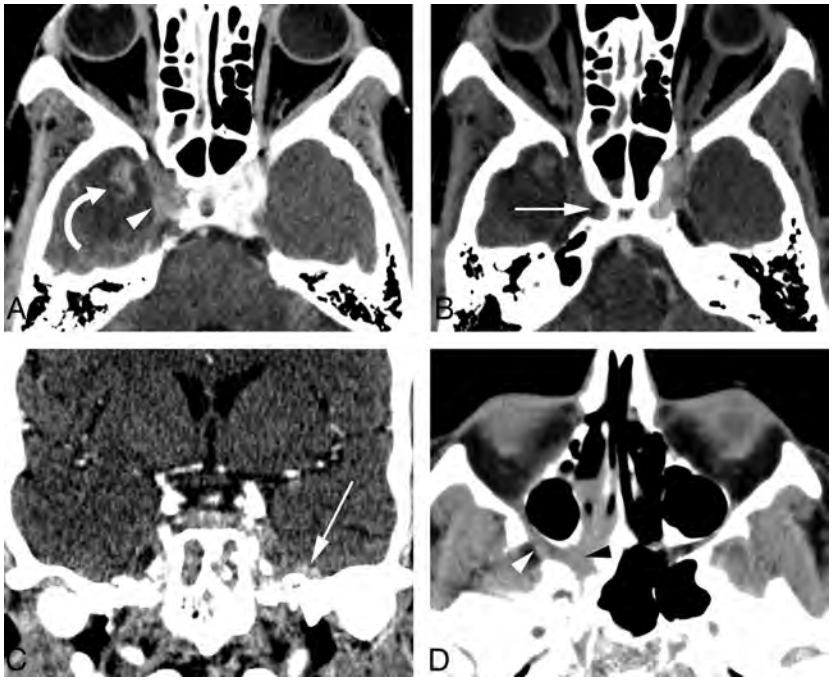

FIG 4. Examples of advanced manifestations of AIFR. *A* and *B*, Axial postcontrast CT images show a filling defect in the right cavernous sinus (*white arrowhead*) with adjacent parenchymal hyperattenuation or focal area of enhancement (*curved arrow*) most consistent with an acute hemorrhagic infarction in the right anterior temporal pole or parenchymal involvement by AIFR, respectively. There is also partial thrombosis of the right internal carotid artery (*white arrow*). *C*, Postcontrast coronal CT in a different patient shows subtle left epidural thickening along the floor of the middle cranial fossa (*white arrow*). *D*, Axial noncontrast CT in a third patient shows soft-tissue infiltration of the right sphenopalatine foramen and pterygopalatine fossa (*black arrowhead*), with extension into the right orbital apex (*white arrowhead*).

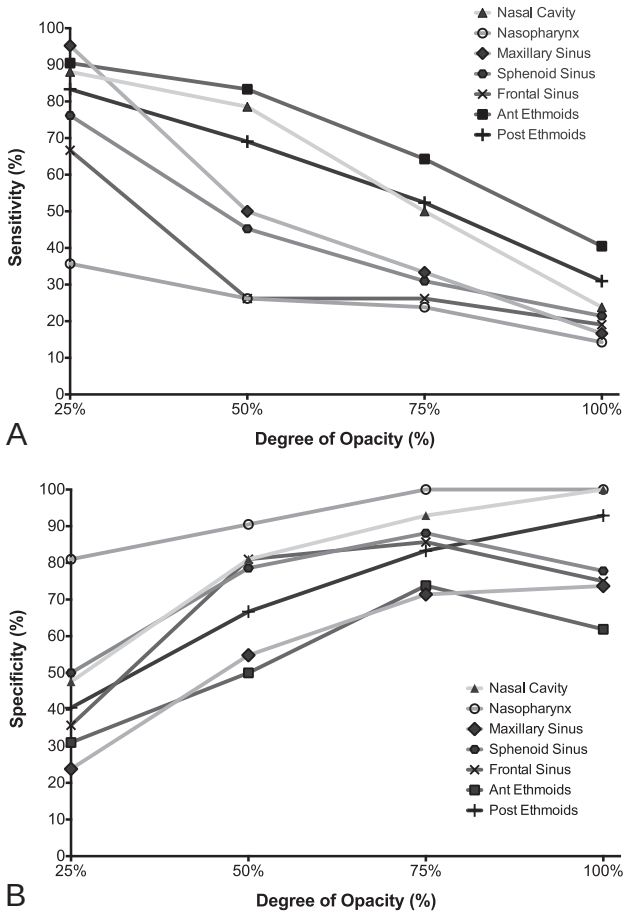

FIG 5. Correlation of the degree of opacity in the nasal cavity and paranasal regions with specificity (*A*) and sensitivity (*B*). Increasing opacity, particularly in the nasal cavity, nasopharynx, and posterior ethmoid air cells, has a strong correlation with specificity for AIFR. A decrease in sensitivity is also evident as the degree of opacity increases.

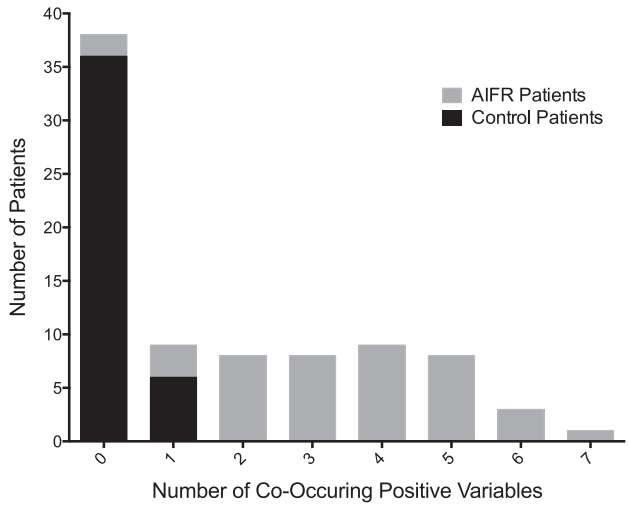

FIG 6. Illustration of the number of co-occurring positive variables (7-variable model) in patients with AIFR versus controls. The graph illustrates that most patients with AIFR have >1 positive area of involvement in the 7-variable model.

therefore, laterality data were consolidated for further analysis using the highest unilateral score.

We balanced statistical rigor of multivariate stepwise regression (minimizing Akaike Information Criterion) with the clinical reality of maximizing positive predictive value (PPV) and negative predictive value (NPV) to generate a 7-variable diagnostic model to predict AIFR (On-line Table). The top 4 variables in the model (periantral fat, pterygopalatine fossa, nasolacrimal duct, and lacrimal sac) were the most correlated with AIFR. These variables highly intercorrelated themselves and were present in most or all of the numerous statistical models generated during this evaluation. With respect to the 7-variable model, the presence of any single positive variable has an 87% PPV, 95% NPV, 95% sensitivity, and 86% specificity. Moreover, a positive outcome in any 2 variables predicted AIFR with 100% specificity, 100% PPV, and 88.1% sensitivity. Our results show that ≥2 of the 7 model variables were positive in 88% (37 of 42) of the patients with AIFR (Fig 6).

DISCUSSION

We present a simple-yet-accurate CT-based clinical model derived from a large single-institution study that can exclude or diagnose AIFR with a higher degree of confidence than suggested previously.[8,9] A key attribute of this model is that within our clinical dataset, the involvement of any 2 of the 7 variables predicted AIFR with 100% specificity. The predictive power is also enhanced because 88% of patients with AIFR presented with findings captured by ≥2 variables. This model has variables that have been previously ascribed to characteristic imaging findings for AIFR[1,8,10,11] (periantral fat, bone dehiscence, orbital invasion, pterygopalatine fossa), as well as uncommonly described markers for AIFR such as nasolacrimal duct and lacrimal sac involvement.[16,17]

The power of the clinical model resides in the aggregate evaluation of all 7 variables because no individual variable had both high PPV and high NPV. For example, disease involvement in the periantral fat—an early indicator of AIFR[10]—was the best individual predictor of AIFR in our study but, by itself, had a sensitivity of only 74%. Bone dehiscence proved to be a specific marker for AIFR (100% specificity) but has low sensitivity (35%), which agrees with previously reported data.[8] Because the fungi tend to spread through vascular channels or along nerves,[18-21] extension outside of the sinus frequently occurs in the absence of bone destruction. Therefore, bone destruction alone is not a useful exclusionary criterion. This phenomenon likely explains the high correlation seen with involvement of the sphenopalatine foramen and ipsilateral pterygopalatine fossa, suggesting extension from the nasal cavity along either posterior superior nasal nerves or the sphenopalatine artery. This is in contradistinction to isolated involvement of the posterior periantral fat, which is more likely related to direct extension from the maxillary sinus along vascular channels.

Our study agrees with previous literature implicating severe nasal cavity mucosal thickening on CT as a common finding in patients with AIFR.[8] This is noteworthy because of the relatively good prognosis when AIFR is limited to the nasal cavity.[2] Unfortunately, unilateral nasal cavity disease has a low specificity though it is one of the more frequent findings in AIFR (78.6% of patients in our study had unilateral predominant disease). Consequently, unilateral nasal cavity disease may not be a reliable individual predictor of AIFR. The correlation of AIFR with the

severity of mucosal thickening was also present in areas outside the nasal cavity. We found a significant relationship between the incidence of AIFR and the degree of mucosal disease in 6 of 8 measured regions; however, incorporating such dependency on variable progression of mucosal disease proved difficult (and unnecessary). We opted for a clinical model that offered high PPV and high NPV, independent of opacity assignments for simpler clinical applicability.

To our knowledge, the mortality rate of our patient group (17%) is one of the lowest published for a study of this scale, which suggests that these patients were diagnosed at a relatively favorable stage of disease. However, we were unable to identify any specific indictors of prognosis from our data—that is, in no region was disease involvement indicative of patient mortality. This was somewhat surprising because findings classically considered early-stage and late-stage factors were both present in our patients. If these monikers are accurate, patients presenting with so-called late-stage symptoms would be expected to have relatively high mortality, but this was not the case. For example, none of the 7 patients who died of AIFR presented with bone dehiscence. This outcome suggests caution in predicting a time course of disease or prognosis based on findings previously considered late-stage findings.

Our results show that CT is an effective screening tool for AIFR. Existing literature directly comparing MR imaging and CT found relatively higher sensitivity and PPV for AIFR by using MR imaging. This finding led to the recommendation that CT be considered a second-line technique.[9] While our study populations were different, our CT-based predictive model nevertheless demonstrated higher sensitivity (95% versus 86%), specificity (86% versus 75%), and NPV (95% versus 60%) than these previously published MR imaging data.[9] Our PPV estimates were similar (87% versus 92%). Moreover, our predictive model even produces higher sensitivity, specificity, and NPV than previously reported with CT.[8,9] The NPV is of particular importance in screening studies because low NPV results in erroneously excluding a patient positive for AIFR. Thus, on the basis of our results, CT with application of our predictive model should be considered a primary technique for evaluating AIFR.

Several limitations in our study are noteworthy. First, the rarity of AIFR necessitated a retrospective study design to capture a large number of cases. Readers were blinded to all clinical data to minimize bias, but that is a concern in retrospective designs. Second, some selection bias is inherent because the control group all progressed to endoscopy or surgery, suggesting higher clinical suspicion of sinus disease. This bias would likely lead to underestimation of the NPV and overestimation of PPV. Third, we purposely selected a patient control group with predisposing conditions to AIFR so that our clinical model would be applicable to the interpreting radiologist evaluating possible AIFR among an at-risk patient population in a real-world clinical environment. Consequently, some caution is warranted in extrapolating our results to other patient groups in which AIFR is not the clinical concern.

CONCLUSIONS

We propose a CT-based model to help exclude or diagnose AIFR with a higher degree of confidence than suggested previously.[9] Application of this proposed 7-variable model may improve evaluation of potential AIFR in an at-risk population and serve as the basis for a subsequent prospective study.

REFERENCES

1. Aribandi M, McCoy VA, Bazan C 3rd. **Imaging features of invasive and noninvasive fungal sinusitis: a review.** *Radiographics* 2007;27:1283–96
2. Gillespie MB, O'Malley BW Jr, Francis HW. **An approach to fulminant invasive fungal rhinosinusitis in the immunocompromised host.** *Arch Otolaryngol Head Neck Surg* 1998;124:520–26
3. Parikh SL, Venkatraman G, DelGaudio JM. **Invasive fungal sinusitis: a 15-year review from a single institution.** *Am J Rhinol* 2004;18:75–81
4. Chakrabarti A, Denning DW, Ferguson BJ, et al. **Fungal rhinosinusitis: a categorization and definitional schema addressing current controversies.** *Laryngoscope* 2009;119:1809–18
5. Kasapoglu F, Coskun H, Ozmen OA, et al. **Acute invasive fungal rhinosinusitis: evaluation of 26 patients treated with endonasal or open surgical procedures.** *Otolaryngol Head Neck Surg* 2010;143:614–20
6. Saghrouni F, Ben Youssef Y, Gheith S, et al. **Twenty-nine cases of invasive aspergillosis in neutropenic patients.** *Med Mal Infect* 2011;41:657–62
7. Turner JH, Soudry E, Nayak JV, et al. **Survival outcomes in acute invasive fungal sinusitis: a systematic review and quantitative synthesis of published evidence.** *Laryngoscope* 2013;123:1112–18
8. DelGaudio JM, Swain RE Jr, Kingdom TT, et al. **Computed tomographic findings in patients with invasive fungal sinusitis.** *Arch Otolaryngol Head Neck Surg* 2003;129:236–40
9. Groppo ER, El-Sayed IH, Aiken AH, et al. **Computed tomography and magnetic resonance imaging characteristics of acute invasive fungal sinusitis.** *Arch Otolaryngol Head Neck Surg* 2011;137:1005–10
10. Silverman CS, Mancuso AA. **Periantral soft-tissue infiltration and its relevance to the early detection of invasive fungal sinusitis: CT and MR findings.** *AJNR Am J Neuroradiol* 1998;19:321–25
11. Gamba JL, Woodruff WW, Djang WT, et al. **Craniofacial mucormycosis: assessment with CT.** *Radiology* 1986;160:207–12
12. Mossa-Basha M, Ilica AT, Maluf F, et al. **The many faces of fungal disease of the paranasal sinuses: CT and MRI findings.** *Diagn Interv Radiol* 2013;19:195–200
13. Centeno RS, Bentson JR, Mancuso AA. **CT scanning in rhinocerebral mucormycosis and aspergillosis.** *Radiology* 1981;140:383–89
14. De Pauw B, Walsh TJ, Donnelly JP, et al. **Revised definitions of invasive fungal disease from the European Organization for Research and Treatment of Cancer/Invasive Fungal Infections Cooperative Group and the National Institute of Allergy and Infectious Diseases Mycoses Study Group (EORTC/MSG) Consensus Group.** *Clin Infect Dis* 2008;46:1813–21
15. Chen CY, Sheng WH, Cheng A, et al. **Invasive fungal sinusitis in patients with hematological malignancy: 15 years' experience in a single university hospital in Taiwan.** *BMC Infect Dis* 2011;11:250
16. Halawa A, Yacoub G, Al Hassan M, et al. **Dacryocystitis: an unusual form of Mucorales infection.** *J Ky Med Assoc* 2008;106:520–24
17. Kapur R, Aakalu VK, August CZ, et al. **Mucormycosis infection of the lacrimal sac.** *Ophthal Plast Reconstr Surg* 2009;25:494–96
18. Margo CE, Linden C, Strickland-Marmol LB, et al. **Rhinocerebral mucormycosis with perineural spread.** *Ophthal Plast Reconstr Surg* 2007;23:326–27
19. McLean FM, Ginsberg LE, Stanton CA. **Perineural spread of rhinocerebral mucormycosis.** *AJNR Am J Neuroradiol* 1996;17:114–16
20. Orguc S, Yuceturk AV, Demir MA, et al. **Rhinocerebral mucormycosis: perineural spread via the trigeminal nerve.** *J Clin Neurosci* 2005;12:484–86
21. Frater JL, Hall GS, Procop GW. **Histologic features of zygomycosis: emphasis on perineural invasion and fungal morphology.** *Arch Pathol Lab Med* 2001;125:375–78

Hyperintense Optic Nerve due to Diffusion Restriction: Diffusion-Weighted Imaging in Traumatic Optic Neuropathy

U.K. Bodanapally, K. Shanmuganathan, R.K. Shin, D. Dreizin, L. Katzman, R.P. Reddy, and D. Mascarenhas

ABSTRACT

BACKGROUND AND PURPOSE: Abnormal signal intensity of the optic nerve due to diffusion restriction may be seen in traumatic optic neuropathy. In addition to evaluating optic nerve hyperintensity on diffusion-weighted imaging, we compared the group differences of ADC values between the injured and uninjured contralateral nerve and identified the relation between measured ADC values and admission visual acuity.

MATERIALS AND METHODS: We retrospectively evaluated 29 patients with traumatic optic neuropathy who underwent MR imaging with DWI. Uninjured contralateral optic nerves were used as controls. Two attending radiologists, blinded to the side of injury, independently reviewed the DWI for the presence of signal-intensity abnormality and obtained ADC values after manually selecting the ROI.

RESULTS: Hyperintensity of the optic nerve was demonstrated in 8 of the 29 patients, with a sensitivity of 27.6% (95% CI, 12.8–47.2) and a specificity of 100% (95% CI, 87.9–100). ADC values were obtained in 25 patients. The mean ADC in the posterior segment of the injured nerve was significantly lower than that in the contralateral uninjured nerve (Welch ANOVA, $F = 9.7$, $P = .003$). There was a moderate-to-strong correlation between low ADC values and poor visual acuity in 10 patients in whom visual acuity could be obtained at admission ($R = 0.7$, $P = .02$). Patients with optic nerve hyperintensity presented with worse visual acuity.

CONCLUSIONS: Hyperintensity of the optic nerve due to diffusion restriction can serve as a specific imaging marker of traumatic optic neuropathy. When paired with reduced ADC values, this finding may be an important surrogate for visual acuity.

ABBREVIATIONS: ON = optic nerve; Q = quartile; TON = traumatic optic neuropathy; VA = visual acuity

Traumatic optic neuropathy (TON) is an acute injury of the optic nerve (ON), typically presenting with severe impairment of visual function. TON is often classified on the basis of the location of the injury. Anterior ON injury is usually associated with ON head avulsion and disruption of circulation at the ON head. These patients present with intraocular hemorrhage and disruption of anatomy at the ON head on funduscopy. Posterior TON involves the nerve at a site proximal to where the ophthalmic artery enters the ON.[1] Clinical diagnosis of posterior TON is based on the presence of a relative afferent pupillary defect, decreased visual acuity (VA), normal funduscopic examination findings, and no apparent intraocular pathology.[2-4] The focus of this study was limited to posterior TON. Contusion, necrosis, concussion, hemorrhage, nerve fiber tears, and infarction due to vascular thrombosis or spasm have all been implicated as potential mechanisms of TON.[5,6] Specific causes include motor vehicle collisions, falls, assaults, blunt force effects of penetrating trauma, and surgical mishaps in and around the optic nerve, with a reported high prevalence among young men.[7]

The architecture of the orbit facilitates transfer of impact forces from facial trauma to the region of the optic canal, where the nerve is vulnerable to injury due to the shearing effect between its fixed and mobile portions.[7-9] The concept of primary and secondary injury in TON has been proposed by Walsh.[10] Primary injury results from immediate shearing of the retinal ganglion cell axons of the nerve. Secondary injury occurs from a complex biochemical cascade of events that follows the primary injury, resulting in edema of the ON within the inflexible optic canal.[11] Edema of the nerve in the optic canal produces a compartment syndrome, resulting in nerve ischemia due to compression of the pial vascular plexus.[12,13]

Received November 3, 2014; accepted after revision December 23.

From the Departments of Radiology, R Adams Cowley Shock Trauma Center (U.K.B., K.S., D.D.) and Ophthalmology and Visual Sciences (R.K.S., L.K.), University of Maryland Medical Center, Baltimore, Maryland; Albert Einstein College of Medicine of Yeshiva University (R.P.R.), Bronx, New York; and University of Maryland School of Medicine (D.M.), Baltimore, Maryland.

Please address correspondence to Uttam K. Bodanapally, MBBS, 22 S Greene St, Department of Radiology, University of Maryland Medical Center, Baltimore, MD 21201; e-mail: ubodanapally@umm.edu

http://dx.doi.org/10.3174/ajnr.A4290

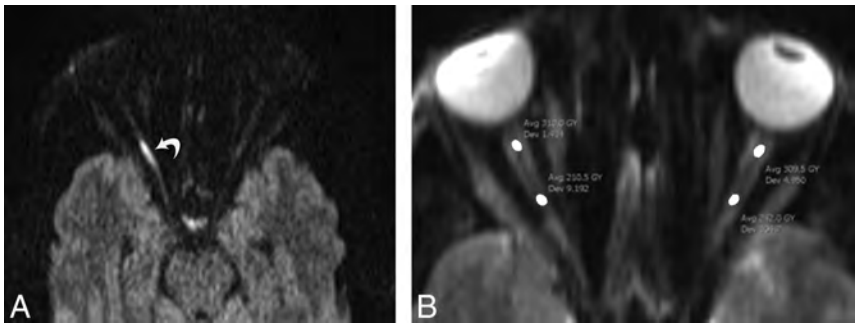

FIG 1. A 37-year-old man with right-sided TON following a motor vehicle collision. Axial diffusion-weighted image (*A*) shows hyperintensity of the posterior segment of the optic nerve (*curved arrow*) due to restricted diffusion. *B*, Axial DWI ($b=0$) of the same patient shows ROI placement on the anterior and posterior segments of intraorbital optic nerve.

Conventional MR imaging findings are normal in most patients with TON.[3,5] An earlier study with DTI in TON showed decreased axial diffusion and ADC values in the posterior segment of the injured ON.[3] In this retrospective study, we aimed to determine the ability of abnormal signal intensity of the ON due to diffusion restriction on DWI to diagnose TON, compare the group differences of ADC values between the injured and uninjured contralateral nerves, and identify the relation between the measured ADC values and admission VA.

MATERIALS AND METHODS

The study was compliant with the Health Insurance Portability and Accountability Act, and permission was obtained from our institutional review board. The study was conducted at a level I trauma center. The inclusion criteria for this retrospective study were the following: 1) history of blunt craniofacial trauma between January 2004 and December 2013, 2) acquisition of DWI as part of the MR imaging examination of the brain or orbits (≤15 days after trauma), 3) 18 years of age or older, and 4) a clinically confirmed diagnosis of TON on formal ophthalmology consultation. Exclusion criteria were the following: 1) TON caused by blunt force or blast effects of penetrating trauma, and 2) abnormal funduscopy findings or traumatic structural intraocular pathology on clinical examination. During the study period, MR imaging was not routinely performed on patients with TON. MR imaging of the brain or orbits was performed at the discretion of the clinicians.

At the study institute, ophthalmology is consulted on all patients with orbital or periorbital soft-tissue trauma and craniofacial fractures, to detect injuries involving the visual system. All patients referred to ophthalmology are evaluated while in the trauma resuscitation unit. A clinical diagnosis of TON is made in the presence of decreased VA, relative afferent pupillary defect, and normal funduscopic examination findings. Testing for VA or funduscopy is usually not possible in patients who are unconscious due to sedation, mechanical ventilation, or associated head injuries. In such patients, a probable diagnosis of TON is made on the basis of the presence of a relative afferent pupillary defect, and the diagnosis is confirmed by re-evaluating the patients after they regain consciousness or after extubation.

MR Imaging Protocol and Image Analysis

All imaging was performed on a 1.5T Avanto scanner (Siemens, Erlangen, Germany) with parallel imaging capacity. Twenty patients underwent DWI as part of MR imaging of the brain; and in the remaining 9 patients, DWI was part of orbital MR imaging. According to our institutional protocol, DWI is performed at a 5-mm section thickness for both orbital and brain imaging. In all patients, DWI was obtained in the axial plane by using a dual spin-echo echo-planar imaging method with diffusion-weighting in 3 orthogonal directions with *b*-values of 0, 500, 1000 s/mm^2. The TE for the DWI was 86 ms with a TR of 5400 ms. A section thickness of 5 mm and an FOV of 220 × 220 mm at an acquisition matrix of 134 × 192 pixels were used.

Image Analysis

The DWI was evaluated on the PACS of our institution by 2 fellowship-trained and board-certified trauma radiologists (U.K.B. and D.D.) with 8 and 3 years of experience, respectively. Images were first evaluated qualitatively and then quantitatively. For qualitative analysis, the reviewers were blinded to the side of injury and individually evaluated the ONs for bilateral or unilateral signal intensity changes at $b=1000$. The reviewers classified the signal intensity into the following categories: higher, equal, or lower than the signal intensity of the contralateral ON and brain parenchyma. In the case of increased signal intensity, the extent of involvement (posterior and anterior segments) was documented (Figs 1 and 2). The usual 20- to 25-mm intraorbital ON was divided into anterior and posterior segments at approximately 10 mm behind the globe. The division was made to evaluate intersegmental differences in signal intensity and ADC values because the blood supply of the posterior segment is different from that of the anterior segment and the posterior segment has a greater propensity for injury.

For quantitative analysis, the ADCs within the ON were measured by ROI analysis. For placement of an ROI, both readers were instructed to include the posterior and anterior segments of the ON separately. Elliptic ROIs of approximately 7 mm^2 (range, 6–8 mm^2) were manually drawn over the long axis of the ON on the spin-echo echo-planar images ($b=0$) (Fig 1*B*) and then were transferred to the ADC maps. The anterior segment ROIs were drawn at a distance of approximately 3–4 mm from the globe, and the posterior ROI, at approximately 15–18 mm from the globe. Data from the posterior and anterior segments were analyzed separately. To avoid CSF partial volume artifacts, the ROI mostly included voxels at the nerve center. In addition, areas of susceptibility artifacts were excluded.

Statistical Analysis

The correlation between the ADC measurements of the 2 reviewers was performed by using a Pearson correlation coefficient. The sensitivity and specificity of signal-intensity abnormality of the

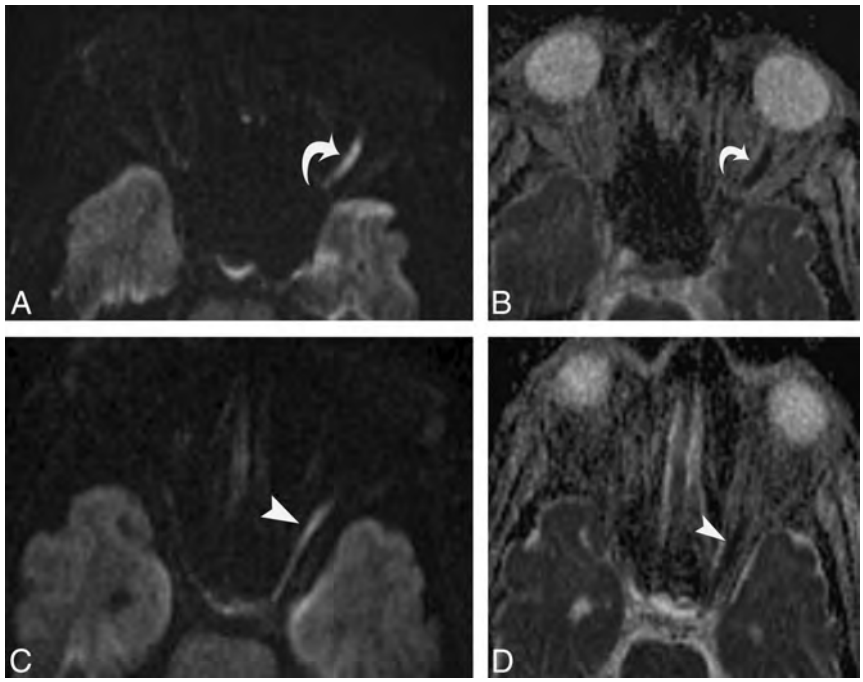

FIG 2. A 64-year-old man with left-sided TON following a fall. Axial diffusion-weighted image (*A*) and ADC map (*B*) show concomitant extension of hyperintensity into the anterior segment of optic nerve (*curved arrow*), with corresponding hypointense signal on the ADC map suggestive of restricted diffusion. Posterior segment involvement on the diffusion-weighted image (*C*) and ADC map (*D*).

ON on DWI was calculated by a contingency table. The mean ADC of both reviewers was used for statistical analysis. A 1-way ANOVA was used to compare the between-group differences of ADC values. After testing for homogeneous variance (Levene test), a post hoc analysis was performed by using the Welch and Wilcoxon tests. Receiver operating characteristic curve analysis was used to evaluate the usefulness of ADC measurements. Linear regression analysis was used to determine the relationship between admission VA and ADC values. For all analysis, a P value $< .05$ was considered statistically significant. Statistical analysis was performed by using JMP 11 software (SAS Institute, Cary, North Carolina).

VA was converted into a logarithm of the minimum angle of resolution units to provide a numeric scale for statistical analysis.

RESULTS

Demographics

A search of the trauma data base of the institution yielded 183 patients with a clinical diagnosis of TON. Twenty-nine patients (21 men, 8 women; mean age, 40.8 years; range, 18–69 years) of the total 183 were evaluated with DWI and were retrospectively recruited for the study. All patients had unilateral TON. The mechanism of injury in patients with TON was a motor vehicle collision in 15, assault in 6, a fall in 4, pedestrian struck in 3, and orbital surgery in 1. A single patient with iatrogenic TON was included in the study. The patient developed visual impairment after simple orbital floor fracture repair without documented perioperative hypotension or elevated intraorbital pressure, thus excluding the possibility of surgical posterior ischemic optic neuropathy and orbital compartment syndrome. On the basis of the information and the clinical findings, the patient was diagnosed with iatrogenic TON. There were 17 left-sided injuries and 12 right-sided ON injuries. The median length from the time of trauma to imaging was 7 days (Q_3–Q_1 = 9.5 days). Table 1 provides the data regarding the time from injury to MR imaging, VA, ON hyperintensity, and ADC values.

Qualitative Analysis

In 8 of the 29 patients with TON, the injured ON demonstrated restricted diffusion with hyperintense signal on DWI and corresponding hypointense signal on ADC maps. None of the contralateral uninjured nerves demonstrated abnormal signal. This restricted diffusion in ON constitutes a sensitivity of 27.6% (8/29) (95% CI, 12.8–47.2) and a specificity of 100% (29/29) (95% CI, 87.9–100). All 8 patients had hyperintense signal involving the posterior segment of the nerve with concomitant involvement of the anterior segment in 2 patients. There was perfect agreement between the 2 reviewers in the assessment of the signal intensity of the ONs.

Quantitative Analysis

The reviewers independently excluded 4 patients because of inaccurate ADC measurements due to susceptibility artifacts caused by the air-bone-tissue interface and/or partial volume effects, which affected the ROI placement over the ONs. The mean posterior segment ADC of the contralateral uninjured ON in the remaining 25 patients was 1.32×10^{-3} mm^2/s (standard error, 0.85×10^{-3} mm^2/s; 95% CI, 1.15×10^{-3} mm^2/s to 1.49×10^{-3} mm^2/s). The mean posterior segment ADC of the injured nerve was 0.94×10^{-3} mm^2/s (standard error, 0.85×10^{-3} mm^2/s; 95% CI, 0.77×10^{-3} mm^2/s to 1.11×10^{-3} mm^2/s) (Fig 3). The posterior segment ADC differed significantly between injured and uninjured nerves in Welch ANOVA analysis ($F = 9.7$, $P = .003$ and Wilcoxon $P = .015$). Receiver operating characteristic curve analysis determined a discrimination ability of 0.7 (area under the curve) between the injured and uninjured contralateral nerve with optimum sensitivity and specificity at a mean ADC value of 0.92×10^{-3} mm^2/s.

There was no statistical difference in the mean anterior segment ADC values between the injured and uninjured nerves ($P = 0.24$) (Table 2). In subsequent analysis, the patients were divided into 2 subgroups. Group 1 consisted of 14 patients with a time from injury to MR imaging examination of ≤7 days, and the remaining 11 patients constituted group 2 with a time from injury to MR imaging of >7 days. In group 1 patients, the mean posterior segment ADC of the injured ON was significantly reduced

Table 1: Results of the 29 cases with traumatic optic neuropathy, their respective time from injury to MRI, and visual acuity

Patient No.	Days between Injury and MRI	VA on Affected Side (logMAR)	Hyperintensity due to Diffusion Restriction	ADC (10^{-3} mm^2/s) in the Posterior Segment of the Injured ON
1	12	NA	−	NE
2	15	NA	−	NE
3	1	−0.7	−	NE
4	7	NA	−	NE
5	7	−4.7	+	0.3
6	15	NA	−	1.25
7	15	NA	−	1.4
8	9	−4.7	−	0.825
9	1	−1	−	1.5
10	2	−4.7	−	0.85
11	2	−0.48	−	1.25
12	12	NA	−	1.3
13	10	NA	−	1.6
14	7	NA	−	1.35
15	5	NA	−	1.35
16	8	−4.7	+	0.15
17	12	−1	−	0.92
18	11	NA	−	1.65
19	12	NA	+	0.75
20	1	−4.7	+	0.38
21	4	−4.7	+	0.05
22	1	NA	−	1.074
23	4	NA	−	1.15
24	3	NA	+	0.6
25	11	NA	−	1.15
26	10	NA	−	1.65
27	5	−4.7	+	0.15
28	1	NA	−	0.65
29	1	NA	+	0.285

Note:—logMAR indicates logarithm of the minimum angle of resolution; NA, not available; NE, not evaluated; +, present; −, absent.

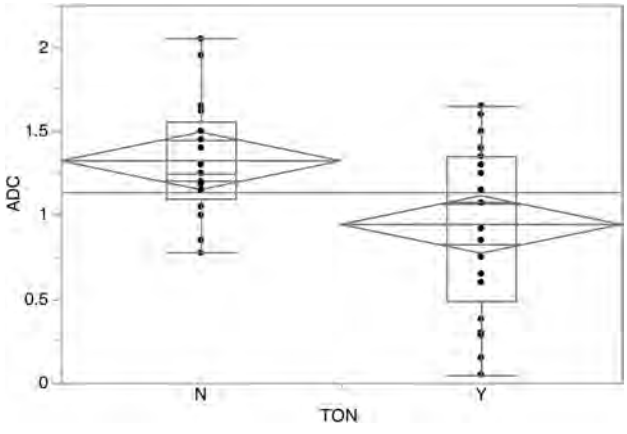

FIG 3. Graph comparing the ADC (10^{-3} mm^2/s) values and the clinical diagnosis of TON. Box-and-whisker plots with *lines* representing medians, interquartile ranges, and greatest and least values. Mean diamond plots with *horizontal lines* represent mean and upper and lower 95% confidence points for each group.

relative to the contralateral posterior ON ($P = .03$). The ADC reduction did not reach statistical significance in group 2 patients ($P = .17$). The interrater reliability in measuring the ADC of the ONs was very good, with a Pearson correlation coefficient of 0.87 (95% CI, 0.79–0.92).

Admission VA was available in 10 of the 29 patients. Admission VA could not be obtained in 19 patients due to associated injuries for which patients were under sedation, on mechanical ventilation, or under the influence of other mind-altering drugs. There was a moderate-to-strong correlation between low ADC values and poor VA in the 10 patients analyzed (ie, a lower logarithm of the minimum angle of resolution) (Pearson $r = 0.7$, $P = .02$; Spearman $\rho = 0.66$, $P = .03$). In patients with ON hyperintensity on qualitative analysis, 5 of the 8 patients had available VA. All 5 patients presented with no light perception. The median logarithm of the minimum angle of resolution in patients with ON hyperintensity was −4.7 (no light perception) (Q_1–$Q_3 = 0$); and in those without hyperintensity, the logarithm of the minimum angle of resolution was −1 (20/200) (Q_1–$Q_3 = -4$, $P = .012$).

DISCUSSION

The results of our study indicate that hyperintensity of the ON predominantly affecting the posterior segment of the intraorbital ON is associated with a clinical diagnosis of TON in the appropriate clinical setting. Although a decreased ADC value of the injured nerve and alterations in other DTI parameters have been previously described,[3] a qualitative visual assessment of ON hyperintensity on DWI can provide a helpful clinical indicator of TON. The sensitivity of this sign was 27.6% (95% CI, 12.8%–47.2%) and the specificity was 100% (95% CI, 87.9%–100%). Hence, the presence of hyperintensity is helpful in making a diagnosis of TON, but its absence should not be interpreted as an absence of TON.

Our results also showed a statistically significant difference between the mean posterior segment ADC values of the injured-versus-uninjured nerves, which can help in the discrimination of TON. In the limited number of patients with TON with available VA, there was a correlation between low ADC values and poor VA, and those with ON hyperintensity due to diffusion restriction had the worst VA (ie, no light perception at presentation). The correlation among ON hyperintensity, low ADC values, and poor VA at admission may help clinicians predict the likelihood of visual recovery in patients with severe trauma, especially in those in whom VA could not be obtained due to various factors, because the initial VA is the strongest predictor of visual recovery.[14-16] This information has the potential to help prioritize therapeutic interventions should new therapies become available.

Acute ischemia and contusions in the brain parenchyma and spinal cord present as hyperintense signal on DWI at measurements with large *b*-values, and the calculated ADC map shows decreased diffusivity.[17,18] Although contusion-related necrosis and ischemia of the ON are implicated in TON at postmortem examination, the signal-intensity changes in DWI corresponding to these histologic findings have not been evaluated in patients with TON, to our knowledge. The hyperintensity of the injured ON seen in our patients, most of whom have involvement of the posterior segment, supports the hypothesis that the nerve segment that is most vulnerable to primary injury is at the level of the optic canal and that secondary injury from compartment syndrome occurs in the optic canal, causing nerve ischemia. The 2 cases with concomitant varying levels of extension of hyperintensity into the anterior segment may be explained by

Table 2: Mean and median ADC values on injured and uninjured contralateral optic nerves in patients with traumatic optic neuropathy

ON Segment	Injured ON		Contralateral ON		*P* Value (between Injured and Contralateral Side)	
	Mean ADC, SE (10^{-3} mm^2/s)	Median ADC, Q_3–Q_1 (10^{-3} mm^2/s)	Mean ADC, SE (10^{-3} mm^2/s)	Median ADC, Q_3–Q_1 (10^{-3} mm^2/s)	Welch Test	Wilcoxon Test
Posterior segment	0.94 (0.85)[a]	1.07 (0.86)[a]	1.32 (0.85)[a]	1.25 (0.46)[a]	.0033[a]	.015[a]
Anterior segment	1.37 (0.73)	1.46 (0.36)	1.49 (0.73)	1.42 (0.47)	.24	.49

Note:—SE indicates standard error.
[a] Statistically significant differences ($P < .05$).

spasm or thrombosis of the axial centrifugal vascular system formed by intraneural branches of the central retinal artery. Subanalysis of patients based on the time from injury to MR imaging examination showed a statistically significant decrease in the posterior segment ADC when the imaging was performed within 7 days after injury. The reduction in ADC did not reach statistical significance when the imaging was performed between 7 and 15 days after trauma, however. This phenomenon is most likely due to ADC normalization, though the time course of the normalization process is not known for the optic nerve in the setting of trauma.

There is limited literature regarding the utility of functional MR imaging of ON injury. An earlier study by Bodanapally et al[3] evaluated the role of DTI in 12 patients with TON and reported a lower axial diffusivity in both of the segments of the ON and a decrease in ADC in the posterior segment. The decrease in ADC, however, was not statistically significant in relation to the contralateral uninjured nerve.[3] The significant decrease in ADC values in our current study can be due to a larger study cohort, difference in the technique of ADC measurements, and/or the inclusion of patients with hyperintense ON due to diffusion restriction. In contrast to the above findings, Yang et al[19] evaluated 6 patients with DTI (mean time from injury to imaging, 5.2 days) and showed an increase in mean ADC values. The authors ascribed this increase to the ischemic demyelination or necrosis of the nerve fiber bundles. Contrary to their explanation, we suggest that the acute injury of the optic nerve is manifested by a decrease in the ADC values similar to the reduced ADC values in acute cerebral and spinal cord injuries.

TON is a clinical diagnosis, but a clinical examination may not be possible in patients with severe polytrauma due to sedation, mechanical ventilation, or the influence of other mind-altering drugs. Even testing for the presence of a relative afferent pupillary defect may not be possible or reliable in some patients due to nonreactive pupils frequently encountered in patients with associated traumatic brain injury, coma, or raised intracranial pressures. In this background, our results may have clinical implications when radiologists who evaluate DWI sequences while reviewing brain MR imaging studies also evaluate the optic nerve for signal abnormality and, if it is present, alert the referring clinicians to the possibility of TON.

Our study has several limitations. First, it has a retrospective design. Second, the small study population may limit the generalizability of the findings. Third, inadequate spatial sampling due to a section thickness of 5 mm may have underestimated the incidence of diffusion restriction by precluding the identification of hyperintense signal in some patients, potentially lowering the sensitivity. DWI was performed at a 5-mm section thickness in our patient cohort. Thin sections (eg, 3 mm) may improve the sensitivity. ADC measurement of the ON is challenging due to the small diameter of the ON because there is the potential of partial volume averaging with surrounding CSF, fat, and osseous structures. Finally, correlations between low ADC values and poor VA should be interpreted with caution because our results were based on patients with varying times from injury to MR imaging examination, which would influence the measured ADC values due to the ADC normalization process. However, the limitations should not negate the conclusion that ON hyperintensity due to diffusion restriction on DWI was seen in approximately one-fourth of our patients with TON and is usually associated with the worst VA (no light perception) at presentation.

CONCLUSIONS

Hyperintensity of the ON due to diffusion restriction after trauma is an imaging marker of TON, and when paired with reduced ADC values in the posterior segment of the ON, it may provide important information regarding VA at presentation and hence the future visual outcome.

Disclosures: Robert K. Shin—*UNRELATED*: *Consultancy*: Novartis; *Grants/Grants Pending*: Novartis,* Biogen Idec,* Teva,* *Comments*: clinical trials (principal investigator or subinvestigator); *Royalties*: Wolters Kluwer, *Comments*: coeditor of *Neurology for the Non-Neurologist*. *Money paid to the institution.

REFERENCES

1. Steinsapir KD, Goldberg RA. **Traumatic optic neuropathy: an evolving understanding.** *Am J Ophthalmol* 2011;151:928–33
2. Bodanapally UK, Van der Byl G, Shanmuganathan K, et al. **Traumatic optic neuropathy prediction after blunt facial trauma: derivation of a risk score based on facial CT findings at admission.** *Radiology* 2014;272:824–31
3. Bodanapally UK, Kathirkamanathan S, Geraymovych E, et al. **Diagnosis of traumatic optic neuropathy: application of diffusion tensor magnetic resonance imaging.** *J Neuroophthalmol* 2013;33:128–33
4. Lessell S. **Indirect optic nerve trauma.** *Arch Ophthalmol* 1989;107:382–86
5. Cockerham KP. **Traumatic optic neuropathy.** In: Lounsbury ED, Bellamy RF, Zajtchuk R, eds. *Textbook of Military Medicine: Ophthalmic Care of the Combat Casualty*. Washington, DC: Office of the Surgeon General at TMM publications; 2003:395–403
6. Crompton MR. **Visual lesions in closed head injury.** *Brain* 1970;93:785–92
7. Steinsapir KD, Goldberg RA. **Traumatic optic neuropathy: a critical update.** *Compr Ophthalmol Update* 2005;6:11–21
8. Anderson RL, Panje WR, Gross CE. **Optic nerve blindness following blunt forehead trauma.** *Ophthalmology* 1982;89:445–55
9. Seiff SR. **High dose corticosteroids for treatment of vision loss due to indirect injury to the optic nerve.** *Ophthalmic Surg* 1990;21:389–95

10. Walsh FB. **Pathological-clinical correlations: I. Indirect trauma to the optic nerves and chiasm. II. Certain cerebral involvements associated with defective blood supply.** *Invest Ophthalmol* 1966; 5:433–49
11. Steinsapir KD, Goldberg RA. **Traumatic optic neuropathy.** *Surv Ophthalmol* 1994;38:487–518
12. Walsh FB, Hoyt WF. *Clinical Neuro-ophthalmology*. 3rd ed. Baltimore: Williams & Wilkins; 1969:2380
13. Sarkies N. **Traumatic optic neuropathy.** *Eye* 2004;18:1122–25
14. Yu-Wai-Man P, Griffiths PG. **Steroids for traumatic optic neuropathy.** *Cochrane Database Syst Rev* 2013;6:CD006032
15. Wang BH, Robertson BC, Girotto JA, et al. **Traumatic optic neuropathy: a review of 61 patients.** *Plast Reconstr Surg* 2001;107: 1655–64
16. Levin LA, Beck RW, Joseph MP, et al. **The treatment of traumatic optic neuropathy: the International Optic Nerve Trauma Study.** *Ophthalmology* 1999;106:1268–77
17. Galloway NR, Tong KA, Ashwal S, et al. **Diffusion-weighted imaging improves outcome prediction in pediatric traumatic brain injury.** *J Neurotrauma* 2008;25:1153–62
18. Schaefer PW, Huisman TA, Sorensen AG, et al. **Diffusion-weighted MR imaging in closed head injury: high correlation with initial Glasgow coma scale score and score on modified Rankin scale at discharge.** *Radiology* 2004;233:58–66
19. Yang QT, Fan YP, Zou Y, et al. **Evaluation of traumatic optic neuropathy in patients with optic canal fracture using diffusion tensor magnetic resonance imaging: a preliminary report.** *ORL J Otorhinolaryngol Relat Spec* 2011;73:301–07

Injury to the Cerebellum in Term Asphyxiated Newborns Treated with Hypothermia

S. Kwan, E. Boudes, G. Gilbert, C. Saint-Martin, S. Albrecht, M. Shevell, and P. Wintermark

ABSTRACT

BACKGROUND AND PURPOSE: Until now, most studies of brain injury related to term neonatal encephalopathy have focused on the cerebrum and ignored the cerebellum. We sought to evaluate whether cerebellar injury occurs in term asphyxiated neonates.

MATERIALS AND METHODS: Asphyxiated neonates treated with hypothermia were enrolled prospectively. Severity of brain injury in the cerebrum was scored on each MR imaging obtained during the first month of life; cerebellar injury was recorded when mentioned in the imaging or autopsy report. In addition, for some of the neonates, the ADC and fractional anisotropy were measured in 4 regions of interest in the cerebellum.

RESULTS: One hundred seventy-two asphyxiated neonates met the criteria for hypothermia. Cerebellar injury was visible only on conventional imaging of 4% of the neonates for whom brain imaging was available, but it was reported in the autopsy report of 72% of the neonates who died. In addition, 41 of the asphyxiated neonates had a total of 84 ADC and fractional anisotropy maps. Neonates with brain injury described only in the cerebrum demonstrated ADC and fractional anisotropy changes similar to those of the neonates with brain injury in the cerebrum and cerebellum—increased ADC around day 10 of life and decreased fractional anisotropy on day 2–3 of life, around day 10 of life, and around 1 month of age.

CONCLUSIONS: The cerebellum may be injured in term neonates after birth asphyxia. These cerebellar injuries are only rarely visible on conventional imaging, but advanced neuroimaging techniques may help to identify them.

ABBREVIATION: FA = fractional anisotropy

Birth asphyxia and its resulting neonatal encephalopathy occur in approximately 2 per 1000 births in developed countries and are responsible for 23% of all neonatal deaths worldwide.[1-3] Children who survive birth asphyxia may develop severe neurodevelopmental complications, such as cerebral palsy, mental retardation, learning difficulties, and other cognitive deficits. Until now, therapeutic hypothermia to an esophageal temperature of 33.5°C initiated within the first 6 hours of life and continued for 72 hours has emerged as the only available safe treatment for possibly improving the long-term outcome of some of these asphyxiated neonates.[4-6]

Parents of these neonates are wondering increasingly about the long-term prognosis while their neonate is still hospitalized in the neonatal intensive care unit. In the past, the prognosis was based on clinical history, clinical examinations, and neurologic tools such as electroencephalography.[7] In the last few years, MR imaging has developed considerably, and conventional MR imaging sequences have become the standard for visualizing the presence and extent of brain injury after hypothermia treatment is completed.[8,9] However, newer advanced MR imaging modalities, such as DTI and subsequent apparent diffusion coefficient and fractional anisotropy (FA) maps, are becoming available tools for use with neonates and may permit an even better definition of brain injury and thus may provide a more accurate prognosis.[10,11]

Typical patterns of injury in term asphyxiated neonates are usually described in the cerebrum, including basal ganglia injury, watershed injury, and near-total injury. Until now, injury to the cerebellum has been reported only rarely after birth asphyxia in term neonates. Nevertheless, the few available imaging studies in

Received December 16, 2014; accepted after revision February 2, 2015.

From the Division of Newborn Medicine, Department of Pediatrics (S.K., E.B., P.W.), Division of Pediatric Radiology (C.S.-M.), Department of Pediatric Pathology (S.A.), and Division of Pediatric Neurology, Department of Pediatrics (M.S.), Montreal Children's Hospital, McGill University, Montreal, Quebec, Canada; and MR Clinical Science (G.G.), Philips Healthcare, Montreal, Quebec, Canada.

Please address correspondence to Pia Wintermark, MD, McGill University/Montreal Children's Hospital, Division of Newborn Medicine, 1001 boul Décarie, Site Glen, Block E, EM0.3244, Montréal, QC H4A 3J1, Canada; e-mail: pia.wintermark@bluemail.ch

Indicates open access to non-subscribers at www.ajnr.org

Indicates article with supplemental on-line table.

http://dx.doi.org/10.3174/ajnr.A4326

which the cerebellum was examined reported cerebellar injury in severe cases of neonatal encephalopathy.[12-15] Sargent et al[15] found cerebellar vermian atrophy on CT and MR imaging acquired from 12 neonates around 10–19 months of age with neonatal encephalopathy and who developed thalamic injury with or without cortical injury; however, they did not find any signs of cerebellar involvement on the imaging performed on these patients during the first 2 weeks of life. Le Strange et al[14] confirmed reduced cerebellar growth, including vermis growth, during the first year after birth in 6 neonates with neonatal encephalopathy who developed severe basal ganglia and thalamic injury. Connolly et al[13] found abnormally high T2 signal intensity in the anterior lobe of the vermis on MR images acquired at various ages (ie, from 1 to 24 years) from 18 neonates with neonatal encephalopathy who had developed near-total injury. As demonstrated in premature neonates,[16] studying the cerebellum in neonates is highly relevant and important, because injury to the cerebellum may create an additional burden on the future neurodevelopment of these neonates.

Thus, this present study was designed to report the incidence of cerebellar injury in asphyxiated neonates treated with hypothermia. We hypothesize that asphyxiated neonates are at risk of injury to the cerebellum and that cerebellar injury may be better identified in these neonates by using advanced neuroimaging techniques.

MATERIALS AND METHODS

Patients

We conducted a prospective cohort study of term asphyxiated neonates admitted to our neonatal intensive care unit between 2008 and 2014 and who met the criteria for induced hypothermia[4-6]: 1) gestational age of ≥36 weeks and birth weight of ≥1800 g; 2) evidence of fetal distress, such as history of an acute perinatal event, cord pH of ≤7.0, or base deficit of −16 mEq/L or lower; 3) evidence of neonatal distress, such as an Apgar score of ≤5 at 10 minutes, postnatal blood gas pH obtained within the first hour of life of ≤7.0, or a base deficit of −16 mEq/L or lower, or continued need for ventilation initiated at birth and continued for at least 10 minutes; and 4) evidence of moderate or severe encephalopathy obtained by physical examination and/or amplitude-integrated electroencephalography. Eligible patients received whole-body cooling to an esophageal temperature of 33.5°C, initiated by 6 hours of life and continued for 72 hours (unless contraindications developed), and then slow rewarming. The research protocol was approved by the Montreal Children's Hospital institutional review board, and informed parental consent was obtained in each case.

Brain MR Imaging

Per standard clinical protocol at our institution, a brain MR imaging scan was performed for all these neonates around day 10 of life. The MR imaging scans were performed by using a 3T clinical system (Achieva X; Philips Healthcare, Best, the Netherlands). Each MR imaging study included a 3D T1-weighted gradient-echo (TR, 24 ms; TE, 4.6 ms; matrix size, 180 × 180; FOV, 180 mm; flip angle, 30°; sagittal sections, 104; section thickness, 1.0 mm; and multiplanar reformations in axial and coronal planes), a TSE high-resolution T2-weighted (TR, 5000 ms; TE, 90 ms; TSE factor, 15; matrix size, 300 × 300; FOV, 150 mm; flip angle, 90°; axial sections, 27; section thickness, 3.0 mm), and a single-shot EPI DWI (TR, 2424.4 ms; TE, 69 ms; matrix size, 200 × 117; FOV, 240 mm; b-values, 600 and 1200 s/mm^2; flip angle, 90°; axial sections, 21; section thickness, 4.0 mm) sequence. These 3 sequences combined are referred to as "conventional MR imaging" throughout the remainder of this article, because they were the ones used by the neuroradiologists to interpret the MR imaging studies and compile their reports.

Pediatric neuroradiologists, who were blind to the clinical conditions of the infants, interpreted the MR imaging studies of the asphyxiated neonates treated with hypothermia. They reported the presence and extent of brain injury in the cerebrum according to a previously described MR imaging scoring system.[17] Cerebellar injury was recorded when mentioned in their report to evaluate the incidence of cerebellar injury in these neonates obtained by conventional imaging. The presented data were based only on the reports from the initial time of the study. We wanted to focus on the reading of the conventional sequences by the neuroradiologists to determine how often cerebellar injury was reported. We did not want to influence or bias them by asking them to specifically review the images for the cerebellum.

Autopsy

If the neonate did not survive, the autopsy result (when available) was also used to assess the presence and extent of brain injury in the cerebrum and the cerebellum. Cerebellar injury was recorded when mentioned in the report to evaluate the incidence of cerebellar injury in these neonates obtained by pathology.

ADC and FA Maps

In addition, since 2010, when possible (ie, when the parents consented for their neonate to have additional MR imaging, when the neonates were hemodynamically stable, and when a team of a nurse and a respiratory therapist was available to assist with the MR imaging), neonates were enrolled in an MR imaging research study, and MR imaging scans were performed on day 1 of life, day 2–3 of life, around day 10 of life, and/or around 1 month of life. These time points were chosen to ensure the absence of antenatal brain injury (day 1 of life), to assess early patterns of injury (day 2–3 of life), and to define the extent of definitive brain injuries (around day 10 of life and around 1 month of life). Patients who underwent hypothermia had therapy maintained during the MR imaging scan without any adverse events.[18] Any ventilation, pressor support, or sedation was maintained during the MR imaging process, and additional sedation was avoided.

A similar imaging protocol was used with these neonates at different time points. However, in addition to the above-mentioned sequences, a single-shot EPI DTI sequence with isotropic resolution (TR, 5937.8 ms; TE, 69 ms; matrix size, 100 × 100; FOV, 180 mm; sensitivity encoding factor, 2; directions, 32; b-value, 750 s/mm^2; axial sections, 46; section thickness, 1.8 mm) was included in the imaging protocol for the neonates enrolled in the MR imaging research study. In addition, the FSL Brain Extraction Tool (http://fsl.fmrib.ox.ac.uk/fsl/fslwiki/BET) was used to remove all extracerebral tissues (ie, eyes, meninges, skull, etc)

from the images.[19] Then, ADC and FA maps were generated for the whole brain by using the tools of the Diffusion Imaging in Python (DIPY) package (Sherbrooke Connectivity Imaging Lab, Sherbrooke University, Sherbrooke, Quebec, Canada).[20]

To assess whether subtle changes in the cerebellum were not recognized on conventional MR imaging of these patients, ADC and FA values were measured in 4 different regions of interest in the cerebellum (ie, the superior cerebellar peduncle, the dentate nucleus, the middle cerebellar peduncle, and the inferior cerebellar peduncle), as described in other study reports.[21-23] The regions of interest were always drawn by the same observer by using ImageJ (Image Processing and Analysis in Java; National Institutes of Health, Bethesda, Maryland).[24] Axial T2-weighted imaging was used in conjunction with the axial ADC and FA maps to accurately identify the regions of interest in the cerebellum. Measurements in the right and left sides in these different regions of interests were obtained and then averaged. The measurements were repeated twice for each region of interest to increase reproducibility.

Statistical Analysis

For the analysis of ADC and FA measurements, asphyxiated neonates treated with hypothermia were categorized into 1 of 3 subgroups on the basis of the presence or absence of brain injury reported from MR imaging and/or autopsy: 1) neonates who did not develop injury, 2) neonates who developed brain injury in the cerebrum, and 3) neonates who developed brain injury in the cerebrum and the cerebellum. Statistical analysis was performed according to the day of life on which MR imaging was performed. For each region of interest, ADC and FA values were compared between the groups by using Mann-Whitney *U* tests. A *P* value of $<.05$ was considered statistically significant. All statistical analyses were performed by using GraphPad Prism software (GraphPad Software, San Diego, California).

RESULTS

Description of the Patients

A total of 172 term asphyxiated neonates met the criteria for hypothermia (On-line Table).

Of the asphyxiated neonates, 83% (143 of 172) survived. Among these patients, only 3% (5 of 143) had a cerebellar injury described on their MR imaging report; these patients presented with an associated watershed injury or with a near-total injury. Injury to the cerebellum was described most often as an abnormal T1 signal in specific regions of the cerebellum (the dentate nuclei or surrounding cerebellar white matter) and/or, more rarely, as a restricted diffusion in the cerebellum. Among the remaining patients without a described cerebellar injury, 56% (77 of 138) did not develop brain injury in the cerebrum, and 44% (61 of 138) did develop brain injury in the cerebrum; 20% (12 of 61) developed basal ganglia injury, 44% (27 of 61) developed watershed injury, and 36% (22 of 61) developed near-total injury. It is notable that 2 neonates had small hematomas within the left cerebellar hemisphere, and 1 neonate had one within the right cerebellar hemisphere; several neonates presented with subdural hematomas in the posterior cerebellar hemisphere, but these hematomas did not exert any mass effect on the underlying cerebellum.

Seventeen percent (29 of 172) of the neonates died as a result of complications of birth asphyxia and neonatal encephalopathy. Among those who died, 48% (14 of 29) had an available autopsy report that described brain injury; 71% (10 of 14) presented with apoptosis clearly identified in the cerebellum at the time of autopsy, 21% (3 of 14) presented with acidophilic neurons in the cerebellum, and 7% (1 of 14) did not have any described injury in the cerebellum. Each patient who died and had an autopsy had brain injury in the cerebrum at the time of the autopsy. It is interesting to note that among the neonates who died and had an autopsy, 2 had brain MR imaging before death, but the presence of cerebellar injury was mentioned in only one of the neonate's MR imaging reports. With respect to this patient born after placental abruption (Fig 1), a restricted diffusion and an increased T1 signal were reported around the bilateral dentate nuclei of the cerebellum; the autopsy of this patient revealed numerous apoptotic neurons throughout the internal granular layer of the cerebellar cortex and a necrosis of the dentate nuclei and the Purkinje cells in the cerebellar cortex. Among the 52% (15 of 29) of neonates who died and did not have an autopsy, only 27% (4 of 15) had brain MR imaging performed, and the presence of cerebellar injury was recognized in only one of the MR imaging reports. In this patient, restricted diffusion was again noted on the ADC map around the bilateral dentate nuclei.

Among the 16 asphyxiated neonates with cerebellar injury reported from their MR imaging and/or autopsy, 3 were born after placental abruption, 1 was born after cord prolapse, 1 was born after placenta previa, 2 were born with tight nuchal cord, 6 presented profound fetal bradycardia of unclear origin, 1 presented poor variability, and 2 did not have a clear cause to explain their asphyxial event.

ADC and FA Maps

A total of 84 ADC and FA maps were obtained for 41 asphyxiated neonates treated with hypothermia, in whom a DTI sequence was performed in addition to the conventional sequences. Ten were obtained on day 1 of life, 22 on day 2–3 of life, 32 around day 10 of life (mean, day 10 of life; range, day 7–15 of life), and 20 around 1 month of life (mean, day 33 of life; range, day 29–42 of life).

ADC values (Fig 2) were significantly increased around day 10 of life in the superior cerebellar peduncle ($P = .0001$), the middle cerebellar peduncle ($P = .0004$), and the inferior cerebellar peduncle ($P = .006$) in neonates with brain injury of the cerebrum and cerebellum compared with those without brain injury; the ADC values in the dentate nucleus were not different around day 10 of life between these 2 groups of neonates. In addition, ADC values were not different between these 2 groups at the other time points except on day 1 of life for the middle cerebellar peduncle ($P = .003$), for which the ADC was significantly increased in the neonates with brain injury in the cerebrum and cerebellum. ADC values in the cerebellum were not different between neonates with a brain injury described only in the cerebrum and those without injury except around day 10 of life for the superior cerebellar peduncle ($P < .0001$), for which the ADC was significantly increased in the neonates with a brain injury described only in the cerebrum.

FA values (Fig 3) were significantly decreased around day 10 of

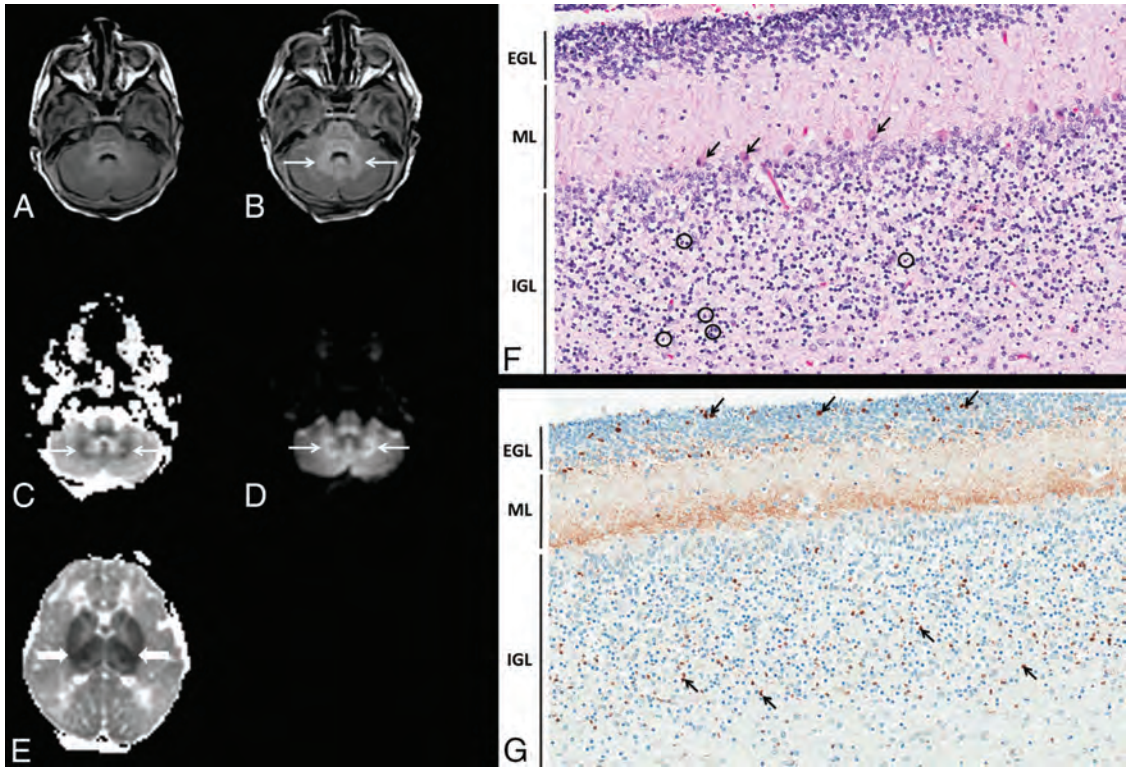

FIG 1. Term asphyxiated neonate treated with hypothermia who presented with cerebellar injury on MR imaging and histopathology. *A*, The cerebellum on day 1 of life (axial T1-weighted image shows a normal signal in the cerebellum). *B–D*, The cerebellum on day 2 of life. Axial T1-weighted image (*B*), ADC map (*C*), and diffusion-weighted image (*D*) show an abnormal signal (*thin arrows*) around the bilateral dentate nuclei. *E*, ADC map of the cerebrum on day 2 of life shows an associated marked basal ganglia injury (*thick arrows*). *F* and *G*, Histopathology of the cerebellum on day 3 of life (magnification ×20). Hematoxylin-eosin–stained section of the cerebellar cortex (*F*) shows the Purkinje cells (*arrows*) with shrunken hypereosinophilic cytoplasm and condensed nuclei, typical of hypoxic-ischemic necrosis ("red and dead" neurons). In addition, in the internal granular layer (IGL), many apoptotic internal granular neurons (*circles*) are present. *G*, Immunostaining of the cerebellar cortex for active caspase 3 (orange-brown staining), highlights the apoptotic internal granular neurons. In addition, the staining of the neuropil of the molecular layer (ML) is consistent with "synapoptosis." Also, apoptotic neuronal precursor cells (*arrows*) are present in the external granular layer (EGL), which occurs as part of the normal involution of this layer.

life in the superior cerebellar peduncle ($P = .007$), the middle cerebellar peduncle ($P < .0001$), and the inferior cerebellar peduncle ($P < .0001$) in neonates with brain injury of the cerebrum and cerebellum compared with those without brain injury; the FA values in the dentate nucleus were not different around day 10 of life between these 2 groups of neonates. Similarly, a decreased FA value also was observed in the 1 neonate with a brain injury of the cerebrum and cerebellum, which was scanned around 1 month of age. The same trend was already observed on day 2–3 of life in the middle cerebellar peduncle ($P < .0001$) and the inferior cerebellar peduncle ($P = .0004$) in the neonates with brain injury of the cerebrum and cerebellum compared with those without brain injury. It is interesting to note that the FA values significantly decreased around 1 month of life in the superior cerebellar peduncle ($P < .0001$), the middle cerebellar peduncle ($P < .0001$), and the inferior cerebellar peduncle ($P < .0001$) in the neonates with a brain injury described only in the cerebrum compared with those without brain injury; the FA values in the dentate nucleus were not different around 1 month of life between these 2 groups of neonates. The same trend was already observed on day 2–3 of life and around day 10 of life in the middle cerebellar peduncle ($P < .0001$ on day 2–3 of life and $P = .03$ around day 10 of life) and in the inferior cerebellar peduncle ($P = .07$ on day 2–3 of life and $P = .003$ around day 10 of life) in the neonates with brain injury of the cerebrum and cerebellum compared with those without brain injury.

DISCUSSION

The results of this study provide insight into cerebellum injury in asphyxiated neonates treated with hypothermia. Cerebellar injury was only rarely reported on conventional MR imaging. Only 6 asphyxiated neonates treated with hypothermia had a cerebellar injury described on their MR imaging report, which represents 4% of the asphyxiated neonates treated with hypothermia from the cohort with brain imaging data available, or 9% of the asphyxiated neonates treated with hypothermia who developed brain injury visible on brain imaging. In these 6 cases, the cerebellar injury was also always associated with an injury of the cerebrum. However, cerebellar injury was a common finding in the autopsies of the asphyxiated neonates treated with hypothermia who died (ie, it was clearly present in 72% of these neonates). The cerebellar injury was always associated with an injury of the cerebrum. Thus, the incidence of a neuroimaging-evident cerebellar injury in asphyxiated neonates treated with hypothermia widely contrasts with the incidence of pathologically evident cerebellar injury in these neonates, as already pointed out by others.[15] It is possible that the asphyxiated neonates who died were among the ones with

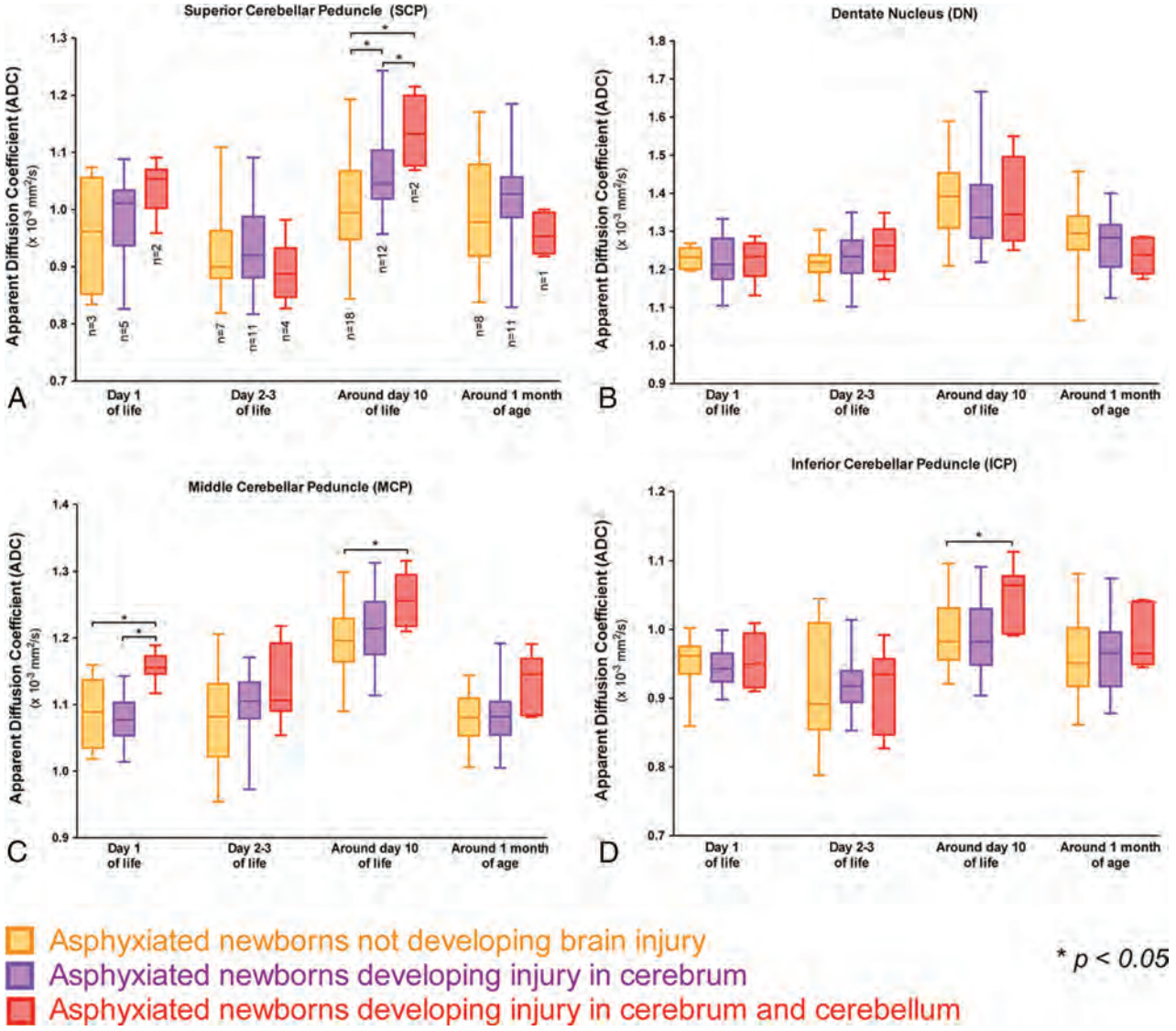

FIG 2. Comparison of ADC values in each region of interest in the cerebellum among the neonates who did not develop injury, neonates who developed brain injury in the cerebrum, and neonates who developed brain injury in the cerebrum and the cerebellum on day 1 of life, day 2–3 of life, around day 10 of life, and around day 30 of life. Each box and pair of whiskers indicate the median and the minimum and maximum ADC values, respectively. The different regions of interest are the superior cerebellar peduncle (*A*), the dentate nucleus (*B*), the middle cerebellar peduncle (*C*), and the inferior cerebellar peduncle (*D*).

the most severe brain injury. It is also possible that the neuroradiologists interpreting the conventional imaging concentrated their attention on the supratentorial injury and overlooked the cerebellar injury when reporting their results. However, it is also possible that cerebellar injuries are subtle on conventional imaging and hard to recognize[14,15] and that they are only clearly visible in asphyxiated neonates with severe brain injury.[13]

In the second part of this study, we used advanced neuroimaging techniques to measure ADC and FA in 4 specific regions of the cerebellum. Of the 149 asphyxiated neonates treated with hypothermia in our cohort, 41 (28% of the neonates with imaging available) had ADC and FA maps available for measurements. Neonates with brain injury of the cerebrum and cerebellum showed ADC and FA changes in some of the measured cerebellar structures, mainly an increased ADC around day 10 of life and a decreased FA on day 2–3 of life and around day 10 of life. It is interesting to note that neonates with brain injury described only in the cerebrum also demonstrated ADC and FA changes in the same cerebellar structures, again mainly an increased ADC around day 10 of life and a decreased FA on day 2–3 of life, around day 10 of life, and around 1 month of age. Neonates with brain injury described only in the cerebrum (and not in the cerebellum) presented ADC and FA values in their cerebellum that were similar to those in the neonates with brain injury described in the cerebrum and cerebellum. These results suggest an unrecognized cerebellum injury in some of the neonates with brain injury described only in the cerebrum when using conventional MR imaging sequences. It is interesting to note that after this analysis, we went back and examined the conventional imaging of some of these neonates with abnormal FA values, and we found the changes to be very subtle and hard to recognize on conventional imaging. Advanced neuroimaging techniques with measurements of ADC and FA values seem to be able to identify these cerebellum injuries that are not visible on conventional imaging, and thus,

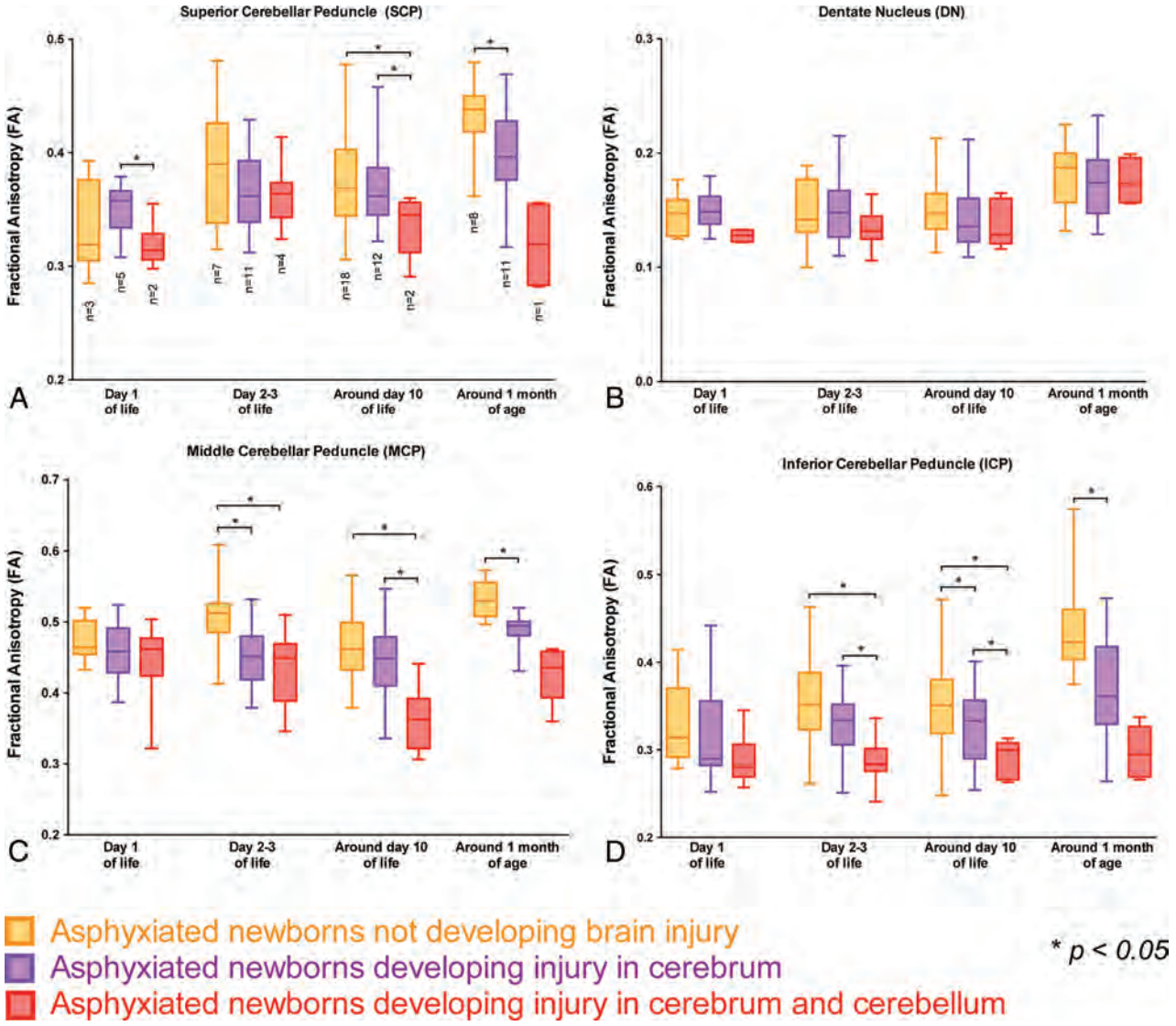

FIG 3. Comparison of FA values in each region of interest in the cerebellum between neonates who did not develop injury, neonates who developed brain injury in the cerebrum, and neonates who developed brain injury in the cerebrum and the cerebellum on day 1 of life, day 2–3 of life, around day 10 of life, and around day 30 of life. Each box and pair of whiskers indicate the median and the minimum and maximum FA values, respectively. The different regions of interest are the superior cerebellar peduncle (*A*), the dentate nucleus (*B*), the middle cerebellar peduncle (*C*), and the inferior cerebellar peduncle (*D*).

they should be used more widely with these neonates to understand the full extent of their injuries.

Typically, brain injury to the cerebrum after neonatal encephalopathy in term neonates has resulted in reduced ADC values during the first days of life, and pseudonormalization after the first week of life[25-27]; similar but slower changes have been shown in conjunction with hypothermia.[10] In our study, the changes in the cerebellum did not follow this typical pattern. No consistent acute change in ADC values was observed during the first days of life[12,15]; the only consistent changes in ADC values were the isolated increased ADC around day 10 of life. Previously, increased ADC values have been linked to extracellular edema, whereas decreased ADC values have been linked to cytotoxic edema, among other causes.[28] Thus, these findings raise a question about whether different mechanisms of injury may be involved in cerebellar injury after neonatal encephalopathy. Fractional anisotropy values tended to decrease around day 2–3 of life in the cerebellar peduncles, and the decrease became more prominent over time and reached significance around day 30 of life. In brain injury to the cerebrum after neonatal encephalopathy, these changes in FA values have been linked with irreversible ischemia, cell death, and loss of structural integrity.[29,30] In addition, in our study, no patient was found with an isolated injury in the cerebellum. All the neonates with a cerebellar injury described on their MR imaging or autopsy report also had an associated injury to the cerebrum (ie, in the basal ganglia and/or in the cortex and subcortical white matter). ADC and FA changes in the cerebellum were noted in neonates with an injury to the cerebrum and cerebellum and the neonates with an injury described only in the cerebrum compared with those in the group of neonates without injury. It is interesting to note that the 3 cerebellar peduncles showed similar trends in ADC and FA changes, but the dentate nucleus did not show similar changes.

These results suggest that injury to the cerebellum in term

asphyxiated neonates treated with hypothermia may directly follow the asphyxial event, but it may be also that injury often occurs indirectly by way of the transneuronal degeneration related to damages in other connected areas of the brain rather than directly by way of damage to the cerebellum at the time of asphyxia.[14,15,29,31] Transneuronal degeneration has been described as the anterograde and retrograde degeneration of neurons synapsing with neurons injured in the initial lesion, related to a disruption of electrical inputs and outputs.[29,32-34] This process can lead to the disappearance of entire white matter tracts.[32-34] The 3 cerebellar peduncles manage the fibers that connect the basal ganglia and widespread cortical areas to the cerebellum.[35,36] An injury to one of these above-mentioned structures can lead to transneuronal degeneration and programmed cell death through the cerebellar peduncles by way of disruption of these pathways. This hypothesis would help to explain the previously reported reduced cerebellar growth in infants with neonatal encephalopathy[14] and would support a mechanism of diffuse cerebellar injury rather than a focal injury.[12]

The cerebellum is increasingly being recognized as an important component of the brain with a role in motor functions,[37] such as coordination and balance, but also with a role in vision, cognition, planning, learning, and language.[38,39] Cerebellar development is known to continue after birth, with continuing cell differentiation and migration and linear growth during the first year after term birth.[14] In premature neonates, cerebellar injury has been related to a constellation of long-term neurodevelopmental deficits, including impaired motor sequencing, fine motor incoordination, cognitive dysfunction, autism, and other neuropsychiatric sequelae.[38,40] Impairment of cerebellar growth has been linked with impairment of brain development.[38] Thus, injury to the cerebellum in term asphyxiated neonates treated with hypothermia may also have a profound impact on the future neurodevelopment of these infants. These cerebellar injuries may explain why some of the asphyxiated neonates still develop more complex impairments, such as an impairment of motor coordination, memory, learning, or visuospatial processing.[4] Follow-up studies are needed to determine what the contribution of these cerebellar injuries is to the neurodevelopmental sequelae described later in these patients.

As for other conditions and disorders that affect the cerebellum,[21] advanced neuroimaging (such as measurements of the apparent diffusion coefficient and fractional anisotropy) has proved to be useful for assessing cerebellar injury in term asphyxiated neonates treated with hypothermia. To our knowledge, our study is the first to show that changes in ADC and FA values can be used to evaluate cerebellar injury in asphyxiated neonates treated with hypothermia. It is unfortunate that ADC and FA maps were not measurable for the whole cohort of patients, because the MR imaging sequences that permitted us to obtain these maps are not yet part of the standard of care for these patients at our institution. It also would have been ideal to study a group of asphyxiated neonates not treated with hypothermia to determine if the hypothermia treatment influenced the magnitude of the severity of the observed cerebellar injuries. However, because cooling is now the standard of care, it is no longer possible to randomly assign infants to undergo or not undergo cooling to assess the impact of hypothermia on cerebellar injuries. Additional studies need to determine whether a wider generalization of the use of such sequences may permit the detection of injuries that are for now invisible on conventional neuroimaging and may improve the prognosis given to the parents of such infants. Neurodevelopmental studies of these patients also are recommended to gain a better understanding of how these injuries unfold into neurodevelopmental impairments. We chose to assess only 4 specific regions in the cerebellum that were easily recognizable from one patient to another to make sure that our measurements were very specific. The method we used did not enable us to measure the separate eigenvectors of the diffusion tensor. Additional studies that measure the 3 principal eigenvectors that can describe diffusion in and around a lesion may provide additional insight into injury evolution and the response of the brain to such an insult.[30] Moreover, values in healthy controls could rule out the possibility that injury occurs only in the cerebellum in asphyxiated neonates treated with hypothermia. An atlas-based DTI analysis in which these results are compared with those of healthy controls would also enable us to better understand these cerebellar injuries.

To calculate the pathologic incidence of cerebellar injury in these neonates, only a description of apoptosis was considered to indicate cerebellar brain injury, because neuronal apoptosis typically requires 24–48 hours to develop after a hypoxic-ischemic insult.[40] Acidophilic changes were not accredited to cerebral brain injury in this study, because they usually take approximately 4–6 hours to develop after a hypoxic-ischemic insult[41] and thus could represent the dying process.

CONCLUSIONS

The cerebellum may be injured in term neonates after birth asphyxia. These cerebellar injuries are evident on conventional imaging for only a few neonates and are not visible for most other neonates whose potential cerebellar injuries may be identified only by advanced neuroimaging techniques. A combination of ADC and FA values may be a useful and reliable tool to use for term asphyxiated neonates treated with hypothermia to quantify and ascertain the extent of their cerebellar injury and its temporal evolution after neonatal encephalopathy. Follow-up studies are needed to determine if these cerebellar injuries predict some of the fine motor and other neurodevelopmental abnormalities that can develop later in these neonates.

ACKNOWLEDGMENTS

We thank the families and their neonates for participating in this study. Special thanks also are due to the neonatal intensive care unit nurses, neonatal intensive care unit respiratory therapists, and MR imaging technicians who made this study possible. We thank Mr. Octavian Dobrescu for his help with the review of the literature and Mr. Wayne Ross Egers for his professional English correction of the manuscript.

Disclosures: Guillaume Gilbert—*UNRELATED*: *Employment*: Philips Healthcare, *Comments*: Clinical scientist who participates in and supports clinical research performed with academic partners. Michael Shevell—*UNRELATED*: *Expert Testimony*: Varied law firms and Canadian Medical Protective Association, *Comments*: Acts as an expert for both defendants and plaintiffs, primarily in perinatal asphyxia cases with regard to issues pertaining to causation, disability, prognosis, and life expectancy; *Grants/Grants Pending*: NeuroDevNet Network of Centres of Excellence,* *Com-*

ments: Funding for national Canadian Cerebral Palsy Registry. Pia Wintermark—*RELATED*: *Grant*: research grant funding from the Fonds de recherche du Québec–Santé Clinical Research Scholar Career Award Junior 1, the New Investigator Research Grant from the SickKids Foundation, and the Canadian Institutes of Health Research Institute of Human Development, Child and Youth Health.* *Money paid to the institution.

REFERENCES

1. Bryce J, Boschi-Pinto C, Shibuya K, et al. **WHO estimates of the causes of death in children.** *Lancet* 2005;365:1147–52
2. Kurinczuk JJ, White-Koning M, Badawi N. **Epidemiology of neonatal encephalopathy and hypoxic-ischaemic encephalopathy.** *Early Hum Dev* 2010;86:329–38
3. Lawn J, Shibuya K, Stein C. **No cry at birth: global estimates of intrapartum stillbirths and intrapartum-related neonatal deaths.** *Bull World Health Organ* 2005;83:409–17
4. Azzopardi D, Strohm B, Marlow N, et al; TOBY Study Group. **Effects of hypothermia for perinatal asphyxia on childhood outcomes.** *N Engl J Med* 2014;371:140–49
5. Jacobs SE, Berg M, Hunt R, et al. **Cooling for newborns with hypoxic ischaemic encephalopathy.** *Cochrane Database Syst Rev* 2013;1:CD003311
6. Shankaran S, Pappas A, McDonald SA, et al. **Childhood outcomes after hypothermia for neonatal encephalopathy.** *N Engl J Med* 2012;366:2085–92
7. Thoresen M, Hellström-Westas L, Liu X, et al. **Effect of hypothermia on amplitude-integrated electroencephalogram in infants with asphyxia**. *Pediatrics* 2010;126:e131–39
8. Inder TE, Hunt RW, Morley CJ, et al. **Randomized trial of systemic hypothermia selectively protects the cortex on MRI in term hypoxic-ischemic encephalopathy.** *J Pediatr* 2004;145:835–37
9. Rutherford M, Ramenghi LA, Edwards AD, et al. **Assessment of brain tissue injury after moderate hypothermia in neonates with hypoxic-ischaemic encephalopathy: a nested substudy of a randomised controlled trial.** *Lancet Neurol* 2010;9:39–45
10. Bednarek N, Mathur A, Inder T, et al. **Impact of therapeutic hypothermia on MRI diffusion changes in neonatal encephalopathy.** *Neurology* 2012;78:1420–27
11. Gano D, Chau V, Poskitt KJ, et al. **Evolution of pattern of injury and quantitative MRI on days 1 and 3 in term newborns with hypoxic-ischemic encephalopathy.** *Pediatr Res* 2013;74:82–87
12. Castillo M. **Selective vulnerability and the cerebellum in neonates.** *AJNR Am J Neuroradiol* 2007;28:20–21
13. Connolly DJ, Widjaja E, Griffiths PD. **Involvement of the anterior lobe of the cerebellar vermis in perinatal profound hypoxia.** *AJNR Am J Neuroradiol* 2007;28:16–19
14. Le Strange E, Saeed N, Cowan FM, et al. **MR imaging quantification of cerebellar growth following hypoxic-ischemic injury to the neonatal brain.** *AJNR Am J Neuroradiol* 2004;25:463–68
15. Sargent MA, Poskitt KJ, Roland EH, et al. **Cerebellar vermian atrophy after neonatal hypoxic-ischemic encephalopathy.** *AJNR Am J Neuroradiol* 2004;25:1008–15
16. Limperopoulos C, Bassan H, Gauvreau K, et al. **Does cerebellar injury in premature infants contribute to the high prevalence of long-term cognitive, learning, and behavioral disability in survivors?** *Pediatrics* 2007;120:584–93
17. Barkovich AJ, Hajnal BL, Vigneron D, et al. **Prediction of neuromotor outcome in perinatal asphyxia: evaluation of MR scoring systems.** *AJNR Am J Neuroradiol* 1998;19:143–49
18. Wintermark P, Labrecque M, Warfield SK, et al. **Can induced hypothermia be assured during brain MRI in neonates with hypoxic-ischemic encephalopathy?** *Pediatr Radiol* 2010;40:1950–54
19. Smith SM. **Fast robust automated brain extraction.** *Hum Brain Mapp* 2002;17:143–55
20. Garyfallidis E, Brett M, Amirbekian B, et al. **DIPY, a library for the analysis of diffusion MRI data.** *Front Neuroinform* 2014;8:8
21. Chokshi FH, Poretti A, Meoded A, et al. **Normal and abnormal development of the cerebellum and brainstem as depicted by diffusion tensor imaging.** *Semin Ultrasound CT MR* 2011;32:539–54
22. Nicoletti G, Manners D, Novellino F, et al. **Diffusion tensor MRI changes in cerebellar structures of patients with familial essential tremor.** *Neurology* 2010;74:988–94
23. Widjaja E, Kis A, Go C, et al. **Abnormal white matter on diffusion tensor imaging in children with new-onset seizures.** *Epilepsy Res* 2013;104:105–11
24. Rasband WS. ImageJ. US National Institutes of Health, Bethesda, Maryland; 1997–2004. Available at: http://imagej.nih.gov/ij/. Accessed December 16, 2014
25. Barkovich AJ. **MR imaging of the neonatal brain.** *Neuroimaging Clin N Am* 2006;16:117–35, viii–ix
26. McKinstry RC, Miller JH, Snyder AZ, et al. **A prospective, longitudinal diffusion tensor imaging study of brain injury in newborns.** *Neurology* 2002;59:824–33
27. Rutherford M, Counsell S, Allsop J, et al. **Diffusion-weighted magnetic resonance imaging in term perinatal brain injury: a comparison with site of lesion and time from birth.** *Pediatrics* 2004;114:1004–14
28. Ito J, Marmarou A, Barzó P, et al. **Characterization of edema by diffusion-weighted imaging in experimental traumatic brain injury.** *J Neurosurg* 1996;84:97–103
29. Groenendaal F, Benders MJ, de Vries LS. **Pre-Wallerian degeneration in the neonatal brain following perinatal cerebral hypoxia-ischemia demonstrated with MRI.** *Semin Perinatol* 2006;30:146–50
30. Ward P, Counsell S, Allsop J, et al. **Reduced fractional anisotropy on diffusion tensor magnetic resonance imaging after hypoxic-ischemic encephalopathy.** *Pediatrics* 2006;117:e619–30
31. Limperopoulos C, Soul JS, Haidar H, et al. **Impaired trophic interactions between the cerebellum and the cerebrum among preterm infants.** *Pediatrics* 2005;116:844–50
32. Bouza H, Dubowitz LM, Rutherford M, et al. **Prediction of outcome in children with congenital hemiplegia: a magnetic resonance imaging study.** *Neuropediatrics* 1994;25:60–66
33. Mazumdar A, Mukherjee P, Miller JH, et al. **Diffusion-weighted imaging of acute corticospinal tract injury preceding Wallerian degeneration in the maturing human brain.** *AJNR Am J Neuroradiol* 2003;24:1057–66
34. De Vries LS, Van der Grond J, Van Haastert IC, et al. **Prediction of outcome in new-born infants with arterial ischaemic stroke using diffusion-weighted magnetic resonance imaging.** *Neuropediatrics* 2005;36:12–20
35. Bostan AC, Strick PL. **The cerebellum and basal ganglia are interconnected.** *Neuropsychol Rev* 2010;20:261–70
36. Salamon N, Sicotte N, Drain A, et al. **White matter fiber tractography and color mapping of the normal human cerebellum with diffusion tensor imaging.** *J Neuroradiol* 2007;34:115–28
37. Allin M, Matsumoto H, Santhouse AM, et al. **Cognitive and motor function and the size of the cerebellum in adolescents born very pre-term.** *Brain* 2001;124:60–66
38. Limperopoulos C, Chilingaryan G, Sullivan N, et al. **Injury to the premature cerebellum: outcome is related to remote cortical development.** *Cereb Cortex* 2014;24:728–36
39. Van Braeckel KN, Taylor HG. **Visuospatial and visuomotor deficits in preterm children: the involvement of cerebellar dysfunctioning.** *Dev Med Child Neurol* 2013;55(suppl 4):19–22
40. Biran V, Verney C, Ferriero DM. **Perinatal cerebellar injury in human and animal models.** *Neurol Res Int* 2012;2012:858929
41. Becher JC, Bell JE, Keeling JW, et al. **The Scottish perinatal neuropathology study: clinicopathological correlation in early neonatal deaths.** *Arch Dis Child Fetal Neonatal Ed* 2004;89:F399–407

Periventricular Location as a Risk Factor for Hemorrhage and Severe Clinical Presentation in Pediatric Patients with Untreated Brain Arteriovenous Malformations

L. Ma, Z. Huang, X.-L. Chen, J. Ma, X.-J. Liu, H. Wang, X. Ye, S.-L. Wang, Y. Cao, S. Wang, Y.-L. Zhao, and J.-Z. Zhao

ABSTRACT

BACKGROUND AND PURPOSE: The morphologic features of brain arteriovenous malformations differ between children and adults; therefore, our aim was to analyze various features of brain arteriovenous malformations to assess the risk of hemorrhage in children.

MATERIALS AND METHODS: We identified all consecutive children admitted to Beijing Tiantan Hospital for brain arteriovenous malformations between July 2009 and April 2014. The effects of demographic characteristics and brain arteriovenous malformation morphology on hemorrhage presentation, annual bleeding rates, postnatal hemorrhage, and immediate posthemorrhagic neurologic outcomes were studied by using univariate and multivariable regression analyses.

RESULTS: A total of 108 pediatric brain arteriovenous malformation cases were identified, 66 (61.1%) of which presented with hemorrhage. Of these, 69.7% of ruptured brain arteriovenous malformations were in a periventricular location. Periventricular nidus location (OR, 3.443; 95% CI, 1.328–8.926; $P = .011$) and nidus size (OR, 0.965; 95% CI, 0.941–0.989; $P = .005$) were independent predictors of hemorrhagic presentation. The annual hemorrhage rates in children with periventricular brain arteriovenous malformations were higher at 6.88% (OR, 1.965; 95% CI, 1.155–3.341; $P < .05$). The hemorrhage-free survival rates were also lower for children with periventricular brain arteriovenous malformations (log-rank, $P = .01$). Periventricular location (hazard ratio, 1.917; 95% CI, 1.131–3.250; $P = .016$) and nidus size (hazard ratio, 0.983; 95% CI, 0.969–0.997; $P = .015$) were associated with hemorrhage after birth in pediatric brain arteriovenous malformations. An ordinal analysis showed lower immediate posthemorrhage mRS in patients with periventricular brain arteriovenous malformations (OR for greater disability, 2.71; 95% CI, 1.03–7.11; $P = .043$).

CONCLUSIONS: Small periventricular brain arteriovenous malformations were associated with increased hemorrhage risk in pediatric patients. Cautious follow-up of children with untreated periventricular brain arteriovenous malformations is recommended because of a higher hemorrhage risk and potentially more severe neurologic outcomes.

ABBREVIATIONS: BAVM = brain arteriovenous malformations; ICH = intracranial hemorrhage; IVH = intraventricular hemorrhage

Hemorrhagic stroke accounts for half of pediatric strokes and is a life-threatening disease with a mortality rate of >30% and permanent deficits in up to 40% of patients.[1-3] Brain arteriovenous malformations (BAVMs) have been proved to be the underlying cause of most intracranial hemorrhage (ICH) in children.[4] In contrast to adult patients, children with BAVMs are more likely to present initially with ICH, while the overall annual hemorrhage rate for pediatric BAVM does not exceed that of adults.[5] A long-term follow-up study revealed that childhood presentation may provide relative protection against subsequent ICH.[6] Recent studies have indicated that the angioarchitectural features of BAVM differed between children and adults, but specific studies of hemorrhagic risk assessment in children have been limited.[7]

Previous studies have been performed primarily in adults or patients of all ages and have shown that presentation with hem-

Received October 20, 2014; accepted after revision December 16.

From the Departments of Neurosurgery (L.M., Z.H., X.-L.C., X.-J.L., H.W., X.Y., S.-L.W., Y.C., S.W., Y.-L.Z., J.-Z.Z.) and Neuroradiology (J.M.), Beijing Tiantan Hospital, Capital Medical University, Beijing, P. R. China; China National Clinical Research Center for Neurological Diseases (L.M., Z.H., X.-L.C., X.-J.L., Y.C., S.W., Y.-L.Z., J.-Z.Z.), Beijing, P. R. China; Center for Stroke (Y.-L.Z., J.-Z.Z.), Beijing Institute for Brain Disorders, Beijing, P. R. China; and Beijing Key Laboratory of Translational Medicine for Cerebrovascular Disease (Y.C., S.W., Y.-L.Z., J.-Z.Z.), Beijing, P. R. China.

This work was supported by the Ministry of Science and Technology of China, National Key Technology Research and Development Program (2013BAI09B03); Beijing Institute for Brain Disorders grant (BIBD-PXM2013_014226_07_000084); and the National Natural Science Foundation of China (H0906 81271313 to Y.-L. Zhao).

Please address correspondence to Yuan-Li Zhao, MD, Beijing Tiantan Hospital, Capital Medical University, Beijing, P. R. China; e-mail: zhaoyuanli@126.com

Indicates open access to non-subscribers at www.ajnr.org
Indicates article with supplemental on-line appendix and tables.
Indicates article with supplemental on-line photo.
http://dx.doi.org/10.3174/ajnr.A4300

orrhage is the most important and widely accepted risk factor for future bleeding from BAVMs.[8-10] Meta-analyses of natural history studies and large-scale cohort studies failed to reach a consensus regarding the role of other factors such as nidus size, exclusive deep venous drainage, associated arterial aneurysm, and deep location.[11-13] A periventricular location has also been found to correlate positively with the risk of hemorrhage before the treatment of BAVMs.[14,15] However, this feature, although amenable to analysis with imaging, has not been studied carefully in the risk assessment of interventional-versus-observational treatment.

This study was based on the hypothesis that a periventricular location, along with other morphologic features such as deep location, posterior fossa location, nidus size, exclusively deep venous drainage, and associated aneurysm, is a potential risk factor for BAVM rupture and unfavorable outcomes in pediatric patients. The study aimed to accomplish the following objectives: 1) to assess the association of these factors with the risk of hemorrhage in children with BAVMs; 2) to evaluate the hemorrhage-free survival of children with and without these factors, assuming that the BAVM had been present from birth; 3) to study the associations of these factors with the time from birth to first hemorrhage; and 4) to compare the hemorrhage site, severity of the acute presentation, and the type of intervention in ruptured periventricular and nonperiventricular BAVMs.

MATERIALS AND METHODS

The study protocol was approved by the institutional review board of Beijing Tiantan Hospital. Written informed consent was obtained from all participants and/or their guardians at admission.

Patients and Study Design

The Tiantan BAVM data base has been previously described and is a prospectively maintained data base collecting demographic, clinical, and neuroradiologic data for all patients with a confirmed angiographic or histologic diagnosis of BAVM treated at Beijing Tiantan Hospital, Capital Medical University.[16] This data base was retrospectively queried to identify all consecutive children diagnosed with BAVMs between July 2009 and April 2014. Pediatric patients were defined as patients who were 18 years of age or younger at the first angiographic diagnosis of BAVM (excluding dural and pial arteriovenous fistulas and vein of Galen malformations).

BAVM hemorrhage was defined as a symptomatic clinical event with signs of fresh intracranial blood on CT or MR imaging and/or in the CSF, with no easily identifiable alternative source that was more likely to be the cause than the BAVM. All hemorrhages before treatment for BAVM were documented. Annual hemorrhage rates were calculated as the ratio of the number of hemorrhages to the total number of patient-years of follow-up. We calculated patient-years of follow-up, assuming that the BAVM was present from birth until the first treatment for BAVM. For the BAVM hemorrhage-free survival analysis, the primary outcome was the first hemorrhage from BAVM, and patients were censored at the time of any interventional treatment for the BAVM or at the time of the last follow-up.

Neurologic function at hemorrhage onset was assessed by using the mRS and Glasgow Coma Scale. The immediate posthemorrhage mRS and Glasgow Coma Scale scores were recorded within 24 hours of the presenting hemorrhage. A clinician who was not directly involved in the care of these patients performed all scale assessments. Emergency intervention for ICH evacuation or drainage was considered in patients with a Glasgow Coma Scale score of $\leq$8, ICH with neurologic deficit, or intraventricular hemorrhage (IVH) with hydrocephalus.

Neuroradiologic Review

MR imaging, CT, and angiographic images available for each patient were evaluated by consensus between 2 neuroradiologists (J.M., with 24 years of experience, and W.B.G., with 10 years of experience) who were blinded to the clinical information. A structured list of angiographic and MR imaging features was retrospectively scored by using a protocol that generally conformed to the consensus recommended by a Joint Writing Group for BAVM research reporting terminology.[17] Variants that were reported to be predictive of BAVM rupture but were not expanded in the recommended protocol were defined with reference to previous studies.[18-20]

BAVM location was dichotomized into deep (basal ganglia, thalamus, cerebellum, and corpus callosum) and superficial (all other locations). A posterior fossa location was defined as brain stem, cerebellum, or both. BAVMs were also classified as having a periventricular location if the nidus (with a contrast-enhancement or flow void) contacted the ependymal lining of the ventricle on contrast-enhanced T1- and T2-weighted images.[14,21,22] To reduce the confounding effects of hematoma on the imaging analysis for patients with hemorrhages, we evaluated all MR images available before treatment (Fig 1). For the few patients who underwent emergency treatment but had no MR images obtained before the BAVM rupture, the BAVM location was identified on CT according to the consensus of the 2 neuroradiologists.

ICHs were classified as intraparenchymal hemorrhage, IVH, SAH, or a combination of the above 2 or 3 locations. Hematoma volume was evaluated with an ellipsoid method.[23] Hematomas were defined as deep if the basal ganglia, thalamus, brain stem, cerebellum, or corpus callosum was involved.

Venous drainage was dichotomized into exclusively deep venous drainage or nonexclusively deep venous drainage (superficial-only drainage or superficial and deep drainage). An aneurysm was defined as a saccular dilation of the lumen $>$2 times the width of the arterial vessel that carried the dilation. An aneurysm was diagnosed when dilation was evident with no obvious overlap of neighboring vessels on 2 orthogonal (both coronal and sagittal) angiographic views. Associated aneurysms included only aneurysms related to shunt flow. For statistical analysis, the associated aneurysm variable was dichotomized into absent or present.

Each nidus was measured in 3 dimensions on the latest contrast-enhanced MR imaging and angiogram before BAVM rupture. The largest diameter (in millimeters) among the 3 dimensions was recorded as the maximal AVM size for further analysis.

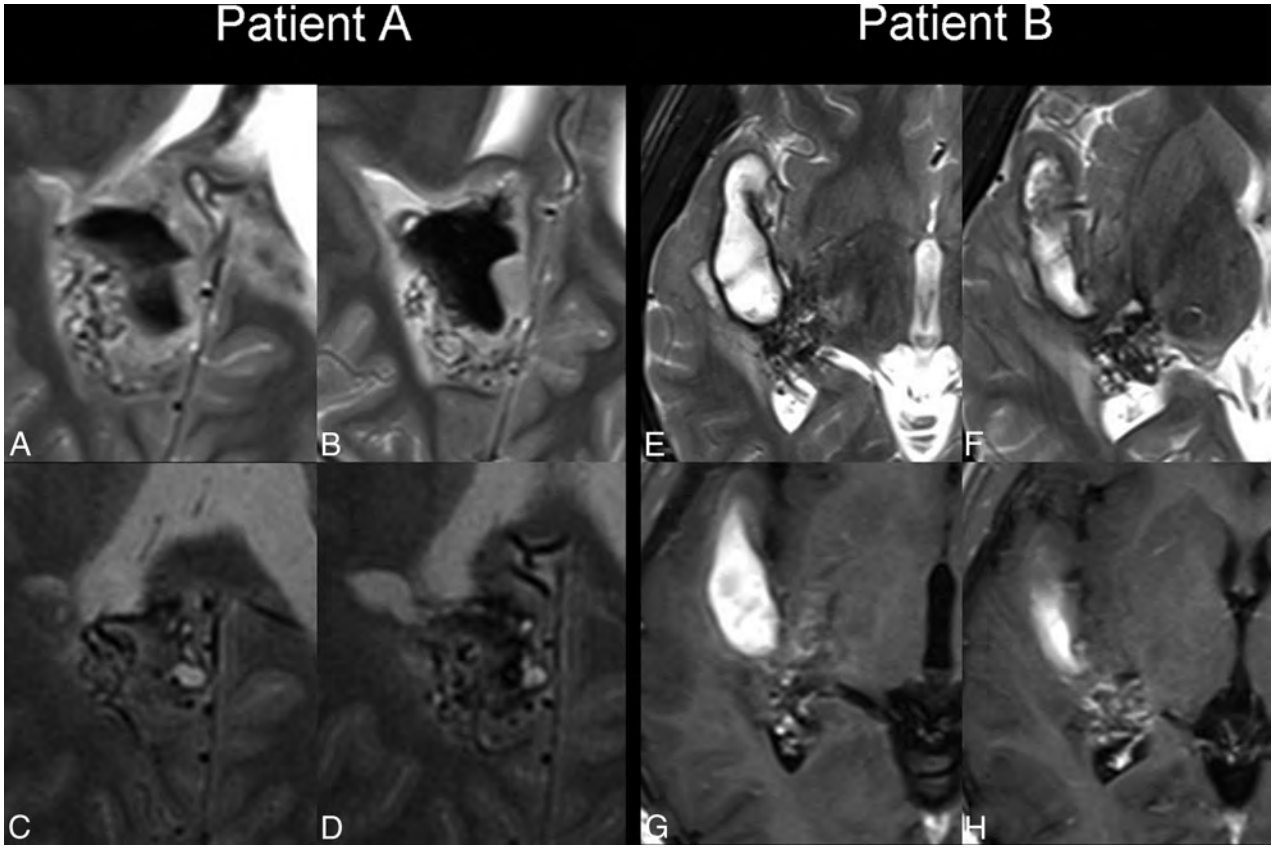

FIG 1. Ruptured BAVMs having a periventricular location. Patient A was diagnosed with right occipital BAVM. Axial T2WI on posthemorrhage day 3 (*A* and *B*) and 1 month later (*C* and *D*). The relationship between the ventricle and BAVM lesion is explicit at 1 month after hemorrhage. Patient B was diagnosed with right temporal BAVM. Axial T2WI (*E* and *F*) and postcontrast T1WI (*G* and *H*) on posthemorrhage day 14. The hematoma does not obscure the nidus edge contacting the ventricle.

Statistical Analysis

Data were analyzed by using SPSS Statistics, Version 20.0 (IBM, Armonk, New York). Statistical significance was set at $P < .05$. For the neuroradiologic and clinical data, patients with and without periventricular BAVMs were compared by using descriptive statistics, including *t* tests for continuous variables and χ^2 tests for categoric variables. The κ coefficient was used to analyze the interobserver agreement between the 2 neuroradiologists.

We first examined the association of periventricular location with the time to hemorrhage, before any treatment. We performed Cox proportional hazards analysis of the time from birth to the first hemorrhage, censoring patients at the time of treatment or last follow-up. Kaplan-Meier survival curves and log-rank tests were used to evaluate hemorrhage-free survival for patients with and without periventricular BAVMs. Both univariate and multivariable Cox proportional hazards analyses were performed, including all potential risk factors for hemorrhage.

The second stage of the analysis examined the relationship between BAVM hemorrhage outcomes at presentation and periventricular location. Both univariate and multivariable logistic regression analyses were performed by using hemorrhage presentation and severe posthemorrhage presentation (mRS >3) as the outcomes, respectively, and periventricular location as the primary predictor. We created a multivariable model that included all the potential risk factors, regardless of whether they were significant on univariate analysis. The mRS scores were also analyzed by using both an unadjusted proportional-odds regression model across all levels of the scale and a proportional-odds regression model that adjusted for other baseline demographic and morphologic variables.

RESULTS

Characteristics of the Study Population

A total of 108 pediatric patients with BAVM were identified. None of the patients had familial BAVM or hereditary hemorrhagic telangiectasia. Baseline characteristics are shown in Table 1. The age at diagnosis ranged from 1 to 18 years (mean age, 10.95 ± 4.13 years). Of these, 66 of 108 patients (61.1%) initially presented with ICH. Most patients experienced their first BAVM rupture during their first 12 years (48/66, 72.7%). The most common initial hemorrhage type was intraparenchymal hemorrhage (34/66, 51.5%), followed by intraparenchymal hemorrhage with IVH (19/66, 28.8%) and IVH (5/66, 7.6%). Exclusively deep venous drainage was found in 9.3% of the BAVMs, and associated aneurysm, in 13%. A deep location was encountered in 34.3%, and 7.4% involved the posterior fossa. Notably, 65 of 108 BAVMs (60.2%) were classified as periventricular, 70.8% of which presented with ICH. In significant contrast, 46.5% of BAVMs without ventricular involvement ruptured ($P = .011$). The periventricular BAVMs were more likely to have a deep location ($P <$

Table 1: Baseline characteristics of periventricular and nonperiventricular BAVMs[a]

Characteristic	Nonperiventricular (*n* = 43)	Periventricular (*n* = 65)	Total (*n* = 108)	*P* Value
Demographic				
Sex				.450
Female	19 (44.2)	24 (36.9)	43 (39.8)	
Male	24 (55.8)	41 (63.1)	65 (60.2)	
Age at diagnosis (yr)	12.07 ± 3.41	10.22 ± 4.42	10.95 ± 4.13	.022[b]
Clinical				
Hemorrhage presentation				.011[b]
No	23 (53.5)	19 (29.2)	42 (38.9)	
Yes	20 (46.5)	46 (70.8)	66 (61.1)	
IVH nonpresence	17 (85.0)	22 (47.8)	39 (59.1)	
IVH presence	3 (15.0)	24 (52.2)	27 (40.9)	
Venous drainage				.315[c]
Not exclusively deep	41 (95.3)	57 (87.7)	98 (90.7)	
Exclusively deep	2 (4.7)	8 (12.3)	10 (9.3)	
Deep location				<.001[b]
No	37 (86.0)	34 (52.3)	71 (65.7)	
Yes	6 (14.0)	31 (47.7)	37 (34.3)	
Posterior fossa location				.374
No	41 (95.3)	59 (90.8)	100 (92.6)	
Yes	2 (4.7)	6 (9.2)	8 (7.4)	
Associated aneurysm				.737
No	38 (88.4)	56 (86.2)	94 (87.0)	
Yes	5 (11.6)	9 (13.8)	14 (13.0)	
Maximal nidus size (mm)	35.74 ± 15.11	41.83 ± 20.87	39.41 ± 18.95	.082[d]

[a] Data are No. (%) or mean ± SD.
[b] Statistically significant.
[c] *P* values are from the χ^2 test (correction for continuity).
[d] *P* values are from the *t* test.

Table 2: Factors associated with hemorrhagic presentation by univariate analysis[a]

Characteristic	Nonhemorrhage (*n* = 42)	Hemorrhage (*n* = 66)	Total (*n* = 108)	*P* Value
Demographic				
Sex				.771
Female	16 (38.1)	27 (40.9)	43 (39.8)	
Male	26 (61.9)	39 (59.1)	65 (60.2)	
Age at diagnosis (yr)	11.71 ± 4.23	10.47 ± 4.03	10.95 ± 4.13	.128
Radiologic				
Venous drainage				.344[b]
Not exclusively deep	40 (95.2)	58 (87.9)	98 (90.7)	
Exclusively deep	2 (4.8)	8 (12.1)	10 (9.3)	
Deep location				.320
No	30 (71.4)	41 (62.1)	71 (65.7)	
Yes	12 (28.6)	25 (37.9)	37 (34.3)	
Periventricular location				.011[c]
No	23 (54.8)	20 (30.3)	43 (39.8)	
Yes	19 (45.2)	46 (69.7)	65 (60.2)	
Posterior fossa location				1.000[d]
No	39 (92.9)	61 (92.4)	100 (92.6)	
Yes	3 (7.1)	5 (7.6)	8 (7.4)	
Associated aneurysm				.396
No	38 (90.5)	56 (84.8)	94 (87.0)	
Yes	4 (9.5)	10 (15.2)	14 (13.0)	
Maximal nidus size (mm)	45.33 ± 18.25	35.64 ± 18.54	39.41 ± 18.95	.009[c]

[a] Data are No. (%) or mean ± SD.
[b] *P* values are from the χ^2 test (correction for continuity).
[c] Statistically significant.
[d] *P* values are from the Fisher exact test.

.001) and to be diagnosed early ($P = .022$). However, these lesions were not more likely to have distinct venous drainage, and there was no significant difference in supra-/infratentorial distribution, associated aneurysm incidence, or nidus size in this series of patients ($P > .05$) (Table 1).

Association of Periventricular Location with Hemorrhage Presentation

Univariate analysis revealed that BAVMs with hemorrhage were more likely to be periventricular (69.7% versus 30.3%, $P = .011$). Moreover, the nidus size was significantly smaller in BAVMs that presented with hemorrhage (35.64 ± 18.54 mm versus 45.33 ± 18.25 mm, $P = .009$). BAVMs with hemorrhagic presentation were not different from the unruptured BAVMs with respect to demographic and morphologic factors, including exclusively deep venous drainage, deep location, infratentorial location, and associated aneurysm (Table 2).

The multivariable model that adjusted for other potential risk factors showed that a periventricular location was highly predictive of hemorrhagic presentation (OR, 3.443; 95% CI, 1.328–8.926; $P = .011$) and that increased nidus size was relatively protective (OR, 0.965; 95% CI, 0.941–0.989; $P = .005$) in children with BAVMs. Age, sex, deep location, posterior fossa involvement, exclusively deep venous drainage, and associated aneurysms did not predict hemorrhagic presentations in these pediatric patients (On-line Table 1).

Association of Periventricular Location with Hemorrhage-Free Survival

If one assumes that the BAVM had been present since birth, there were 1279 patient-years of follow-up for this population of 108 patients (mean, 11.8 years). A total of 70 hemorrhages occurred in 66 patients with ruptured BAVMs, yielding an overall annual BAVM hemorrhage rate of 5.47% for pediatric patients. A total of 50 hemorrhages occurred in 46 patients with ruptured periventricular BAVMs during 727 patient-years of follow-up, yielding an annual hemorrhage rate of 6.88%. In contrast, of the 552 patient-years of follow-up in 20 patients with ruptured nonperiventricular BAVMs, only 20 hemorrhages occurred, yielding an annual hemorrhage rate of 3.62%. The odds ratio for rupture of periventricular BAVMs, compared with nonperiventricular BAVMs, was 1.965 (95% CI, 1.155–3.341).

There was a significant difference between the time to hemorrhage for patients with periventricular and nonperiventricular BAVMs (log-rank, $P = .01$). Periventricular BAVMs ruptured

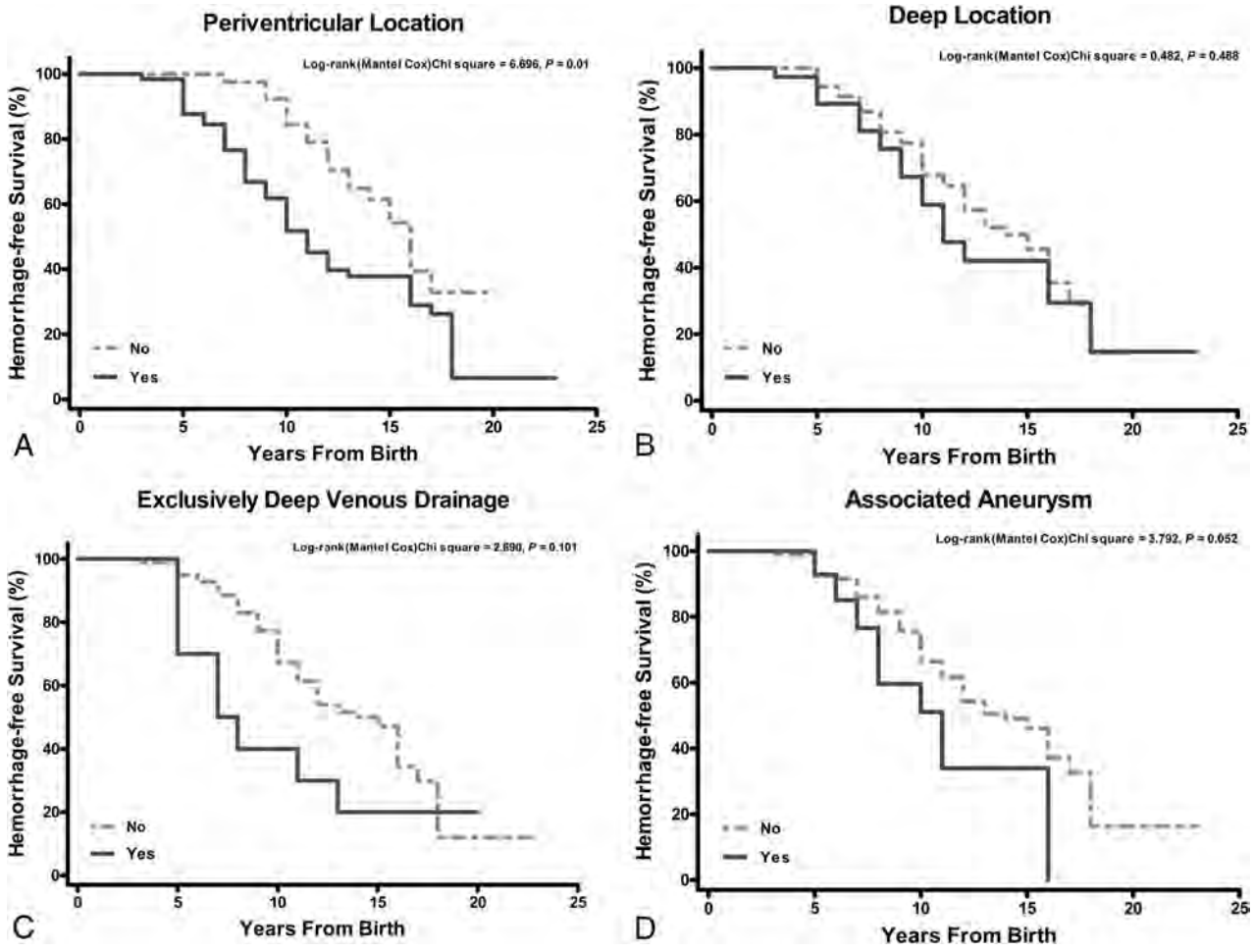

FIG 2. Kaplan-Meier curves demonstrating the hemorrhage-free survival difference between BAVMs with and without certain morphologic features.

earlier before treatment, with a median hemorrhage-free survival of 11.00 years (95% CI, 9.31–12.69) for periventricular BAVMs and 16.00 years (95% CI, 14.29–17.71) for nonperiventricular BAVMs (Fig 2). There was a borderline significant association between the presence of an aneurysm and hemorrhage-free survival (log-rank, $P = .052$). We do not have sufficient data to support an association of deep location (log-rank, $P = .488$) or exclusively deep venous drainage (log-rank, $P = .101$) with earlier BAVM rupture in childhood before any treatment.

Both univariate and multivariable Cox regression analyses were performed on the 108 pediatric patients (On-line Table 1). Although the univariate analysis identified a periventricular nidus location (hazard ratio, 1.917; 95% CI, 1.131–3.250; $P = .016$) and nidus size (hazard ratio, 0.983; 95% CI, 0.969–0.997; $P = .015$) as predictors of future hemorrhage risk in pediatric BAVMs, neither of these variables was significantly associated with earlier BAVM rupture independent of other characteristics in the multivariable model. Most unsurprising, the later the BAVM was diagnosed, the later the lesion ruptured, according to this follow-up approach.

Associations of Periventricular Location with Severe Presentation in Ruptured BAVMs

In the 66 pediatric patients with ruptured BAVMs, deep, large (>30 mL) hematomas and acute hydrocephalus were associated with a severe posthemorrhage presentation (On-line Table 2). There was a trend toward a higher risk of having an immediate posthemorrhage mRS of >3 in patients with periventricular BAVMs than in patients with nonperiventricular BAVMs (50% versus 25%, $P = .059$) (On-line Table 2 and On-line Fig 1). The unadjusted ordinal analysis showed a significant unfavorable shift in the distribution of immediate posthemorrhage mRS scores in patients with a periventricular nidus location (pooled odds ratio for a shift to a higher mRS score, 2.71; 95% CI, 1.03–7.11) (Table 3). In addition, periventricular BAVMs were significantly associated with ICH involving the ventricles (pure IVH, IVH with intraparenchymal hemorrhage, IVH with SAH, IVH with intraparenchymal hemorrhage and SAH) (52.17% versus 15.00%, $P = .005$). IVH with intraparenchymal hemorrhage was present in 17/46 (37%) ruptured periventricular BAVMs in contrast to only 2/20 (10%) nonperiventricular BAVMs (Fig 3 and On-line Fig 1). Further analysis revealed a higher frequency of deep (30.4%), large (26.1%) hematomas and acute hydrocephalus (21.7%) in ruptured periventricular BAVMs than in nonperiventricular BAVMs (On-line Fig 2).

Immediate posthemorrhage Glasgow Coma Scale score of ≤8 occurred in 26.1% of children with periventricular BAVMs and 20.0% with BAVMs in other locations. Emergent interventions (craniotomy or external ventricular drainage for blood evacuation with or without decompressive craniectomy) were per-

Table 3: Immediate posthemorrhage presentation severity according to different methods of analysis of scores on the mRS

Characteristic of mRS Scores	Ruptured BAVM		OR (95% CI)	*P* Value	OR adjusted (95% CI)[a]	*P* Value
	Nonperiventricular (*n* = 20)	Periventricular (*n* = 46)				
Severe presentation (No.) (%)			3.00 (0.94 to 9.62)	.065	2.02 (0.51–7.96)	.316
0–3	15 (75.0)	23 (50)				
4–6	5 (25.0)	23 (50)				
Immediate posthemorrhage mRS, shift on scores (No.) (%)			2.71 (1.03–7.11)	.043[b]	1.96 (0.64–6.04)	.242
0 (no symptoms at all)						
1 (no significant disability despite symptoms)	0 (0)	0 (0)				
2 (slight disability)	2 (10.0)	2 (4.3)				
3 (moderate disability requiring some help)	7 (35.0)	8 (17.4)				
4 (moderate-to-severe disability, much help)	6 (30.0)	13 (28.3)				
5 (severe disability, requiring full care)	1 (5.0)	8 (17.4)				
	4 (20.0)	15 (32.6)				

[a] Adjusted for age at diagnosis, sex, deep location, infratentorial location, exclusively deep venous drainage, associated aneurysm, and maximal nidus size.
[b] Statistically significant.

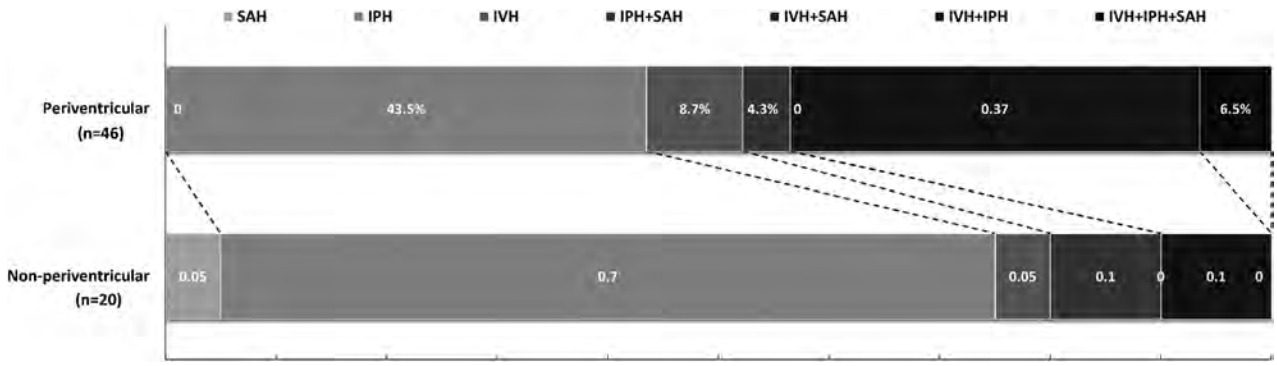

FIG 3. Hemorrhage location of ruptured periventricular BAVMs and nonperiventricular BAVMs.

formed in 34.8% of children with periventricular BAVMs and in 20.0% with BAVMs in other locations. However, these differences were not statistically significant (On-line Fig 1).

DISCUSSION

BAVM Hemorrhage Risk Predictors in Pediatric Patients

Many studies aimed at identifying morphologic features associated with BAVM hemorrhagic presentations and the risk of subsequent hemorrhage have been performed, mainly in adult patients.[8-13] A recent angiographic study revealed that the angioarchitectural features of BAVM, some of which confer a higher risk for future hemorrhage in adults, differ between children and adults.[7] However, only a few studies have specifically been conducted to assess the risk of pediatric BAVM hemorrhage and provide a prognosis before treatment (On-line Table 3).

Previous studies have reported the following factors to be associated with hemorrhage at presentation in children with BAVMs: smaller AVM nidus size, deep/exclusively deep venous drainage, single draining vein, and eloquent nidus location.[24-28] Most of these factors and results were obtained from a retrospective cohort (younger than 22 years of age) at Columbia University Medical Center.[24,26,28] Two larger studies reported results with a relatively distinct bias (a wide range of odds ratio or only radiosurgery patients), suggesting that these studies might have been underpowered to assess the impact of certain features on BAVM hemorrhage.[25,27]

In this exclusively pediatric cohort (18 years old or younger) of patients with BAVMs referred to a high-volume Chinese neurosurgery center during the past 5 years, we identified periventricular nidus location and smaller nidus size as independent predictors of hemorrhagic presentation. In contrast to adult patients, deep location, exclusively deep venous drainage, and associated aneurysms were not significantly correlated with the appearance of hemorrhage in these children. A recent study of the Columbia pediatric BAVM cohort (of 81 children) identified deep venous drainage, rather than exclusively deep venous drainage, as a predictor for hemorrhage presentation.[28] Another report on 135 children with BAVMs indicated the presence of an association of exclusively deep venous drainage with hemorrhage.[25] The role of exclusively deep venous drainage should be analyzed in further studies with larger sample sizes by using standard angiographic methods, because only 9.3% of children with BAVMs had exclusively deep venous drainage in our study, which is much less than the 17%–28% rate reported in other studies.[7] The presence of an associated aneurysm and deep nidus location has failed to correlate with BAVM hemorrhage in all previous pediatric studies, and our data corroborate these findings.[24-27]

Periventricular Nidus with Higher Hemorrhage Risk and More Severe Presentation

More than one-third (34%–37%) of BAVMs in patients of all ages have been found to be periventricular.[14,15] Our data showed a higher frequency of periventricular BAVMs in pediatric patients (60.2%). This heterogeneity related to patient age is congruent

with another finding that periventricular BAVMs were more likely to present at a young age than nonperiventricular lesions. In previous studies (On-line Table 4), a periventricular location correlated with an increased risk of BAVM hemorrhage.[14,15,21,22,29] In general, 70%–90% of periventricular BAVMs presented with hemorrhage initially.[14,29] The underlying mechanism may be related to silent intralesional hemorrhage and clot breakdown in CSF, as reported in previous studies.[14] Our data partially verified this theory, indicating that periventricular locations were associated with more intraventricular hemorrhages (52.2%). However, periventricular BAVMs were, as expected, more often located deep within the brain, raising the possibility that a deep location and venous drainage might play confounding roles in periventricular BAVM hemorrhages. Nonetheless, the present study in children did not reveal a significantly increased frequency of exclusively deep venous drainage in periventricular BAVMs, and the multivariable analysis indicated that periventricular location was a risk factor for hemorrhage, independent of deep location or venous drainage pattern.

Previous studies have identified some morphologic factors that are significant at presentation but do not necessarily predict future hemorrhages in pediatric patients with BAVMs.[24-28] While the long-term follow-up of prospective studies such as A Randomized Trial of Unruptured Brain Arteriovenous Malformations will clarify features that predict future hemorrhage in adults with BAVMs, these studies are less likely to be performed in pediatric patients, a group in which most patients present with hemorrhage; ethical dilemmas could arise during conservative treatment with observation of known BAVMs.[30] Assuming that the BAVM had been present since birth, thereby accumulating a large number of patient-years of follow-up, we found an overall annual hemorrhage rate of 5.47% in children with BAVMs, which is much higher than the 2.0% reported in a previous study.[6] The annual hemorrhage rate of periventricular BAVMs (6.88%) was almost twice that of nonperiventricular BAVMs. The differences in hemorrhage-free survival between patients with periventricular and nonperiventricular BAVMs were also pronounced. This follow-up approach has been used in many previous studies of BAVMs (On-line Table 5). To consolidate this result, we also reanalyzed the data with an assumption-free follow-up approach (On-line Appendix); this analysis also indicated that periventricular BAVMs had a higher hemorrhage rate (On-line Table 6).

Furthermore, our data indicated a potential association between a periventricular nidus location and a severe clinical presentation after hemorrhage. Further analysis revealed that the poor outcome at presentation of patients with periventricular BAVMs might be associated with deep, large hematomas and acute hydrocephalus. However, <40% of the periventricular BAVMs with unfavorable outcomes presented with hydrocephalus that could be reversed with external ventricular drainage.

Study Limitations

This study was limited by its sample size, single-institutional population, and the assumptions used in the follow-up method. For the BAVM natural history study, the most valid follow-up model is to use the time from diagnosis to an event.[8,9,31] However, investigators from our study group and other institutes have also reported the hemorrhage rate on the basis of a follow-up method that assumes that the lesion is present from birth and has a subsequent constant annual hemorrhage risk (On-line Table 5).[16,32-35] A recent study comparing the 2 approaches suggested that the latter follow-up method is a valid alternative for a BAVM natural history study.[36]

CONCLUSIONS

Small periventricular BAVMs were associated with an increased hemorrhage risk in pediatric patients. Cautious follow-up of children with untreated periventricular BAVMs is recommended due to the higher hemorrhage risk and the likelihood of severe neurologic outcomes at the time of hemorrhage onset.

ACKNOWLEDGMENTS

The authors thank Dr Gu Wei-Bin of the Department of Neuroradiology at Beijing Tiantan Hospital for his assistance with the image analysis; and Dr Wang Chen-Xi of the Department of Surgery, West China School of Medicine, at Sichuan University, and Dr Yuan Lian-Xiong of the Department of Statistics and Epidemiology, School of Public Health, at Sun Yat-Sen University for their assistance with the manuscript preparation and data analysis.

Disclosures: Li Ma—*RELATED*: *Grant*: The Ministry of Science and Technology of China, Beijing Institute for Brain Disorders, National Natural Science Foundation of China,* *Comments*: This project was supported by the Ministry of Science and Technology of China, National Key Technology Research and Development Program (2013BAI09B03); Beijing Institute for Brain Disorders grant (BIBD-PXM2013_014226_07_000084); and the National Natural Science Foundation of China (H0906 81271313 to Y.-L. Zhao). *Money paid to the institution.

REFERENCES

1. Fullerton HJ, Wu YW, Zhao S, et al. **Risk of stroke in children: ethnic and gender disparities.** *Neurology* 2003;61:189–94
2. Blom I, De Schryver EL, Kappelle LJ, et al. **Prognosis of haemorrhagic stroke in childhood: a long-term follow-up study.** *Dev Med Child Neurol* 2003;45:233–39
3. Broderick J, Talbot GT, Prenger E, et al. **Stroke in children within a major metropolitan area: the surprising importance of intracerebral hemorrhage.** *J Child Neurol* 1993;8:250–55
4. Meyer-Heim AD, Boltshauser E. **Spontaneous intracranial haemorrhage in children: aetiology, presentation and outcome.** *Brain Dev* 2003;25:416–21
5. Stapf C, Khaw AV, Sciacca RR, et al. **Effect of age on clinical and morphological characteristics in patients with brain arteriovenous malformation.** *Stroke* 2003;34:2664–69
6. Fullerton HJ, Achrol AS, Johnston SC, et al. **Long-term hemorrhage risk in children versus adults with brain arteriovenous malformations.** *Stroke* 2005;36:2099–104
7. Hetts SW, Cooke DL, Nelson J, et al. **Influence of patient age on angioarchitecture of brain arteriovenous malformations.** *AJNR Am J Neuroradiol* 2014;35:1376–80
8. Stapf C, Mast H, Sciacca RR, et al. **Predictors of hemorrhage in patients with untreated brain arteriovenous malformation.** *Neurology* 2006;66:1350–55
9. Kim H, Sidney S, McCulloch CE, et al. **Racial/ethnic differences in longitudinal risk of intracranial hemorrhage in brain arteriovenous malformation patients.** *Stroke* 2007;38:2430–37
10. da Costa L, Wallace MC, Ter Brugge KG, et al. **The natural history and predictive features of hemorrhage from brain arteriovenous malformations.** *Stroke* 2009;40:100–05
11. Kim H, Al-Shahi Salman R, McCulloch CE, et al. **Untreated brain**

arteriovenous malformation: patient-level meta-analysis of hemorrhage predictors. *Neurology* 2014;83:590–97
12. Gross BA, Du R. **Natural history of cerebral arteriovenous malformations: a meta-analysis.** *J Neurosurg* 2013;118:437–43
13. Abecassis IJ, Xu DS, Batjer HH, et al. **Natural history of brain arteriovenous malformations: a systematic review.** *Neurosurg Focus* 2014;37:E7
14. Marks MP, Lane B, Steinberg GK, et al. **Hemorrhage in intracerebral arteriovenous malformations: angiographic determinants.** *Radiology* 1990;176:807–13
15. Zipfel GJ, Bradshaw P, Bova FJ, et al. **Do the morphological characteristics of arteriovenous malformations affect the results of radiosurgery?** *J Neurosurg* 2004;101:393–401
16. Liu XJ, Wang S, Zhao YL, et al. **Risk of cerebral arteriovenous malformation rupture during pregnancy and puerperium.** *Neurology* 2014;82:1798–803
17. Atkinson RP, Awad IA, Batjer HH, et al. **Reporting terminology for brain arteriovenous malformation clinical and radiographic features for use in clinical trials.** *Stroke* 2001;32:1430–42
18. Duong DH, Young WL, Vang MC, et al. **Feeding artery pressure and venous drainage pattern are primary determinants of hemorrhage from cerebral arteriovenous malformations.** *Stroke* 1998; 29:1167–76
19. Stefani MA, Porter PJ, terBrugge KG, et al. **Large and deep brain arteriovenous malformations are associated with risk of future hemorrhage.** *Stroke* 2002;33:1220–24
20. Khaw AV, Mohr JP, Sciacca RR, et al. **Association of infratentorial brain arteriovenous malformations with hemorrhage at initial presentation.** *Stroke* 2004;35:660–63
21. Friedman WA, Blatt DL, Bova FJ, et al. **The risk of hemorrhage after radiosurgery for arteriovenous malformations.** *J Neurosurg* 1996; 84:912–19
22. Meder JF, Oppenheim C, Blustajn J, et al. **Cerebral arteriovenous malformations: the value of radiologic parameters in predicting response to radiosurgery.** *AJNR Am J Neuroradiol* 1997;18:1473–83
23. Stocchetti N, Croci M, Spagnoli D, et al. **Mass volume measurement in severe head injury: accuracy and feasibility of two pragmatic methods.** *J Neurol Neurosurg Psychiatry* 2000;68:14–17
24. Anderson RC, McDowell MM, Kellner CP, et al. **Arteriovenous malformation-associated aneurysms in the pediatric population.** *J Neurosurg Pediatr* 2012;9:11–16
25. Ellis MJ, Armstrong D, Vachhrajani S, et al. **Angioarchitectural features associated with hemorrhagic presentation in pediatric cerebral arteriovenous malformations.** *J Neurointerv Surg* 2013;5: 191–95
26. Kellner CP, McDowell MM, Appelboom G. **Analysis of hemorrhage risk factors in pediatric arteriovenous malformations** [abstract 105]. *Neurosurg Focus* 2011;30:A1–35
27. Zheng T, Wang QJ, Liu YQ, et al. **Clinical features and endovascular treatment of intracranial arteriovenous malformations in pediatric patients.** *Childs Nerv Syst* 2014;30:647–53
28. Kellner CP, McDowell MM, Phan MQ, et al. **Number and location of draining veins in pediatric arteriovenous malformations: association with hemorrhage.** *J Neurosurg Pediatr* 2014;14:538–45
29. Kasliwal MK, Kale SS, Gupta A, et al. **Outcome after hemorrhage following gamma knife surgery for cerebral arteriovenous malformations.** *J Neurosurg* 2009;110:1003–09
30. Al-Shahi Salman R, White PM, Counsell CE, et al; Scottish Audit of Intracranial Vascular Malformations Collaborators. **Outcome after conservative management or intervention for unruptured brain arteriovenous malformations.** *JAMA* 2014;311:1661–69
31. Halim AX, Johnston SC, Singh V, et al. **Longitudinal risk of intracranial hemorrhage in patients with arteriovenous malformation of the brain within a defined population.** *Stroke* 2004;35:1697–702
32. Horton JC, Chambers WA, Lyons SL, et al. **Pregnancy and the risk of hemorrhage from cerebral arteriovenous malformations.** *Neurosurgery* 1990;27:867–71; discussion 871–72
33. Pollock BE, Flickinger JC, Lunsford LD, et al. **Factors that predict the bleeding risk of cerebral arteriovenous malformations.** *Stroke* 1996; 27:1–6
34. Han PP, Ponce FA, Spetzler RF. **Intention-to-treat analysis of Spetzler-Martin grades IV and V arteriovenous malformations: natural history and treatment paradigm.** *J Neurosurg* 2003;98:3–7
35. Gross BA, Du R. **Hemorrhage from arteriovenous malformations during pregnancy.** *Neurosurgery* 2012;71:349–55; discussion 355–56
36. Kim H, McCulloch CE, Johnston SC, et al. **Comparison of 2 approaches for determining the natural history risk of brain arteriovenous malformation rupture.** *Am J Epidemiol* 2010;171:1317–22

Diffusion Tensor Imaging and Fiber Tractography in Children with Craniosynostosis Syndromes

B.F.M. Rijken, A. Leemans, Y. Lucas, K. van Montfort, I.M.J. Mathijssen, and M.H. Lequin

ABSTRACT

BACKGROUND AND PURPOSE: Patients with craniosynostosis syndromes caused by mutations in *FGFR-2*, *FGFR-3*, and *TWIST1* genes are characterized by having prematurely fused skull sutures and skull base synchondroses, which result in a skull deformity and are accompanied by brain anomalies, including altered white matter microarchitecture. In this study, the reliability and reproducibility of DTI fiber tractography was investigated in these patients. The outcomes were compared with those of controls.

MATERIALS AND METHODS: DTI datasets were acquired with a 1.5T MR imaging system with 25 diffusion gradient orientations (voxel size = $1.8 \times 1.8 \times 3.0$ mm^3, b-value = 1000 s/mm^2). White matter tracts studied included the following: corpus callosum, cingulate gyrus, fornix, corticospinal tracts, and medial cerebellar peduncle. Tract pathways were reconstructed with ExploreDTI in 58 surgically treated patients with craniosynostosis syndromes and 7 controls (age range, 6–18 years).

RESULTS: Because of the brain deformity and abnormal ventricular shape and size, DTI fiber tractography was challenging to perform in patients with craniosynostosis syndromes. To provide reliable tracts, we adapted standard tracking protocols. Fractional anisotropy was equal to that in controls (0.44 versus 0.45 $\pm$ 0.02, $P = .536$), whereas mean, axial, and radial diffusivity parameters of the mean white matter were increased in patients with craniosynostosis syndromes ($P < .001$). No craniosynostosis syndrome–specific difference in DTI properties was seen for any of the fiber tracts studied in this work.

CONCLUSIONS: Performing DTI fiber tractography in patients with craniosynostosis syndromes was difficult due to partial volume effects caused by an anisotropic voxel size and deformed brain structures. Although these patients have a normal fiber organization, increased diffusivity parameters suggest abnormal microstructural tissue properties of the investigated white matter tracts.

ABBREVIATIONS: AD = axial diffusivity; FA = fractional anisotropy; FT = fiber tractography; MD = mean diffusivity; RD = radial diffusivity

Craniosynostosis occurs in 1:2100–2500 neonates, of which at least 20% is caused by an identified genetic mutation. *FGFR-2* (32%), *FGFR-3* (25%), and *TWIST1* (19%) are the most commonly involved genes, responsible for Apert and Crouzon-Pfeiffer, Muenke, and Saethre-Chotzen syndromes, respectively. Patients in whom ≥2 cranial sutures have fused prematurely but for whom no responsible gene mutation has been found are referred to as having complex craniosynostosis (5.5%).[1]

Patients with complex and syndromic craniosynostosis syndromes are characterized by the premature fusion of skull sutures and skull base synchondroses, which induces an abnormal growth of the skull, skull base, and midface. Not only are bony structures involved in craniosynostosis, but brain and CSF circulation appear to be directly affected by the genetic defect as well.[2-5] Because genes responsible for craniosynostosis syndromes are expressed during early embryonic development of the head,[6] it is likely that these intrinsic factors can also induce disturbances in microstructural WM organization.[4,7]

Structural or mechanical cerebral abnormalities such as Chiari malformation type I are often reported in these patients.[8] Additionally, ventriculomegaly, hypoplasia of the corpus callosum or hippocampus, agenesis of the septum pellucidum, and even aberrations in WM are seen.[4,9-13] Patients with craniosynostosis syndromes have a 2-fold higher risk for de-

Received November 12, 2014; accepted after revision January 2, 2015.

From the Departments of Plastic and Reconstructive Surgery and Hand Surgery (B.F.M.R., Y.L., I.M.J.M.) and Radiology (M.H.L.), Erasmus Medical Center/Sophia Children's Hospital, Rotterdam, the Netherlands; Image Sciences Institute (A.L.), University Medical Center, Utrecht, the Netherlands; and Department of Biostatics (K.v.M.), Erasmus Medical Center, Rotterdam, the Netherlands.

The research of A.L. was supported by VIDI Grant 639.072.411 from the Netherlands Organisation for Scientific Research.

Please address correspondence to B.F.M. Rijken, MD, Erasmus MC Rotterdam, Department of Plastic and Reconstructive Surgery and Hand Surgery, Room Ee 15.91b, PO Box 2040, 3000 CA Rotterdam, the Netherlands; e-mail: b.rijken@erasmusmc.nl

Indicates open access to non-subscribers at www.ajnr.org

Indicates article with supplemental on-line tables.

http://dx.doi.org/10.3174/ajnr.A4301

veloping intellectual disability than the normative population, while they also have more behavioral and emotional functioning problems.[14]

In this study, we investigated whether diffusion tensor imaging and fiber tractography (FT) can be used for studying WM organization in patients with craniosynostosis syndromes. This technique should give more objective and anatomically complete information about WM tracts than the subjective single ROI approach that has been used before,[7] because parameters will be defined over the total length of a particular WM tract rather than at 1 certain location in the tract. Additionally, we wanted to focus on different types of fiber tracts (commissural, projection, and association) and to study whether DTI properties differ between patients with craniosynostosis syndromes and control subjects. Fractional anisotropy (FA), mean diffusivity (MD), axial diffusivity (AD), and radial diffusivity (RD) are common diffusion properties for characterizing fiber structural features and providing information about axonal tissue organization.[15-17]

We hypothesized that FA would be reduced and diffusivity properties would be increased in patients with craniosynostosis syndromes compared with controls; these changes would indicate an abnormal microstructural tissue organization.

MATERIALS AND METHODS

The medical ethics committee approved this prospective study (MEC-2014–461), performed at the Dutch Craniofacial Center, the national referral center for patients with craniosynostosis syndromes in a population of 16 million inhabitants. MR imaging data were acquired between July 2006 and October 2013 as part of the standard clinical follow-up protocol for patients with syndromic or complex craniosynostosis.

Subjects

In this study, we included 58 patients with craniosynostosis syndromes, including Apert, Crouzon-Pfeiffer, Muenke, and Saethre-Chotzen syndromes and patients with complex craniosynostosis. The latter group included patients who had at least 2 prematurely closed skull sutures, for which a responsible gene mutation has not yet been found. The study population incorporated that of Florisson et al.[7] However, the inclusion period of this study was longer; therefore, we included more patients. In this study, we added 6 patients with Apert syndrome, 2 with Crouzon-Pfeiffer syndrome, 2 with Muenke syndrome, and 5 with complex craniosynostosis. Sixty-nine patients underwent both genetic testing and MR imaging, including DTI. Patients with craniosynostosis syndromes are at risk for developing episodes of increased intracranial pressure; therefore, they routinely underwent a cranial vault expansion within the first year of life to prevent or treat increased intracranial pressure. However, they still might develop enlarged ventricles, mostly because of disturbed CSF absorption due to venous hypertension.[2] Enlarged ventricles can induce periventricular WM atrophy but also affect the shape of surrounding brain structures. Therefore, we included the frontal occipital horn ratio in our analyses to correct for ventricular size.

Only the first MR image of our patients with craniosynostosis syndromes between 6 and 18 years of age was included. In addition, we included 7 healthy control subjects within the same age range who were previously neuropsychologically tested and scanned (identical scanner and MR imaging protocol) for another study.[18] Exclusion criteria for all subjects were the following: insufficient quality of the collected DTI dataset due to incomplete scanning, motion artifacts, or inhomogeneity of the MR imaging field due to braces or metallic remains from operations. In total, we excluded 7 patients with craniosynostosis syndromes: 1 had Apert syndrome, 1 had Crouzon-Pfeiffer syndrome, 2 had Muenke syndrome, 1 had Saethre-Chotzen syndrome, and 2 had complex craniosynostosis. In addition, 1 patient with Apert and 3 with Crouzon-Pfeiffer syndrome with a ventriculoperitoneal-shunt were also excluded from the study because this may influence the specificity of the collected DTI dataset. Consequently, the final study population included 58 patients with craniosynostosis syndromes and 7 control subjects.

Image Acquisition

All MR imaging data were acquired with a 1.5T unit (General Electric Healthcare, Milwaukee, Wisconsin), including 3D T1 spoiled gradient-recalled, 3D T2 Cube, and DTI sequences. DTI was obtained by using a multirepetition single-shot echo-planar sequence with a section thickness of 3 mm without a gap. Images were obtained in 25 gradient directions with the following parameters: sensitivity, $b=1000$ s/mm^2; TR = 15,000 ms; TE = 82.1 ms; FOV = 240 × 240 mm^2; and matrix = 128 × 128, resulting in a voxel size of 1.8 × 1.8 × 3.0 mm.[7] This protocol was identical throughout the entire study period.

Data Collection

All DTI processing was performed by using ExploreDTI (http://exploredti.com/).[19] In summary, processing consisted of correction of subject motion and eddy current distortions[20] and a weighted linear least-squares estimation of the diffusion tensor with the robust extraction of kurtosis indices with linear estimation (REKINDLE) approach.[21,22] The *MRI Atlas of Human White Matter* of Oishi et al[23] was used as a guideline to reconstruct the fiber pathways. WM tracts for tractography included projection fibers (corticospinal tract), commissural/callosal fibers (corpus callosum, anterior commissure), association fibers (uncinate fasciculus), tracts of the limbic system (fornix, cingulate gyrus), and tracts in the brain stem (medial cerebellar peduncle).

Tractography was performed by placing ROIs on each dataset by using "OR/SEED" and "AND" operators to allow tracts to pass through, and "NOT" operators when tracts were not allowed to pass through.[24] In addition, "NOT" operators were occasionally placed in the midline to avoid crossing fibers from other bundles. Furthermore, 2 ANDs were placed to extract a certain segment of a WM tract; thereby, identical tract parts of each subject were measured. The FA threshold was set at 0.1, and the maximum angle threshold, at 45°. For all included WM tracts, ROI definitions were adjusted to established publications presenting good validity and reliability.[25,26] The adapted protocol for DTI FT was exactly the same in both control and craniosynostosis groups and is described in more detail below.

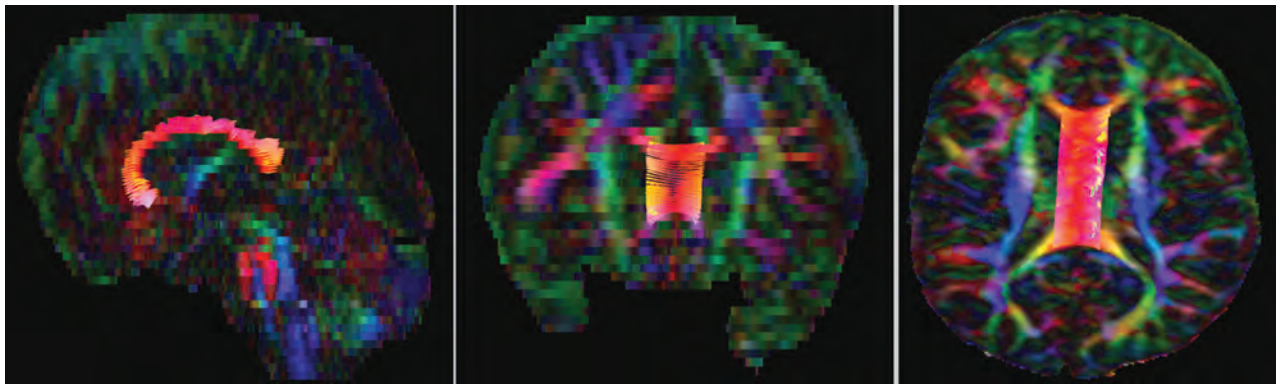

FIG 1. Midsagittal 10 mm of the corpus callosum in a 6-year-old female patient with Muenke syndrome.

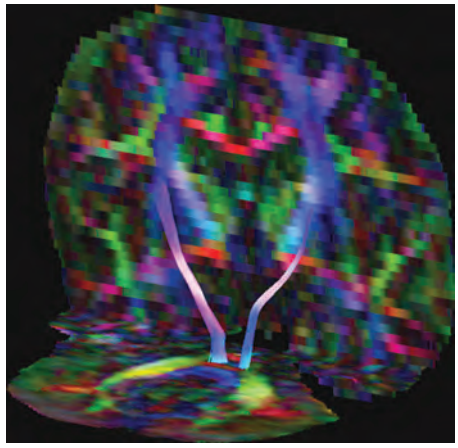

FIG 2. Midsegment of bilateral corticospinal tracts in a 6-year-old female patient with Muenke syndrome.

Commissural Fibers

Corpus Callosum. The genu, corpus, and splenium of the corpus callosum were measured separately; for all 3 parts, a OR/SEED was placed similarly in the midsagittal plane around the relevant part of the corpus callosum. To exclude regions of crossing fibers and partial volume effects, we set the maximum fiber length at 10 mm; thus, only the midsagittal segment of the corpus callosum was selected (Fig 1).[27]

Projection Fibers

Corticospinal Tracts. Fiber tracts of the corticospinal tracts (Fig 2) were generated for both sides, by placing a OR/SEED at the level of the medial cerebellar peduncle, where it was clearly separated from the pontine crossing tract and corticospinal tracts. An AND was placed at the same level, 1 additional AND at the level of the decussation of the superior cerebellar peduncle, and 1 AND around the posterior limb of the internal capsule.

Limbic System Fibers

Cingulate Gyrus. The cingulate gyrus was divided into central and hippocampal parts (Fig 3*A*, -*B*). For the first part, a OR/SEED was placed in the coronal plane above the middle part of the corpus of the corpus callosum. Additionally, 1 AND was placed posterior to it, while another AND was placed anterior to the splenium; therefore, only the middle part of the cingulate gyrus was tracked. The hippocampal part was measured by a OR/SEED placed in the coronal plane underneath the splenium, followed by 1 AND placed in the transverse plane just below the splenium and a second AND, over the cingulate gyrus at the temporal lobe, which was already labeled by tracking.

Fornix. With regard to FT of the fornix, a OR/SEED was placed in the transverse plane around the turquois body of the fornix located at the level of the thalamus. An AND was placed at the body of the fornix in the coronal plane and separately in the transverse plane around the left or right bundle that was labeled by tracking. By placing 2 additional ANDs, 1 around the fornix at the level of the anterior commissure and the other at the level of the temporal lobe, an identical segment of the fornix was labeled in all patients (Fig 3*C*).

Tracts in the Brain Stem

Medial Cerebellar Peduncle. Fiber tracts of the medial cerebellar peduncle (Fig 4) were tracked by placing a OR/SEED around the relevant structure in the coronal view and by placing 2 ANDs around each peduncle at the level of the pontine crossing tract and posterior from the pons.

Statistical Analysis

A linear regression analysis was performed for each dependent variable: FA, MD, AD, and RD of each WM structure, while tract volume and the frontal occipital horn ratio were added to the model as independent variables to correct for tract volume and ventricular size. Similar to findings in the study of Florisson et al,[7] age did not have a statistically significant effect on DTI parameters and was therefore excluded from our model. In total, we tested 4 diffusion properties (FA, MD, AD, and RD) and 11 WM structures (corpus callosum [genu, corpus, splenium, and total], bilateral cingulate gyrus, fornix, bilateral corticospinal tracts, medial cerebellar peduncle, and mean WM), resulting in 44 comparisons between patients with craniosynostosis syndromes and controls. A Bonferroni correction was performed, and a P value $< .001$ (P value $= .05/44$) was considered statistically significant. The intra- and interobserver reliability was tested by average-measures 2-way mixed intraclass correlation coefficients.

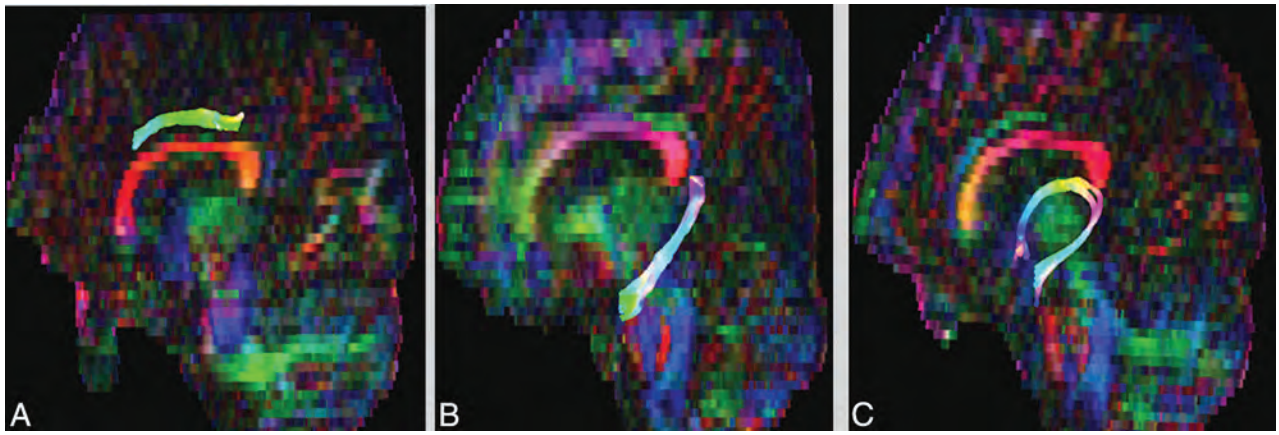

FIG 3. *A,* Central segment of cingulate gyrus. *B,* hippocampal segment of cingulate gyrus. *C,* Segmental part of the fornix.

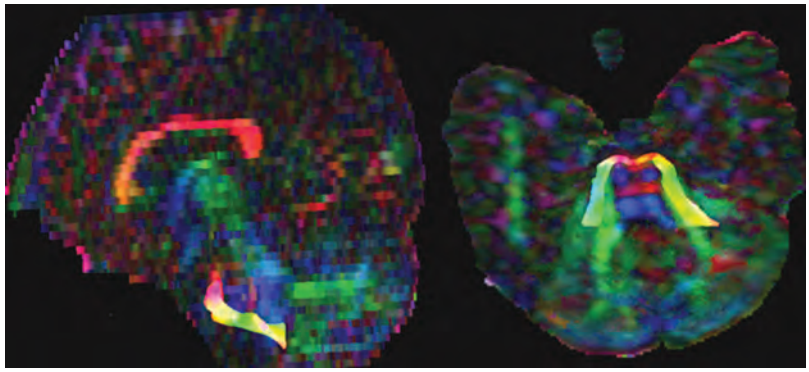

FIG 4. Segmental part of the medial cerebellar peduncle.

Patient characteristics

Syndrome	Apert	Crouzon-Pfeiffer	Muenke	Saethre-Chotzen	Complex	Total Craniosynostosis	Controls
No. of subjects	10	16	10	9	13	58	7
M/F sex	5:5	9:7	4:6	6:3	7:6	31:27	2:5
Mean age (yr)	11.1	10.1	7.9	8.9	8.9	9.4	10.7

RESULTS

Subjects

This study included 7 control subjects (mean age, 10.7 years; range, 7.5–15 years) and 58 patients with syndromic or complex craniosynostosis (mean age, 9.4 years; range, 6–18 years). The distribution for the different syndromes is presented in Table.

Measurement: Reliability and Reproducibility

DTI FT in patients with craniosynostosis syndromes was challenging because of partial volume effects due to the brain deformity and abnormal ventricular size and shape. Therefore, standard FT protocols could not be used, and measurements of all tracts needed to be adapted to track reliable and comparable fiber tracts in all subjects. Although an FA threshold of 0.2 is commonly used, an FA threshold of 0.1 made it possible to track all structures in the control group and almost all included structures in the craniosynostosis group. Consequently, by using an FA threshold of 0.1, more aberrant tracts were generated and additional AND and NOT ROIs were required to exclude aberrant fibers. Additionally, by extracting particular segments from a WM tract (by using 2 AND operators), we could measure identical WM structures and make fair comparisons between patients with craniosynostosis syndromes and control subjects. Unfortunately, the anterior commissure was not measurable in either controls or patients with craniosynostosis syndromes. Probably the anisotropic voxel size used in our protocol was too large to reconstruct such a small structure. The uncinate fasciculus showed implausible tractography in patients with craniosynostosis syndromes; therefore, both structures were excluded from the study. Furthermore, in different patients with craniosynostosis syndromes, fiber tracts could not be measured due to partial volume effects, mainly involving the cingulate gyrus and fornix (13 patients with Apert syndrome and 1 with Crouzon-Pfeiffer syndrome).

Intra- and Interobserver Reliability

Observers (B.F.M.R. and Y.L.) had 2 years of experience in DTI-FT and were supervised by A.L. with 12 years of experience in DTI and by M.H.L. with 20 years of experience in pediatric neuroradiology. Intraobserver reliability of measurements was determined by observer 1 (Y.L.), who performed all structural measurements twice in 10 subjects, 5 patients and 5 control subjects. This process resulted in an intraclass correlation coefficient of 0.93. Interobserver reliability was measured by comparing the results of observer 1 with those of a second observer (B.F.M.R.), who measured the same 10 subjects; this procedure resulted in an interclass correlation coefficient of 0.94.

WM Tracts and Ventriculomegaly

The frontal occipital horn ratio was more constant in control subjects (range, 0.31–0.37; mean, 0.35 $\pm$ 0.02) than in patients with craniosynostosis syndromes (range, 0.25–0.53; mean, 0.38 $\pm$ 0.05) and was highest in patients with Apert and Crouzon-Pfeiffer syndromes, indicating that these patients had the largest

ventricles. The frontal occipital horn ratio was not significantly correlated to the FA, MD, AD, and RD of mean WM. However, it was significantly correlated to a reduced FA and increased diffusivity properties of the genu and corpus of the corpus callosum ($P < .001$), but it had no significant effect on the splenium.

WM Measures and Craniosynostosis

Mean WM DTI properties were calculated by the sum of the properties of the individual structures and divided by the number of brain structures that could be measured.

FA. The mean FA of the total group of patients with craniosynostosis syndromes showed an FA of the mean WM similar to that of control subjects (0.44 versus 0.45, $P = .536$), as well as for the separate WM tracts.

Diffusivity Properties. MD, AD, and RD of the mean WM were significantly higher in patients with craniosynostosis syndromes compared with the control group ($P < .001$). Whereas all diffusivity properties were significantly increased in the cingulate gyrus and corticospinal tracts, only AD was significantly increased in the corpus and splenium of the corpus callosum (On-line Table 1).

With regard to the different craniosynostosis syndromes, FA of mean WM and separate WM tracts was equal to that of control subjects (On-line Table 2). However, MD, AD, and RD of mean WM were significantly higher in each syndrome compared with controls ($P < .001$). While the cingulate gyrus and corticospinal tracts were affected the most, diffusivity properties of the fornix and medial cerebellar peduncle were similar between each craniosynostosis group and the control group. For an overview see On-line Tables 3–5.

DISCUSSION

Following DTI studies on ROIs, we now performed DTI FT to study WM tracts in patients with syndromic and complex craniosynostosis. The aim of the study was to investigate the reliability of this technique in an unusual patient group with skull and brain deformities and to compare DTI properties between these patients and controls. Due to the premature fusion of skull sutures, patients with craniosynostosis syndromes develop abnormal skull and brain shapes. For instance, when coronal sutures are involved, a brachycephalic skull shape will develop. Consequently, brain structures running in the anteroposterior direction will be bent or even compressed, while structures running from left to right might be stretched out by the compensatory growth of the skull and brain parallel to the premature fused skull suture. Patients with craniosynostosis syndromes often develop ventriculomegaly, which may induce periventricular WM atrophy but also changes the shape of surrounding brain structures. Particularly the corpus callosum is at risk for CSF contamination, and DTI FT has previously been described as being difficult to conduct in patients with hydrocephalus.[28] Hence, difficulties in fiber tracking is (among others) caused by partial volume effects, we discovered that DTI FT in patients with craniosynostosis syndromes is more challenging than in controls; the combination of structural brain abnormalities and anisotropic voxels gives rise to less realistic fiber tract reconstructions. Unfortunately less is known about the effects of anisotropic voxels on the outcome of the FT, though it is assumed that isotropic voxels may be more beneficial for FT.[29] The use of an anisotropic voxel size in our study might be seen as a limitation; however, FT in our control group without skull shape abnormalities did not cause any difficulties. Therefore, we believe that the deformity of WM structures itself caused by the genetic defect, prematurely fused skull sutures, and/or large CSF spaces nearby has a greater influence on fiber tract reconstructions than the anisotropic voxel size.

Another limitation of our study includes the inability for total blinding of the observers; the altered brain shape in our patient population could often be visually detected during the measurements. In addition, we were able to include only a small number of control subjects within the same age range as our patients with craniosynostosis syndromes, who were not age and sex matched. However, because the age of all subjects ranged from 6 to 18 years and the brain has matured thoroughly enough from 6 years of age to yield stable anisotropic indexes, DTI properties seem to change only slightly afterward.

Regarding DTI properties between controls and patients with craniosynostosis syndromes, we found that FA was similar between both groups, in contrast to the findings in the study of Florisson et al.[7] Our study showed lower FA in almost all structures of both controls and patients with craniosynostosis syndromes, probably caused by the different postprocessing pipeline and data-acquisition protocol. In addition, placing a single ROI may be more subjective and could cause an overestimate of the FA of the structure of interest. Furthermore, the FA is typically underestimated in areas with crossing fibers and is further affected by an anisotropic voxel size.[29,30] Comparable with results of the study of Florisson et al,[7] diffusivity properties of the mean WM in our study were significantly higher in the total group of patients with craniosynostosis syndromes than in the control group. Although diffusivity parameters per craniosynostosis syndrome were higher than those in controls as well, regarding particular WM tracts there was no clear distinction between any craniosynostosis syndrome and the control group. One could argue that this is remarkable because *FGFR* genes have a major influence on myelinization of WM tracts by involving the development of oligodendrocytes,[31] while the *TWIST1* gene responsible for Saethre-Chotzen syndrome is important in mesenchymal cell lineage.[32,33]

Similar to the findings in the study of Yuan et al[34] regarding DTI in infants with hydrocephalus, the frontal occipital horn ratio (ie, ventricular size) was significantly related to a lower FA and higher diffusivity properties in the genu and corpus of the corpus callosum in our study. This finding might be caused by the increased amount of water or edema in the extracellular space,[35,36] because these structures are located closest to the ventricles. We assume that the role of the central CSF spaces is at least as big as the genetic influence in causing WM alterations. As in patients with sagittal craniosynostosis in whom altered DTI parameters may underlie their neuropsychological deficits,[37] WM abnormalities of the cingulate gyrus and corpus callosum in syndromic patients with craniosynostosis syndromes may be responsible for existing attention and memory problems.[14] However, neurologic assessment of our patients with craniosynostosis syndromes cannot explain diffusivity abnormalities in the corticospinal tracts, and motor deficits might rather be caused by impair-

ment of the frontal WM.[38] Remarkably, the fornix seems to be spared by the mechanical pressure or stretching caused by ventriculomegaly and altered brain shape. By contrast, Hattori et al[13] did show reduced FA values in the fornix of patients with normal pressure hydrocephalus compared with controls.

If we take these results together, our findings demonstrate that patients with craniosynostosis syndromes have a normal fiber organization but exhibit abnormal diffusivity values that may be related to differences in microstructural tissue properties. Performing DTI FT in very young patients with craniosynostosis syndromes without an operation, in whom secondary changes of the WM microarchitecture are unlikely to have occurred yet, would be interesting, to relate WM disturbances to either genetic influences or secondary changes including enlarged ventricles.

CONCLUSIONS

DTI FT is challenging to perform in patients with craniosynostosis syndromes, most likely because of their deformed brain and abnormal ventricular size and shape. This study showed that patients with craniosynostosis syndromes have FA equal to that in control subjects, while MD, AD, and RD were significantly higher in different brain structures in these patients. Although these differences may indicate abnormalities in tissue microstructural properties, such as myelin deficiency and axonal loss, we cannot exclude confounding contributions of partial volume effects related to the enlarged CSF spaces. No craniosynostosis syndrome–specific differences in DTI properties were seen in any particular type of fiber tract.

REFERENCES

1. Johnson D, Wilkie AO. **Craniosynostosis.** *Eur J Hum Genet* 2011;19:369–76
2. Di Rocco C, Frassanito P, Massimi L, et al. **Hydrocephalus and Chiari type I malformation.** *Childs Nerv Syst* 2011;27:1653–64
3. Britto JA, Evans RD, Hayward RD, et al. **From genotype to phenotype: the differential expression of FGF, FGFR, and TGFbeta genes characterizes human cranioskeletal development and reflects clinical presentation in FGFR syndromes.** *Plast Reconstr Surg* 2001; 108:2026–39; discussion 2040–46
4. Raybaud C, Di Rocco C. **Brain malformation in syndromic craniosynostoses, a primary disorder of white matter: a review.** *Childs Nerv Syst* 2007;23:1379–88
5. de Jong T, Rijken BF, Lequin MH, et al. **Brain and ventricular volume in patients with syndromic and complex craniosynostosis.** *Childs Nerv Syst* 2012;28:137–40
6. Morriss-Kay GM, Wilkie AO. **Growth of the normal skull vault and its alteration in craniosynostosis: insights from human genetics and experimental studies.** *J Anat* 2005;207:637–53
7. Florisson JM, Dudink J, Koning IV, et al. **Assessment of white matter microstructural integrity in children with syndromic craniosynostosis: a diffusion-tensor imaging study.** *Radiology* 2011;261: 534–41
8. Cinalli G, Renier D, Sebag G, et al. **Chronic tonsillar herniation in Crouzon's and Apert's syndromes: the role of premature synostosis of the lambdoid suture.** *J Neurosurg* 1995;83:575–82
9. Cinalli G, Spennato P, Sainte-Rose C, et al. **Chiari malformation in craniosynostosis.** *Childs Nerv Syst* 2005;21:889–901
10. Jeevan DS, Anlsow P, Jayamohan J. **Abnormal venous drainage in syndromic craniosynostosis and the role of CT venography.** *Childs Nerv Syst* 2008;24:1413–20
11. Quintero-Rivera F, Robson CD, Reiss RE, et al. **Intracranial anomalies detected by imaging studies in 30 patients with Apert syndrome.** *Am J Med Genet A* 2006;140:1337–38
12. Cohen MM Jr. **Pfeiffer syndrome update, clinical subtypes, and guidelines for differential diagnosis.** *Am J Med Genet* 1993;45: 300–07
13. Hattori T, Ito K, Aoki S, et al. **White matter alteration in idiopathic normal pressure hydrocephalus: tract-based spatial statistics study.** *AJNR Am J Neuroradiol* 2012;33:97–103
14. Maliepaard M, Mathijssen IM, Oosterlaan J, et al. **Intellectual, behavioral, and emotional functioning in children with syndromic craniosynostosis.** *Pediatrics* 2014;133:e1608–15
15. Basser PJ, Mattiello J, LeBihan D. **MR diffusion tensor spectroscopy and imaging.** *Biophys J* 1994;66:259–67
16. Beaulieu C. **The basis of anisotropic water diffusion in the nervous system: a technical review.** *NMR Biomed* 2002;15:435–55
17. Le Bihan D. **Looking into the functional architecture of the brain with diffusion MRI.** *Nat Rev Neurosci* 2003;4:469–80
18. van Engelen SJ, Krab LC, Moll HA, et al. **Quantitative differentiation between healthy and disordered brain matter in patients with neurofibromatosis type I using diffusion tensor imaging.** *AJNR Am J Neuroradiol* 2008;29:816–22
19. Leemans A, Jeurrissen B, Sijbers J, Jones DK. **ExploreDTI: a graphical toolbox for processing, analyzing, and visualizing diffusion MR data.** In: *Proceedings of the 17th Annual Meeting of International Society of Magnetic Resonance in Medicine,* Honolulu, Hawaii. April 18–24, 2009:3537
20. Leemans A, Jones DK. **The B-matrix must be rotated when correcting for subject motion in DTI data.** *Magn Reson Med* 2009;61: 1336–49
21. Tax CM, Otte WM, Viergever MA, et al. **REKINDLE: robust extraction of kurtosis INDices with linear estimation.** *Magn Reson Med* 2015;73:794–808
22. Veraart J, Sijbers J, Sunaert S, et al. **Weighted linear least squares estimation of diffusion MRI parameters: strengths, limitations, and pitfalls.** *Neuroimage* 2013;81:335–46
23. Oishi K, Faria AV, van Zijl PC, et al. *MRI Atlas of Human White Matter.* 2nd ed. Amsterdam: Elsevier; 2010
24. Basser PJ, Pajevic S, Pierpaoli C, et al. **In vivo fiber tractography using DT-MRI data.** *Magn Reson Med* 2000;44:625–32
25. Malykhin N, Concha L, Seres P, et al. **Diffusion tensor imaging tractography and reliability analysis for limbic and paralimbic white matter tracts.** *Psychiatry Res* 2008;164:132–42
26. Kumar A, Sundaram SK, Sivaswamy L, et al. **Alterations in frontal lobe tracts and corpus callosum in young children with autism spectrum disorder.** *Cereb Cortex* 2010;20:2103–13
27. Reijmer YD, Leemans A, Heringa SM, et al. **Improved sensitivity to cerebral white matter abnormalities in Alzheimer's disease with spherical deconvolution based tractography.** *PLoS One* 2012;7:e44074
28. Rajagopal A, Shimony JS, McKinstry RC, et al. **White matter microstructural abnormality in children with hydrocephalus detected by probabilistic diffusion tractography.** *AJNR Am J Neuroradiol* 2013;34:2379–85
29. Oouchi H, Yamada K, Sakai K, et al. **Diffusion anisotropy measurement of brain white matter is affected by voxel size: underestimation occurs in areas with crossing fibers.** *AJNR Am J Neuroradiol* 2007;28:1102–06
30. Vos SB, Jones DK, Jeurissen B, et al. **The influence of complex white matter architecture on the mean diffusivity in diffusion tensor MRI of the human brain.** *Neuroimage* 2012;59:2208–16
31. Furusho M, Dupree JL, Nave KA, et al. **Fibroblast growth factor receptor signaling in oligodendrocytes regulates myelin sheath thickness.** *J Neurosci* 2012;32:6631–41
32. Chen ZF, Behringer RR. **Twist is required in head mesenchyme for cranial neural tube morphogenesis.** *Genes Dev* 1995;9:686–99
33. el Ghouzzi V, Le Merrer M, Perrin-Schmitt F, et al. **Mutations of the**

TWIST gene in the Saethre-Chotzen syndrome. *Nat Genet* 1997; 15:42–46
34. Yuan W, Mangano FT, Air EL, et al. **Anisotropic diffusion properties in infants with hydrocephalus: a diffusion tensor imaging study.** *AJNR Am J Neuroradiol* 2009;30:1792–98
35. Berlot R, Metzler-Baddeley C, Jones DK, et al. **CSF contamination contributes to apparent microstructural alterations in mild cognitive impairment.** *Neuroimage* 2014;92:27–35
36. Vos SB, Jones DK, Viergever MA, et al. **Partial volume effect as a hidden covariate in DTI analyses.** *Neuroimage* 2011;55:1566–76
37. Beckett JS, Brooks ED, Lacadie C, et al. **Altered brain connectivity in sagittal craniosynostosis.** *J Neurosurg Pediatr* 2014;13:690–98
38. Lenfeldt N, Larsson A, Nyberg L, et al. **Diffusion tensor imaging reveals supplementary lesions to frontal white matter in idiopathic normal pressure hydrocephalus.** *Neurosurgery* 2011;68:1586–93; discussion 1593

Tract-Based Spatial Statistics in Preterm-Born Neonates Predicts Cognitive and Motor Outcomes at 18 Months

E.G. Duerden, J. Foong, V. Chau, H. Branson, K.J. Poskitt, R.E. Grunau, A. Synnes, J.G. Zwicker, and S.P. Miller

ABSTRACT

BACKGROUND AND PURPOSE: Adverse neurodevelopmental outcome is common in children born preterm. Early sensitive predictors of neurodevelopmental outcome such as MR imaging are needed. Tract-based spatial statistics, a diffusion MR imaging analysis method, performed at term-equivalent age (40 weeks) is a promising predictor of neurodevelopmental outcomes in children born very preterm. We sought to determine the association of tract-based spatial statistics findings before term-equivalent age with neurodevelopmental outcome at 18-months corrected age.

MATERIALS AND METHODS: Of 180 neonates (born at 24–32-weeks' gestation) enrolled, 153 had DTI acquired early at 32 weeks' postmenstrual age and 105 had DTI acquired later at 39.6 weeks' postmenstrual age. Voxelwise statistics were calculated by performing tract-based spatial statistics on DTI that was aligned to age-appropriate templates. At 18-month corrected age, 166 neonates underwent neurodevelopmental assessment by using the Bayley Scales of Infant Development, 3rd ed, and the Peabody Developmental Motor Scales, 2nd ed.

RESULTS: Tract-based spatial statistics analysis applied to early-acquired scans (postmenstrual age of 30–33 weeks) indicated a limited significant positive association between motor skills and axial diffusivity and radial diffusivity values in the corpus callosum, internal and external/extreme capsules, and midbrain ($P < .05$, corrected). In contrast, for term scans (postmenstrual age of 37–41 weeks), tract-based spatial statistics analysis showed a significant relationship between both motor and cognitive scores with fractional anisotropy in the corpus callosum and corticospinal tracts ($P < .05$, corrected). Tract-based spatial statistics in a limited subset of neonates ($n = 22$) scanned at <30 weeks did not significantly predict neurodevelopmental outcomes.

CONCLUSIONS: The strength of the association between fractional anisotropy values and neurodevelopmental outcome scores increased from early-to-late-acquired scans in preterm-born neonates, consistent with brain dysmaturation in this population.

ABBREVIATIONS: AD = axial diffusivity; Bayley-III = Bayley Scales of Infant Development, 3rd ed; FA = fractional anisotropy; IVH = intraventricular hemorrhage; IQR = interquartile range; PDMS-2 = Peabody Developmental Motor Scales, 2nd ed; PMA = postmenstrual age; RD = radial diffusivity; TBSS = tract-based spatial statistics

The incidence of very preterm birth (24–32 weeks' gestation) is increasing worldwide,[1-4] yet surviving neonates still have high rates of adverse neurodevelopmental outcomes.[5-7] While childhood impairment in very preterm born neonates is related to a number of factors, evidence suggests that the severity of white matter injury in the neonatal period is predictive of neurodevelopmental impairment. Examination of white matter development in preterm neonates by using DTI, sensitive to microstructural organization, is increasingly recognized as a promising tool to identify neonates at high risk of neurodevelopmental impairment.[8]

Received November 28, 2014; accepted December 23.

From the Department of Paediatrics (E.G.D., J.F., V.C., H.B., S.P.M.), Hospital for Sick Children and University of Toronto, Toronto, Ontario, Canada; Department of Pediatrics (V.C., K.J.P., R.E.G., A.S., J.G.Z., S.P.M.), University of British Columbia, BC Children's and Women's Hospitals, Child and Family Research Institute, Vancouver, British Columbia, Canada; and Department of Occupational Science and Occupational Therapy (J.G.Z.), University of British Columbia, Vancouver, British Columbia, Canada.

This work was supported by the Canadian Institutes of Health Research (MOP79262 to S.P.M. and MOP86489 to R.E.G.) and the NeuroDevNet National Centres of Excellence. S.P.M. is currently Bloorview Children's Hospital Chair in Paediatric Neuroscience and was supported by a Tier 2 Canadian Research Chair in Neonatal Neuroscience and the Michael Smith Foundation for Health Research Scholar Award. R.E.G. is supported by a Senior Scientist award from the Child and Family Research Institute. J.G.Z. is funded by a Michael Smith Foundation for Health Research Scholar Award and the Canadian Child Health Clinician Scientist Program.

Paper previously presented in part at: Annual Meeting of the Pediatric Academic Societies, May 3–6, 2014; Vancouver, British Columbia, Canada.

Please address correspondence to Steven P. Miller, MDCM, MAS, FRCPC, Division of Neurology, Hospital for Sick Children, 555 University Ave, Toronto, ON, Canada M5G, 1X8; e-mail: steven.miller@sickkids.ca

Indicates open access to non-subscribers at www.ajnr.org
Indicates article with supplemental on-line photo.
http://dx.doi.org/10.3174/ajnr.A4312

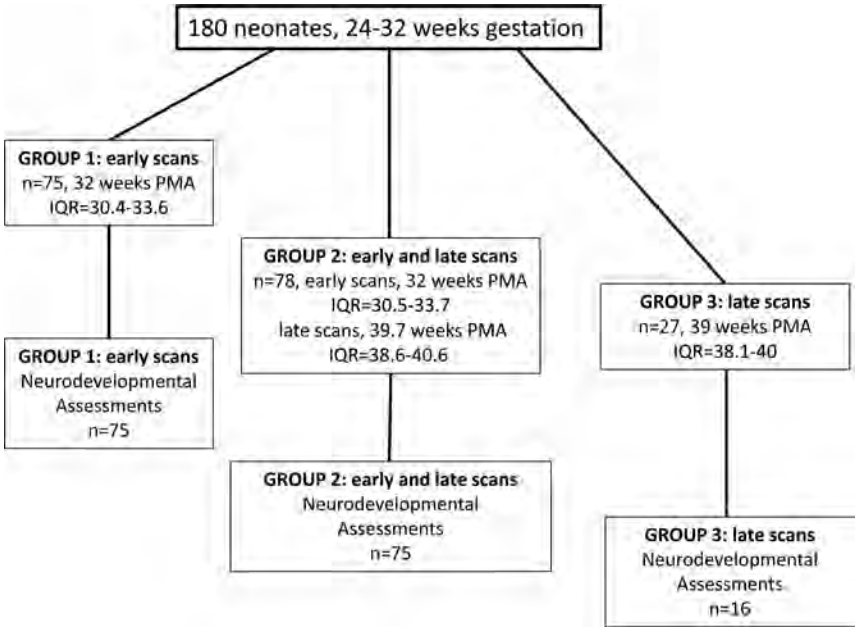

FIG 1. Participant flow chart. Neonate data (180 very preterm-born infants of <32 weeks' gestation, with 1 or 2 MR imaging scanning sessions including DTI) are separated into 3 groups: group 1, 75 neonates with only 1 early scan near the time of birth (median postmenstrual age at scanning, 32 weeks) (all 75 neonates have neurodevelopmental follow-up data at 18-month corrected age); group 2, 78 neonates with 2 scans, both early (PMA, 32 weeks) and at term-equivalent age (PMA, 39.7 weeks) (75 neonates have follow-up data); group 3, 27 neonates with a late scan (PMA, 39 weeks) (16 neonates have follow-up data).

Previous neonatal brain DTI studies indicated that white matter fractional anisotropy (FA) increases with age, even before myelin is evident on conventional MR imaging sequences.[9-11] The developmental increase in FA is largely driven by changes in diffusion measures of radial diffusivity (RD) that reflect decreases in membrane permeability of myelinating and premyelinating white matter fiber pathways.[11] Furthermore, with an ROI approach, FA extracted from DTI scans acquired near birth and term-equivalent age indicated that diffusion parameters correlated with cognitive, language, and motor outcomes.[8]

An alternative to the ROI approach is to analyze the DTI data in a 3D MR image space by using tract-based spatial statistics (TBSS; http://fsl.fmrib.ox.ac.uk/fsl/fslwiki/TBSS), permitting the voxelwise statistical analysis of DTI measures. For example, TBSS performed on scans acquired at term-equivalent age (40 weeks' postmenstrual age [PMA]) in preterm-born neonates detected alterations in white matter microstructure in the absence of overt brain injury.[12,13] Furthermore, TBSS has been used to examine diffusion measures acquired at term-equivalent age and has related them to cognitive and motor outcomes in young preterm-born children.[14,15] Previous TBSS studies examining outcome measures at 2 years (corrected age) in children born preterm reported that increased FA levels were associated with better outcome.[14,15] For example, Van Kooij et al[16] reported that the increase in FA in the corpus callosum, fornix, external and internal capsules, superior longitudinal fasciculus, inferior longitudinal and fronto-occipital fasciculi, cingulum, and uncinate fasciculus in their preterm population was positively associated with improved fine motor scores, explained by a decrease in RD. Conversely, the findings of lower FA and increased RD values associated with poorer fine motor scores were interpreted to reflect disruptions in premyelination processes.

Previous TBSS studies have largely focused on scans acquired at term-equivalent age in preterm neonates, coinciding with the myelination of major white matter fiber pathways, such as the posterior limb of the internal capsule and the brain stem.[13,16] However, evidence from histologic and MR imaging studies has indicated that some subcortical structures myelinate at <30 weeks of gestation.[14,15,17] Furthermore, TBSS permits voxelwise statistical analysis of the entire white matter skeleton, a more robust technique compared with an ROI-based approach. Furthermore, DTI analyses performed by using TBSS analysis of DTI measures obtained in neonates have demonstrated that alterations in FA with time were associated with poor outcome.[8] Therefore, using TBSS applied to early-acquired scans may provide a useful predictive measure of developmental outcome in the first weeks of life. Earlier prediction of neurodevelopmental outcome is highly relevant to clinicians making essential care decisions.

The aim of the present study was to determine whether TBSS analysis of early scans would show a similar association, as seen for term-equivalent-age scans, between white matter microstructure and neurodevelopmental performance assessed at 18-month corrected age.

MATERIALS AND METHODS

Participants

A total of 180 neonates born very preterm (51% male, 24–32 weeks' gestation) who were admitted to BC Women's Hospital, Vancouver British Columbia, Canada, were enrolled in the study between April 2006 and September 2010 (Fig 1), as described previously.[8] The primary inclusion criterion was being born between 24 and 32 weeks of gestation. Neonates with a congenital malformation or syndrome, antenatal infection, or sonographic evidence of a large parenchymal hemorrhagic infarction of >2 cm were excluded from the study. The Clinical Research Ethics Board at the University of British Columbia and Children's and Women's Health Centre of British Columbia approved this study, and written informed consent was obtained from the parent or legal caregiver of each infant.

MR Imaging

Neonates were scanned on an Avanto (Siemens, Erlangen, Germany) 1.5T MR imaging scanner by using VB 13A software. The neonates rested quietly or slept inside a MR-conditional incubator (Lammers Medical Technology, Luebeck, Germany)

and neonatal head coil (Advanced Imaging Research, Cleveland, Ohio). MR images were obtained as soon the neonate was clinically stable for transport (early scans: median age, 32 weeks; interquartile range [IQR], 30.4–33.7 weeks) and again at term-equivalent age (late scans: median age, 39.6 weeks; IQR, 38.4–40.4 weeks). Neonates underwent anatomic imaging (coronal volumetric T1-weighted images: TR, 36 ms; TE, 9.2 ms; FOV, 200 mm; section thickness, 1 mm; no gap) and axial fast spin-echo T2-weighted imaging (TR, 4610 ms; TE, 107 ms; FOV, 160 mm; section thickness, 4 mm; gap, 0.2 mm), followed by a DTI sequence (multirepetition, single-shot echo-planar sequence with 12 gradient directions; TR, 4900 ms; TE, 104 ms; FOV, 160 mm; section thickness, 3 mm; no gap), 3 averages of 2 diffusion weightings of 600 and 700 s/mm^2 (b-values), and an image without diffusion weighting, resulting in an in-plane resolution of 1.3 mm.

A neuroradiologist (K.J.P.) scored the anatomic images for the severity of white matter injury (none = 0, minimal = 1, moderate-severe = 2–3 combined) and intraventricular hemorrhage (IVH) (none = 0, mild = 1–2, and moderate-severe = 3–4) as reported previously.[8]

Image Analysis

DTI analyses were performed by using the fMRI of the Brain software library (FSL; http://www.fmrib.ox.ac.uk/fsl/).[18] Preprocessing included correction for eddy current effects. All diffusion-weighted volumes were linearly registered to 1 non-diffusion-weighted volume for each participant by using affine transformations.[19,20]

The estimated diffusion tensor data were masked to include only the brain by using the Brain Extraction Tool (http://fsl.fmrib.ox.ac.uk/fsl/fslwiki/BET).[21] A diffusion tensor model was fit to the data at each voxel and to calculate voxelwise fractional anisotropy, mean diffusivity (average of total diffusion within a given voxel), axial diffusivity (AD = first eigenvalue: λ1), and radial diffusivity (average of second and third eigenvalues: λ2, λ3).

To determine the spatial location of alterations in diffusion measures (FA, mean diffusivity, AD, RD), we processed volumes by using the TBSS pipeline.[22] FA images were nonlinearly aligned[23,24] to age-appropriate templates (early preterm scans: $n = 24$, 27–29 weeks; midpreterm scans: $n = 99$, 30–33 weeks; late preterm scans: $n = 34$, 34–36 weeks; term scans: $n = 101$, 37–41 weeks) to calculate voxelwise statistics.

Data Analysis of TBSS. Voxelwise regression analyses were performed to assess the association of diffusion measures and outcome scores of the Bayley Scales of Infant Development, 3rd ed (Bayley-III) and the Peabody Developmental Motor Scales, 2nd ed (PDMS-2). Cluster-size thresholding was applied to the data, in which the size of the cluster was determined by 500 permutations by using Randomise v.2.9 within the fMRI of the Brain Software Library (http://fsl.fmrib.ox.ac.uk/fsl/fslwiki/Randomise). A threshold of $P < .05$ (95th percentile of the distribution) was set for the clusters, corrected for multiple comparisons across space. Average FA, AD, and RD values were then extracted for the whole brain and an ROI in the corpus callosum.

Demographic and Clinical Data Collection

A neonatal research nurse and neonatal neurologist collected demographic data and clinical variables systematically. Variables of interest included gestational age at birth, cord pH, intensity of resuscitation, days of intubation, any postnatal infections (including positive-culture infection, confirmed necrotizing enterocolitis), patent ductus arteriosus, and chronic lung disease.

Neurodevelopmental Outcomes at 18-Month Corrected Age

Of the 180 subjects enrolled, 166 children returned for neurodevelopmental follow-up at BC Women's Hospital. Most of the children ($n = 155$) were assessed at 18- to 21-month corrected age (median age, 18.7 months; IQR, 18.3–19.5 months), but 11 children were seen between 22 and 37 months. Of the 166 preterm-born children, 75 had early scans, 75 had early and late scans, and 16 were scanned at term-equivalent age. The children's neurodevelopmental abilities were assessed by using the Bayley-III and the PDMS-2 (5 infants were not assessed, total $n = 161$).

The Bayley-III cognitive, motor, and language composite scores (mean, 100 ± 15) were calculated. Only the cognitive and language scales were used in the subsequent TBSS analyses. Motor abilities were also assessed by using the PDMS-2, which comprises 6 subtests and generates a Gross Motor and Fine Motor and Total Motor Quotient.

RESULTS

Clinical Characteristics

The median gestational age at birth of the 180 neonates included in the study was 27.7 weeks (IQR, 26–29.7 weeks), and the median birth weight was 1022 g (IQR, 820–1281.3 g). The neonates were grouped on the basis of the number of scans that were included in the final TBSS analyses (group 1, early scans; group 2, early and late scans; group 3, late scans, Fig 1). The details of the clinical characteristics for the groups based on gestational age at MR imaging are listed in Table 1.

Diagnostic MR Imaging Findings

On the anatomic images, white matter injury was present in up to one-quarter of the most premature babies, but severe IVH was uncommon in this cohort. Diagnostic imaging findings for the groups of neonates stratified by postmenstrual age at the time of the MR imaging are listed in Table 2.

Neurodevelopmental Outcome

The median age at which the neonates returned for neurodevelopmental follow-up was 18.7-month (IQR, 18.3–19.5 months) corrected age. The median scores on the Bayley-III and on the PDMS-2 were in the normal range. However, between 6% and 21% of neonates scored 1 SD or below (<84) on the Bayley-III or the PDMS-2 (6%, Bayley-III: cognitive; 21%, Bayley-III: language; 19%, PDMS-2: Gross Motor Quotient; 6%, PDMS-2: Fine Motor Quotient; 16%, PDMS-2: Total Motor Quotient). The results of the standardized neurodevelopmental assessment scores stratified into groups based on the postmenstrual age at scanning are described in Table 3.

Table 1: Clinical characteristics: separated into groups based on the postmenstrual age at scanning[a]

	27–29 Weeks (*n* = 24) (Median) (IQR) or (No.) (%)	30–33 Weeks (*n* = 99) (Median) (IQR) or (No.) (%)	34–36 Weeks (*n* = 34) (Median) (IQR) or (No.) (%)	37–41 Weeks (*n* = 101) (Median) (IQR) or (No.) (%)
Birth GA (wks)	27.3 (26.1–27.8)	29.3 (27.5–30.6)	26.1 (25–27.7)	26.9 (25.9–29.7)
Age at MRI (wks)	29 (28.5–29.4)	32 (30.9–32.9)	35.1 (34.5–36.3)	39.7 (38.6–40.6)
Sex (male)	12 (50%)	57 (57%)	16 (47%)	54 (53%)
Birth weight (g)	1022.5 (911.5–1171.3)	1140 (957.5–1377.5)	749 (607.5–1002.5)	970 (805–1270)
Days of mechanical ventilation	2 (1–5.8)	3 (1–10.5)	37.5 (20.5–51.3)	11.5 (2–51)
Infection[b]	11 (46%)	31 (31%)	19 (56%)	49 (49%)
Patent ductus arteriosus	9 (38%)	38 (38%)	27 (79%)	47 (47%)
Chronic lung disease	5 (21%)	10 (10%)	17 (50%)	27 (27%)

Note:—GA indicates gestational age.

[a] One hundred eighty neonates participated. Seventy-five neonates had early scans (near birth), 78 neonates were scanned early and late (birth, term-equivalent age), and 27 neonates were scanned late (term-equivalent age), for a total of 258 scans.

[b] Infection, culture-positive infection, confirmed necrotizing enterocolitis.

Table 2: Radiologic findings: separated into groups based on the postmenstrual age at scanning[a]

	27–29 Weeks (*n* = 24) (No.) (%)	30–33 Weeks (*n* = 99) (No.) (%)	34–36 Weeks (*n* = 34) (No.) (%)	37–41 Weeks (*n* = 101) (No.) (%)
WMI (moderate/severe)[b]	6 (25%)	15 (15%)	4 (12%)	12 (12%)
IVH (grade 1/2)[c]	10 (42%)	40 (40%)	18 (53%)	33 (33%)
IVH (grade 3/4)[c]	1 (4%)	2 (2%)	1 (3%)	2 (2%)
Cerebellar hemorrhage	2 (8%)	11 (11%)	5 (15%)	12 (12%)

Note:—WMI indicates white matter injury.

[a] One hundred eighty neonates participated. Seventy-five neonates had early scans (near birth), 78 neonates were scanned early and late (birth, term-equivalent age), and 27 neonates were scanned late, for a total of 258 scans.

[b] WMI defined as foci exhibiting T1 hyperintensity without T2 hypointensity or by low-intensity T1 foci.

[c] IVH was graded (none = 0, mild = 1–2, and moderate-severe = 3–4) using the Papile system.

Table 3: Neurodevelopmental outcome: separated into groups by postmenstrual age at scanning[a]

	27–29 Weeks (*n* = 22) (Median) (IQR)	30–33 Weeks (*n* = 93) (Median) (IQR)	34–36 Weeks (*n* = 32) (Median) (IQR)	37–41 Weeks (*n* = 94) (Median) (IQR)
Age at follow-up (mo)[b]	18.7 (18.4–19.2)	18.7 (18.3–19.7)	18.6 (18.3–19.1)	18.8 (18.4–19.4)
Bayley-III cognitive[c]	105 (100–110)	110 (100–115)	102.5 (92.5–110)	105 (95–110)
Bayley-III language[c]	101.5 (83.5–111.3)	100 (91–109)	95.5 (83–109)	100 (86.8–108.3)
Bayley-III motor[c]	98.5 (88.8–105.3)	100 (91.8–107)	92.5 (84.3–104)	97 (88–107)
PDMS-2 Gross Motor[c]	91 (87–96)	94 (87–98)	89 (79–96)	91 (87–98)
PDMS-2 Fine Motor[c]	100 (97–106)	100 (97–103)	97 (89.5–103)	100 (94–103)
PDMS-2 Total Motor[c]	96 (90–101)	96 (92–98)	92 (84–97)	94 (89–98)

[a] One hundred sixty-six neonates returned for neurodevelopmental follow-up. DTI data were acquired in 75 of the neonates early and in 75 of the neonates at early and late time points (150 scans). Sixteen neonates had late scans for a total of 241 scans.

[b] Age corrected for prematurity.

[c] The mean composite score in a normative population is 100 ± 15.

Diffusion Measures and Neurodevelopmental Outcome

Cognitive and Language Outcome. The TBSS analysis performed on the diffusion data acquired in neonates scanned at early postmenstrual ages (27–29 weeks, 30–33 weeks, 34–36 weeks) indicated no significant positive or negative association between cognitive and language outcomes and FA, AD, or RD values in the white matter skeleton ($P > .05$).

The TBSS analysis applied to the diffusion data from neonates scanned at 37–41 weeks showed a positive association between FA in a number of white matter tracts and cognitive scores (Fig 2, $P = .02$). Specifically, neonates scanned at a postmenstrual age of 37–41 weeks showed a positive relationship between cognitive outcome and FA values in the superior portion of the corona radiata, corticospinal tracts, genu of the corpus callosum, internal capsule, external/extreme capsules, optic radiations, and cerebral peduncle. No voxels demonstrated a negative correlation between FA and cognitive scores. The mean AD and RD values were extracted from the regions showing a significant association between FA and cognitive outcome and are plotted in Fig 2. Results indicated that FA ($R = 0.3$, $P = .03$) and RD ($R = -0.2$, $P = .03$) excluding AD ($R = -0.1$, $P = .2$), were associated with cognitive outcome scores based on Spearman ρ correlations. TBSS applied to the non-FA images indicated a significant negative association with cognitive outcome scores and RD images ($P = .04$). No association between cognitive outcome scores and AD images was found. Results were maintained when removing the data from neonates who had a moderate-severe white matter injury and/or severe IVH (On-line Fig 1). FA values were not significantly associated with language outcomes in neonates scanned at 37–41 weeks ($P = .13$).

Motor Outcome

In neonates scanned at early time periods (30–33 weeks), AD and RD images were positively associated with fine motor scores on the PDMS-2, specifically in the territories of the corpus callosum and internal, external/extreme capsules and extending to the cerebral peduncles in the midbrain ($P < .05$). No association between fine motor scores and FA was evident in neonates scanned at a PMA of 30–33 weeks ($P = .1$). Additionally, gross and total motor scores were not predicted by diffusion parameters (all $P > .05$).

Neonates scanned at later postmenstrual ages (37–41 weeks) also showed a significant positive association of FA with total motor scores in the superior portion of the corona radiata, corticospinal tracts, and the genu of the corpus callosum ($P = .02$). FA, AD, and RD values were not significantly positively or negatively associated with gross or fine motor scores ($P > .05$).

In smaller subsets of neonates scanned at other postmenstrual ages (27–29 weeks, 34–36 weeks), FA, AD, and RD were not significantly associated with motor scores ($P > .05$).

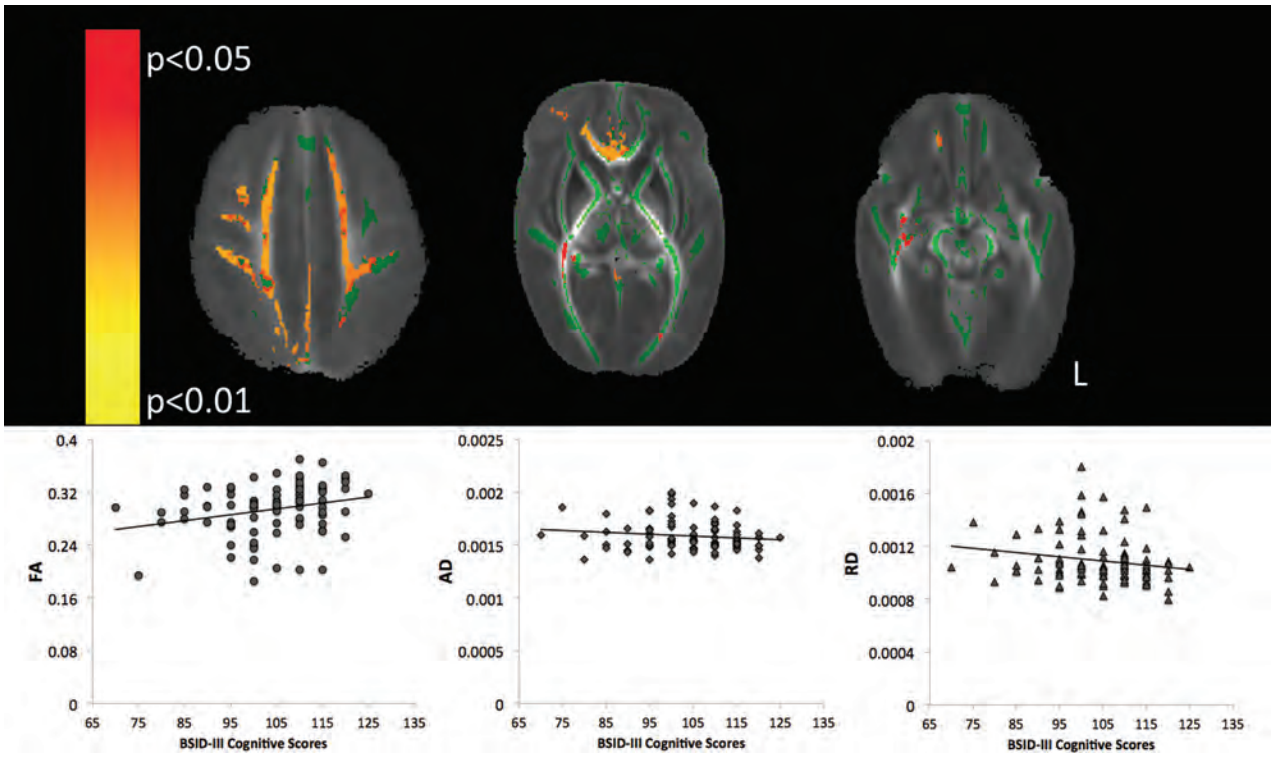

FIG 2. TBSS analysis of term scans (PMA of 37–41-weeks). *Top*: Mean FA map (red-yellow) demonstrating the significant positive linear association between cognitive scores on the Bayley-III and FA in the territory of the medial prefrontal cortex (*left*), the genu of the corpus callosum (*middle*), and portions of the inferior fronto-occipital fasciculus (*right*, $P < .05$, corrected for multiple comparisons). The mean FA skeleton is shown in green. *Bottom*: FA ($R = 0.3$, $P = .03$), AD ($R = -0.1$, $P = .2$), and RD ($R = -0.2$, $P = .03$) values from the significant clusters in the FA map. Spearman ρ correlation and an α level are set at .05.

DISCUSSION

Using TBSS analysis of diffusion-tensor images, we demonstrated that FA values can be used to predict cognitive outcome at 18 months (corrected age) in preterm-born neonates at term age. Moreover, we demonstrated the utility of using age-specific templates scanned at both early postmenstrual ages (27–29 weeks, 30–33 weeks, 34–36 weeks) and at term age (37–41 weeks) for TBSS analysis in very preterm-born neonates. The analytic method of TBSS offers a number of advantages over hypothesis-directed ROI analyses, in that it describes changes in white matter microstructure in a 3D image space.

TBSS applied to scans acquired around term age, 37–41 weeks' gestation, showed a robust association between FA values in major white matter tracts, with better cognitive and motor performance assessed at 18-month corrected age. The significant findings of higher FA values at 37–41 weeks being correlated with cognitive outcome was largely driven by decreases in RD. Findings are in agreement with a previous TBSS study with preterm-born neonates scanned at term-equivalent age that also reported increased FA in relation to higher cognitive scores and fine motor skills assessed at 2 years.[16] The biologic significance of increased FA and decreased RD in the absence of changes in AD is thought to reflect myelination processes leading to reduced permeability.[9,25] Reductions in RD are associated with the development of oligodendrocyte precursor cells,[26] while AD increases with the rise in axonal number or increase in axonal caliber. The neonates with relatively lower FA values and higher RD values with poor cognitive outcome may have experienced a disruption in premyelination or myelination processes.[27]

The use of TBSS to predict motor outcome was predictive for neonates scanned as early as 30–33 weeks. Results indicated that fine motor scores were negatively associated with AD and RD in white matter fiber pathways located in subcortical regions and the brain stem. Neonates with high AD and RD values may be at higher risk for the development of motor abnormalities. Given the widespread changes in AD and RD in several white matter fiber pathways, findings may be reflective of the loss of placental growth factors and nutrients due to the early exposure to the extrauterine environment or early systemic illness.

The higher FA values and lower RD values as revealed by using TBSS applied to scans acquired at 30–33 weeks and 37–41 weeks are consistent with myelination patterns seen during typical development.[23] Myelination does not occur in a uniform process, but rather, different sites myelinate at distinctive times during different time intervals.[15] Portions of white matter tracts in the forebrain begin to myelinate at 28–29 weeks.[23] At 37–40 weeks of gestation, the posterior limb of the internal capsule and the lateral white matter of the cerebellum are myelinated, while regions of the frontal pole begin to myelinate after 40 weeks.[17,18] In the current study, FA values in the anterior portion of the corpus callosum extracted from data acquired in neonates scanned at 30–33 weeks were significantly associated with motor outcome. The probabilistic analytic method used by TBSS can detect white matter tracts in areas of low FA, including those regions that are

sparsely myelinated or unmyelinated.[24,28] The early-acquired scans (27–29 weeks) analyzed with TBSS did not predict neurodevelopmental outcome, thus indicating a time lag to detect the abnormal white matter maturation that is predictive of cognitive outcome in preterm neonates. The lack of predictive findings from TBSS applied to the early scans is likely reflective of dysmaturation of the white matter, which is an important brain abnormality in preterm neonates.[27]

Language outcomes were not found to be significantly associated with FA values extracted in any of the postmenstrual age groups of interest. Language capabilities in infants of 18–24 months can be strongly influenced by environmental factors. Therefore, the lack of association between linguistic ability and diffusion measures of white matter microstructure seen in the current work may reflect the broad range of language capabilities in children at 18 months of age. An additional consideration is that methodologic limitations of TBSS may have affected the resolution of the arcuate fasciculus, the main white matter fiber pathway subserving speech and language.[29]

CONCLUSIONS

The development of sensitive MR imaging–based measures of white matter microstructural development in preterm-born neonates is important for the understanding of neurodevelopmental outcome, not only for the early diagnosis and treatment of neonatal brain injury and dysmaturation but also to optimize outcomes for preterm babies. In this study, we have demonstrated that through the development of age-appropriate templates, it was possible to use TBSS to predict motor outcome in scans acquired as early as postmenstrual age of 30–33 weeks. TBSS analysis applied to earlier-acquired scans was not found to be predictive of cognitive outcome. However, cognitive and motor outcomes were predicted by TBSS analysis applied to scans acquired at 37–41 weeks, even when neonates with brain injury were excluded. White matter dysmaturation is increasingly recognized as the primary pathology in contemporary cohorts of preterm neonates.[27] Thus, the full extent of white matter abnormalities in the preterm neonate may not be apparent on early scans, necessitating follow-up at term-equivalent age.

ACKNOWLEDGMENTS

The authors thank the families who participated in this research. We also thank Janet Rigney, Sandra Belanger, RN, and Mark Chalmers, RRT (University of British Columbia), for research support, and the staff of the Neonatal Follow-Up Clinic at BC Women's Hospital.

Disclosures: Emma G. Duerden—*RELATED*: *Grant*: Canadian Institutes of Health Research,* *Comments*: This grant provided the funds to conduct the research. Vann Chau—*RELATED*: *Grant*: Canadian Institutes of Health Research,* NeuroDevNet National Centres of Excellence; Helen Branson—*RELATED*: *Grant*: Canadian Institutes of Health Research,* NeuroDevNet.* Anne Synnes—*RELATED*: *Grant*: Canadian Institutes of Health Research grant,* *Comments*: Canadian Institutes of Health Research grant funded MRI and 18-month patient assessments and research staff; public funding agency/program in Canada;* NeuroDevNet; *UNRELATED*: *Grants/Grants Pending*: Canadian Institutes of Health Research grant.* Jill G. Zwicker—*RELATED*: *Grant*: Michael Smith Foundation for Health Research Scholar Award,* Canadian Child Health Clinician Scientist Program Career Enhancement Award*; *UNRELATED*: *Grants/Grants Pending*: Michael Smith Foundation for Health Research Scholar Award,* Canadian Child Health Clinician Scientist Program Career Enhancement Award*; *Travel/Accommodations/Meeting Expenses Unrelated to Activities Listed*: used start-up funds and professional development funds from my institution to pay for conference travel/accommodations/registration. Steven P. Miller—*RELATED*: *Grant*: Canadian Institutes of Health Research (Principal Investigator) and NeuroDevNet. Ruth E. Grunau—Canadian Institutes of Health Research grant MOP86489 and the NeuroDevNet. *Money paid to the Institution.

REFERENCES

1. Beck S, Wojdyla D, Say L, et al. **The worldwide incidence of preterm birth: a systematic review of maternal mortality and morbidity.** *Bull World Health Organ* 2010;88:31–38
2. Blencowe H, Cousens S, Chou D, et al. **Born too soon: the global epidemiology of 15 million preterm births**. *Reprod Health* 2013; 10(suppl 1):S2
3. Chang HH, Larson J, Blencowe H, et al. **Preventing preterm births: analysis of trends and potential reductions with interventions in 39 countries with very high human development index.** *Lancet* 2013;381:223–34
4. Blencowe H, Cousens S, Oestergaard MZ, et al. **National, regional, and worldwide estimates of preterm birth rates in the year 2010 with time trends since 1990 for selected countries: a systematic analysis and implications.** *Lancet* 2012;379:2162–72
5. D'Onofrio BM, Class QA, Rickert ME, et al. **Preterm birth and mortality and morbidity: a population-based quasi-experimental study.** *JAMA Psychiatry* 2013;70:1231–40
6. Herber-Jonat S, Streiftau S, Knauss E, et al. **Long-term outcome at age 7–10 years after extreme prematurity: a prospective, two centre cohort study of children born before 25 completed weeks of gestation (1999–2003).** *J Matern Fetal Neonatal Med* 2014;27:1620–26
7. Edwards J, Berube M, Erlandson K, et al. **Developmental coordination disorder in school-aged children born very preterm and/or at very low birth weight: a systematic review.** *J Dev Behav Pediatr* 2011;32:678–87
8. Chau V, Synnes A, Grunau RE, et al. **Abnormal brain maturation in preterm neonates associated with adverse developmental outcomes.** *Neurology* 2013;81:2082–89
9. Dubois A, Bringuier S, Capdevilla X, et al. **Vocal and verbal expression of postoperative pain in preschoolers.** *Pain Manag Nurs* 2008;9:160–65
10. Hüppi PS, Maier SE, Peled S, et al. **Microstructural development of human newborn cerebral white matter assessed in vivo by diffusion tensor magnetic resonance imaging.** *Pediatr Res* 1998;44:584–90
11. Partridge SC, Mukherjee P, Henry RG, et al. **Diffusion tensor imaging: serial quantitation of white matter tract maturity in premature newborns.** *Neuroimage* 2004;22:1302–14
12. Anjari M, Srinivasan L, Allsop JM, et al. **Diffusion tensor imaging with tract-based spatial statistics reveals local white matter abnormalities in preterm infants.** *Neuroimage* 2007;35:1021–27
13. Alexandrou G, Mårtensson G, Skiold B, et al. **White matter microstructure is influenced by extremely preterm birth and neonatal respiratory factors.** *Acta Paediatr* 2014;103:48–56
14. Counsell SJ, Maalouf EF, Fletcher AM, et al. **MR imaging assessment of myelination in the very preterm brain.** *AJNR Am J Neuroradiol* 2002;23:872–81
15. Kinney HC, Brody BA, Kloman AS, et al. **Sequence of central nervous system myelination in human infancy. II. Patterns of myelination in autopsied infants.** *J Neuropathol Exp Neurol* 1988;47:217–34
16. van Kooij BJ, de Vries LS, Ball G, et al. **Neonatal tract-based spatial statistics findings and outcome in preterm infants.** *AJNR Am J Neuroradiol* 2012;33:188–94
17. Barkovich AJ. **Concepts of myelin and myelination in neuroradiology.** *AJNR Am J Neuroradiol* 2000;21:1099–109
18. Jenkinson M, Beckmann CF, Behrens TE, et al. **FSL.** *Neuroimage* 2012;62:782–90
19. Jenkinson M, Smith SM. **A global optimisation method for robust affine registration of brain images.** *Med Image Anal* 2001;5:143–56
20. Jenkinson M, Bannister PR, Brady JM, et al. **Improved optimisation for the robust and accurate linear registration and motion correction of brain images.** *Neuroimage* 2002;17:825–41

21. Smith SM. **Fast robust automated brain extraction.** *Hum Brain Mapp* 2002;17:143–55
22. Smith SM, Jenkinson M, Johansen-Berg H, et al. **Tract-based spatial statistics: voxelwise analysis of multi-subject diffusion data.** *Neuroimage* 2006;31:1487–505
23. Gilles FH, Shankle W, Dooling EC. **Myelinated tracts: growth patterns**. In: Gilles FH, Leviton A, Dooling EC, eds. *The Developing Human Brain: Growth and Epidemiologic Neuropathology*. Littleton: John Wright; 1983:118–82
24. Bassi L, Chew A, Merchant N, et al. **Diffusion tensor imaging in preterm infants with punctate white matter lesions.** *Pediatr Res* 2011;69:561–66
25. Dubois J, Hertz-Pannier L, Dehaene-Lambertz G, et al. **Assessment of the early organization and maturation of infants' cerebral white matter fiber bundles: a feasibility study using quantitative diffusion tensor imaging and tractography.** *Neuroimage* 2006;30:1121–32
26. Drobyshevsky A, Song SK, Gamkrelidze G, et al. **Developmental changes in diffusion anisotropy coincide with immature oligodendrocyte progression and maturation of compound action potential.** *J Neurosci* 2005;25:5988–97
27. Back SA, Miller SP. **Brain injury in premature neonates: a primary cerebral dysmaturation disorder?** *Ann Neurol* 2014;75:469–86
28. Bassi L, Ricci D, Volzone A, et al. **Probabilistic diffusion tractography of the optic radiations and visual function in preterm infants at term equivalent age.** *Brain* 2008;131:573–82
29. Catani M, Jones DK, ffytche DH. **Perisylvian language networks of the human brain.** *Ann Neurol* 2005;57:8–16

Radiation Necrosis in Pediatric Patients with Brain Tumors Treated with Proton Radiotherapy

S.F. Kralik, C.Y. Ho, W. Finke, J.C. Buchsbaum, C.P. Haskins, and C.-S. Shih

ABSTRACT

BACKGROUND AND PURPOSE: Proton radiotherapy has been increasingly utilized to treat pediatric brain tumors, however, limited information exists regarding radiation necrosis among these patients. Our aim was to evaluate the incidence, timing, clinical significance, risk factors, and imaging patterns of radiation necrosis in pediatric patients with brain tumors treated with proton radiation therapy.

MATERIALS AND METHODS: A retrospective study was performed on 60 consecutive pediatric patients with primary brain tumors treated with proton radiation therapy. Radiation necrosis was assessed by examining serial MRIs and clinical records to determine the incidence, timing, risk factors, imaging patterns, and clinical significance associated with the development of radiation necrosis in these patients. Radiation necrosis was defined as areas of new enhancement within an anatomic region with previous exposure to proton beam therapy with subsequent decrease on follow-up imaging without changes in chemotherapy.

RESULTS: Thirty-one percent of patients developed radiation necrosis with a median time to development of 5.0 months (range, 3–11 months). Risk factors included multiple chemotherapy agents (>3 cytotoxic agents) and atypical teratoid rhabdoid tumor pathology ($P = .03$ and $P = .03$, respectively). The most common imaging patterns were small (median, 0.9 cm) and multifocal (63% of patients) areas of parenchymal enhancement remote from the surgical site. The median time to complete resolution on imaging was 5.3 months (range, 3–12 months). Among patients with imaging findings of radiation necrosis, 25% demonstrated severe symptoms with medical intervention indicated.

CONCLUSIONS: Pediatric patients with brain tumors treated with proton radiation therapy demonstrate a high incidence of radiation necrosis and a short time to development of necrosis. Multiple small areas of necrosis are frequently identified on imaging. Exposure to multiple chemotherapy agents was a significant risk factor associated with radiation necrosis in these patients.

ABBREVIATIONS: CTCAE = Common Terminology Criteria for Adverse Events; PBT = proton beam radiotherapy

Radiation necrosis is a well-described toxicity that has been reported over a wide range of tumor pathologies and radiation doses.[1] Although histopathology can be used to establish a diagnosis of radiation necrosis, more commonly a clinicoradiologic diagnosis of radiation necrosis is used to avoid surgical morbidity and potential complications. Most of the literature regarding radiation necrosis involves adult patients, but the incidence of radiation necrosis in the pediatric brain tumor population with photon radiation therapy has also been described with an incidence of 5% and is potentially exacerbated by chemotherapy so that radiation necrosis may be attributable to the combination of radiation therapy and chemotherapy.[2,3] Although radiation therapy remains an important form of treatment for pediatric brain tumors, the brains of young children may respond differently to radiation therapy compared with adults. Potential etiologies reported from a limited number of animal studies have demonstrated differences in progenitor cells, local microenvironment, inflammatory response, and effects on oligodendrocytes and microglia.[4-7] Consequently, there is poor understanding of the effect of radiation therapy combined with chemotherapy on the normal brain tissue of pediatric patients. Therefore, continued investigation of radiation necrosis in pediatric patients remains important to understand these differences in susceptibility to radiation injury.

Compared with conventional (photon) radiation therapy, proton beam therapy (PBT) offers the theoretic advantages of the

Received December 8, 2014; accepted after revision January 15, 2015.

From the Departments of Radiology and Imaging Sciences (S.F.K., C.Y.H., W.F.), Radiation Oncology (J.C.B.), and Pediatrics, Hematology/Oncology Section (C.-S.S.), Indiana University School of Medicine (C.P.H.), Indianapolis, Indiana.

Please address correspondence to Stephen F. Kralik, MD, 705 Riley Hospital Dr, Indianapolis, IN, 46202; e-mail: steve.kralik@gmail.com

Indicates article with supplemental on-line table.

http://dx.doi.org/10.3174/ajnr.A4333

absence of an exit dose, a highly conformal dose distribution, and a reduced radiation dose to adjacent normal tissue.[8] Therefore, potential benefits of proton radiation therapy in patients with pediatric brain tumors may include the reduction of negative long-term effects of radiation, such as cognitive deficits, endocrine abnormalities, vascular abnormalities, and secondary malignancies.[9] PBT has been used increasingly to treat pediatric brain tumors, including craniopharyngiomas, ependymomas, germinomas, and medulloblastomas; however, limited data exist regarding radiation necrosis with proton radiation therapy in this population, with only 1 small series reporting an incidence of 47%.[10-14] The purpose of this research was to evaluate the incidence, timing, clinical significance, risk factors, and imaging patterns of radiation necrosis in patients with pediatric brain tumor with PBT.

MATERIALS AND METHODS

Following institutional review board approval, a search of the pediatric neuro-oncology patient data base at our institution identified patients with primary brain tumors who were treated with PBT, and verification of PBT treatment and doses was obtained from the radiation oncology PBT treatment data base. All patients were either those with a newly diagnosed primary brain tumor who were subsequently treated with PBT or those who had low-grade gliomas without prior treatment with radiation therapy who demonstrated tumor progression on chemotherapy necessitating treatment with PBT. Therefore, patients were excluded if there was any history of treatment with photon radiation therapy, including before PBT, concurrent with PBT, or after PBT. Patients were also excluded if there was >1 course of PBT. Subsequently, a retrospective review of clinical and radiologic data was performed on 60 consecutive pediatric patients with primary brain tumors who had undergone cranial PBT from January 11, 2010, to October 25, 2012, and had clinical and MR imaging follow-up performed at our institution. Patients were scanned at approximately 3-month intervals or sooner with suspicious findings on imaging. Patients without both 6 months of clinical follow-up and MR imaging follow-up from the completion of PBT were excluded from the statistical analysis for cerebral necrosis, including if death occurred before 6 months.

PBT treatment doses followed the standard of care in the United States at a Children's Oncology Group treatment center with a continuum of radiation doses ranging from 50 to 60 Gy total for most. The radiation oncologist (J.C.B.) approved 3D image guidance treatment plans before every single field in real-time each day in every patient. Typical target volumes with PBT included gross tumor volume (any visible residual tumor and/or resection cavity) to a clinical target volume (area of concern) margin of 5 mm; and the planning tumor volume (gross tumor volume plus clinical target volume) margin was set as 2 mm with a 5-mm margin when accounting for additional factors including smearing. All craniospinal radiation therapy was performed with PBT, not photon radiation therapy. Twenty-one patients received craniospinal radiation therapy with doses ranging from 23.4 to 36 Gy, which was performed with 1 treatment per day with no break right into the boost. Those with medulloblastoma received craniospinal irradiation while the remainder received focal PBT.

Brain MRI consisted of imaging performed with 1.5T or 3T (Avanto and Verio; Siemens, Erlangen, Germany) MR imaging units with axial and sagittal T1-weighted TSE, axial T2-weighted TSE, axial FLAIR, axial DWI, coronal T1-weighted TSE postcontrast with fat saturation, and axial T1-weighted MPRAGE pulse sequences. Postcontrast imaging was performed in all patients after 0.1-mmol/kg intravenous administration of gadobenate dimeglumine (MultiHance; Bracco Diagnostics, Princeton, New Jersey).

Two fellowship-trained, board-certified neuroradiologists (C.Y.H., S.F.K.) with Certificates of Added Qualification in neuroradiology independently evaluated all preoperative, immediate postoperative, and subsequent follow-up brain MRI of included patients. All sequences on preoperative and immediate postoperative brain MRI were evaluated for imaging abnormalities, with particular attention to preoperative tumor location and size, the presence of multifocal or leptomeningeal tumor, hydrocephalus, extent of tumor resection (gross total resection or subtotal resection), and immediate postoperative complications, including cytotoxic edema or hemorrhage. A gross total resection was defined as no MR imaging evidence of residual tumor on postoperative imaging. Subtotal resection was defined as any evidence of residual tumor remaining on the postoperative MR imaging. All sequences on postradiation therapy MRI were evaluated for imaging abnormalities with particular attention to new areas of parenchymal enhancement and subsequent changes of the enhancement on serial follow-up MRI. New areas of cerebral enhancement on postcontrast sequences were evaluated for locations, diameter of the largest area of enhancement, and serial changes on follow-up MRI.

Radiation necrosis was defined after consensus agreement between the 2 neuroradiologists in conjunction with a pediatric neuro-oncologist and a pediatric radiation oncologist as the following: 1) A new area of contrast enhancement occurs in the brain parenchyma, which did not demonstrate abnormal signal or enhancement before radiation therapy. 2) The enhancement must either spontaneously decrease or resolve within 6 months of development on follow-up MR imaging without additional tumor treatment intervention and without evidence of an alternate etiology (ie, stroke, hemorrhage, or infection) in conjunction with a review of clinical records performed by a board-certified pediatric neuro-oncologist. 3) The area of enhancement is confirmed to be within an area receiving a radiation dose by a board-certified pediatric radiation oncologist. Patients with subtotal resections demonstrating enlargement of residual tumor due to new areas of nonenhancement within the residual tumor followed by a spontaneous decrease in the size of the tumor were defined as having tumoral necrosis rather than radiation necrosis. Timing from the completion of PBT to the development of radiation necrosis and timing from the appearance of radiation necrosis to complete resolution of enhancement were recorded.

Among patients with imaging findings of radiation necrosis, the clinical significance of radiation necrosis was determined by a pediatric neuro-oncologist following a review of the medical records and was graded by using the Common Terminology Criteria for Adverse Events, Version 4.0 (CTCAE) grading scale for CNS necrosis seen in Table 1.[15] Clinical risk factors that were

Table 1: Common Terminology Criteria for Adverse Events, Version 4.0: central nervous system necrosis[a]

Grade	Criteria
1	Asymptomatic; clinical, or diagnostic observations only; intervention not indicated
2	Moderate symptoms; corticosteroids indicated
3	Severe symptoms; medical intervention indicated
4	Life-threatening consequences; urgent intervention indicated
5	Death

[a] Adapted from Department of Health and Human Services.[15]

Table 2: Patient characteristics

Category	Characteristics
Age	Average, 7.2 ± 5.1 yr (range, 0.8–18 yr) 14/52 (27%) 3 years of age or younger
Sex	Male/female, 2.5:1
Tumor pathology	Medulloblastoma and PNET ($n = 19$) Ependymoma ($n = 12$) Germinoma ($n = 4$) Brain stem glioma ($n = 3$) ATRT ($n = 3$) Craniopharyngioma ($n = 3$) Mature teratoma ($n = 2$) Pilocytic astrocytoma ($n = 2$) High-grade neuroepithelial tumor ($n = 1$) Pilomyxoid astrocytoma ($n = 1$) Pineal parenchymal tumor ($n = 1$) Chordoid meningioma ($n = 1$)
Total cranial radiation	Average, 54.0 Gy (range, 21–59.4 Gy)

Note:—ATRT indicates atypical teratoid rhabdoid tumor; PNET, primitive neuroectodermal tumor.

recorded included age at the time of radiation therapy, sex, tumor pathology, tumor location, total radiation therapy dose, craniospinal radiation therapy, and chemotherapy agents. Patients who received >3 cytotoxic chemotherapeutic agents, not including biologic agents such as tyrosine kinase or vascular endothelial growth factor inhibitors, at any time during therapy, whether before, concurrent, or after proton beam treatment, were defined as having received "multiple chemotherapeutic agents" for the purposes of determining the statistical significance of chemotherapy agents as a clinical risk factor associated with radiation necrosis. Statistical analysis of radiation necrosis and clinical risk factors was performed by using a 2-tailed Fisher exact test. A P value of <.05 was considered statistically significant.

RESULTS

No patients were excluded due to nondiagnostic imaging. Eight patients were excluded due to not meeting the minimum 6 months of follow-up imaging. Three of these patients (2 with diffuse infiltrative pontine gliomas and 1 with a large supratentorial primitive neuroectodermal tumor) died before 6-month follow-up imaging. Fifty-two patients were evaluated for radiation necrosis. Patient characteristics are seen in Table 2. Seventeen of 52 (33%) patients had supratentorial tumors involving the pineal (6, 12%), sella (6, 12%), and parenchyma or meninges (5, 10%). Thirty-three of 52 (63%) patients had infratentorial tumors with involvement of the brain stem (3, 6%) and fourth ventricle/cerebellar hemisphere (30, 58%). Multifocal tumor occurred in 2/52 (4%). Surgical treatment included gross total resection (28, 53.8%), subtotal resection (23, 44.2%), and none (1, 1.9%). The 1 nonsurgical case involved a brain stem tumor.

Median follow-up imaging following PBT was 18 months (average, 18.4 months; range, 6–34 months). Six patients died, including the 3 excluded patients who died before 6-month follow up. The median time from surgery to completion of radiation therapy was 72 days (average, 104 days; range, 34–434 days). Sixteen of 52 (31%) patients developed radiation necrosis as defined above with all of these patients (16/16, 100%) demonstrating areas of enhancement that were not directly adjacent to the resection cavity. Figures 1 and 2 show examples of patients with radiologic findings consistent with radiation necrosis. The median time to the development of radiation necrosis was 5.0 months (average, 5.5 months; range, 3–11 months). One patient demonstrated tumoral necrosis beginning at 1 month following PBT, which progressively decreased starting at 4 months following PBT. Two patients demonstrated a combination of tumoral necrosis and radiation necrosis with the tumoral necrosis in both patients beginning at 3 months following PBT and progressively decreasing at 9 and 12 months following PBT, respectively.

Radiation necrosis was identified with multiple tumor pathologies: medulloblastoma and primitive neuroectodermal tumor (5/19, 26%), ependymoma (6/12, 50%), atypical teratoid rhabdoid tumor (3/3, 100%), craniopharyngioma (1/3, 33%), pilocytic astrocytoma (1/2, 50%), and pilomyxoid astrocytoma (1/1, 100%), while the remainder did not demonstrate radiation necrosis. Radiation necrosis was identified in multiple intracranial locations including the brain stem (56%); cerebellum (62%); globus pallidus and thalamus (31%); hippocampus (13%); and corpus callosum, periventricular white matter, and corona radiata (13%). Multiple areas of necrosis were identified in 63% of patients, while the remainder demonstrated a solitary focus of necrosis. The median size of the largest focus of enhancement measured 0.9 cm (average, 1.2 cm; range, 0.3–5.7 cm). The median time to complete resolution of all enhancing areas was 5.3 months (range, 3–12 months), with complete resolution of enhancement seen in 50% of patients at 3 months, in 75% of patients at 6 months, and in 100% of patients at 12 months.

Clinical risk factors associated with radiation necrosis are listed in Table 3. Patients who received multiple chemotherapeutic agents and atypical teratoid rhabdoid tumor pathology were more likely to develop radiation necrosis ($P = .03$ and $P = .03$, respectively). Chemotherapy details are demonstrated in the Online Table. Five patients who received multiple chemotherapeutic agents before PBT developed radiation necrosis, while 3 patients who received multiple chemotherapeutic agents before PBT did not develop radiation necrosis. No patients received >3 chemotherapeutic agents during PBT. Among patients with imaging findings of radiation necrosis, 12/16 (75%) were categorized as having grade 1(asymptomatic) and 4/16 (25%) had grade 3 (severe symptoms) according to the CTCAE central nervous system necrosis grading scale. One patient with severe symptoms was treated with hyperbaric oxygen therapy. Among all patients treated with PBT, symptomatic radiation necrosis was present in 4/52 (7.7%).

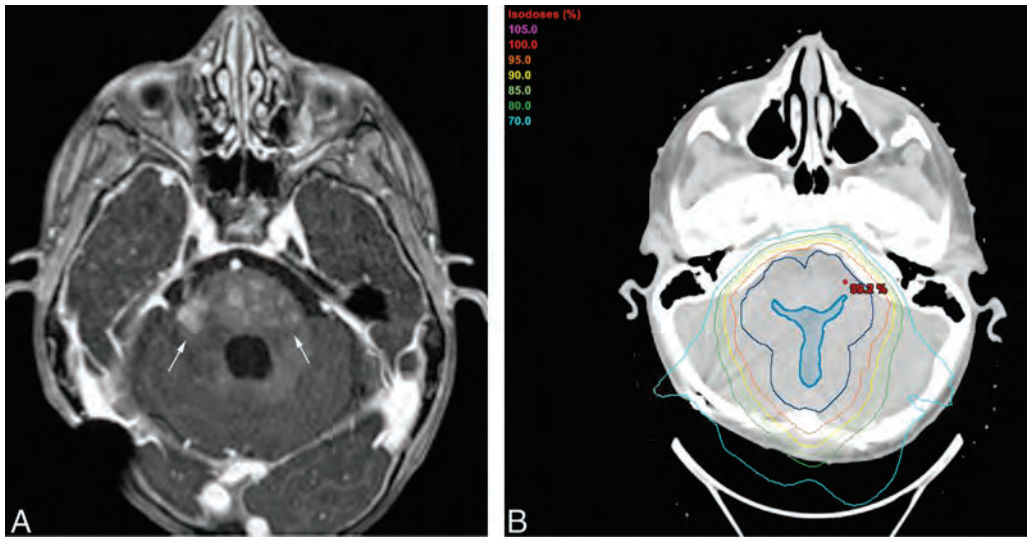

FIG 1. A 2-year-old child with a posterior fossa ependymoma status post gross total resection who developed multiple small foci of abnormal enhancement (*arrows*) in the pons and middle cerebellar peduncles, seen on an axial T1WI+C image (*A*), located within the radiation field (*B*) at 6 months following completion of PBT. Shown in the radiation treatment image (*B*) are the target structures of the gross tumor volume (dark blue filled) and the clinical target volume (darker blue, not filled). The dose lines of the proton beam treatment plan (analogous to the elevation lines of a topographic map) are shown as percentages of the prescription dose (59.4 Gy) in light purple (105%), red (100%), orange (95%), yellow (90%), light green (85%), forest green (80%), and cyan (70%).

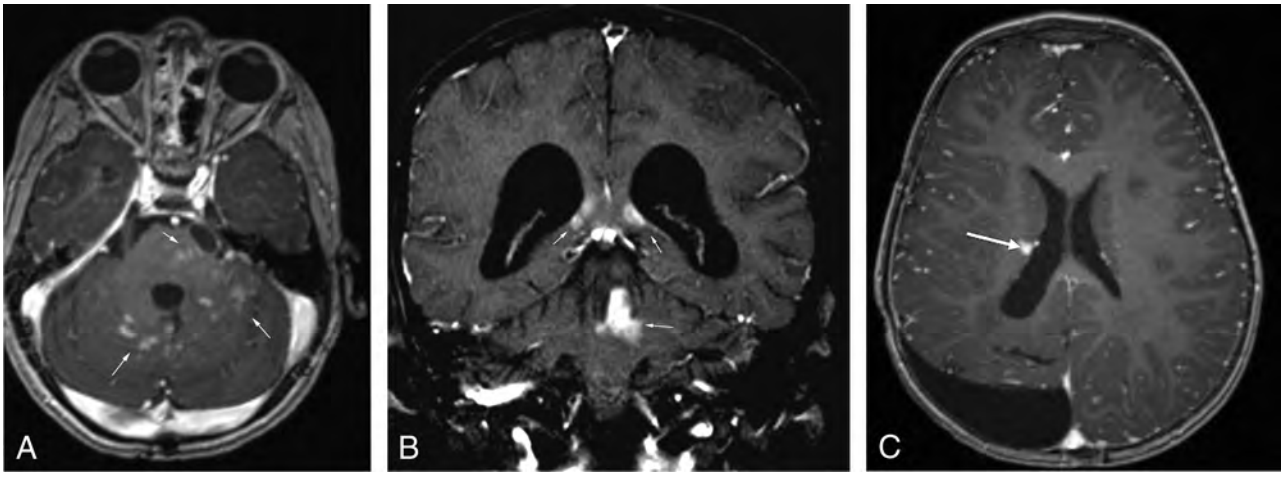

FIG 2. Examples of radiation necrosis in patients with pediatric brain tumor treated with proton radiation therapy. *A*, A 4-year-old child with a posterior fossa ependymoma status post subtotal resection who developed multiple small foci of abnormal parenchymal enhancement (*arrows*) in the pons and cerebellum seen on an axial T1WI+C image at 4 months following completion of PBT. *B*, A 7-year-old child with a posterior fossa medulloblastoma status post subtotal resection who developed multiple small foci of abnormal parenchymal enhancement (*arrows*) in the corpus callosum/periventricular white matter and the cerebellum and left superior cerebellar peduncle seen on a coronal T1WI+C image at 7 months following completion of PBT. *C*, A 2-year-old child with a supratentorial ependymoma status post gross total resection who developed a single small foci of abnormal parenchymal enhancement (*arrow*) in the right periventricular white matter seen on an axial T1WI+C image at 11 months following completion of PBT.

DISCUSSION

The prospective diagnosis of radiation necrosis in patients with brain tumor remains challenging and strongly reliant on clinical and radiologic data because biopsy of new imaging findings is uncommon, particularly in pediatric patients who may develop new lesions in critical structures such as the brain stem. Because a myriad of imaging appearances have been described with radiation necrosis, prospectively diagnosing radiation necrosis relies on a multitude of factors, including the imaging appearance and timing of necrosis and the larger clinical picture from the multidisciplinary care of these patients. In most cases, the confirmation of radiation necrosis is the result of the serial clinical and radiologic follow-up of these patients. The imaging pattern most frequently encountered among our patients treated with PBT was that of multifocal small areas of parenchymal enhancement not immediately adjacent to the resection cavity, which resolved at a median of 5.0 months. These findings are similar to those from a smaller series of patients treated with PBT by Sabin et al.[10] The imaging pattern we identified may help radiologists avoid misdiagnosis of tumor progression or at least consider the diagnosis of radiation necrosis in pediatric patients with brain tumor with PBT.

Radiation necrosis has been more extensively evaluated in adults compared with children. The Quantitative Analyses of

Table 3: Clinical variables associated with radiation necrosis

Statistically Significant	Not Statistically Significant
>3 Chemotherapy agents ($P = .03$)	Age, 2 years or younger ($P = .11$)
ATRT pathology ($P = .03$)	Age, 3 years or younger ($P = .34$)
	Sex ($P = 1.0$)
	Gross total surgical resection ($P = .77$)
	Medulloblastoma tumor pathology ($P = .35$)
	Ependymoma tumor pathology ($P = .15$)
	Germinoma[a] ($P = .3$)
	Infratentorial tumor location ($P = 1.0$)
	Pineal tumor location[a] ($P = .16$)
	Craniospinal radiation ($P = .48$)
	Total radiation dose ($P = .66$)

Note:—ATRT indicates atypical teratoid rhabdoid tumor.
[a] No pineal tumors or germinomas demonstrated radiation necrosis.

Normal Tissue Effects in the Clinic group reviewed 8 adult studies, including nearly 3700 patients, and estimated a 5% and 10% risk of symptomatic radiation necrosis in patients who received fractionated radiation with total doses of 72 and 90 Gy.[16] In contrast, there are few reported large series of radiation necrosis in patients with pediatric brain tumors. In 1 study of 101 children treated with photon radiation therapy, 5% of patients developed radiation necrosis based on clinicoradiologic follow-up.[2] In another study of 49 patients with malignant brain tumors treated with photon radiation therapy, high-dose thiotepa, and autologous stem cell rescue, 37% of patients developed posttreatment abnormal brain imaging findings, which were defined broadly to include contrast-enhancing lesions, T2-weighted or FLAIR hyperintense lesions, hemorrhage, or subdural fluid, though the percentage of radiation necrosis was not reported.[3] In our series, 31% of patients developed radiation necrosis based on imaging, indicating a trend toward a higher incidence of necrosis with PBT compared with the incidence reported for photon radiation therapy, which was similar to the high percentage in a series of 17 patients treated with PBT, of whom 47% developed an imaging diagnosis of radiation necrosis.[10] Our results differed, however, from those of 2 separate series of pediatric patients treated with PBT for ependymoma and medulloblastoma/primitive neuroectodermal tumor, in which no cases of radiation necrosis were reported; however, neither series described the methodology for detection of radiation necrosis to determine the significance of this difference.[12,13]

Potential reasons for the differences in the reported incidence of radiation necrosis between photon and proton radiation therapy include differences in the clinicoradiologic definition, exclusion of patients or certain tumors, and differences in medical or radiation therapy. We chose to exclude patients who did not have 6-month follow-up imaging because our median timing to development of necrosis occurred at 5 months. We chose to require radiation necrosis to demonstrate contrast enhancement rather than any new signal abnormality on imaging, which may decrease the percentage of radiation necrosis in our series. In studies that rely on a clinicoradiologic diagnosis of radiation necrosis, there is no strict timeframe in which radiation necrosis must resolve, remain stable, or begin to decrease. A time requirement is ultimately necessary, however, to establish a basis from which a clinicoradiologic diagnosis of radiation necrosis is determined. We used a relatively conservative requirement that the enhancement resolve or begin to decrease at 6 months, and this may lower the incidence of radiation necrosis in our patients. Last, studies relying on a clinicoradiologic diagnosis of radiation necrosis without histopathology cannot be directly compared with studies describing radiation necrosis on the basis of histopathology. In our study, we cannot definitively conclude that these areas of enhancement represent radiation necrosis on histopathology versus an alternate process that is exacerbated by the effects of chemotherapy.

Pseudoprogression is one such potential consideration for an alternate process occurring in these patients. The pathophysiology of pseudoprogression is poorly understood, and there is overlap in both terminology and appearance with radiation necrosis; however, tissue obtained from patients with pseudoprogression does not demonstrate the same findings seen in radiation necrosis.[17] Pseudoprogression typically is defined as occurring within 3 months after completion of treatment but can range up to 6 months after therapy completion.[17,18] In addition to relatively late timing encountered in our patients, the areas of necrosis were not within areas of resected tumor and were not within adjacent structures in which tumor growth would characteristically occur, both of which are atypical for pseudoprogression. Therefore, the current definition, description, and understanding of pseudoprogression do not provide an adequate explanation of our findings. If one recognizes the potential effects of chemotherapy in conjunction with PBT and the lack of histologic proof in our patients, "treatment-related cerebral necrosis" may be a more preferable description of the findings among our patients and more indicative of potential multifactorial causes than radiation alone. Ultimately, the major point of emphasis is that PBT may result in a significant degree of necrosis and the effects of PBT may be potentiated by additional factors, particularly chemotherapy.

The potential for chemotherapeutic interactions with radiation therapy has been well-documented, albeit not well-understood. For example, as chemosensitizers, temozolomide and bevacizumab have been used concurrently with radiation therapy in high-grade gliomas, and carboplatin has been studied as a radiation sensitizer with medulloblastomas and other CNS tumors.[19-22] In addition, chemotherapeutics such as anthracycline and doxorubicin are commonly avoided during radiation and can even remotely result in radiation recall with a later insult.[23] Finally, there are many chemotherapeutics that may have direct CNS toxicity such as methotrexate and ifosfamide, which could potentiate CNS radiation necrosis. With this in mind, the presence, timing, and dosage of single or multiple chemotherapeutic agents in conjunction with radiation may influence the incidence and severity of radiation necrosis. Although we are not able to implicate specific agents in our study, due to different treatment protocols for different tumors, we are able to show that the presence of multiple chemotherapeutic agents significantly increases the risk of radiation necrosis in our study. Fifty percent of the patients in this study received multiple chemotherapeutic agents and therefore compose a large percentage of our patients who

received radiation. Furthermore, the risk factor of atypical teratoid rhabdoid tumor pathology may be related to intensive chemotherapy because all patients with atypical teratoid rhabdoid tumors received high-dose neoadjuvant chemotherapy with stem cell rescue before radiation therapy at our institution. These findings together underscore the importance of further study in understanding the interaction of chemotherapy and radiation therapy in the context of designing a brain tumor treatment plan.

Predicting the timing of radiation necrosis remains challenging, and a wide range from months to years has been reported. Understanding of the timing to development of necrosis, however, remains an important factor when imaging findings potentially representing radiation necrosis are encountered. In our series, radiation necrosis was seen at a median of 5.0 months (range, 3–11 months). This compares with radiation necrosis described at a median of 1.2 months (range, 0.5–8.0 months) and 8 months (range, 2–39 months) in 2 large series of patients with pediatric brain tumors treated with photon radiation therapy and a median time of 3.9 months in a smaller series of patients treated with PBT.[2,3] It remains uncertain which factors in patients with pediatric brain tumor account for the difference in time to development of radiation necrosis compared with adult patients, which is more typical at or greater than 12 months.[1,24] Based on the proposed pathogenesis of radiation necrosis, there may be differences in the vascular endothelium, progenitor cells, oligodendrocytes, microglia, local microenvironment, and inflammatory response in the developing brain compared with adults accounting for the differences in timing.[4-7] Last, differences in imaging-frequency practice patterns likely contribute to differences in the reported timing to the development of radiation necrosis, particularly because many patients may be asymptomatic. Therefore, the median time and range of the time to development of radiation necrosis encountered in our patients should be considered an approximation rather than an absolute time period.

The clinical significance of MR imaging changes suggestive of radiation necrosis is a common question for the health care provider and his or her patients. Among our series of patients with pediatric brain tumors treated with PBT who demonstrated radiation necrosis, 25% demonstrated severe symptoms (based on the CTCAE grading scale) with medical intervention indicated. On the basis of these findings, any patient who develops similar MR imaging findings suggestive of radiation necrosis should raise high suspicion by the clinician for the current or later development of clinical symptoms, though most subjects may remain symptom-free.

Because radiation therapy remains the mainstay for many CNS tumor types, it is common for patients to receive fairly standardized maximum doses, depending on the location of the tumor. Thus, because the given radiation doses were not sufficiently heterogeneous, we were not able to document dose dependence in necrosis. However, the target doses typically used for PBT are frequently based on prescribed doses determined for photon radiation therapy. Whether similar doses using protons is required to maintain equivalent cure rates or whether lower doses with equivalent volumes may be as effective with less toxicity is not well understood.

Limitations

In our center, most patients with pediatric brain tumor are referred for proton radiation therapy because of the real or perceived benefits from PBT. However, there is still the possibility of selection bias regarding certain disease types such as glioblastoma multiforme or diffuse intrinsic pontine glioma that may be recommended for photon radiation therapy and, thus, not included in the sample. Our patient population is heterogeneous, and different tumor types necessitate different surgical or medical treatment. While we show that multiple chemotherapeutic agents increase the risk of developing radiation necrosis following PBT, our study was not able to distinguish whether any particular agent or combination of agents plays a more or less significant role. An associated limitation is the possibility that enhancing areas described in our study may represent a process that is different from the previously described histopathology of radiation necrosis and that this process is affected by chemotherapy. While the total given radiation dose did not demonstrate a statistically significant association with the development of radiation necrosis, further evaluation of the absorbed doses in areas that develop necrosis will be necessary, but this is beyond the scope of this study.

CONCLUSIONS

Pediatric patients with brain tumors treated with proton radiation therapy have a high incidence of radiation necrosis, demonstrating a short timeframe to development, which frequently occurs as multiple small areas of enhancement that are remote from the tumor site. Knowledge of the timing, incidence, and imaging appearance of radiation necrosis in patients with pediatric brain tumor treated with PBT can help with the radiologic differentiation from tumor recurrence. The presence of multiple chemotherapeutic agents was found to be a statistically significant risk factor associated with radiation necrosis. Additional analysis regarding the interaction of specific chemotherapeutic agents with PBT and the further investigation of PBT doses relative to photon radiation therapy are necessary to reduce these adverse treatment effects.

REFERENCES

1. Ruben JD, Dally M, Bailey M, et al. **Cerebral radiation necrosis: incidence, outcomes, and risk factors with emphasis on radiation parameters and chemotherapy.** *Int J Radiat Oncol Biol Phys* 2006;65:499–508
2. Plimpton SR, Stence N, Hemenway M, et al. **Cerebral radiation necrosis in pediatric patients.** *J Pediatr Hematol Oncol* 2015;32:78–83
3. Spreafico F, Gandola L, Marchiano A, et al. **Brain magnetic resonance imaging after high-dose chemotherapy and radiotherapy for childhood brain tumors.** *Int J Radiat Oncol Biol Phys* 2008;70:1011–19
4. Fukuda A, Fukuda H, Swanpalmer, J, et al. **Age-dependent sensitivity of the developing brain to irradiation is correlated with the number and vulnerability of progenitor cells.** *J Neurochem* 2005;92:569–84
5. Kalm M, Lannering B, Björk-Eriksson T, et al. **Irradiation-induced loss of microglia in the young brain.** *J Neuroimmunol* 2009;206:70–75
6. Schindler MK, Forbes ME, Robbins ME, et al. **Aging-dependent changes in the radiation response of the adult rat brain.** *Int J Radiat Oncol Biol Phys* 2008;70:826–34

7. Bustamante J, Czerniczyniec A, Cymeryng C, et al. **Age-related changes from youth to adulthood in rat brain cortex: nitric oxide synthase and mitochondrial respiratory function.** *Neurochem Res* 2008;33:1216–23
8. Levin WP, Kooy H, Loeffler JS, et al. **Proton beam therapy.** *Br J Cancer* 2005;93:849–54
9. Boehling NS, Grosshans DR, Bluett JB, et al. **Dosimetric comparison of three-dimensional conformal proton radiotherapy, intensity-modulated proton therapy, and intensity-modulated radiotherapy for treatment of pediatric craniopharyngiomas.** *Int J Radiat Oncol Biol Phys* 2012;82:643–52
10. Sabin ND, Merchant TE, Harreld JH, et al. **Imaging changes in very young children with brain tumors treated with proton therapy and chemotherapy.** *AJNR Am J Neuroradiol* 2013;34:446–50
11. Howell RM, Giebeler A, Koontz-Raisig W, et al. **Comparison of therapeutic dosimetric data from passively scattered proton and photon craniospinal irradiations for medulloblastoma.** *Radiat Oncol* 2012;7:116
12. MacDonald SM, Safai S, Trofimov A, et al. **Proton radiotherapy for childhood ependymoma: initial clinical outcomes and dose comparisons.** *Int J Radiat Oncol Biol Phys* 2008;71:979–86
13. Jimenez RB, Sethi R, Depauw N, et al. **Proton radiation therapy for pediatric medulloblastoma and supratentorial primitive neuroectodermal tumors: outcomes for very young children treated with upfront chemotherapy.** *Int J Radiat Oncol Biol Phys* 2013;87:120–26
14. MacDonald SM, Trofimov A, Safai S, et al. **Proton radiotherapy for pediatric central nervous system germ cell tumors: early clinical outcomes.** *Int J Radiat Oncol Biol Phys* 2011;79:121–29
15. Department of Health and Human Services. National Institutes of Health. National Cancer Institute. Common Terminology Criteria for Adverse Events, Version 4.0. http://www.acrin.org/Portals/0/Administration/Regulatory/CTCAE_4.02_2009-09-15_QuickReference_5x7.pdf. Published May 28, 2009. Accessed November 5, 2014
16. Lawrence YR, Li XA, el Naqa I, et al. **Radiation dose-volume effects in the brain.** *Int J Radiat Oncol Biol Phys* 2010;76:S20–27
17. Parvez K, Parvez A, Zadeh G. **The diagnosis and treatment of pseudoprogression: radiation necrosis and brain tumor recurrence.** *Int J Mol Sci* 2014;15:11832–46
18. Hygino da Cruz LC Jr, Rodriguez I, Domingues RC, et al. **Pseudoprogression and pseudoresponse: imaging challenges in the assessment of posttreatment glioma.** *AJNR Am J Neuroradiol* 2011;32:1978–85
19. Aguilera DG, Mazewski C, Hayes L, et al. **Prolonged survival after treatment of diffuse intrinsic pontine glioma with radiation, temozolomide, and bevacizumab: report of 2 cases.** *J Pediatr Hematol Oncol* 2013;35:e42–46
20. Anand AK, Chaudhory AR, Aggarwal HN, et al. **Survival outcome and neurotoxicity in patients of high-grade gliomas treated with conformal radiation and temozolomide.** *J Cancer Res Ther* 2012;8:50–56
21. Floyd SR, Kasper EM, Uhlmann EJ, et al. **Hypofractionated radiotherapy and stereotactic boost with concurrent and adjuvant temozolomide for glioblastoma in good performance status elderly patients: early results of a phase II trial.** *Front Oncol* 2012;2:122
22. Jakacki RI, Burger PC, Zhou T, et al. **Outcome of children with metastatic medulloblastoma treated with carboplatin during craniospinal radiotherapy: a Children's Oncology Group Phase I/II study.** *J Clin Oncol* 2012;30:2648–53
23. Haas RL, de Klerk G. **An illustrated case of doxorubicin-induced radiation recall dermatitis and a review of the literature.** *Neth J Med* 2011;69:72–75
24. Peterson K, Clark HB, Hall WA, et al. **Multifocal enhancing magnetic resonance imaging lesions following cranial irradiation.** *Ann Neurol* 1995;38:237–44

PHYSICIANS BOOST THE ECONOMY.

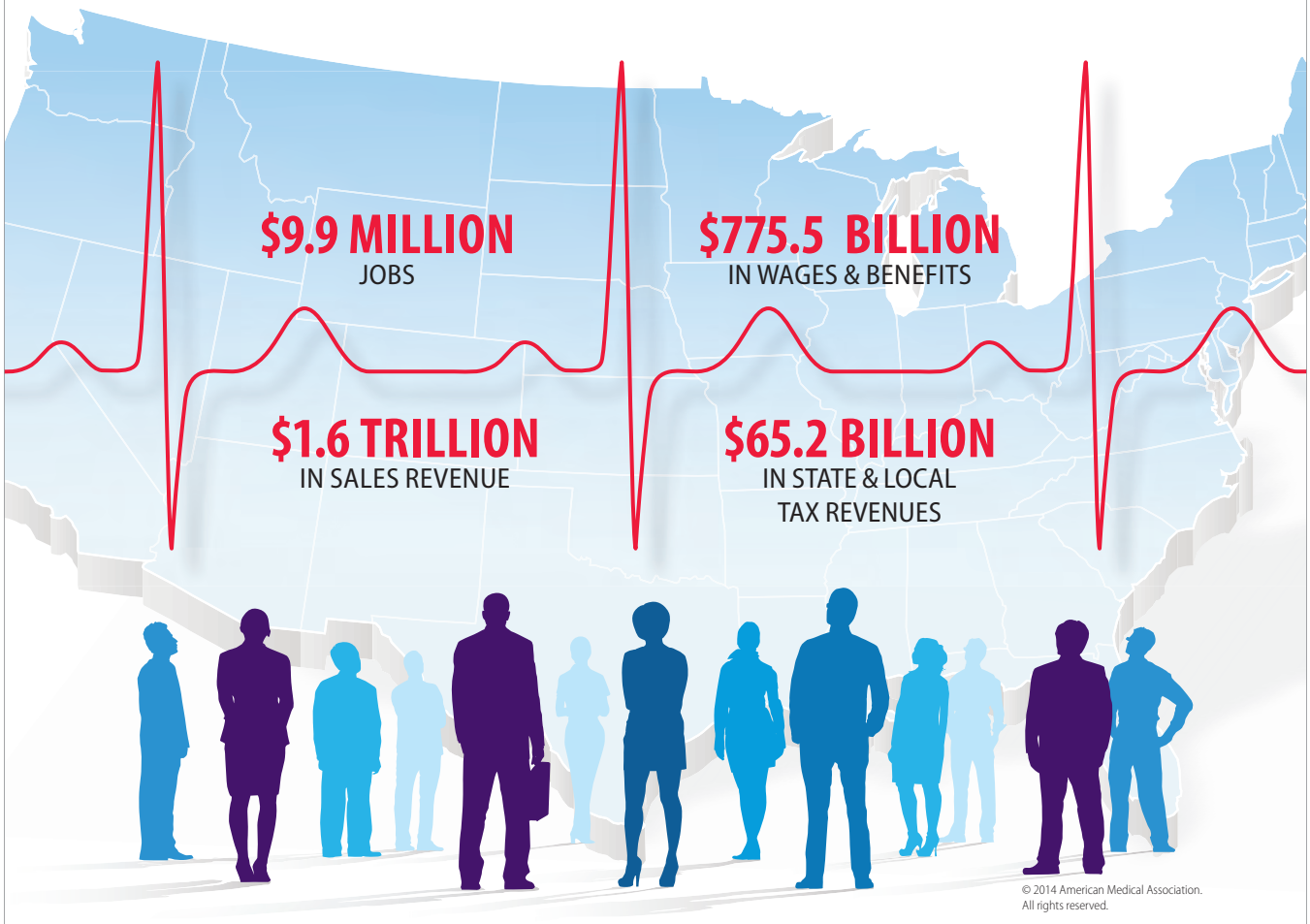

See the effects across the nation.

The American Medical Association 2014 Economic Impact Study shows how much physicians add to the economic health of our nation.

Check the effect physicians have on the U.S. economy by viewing the entire national report from the AMA Advocacy Resource Center at **ama-assn.org/go/eis**.

AMA
AMERICAN MEDICAL ASSOCIATION

Please activate your 2015 AMA membership by calling (800) 262-3211 or visit ama-assn.org/go/join.

10th Annual Meeting of the

American Society of

FUNCTIONAL NEURORADIOLOGY

February 29 - March 2, 2016

in co-sponsorship with the

American Society of

PEDIATRIC NEURORADIOLOGY

February 28 - 29, 2016

Renaissance Austin Hotel
Austin, Texas

Optional BOLD Functional MRI Hands On Workshop
Saturday, February 27, 2016

Separate Registration Required
Registration is Limited to 20 Attendees Per Session.

For More Information, visit **www.asfnr.org**

Target® Detachable Coil

See package insert for complete indications, contraindications, warnings and instructions for use.

INTENDED USE / INDICATIONS FOR USE
Target Detachable Coils are intended to endovascularly obstruct or occlude blood flow in vascular abnormalities of the neurovascular and peripheral vessels.

Target Detachable Coils are indicated for endovascular embolization of:
- Intracranial aneurysms
- Other neurovascular abnormalities such as arteriovenous malformations and arteriovenous fistulae
- Arterial and venous embolizations in the peripheral vasculature

CONTRAINDICATIONS
None known.

POTENTIAL ADVERSE EVENTS
Potential complications include, but are not limited to: allergic reaction, aneurysm perforation and rupture, arrhythmia, death, edema, embolus, headache, hemorrhage, infection, ischemia, neurological/intracranial sequelae, post-embolization syndrome (fever, increased white blood cell count, discomfort), TIA/stroke, vasospasm, vessel occlusion or closure, vessel perforation, dissection, trauma or damage, vessel rupture, vessel thrombosis. Other procedural complications including but not limited to: anesthetic and contrast media risks, hypotension, hypertension, access site complications.

WARNINGS
- Contents supplied STERILE using an ethylene oxide (EO) process. Do not use if sterile barrier is damaged. If damage is found, call your Stryker Neurovascular representative.
- For single use only. Do not reuse, reprocess or resterilize. Reuse, reprocessing or resterilization may compromise the structural integrity of the device and/or lead to device failure which, in turn, may result in patient injury, illness or death. Reuse, reprocessing or resterilization may also create a risk of contamination of the device and/or cause patient infection or cross-infection, including, but not limited to, the transmission of infectious disease(s) from one patient to another. Contamination of the device may lead to injury, illness or death of the patient.
- After use, dispose of product and packaging in accordance with hospital, administrative and/or local government policy.
- **This device should only be used by physicians who have received appropriate training in interventional neuroradiology or interventional radiology and preclinical training on the use of this device as established by Stryker Neurovascular.**
- Patients with hypersensitivity to 316LVM stainless steel may suffer an allergic reaction to this implant.
- MR temperature testing was not conducted in peripheral vasculature, arteriovenous malformations or fistulae models.
- The safety and performance characteristics of the Target Detachable Coil System (Target Detachable Coils, InZone Detachment Systems, delivery systems and accessories) have not been demonstrated with other manufacturer's devices (whether coils, coil delivery devices, coil detachment systems, catheters, guidewires, and/or other accessories). Due to the potential incompatibility of non Stryker Neurovascular devices with the Target Detachable Coil System, the use of other manufacturer's device(s) with the Target Detachable Coil System is not recommended.
- To reduce risk of coil migration, the diameter of the first and second coil should never be less than the width of the ostium.
- In order to achieve optimal performance of the Target Detachable Coil System and to reduce the risk of thromboembolic complications, it is critical that a continuous infusion of appropriate flush solution be maintained between a) the femoral sheath and guiding catheter, b) the 2-tip microcatheter and guiding catheters, and c) the 2-tip microcatheter and Stryker Neurovascular guidewire and delivery wire. Continuous flush also reduces the potential for thrombus formation on, and crystallization of infusate around, the detachment zone of the Target Detachable Coil.
- Do not use the product after the "Use By" date specified on the package.
- Reuse of the flush port/dispenser coil or use with any coil other than the original coil may result in contamination of, or damage to, the coil.
- Utilization of damaged coils may affect coil delivery to, and stability inside, the vessel or aneurysm, possibly resulting in coil migration and/or stretching.
- The fluoro-saver marker is designed for use with a Rotating Hemostatic Valve (RHV). If used without an RHV, the distal end of the coil may be beyond the alignment marker when the fluoro-saver marker reaches the microcatheter hub.
- If the fluoro-saver marker is not visible, do not advance the coil without fluoroscopy.
- Do not rotate delivery wire during or after delivery of the coil. Rotating the Target Detachable Coil delivery wire may result in a stretched coil or premature detachment of the coil from the delivery wire, which could result in coil migration.
- Verify there is no coil loop protrusion into the parent vessel after coil placement and prior to coil detachment. Coil loop protrusion after coil placement may result in thromboembolic events if the coil is detached.
- Verify there is no movement of the coil after coil placement and prior to coil detachment. Movement of the coil after coil placement may indicate that the coil could migrate once it is detached.
- Failure to properly close the RHV compression fitting over the delivery wire before attaching the InZone® Detachment System could result in coil movement, aneurysm rupture or vessel perforation.
- Verify repeatedly that the distal shaft of the catheter is not under stress before detaching the Target Detachable Coil. Axial compression or tension forces could be stored in the 2-tip microcatheter causing the tip to move during coil delivery. Microcatheter tip movement could cause the aneurysm or vessel to rupture.
- Advancing the delivery wire beyond the microcatheter tip once the coil has been detached involves risk of aneurysm or vessel perforation.
- The long term effect of this product on extravascular tissues has not been established so care should be taken to retain this device in the intravascular space.

Damaged delivery wires may cause detachment failures, vessel injury or unpredictable distal tip response during coil deployment. If a delivery wire is damaged at any point during the procedure, do not attempt to straighten or otherwise repair it. Do not proceed with deployment or detachment. Remove the entire coil and replace with undamaged product.

- After use, dispose of product and packaging in accordance with hospital, administrative and/or local government policy.

CAUTIONS / PRECAUTIONS
- Federal Law (USA) restricts this device to sale by or on the order of a physician.
- Besides the number of InZone Detachment System units needed to complete the case, there must be an extra InZone Detachment System unit as back up.
- Removing the delivery wire without grasping the introducer sheath and delivery wire together may result in the detachable coil sliding out of the introducer sheath.
- Failure to remove the introducer sheath after inserting the delivery wire into the RHV of the microcatheter will interrupt normal infusion of flush solution and allow back flow of blood into the microcatheter.
- Some low level overhead light near or adjacent to the patient is required to visualize the fluoro-saver marker; monitor light alone will not allow sufficient visualization of the fluoro-saver marker.
- Advance and retract the Target Detachable Coil carefully and smoothly without excessive force. If unusual friction is noticed, slowly withdraw the Target Detachable Coil and examine for damage. If damage is present, remove and use a new Target Detachable Coil. If friction or resistance is still noted, carefully remove the Target Detachable Coil and microcatheter and examine the microcatheter for damage.
- If it is necessary to reposition the Target Detachable Coil, verify under fluoroscopy that the coil moves with a one-to-one motion. If the coil does not move with a one-to-one motion or movement is difficult, the coil may have stretched and could possibly migrate or break. Gently remove both the coil and microcatheter and replace with new devices.
- Increased detachment times may occur when:
  - Other embolic agents are present.
  - Delivery wire and microcatheter markers are not properly aligned.
  - Thrombus is present on the coil detachment zone.
- Do not use detachment systems other than the InZone Detachment System.
- Increased detachment times may occur when delivery wire and microcatheter markers are not properly aligned.
- Do not use detachment systems other than the InZone Detachment System.

Stryker Neurovascular
47900 Bayside Parkway
Fremont, CA 94538-6515

stryker.com/neurovascular

Date of Release: FEB/2014

EX_EN_US

Trevo® XP ProVue Retrievers

See package insert for complete indications, complications, warnings, and instructions for use.

INDICATIONS FOR USE
The Trevo Retriever is intended to restore blood flow in the neurovasculature by removing thrombus in patients experiencing ischemic stroke within 8 hours of symptom onset. Patients who are ineligible for intravenous tissue plasminogen activator (IV t-PA) or who fail IV t-PA therapy are candidates for treatment.

COMPLICATIONS
Procedures requiring percutaneous catheter introduction should not be attempted by physicians unfamiliar with possible complications which may occur during or after the procedure. Possible complications include, but are not limited to, the following: air embolism; hematoma or hemorrhage at puncture site; infection; distal embolization; pain/headache; vessel spasm, thrombosis, dissection, or perforation; emboli; acute occlusion; ischemia; intracranial hemorrhage; false aneurysm formation; neurological deficits including stroke; and death.

COMPATIBILITY
3x20 mm retrievers are compatible with Trevo® Pro 14 Microcatheters (REF 90231) and Trevo® Pro 18 Microcatheters (REF 90238). 4x20 mm retrievers are compatible with Trevo® Pro 18 Microcatheters (REF 90238). Compatibility of the Retriever with other microcatheters has not been established. Performance of the Retriever device may be impacted if a different microcatheter is used. The Merci® Balloon Guide Catheters are recommended for use during thrombus removal procedures. Retrievers are compatible with the Abbott Vascular DOC® Guide Wire Extension (REF 22260).

WARNINGS
- Contents supplied STERILE, using an ethylene oxide (EO) process. Nonpyrogenic.
- To reduce risk of vessel damage, adhere to the following recommendations:
  - Take care to appropriately size Retriever to vessel diameter at intended site of deployment.
  - Do not perform more than six (6) retrieval attempts in same vessel using Retriever devices.
  - Maintain Retriever position in vessel when removing or exchanging Microcatheter.
- To reduce risk of kinking/fracture, adhere to the following recommendations:
  - Immediately after unsheathing Retriever, position Microcatheter tip marker just proximal to shaped section. Maintain Microcatheter tip marker just proximal to shaped section of Retriever during manipulation and withdrawal.
  - Do not rotate or torque Retriever.
  - Use caution when passing Retriever through stented arteries.
- Do not resterilize and reuse. Structural integrity and/or function may be impaired by reuse or cleaning.
- The Retriever is a delicate instrument and should be handled carefully. Before use and when possible during procedure, inspect device carefully for damage. Do not use a device that shows signs of damage. Damage may prevent device from functioning and may cause complications.
- Do not advance or withdraw Retriever against resistance or significant vasospasm. Moving or torquing device against resistance or significant vasospasm may result in damage to vessel or device. Assess cause of resistance using fluoroscopy and if needed resheath the device to withdraw.
- If Retriever is difficult to withdraw from the vessel, do not torque Retriever. Advance Microcatheter distally, gently pull Retriever back into Microcatheter, and remove Retriever and Microcatheter as a unit. If undue resistance is met when withdrawing the Retriever into the Microcatheter, consider extending the Retriever using the Abbott Vascular DOC guidewire extension (REF 22260) so that the Microcatheter can be exchanged for a larger diameter catheter such as a DAC® catheter. Gently withdraw the Retriever into the larger diameter catheter.
- Administer anti-coagulation and anti-platelet medications per standard institutional guidelines.

PRECAUTIONS
- Prescription only – device restricted to use by or on order of a physician.
- Store in cool, dry, dark place.
- Do not use open or damaged packages.
- Use by "Use By" date.
- Exposure to temperatures above 54°C (130°F) may damage device and accessories. Do not autoclave.
- Do not expose Retriever to solvents.
- Use Retriever in conjunction with fluoroscopic visualization and proper anti-coagulation agents.
- To prevent thrombus formation and contrast media crystal formation, maintain a constant infusion of appropriate flush solution between guide catheter and Microcatheter and between Microcatheter and Retriever or guidewire.
- Do not attach a torque device to the shaped proximal end of DOC® Compatible Retriever. Damage may occur, preventing ability to attach DOC® Guide Wire Extension.

Concentric Medical
301 East Evelyn
Mountain View, CA 94041

EC REP

EMERGO Europe
Molenstraat 15
2513 BH, The Hague
The Netherlands

Stryker Neurovascular
47900 Bayside Parkway
Fremont, CA 94538-6515

stryker.com/neurovascular
stryker.com/emea/neurovascular

Date of Release: JUN/2014

EX_EN_GL

CE 0459

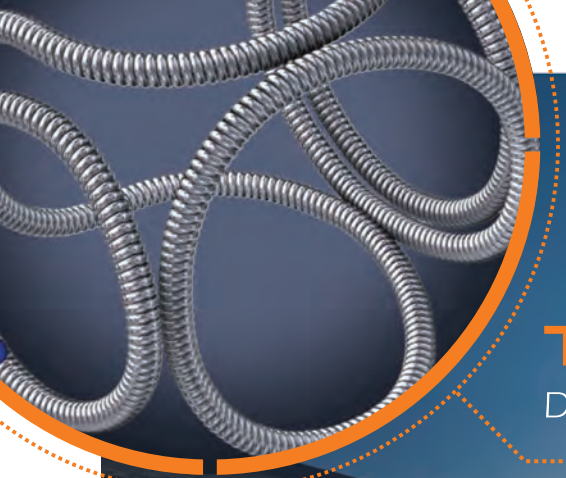

Target®
DETACHABLE COILS

Smooth and Stable

Whether you are framing, filling or finishing, Target Detachable Coils deliver consistently smooth deployment and exceptional microcatheter stability. Focused on design, Target Coils feature a host of advantages to ensure the high-powered performance you demand.

For more information, please visit www.strykerneurovascular.com/Target or contact your local Stryker Neurovascular sales representative.

stryker® Neurovascular

Stroke: *Our Only Focus. Our Ongoing Promise.*